GUARANTEED VERIFICATION OF FINITE ELEMENT SOLUTIONS OF HEAT CONDUCTION

A Dissertation

by

DELIN WANG

Submitted to the Office of Graduate Studies of
Texas A&M University
in partial fulfillment of the requirements for the degree of

DOCTOR OF PHILOSOPHY

May 2011

Major Subject: Aerospace Engineering

GUARANTEED VERIFICATION OF FINITE ELEMENT SOLUTIONS OF HEAT CONDUCTION

A Dissertation

by

DELIN WANG

Submitted to the Office of Graduate Studies of
Texas A&M University
in partial fulfillment of the requirements for the degree of

DOCTOR OF PHILOSOPHY

Approved by:

Chair of Committee,	Theofanis Strouboulis
Committee Members,	Joseph E. Pasciak
	Yalchin Efendiev
	Wolfgang Bangerth
Head of Department,	Dimitris Lagoudas

May 2011

Major Subject: Aerospace Engineering

ABSTRACT

Guaranteed Verification of Finite Element Solutions of Heat Conduction.

(May 2011)

Delin Wang, B.E., Qingdao University of Science & Technology, China;

M.S., Jilin University, China;

M.E., Texas A&M University

Chair of Advisory Committee: Dr. Theofanis Strouboulis

This dissertation addresses the accuracy of a-posteriori error estimators for finite element solutions of problems with high orthotropy especially for cases where rather coarse meshes are used, which are often encountered in engineering computations. We present sample computations which indicate lack of robustness of all standard residual estimators with respect to high orthotropy. The investigation shows that the main culprit behind the lack of robustness of residual estimators is the coarseness of the finite element meshes relative to the thickness of the boundary and interface layers in the solution.

With the introduction of an elliptic reconstruction procedure, a new error estimator based on the solution of the elliptic reconstruction problem is invented to estimate the exact error measured in space-time $\mathscr{C}$-norm for both semi-discrete and fully discrete finite element solutions to linear parabolic problem. For a fully discrete solution, a temporal error estimator is also introduced to evaluate the discretization

error in the temporal field. In the meantime, the implicit Neumann subdomain residual estimator for elliptic equations, which involves the solution of the local residual problem, is combined with the elliptic reconstruction procedure to carry out a posteriori error estimation for the linear parabolic problem. Numerical examples are presented to illustrate the superconvergence properties in the elliptic reconstruction and the performance of the bounds based on the space-time $\mathscr{C}$-norm.

The results show that in the case of L^2 norm for smooth solution there is no superconvergence in elliptic reconstruction for linear element, and for singular solution the superconvergence does not exist for element of any order while in the case of energy norm the superconvergence always exists in elliptic reconstruction. The research also shows that the performance of the bounds based on space-time $\mathscr{C}$-norm is robust, and in the case of fully discrete finite element solution the bounds for the temporal error are sharp.

To my family: my wife, *Qian*, and my daughter and son, *Claire* and *Ethan*

ACKNOWLEDGMENTS

First I would like to express my deep appreciation to the chairman of my advisory committee, Dr. Theofanis Strouboulis, for his invaluable assistance, encouragement and guidance which gives me the strength and motivation to finish this dissertation. His enthusiasm regarding research is the example that I will endeavor to follow.

I would like to thank Dr. J. Pasciak, Dr. W. Bangerth, and Dr. Y. Efendiev, for serving on my advisory committee. Thanks also to Dr. Cizmas for his presence at my defense to substitute for Dr. Y. Efendiev.

I would like also to express my sincere appreciation to Professor Ivo Babuška for his advice and encouragement during the course of this work.

Many thanks are due to past colleagues. In particular, I would like to thank Dr. Lin Zhang and Dr. Realino Hidajat for their help and support. Appreciation also goes to Dr. Dibyendu Datta for his help in taking over the GFEM code.

I would like also to acknowledge Dr. Jessica Li and Dr. Goodson for their support and help. I also thank Dr. Walter Haisler and my boss, Tony Paulin, for facilitating all the paperwork to make the part-time Ph.D. possible. Thanks also to Ms. Karen Knabe for her help in dealing with all the relevant documents and forms.

Truly unbounded thanks are due to my parents and brothers who have been a tremendous moral support throughout these years.

Finally, my utmost gratitude is due my wife, who has always been present to help me overcome all the difficulties along the way. Her love, patience, sacrifice and

emotional support were essential for the completion of the dissertation. I also thank my daughter, Claire, and my son, Ethan, who are the source of all joy.

TABLE OF CONTENTS

CHAPTER Page

LIST OF TABLES

TABLE Page

TABLE Page

TABLE Page

TABLE Page

TABLE Page

LIST OF FIGURES

FIGURE Page

FIGURE Page

FIGURE Page

FIGURE Page

FIGURE Page

FIGURE Page

FIGURE Page

FIGURE Page

FIGURE Page

FIGURE Page

FIGURE Page

FIGURE Page

FIGURE Page

FIGURE Page

FIGURE Page

FIGURE Page

FIGURE Page

FIGURE Page

FIGURE Page

FIGURE Page

FIGURE Page

FIGURE Page

FIGURE Page

FIGURE Page

FIGURE Page

FIGURE Page

FIGURE Page

FIGURE Page

FIGURE Page

FIGURE Page

FIGURE Page

FIGURE Page

FIGURE Page

FIGURE Page

FIGURE Page

FIGURE Page

FIGURE Page

FIGURE Page

FIGURE Page

CHAPTER I

INTRODUCTION

1.1 Motivation and background

A posteriori error estimation has become increasingly important in engineering computations because it is the main tool for "solution verification"[1, 2], which is needed as part of verification of computed solutions, namely for checking "if the mathematical problem is solved right"[3]. In practice we are primarily interested in obtaining certain outputs expressed in terms of the solution of the employed mathematical model which are pre-specified goals of the analysis and are referred to as "quantities of interest" (q.o.i)[2]. It follows that the objective of a posteriori error estimation is mostly to be able to obtain reliable estimates of the approximation error in the computed q.o.i. A prerequisite for this is mostly to be able to compute reliable estimates for the energy norm of the error and this is the topic addressed in this paper.

Various aspects of the state of the art of a-posteriori estimation including the formulation of the various estimators, related theoretical aspects, their robustness with respect to the topology, distortion of the mesh, and class of solutions, and how to construct "guaranteed" estimates for the q.o.i. are addressed in [4–6] and in the references therein. Recently, the focus of many efforts in a posteriori error estimation has been the construction of computable guaranteed upper and lower bounds of the error in the q.o.i. based on the developed infrastructure of residual estimators. This subject is not new, it was addressed in [7] 30 years ago employing the framework of the hypercircle from the book [8] which appeared more than 50 years ago. This approach

---

This dissertation follows the style of Computer Methods in Applied Mechanics and Engineering.

was recently extended to more general classes of problems like e.g. viscoelasticity, and inelasticity etc in [5, 9–13]. Various approaches for constructing bounds for the error in finite element solutions of heat-conduction and elasticity type problems based on residual computations can be found in [5, 9], in Chapter 6 of [6], in [14–18], and the references therein.

In this paper we will study the robustness of several residual estimators for the error in finite element solutions of a model problem of heat conduction in a multimaterial domain with highly orthotropic subdomains. We will be interested in the deterioration of the quality of the estimators with the high orthotropy, which can occur in certain important practical applications [19]. This paper is an extension of earlier work presented in the Ph.D. dissertation of Datta [20].

As for parabolic problems, a posteriori error estimates are derived in [21–23] for one-dimensional and in [24–26] for multidimensional linear and mildly nonlinear problems. A theoretical and numerical study of the effectivity index is proposed in [24] for the linear heat conduction. The L^2 in time and H^1 in space error is bounded above and below by an explicit error estimator based on equation residual. In [25, 26], a posteriori error estimate are derived for linear and nonlinear parabolic problems when using the discontinuous Galerkin methods. The L^∞ in time, L^2 in space error is bounded above by an explicit error estimator using sharp a priori estimates for the dual problem. In [27] a general framework is developed for nonlinear evolution equations and a posteriori error estimates are derived in the L^∞ in time, L^2 in space error. In [28, 29], the general framework introduced in [30] is extended to a wide class of nonlinear parabolic problems. A posteriori error estimates are obtained for several norms, upper and lower bounds are proposed. In [31, 32], it is proven that a posteriori error estimation of a linear elliptic problem yields an estimator for the semidiscrete solutions of parabolic problems by employing appropriate space-time energy norms.

For a posteriori error estimation of fully discrete solutions of parabolic problems, see [33]. Efficient adaptive procedures based on a posteriori error estimates are developed in [34, 35] for solving nonlinear partial differential equations arising from physical and industrial processes. In [36–39], a postprocessing technique is applied for the semidiscrete finite element solution to nonlinear parabolic problems, which solves a linear elliptic problem on a finer grid (or higher order space) once the time integration on the coarser mesh is completed. This technique increases the convergence rate of the finite element method to which it is applied. Numerical experiments show that the technique is computationally more efficient than the method to which it is applied. The study on the application of the a posteriori error estimation introduced in [36–39] to the fully discrete nonlinear parabolic case is addressed in [40]. In [41, 42], an auxiliary function called elliptic reconstruction is introduced to derive a posteriori error estimators for linear parabolic case, which is essentially the postprocessed approximation in [36–39]. Based on the strategies from [43, 44], a methodology is provided in [45, 46] to obtain computable strict bounds for quantities of interest for parabolic problems.

1.2 Research goals

The goal of this research can be summarized as follows:

1. To find the culprit behind the poor performance of existing implicit residual estimators for elliptic problem when applied to the thermal battery problem with high orthotropy.

2. To employ the elliptic reconstruction procedure to carry out the error estimation for both semi-discrete and fully discrete finite element solutions of linear parabolic problem.

3. To combine the available a posteriori error estimation technology for elliptic problems with the elliptic reconstruction procedure in attempt to practice a posteriori error estimation for linear parabolic problem.

4. To investigate the performance of the elliptic reconstruction procedure in the case of nonsmooth solution.

1.3 Outline of the dissertation

Following this Introduction, in Chapter II we formulate the model problem of heat-conduction in a thermal battery [19] and its finite element approximations and we report the effectivity of several residual estimators and its deterioration in the case of extreme orthotropy. To clearly illustrate the main difficulty, which is the coarseness of the mesh relative to the size of sharp layers in the solution, in Chapter III we construct simpler model problems for which we are able to analyze further the results. We show that if we do not have available capabilities for adaptive meshing, which is often the case in practical computations, then the estimators may grossly overestimate the true error.

Chapter IV is about the error estimation of semi-discrete finite element solution of linear parabolic problem based on elliptic reconstruction. Several numerical examples are employed to verify the newly invented space-time error estimator. In the meantime, the residual estimators for elliptic problem is combined with elliptic reconstruction procedure. Similar work is extended to the fully discrete finite element solution and we also introduce a new error estimator to evaluate the temporal error, all of which is addressed in Chapter V. Then we close by formulating conclusions and future work.

CHAPTER II

A POSTERIORI ERROR ESTIMATION OF A THERMAL BATTERY PROBLEM WITH HIGH ORTHOTROPY

2.1 Thermal battery problem and its finite element solution

Let Ω be the domain consisting of five subdomains Ω_k, $\overline{\Omega} = \bigcup_{k=1}^{5} \Omega_k$, with boundary Γ_{N} consisting of four parts Γ_{N}^i, $\overline{\Gamma}_{\mathrm{N}} = \bigcup_{k=1}^{4} \overline{\Gamma}_{\mathrm{N}}^i$, as shown in Fig. 2.1. We will be interested in the temperature distribution u, which satisfies the orthotropic Poisson equation.

$$-\nabla \cdot \big(\mathbf{K}\ \nabla u\big) = f \stackrel{\text{def}}{=} \begin{cases} 1 & \text{in } \Omega_2,\ \Omega_3 \\ 0 & \text{elsewhere} \end{cases} \tag{2.1a}$$

with the Robin boundary condition

$$\mathbf{K}\nabla u \cdot \mathbf{n} = g^{(i)} - \alpha^{(i)}\ u \qquad \text{on } \Gamma_N^i \tag{2.1b}$$

for $i = 1, 2, 3, 4$, where

$$\alpha^{(i)} = \begin{cases} 0, & i = 1 \\ 1, & i = 2 \\ 2, & i = 3 \\ 3, & i = 4 \end{cases} \qquad g^{(i)} = \begin{cases} 0, & i = 1 \\ 3, & i = 2 \\ 2, & i = 3 \\ 1, & i = 4 \end{cases} \tag{2.1c}$$

with $\mathbf{K}$ is constant in each Ω_k, with value $\mathbf{K}^{(k)}_{\text{Orth}} = \begin{bmatrix} K_x^{(k)} & 0 \\ 0 & K_y^{(k)} \end{bmatrix}$ with

$$K_x^{(k)} = \begin{cases} 25.0, & k=1 \\ 7.0, & k=2 \\ k_x, & k=3 \\ 0.2, & k=4 \\ 0.05, & k=5 \end{cases} \qquad K_y^{(k)} = \begin{cases} 25.0, & k=1 \\ 0.8, & k=2 \\ k_y, & k=3 \\ 0.2, & k=4 \\ 0.05, & k=5 \end{cases} \tag{2.2}$$

where we employ $k_x = 5.0$, and we choose k_y such that $\frac{k_x}{k_y} = 1000$, 2500, 5000, 10000, 25000, 50000.

We will also consider the isotropic case in which $\mathbf{K}^{(k)}_{\text{Iso}} = \begin{bmatrix} K_x^{(k)} & 0 \\ 0 & K_x^{(k)} \end{bmatrix}$

The variational formulation of the model problem reads:

Find $u \in \mathcal{U}(\Omega)$ such that

$$\mathcal{B}_\Omega(u,v) \stackrel{\text{def}}{=} \int_\Omega \nabla v^T \mathbf{K}\, \nabla u \; + \int_{\Gamma_N} \alpha\; u\; v = \mathcal{L}(v) \stackrel{\text{def}}{=} \int_\Omega f\; v + \int_{\Gamma_N} g\; v \qquad \forall\; v \in \mathcal{U}(\Omega) \tag{2.3a}$$

Here

$$\mathcal{U}(\Omega) \stackrel{\text{def}}{=} \left\{ v \;\middle|\; ||v||_{\mathcal{U}} \stackrel{\text{def}}{=} \sqrt{\mathcal{B}_\Omega(v,v)} < \infty \right\} \tag{2.3b}$$

is the energy space and $||\cdot||_{\mathcal{U}}$ is the energy norm. Below, we will denote the exact solution of this problem by u_{EX}.

Let Δ_h be a mesh of rectangles as shown in Fig. 2.2 a-c. We introduce the finite element solution $u_{S^p_{\Delta_h}}$ of degree p as the solution of the discrete problem:

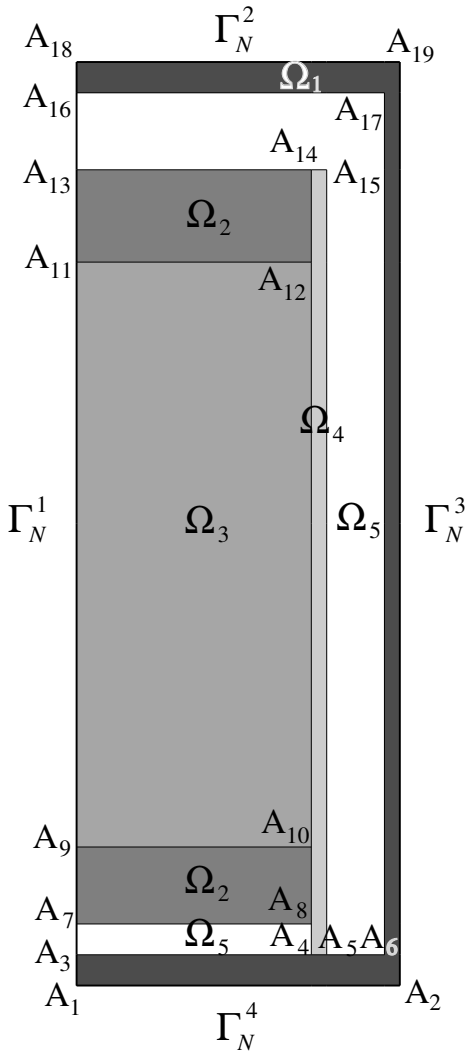

Fig. 2.1. Heat conduction in a thermal battery. The problem domain, its subdomains and the boundary with its subdomains. [1]

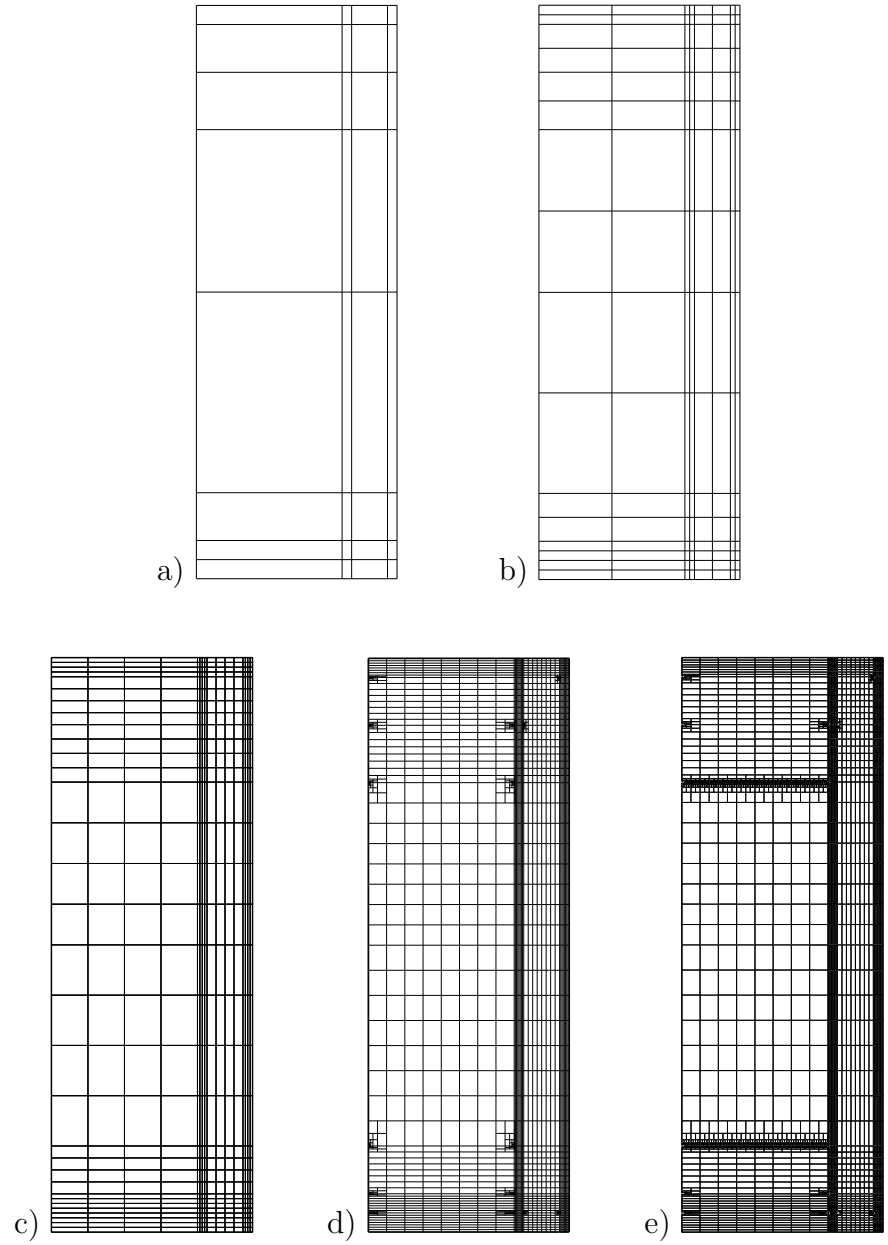

Fig. 2.2. Heat conduction in a thermal battery. The meshes Δ_h, with a) Mesh I; b) Mesh II; c) Mesh III; d)The overkill mesh Δ_h^{ovk}; e)The overkill mesh $\Delta_h^{ovk'}$. [1]

Find $u_{S^p_{\Delta_h}} \in S^p_{\Delta_h}$ such that

$$\mathscr{B}_\Omega(u_{S^p_{\Delta_h}}, v) = \mathscr{L}(v) \qquad \forall\, v \in S^p_{\Delta_h} \tag{2.4}$$

Here $S^p_{\Delta_h} \subset \mathcal{U}(\Omega)$, is the finite element space defined using tensor-product rectangular elements of degree p over the mesh Δ_h

We will denote the error in the finite element solution $u_{S^p_{\Delta_h}}$ by

$$e_{S^p_{\Delta_h}} \stackrel{\text{def}}{=} u_{EX} - u_{S^p_{\Delta_h}} \tag{2.5}$$

For the analysis, we will replace u_{EX} by an overkill solution $u_{S^{p'}_{\Delta_h^{ovk}}}$, with Δ_h^{ovk} denoting the overkill mesh, and $p' > p$ the employed degree of overkill approximation. We will assume that the overkill approximation $u_{S^{p'}_{\Delta_h^{ovk}}}$ is sufficiently accurate so that we can use it instead of the exact solution u_{EX} to analyze our results.

In the computations we employed the meshes Mesh I, Mesh II, Mesh III, shown respectively in Fig. 2.2 a, b, c, and $p = 1, 2, 3$ for the finite element solution. In the computation of the overkill solution, it should be noted that there are two interface layers at the top and bottom of domain Ω_3 in the case of high orthotropy with the magnitude of characteristic thickness of the interface layer equal to $\sqrt{\frac{k_y}{k_x}}$. The interface layer will be addressed in details in the later sections. Therefore two types of overkill meshes Δ_h^{ovk} and $\Delta_h^{ovk'}$ as shown in Fig. 2.2 d and e are adopted. Both the mesh Δ_h^{ovk} and the mesh $\Delta_h^{ovk'}$ were constructed starting from Mesh II, by employing two uniform refinements followed by five nested refinements of the elements with a vertex at a multi-material point. In the case of the mesh $\Delta_h^{ovk'}$, further adaptive refinement was adopted at the two interface layers of domain Ω_3 such that the smallest mesh size is about the same magnitude as the characteristic thickness of the interface layers. The polynomial order in the overkill solution is chosen to be $p' = 8$.

Table 2.1 lists the energy norm of the overkill solutions based on two overkill meshes. It can be seen that the interface layers have negligible effect on the energy norm of the overkill solution. Therefore the overkill solution based on mesh Δ_h^{ovk} can be considered as the exact solution.

Table 2.1. Comparision of the energy norm of the overkill solutions based on two overkill meshes Δ_h^{ovk} and $\Delta_h^{ovk'}$ vs. the orthotropy $\frac{k_x}{k_y}$ of domain Ω_3. Note that $||u_{S^{p'}_{\Delta_h^{ovk}}}||_{\mathcal{U}}$ denotes the energy norm of the overkill solution from the mesh Δ_h^{ovk} while $||u_{S^{p'}_{\Delta_h^{ovk'}}}||_{\mathcal{U}}$ from the mesh $\Delta_h^{ovk'}$.

$\frac{k_x}{k_y}$	$\left\|\left\|u_{S^{p'}_{\Delta_h^{ovk}}}\right\|\right\|_{\mathcal{U}}$	$\left\|\left\|u_{S^{p'}_{\Delta_h^{ovk'}}}\right\|\right\|_{\mathcal{U}}$	$\frac{\left\|\left\|\left\|u_{S^{p'}_{\Delta_h^{ovk'}}}\right\|\right\|_{\mathcal{U}}-\left\|\left\|u_{S^{p'}_{\Delta_h^{ovk}}}\right\|\right\|_{\mathcal{U}}\right\|}{\left\|\left\|u_{S^{p'}_{\Delta_h^{ovk'}}}\right\|\right\|_{\mathcal{U}}} \times 100\%$
1	1.1081536458E+02	1.1081538842E+02	0.2147716156E-04 %
1000	1.3288518146E+02	1.3288537701E+02	0.1471192726E-03 %
2500	1.3370199254E+02	1.3370282712E+02	0.6242201591E-03 %
5000	1.3402794093E+02	1.3402971341E+02	0.1322467948E-02 %
10000	1.3421257854E+02	1.3421560030E+02	0.2251452136E-02 %
25000	1.3433794621E+02	1.3434295997E+02	0.3732089869E-02 %
50000	1.3438483324E+02	1.3439169401E+02	0.5105077402E-02 %

Fig. 2.3 illustrates the values of $||u_{S^{p'}_{\Delta_h^{ovk}}}||_{\mathcal{U}}$, and relative error

$$E^{rel}_{S^p_{\Delta_h}} = \frac{||e_{S^p_{\Delta_h}}||_{\mathcal{U}}}{||u_{S^{p'}_{\Delta_h^{ovk}}}||_{\mathcal{U}}} \times 100\% \tag{2.6}$$

as a function of the orthotropy $\frac{k_x}{k_y}$.

We see that the relative error is significant e.g. for Mesh II and $p = 2$, $E^{rel}_{S^p_{\Delta_h}} > 10\%$. Also note that for high orthotropy, e.g. $\frac{k_x}{k_y} > 5000$, the relative error is twice of

that of the isotropic case.

Let us also note that in all the computations presented in this paper we employ meshes of rectangles alligned with the axes of orthotropy. The more general case where the orthotropy is oblique to the mesh is more challenging because it is related with the problem of locking [47].

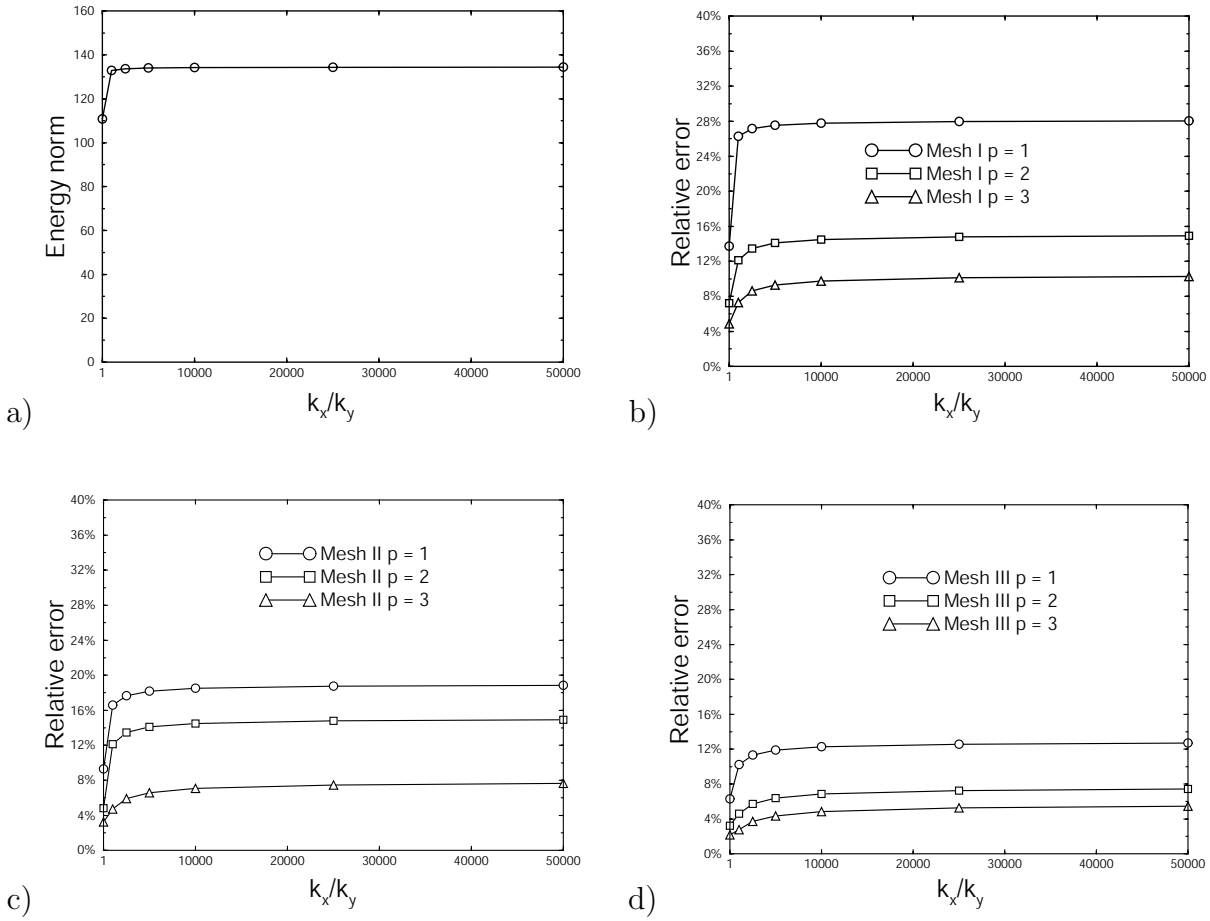

Fig. 2.3. Heat conduction in a thermal battery. a) The energy norm of the overkill solution $||u_{S^8_{\Delta_h^{ovk}}}||_{\mathcal{U}}$ versus the orthotropy $\frac{k_x}{k_y}$, and b-d) the values of the relative error $E^{rel}_{S^p_{\Delta_h}}$, for the finite element solution versus $\frac{k_x}{k_y}$ for Mesh I, Mesh II, and Mesh III, respectively. Note that the relative error increases with the orthotropy, and it is relatively high for all the meshes and element degrees employed. [1]

2.2 Upper and lower bounds based on residual estimators

In order to introduce the estimators we will need the global residual $\mathcal{R}_{\Omega}^{\Delta_h,p} : \mathcal{U} \longmapsto \mathbb{R}$ defined by

$$\mathcal{R}_{\Omega}^{\Delta_h,p}(v) \stackrel{\text{def}}{=} \mathcal{L}(v) - \mathcal{B}_{\Omega}(u_{S^p_{\Delta_h}}, v) = \mathcal{B}_{\Omega}(e_{S^p_{\Delta_h}}, v) \quad v \in \mathcal{U}(\Omega) \tag{2.7}$$

and its splitting

$$\mathcal{R}_{\Omega}^{\Delta_h,p}(v) = \sum_{\tau \in \Delta_h} \mathcal{R}_{\tau}^{\Delta_h,p}(v\big|_{\tau}) \quad v \in \mathcal{U}(\Omega) \tag{2.8}$$

where $\mathcal{R}_{\tau}^{\Delta_h,p} : \mathcal{U}(\tau) \longmapsto \mathbb{R}$, are the equilibrated element residua, and $\mathcal{U}(\tau)$ denotes the energy-space over the element τ. For the various construction of $\mathcal{R}_{\tau}^{\Delta_h,p}$, see [4–6, 9].

We are going to address two types of residual estimators which are Neumann patch residual estimators and subdomain residual estimators respectively.

First for Neumann patch residual estimators, let $\Omega_h \stackrel{\text{def}}{=} \left\{\omega_j\right\}_{j=1}^{npatches}$, denote a partition of the mesh Δ_h into non-overlapping patches of elements as is, for example, shown in Fig. 2.4. Let $\hat{e}_{\omega_j}^{\text{Neum}}$, denote the exact solution of the Neumann patch residual problem:

Find $\hat{e}_{\omega_j}^{\text{Neum}} \in \mathcal{U}(\omega_j)$ such that:

$$\mathcal{B}_{\omega_j}\left(\hat{e}_{\omega_j}^{\text{Neum}}, v\right) = \mathcal{R}_{\omega_j}^{\Delta_h,p}(v) \quad \forall v \in \mathcal{U}(\omega_j) \tag{2.9a}$$

where

$$\mathcal{B}_{\omega_j}\left(\hat{e}_{\omega_j}^{\text{Neum}}, v\right) \stackrel{\text{def}}{=} \int_{\omega_j} \nabla v^T \mathbf{K} \nabla \hat{e}_{\omega_j}^{\text{Neum}} + \int_{\partial\omega_j \cap \Gamma_N} \alpha\ \hat{e}_{\omega_j}^{\text{Neum}}\ v \tag{2.9b}$$

and

$$\mathcal{R}_{\omega_j}^{\Delta_h,p}(v) \stackrel{\text{def}}{=} \sum_{\tau \in \Delta, \tau \subseteq \omega_j} \mathcal{R}_{\tau}^{\Delta_h,p}(v\big|_{\tau}) \quad \forall v \in \mathcal{U}(\omega_j) \tag{2.9c}$$

Then, we have (see [4–6, 9]) the constant-free upper bound

$$||e_{S^p_{\Delta_h}}||_{\mathcal{U}} = \mathcal{R}_\Omega^{\Delta_h,p}(e_{S^p_{\Delta_h}}) \leq \mathcal{E}^{\text{Neum}}_{\Omega_h} \stackrel{\text{def}}{=} \sqrt{\sum_{\omega_j \in \Omega_h} ||\hat{e}^{\text{Neum}}_{\omega_j}||^2_{\mathcal{U}}} \tag{2.10}$$

Here $\mathcal{U}(\omega_j)$ is the energy space over ω_j, $\hat{e}^{\text{Neum}}_{\omega_j}$ are the Neumann patch residual indicator functions, and $\mathcal{E}^{\text{Neum}}_{\Omega_h}$ the Neumann patch residual estimator. In the special case that $\Omega_h \equiv \Delta_h$ we obtain the element residual estimator denoted by $\mathcal{E}^{\text{Neum}}_{\Delta_h}$.

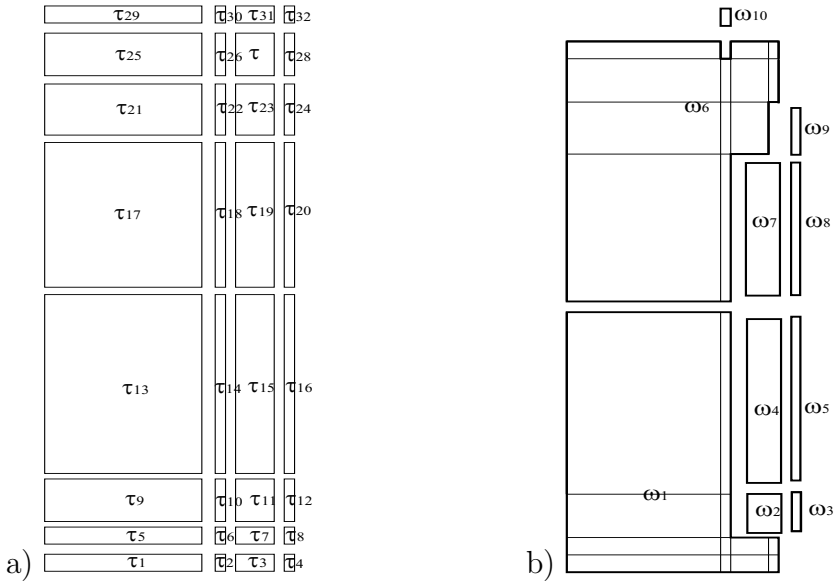

Fig. 2.4. Patch residual problems: Example of partitions of a mesh into patches of elements. a) The patches are identical with the elements; b) The patches consist of the vertex patches of elements which are connected to the reentrant corners, and the elements which remain after the re-entrant corner vertex patches have been formed. [1]

Second for subdomain residual estimators, let $\omega_X^{\Delta_h} = \bigcup_{\substack{\tau \in \Delta_h \\ X \in \partial\tau}} \tau = \text{supp}(\phi_X^{\Delta_h})$, denote the subdomain associated with the mesh-vertex X, where $\phi_X^{\Delta_h}$ is the piecewise bilinear basis function supported over $\omega_X^{\Delta_h}$ as is e.g. shown in Fig 2.5, and let $\hat{e}^{\text{Dir}}_{\omega_X^{\Delta_h}}$ denote the exact solution of the following Dirichlet problem:

Find $\hat{e}^{\mathrm{Dir}}_{\omega_X^{\Delta_h}} \in \mathcal{U}_0(\omega_X^{\Delta_h})$ such that

$$\mathcal{B}_{\omega_X^{\Delta_h}}(\hat{e}^{\mathrm{Dir}}_{\omega_X^{\Delta_h}}, v) = \mathcal{R}^{\Delta_h,p}_{\omega_X^{\Delta_h}}(v) \quad \forall v \in \mathcal{U}_0^{\mathrm{Dir}}(\omega_X^{\Delta_h}) \tag{2.11}$$

Here $\mathcal{U}_0(\omega_X^{\Delta_h})$ is the energy space of functions which vanish on $\partial\omega_{X,D}^{\Delta_h} = \partial\omega_X^{\Delta_h} - (\partial\omega_X^{\Delta_h} \bigcap \Gamma_N)$, and $\mathcal{B}_{\omega_X^{\Delta_h}}$ and $\mathcal{R}^{\Delta_h,p}_{\omega_X^{\Delta_h}}$ are defined by assembling the corresponding element contributions. We then have [6]

$$\frac{1}{\sqrt{M}}\mathscr{E}^{\mathrm{Dir}}_{Subd} \leq ||u_{S^p_{\Delta_h}}||_{\mathcal{U}} \leq \mathscr{K}\mathscr{E}^{\mathrm{Dir}}_{Subd} \tag{2.12}$$

where

$$\mathscr{E}^{\mathrm{Dir}}_{Subd} \stackrel{\mathrm{def}}{=} \sqrt{\sum_{X\in\mathcal{N}(\Delta_h)} ||\hat{e}^{\mathrm{Dir}}_{\omega_X^{\Delta_h}}||^2_{\mathcal{U}(\omega_X^{\Delta_h})}} \tag{2.13}$$

is the Dirichlet subdomain residual estimator, $\hat{e}^{\mathrm{Dir}}_{\omega_X^{\Delta_h}}$ is the Dirichlet subdomain residual error indicator function, M is the overlap index namely the maximum number of elements connected to a vertex (for Mesh I, Mesh II, and Mesh III, $M = 4$), and $\mathscr{K}$ is a constant depending on the admissible classes of meshes, material orthotropies, and the degree p of the elements (see [6] for details).

We will also introduce two Neumann subdomain residual estimators which lead to constant-free upper bounds. We employ the following problems:

Find $\hat{e}^{\mathrm{Neum,I}}_{\omega_X^{\Delta_h}} \in \mathcal{U}(\omega_X^{\Delta_h})$, such that

$$\mathcal{B}^{\phi_X^{\Delta_h}}_{\omega_X^{\Delta_h}}(\hat{e}^{\mathrm{Neum,I}}_{\omega_X^{\Delta_h}}, v) = \mathcal{R}_{\omega_X^{\Delta_h}}(\phi_X^{\Delta_h}\ v) \qquad \forall v \in \mathcal{U}(\omega_X^{\Delta_h}) \tag{2.14a}$$

where

$$\mathcal{B}^{\phi_X^{\Delta_h}}_{\omega_X^{\Delta_h}}(\hat{e}^{\mathrm{Neum,I}}_{\omega_X^{\Delta_h}}, v) \stackrel{\mathrm{def}}{=} \int_{\omega_X^{\Delta_h}} \phi_X^{\Delta_h}\ \nabla v^T \mathbf{K}\ \nabla \hat{e}^{\mathrm{Neum,I}}_{\omega_X^{\Delta_h}} + \int_{\partial\omega_X^{\Delta_h}} \phi_X^{\Delta_h}\ \alpha\ \hat{e}^{\mathrm{Neum,I}}_{\omega_X^{\Delta_h}}\ v \tag{2.14b}$$

and

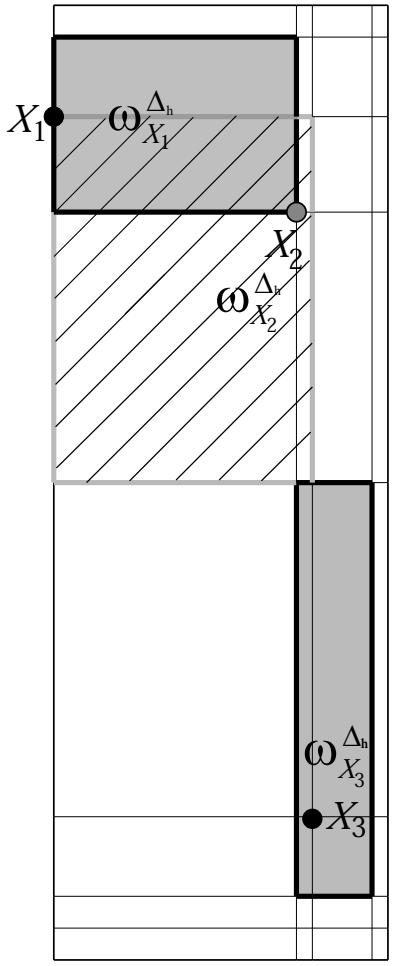

Fig. 2.5. Examples of subdomains $\omega_X^{\Delta_h} = supp(\phi_X^{\Delta_h})$, for Mesh I. [1]

Find $\hat{e}^{\text{Neum,II}}_{\omega_X^{\Delta_h}} \in \mathcal{U}(\omega_X^{\Delta_h})$, such that

$$\mathcal{B}_{\omega_X^{\Delta_h}}(\hat{e}^{\text{Neum,II}}_{\omega_X^{\Delta_h}}, v) = \mathcal{R}_{\omega_X^{\Delta_h}}(\phi_X^{\Delta_h}\ v) \qquad \forall v \in \mathcal{U}(\omega_X^{\Delta_h}) \tag{2.15a}$$

where

$$\mathcal{B}_{\omega_X^{\Delta_h}}(\hat{e}^{\text{Neum,II}}_{\omega_X^{\Delta_h}}, v) \stackrel{\text{def}}{=} \int_{\omega_X^{\Delta_h}} \nabla v^T \mathbf{K}\ \nabla \hat{e}^{\text{Neum,II}} + \int_{\partial\omega_X^{\Delta_h}} \alpha\ \hat{e}^{\text{Neum,II}}\ v \tag{2.15b}$$

Note that the only difference between the two problems is the employment of a $\phi_X^{\Delta_h}$

weighted bilinear form in (2.14a). We then have

$$||e_{S^p_{\Delta_h}}||_{\mathcal{U}} \leq \mathscr{E}^{\text{Neum,I}}_{Subd} \overset{\text{def}}{=} \sqrt{\sum_X \left|\left|\hat{e}^{\text{Neum,I}}_{\omega_X^{\Delta_h}}\right|\right|^2_{\mathcal{U}(\omega_X^{\Delta_h}),\phi_X^{\Delta_h}}} \tag{2.16}$$

where $\left|\left|\cdot\right|\right|_{\mathcal{U}(\omega_X^{\Delta_h}),\phi_X^{\Delta_h}}$ is the energy norm corresponding to the weighted bilinear form $\mathcal{B}^{\phi_X^{\Delta_h}}_{\omega_X^{\Delta_h}}(\cdot,\cdot)$, and

$$||e_{S^p_{\Delta_h}}||_{\mathcal{U}} \leq \mathscr{E}^{\text{Neum,II}}_{Subd} \overset{\text{def}}{=} \sqrt{\sum_{\tau\in\Delta_h} \left|\left| \sum_{X\in\mathcal{N}(\Delta_h)} \hat{e}^{\text{Neum,II}}_{\omega_X^{\Delta_h}}\right|\right|^2_{\mathcal{U}}} \tag{2.17}$$

Here $\hat{e}^{\text{Neum,I}}_{\omega_X^{\Delta_h}}$ (resp. $\hat{e}^{\text{Neum,II}}_{\omega_X^{\Delta_h}}$) are the subdomain error indicator functions of type I (resp. type II) and $\mathscr{E}^{\text{Neum,I}}_{Subd}$ (resp. $\mathscr{E}^{\text{Neum,II}}_{Subd}$) are the corresponding estimators. Note that (2.16) was proposed in [48], while (2.17) was established in [16]. Both subdomain residual estimators provide constant free upper bound for the energy norm of the error, similiarly as the Neumann patch and element residual estimators.

Let us now illustrate the sensitivity of the above residual estimators to the orthotropy of subdomain Ω_3 for the finite element solutions $u_{S^p_{\Delta_h}}$, with Mesh I, Mesh II, Mesh III and $p = 1, 2, 3$. Figs. 2.6, 2.7 and 2.8 show the variation of the effectivity index

$$\kappa = \frac{\mathscr{E}}{||e_{S^p_{\Delta_h}}||_{\mathcal{U}}} \tag{2.18}$$

versus $\frac{k_x}{k_y}$, respectively for the Neumann element residual estimator $\mathscr{E}^{\text{Neum}}_{\Delta_h}$, Neumann patch residual estimator $\mathscr{E}^{\text{Neum}}_{\Omega_h}$, the Dirichlet subdomain residual estimator $\mathscr{E}^{\text{Dir}}_{\Delta_h}$, and the Neumann subdomain residual estimators $\mathscr{E}^{\text{Neum,I}}_{\text{Subd}}$, and $\mathscr{E}^{\text{Neum,II}}_{\text{Subd}}$. In each case we estimated the energy norm of the exact error by employing the overkill mesh, namely

$$||e_{S^p_{\Delta_h}}||_{\mathcal{U}} \approx ||u_{S^{p'}_{\Delta_h^{ovk}}} - u_{S^p_{\Delta_h}}||_{\mathcal{U}} = \sqrt{||u_{S^{p'}_{\Delta_h^{ovk}}}||^2_{\mathcal{U}} - ||u_{S^p_{\Delta_h}}||^2_{\mathcal{U}}} \tag{2.19}$$

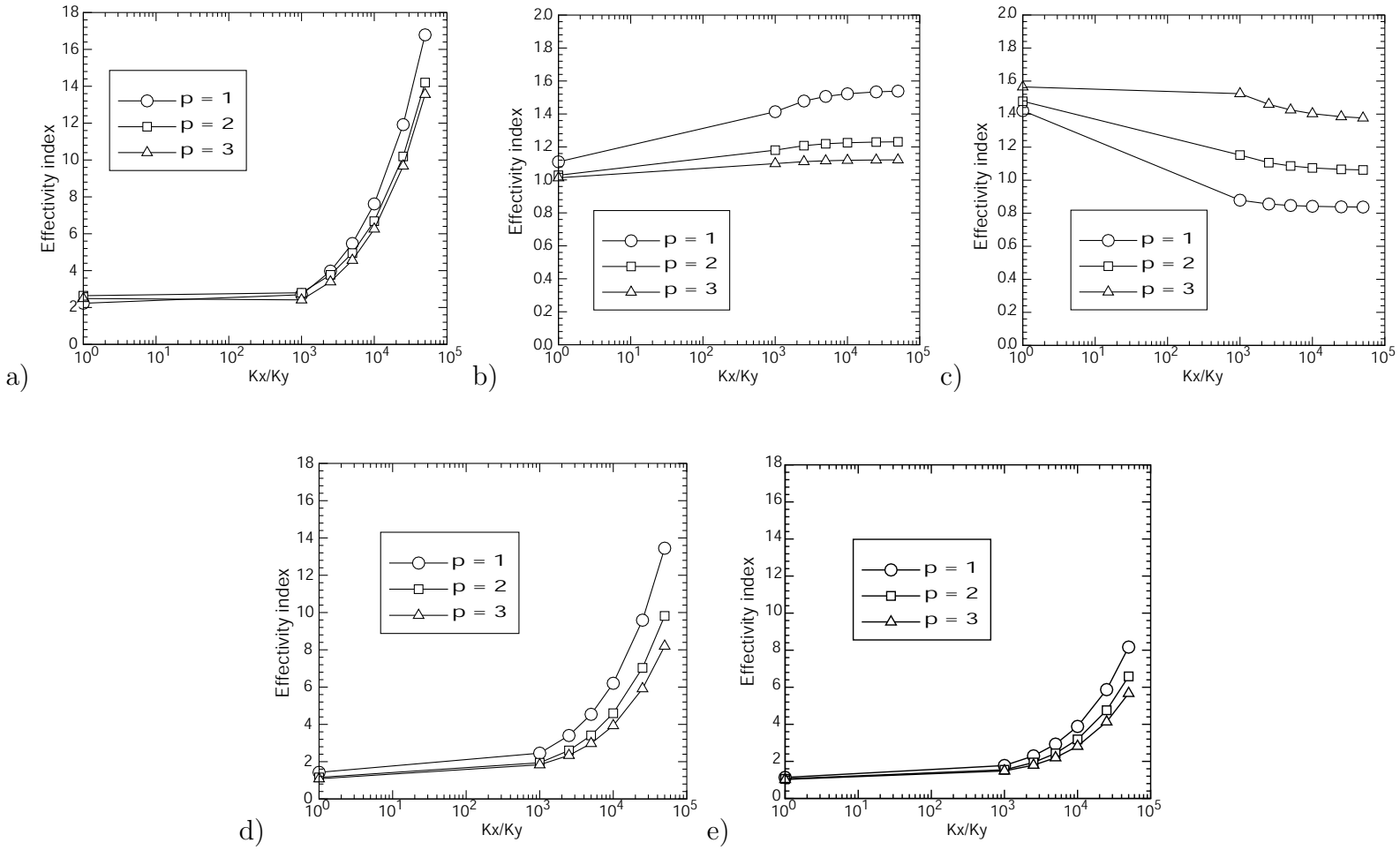

Fig. 2.6. Heat conduction in a thermal battery. The variation of the effectivity indices κ vs. $\dfrac{k_x}{k_y}$, of the exact estimators for Mesh I: a)Neumann element residual $\mathscr{E}^{\text{Neum}}_{\Delta_h}$; b)Neumann patch residual $\mathscr{E}^{\text{Neum}}_{\Omega_h}$; c) Dirichlet subdomain residual $\mathscr{E}^{\text{Dir}}_{Subd}$; d) Neumann subdomain residual I $\mathscr{E}^{\text{Neum,I}}_{Subd}$; e)Neumann subdomain residual II $\mathscr{E}^{\text{Neum,II}}_{Subd}$, using elements of degree $p = 1, 2$, and 3. [1]

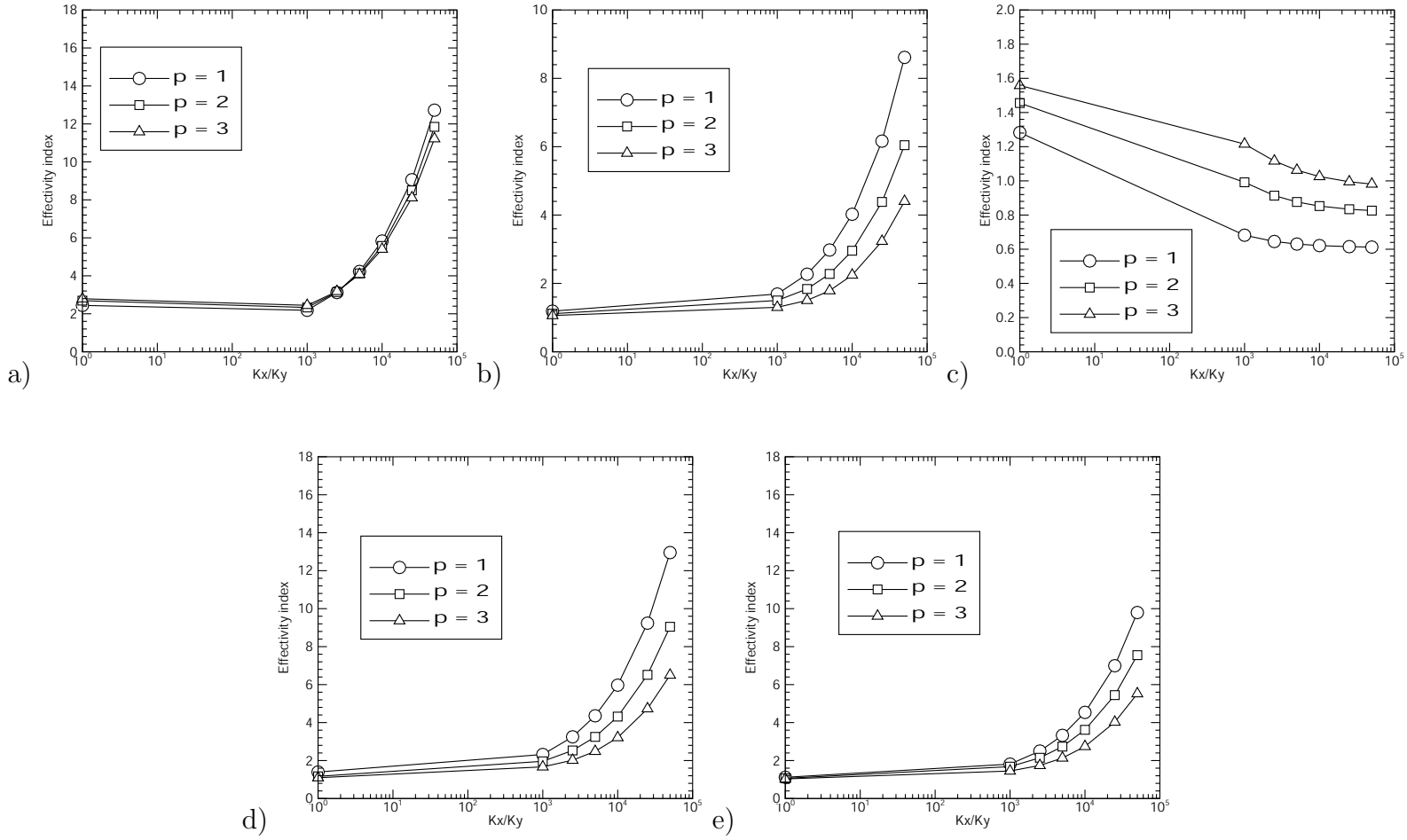

Fig. 2.7. Heat conduction in a thermal battery. The variation of the effectivity indices κ vs. $\dfrac{k_x}{k_y}$, of the exact estimators for Mesh II: a)Neumann element residual $\mathscr{E}^{\text{Neum}}_{\Delta_h}$; (b)Neumann patch residual $\mathscr{E}^{\text{Neum}}_{\Omega_h}$; c) Dirichlet subdomain residual $\mathscr{E}^{\text{Dir}}_{Subd}$; d) Neumann subdomain residual I $\mathscr{E}^{\text{Neum,I}}_{Subd}$; (e)Neumann subdomain residual II $\mathscr{E}^{\text{Neum,II}}_{Subd}$, using elements of degree $p = 1, 2$, and 3.

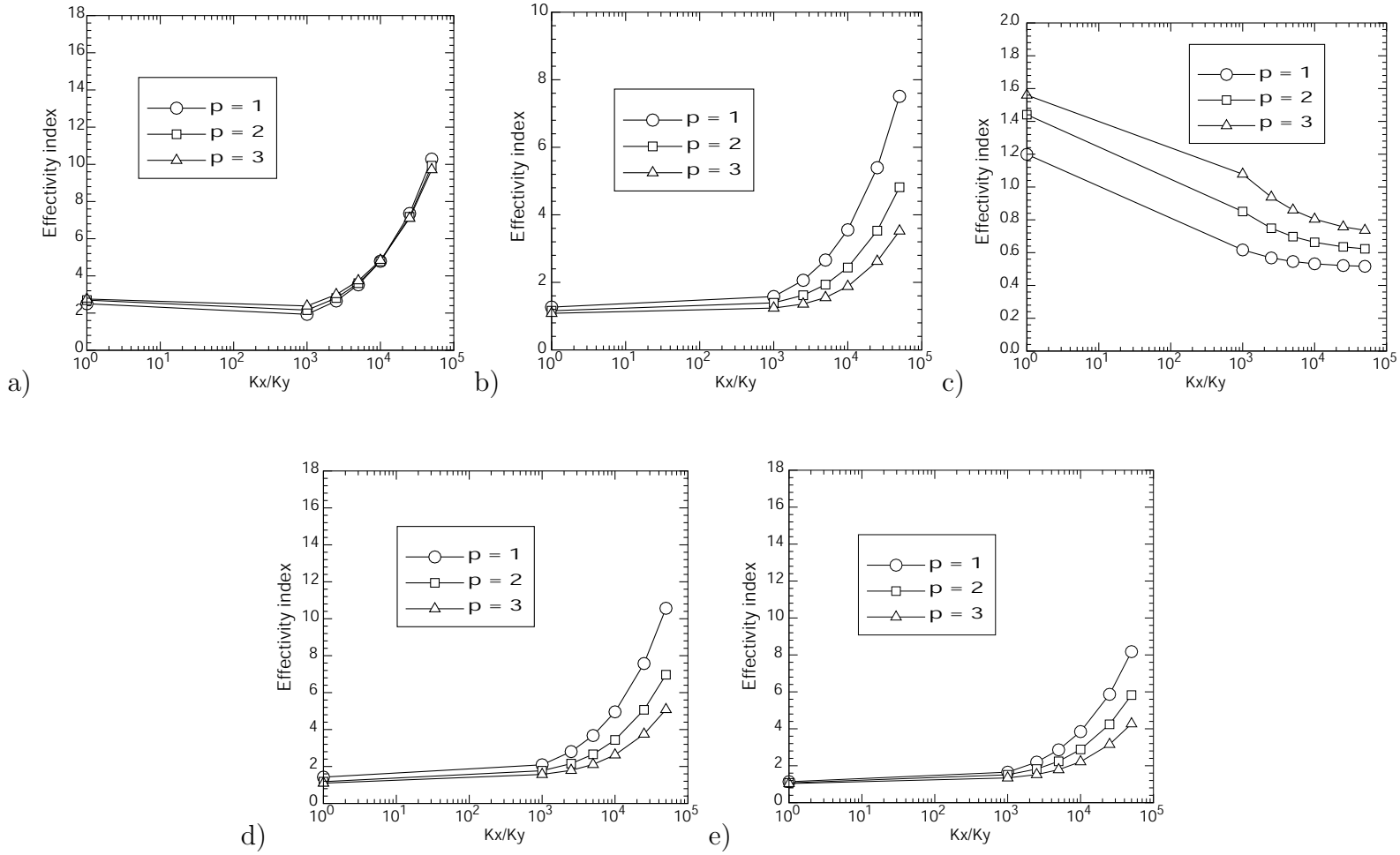

Fig. 2.8. Heat conduction in a thermal battery. The variation of the effectivity indices κ vs. $\dfrac{k_x}{k_y}$, of the exact estimators for Mesh III: a)Neumann element residual $\mathscr{E}^{\text{Neum}}_{\Delta_h}$; b)Neumann patch residual $\mathscr{E}^{\text{Neum}}_{\Omega_h}$; c) Dirichlet subdomain residual $\mathscr{E}^{\text{Dir}}_{Subd}$; d) Neumann subdomain residual I $\mathscr{E}^{\text{Neum,I}}_{Subd}$; e)Neumann subdomain residual II $\mathscr{E}^{\text{Neum,II}}_{Subd}$, using elements of degree $p = 1, 2$, and 3. [1]

We computed the "exact" indicator functions in each case by employing the restriction of the overkill space $S^8_{\Delta_h^{ovk}}$ in the elements and subdomains. We note that all three Neumann estimators which are guaranteed bounds of the energy norm of the error grossly overestimate as the orthotropy ratio $\frac{k_x}{k_y}$ is increased, while the Dirichlet subdomain residual estimator underestimates.

Similar results were obtained for computed versions of the estimators as shown in Figs. 2.9, 2.10 and 2.11 with Mesh I, II, and III in which we employed the p-version with elements of degree $p+k$ to approximate the indicator functions, and we have for the Neumann element residual estimator

$$\mathscr{E}^{\text{Neum}}_{\Delta_h,p+k} \stackrel{\text{def}}{=} \sqrt{\sum_{\tau\in\Delta_h} ||\hat{e}^{\text{Neum}}_{\tau,p+k}||^2_{\mathscr{U}}} \tag{2.20}$$

where $\hat{e}^{\text{Neum}}_{\tau,p+k}$ denote the $(p+k)$ degree finite element approximation of the exact indicator functions $\hat{e}^{\text{Neum}}_{\tau}$. The computed estimators $\mathscr{E}^{\text{Dir}}_{\Delta_h,p+k}$, $\mathscr{E}^{\text{Neum,I}}_{Subd,p+k}$, $\mathscr{E}^{\text{Neum,II}}_{Subd,p+k}$ are defined analogously.

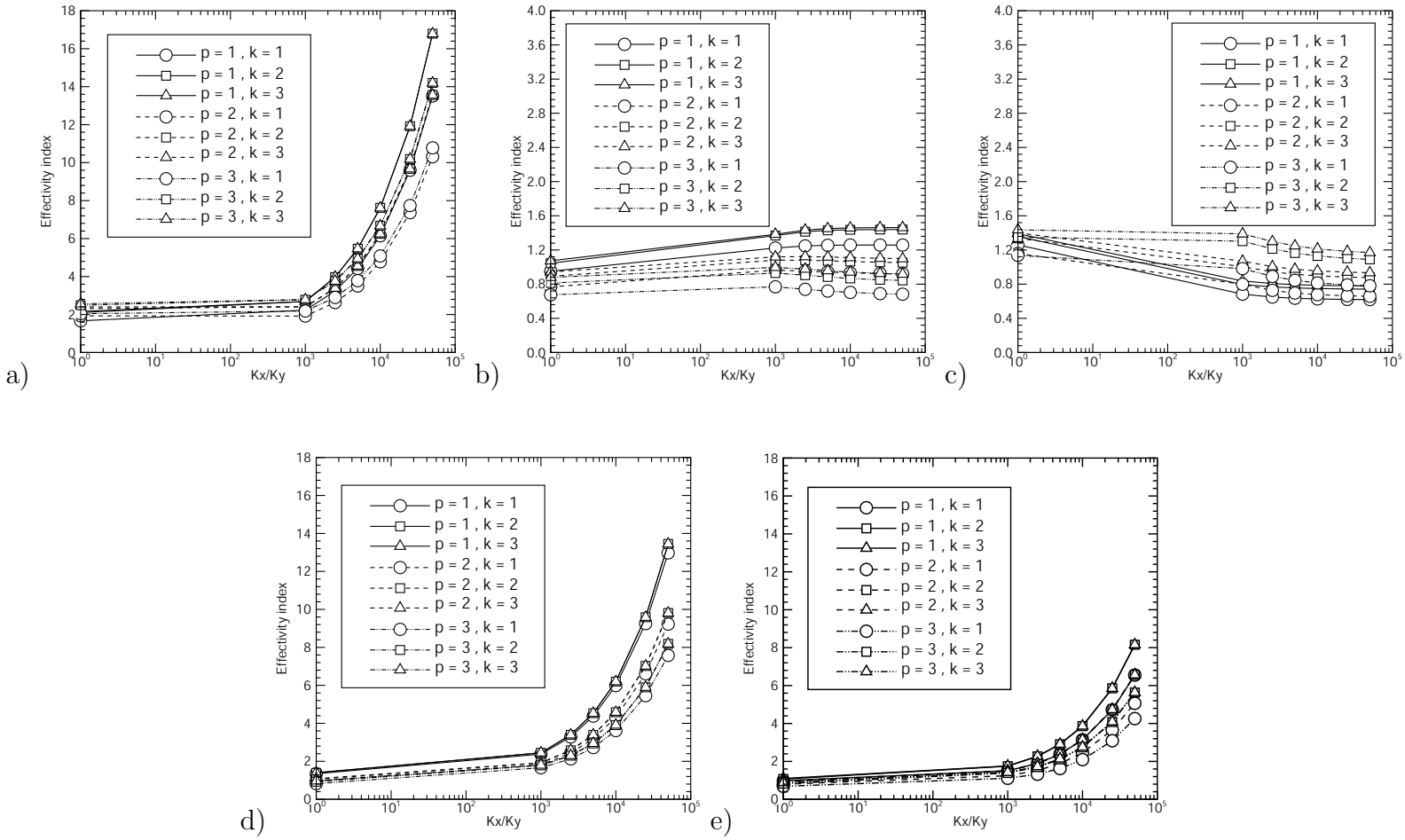

Fig. 2.9. Heat conduction in a thermal battery. The variation of the effectivity indices κ vs. $\dfrac{k_x}{k_y}$, of the computed estimators for Mesh I: a)Neumann element residual $\mathscr{E}^{\mathrm{Neum}}_{\Delta_h,p+k}$; b)Neumann patch residual $\mathscr{E}^{\mathrm{Neum}}_{\Omega_h,p+k}$; c) Dirichlet subdomain residual $\mathscr{E}^{\mathrm{Dir}}_{Subd,p+k}$; d) Neumann subdomain residual I $\mathscr{E}^{\mathrm{Neum,I}}_{Subd,p+k}$; e)Neumann subdomain residual II $\mathscr{E}^{\mathrm{Neum,II}}_{Subd,p+k}$, using elements of degree $p = 1, 2$, and 3 and $k = 1, 2$, and 3.

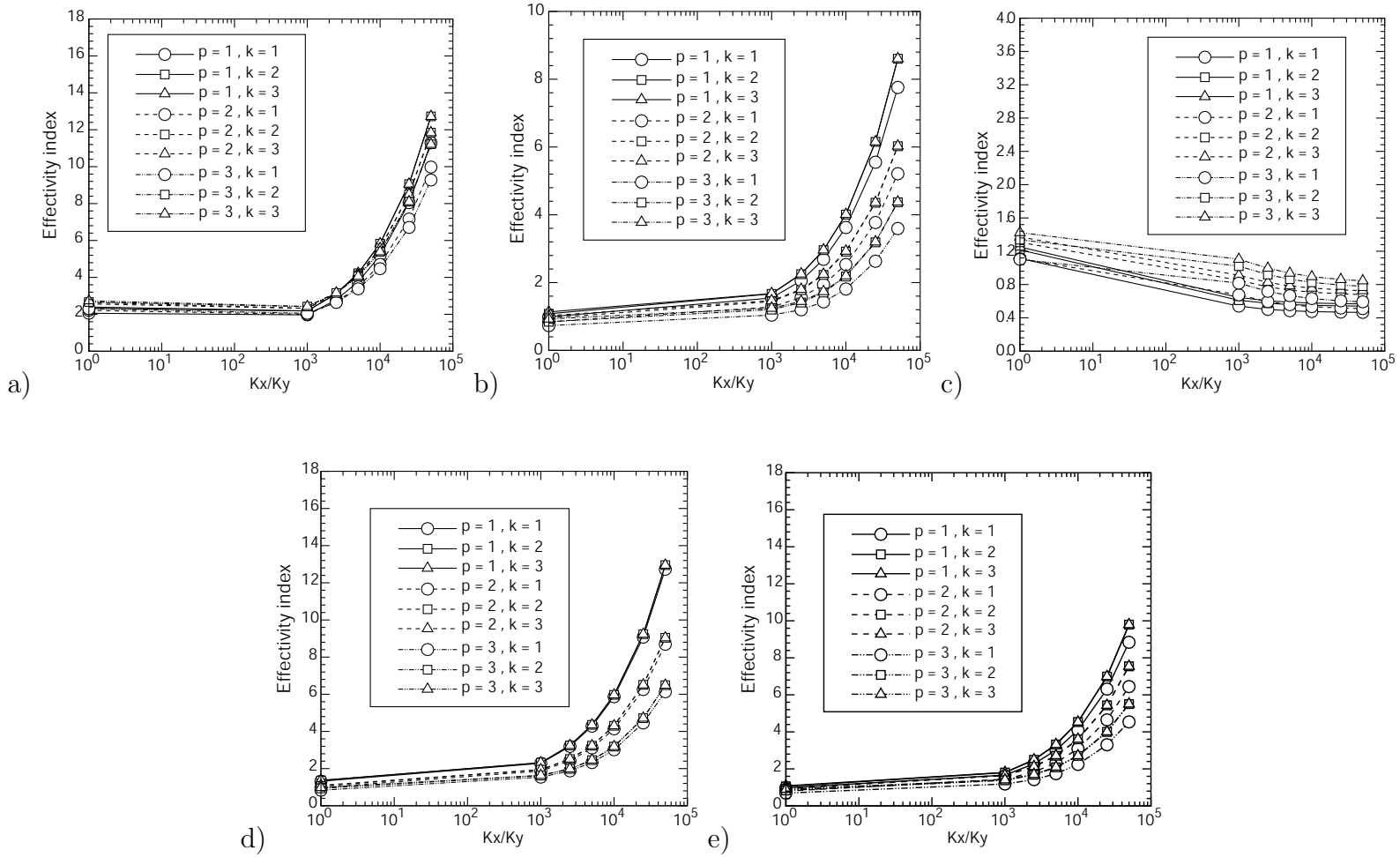

Fig. 2.10. Heat conduction in a thermal battery. The variation of the effectivity indices κ vs. $\dfrac{k_x}{k_y}$, of the computed estimators for Mesh II: a)Neumann element residual $\mathscr{E}^{\text{Neum}}_{\Delta_h,p+k}$; b)Neumann patch residual $\mathscr{E}^{\text{Neum}}_{\Omega_h,p+k}$; c) Dirichlet subdomain residual $\mathscr{E}^{\text{Dir}}_{Subd,p+k}$; d) Neumann subdomain residual I $\mathscr{E}^{\text{Neum,I}}_{Subd,p+k}$; e)Neumann subdomain residual II $\mathscr{E}^{\text{Neum,II}}_{Subd,p+k}$, using elements of degree $p = 1, 2$, and 3 and $k = 1, 2$, and 3. [1]

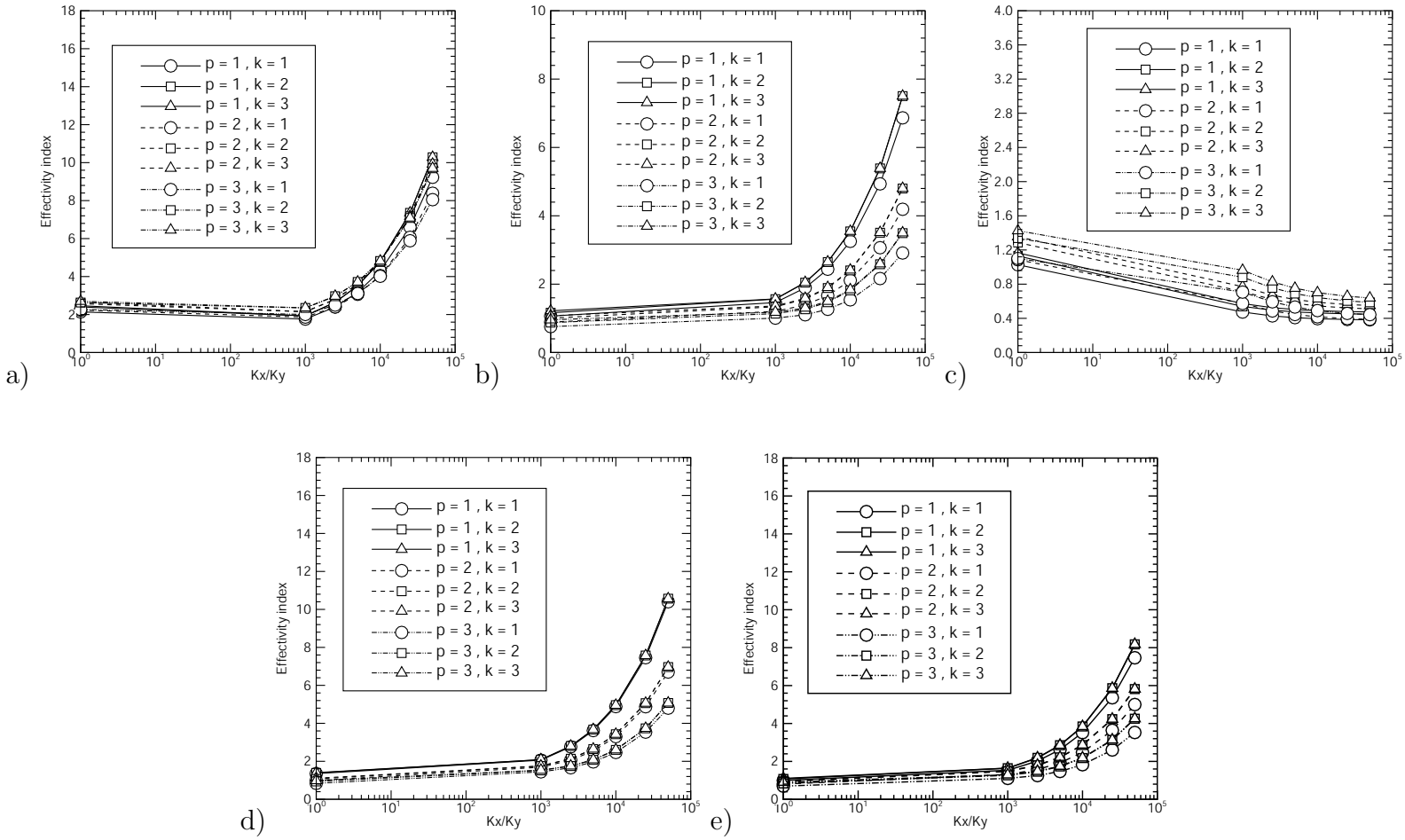

Fig. 2.11. Heat conduction in a thermal battery. The variation of the effectivity indices κ vs. $\dfrac{k_x}{k_y}$, of the computed estimators for Mesh III: a)Neumann element residual $\mathscr{E}^{\text{Neum}}_{\Delta_h,p+k}$; b)Neumann patch residual $\mathscr{E}^{\text{Neum}}_{\Omega_h,p+k}$; c) Dirichlet subdomain residual $\mathscr{E}^{\text{Dir}}_{Subd,p+k}$; d) Neumann subdomain residual I $\mathscr{E}^{\text{Neum,I}}_{Subd,p+k}$; e)Neumann subdomain residual II $\mathscr{E}^{\text{Neum,II}}_{Subd,p+k}$, using elements of degree $p = 1, 2$, and 3 and $k = 1, 2$, and 3.

As expected, the computed estimators are smaller than those of the exact ones. Nevertheless, we cannot use this fact to "improve" the estimators, namely it is not possible in general, to employ a low k to improve the accuracy of the estimator to the high orthotropy.

Above, we have examined the sensitivity of the estimators computed directly for the indicators with respect to the orthotropy. We have seen that the Neumann estimators $\mathscr{E}_{\Delta_h}^{\text{Neum}}$, $\mathscr{E}_{Subd}^{\text{Neum,I}}$, $\mathscr{E}_{Subd}^{\text{Neum,II}}$, which are upper estimators, grossly overestimate the energy-norm of the error $||e_{S_{\Delta_h}^p}||_{\mathscr{U}}$, and the same is true for their computed versions $\mathscr{E}_{\Delta_h,p+k}^{\text{Neum}}$, $\mathscr{E}_{Subd,p+k}^{\text{Neum,I}}$, $\mathscr{E}_{Subd,p+k}^{\text{Neum,II}}$.

Let us now examine the sensitivity of lower bounds for the error constructed using the same indicators. We obtain lower bounds using

$$\mathscr{E}^L(\tilde{e}_{\Delta_h}^{p+k}) \stackrel{\text{def}}{=} \frac{\mathscr{R}_\Omega^{\Delta_h,p}(\tilde{e}_\Delta^{p+k})}{||\tilde{e}_{\Delta_h}^{p+k}||_{\mathscr{U}}} \leq \mathscr{E}^{L,opt}(\tilde{e}_\Delta^{p+k}) \stackrel{\text{def}}{=} \frac{\mathscr{R}_\Omega^{\Delta_h,p}(\tilde{e}_{\Delta_h}^{p+k})}{\min\limits_{q\in S_{\Delta_h}^p} ||\tilde{e}_{\Delta_h}^{p+k}+q||_{\mathscr{U}}} \leq ||e_{S_{\Delta_h}^p}||_{\mathscr{U}} \tag{2.21}$$

We call $\mathscr{E}^{L,opt}(\tilde{e}_{\Delta_h}^{p+k})$ the optimized lower bound and its computation requires only the processing of an additional right hand side employing the factorized stiffness matrix used in the computation of $u_{S_{\Delta_h}^p}$. Here $\tilde{e}_{\Delta_h}^{p+k} \in \mathscr{U}(\Omega)$ denotes a smoothened error indicator function employed in the construction of the lower bound.

For example, in the case of the Neumann element residual indicators $\hat{e}_{p+k}^{\text{Neum}}$ have been computed, we can employ

$$\tilde{e}_{\Delta_h}^{p+k} = \hat{e}_{p+k}^{\text{Neum}} + \Phi_{p+k}^{\text{Neum}} \in \mathscr{U}(\Omega) \tag{2.22}$$

where Φ_{p+k}^{Neum} is a gap function obtained using local averaging as is e.g. discussed in [6]. For the subdomain residual indicators we employ the partition of unity used in the

construction of the estimator, for patching together the indicator functions namely

$$\tilde{e}^{p+k}_{\Delta_h} = \sum_{X \in \mathcal{N}(\Delta_h)} \phi^{\Delta_h}_X \ \hat{e}^{\text{Type}}_{\omega^{\Delta_h}_X, p+k} \tag{2.23}$$

where Type = Dir, Neum, I, or Neum, II.

The effectivity index for the lower bounds will be denoted by

$$\kappa^{L}_{\Delta_h, p+k} \stackrel{\text{def}}{=} \frac{\mathscr{E}^{L}(\tilde{e}^{p+k}_{\Delta_h})}{||e_{S^p_{\Delta_h}}||_{\mathscr{U}}} \qquad \kappa^{L,opt}_{\Delta_h, p+k} \stackrel{\text{def}}{=} \frac{\mathscr{E}^{L,opt}(\tilde{e}^{p+k}_{\Delta_h})}{||e_{S^p_{\Delta_h}}||_{\mathscr{U}}} \tag{2.24}$$

Figs. 2.12, 2.13, 2.14, 2.15, and 2.16 show the variation of $\kappa^{L}_{\Delta_h, p+k}$ and $\kappa^{L,opt}_{\Delta_h, p+k}$ for the Neumann element residual, Neumann patch residual, Dirichlet subdomain residual, Neumann subdomain residual I, and Neumann subdomain residual II, versus the orthotropy $\frac{k_x}{k_y}$ for Mesh I, II, and III, $p = 1, 2, 3$ and $k = 1, 2, 3$. Note the improvement in the lower estimate when the extra computation of $q \in S^p_{\Delta_h}$ which minimizes the denominator is employed. Among all the residual based bounds, the improvement of the optimized version of the lower bound was marked only for Neumann subdomain residual I based lower bound in the case that the orthotropy $\frac{k_x}{k_y}$ is equal to 1. Note also the lower bound is less sensitive to the high orthotropy $\frac{k_x}{k_y}$ than the Neumann patch residual estimator the exact version of which is a guaranteed upper estimate. Let us reiterate that the cost of the extra computation of $q \in S^p_{\Delta_h}$ which minimizes the denominator $||\tilde{e}^{p+k}_{\Delta_h} + q||_{\mathscr{U}}$ is negligible because it employs the factorized stiffness matrix which was used to compute the finite element solution $u_{S^p_{\Delta_h}}$.

Note that for this example problem, the best lower bounds seem to be the ones obtained by employing Neumann element residual indicator functions. For isotropic case the best lower lower bounds are obtained from the subdomain residual indicators using optimization.

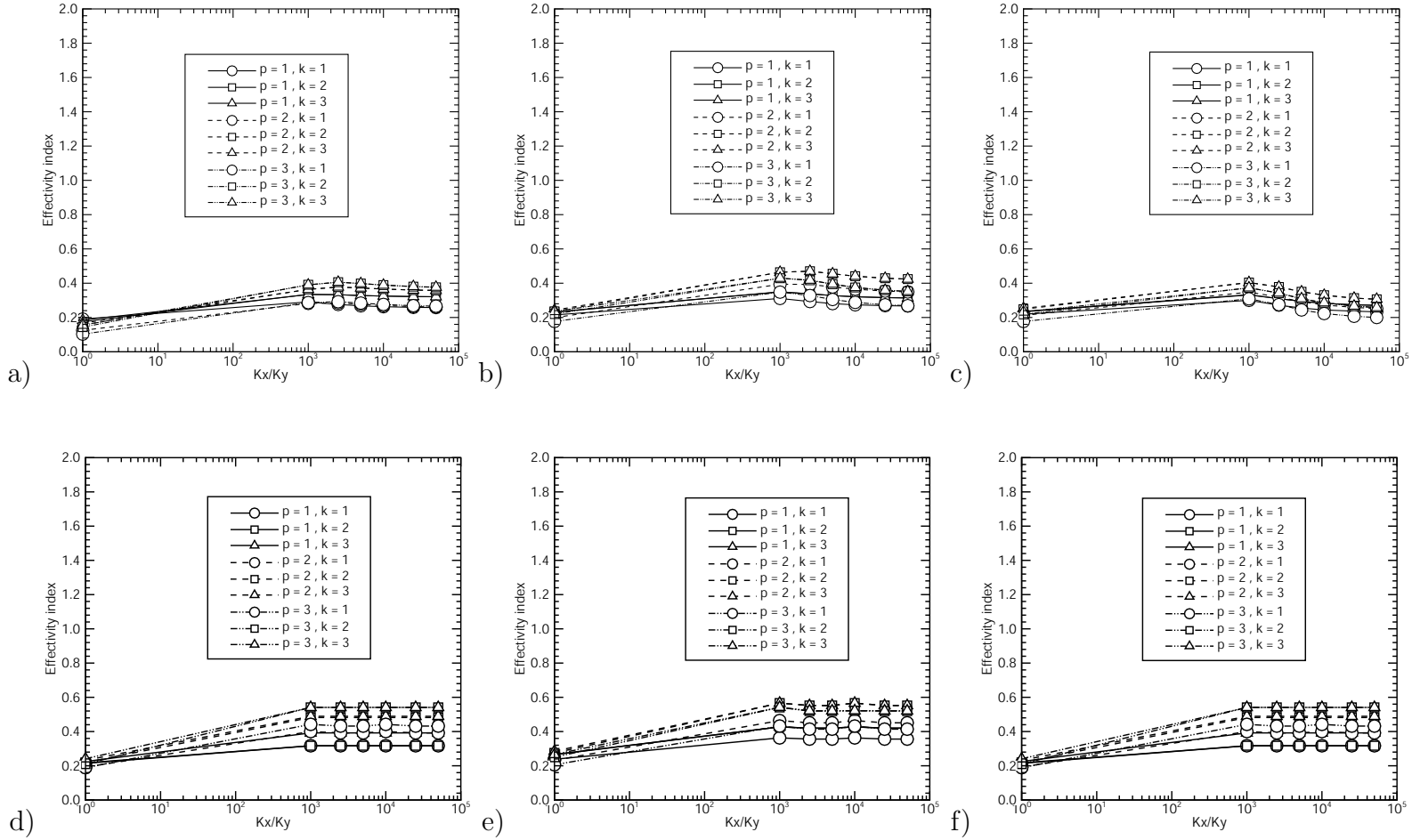

Fig. 2.12. Heat conduction in a thermal battery. The variation of effectivity indices $\kappa^{L}_{\Delta_h,p+k}$ (a) Mesh I; b) Mesh II; c) Mesh III.) and $\kappa^{L,opt}_{\Delta_h,p+k}$ vs. $\dfrac{k_x}{k_y}$ (d) Mesh I; e) Mesh II; f) Mesh III.) of the Neumann element residual based lower bound, for Mesh I, Mesh II, and Mesh III finite element solutions using elements of degree $p = 1, 2,$ and 3 and $k = 1, 2,$ and 3.

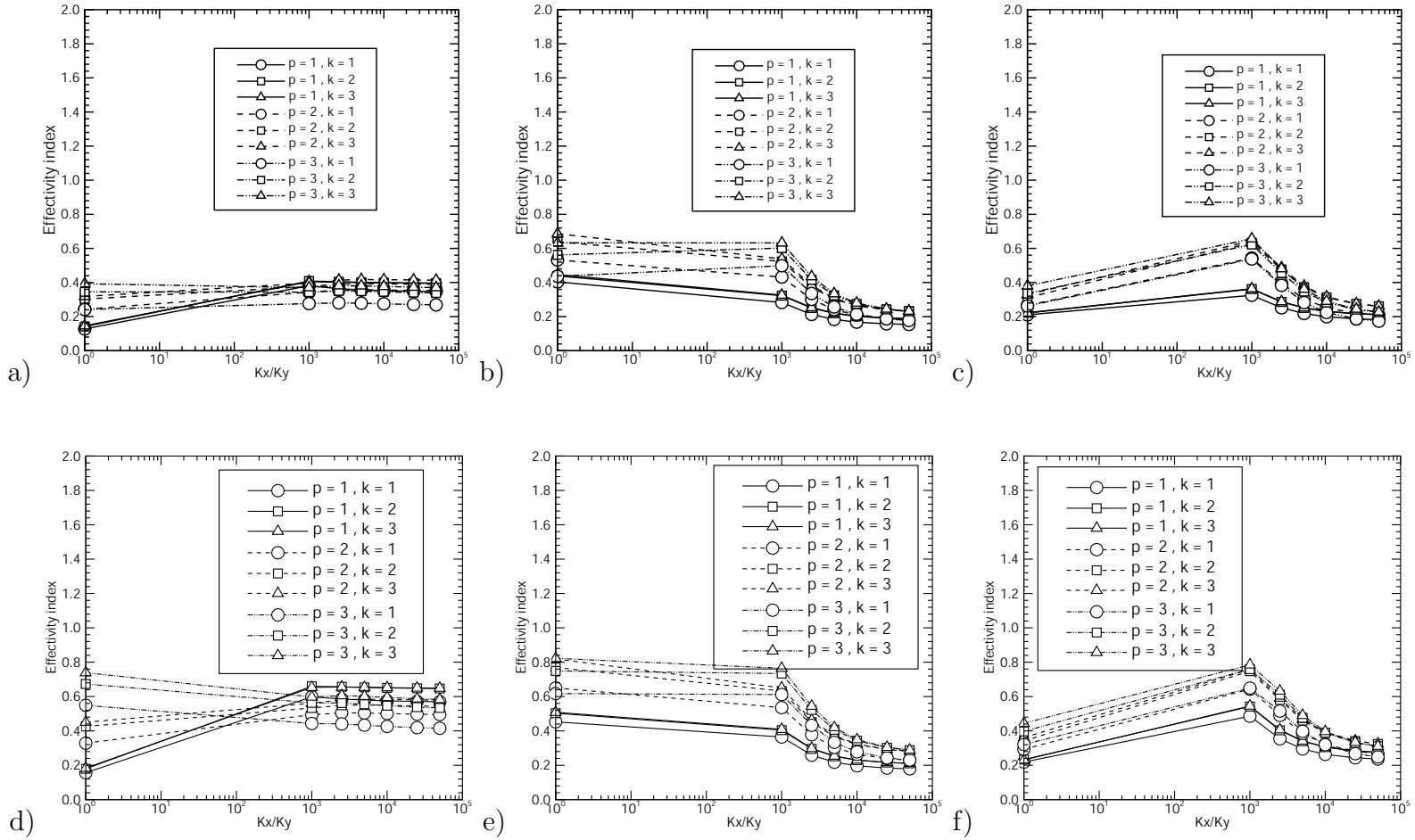

Fig. 2.13. Heat conduction in a thermal battery. The variation of effectivity indices $\kappa^L_{\Delta,p+k}$ (a) Mesh I; b) Mesh II; c) Mesh III.) and $\kappa^{L,opt}_{\Delta_h,p+k}$ vs. $\dfrac{k_x}{k_y}$ (d) Mesh I; e) Mesh II; f) Mesh III.) of the Neumann patch residual based lower bound, for Mesh I, Mesh II, and Mesh III finite element solutions using elements of degree $p = 1, 2,$ and 3 and $k = 1, 2,$ and 3.

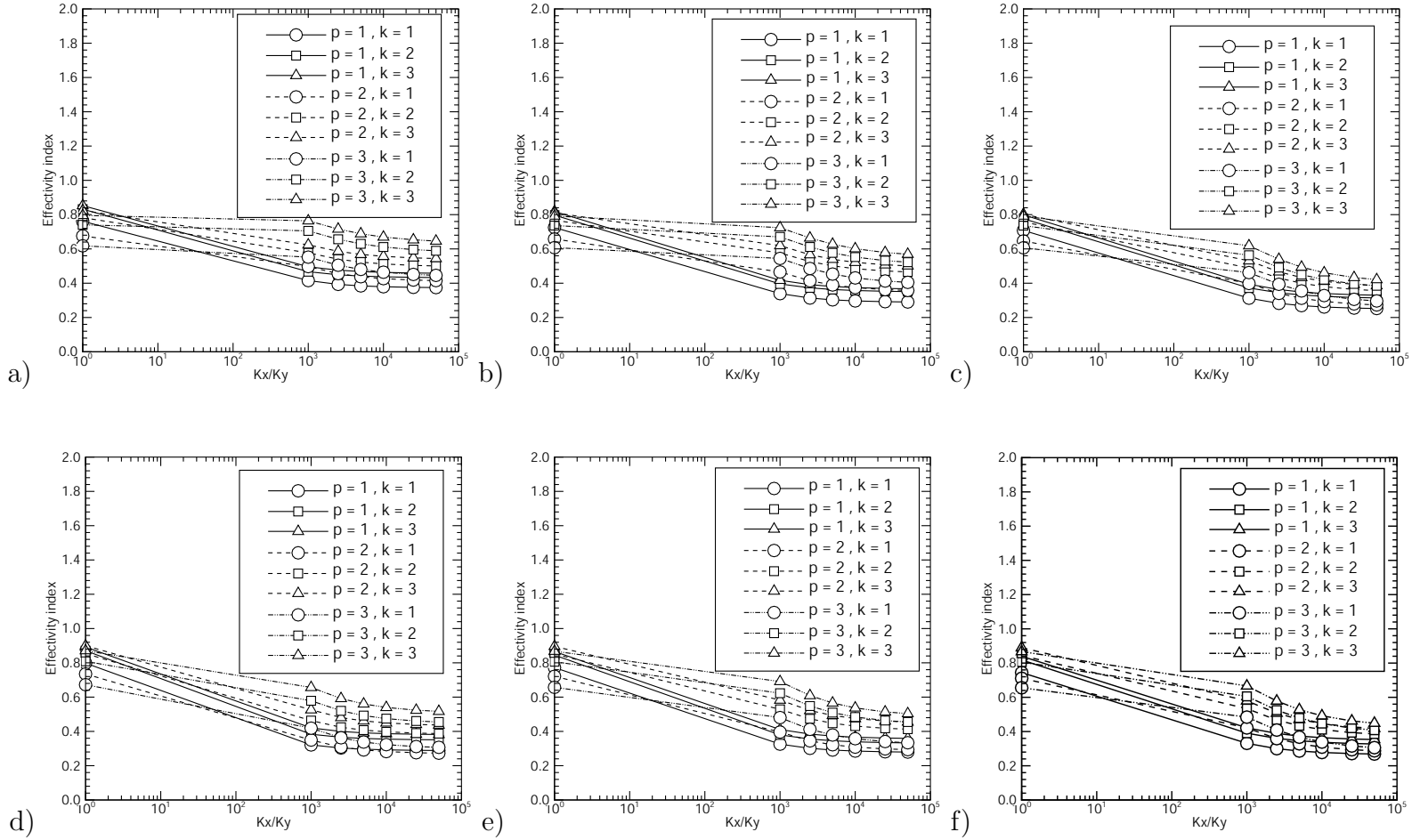

Fig. 2.14. Heat conduction in a thermal battery. The variation of effectivity indices $\kappa^{L}_{\Delta_h,p+k}$ (a) Mesh I; b) Mesh II; c) Mesh III.) and $\kappa^{L,opt}_{\Delta_h,p+k}$ vs. $\dfrac{k_x}{k_y}$ (d) Mesh I; e) Mesh II; f) Mesh III.) of the Dirichlet subdomain residual based lower bound, for Mesh I, Mesh II, and Mesh III finite element solutions using elements of degree $p = 1, 2,$ and 3 and $k = 1, 2,$ and 3.

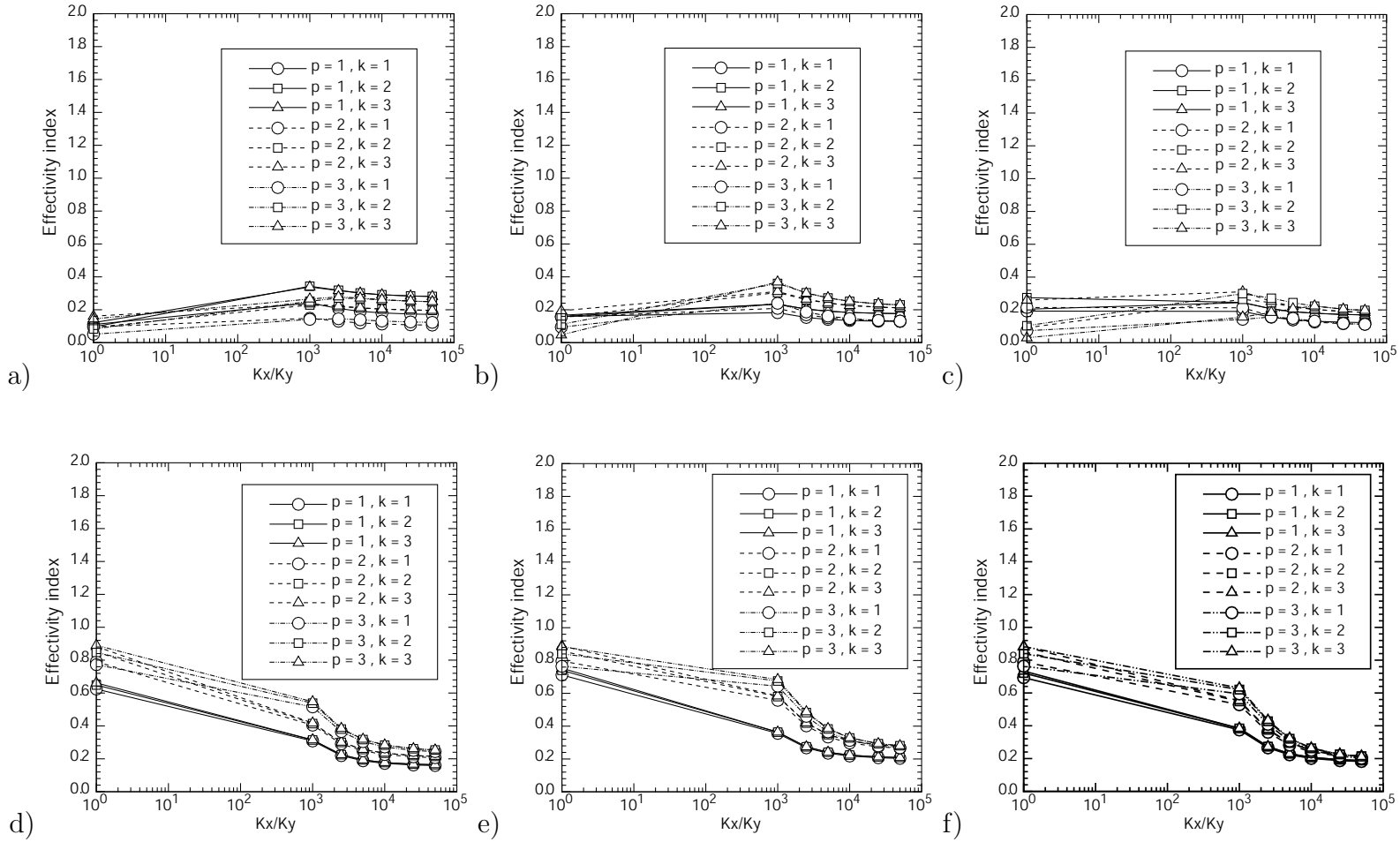

Fig. 2.15. Heat conduction in a thermal battery. The variation of effectivity indices $\kappa^L_{\Delta_h,p+k}$ (a) Mesh I; b) Mesh II; c) Mesh III.) and $\kappa^{L,opt}_{\Delta_h,p+k}$ vs. $\dfrac{k_x}{k_y}$ (d) Mesh I; e) Mesh II; f) Mesh III.) of the Neumann subdomain residual I based lower bound, for Mesh I, Mesh II, and Mesh III finite element solutions using elements of degree $p = 1, 2,$ and 3 and $k = 1, 2,$ and 3. [1]

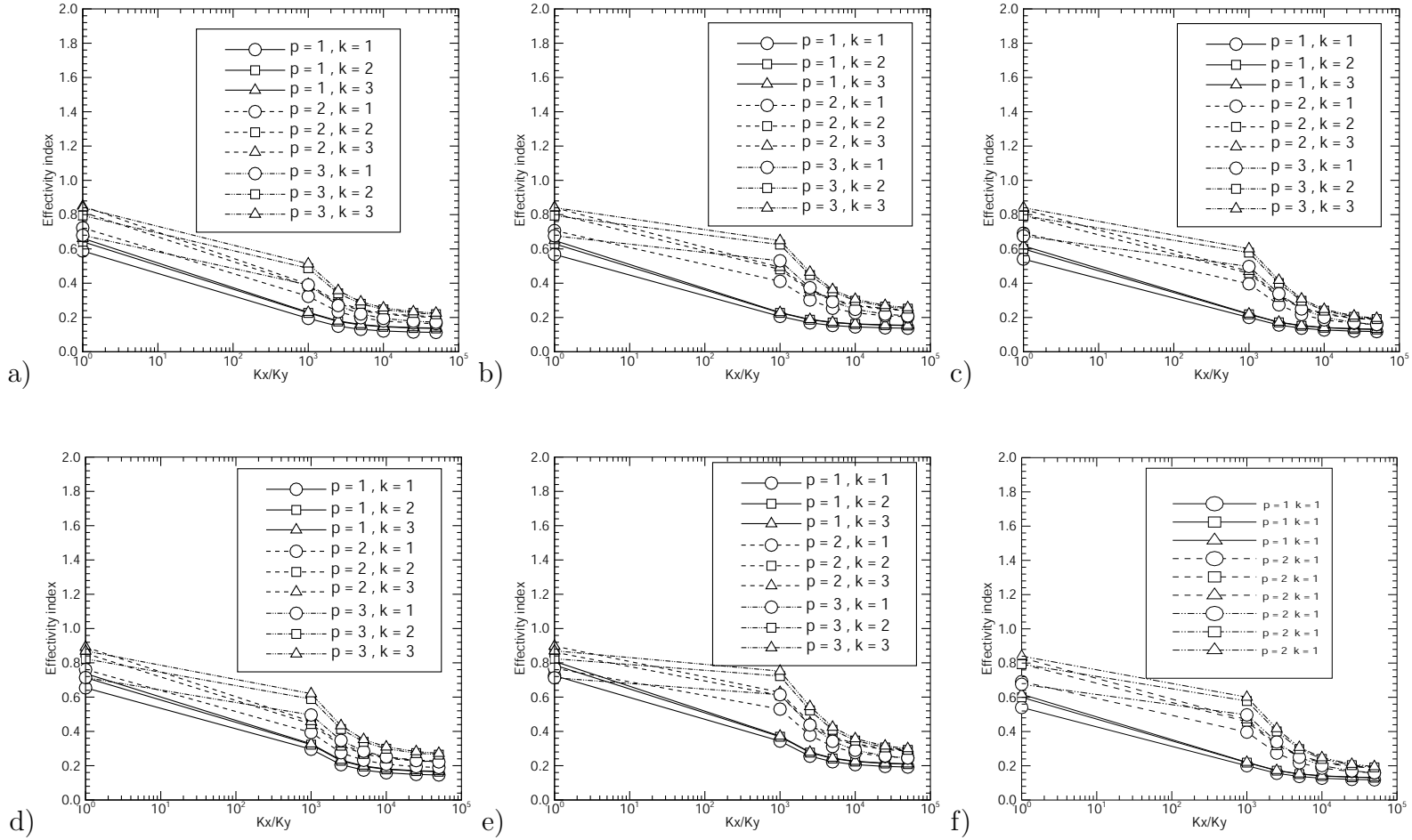

Fig. 2.16. Heat conduction in a thermal battery. The variation of effectivity indices $\kappa^L_{\Delta_h,p+k}$ (a) Mesh I; b) Mesh II; c) Mesh III.) and $\kappa^{L,opt}_{\Delta,p+k}$ vs. $\dfrac{k_x}{k_y}$ (d) Mesh I; e) Mesh II; f) Mesh III.) of the Neumann subdomain residual II based lower bound, for Mesh I, Mesh II, and Mesh III finite element solutions using elements of degree $p = 1, 2,$ and 3 and $k = 1, 2,$ and 3.

CHAPTER III

ILLUSTRATION OF THE MAIN DIFFICULTY

Above we have examined the variation of the effectivity indices for four types of residual estimators with respect to the orthotropy $\frac{k_x}{k_y}$ in the thermal battery model problem. We have seen that:

a) The exact and computed versions of the Neumann patch residual estimator, and the two types of the Neumann subdomain residual estimators grossly overestimate the energy norm of the error as the orthotropy is increased .

b) All lower estimators constructed using the indicator functions of the various residual estimators also deteriorate with the orthotropy. Nevertheless the underestimation is less than the overestimation of the three versions of the upper estimator.

b) The lack of efficiency of the employed estimators can be detected by taking the ratio $\frac{\mathscr{E}^U}{\mathscr{E}^L}$, where $\mathscr{E}^U$ (resp. $\mathscr{E}^L$) is guaranteed upper (resp. lower) estimator.

We will now illustrate the main culprit causing the lack of robustness of the estimators in the employed thermal battery model problem. For this purpose we will employ two simple model problems obtained from the thermal battery problem.

3.1 Model problem with boundary layer

The simplest possible problem which can be used to address the main difficulty is:

Example 3.1. *Model problem with boundary layer.* We seek u which satisfies

$$\begin{aligned} -k_x\frac{\partial^2 u}{\partial x^2} - k_y\frac{\partial^2 u}{\partial y^2} &= 0 \qquad \text{on } \Omega_1 = (0,a)\times(0,b) \\ -k_y\frac{\partial u}{\partial y} &= \sin(\frac{\pi}{a}x) \qquad \text{on } \Gamma_{N_1} \\ -k_y\frac{\partial u}{\partial y} &= 0 \qquad \text{on } \Gamma_{N_2} \\ u &= 0 \qquad \text{on } \Gamma_D \end{aligned} \tag{3.1a}$$

where $a = 6.1$ and $b = 7.2$, and Ω_1 is the problem domain which was cut out of the domain Ω_3 of the thermal battery as shown by the dashed line in Fig. 3.1. The analytical expression of the exact solution is:

$$u_{EX}(x,y) = \frac{1}{k_y C_1\Big(1-e^{-2C_1 b}\Big)}\Big(e^{C_1(y-2b)} + e^{-C_1 y}\Big)\sin(\frac{\pi}{a}x) \quad \text{on } \Omega_1 \tag{3.2}$$

where $C_1 = \frac{\pi}{a}\sqrt{\frac{k_x}{k_y}}$, $k_x = 5.0$ and $k_y = \epsilon$. The orthotropy $\frac{k_x}{k_y}$ of domain Ω_1 is chosen to be $5, 50, 500, 5000, 50000,$ and 500000 respectively. Using (3.2) we can see that the u_{EX} has a boundary layer with thickness of $\sqrt{\frac{k_y}{k_x}}$. In the extreme case of $\frac{k_x}{k_y} = 500,000$, the size of boundary layer is about 0.001414. In order for the mesh size h to be less than or equal to the thickness of the boundary layer we must employ 12 of nested refinement of the rectangular domain leading to a mesh of more than 16 million elements.

Here we will employ bilinear elements ($p = 1$) and meshes of rectangles as shown in the figure in Appendix A. For these meshes it is also possible to obtain an analytical expression for the finite element solution $u_{S^p_{\Delta_h}}$ of degree $p = 1$ in order to analyze the convergence and error estimation for the entire sequence of meshes. The detailed derivations are given in Appendix A. This analytical approach allows us to analyze the estimators without the effect of the roundoff error which must be addressed separately.

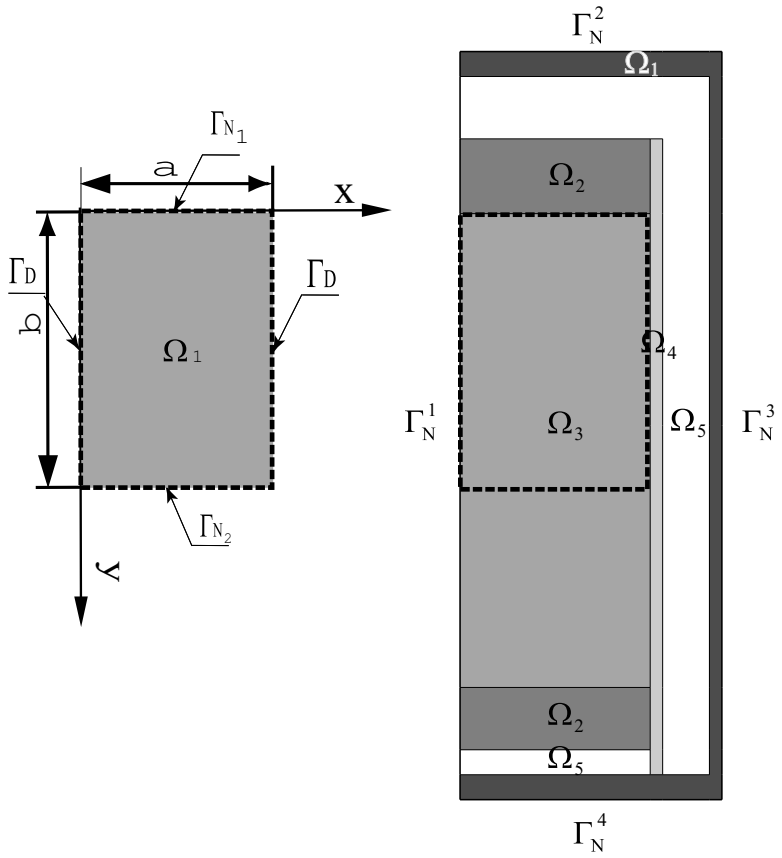

Fig. 3.1. Model problem with boundary layer. [1]

Tables 3.1, 3.2, and 3.3 respectively report the relative error in energy norm, H^1 norm, and L^2 norm of $e_{S^p_{\Delta_h}}$. Note that the number of elements from uniform mesh refinement can be up to 2^{22}. Figs. 3.2, 3.3, and 3.4 show the convergence with respect to the energy norm, the H^1 norm, and the L^2 norm respectively, for various values of the orthotropy $\frac{k_x}{k_y}$, Table 3.4 compares the characteristic thickness of boundary layer $\sqrt{\frac{k_y}{k_x}}$ with the mesh sizes for various orthotropies. It can be seen that the error in finite element solution is within its asymptotic range only when the element size is about the same order of magnitude of the characteristic size of bounday layer. In the case of extreme orthotropy $\frac{k_x}{k_y} = 500,0000$, the mesh has to be refined more than 10 times before the asymptotic range in the finite element solution can be reached.

Table 3.1. Model problem with boundary layer. The relative value of the energy norm of the error $E_{\mathcal{U}}^{rel} \stackrel{\text{def}}{=} ||e_{S^p_{\Delta_h}}||_{\mathcal{U}} \Big/ ||u_{EX}||_{\mathcal{U}} \times 100\%$ versus ϵ for $n = 1, 2, 3, ..., 11$.

$E_{\mathcal{U}}^{rel} = \frac{\|e_{S^p_{\Delta_h}}\|_{\mathcal{U}}}{\|u_{EX}\|_{\mathcal{U}}} \times 100\%$						
n	$\epsilon = 1$	$\epsilon = 0.1$	$\epsilon = 0.01$	$\epsilon = 0.001$	$\epsilon = 0.0001$	$\epsilon = 0.00001$
1	69.1313 %	89.4660 %	96.7135 %	98.9699 %	99.6753 %	99.8974 %
2	42.7122 %	75.6787 %	92.2717 %	97.5966 %	99.2455 %	99.7620 %
3	23.0459 %	54.7030 %	83.7747 %	94.9545 %	98.4254 %	99.5046 %
4	11.7749 %	32.7209 %	68.2975 %	89.6804 %	96.7988 %	98.9971 %
5	5.92049 %	17.3771 %	46.4308 %	79.2763 %	93.5120 %	97.9802 %
6	2.9645 %	8.8330 %	26.4375 %	61.2285 %	86.8616 %	95.9254 %
7	1.4827 %	4.4359 %	13.7627 %	38.9492 %	74.0325 %	91.7506 %
8	0.7414 %	2.2202 %	6.95780 %	21.2986 %	53.6895 %	83.3588 %
9	0.3707 %	1.1104 %	3.48856 %	10.9335 %	32.1221 %	67.8554 %
10	0.1853 %	0.5552 %	1.74543 %	5.50510 %	17.0546 %	45.9994 %
11	0.0926 %	0.2776 %	0.87285 %	2.75727 %	8.6733 %	26.1364 %

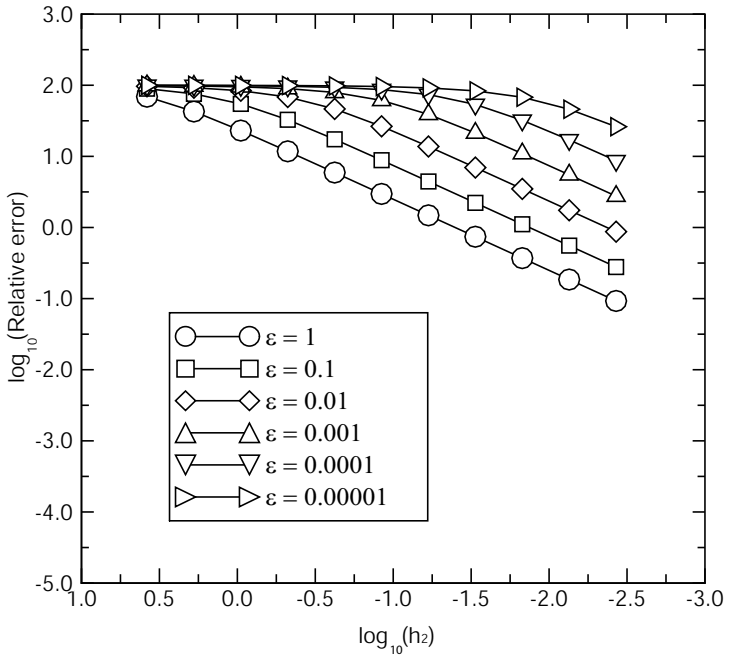

Fig. 3.2. Model problem with boundary layer. The convergence of $E_{\mathcal{U}}^{rel}$ versus $h_2 = \frac{b}{2^n}$, $n = 1, 2, ..., 11$ for various orthotropies ϵ. [1]

Table 3.2. Model problem with boundary layer. The relative value of the H_1 norm of the error $E_{H_1}^{rel} \stackrel{\text{def}}{=} ||e_{S^p_{\Delta_h}}||_{H^1} \Big/ ||u_{EX}||_{H^1} \times 100\%$, versus ϵ for $n = 1, 2, 3, ..., 11$.

$E_{H^1}^{rel} = \frac{\|e_{S^p_{\Delta_h}}\|_{H^1}}{\|u_{EX}\|_{H^1}} \times 100\%$						
n	$\epsilon = 1$	$\epsilon = 0.1$	$\epsilon = 0.01$	$\epsilon = 0.001$	$\epsilon = 0.0001$	$\epsilon = 0.00001$
1	76.0744 %	96.5228 %	99.6261 %	99.9621 %	99.9962 %	99.9996 %
2	50.0269 %	87.9535 %	98.4222 %	99.8306 %	99.9827 %	99.9983 %
3	27.9285 %	69.2108 %	94.3543 %	99.3245 %	99.9291 %	99.9928 %
4	14.4315 %	43.9841 %	83.0769 %	97.4929 %	99.7202 %	99.9711 %
5	7.27848 %	23.9441 %	61.1670 %	91.6191 %	98.9324 %	99.8859 %
6	3.6472 %	12.2611 %	36.5088 %	76.7868 %	96.1656 %	99.5569 %
7	1.8246 %	6.1684 %	19.3192 %	52.4480 %	87.8476 %	98.3375 %
8	0.9124 %	3.0890 %	9.8083 %	29.6933 %	69.2229 %	94.2256 %
9	0.4562 %	1.5451 %	4.9233 %	15.4030 %	43.9494 %	82.8197 %
10	0.2281 %	0.7726 %	2.4640 %	7.7762 %	23.9042 %	60.7737 %
11	0.1140 %	0.3863 %	1.2323 %	3.8976 %	12.2369 %	36.1724 %

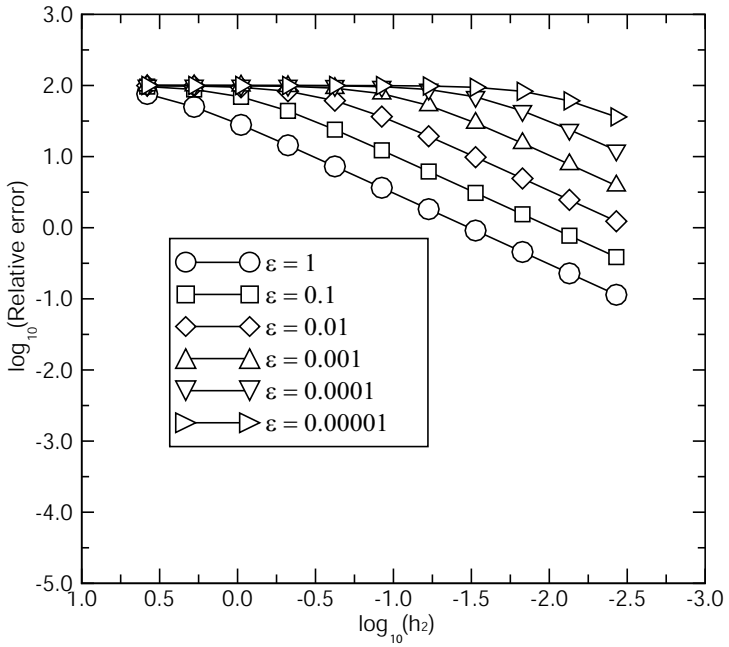

Fig. 3.3. Model problem with boundary layer. The convergence of $E_{H^1}^{rel}$ versus $h_2 = \frac{b}{2^n}$, $n = 1, 2, ..., 11$ for various orthotropies ϵ. [1]

Table 3.3. Model problem with boundary layer. The relative value of the L^2 norm of the error $E^{rel}_{L^2} = ||e_{S^p_{\Delta_h}}||_{L^2} \Big/ ||u_{EX}||_{L^2} \times 100\%$ versus ϵ for $n = 1, 2, 3, ..., 11$.

$E^{rel}_{L^2} = \frac{\|e_{S^p_{\Delta_h}}\|_{L^2}}{\|u_{EX}\|_{L^2}} \times 100\%$						
n	$\epsilon = 1$	$\epsilon = 0.1$	$\epsilon = 0.01$	$\epsilon = 0.001$	$\epsilon = 0.0001$	$\epsilon = 0.00001$
1	41.6445 %	77.1227 %	92.4684 %	97.5953 %	99.2375 %	99.7587 %
2	16.7169 %	57.0287 %	84.7956 %	95.0613 %	98.4267 %	99.5014 %
3	5.09582 %	31.4175 %	71.0879 %	90.2334 %	96.8573 %	99.0012 %
4	1.35193 %	11.7083 %	48.8778 %	81.0394 %	93.7649 %	98.0068 %
5	0.3433 %	3.3595 %	23.5617 %	64.5677 %	87.7457 %	96.0334 %
6	0.0861 %	0.8726 %	7.8547 %	39.9897 %	76.4266 %	92.1492 %
7	0.0215 %	0.2203 %	2.1492 %	16.8105 %	56.9569 %	84.6518 %
8	0.0053 %	0.0552 %	0.5504 %	5.1322 %	31.1975 %	70.8439 %
9	0.0013 %	0.0138 %	0.1384 %	1.3601 %	11.5431 %	48.4759 %
10	0.0003 %	0.0034 %	0.0346 %	0.3452 %	3.3010 %	23.2022 %
11	0.0001 %	0.0008 %	0.0086 %	0.0866 %	0.8565 %	7.6955 %

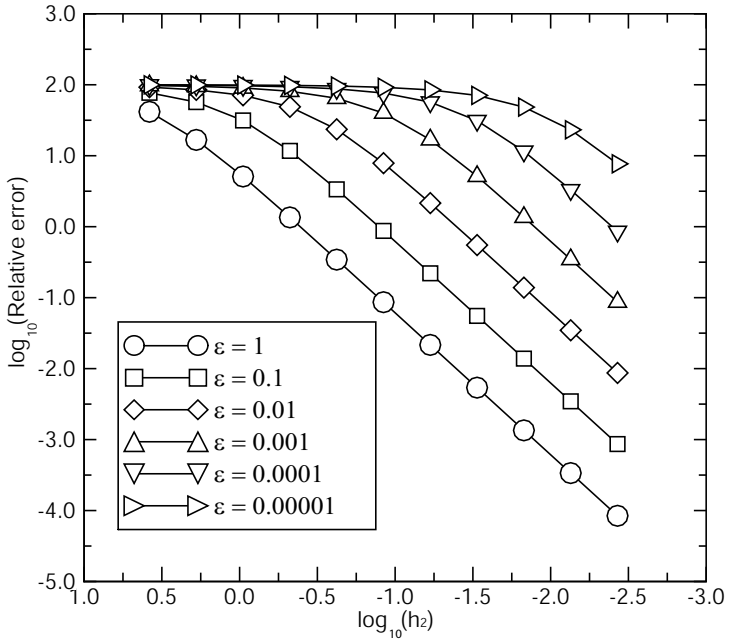

Fig. 3.4. Model problem with boundary layer. The convergence of $E^{rel}_{L^2}$ versus $h_2 = \frac{b}{2^n}$, $n = 1, 2, ..., 11$ for various orthotropies ϵ. [1]

Table 3.4. Model problem with boundary layer. Comparison between the element size at which the error in finite element solution is in asymptotic range and the characteristic thickness of the boundary layer with respect to different orthotropies $\frac{k_x}{k_y}$. $h_c = \frac{b}{2^{n_c}}$ is the element size in asymptotic range, n_c is the mesh refinement level and $\sqrt{\frac{k_y}{k_x}}$ is the characteristic thickness of the boundary layer.

ϵ	n_c	$h_c = \frac{b}{2^{n_c}}$	$\sqrt{\frac{k_y}{k_x}}$
1	2	1.8	0.44721360
0.1	4	0.45	0.14142136
0.01	6	0.1125	0.04472136
0.001	7	0.05625	0.01414214
0.0001	9	0.0140625	0.00447214
0.00001	10	0.00703125	0.00141421

The above framework allows us to analyze the effectivity of the estimators for the entire range of orthotropies without any effect from roundoff error. We will see that the estimator is reliable once the approximation has reached its asymptotic range. For simplicity we will illustrate this by employing the explicit estimator $\mathscr{E}^{EXPL}$ given below. Although there are some differences between the explicit residual estimators and the patch and subdomain implicit estimators considered earlier, the trend should be the same.

We have,

$$||e_{S^p_{\Delta_h}}|| \leq \mathscr{E}^{EXPL} = \sqrt{C_1\Big(\sum_{\tau}|\tau|^{\delta}||r_\tau||^2_{L^2(\tau)}\Big) + C_2\Big(\sum_{\tau}\big(\sum_{\varepsilon\subset\partial\tau}h_\varepsilon^{\alpha}\Big|\Big|\frac{J_\varepsilon^\tau}{\sqrt{2}}\Big|\Big|^2_{L^2(\varepsilon)}\big)\Big)} \quad (3.3)$$

where $||\cdot||$ here denotes the norm of interest, e.g. the energy, H^1, or L^2-norm.

$$r_\tau \stackrel{\text{def}}{=} f+\nabla\cdot\big(\mathbf{K}\nabla u_{S^p_{\Delta_h}}|_\tau\big), \qquad J^\tau_\varepsilon \stackrel{\text{def}}{=} \begin{cases} \Big(\mathbf{K}\nabla u_{S^p_{\Delta_h}}|_{\tau^*} - \mathbf{K}\nabla u_{S^p_{\Delta_h}}|_\tau\Big)\cdot\mathbf{n}_\varepsilon, & \varepsilon = \partial\tau^* \bigcap \partial\tau \\ \sqrt{2}\Big(g - \mathbf{K}\nabla u_{S^p_{\Delta_h}}\cdot\mathbf{n}_{\Gamma_N}\Big), & \varepsilon \subseteq \Gamma_N \end{cases} \tag{3.4}$$

The constants C_1, C_2, δ, and α have to be determined from a calibration of the estimator; for the proof of (3.3) in the case that $||\cdot||$ is the energy norm see [6] and the references therein. For linear finite element solution $p = 1$, $r_\tau \equiv 0$, and hence

$$||e_{S^p_{\Delta_h}}|| \leq \mathscr{E}^{\text{EXPL}} = \sqrt{C_2\Big(\sum_\tau \big(\sum_{\varepsilon\subset\partial\tau} h^\alpha_\varepsilon \Big|\Big|\frac{J^\tau_\varepsilon}{\sqrt{2}}\Big|\Big|^2_{L^2(\varepsilon)}\big)\Big)} \tag{3.5}$$

See Appendix B for more details.

Figs. 3.5, 3.6, and 3.7 illustrate the convergence of the effectivity indices for the explicit estimators for the energy, H^1, and L^2 norms of the error for various values of the orthotropy $\frac{k_x}{\epsilon}$. It can be seen that the effectivity indices of the energy norm and H^1 norm estimators converge to 1 while the effectivity index of the L^2 norm estimator converges to a value between 1.7 and 2. The reason for this behavior is due to the pollution error which is well known in the case of L^2 norm. This can be clearly seen by employing the interpolated exact solution to calculate the estimator as shown in Fig. 3.8, in which case the effectivity indices of $\mathscr{E}^{EXPL}_{L^2}$ converge to 1.

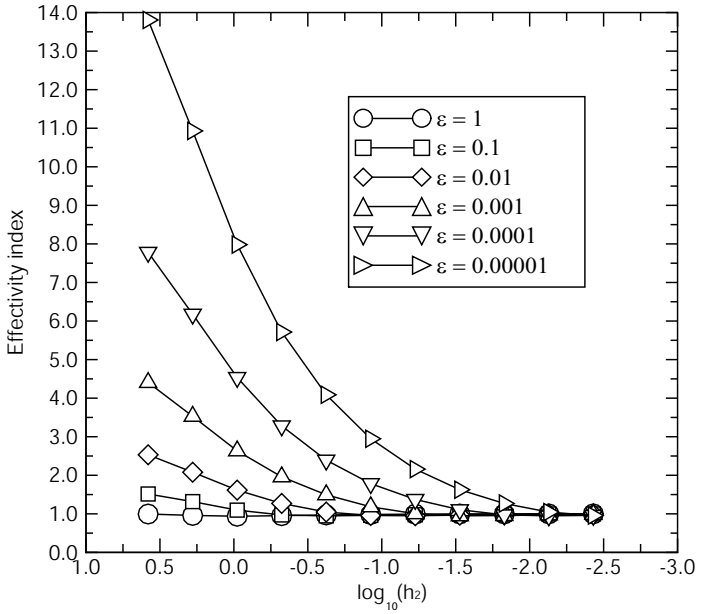

Fig. 3.5. Model problem with boundary layer. Effectivity indices $\kappa_{\mathcal{U}}^{EXPL} \stackrel{\text{def}}{=} \mathcal{C}_{\mathcal{U}}^{\text{EXPL}} / \left|\left| e_{S^p_{\Delta_h}} \right|\right|_{\mathcal{U}}$ for error measured in energy norm with respect to various mesh size $h_2 = \frac{b}{2^n}$, $n = 1, 2, ..., 11$ and different orthotropies $\frac{k_x}{k_y} = \frac{k_x}{\epsilon}$. [1]

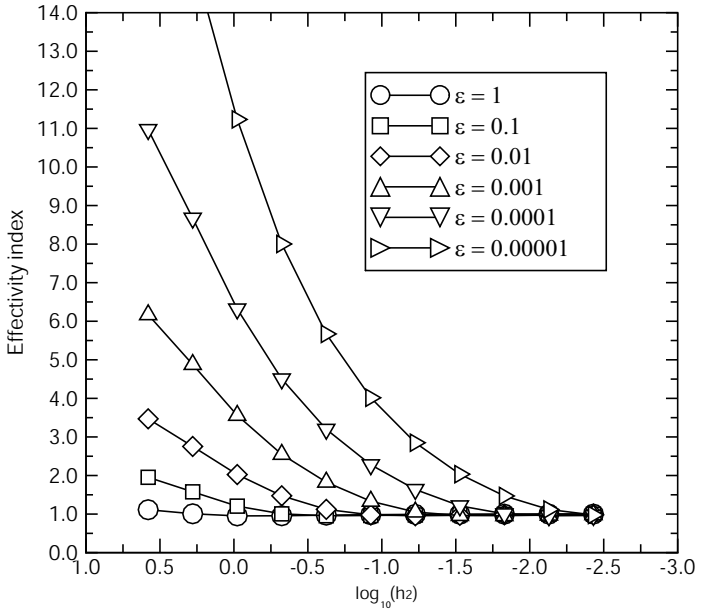

Fig. 3.6. Model problem with boundary layer. Effectivity indices $\kappa_{H^1}^{EXPL} \stackrel{\text{def}}{=} \mathcal{C}_{H_1}^{\text{EXPL}} / \left|\left| e_{S^p_{\Delta_h}} \right|\right|_{H_1}$ for error measured in H_1 norm with respect to various mesh size $h_2 = \frac{b}{2^n}$, $n = 1, 2, ..., 11$ and different orthotropies $\frac{k_x}{k_y} = \frac{k_x}{\epsilon}$. [1]

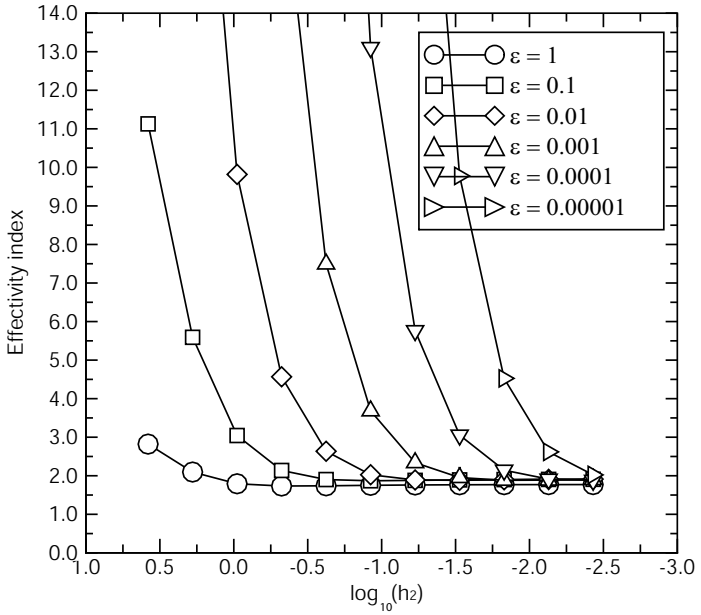

Fig. 3.7. Model problem with boundary layer. Effectivity indices $\kappa_{L^2}^{EXPL} \stackrel{\text{def}}{=} \mathscr{C}_{L^2}^{\text{EXPL}} / ||e_{S^p_{\Delta_h}}||_{L^2}$ for error measured in L^2 norm with respect to various mesh size $h_2 = \frac{b}{2^n}$, $n = 1, 2, ..., 11$ and different orthotropies $\frac{k_x}{k_y} = \frac{k_x}{\epsilon}$. [1]

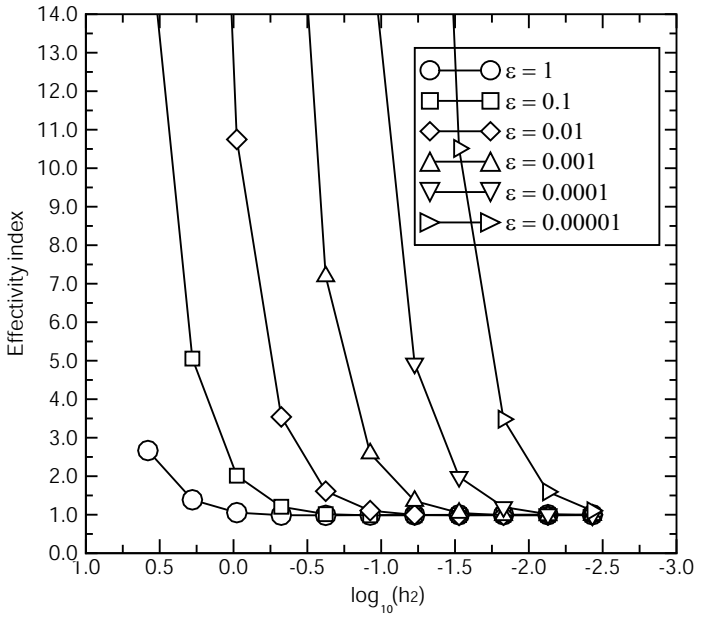

Fig. 3.8. Model problem with boundary layer. Effectivity indices $\kappa_{L^2}^{EXPL} \stackrel{\text{def}}{=} \mathscr{C}_{L^2}^{\text{EXPL}} / ||e_{S^p_{\Delta_h}}||_{L^2}$ for interpolation error measured in L^2 norm with respect to various mesh size $h_2 = \frac{b}{2^n}$, $n = 1, 2, ..., 11$ and different orthotropies $\frac{k_x}{k_y} = \frac{k_x}{\epsilon}$. [1]

Above we analyzed the effectivity indices of the explicit residual estimators which are upper bounds for the enery-norm of the error. Fig. 3.9 is an illustration of the convergence of the well known ZZ estimator (see [4–6, 9]) which is not an upper bound. It can be seen that ZZ estimator converges to the energy norm of the error from below as the mesh refinement level is increased. Again the finite element solution has to be in the asymptotic range before the good effectivity indices can be achieved.

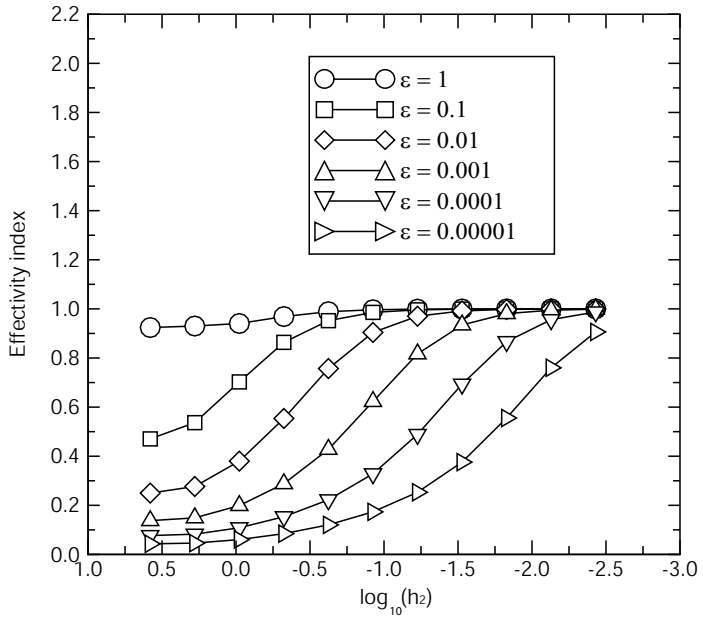

Fig. 3.9. Model problem with boundary layer. Effectivity indices of ZZ estimator $\kappa^{ZZ} \stackrel{\text{def}}{=} \mathscr{E}^{ZZ} / \left|\left| e_{S^p_{\Delta_h}} \right|\right|_{\mathscr{U}}$ with respect to various mesh size $h_2 = \frac{b}{2^n}$, $n = 1, 2, ..., 11$ and different orthotropies $\frac{k_x}{k_y} = \frac{k_x}{\epsilon}$. [1]

3.2 Model problem with interface layer

Above we have employed the simplest possible model problem of heat conduction in an orthotropic domain and we have clearly seen that the accuracy of the estimation is governed by the size of mesh relative to the size of the boundary layer. Let us now

employ another model problem which has an interface layer in the solution which is closer to the original battery model problem.

Example 3.2. *Model problem with interface layer.* We seek u such that

$$\begin{aligned} -\nabla \cdot \big(\mathbf{K}\ \nabla u\big) &= 0 \\ -k'_y \frac{\partial u}{\partial y} &= \sin(\frac{\pi}{a}x) \qquad \text{on } \Gamma_{N_1} \\ -k_y \frac{\partial u}{\partial y} &= 0 \qquad\qquad \text{on } \Gamma_{N_2} \\ u &= 0 \qquad\qquad \text{on } \Gamma_D \end{aligned} \tag{3.6a}$$

where k_x, k_y (resp. k'_x, k'_y) are the principal orthotropies in $\Omega_1 \stackrel{\text{def}}{=} (0,a)\times(0,b)$ (resp. $\Omega_2 \stackrel{\text{def}}{=} (0,a)\times(0,-d)$), where the relation of the problem domain with the thermal battery domain is shown in Fig. 3.10, and we have

$$u_{EX}(x,y) = \begin{cases} A\Big(e^{C_2(y-2b)} + e^{-C_2 y}\Big)\ \sin(\frac{\pi}{a}x) \quad (x,y)\ \in\ \Omega_1 \\ \\ \frac{e^{-C_1 d}}{k'_y C_1}\Big(B_1 e^{C_1 y} + B_2 e^{-C_1 y}\Big)\ \sin(\frac{\pi}{a}x) \quad (x,y)\ \in\ \Omega_2 \end{cases} \tag{3.7}$$

where

$$\begin{aligned} A &= \frac{2e^{-C_1 d}}{k'_y C_1\Big(1+e^{-2C_2 b}\Big)\Big(1-e^{-2C_1 d}\Big) + k_y C_2\Big(1+e^{-2C_1 d}\Big)\Big(1-e^{-2C_2 b}\Big)} \\ B_1 &= \frac{k'_y C_1\Big(1+e^{-2C_2 b}\Big) - k_y C_2\Big(1-e^{-2C_2 b}\Big)}{k'_y C_1\Big(1+e^{-2C_2 b}\Big)\Big(1-e^{-2C_1 d}\Big) + k_y C_2\Big(1+e^{-2C_1 d}\Big)\Big(1-e^{-2C_2 b}\Big)} \\ B_2 &= \frac{k'_y C_1\Big(1+e^{-2C_2 b}\Big) + k_y C_2\Big(1-e^{-2C_2 b}\Big)}{k'_y C_1\Big(1+e^{-2C_2 b}\Big)\Big(1-e^{-2C_1 d}\Big) + k_y C_2\Big(1+e^{-2C_1 d}\Big)\Big(1-e^{-2C_2 b}\Big)} \end{aligned}$$

with $C_1 = \sqrt{\frac{k'_x}{k'_y}}\frac{\pi}{a}$ and $C_2 = \sqrt{\frac{k_x}{k_y}}\frac{\pi}{a}$. The orthotropy $\frac{k_x}{k_y}$ of domain Ω_1 is chosen to be $5, 50, 500, 5000, 50000,$ and 500000 respectively with $k_x = 5$ and $k_y = \epsilon$.

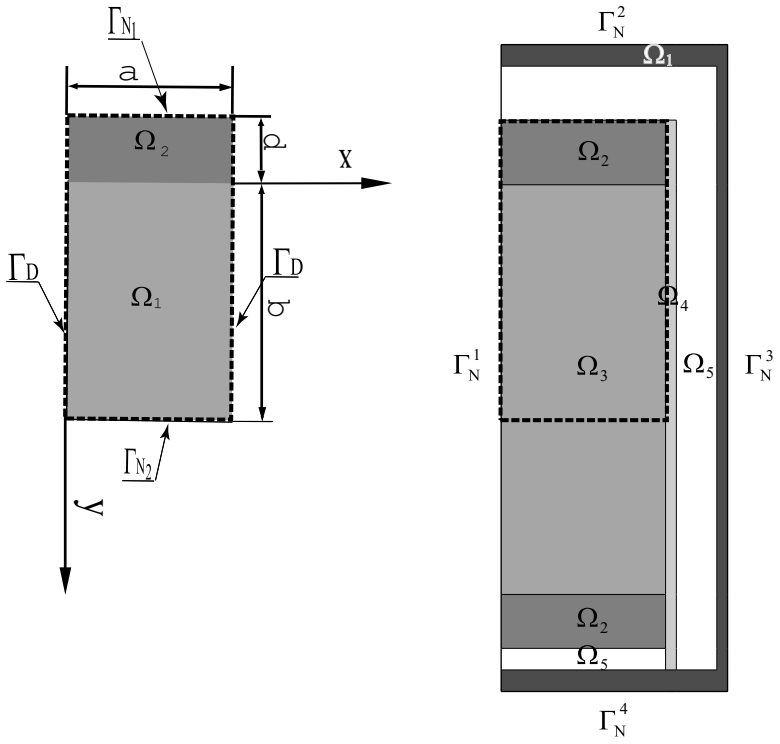

Fig. 3.10. Model problem with interface layer. [1]

Once more, we employed bilinear finite elements ($p = 1$) and meshes of rectangles obtained from the nested refinement of an initial coarse mesh of rectangles, and obtained analytical expressions for the finite element solution as discussed in Appendix C. Tables 3.5, 3.6, and 3.7 respectively report the energy norm, H^1 norm, and L^2 norm of e^1_Δ while their corresponding convergence curves are illustrated in Figs. 3.11, 3.12, and 3.13 respectively.

Table 3.5. Model problem with interface layer. The relative value of the energy norm of the error $E^{rel}_{\mathcal{U}} = ||e_{S^p_{\Delta_h}}||_{\mathcal{U}} \Big/ ||u_{EX}||_{\mathcal{U}} \times 100\%$ versus ϵ for $n = 1, 2, 3, ..., 11$.

$E^{rel}_{\mathcal{U}} = \frac{\|e_{S^p_{\Delta_h}}\|_{\mathcal{U}}}{\|u_{EX}\|_{\mathcal{U}}} \times 100\%$						
n	$\epsilon = 1$	$\epsilon = 0.1$	$\epsilon = 0.01$	$\epsilon = 0.001$	$\epsilon = 0.0001$	$\epsilon = 0.00001$
1	47.6999 %	47.7547 %	47.7857 %	47.7980 %	47.8023 %	47.8036 %
2	24.4360 %	24.5283 %	24.5946 %	24.6230 %	24.6330 %	24.6362 %
3	12.2890 %	12.3714 %	12.4688 %	12.5219 %	12.5418 %	12.5484 %
4	6.15340 %	6.20494 %	6.30360 %	6.38705 %	6.42378 %	6.43656 %
5	3.07796 %	3.10541 %	3.17527 %	3.27383 %	3.33281 %	3.35527 %
6	1.53907 %	1.55311 %	1.59334 %	1.68047 %	1.76480 %	1.80409 %
7	0.76954 %	0.77660 %	0.79760 %	0.85421 %	0.94423 %	1.00429 %
8	0.38477 %	0.38830 %	0.39892 %	0.42983 %	0.49879 %	0.57257 %
9	0.19238 %	0.19415 %	0.19947 %	0.21534 %	0.25635 %	0.32353 %
10	0.09619 %	0.09707 %	0.09973 %	0.10772 %	0.12938 %	0.17484 %
11	0.04809 %	0.04853 %	0.04986 %	0.05386 %	0.06486 %	0.09024 %

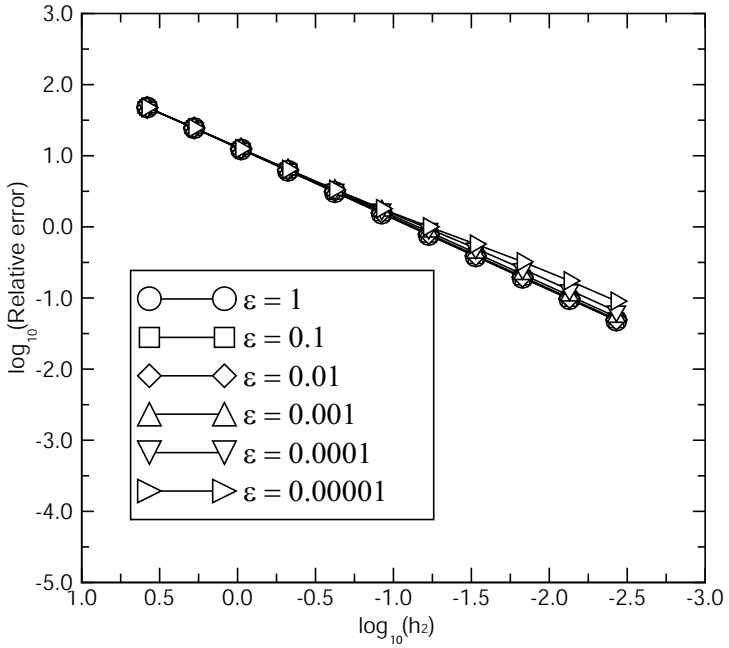

Fig. 3.11. Model problem with interface layer. The convergence of $E^{rel}_{\mathcal{U}}$ versus $h_2 = \frac{b}{2^n}$, $n = 1, 2, ..., 11$ for various orthotropies ϵ. [1]

Table 3.6. Model problem with interface layer. The relative value of the H^1 norm of the error $E^{rel}_{H^1} = ||e_{S^p_{\Delta_h}}||_{H^1} \Big/ ||u_{EX}||_{H^1} \times 100\%$ versus ϵ for $n = 1, 2, 3, ..., 11$.

$E^{rel}_{H^1} = \frac{\|e_{S^p_{\Delta_h}}\|_{H^1}}{\|u_{EX}\|_{H^1}} \times 100\%$						
n	$\epsilon = 1$	$\epsilon = 0.1$	$\epsilon = 0.01$	$\epsilon = 0.001$	$\epsilon = 0.0001$	$\epsilon = 0.00001$
1	48.8323 %	49.1054 %	50.0292 %	52.7528 %	59.5515 %	71.8639 %
2	25.5305 %	26.0349 %	28.0426 %	33.5997 %	45.4640 %	63.6854 %
3	12.9612 %	13.5795 %	17.0949 %	25.5107 %	40.4797 %	61.1118 %
4	6.50748 %	7.00688 %	11.8718 %	22.4378 %	38.8051 %	60.2897 %
5	3.25721 %	3.55289 %	8.11422 %	20.4900 %	37.8452 %	59.8280 %
6	1.62903 %	1.78402 %	4.75212 %	17.2891 %	36.4949 %	59.2095 %
7	0.814568 %	0.89301 %	2.50210 %	11.9046 %	33.5393 %	58.0194 %
8	0.407290 %	0.44663 %	1.26867 %	6.75239 %	26.7948 %	55.4472 %
9	0.20364 %	0.22333 %	0.63660 %	3.50365 %	17.1093 %	49.2612 %
10	0.10182 %	0.11166 %	0.31858 %	1.76889 %	9.31418 %	36.5633 %
11	0.05091 %	0.05583 %	0.15932 %	0.88661 %	4.76857 %	21.8293 %

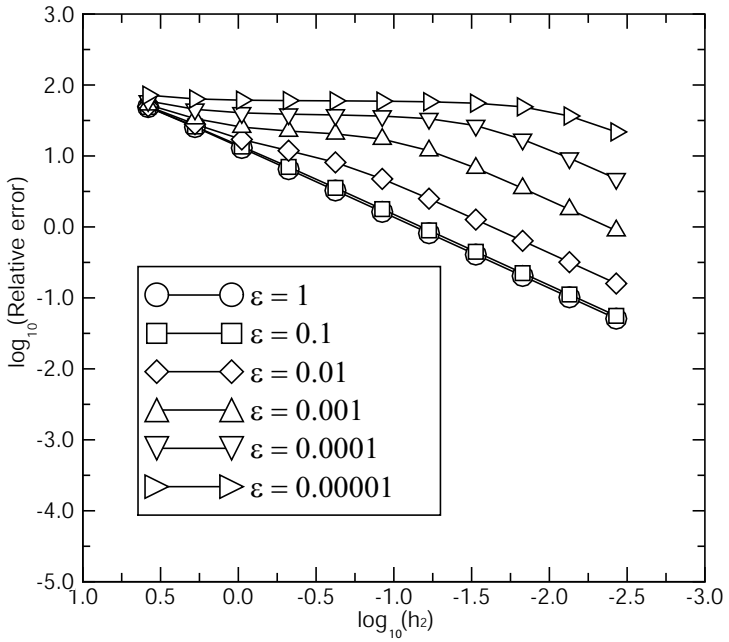

Fig. 3.12. Model problem with interface layer. The convergence of $E^{rel}_{H^1}$ versus $h_2 = \frac{b}{2^n}$, $n = 1, 2, ..., 11$ for various orthotropies ϵ. [1]

Table 3.7. Model problem with interface layer. The relative value of the L^2 norm of the error $E^{rel}_{L^2} = ||e_{S^p_{\Delta_h}}||_{L^2} \Big/ ||u_{EX}||_{L^2} \times 100\%$ versus for $n = 1, 2, 3, ..., 11$.

$E^{rel}_{L^2} = \frac{\|e_{S^p_{\Delta_h}}\|_{L^2}}{\|u_{EX}\|_{L^2}}\%$						
n	$\epsilon = 1$	$\epsilon = 0.1$	$\epsilon = 0.01$	$\epsilon = 0.001$	$\epsilon = 0.0001$	$\epsilon = 0.00001$
1	20.5214 %	20.9277 %	21.1552 %	21.2441 %	21.2787 %	21.2855 %
2	5.31980 %	5.89910 %	6.54323 %	6.83128 %	6.93297 %	6.96465 %
3	1.35197 %	1.86176 %	3.05850 %	3.67595 %	3.89132 %	3.96035 %
4	0.33965 %	0.56622 %	1.64072 %	2.49834 %	2.81965 %	2.92416 %
5	0.08505 %	0.15319 %	0.68628 %	1.55962 %	1.99624 %	2.14435 %
6	0.02126 %	0.03917 %	0.21439 %	0.78512 %	1.30863 %	1.51338 %
7	0.00531 %	0.00985 %	0.05744 %	0.29076 %	0.75042 %	1.01904 %
8	0.00132 %	0.00246 %	0.01462 %	0.08437 %	0.33773 %	0.63433 %
9	0.00033 %	0.00061 %	0.00367 %	0.02202 %	0.11284 %	0.33711 %
10	0.00008 %	0.00015 %	0.00091 %	0.00556 %	0.03113 %	0.13639 %
11	0.00002 %	0.00003 %	0.00022 %	0.00139 %	0.00799 %	0.04195 %

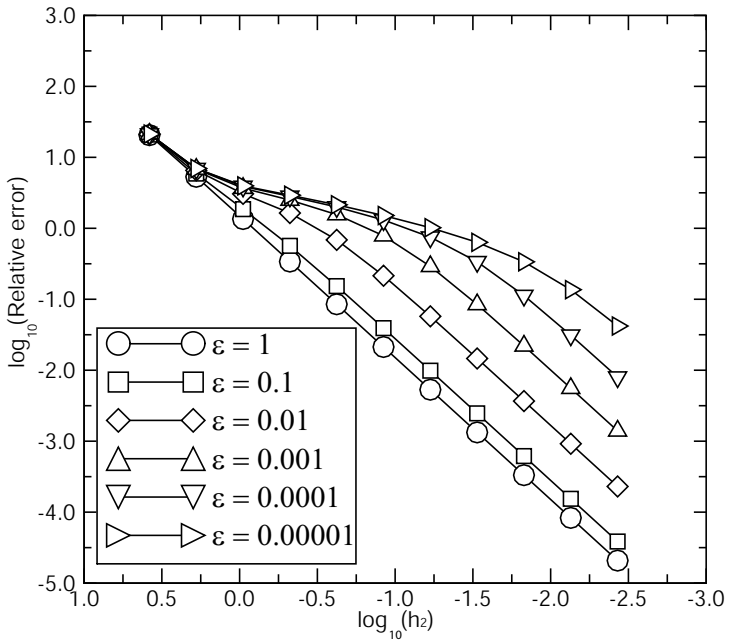

Fig. 3.13. Model problem with interface layer. The convergence of $E^{rel}_{L^2}$ versus $h_2 = \frac{b}{2^n}$, $n = 1, 2, ..., 11$ for various orthotropies ϵ. [1]

From the convergence curve as shown Fig. 3.11 in terms of energy norm, it can be seen that the solutions from different orthotropies converge in the same manner before the $7th$ mesh refinement is reached since the error contribution from Ω_2 is dominant. However, the solutions in the cases of $\epsilon = 0.0001, 0.00001$ converge in a different way once the error from Ω_2 is killed and the error from Ω_1 becomes dominant after the $7th$ mesh refinement.

Fig. 3.12 is the illustration of convergence curve in H^1 norm. It can be seen that for low orthotropies with ϵ equal to 1 and 0.1, the error measured in H^1 norm from Ω_2 is dominant for all the mesh refinements, and hence the H^1 convergence is basically determined by the error from Ω_2. As the orthotropies go up, the error contribution from Ω_1 becomes dominant quickly and the convergence behavior is controlled by the error from Ω_1, which is similar to Example 3.1 as shown in Figs. 3.2, 3.3, and 3.4. Note that for $\epsilon = 0.01, 0.001, 0.0001$ the number of mesh refinements for the error from Ω_1 to become dominant and the error from Ω_2 to be killed is 3, 2, and 1 respectively. In the case of $\epsilon = 0.00001$, the error from Ω_1 is dominant for all the mesh refinements, which means the convergence behavior is completely controlled by the error in highly orthotropic Ω_1. Similar convergence behavior can also be observed in the case of the error measured in L^2 norm as shown in Fig. 3.13.

The explicit estimator as defined in example 3.1 is employed to observe the asymptotic behavior in the existence of interface layer as shown in Figs. 3.14, 3.15, and 3.16 with calibration carried out on domain Ω_1 and Ω_2 separately. It should be noted that explicit estimator is not necessary an upper bound since the calibration does not enforce the continuity condition at the interface. Again we can observe that the effectivity index of the L^2 norm estimator does not converge 1 due to the pollution error. If we employ the interpolated exact solution, we can see that the effectivity index of $\mathscr{E}_{L^2}^{EXPL}$ converges to 1 with the refinement of the mesh as shown in Fig. 3.17.

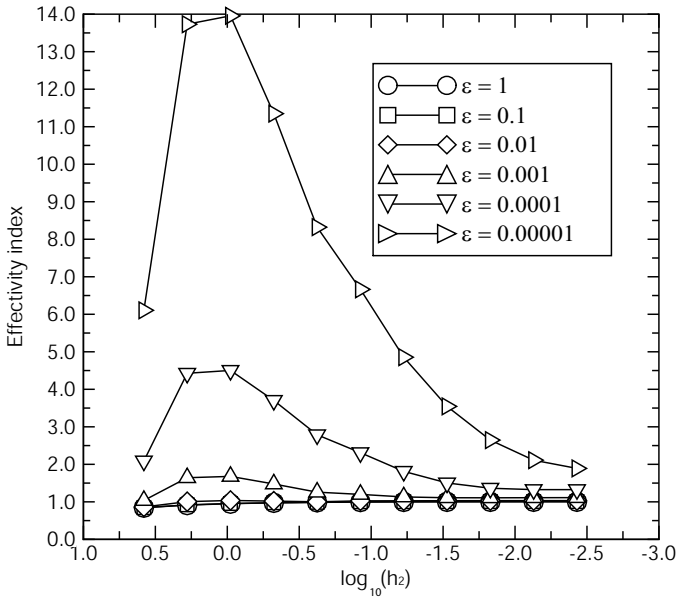

Fig. 3.14. Model problem with interface layer. Effectivity indices $\kappa_{\mathcal{U}}^{EXPL} = \mathscr{E}_{\mathcal{U}}^{\mathrm{EXPL}} / \left|\left| e_{S^p_{\Delta_h}} \right|\right|_{\mathcal{U}}$ for error measured in energy norm with respect to various mesh size $h_2 = \frac{b}{2^n}$, $n = 1, 2, ..., 11$ and different orthotropies $\frac{k_x}{k_y} = \frac{k_x}{\epsilon}$. [1]

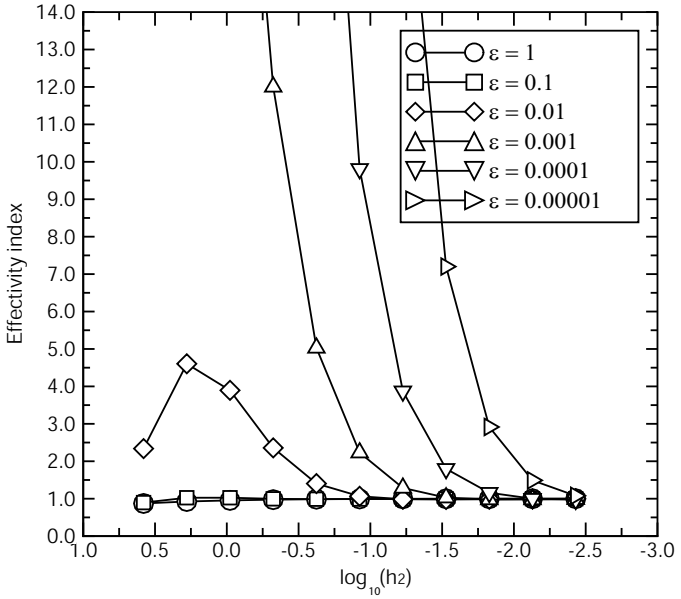

Fig. 3.15. Model problem with interface layer. Effectivity indices $\kappa_{H^1}^{EXPL} = \mathscr{E}_{H_1}^{\mathrm{EXPL}} / \left|\left| e_{S^p_{\Delta_h}} \right|\right|_{H_1}$ for error measured in H_1 norm with respect to various mesh size $h_2 = \frac{b}{2^n}$, $n = 1, 2, ..., 11$ and different orthotropies $\frac{k_x}{k_y} = \frac{k_x}{\epsilon}$. [1]

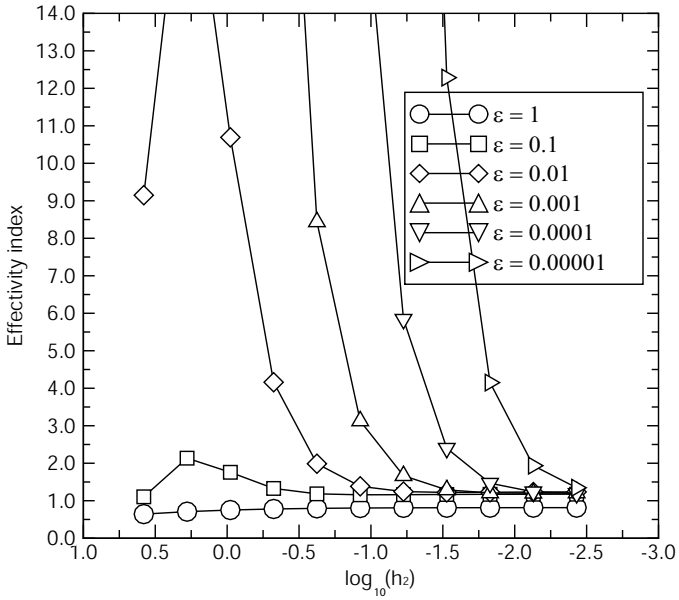

Fig. 3.16. Model problem with interface layer. Effectivity indices $\kappa_{L^2}^{EXPL} = \mathscr{C}_{L^2}^{\mathrm{EXPL}} / \left|\left| e_{S_{\Delta_h}^p} \right|\right|_{L^2}$ for error measured in L^2 norm with respect to various mesh size $h_2 = \frac{b}{2^n}$, $n = 1, 2, ..., 11$ and different orthotropies $\frac{k_x}{k_y} = \frac{k_x}{\epsilon}$. [1]

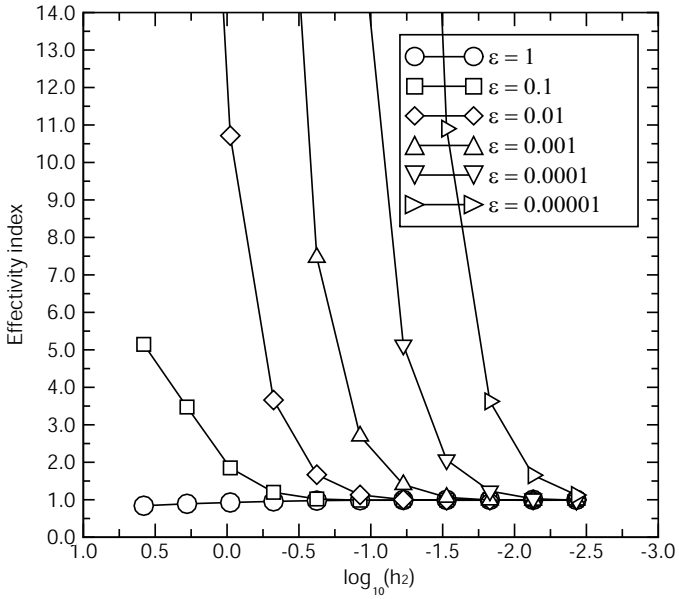

Fig. 3.17. Model problem with interface layer. Effectivity indices $\kappa_{L^2}^{EXPL} = \mathscr{C}_{L^2}^{\mathrm{EXPL}} / \left|\left| e_{S_{\Delta_h}^p} \right|\right|_{L^2}$ for interpolation error measured in L^2 norm with respect to various mesh size $h_2 = \frac{b}{2^n}$, $n = 1, 2, ..., 11$ and different orthotropies $\frac{k_x}{k_y} = \frac{k_x}{\epsilon}$. [1]

3.3 A posteriori error estimation of the two model problems

Above, we have analyzed the effectivity indices of explicit and ZZ estimators for the simplest possible model problems, Example 3.1 and 3.2. We will now employ exact Neumann element residual estimator and Neumann subdomain residual estimator for the above-mentioned two model problems. In the computations below we employed finite element solution computed by employing a direct solver as in the earlier computations for the thermal battery model problem.

It can be seen that for the two model problems in the case of high orthotropy the boundary layer has the characteristic thickness of $\sqrt{\frac{k_y}{k_x}}$. To obtain a converged finite element solution, the element size along the direction of heat conduction coefficient $k_y = \epsilon$ has to be about the same magnitude of the characteristic thickness as shown in Table 3.4.

It is known that for the implicit estimator an element residual problem needs to be solved. For Neumann element/patch residual estimator, the residual problem usually has pure Neumann boundary condition, which can pose a problem in calculating the exact estimators due to the boundary layer effect. The conjecture is that to obtain the exact estimator for Neumann element residual estimator the mesh size has to be about the magnitude of the characteristic thickness in solving the local residual problem. However for Neumann subdomain residual estimator, there is no boundary layer problem since the local residual problem has homogeneous Neumann boundary condition.

In order to check our conjecture, we considered the coarse meshes with two levels of refinement for both model problems employed overkill to obtain the exact Neumann element/subdomain residual estimators using overkill meshes shown in Figs. 3.18 and 3.19 for boundary layer and interface layer problems respectively. One type of overkill mesh is to uniformly refine each element three times and the polynomial order is 8 while the other type of mesh is obtained by adaptively refining the element edges having the boundary layer with polynomial order equal to 3. For the adaptive mesh, the smallest element size is $\frac{h_2}{2^7}$ and therefore for orthotropy $\frac{k_x}{k_y}$ lower than $5,000$, namely $\epsilon < 0.001$, the estimator should be exact as indicated in Table 3.4. The exact Neumann element/subdomain residual estimators based on two types of overkill meshes are listed in Tables 3.8 and 3.9. It can be seen that the boundary layer has negligible effect on the accuracy of the exact estimators and hence the uniform overkill mesh can be employed to obtain the exact estimator.

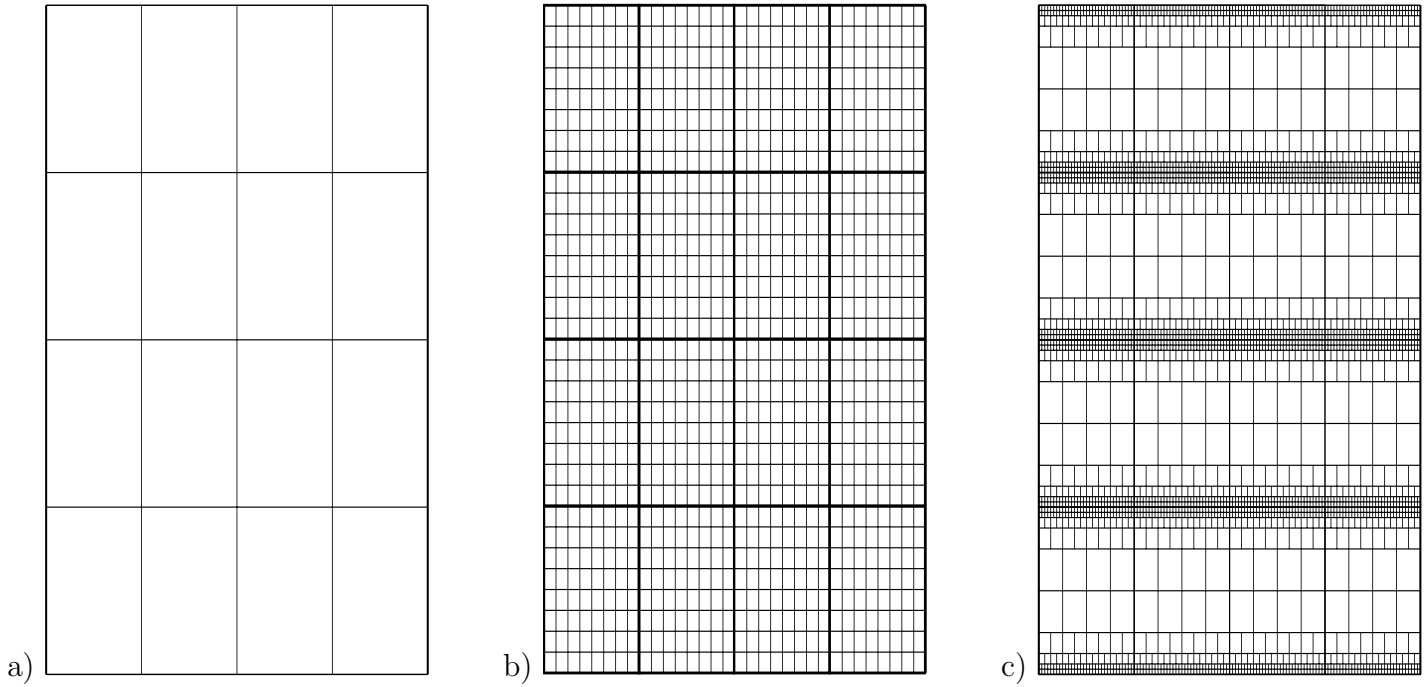

Fig. 3.18. Model problem with boundary layer. a)Mesh for linear finite element solution; b)Uniform mesh for exact Neumann element/subdomain residual restimator estimator. The uniform mesh with polynomial order equal to 8 is obtained by refining uniformly three times for the finite element solution mesh; c)Adpative mesh for exact Neumann element/subdomain residual estimator. The adaptive mesh with polynomial order equal to 3 is obtained by refining adaptively five times for the finite element solution mesh along the ϵ direction which results in the smallest size $\frac{h_2}{2^7}$. [1]

Table 3.8. Model problem with boundary layer. Exact Neumann element residual estimator $\mathscr{E}_{\Delta_h}^{\text{Neum}}$ and exact Neumann subdomain residual estimator $\mathscr{E}_{Subd}^{\text{Neum,II}}$ based on uniform and adaptive overkill meshes. The uniform mesh is from the three further uniform refinements of the finite element solution mesh with polynomial order equal to 8 while the adaptive mesh is obtained by refining adaptively the finite element solution mesh along the direction of ϵ five more times with polynomial order equal to 3. For adaptive overkill mesh the smallest mesh size along the ϵ direction is $\frac{h_2}{2^7}$.

	$\mathscr{E}_{\Delta_h}^{\text{Neum}}$		$\mathscr{E}_{Subd}^{\text{Neum,II}}$	
ϵ	Uniform Mesh	Adaptive Mesh	Uniform Mesh	Adaptive Mesh
1	7.31353267E − 01	7.31355446E − 01	7.02505141E − 01	7.02505104E − 01
0.1	2.78092205E + 00	2.78097757E + 00	2.37541117E + 00	2.37540563E + 00
0.01	8.97043367E + 00	8.97200650E + 00	6.27822847E + 00	6.27871385E + 00
0.001	2.81455046E + 01	2.81794157E + 01	1.68732637E + 01	1.69207737E + 01
0.0001	8.86745092E + 01	8.87515113E + 01	4.88178399E + 01	4.95042831E + 01
0.00001	2.80258825E + 02	2.80298061E + 02	1.50865404E + 02	1.51646393E + 02

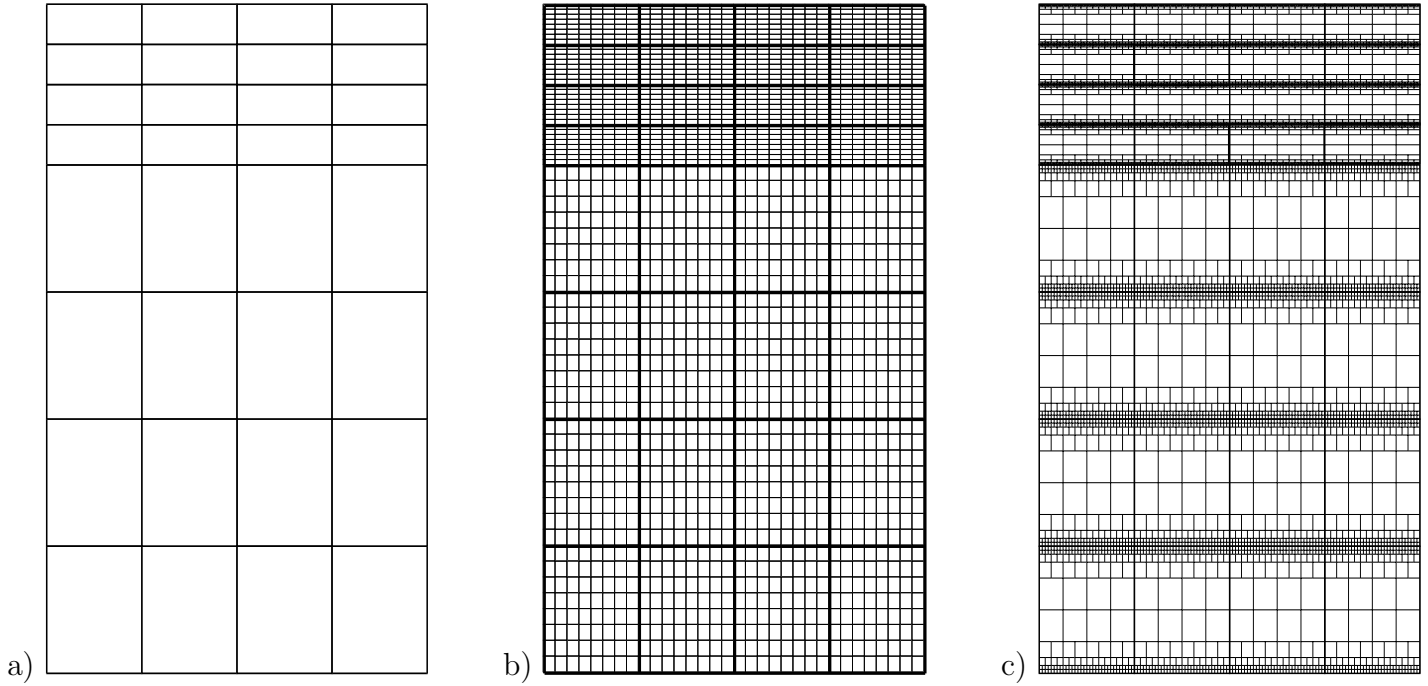

Fig. 3.19. Model problem with interface layer. a)Mesh for linear finite element solution; b)Uniform mesh for exact Neumann element/subdomain residual restimator estimator. The uniform mesh with polynomial order equal to 8 is obtained by refining uniformly three times for the finite element solution mesh; c)Adpative mesh for exact Neumann element/subdomain residual estimator. The adaptive mesh with polynomial order equal to 3 is obtained by refining adaptively five times for the finite element solution mesh along the ϵ direction which results in the smallest size $\frac{h_2}{2^7}$. [1]

Table 3.9. Model problem with interface layer. Exact Neuman element residual estimator $\mathscr{E}_{\Delta_h}^{\text{Neum}}$ and exact Neumann subdomain residual estimator $\mathscr{E}_{Subd}^{\text{Neum,II}}$ based on uniform and adaptive overkill meshes. The uniform mesh is from the three further uniform refinements of the finite element solution mesh with polynomial order equal to 8 while the adaptive mesh is obtained by refining adaptively the finite element solution mesh along the direction of ϵ five more times with polynomial order equal to 3. For adaptive overkill mesh the smallest mesh size along the ϵ direction is $\frac{h_2}{2^7}$.

	$\mathscr{E}_{\Delta_h}^{\text{Neum}}$		$\mathscr{E}_{Subd}^{\text{Neum,II}}$	
ϵ	Uniform Mesh	Adaptive Mesh	Uniform Mesh	Adaptive Mesh
1	3.92759857E − 01	3.92758113E − 01	3.88612634E − 01	3.88611413E − 01
0.1	3.95323230E − 01	3.95345453E − 01	3.90233982E − 01	3.90243604E − 01
0.01	4.15460932E − 01	4.15631419E − 01	3.96739178E − 01	3.96794280E − 01
0.001	5.75903418E − 01	5.77373696E − 01	4.50614912E − 01	4.51054192E − 01
0.0001	1.38276655E + 00	1.38838225E + 00	8.10576902E − 01	8.12980909E − 01
0.00001	4.20828043E + 00	4.22367882E + 00	2.27950171E + 00	2.28799193E + 00

Figs. 3.20 and 3.21 are the effectivity indices of Neumann element residual estimator $\mathscr{E}_{\Delta_h}^{\text{Neum}}$ and Neumann subdomain residual estimator $\mathscr{E}_{Subd}^{\text{Neum,II}}$ for the one battery domain problem. The effectivity indices for both exact estimators are equal to 1 for first level of mesh refinement because in this case the error estimation recovers the exact error obtained from the overkill. In comparison of the convergence curves as shown in Figs. 3.2, 3.3, and 3.4, it can be seen that the effectivity indices for both estimators are close to 1 once the finite element solution is in asymptotic range. For instance for $\epsilon = 0.001$, i.e. the orthotropy equal to 5000, the finite element solution starts to converge at the $4th$ level of refinement and the corresponding effectivity indices for both exact estimators are close to 1.9. At the $5th$ level of refinement when the convergence behavior becomes significant, the effectivity indices for both exact estimators are close to 1.5. It can be expected that the effectivity indices for both estimators can be close to 1 at the $6th$ level of refinements where the finite element solution falls into asymptotic range. This fact is obvious in the case of $\epsilon = 0.01$ in which the finite element solution is asymptotic range at the $5th$ iteration and the corresponding effectivity indices for both estimators are close to 1. It can be anticipated that for the extreme orthotropies with ϵ equal to 0.0001 and 0.00001 the effectivity indices for both estimators will be close to one once the finite element solution is in the asymptotic range.

Figs. 3.22 and 3.23 illustrate the effectivity indices of Neumann element residual estimator $\mathscr{E}_{\Delta_h}^{\text{Neum}}$ and Neumann subdomain residual estimator $\mathscr{E}_{Subd}^{\text{Neum,II}}$ for the two battery domain problem. It can be seen that the convergence curve measured in energy norm as shown in Fig. 3.14 cannot provide any indication about the performance of the two estimators since the curve indicates that the finite element solution is in asymptotic range for all levels of mesh refinements.

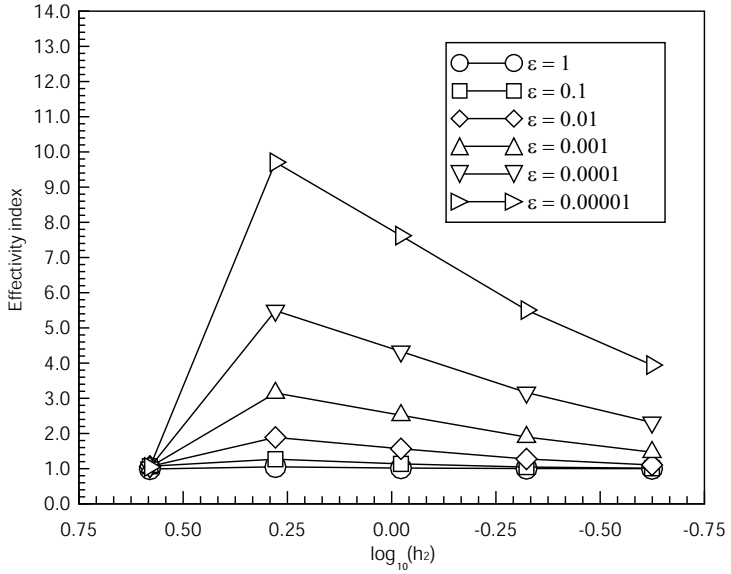

Fig. 3.20. Model problem with boundary layer. The effectivity indices of Neumann element residual estimator $\mathscr{E}_{\Delta_h}^{\mathrm{Neum}}$ with respect to different orthotropies and mesh sizes. [1]

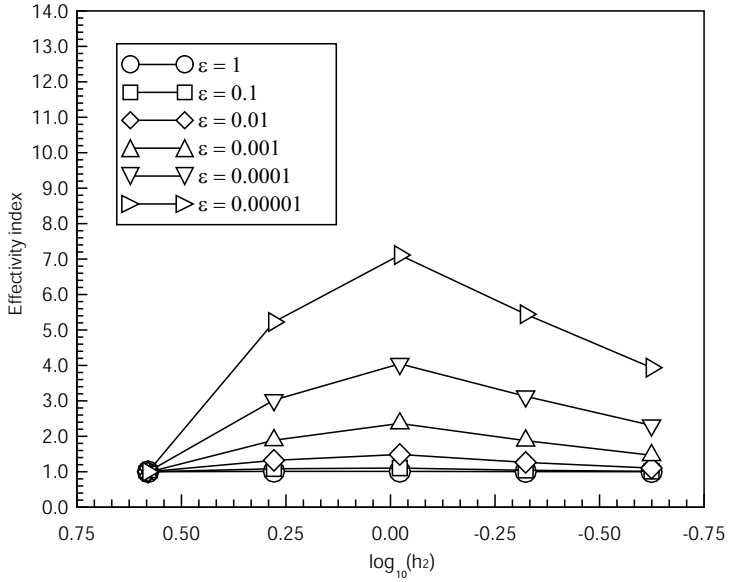

Fig. 3.21. Model problem with boundary layer. The effectivity indices of exact Neumann subdomain residual estimator $\mathscr{E}_{Subd}^{\mathrm{Neum,II}}$ with respect to different orthotropies and mesh sizes. [1]

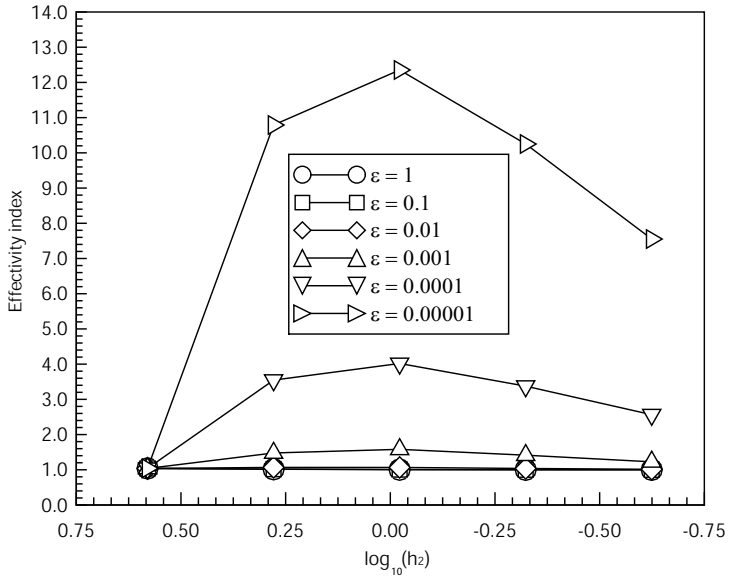

Fig. 3.22. Model problem with interface layer. The effectivity indices of exact Neumann element residual estimator $\mathscr{E}_{\Delta_h}^{\mathrm{Neum}}$ with respect to different orthotropies and mesh sizes. [1]

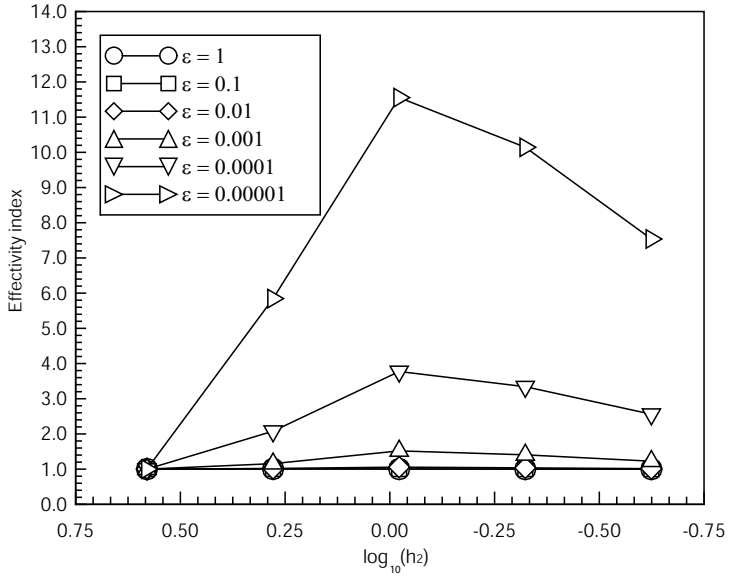

Fig. 3.23. Model problem with interface layer. The effectivity indices of exact Neumann subdomain residual estimator $\mathscr{E}_{Subd}^{\mathrm{Neum,II}}$ with respect to different orthotropies and mesh sizes. [1]

CHAPTER IV

GUARANTEED ERROR ESTIMATION FOR SEMI-DISCRETE SOLUTIONS OF PARABOLIC PROBLEMS BASED ON ELLIPTIC RECONSTRUCTION

4.1 Model problem, semi-discrete solutions, and postprocessing based on elliptic reconstruction

Let Ω be a bounded two-dimensional polygonal domain which consists of several material subdomains, Ω_i, $i = 1, ..., nsubd$, with boundary $\partial\Omega$ consisting of the Dirichlet part Γ_D, and the Neumann part Γ_N, namely, $\partial\Omega = \Gamma_D \cup \Gamma_N$, and $\Gamma_{ij} \stackrel{\text{def}}{=} \partial\Omega_i \cap \partial\Omega_j$, the intersection of $\partial\Omega_i$, and $\partial\Omega_j$, which could be empty. Let $Q_T \stackrel{\text{def}}{=} \Omega \times (0, T)$ denote the space-time domain. We will be interested in solving the transient heat conduction problem with the orthotropic Laplacian in Ω given by:

Find $u = u(\mathbf{x}, t)$, such that

$$-\nabla \cdot (\mathbf{K}_i \, \nabla u) + \gamma_i \frac{\partial u}{\partial t} = f \qquad \text{in} \;\; Q_T^i \stackrel{\text{def}}{=} \Omega_i \times (0, T), \qquad i = 1, ..., nsubd \tag{4.1a}$$

$$u = 0 \qquad \text{on} \;\; \Gamma_D \times (0, T) \tag{4.1b}$$

$$\mathbf{K}_i(s) \nabla u \cdot \mathbf{n} = g - \alpha(s) u \qquad \text{on} \;\; \big(\Gamma_N \cap \partial\Omega_i\big) \times (0, T) \tag{4.1c}$$

$$u(\cdot, 0) = 0 \qquad \text{in} \;\; \Omega \tag{4.1d}$$

where $\mathbf{n}$ is the exterior unit normal.

From [49] there exists a solution u of (4.1), which satisfies the variational equation

$$\big(\gamma \frac{\partial u}{\partial t}, v\big)_{L^2(\Omega)} + \mathcal{B}_\Omega(u, v) = \mathcal{L}(v) \qquad \forall v \in \mathcal{U}(\Omega), \qquad \forall t \in (0, T) \tag{4.2}$$

where

$$\big(\gamma\frac{\partial u}{\partial t},v\big)_{L^2(\Omega)} \stackrel{\text{def}}{=} \sum_{i=1}^{nsubd}\int_{\Omega_i}\gamma_i\frac{\partial u}{\partial t}v \tag{4.3}$$

The semi-discrete finite element solution is defined as the solution of the following problems

Find $u_{S^p_{\Delta_h}} \in S^p_{\Delta_h}$, such that

$$\big(\gamma\frac{\partial}{\partial t}u_{S^p_{\Delta_h}},v\big)_{L^2(\Omega)} + \mathcal{B}_\Omega(u_{S^p_{\Delta_h}},v) = \mathcal{L}(v) \qquad \forall v \in S^p_{\Delta_h}, \qquad \forall t \in (0,T) \tag{4.4}$$

where $S^p_{\Delta_h} \subset \mathcal{U}(\Omega)$ is the finite element space defined using tensor-product rectangular elements of degree p over mesh Δ_h.

The post-processed or reconstructed solution $\hat{u}$ is defined by, [36]

Find $\hat{u} \in \mathcal{U}(\Omega)$ such that

$$\mathcal{B}_\Omega(\hat{u},v) = \mathcal{L}(v) - \big(\gamma\frac{\partial}{\partial t}u_{S^p_{\Delta_h}},v\big)_{L^2(\Omega)} \qquad \forall t \in (0,T) \tag{4.5}$$

It follows that

$$\mathcal{B}_\Omega(\hat{u},v) = \mathcal{L}(v) - \big(\gamma\frac{\partial u_{S^p_{\Delta_h}}}{\partial t},v\big)_{L^2(\Omega)} = \mathcal{B}_\Omega(u_{S^p_{\Delta_h}},v) \qquad \forall v \in S^p_{\Delta_h}, \qquad \forall t \in (0,T) \tag{4.6}$$

and hence $u_{S^p_{\Delta_h}}$ is the finite element approximation of $\hat{u}$. In [36, 37] $\hat{u}$ is called post-processed solution and in [50] the elliptic reconstruction.

Theorem 4.1. For any time instant $T'(0 < T' \leq T)$, there exists a constant $C > 0$ which depends on $K(u)$ where $K(u) = \max\limits_{0\leq t\leq T'} K(u,t)$ and $K(u,t) \stackrel{\text{def}}{=} ||u||_{H^{p+1}} + ||\frac{\partial u}{\partial t}||_{H^{p+1}}$, such that for sufficiently smooth u and $\frac{\partial u}{\partial t}$, and sufficiently small h,

A) For $p \geq 2$ [36], and $l = 0, 1$:

$$||u - \hat{u}||_{H^l} \leq Ch^{p+\bar{\mu}+1-l}|\log h|^{\bar{r}} \tag{4.7}$$

where $\bar{\mu}$ and $\bar{r}$ are

$$\bar{\mu} = \begin{cases} 2 & \text{if } p \geq 3 \\ 1 & \text{otherwise} \end{cases} \qquad \bar{r} = \begin{cases} 0 & \text{if } p = 2 \\ 1 & \text{otherwise} \end{cases} \tag{4.8}$$

where $||v||_{H^0} \stackrel{\text{def}}{=} ||v||_{L^2} \stackrel{\text{def}}{=} \int_\Omega |\nabla v|^2$ and $||v||_{H^1} \stackrel{\text{def}}{=} \int_\Omega |\nabla v|^2$

B) For $p = 1$ [37], and $l = 0, 1$:

$$||u - \hat{u}||_{H^l} \approx Ch^2|\log h| \tag{4.9}$$

For the details of the proof see [36] and [37].

Recall now, standard Galerkin error bound for the semi-discrete solution $u_{S^p_{\Delta_h}}$ [49]

$$||u - u_{S^p_{\Delta_h}}||_{H^l} \leq Ch^{p+1-l}, l = 0, 1 \tag{4.10}$$

Employing the triangle inequality, we have

$$\left|||\hat{u} - u_{S^p_{\Delta_h}}||_{H^l} - ||u - \hat{u}||_{H^l}\right| \leq ||u - u_{S^p_{\Delta_h}}||_{H^l} \leq ||\hat{u} - u_{S^p_{\Delta_h}}||_{H^l} + ||u - \hat{u}||_{H^l} \tag{4.11}$$

and neglecting $||u - \hat{u}||_{H^l}$, according to (4.7), and (4.9), we obtain the asymptotic estimates,

$$||u - u_{S^p_{\Delta_h}}||_{H^l} \approx ||\hat{u} - u_{S^p_{\Delta_h}}||_{H^l}, \quad p \geq 2 - l, \quad l = 0, 1 \tag{4.12}$$

4.2 Upper bound in space-time norm for the exact error in semi-discrete finite element solutions

Let

$$||v||_{\mathscr{C}} \stackrel{\text{def}}{=} \sqrt{\int_0^T ||\sqrt{\gamma}v||^2_{L^2}\, dt + \int_0^T (T - t)\, ||v||^2_{\mathscr{U}}\, dt} \tag{4.13}$$

Let denote the exact error of the parabolic problem by $e_h \stackrel{\text{def}}{=} u - u_{S^p_{\Delta_h}}$ in order to be different from the exact error $e_{S^p_{\Delta_h}}$ for elliptic problem. Then we have:

Theorem 4.2. Under the assumptions which are sufficient for existence of solutions of (4.2)

$$||e_h||_{\mathscr{E}} \leq \mathfrak{E}_{EX} \stackrel{\text{def}}{=} \sqrt{\int_0^T (T-t)||\hat{u} - u_{S^p_{\Delta_h}}||^2_{\mathscr{U}}\, dt + T||\sqrt{\gamma}e_h(0)||^2_{L^2}} \tag{4.14}$$

where $e_h(0)$ denotes the exact error at time instant $t = 0$ and $||\sqrt{\gamma}v||^2_{L^2} \stackrel{\text{def}}{=} \sum_{i=1}^{nsubd} ||\sqrt{\gamma_i}v||^2_{L^2}$

Proof: Substracting equation (4.5) from the equation (4.2), we have

$$\big(\gamma\frac{\partial e_h}{\partial t}, v\big)_{L^2(\Omega)} + \mathscr{B}_\Omega(u - \hat{u}, v) = 0 \qquad \forall v \in \mathscr{U}(\Omega), \qquad \forall t \in (0,T) \tag{4.15}$$

Let $v = e_h$, we have

$$\frac{1}{2}\frac{d}{dt}||\sqrt{\gamma}e_h||^2_{L^2} + \mathscr{B}_\Omega(u - \hat{u}, e_h) = 0 \qquad \forall t \in (0,T) \tag{4.16}$$

It can be shown that

$$\begin{aligned}
\mathscr{B}_\Omega(u - \hat{u}, e_h) &= \mathscr{B}_\Omega(e_h + u_{S^p_{\Delta_h}} - \hat{u}, e_h) = ||e_h||^2_{\mathscr{U}} + \mathscr{B}_\Omega(u_{S^p_{\Delta_h}} - \hat{u}, e_h) \\
&= ||e_h||^2_{\mathscr{U}} + \mathscr{B}_\Omega(u_{S^p_{\Delta_h}} - \hat{u}, u - \hat{u} + \hat{u} - u_{S^p_{\Delta_h}}) \\
&= ||e_h||^2_{\mathscr{U}} - ||\hat{u} - u_{S^p_{\Delta_h}}||^2_{\mathscr{U}} + \mathscr{B}_\Omega(u_{S^p_{\Delta_h}} - \hat{u}, u - \hat{u}) \\
&= ||e_h||^2_{\mathscr{U}} - ||\hat{u} - u_{S^p_{\Delta_h}}||^2_{\mathscr{U}} + \mathscr{B}_\Omega(u_{S^p_{\Delta_h}} - u + u - \hat{u}, u - \hat{u}) \\
&= ||e_h||^2_{\mathscr{U}} - ||\hat{u} - u_{S^p_{\Delta_h}}||^2_{\mathscr{U}} + ||u - \hat{u}||^2_{\mathscr{U}} - \mathscr{B}_\Omega(e_h, u - \hat{u})
\end{aligned} \tag{4.17}$$

Then we obtain

$$\mathscr{B}_\Omega(u - \hat{u}, e_h) = \frac{1}{2}\big(||e_h||^2_{\mathscr{U}} + ||u - \hat{u}||^2_{\mathscr{U}} - ||\hat{u} - u_{S^p_{\Delta_h}}||^2_{\mathscr{U}}\big) \tag{4.18}$$

Therefore (4.16) becomes

$$\frac{d}{dt}||\sqrt{\gamma}e_h||^2_{L^2} + ||e_h||^2_{\mathscr{U}} + ||u-\hat{u}||^2_{\mathscr{U}} = ||\hat{u} - u_{S^p_{\Delta_h}}||^2_{\mathscr{U}} \tag{4.19}$$

Take time integration $\int_0^T \int_0^\tau$ on both sides of (4.19) and employ Fubini's theorem, we have

$$\begin{aligned}\int_0^T \left(||\sqrt{\gamma}e_h||^2_{L^2} + (T-t)||e_h||^2_{\mathscr{U}}\right)dt + \int_0^T (T-t)||u-\hat{u}||^2_{\mathscr{U}}\, dt \\ = \int_0^T (T-t)||\hat{u} - u_{S^p_{\Delta_h}}||^2_{\mathscr{U}}\, dt + T||\sqrt{\gamma}e_h(0)||^2_{L^2}\end{aligned} \tag{4.20}$$

By dropping the term $\int_0^T (T-t)||u-\hat{u}||^2_{\mathscr{U}}\, dt$, (4.20) immediately yields (4.14).

□

Remark 4.1. Note that here we take double integration over time $\int_0^T \int_0^\tau$ in order to have a norm similar to the one defined in [31–33] which is called space-time $\mathscr{A}$-norm as shown below

$$||v||_{\mathscr{A}} \stackrel{\text{def}}{=} \sqrt{\int_0^T \frac{1}{2}||\sqrt{\gamma}v||^2_{L^2}\, dt + \int_0^T (T-t)\, ||v||^2_{\mathscr{U}}\, dt} \tag{4.21}$$

The introduction of space-time $\mathscr{A}$-norm in [31–33] is for the purpose of employing duality approach in order to have upper bound. It can be seen that the only difference between $||v||_{\mathscr{C}}$ and $||v||_{\mathscr{A}}$ is that there is a factor of $\frac{1}{2}$ for the L^2 norm of $||\sqrt{\gamma}v||^2_{L^2}$.

Remark 4.2. When $||u-\hat{u}||_{\mathscr{U}}$ is superconvergent the upper bound $\mathfrak{E}_{EX}$ is sharp.

To get a computable estimate, we replace the exact $\hat{u}$ by its approximation $\hat{u}_{S^{p+k}_{\Delta_{h'}}}$ where $\Delta_{h'}$is obtained from nested subdivision of the mesh Δ_h to obtain

$$\mathfrak{E}_{S^{p+k}_{\Delta_{h'}}} \stackrel{\text{def}}{=} \sqrt{\int_0^T (T-t)\, ||\hat{u}_{S^{p+k}_{\Delta_{h'}}} - u_{S^p_{\Delta_h}}||^2_{\mathscr{U}}\, dt + T\, ||\sqrt{\gamma}e_h(0)||^2_{L^2}} \tag{4.22}$$

which is not necessary a guaranteed upper bound.

4.3 Numerical examples

Let us analyze the performance of the upper bound $\mathfrak{E}_{EX}$ and its computable version $\mathfrak{E}_{S^{p+k}_{\Delta_{h'}}}$ using examples.

Example 4.1. *Heat transition problem in one dimension* [31]. We consider the equation

$$\frac{\partial u}{\partial t} - \frac{\partial^2 u}{\partial x^2} = f \text{ on } \Omega_T = (0, L) \times (0, T] \tag{4.23a}$$

$$u(x, 0) = 0,\ 0 < x < L \tag{4.23b}$$

$$u(0, t) = u(L, t) = 0 \tag{4.23c}$$

with $L = 4$, $T = 4$, and $f(x, t)$ such that

$$u(x, t) = \frac{L^2}{\pi^2} \sin\big(\frac{\pi x}{L}\big)\big(1 - e^{-\frac{\pi^2 t}{L^2}}\big) \tag{4.23d}$$

Fig. 4.1 shows $||u||_{H^l}, l = 0, 1$, for $0 \leq t \leq T = 4$. We choose the time instants $t = \frac{T}{16}, \frac{T}{2}$ at which the solution reflects obvious transient behavior to study the relevant convergence behaviors.

Fig. 4.2 illustrates the superconvergence properties of the elliptic reconstruction measured in the energy norm and L^2 norm at time instant $t = \frac{T}{16}, \frac{T}{2}$, for the semi-discrete solution $u_{S^p_{\Delta_h}}$ computed using elements of degree $p = 1$, 2, and 3, and uniform meshes with mesh size $h = \frac{L}{2^n}$, $n = 1, 2, 3$, and 4 respectively. It can be seen that the convergence rate of $||u - \hat{u}||_{\mathfrak{u}}$ is 2, 4, and 5 for $p = 1, 2$, and 3 respectively while the convergence rate of $||u - u_{S^p_{\Delta_h}}||_{\mathfrak{u}}$ is 1, 2, and 3. For L^2 norm, $||u - \hat{u}||_{L^2}$ and $||u - u_{S^p_{\Delta_h}}||_{L^2}$ have the same convergence rate of 2 in the case of linear element, which means that the values of $\hat{u}$ are not superconvergent for $p = 1$. For quadratic element, $||u - \hat{u}||_{L^2}$ has a convergence rate of 4 while $||u - u_{S^p_{\Delta_h}}||_{L^2}$ is 3. For cubic element, the

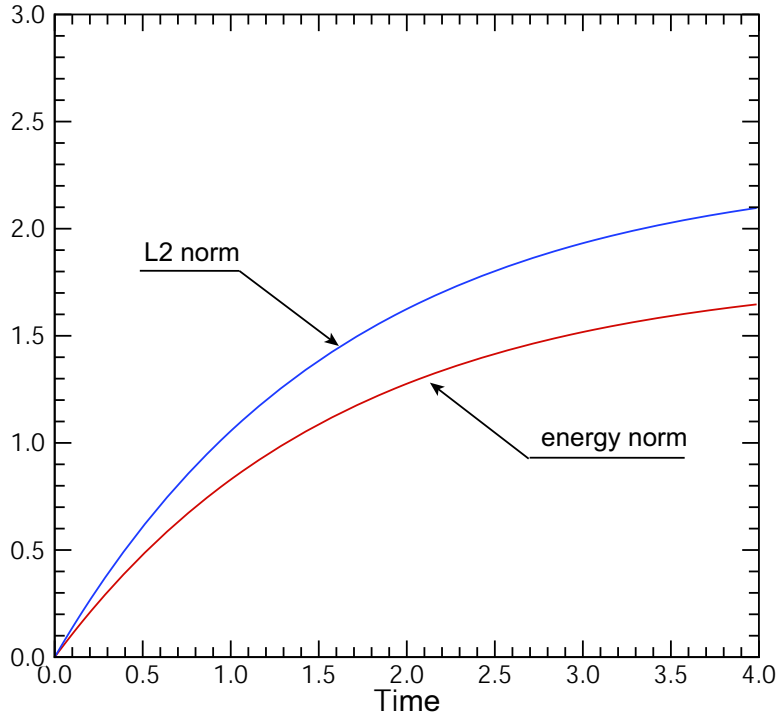

Fig. 4.1. Heat transition problem in one dimension. Plots of evolution of energy norm $||u||_{\mathcal{U}}$ and L^2 norm $||u||_{L^2}$ with respect to time t. Note that $T = 4$.

convergence rate of $||u - \hat{u}||_{L^2}$ is 6 while $||u - u_{S^p_{\Delta_h}}||_{L^2}$ is 4. It can be seen that the elliptic reconstruction does achieve the superconvergence behavior as shown in (4.7) and (4.9).

Remark 4.3. In this paper discontinuous Galerkin method [51, 52] was employed to obtain the "exact" semi-discrete finite solution $u_{S^p_{\Delta_h}}$ by adopting overkill mesh in time. The overkill mesh is obtained by the use of finer refinement in time intervals, the polynomial order up to 8, and the geometric refinement towards to the singularity at $t = 0$ at which time instant the initial and boundary conditions are suddenly applied.

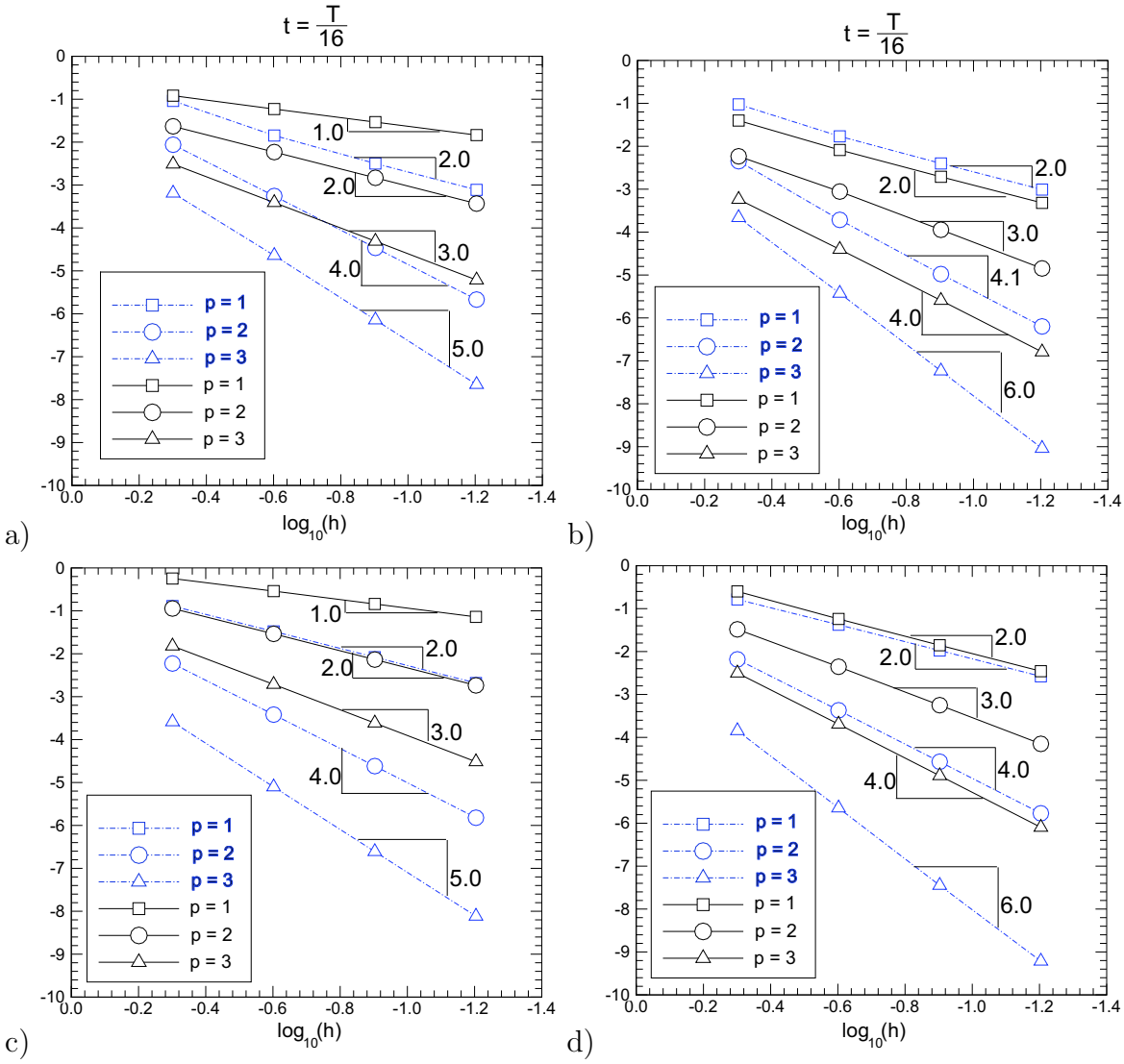

Fig. 4.2. Heat transition problem in one dimension. a) $||u-\hat{u}||_{\mathcal{U}}$ and $||u-u_{S^p_{\Delta_h}}||_{\mathcal{U}}$ at $t=\frac{T}{16}$; b) $||u-\hat{u}||_{L^2}$ and $||u-u_{S^p_{\Delta_h}}||_{L^2}$ at $t=\frac{T}{16}$; c) $||u-\hat{u}||_{\mathcal{U}}$ and $||u-u_{S^p_{\Delta_h}}||_{\mathcal{U}}$ at $t=\frac{T}{2}$; d) $||u-\hat{u}||_{L^2}$ and $||u-u_{S^p_{\Delta_h}}||_{L^2}$ at $t=\frac{T}{2}$, for the semi-discrete finite element solutions of degree $p=1,2$, and 3 with mesh size $h \stackrel{\text{def}}{=} \frac{L}{2^n}$, $n=1,2,3$, and 4 respectively. The dashdot line is about $u-\hat{u}$ measured in energy norm and L^2 norm while the solid line about $u-u_{S^p_{\Delta_h}}$.

Table 4.1 gives the space-time $\mathscr{C}$-norm of the semi-discrete finite element solution $||u_{S^p_{\Delta_h}}||_{\mathscr{C}}$, and the relative value of the $\mathscr{C}$-norm of the error $||e_h||_{\mathscr{C}} \Big/ ||u||_{\mathscr{C}}$, for the semi-discrete solution of degree $p = 1$, 2 and 3, computed using uniform meshes with mesh size $h = \frac{L}{2^n}$, $n = 1, 2, 3,$ and 4 respectively. The uniform meshes are denoted as Mesh I, Mesh II, Mesh III, and Mesh IV, which corresponds to the refinement level $n = 1, 2, 3,$ and 4 respectively.

Table 4.1. Heat transition problem in one dimension. The $\mathscr{C}$-norm of the semi-discrete solution $||u_{S^p_{\Delta_h}}||_{\mathscr{C}}$, and the relative value of $\mathscr{C}$-norm of the error $||e_h||_{\mathscr{C}} \Big/ ||u||_{\mathscr{C}}$, for the semi-discrete solutions of degree $p = 1$, 2 and 3, computed using uniform meshes with mesh size $h = \frac{L}{2^n}$, $n = 1, 2, 3,$ and 4 respectively.

$\|\|u\|\|_{\mathscr{C}} = 4.18817232$								
	Mesh I		Mesh II		Mesh III		Mesh IV	
p	$\|\|u_{S^p_{\Delta_h}}\|\|_{\mathscr{C}}$	$\frac{\|\|e_h\|\|_{\mathscr{C}}}{\|\|u\|\|_{\mathscr{C}}}$	$\|\|u_{S^p_{\Delta_h}}\|\|_{\mathscr{C}}$	$\frac{\|\|e_h\|\|_{\mathscr{C}}}{\|\|u\|\|_{\mathscr{C}}}$	$\|\|u_{S^p_{\Delta_h}}\|\|_{\mathscr{C}}$	$\frac{\|\|e_h\|\|_{\mathscr{C}}}{\|\|u\|\|_{\mathscr{C}}}$	$\|\|u_{S^p_{\Delta_h}}\|\|_{\mathscr{C}}$	$\frac{\|\|e_h\|\|_{\mathscr{C}}}{\|\|u\|\|_{\mathscr{C}}}$
1	3.89636	32.33888 %	4.11854	15.43148 %	4.17095	7.62816 %	4.18387	3.80335 %
2	4.17730	6.15057 %	4.18747	1.54107 %	4.18812	0.38529 %	4.18816	0.09632 %
3	4.18798	0.80787 %	4.18816	0.10197 %	4.18817	0.01278 %	4.18817	0.00160 %

Table 4.2 shows the effectivity index

$$\kappa \stackrel{\text{def}}{=} \frac{\mathfrak{E}_{EX}}{||e_h||_{\mathscr{E}}} \tag{4.24}$$

for the upper bound $\mathfrak{E}_{EX}$ based one the exact solution $\hat{u}$ of the elliptic reconstruction problem, for the semi-discrete finite element solution $u_{S^p_{\Delta_h}}$, computed using elements of degree $p = 1, 2$, and 3, and uniform meshes with mesh size $h = \frac{L}{2^n}$, $n = 1, 2, 3$, and 4 respectively. It can be observed that the effectivity indices are all close to 1 even for the case where the relative error is over 32%.

Table 4.2 also lists the effectivity index

$$\kappa_{S^{p+k}_{\Delta_{h'}}} \stackrel{\text{def}}{=} \frac{\mathfrak{E}_{S^{p+k}_{\Delta_{h'}}}}{||e_h||_{\mathscr{E}}} \tag{4.25}$$

for the computable estimate $\mathfrak{E}_{S^{p+k}_{\Delta_{h'}}}$ where the finite element solution $\hat{u}_{S^{p+k}_{\Delta_{h'}}}$ of the elliptic reconstruction problem is computed with the elements of higher degree $p + k$ (p method), the finer mesh $\Delta_{h'}$ from the nested subdivision of the original mesh Δ_h (h method), and the combination of the two (hp method). It can be seen that the effectivity indices based on the computable $\mathfrak{E}_{S^{p+k}_{\Delta_{h'}}}$ are all close to 1. Clearly as the mesh is refined and the element order is increased, the effectivity indices from the computable $\mathfrak{E}_{S^{p+k}_{\Delta_{h'}}}$ converge to the ones corresponding to the exact $\mathfrak{E}_{EX}$.

Table 4.2. Heat transition problem in one dimension. The effectivity indices κ based on the exact solution $\hat{u}$ and $\kappa_{S^{p+k}_{\Delta_{h'}}} = \mathfrak{E}_{S^{p+k}_{\Delta_{h'}}}/||e_h||_{\mathscr{C}}$ based on the finite element solution $\hat{u}_{S^{p+k}_{\Delta_{h'}}}$ ($k = 1, 2, 3$, and $\Delta_{h'}$ from the nest subdivision of the original mesh Δ_h) of elliptic reconstruction problem obtained with *hp* method, for the semi-discrete finite element solution $u_{S^p_{\Delta_h}}$, computed using elements of degree $p = 1$, 2, and 3, and uniform meshes with mesh size $h = \frac{L}{2^n}$, $n = 1, 2, 3$, and 4 respectively.

$\hat{u}_{S^{p+k}_{\Delta_{h'}}}$		Mesh I			Mesh II			Mesh III			Mesh IV		
Mesh	$p+k$	$p=1$	$p=2$	$p=3$	$p=1$	$p=2$	$p=3$	$p=1$	$p=2$	$p=3$	$p=1$	$p=2$	$p=3$
Mesh I	1	-	-	-	-	-	-	-	-	-	-	-	-
	2	1.0122	-	-	-	-	-	-	-	-	-	-	-
	3	1.0294	0.9942	-	-	-	-	-	-	-	-	-	-
	4	1.0304	1.0027	0.9957	-	-	-	-	-	-	-	-	-
Mesh II	1	0.8902	-	-	-	-	-	-	-	-	-	-	-
	2	1.0289	0.9711	-	1.0024	-	-	-	-	-	-	-	-
	3	1.0304	1.0028	0.9929	1.0073	0.9980	-	-	-	-	-	-	-
	4	1.0304	1.0030	1.0007	1.0073	1.0002	0.9988	-	-	-	-	-	-
Mesh III	1	0.9968	-	-	0.8716	-	-	-	-	-	-	-	-
	2	1.0303	1.0010	-	1.0070	0.9684	-	1.0006	-	-	-	-	-
	3	1.0304	1.0030	1.0006	1.0073	1.0002	0.9922	1.0018	0.9995	-	-	-	-
	4	1.0304	1.0030	1.0007	1.0073	1.0002	1.0000	1.0018	1.0000	0.9997	-	-	-
Mesh IV	1	1.0221	-	-	0.9751	-	-	0.8674	-	-	-	-	-
	2	1.0304	1.0029	-	1.0073	0.9982	-	1.0018	0.9682	-	1.0001	-	-
	3	1.0304	1.0030	1.0007	1.0073	1.0002	0.9999	1.0018	1.0000	0.9922	1.0005	0.9999	-
	4	1.0304	1.0030	1.0007	1.0073	1.0002	1.0000	1.0018	1.0000	1.0000	1.0005	1.0000	0.9999
$\kappa = \frac{\mathfrak{E}_{EX}}{\|\|e_h\|\|_{\mathscr{C}(\Omega)}}$		1.0304	1.0030	1.0007	1.0073	1.0002	1.0000	1.0018	1.0000	1.0000	1.0005	1.0000	1.0000

Example 4.2. *Two dimensional synthetic problem*[53]. We consider the problem

$$\frac{\partial u}{\partial t} - \frac{\partial^2 u}{\partial x^2} - \frac{\partial^2 u}{\partial y^2} = f \quad \text{on} \quad \Omega_T = \Omega \times (0, T] \tag{4.26a}$$

$$u = 0 \quad \text{on} \quad \partial\Omega \tag{4.26b}$$

$$u(x, y, 0) = 100e^{-800(x-x_m)^2(y-y_m)^2}\sin(\pi x)\sin^2(\pi y) \tag{4.26c}$$

The exact solution is

$$u_{EX}(x, y, t) = 100e^{-10t-800(x-x_m)^2(y-y_m)^2}\sin(\pi x)\sin^2(\pi y) \tag{4.26d}$$

Note that $\Omega \stackrel{\text{def}}{=} (0, L) \times (0, L)$, $L = 1$, $T = 0.2$, and $x_m = y_m = 0.1$

Fig. 4.3 shows the evolution of the exact solution measured in energy norm and L^2 norm respectively. We choose the time instants $t = \frac{T}{16}, \frac{T}{2}$ at which the solution contour as shown in Fig. 4.4 reflects obvious transient behavior.

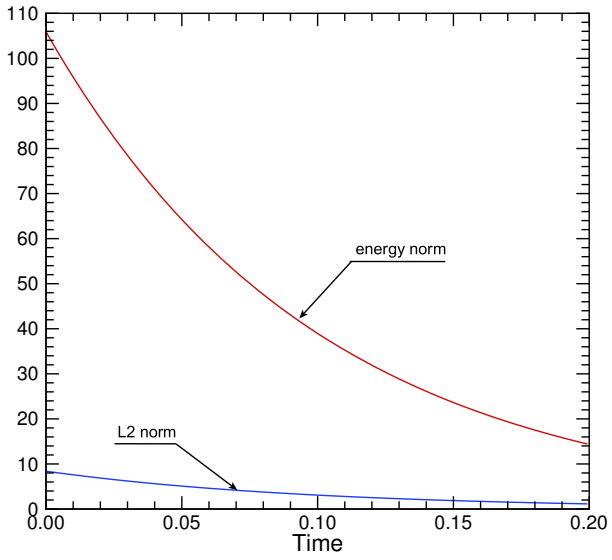

Fig. 4.3. Two dimensional synthetic problem. Plots of evolution of energy norm $||u||_{\mathcal{U}}$ and L^2 norm $||u||_{L^2}$ with respect to time t. Note that $T = 0.2$.

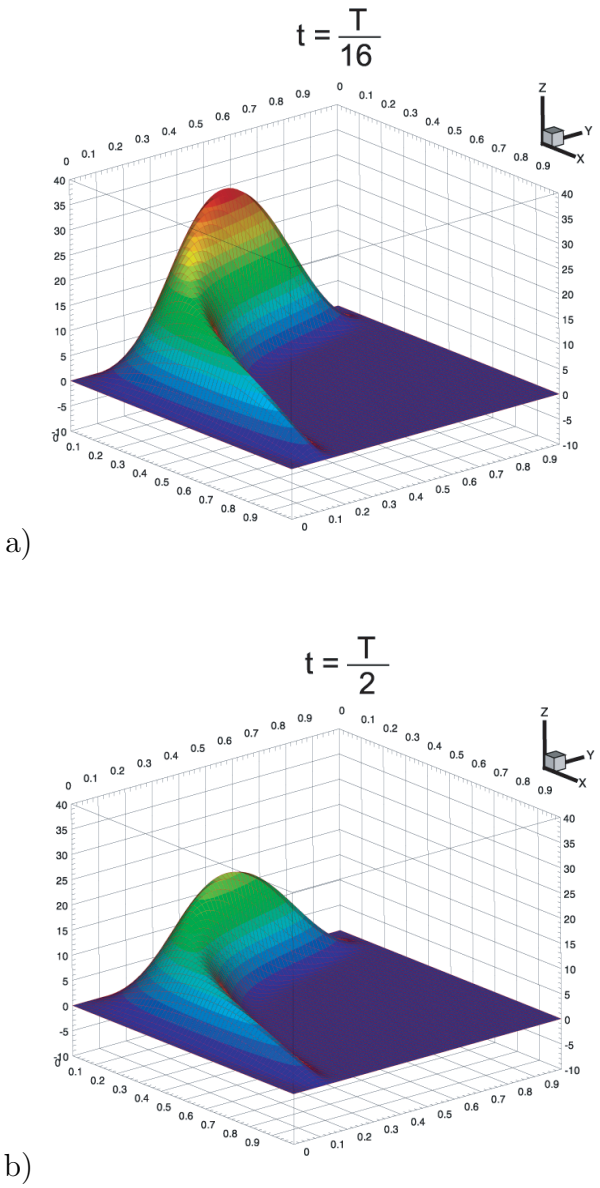

Fig. 4.4. Two dimensional synthetic problem. Plots of $u(x, y, t)$ at time instants: a) $t = \frac{T}{16}$; b) $t = \frac{T}{2}$.

Fig. 4.5 is the illustration of superconvergence properties based on elliptic reconstruction in terms of energy norm and L^2 norm at time instant $t = \frac{T}{16}, \frac{T}{2}$, for the semi-discrete solution $u_{S^p_{\Delta_h}}$ computed using elements of degree $p = 1$, 2, and 3, and uniform meshes with mesh size $h = \frac{L}{2^n}$, $n = 1, 2, 3$, 4, and 5 respectively. It can

be seen that for energy norm the convergence rate of $||u - \hat{u}||_{\mathscr{U}}$ is 1.9, 4, and 4.9 for semi-discrete finite element solution $u_{S^p_{\Delta_h}}$ of element order $p = 1, 2$, and 3 respectively while the convergence rate of $||u - u_{S^p_{\Delta_h}}||_{\mathscr{U}}$ is 0.8, 2.1, and 3.0.

For L^2 norm, in the case of linear element $||u - \hat{u}||_{L^2}$ has convergene rate of 1.8 while $||u - u_{S^p_{\Delta_h}}||_{L^2}$ converges at the rate 2.0 . Clearly there is no superconvergence property for L^2 norm in the case of linear element. For quadratic element, $||u - \hat{u}||_{L^2}$ has a convergence rate of 4 while $||u - u_{S^p_{\Delta_h}}||_{L^2}$ is 3.1. For cubic element, the convergence rate of $||u - \hat{u}||_{L^2}$ is 6.0 while $||u - u_{S^p_{\Delta_h}}||_{L^2}$ is 3.9.

Remark 4.4. It should be noted that the improved convergence rate of the elliptic reconstruction solution happens only under the condition that the classical semi-discrete finite element solution is in asymptotic range. However even when the finite element solution $u_{S^p_{\Delta_h}}$ is out of asymptotic range, the magnitude of the term $u - \hat{u}$ measured in energy norm and L^2 norm is much smaller than the corresponding terms of $u - u_{S^p_{\Delta_h}}$.

Table 4.3 gives the space-time $\mathscr{C}$-norm of the semi-discrete finite element solution $||u_{S^p_{\Delta_h}}||_{\mathscr{C}}$, and the relative value of the $\mathscr{C}$-norm of the error $||e_h||_{\mathscr{C}} \Big/ ||u||_{\mathscr{C}}$, for the semi-discrete solution of degree $p = 1$, 2 and 3, computed using uniform meshes with mesh size $h = \frac{L}{2^n}$, $n = 1, 2, 3$, and 4 respectively. Note that the mesh type, namely, Mesh I, II, III, and IV, corresponds to the refinement level n. It can be seen that the semi-discrete finite element solution starts converging only when finer meshes, such as Mesh III and Mesh IV, are employed. In the case of coarse mesh, such as Mesh I and II with element degree of $p = 1$, the relative error is close to 100%.

Table 4.4 shows the effectivity index κ based on the exact solution $\hat{u}$ of the elliptic reconstruction problem, for the semi-discrete finite element solution $u_{S^p_{\Delta_h}}$, computed using elements of degree $p = 1, 2$, and 3, and uniform meshes with mesh size $h = \frac{L}{2^n}$,

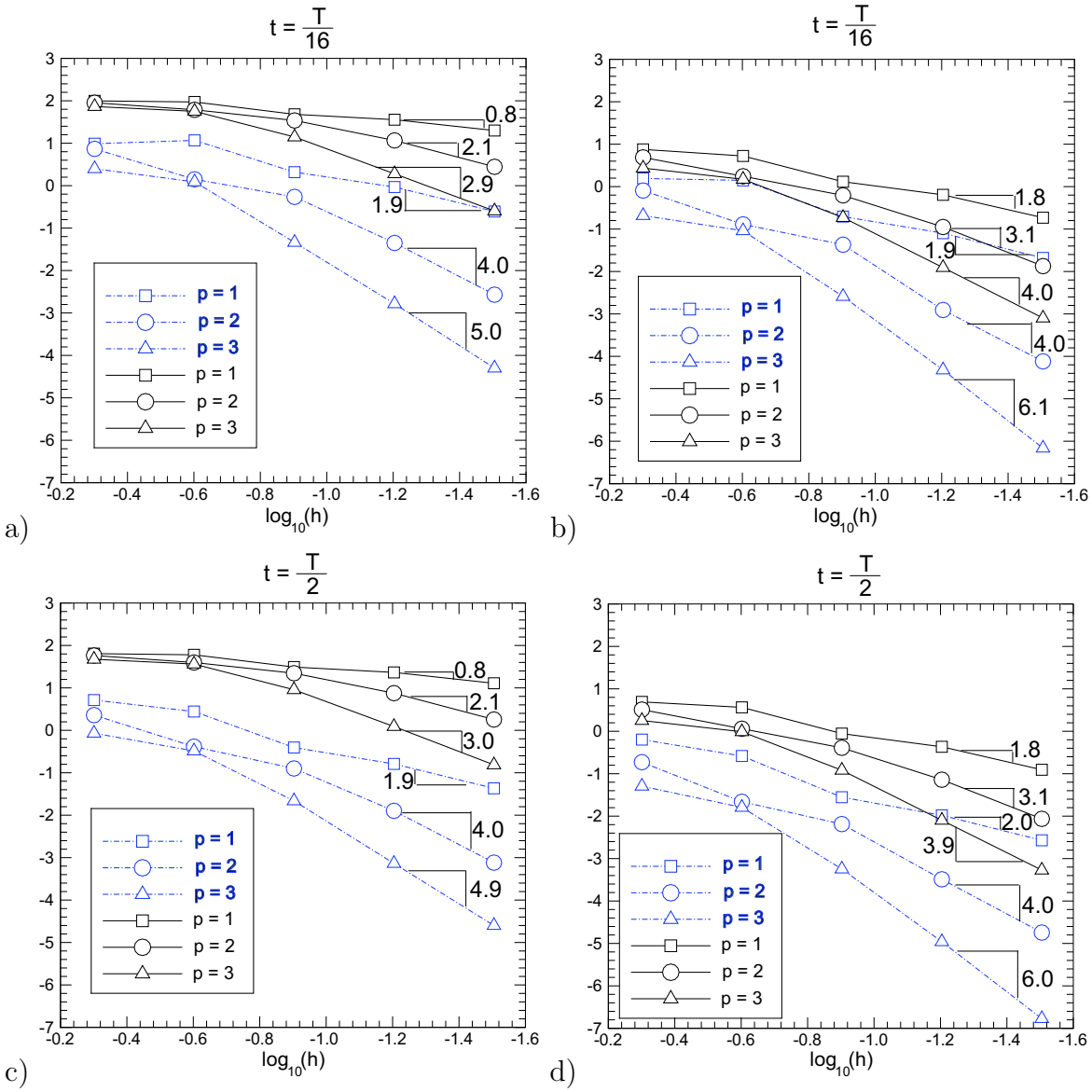

Fig. 4.5. Two dimensional synthetic problem. a) $||u-\hat{u}||_{\mathcal{U}}$ and $||u-u_{S^p_{\Delta_h}}||_{\mathcal{U}}$ at $t=\frac{T}{16}$; b) $||u-\hat{u}||_{L^2}$ and $||u-u_{S^p_{\Delta_h}}||_{L^2}$ at $t=\frac{T}{16}$; c) $||u-\hat{u}||_{\mathcal{U}}$ and $||u-u_{S^p_{\Delta_h}}||_{\mathcal{U}}$ at $t=\frac{T}{2}$; d) $||u-\hat{u}||_{L^2}$ and $||u-u_{S^p_{\Delta_h}}||_{L^2}$ at $t=\frac{T}{2}$, for the semi-discrete finite element solutions of degree $p=1,2,$ and 3 with mesh size $h \stackrel{\text{def}}{=} \frac{L}{2^n}$, $n=1,2,3,$ 4 and 5 respectively. The dashdot line is about $u-\hat{u}$ measured in energy norm and L^2 norm while the solid line about $u-u_{S^p_{\Delta_h}}$.

Table 4.3. Two dimensional synthetic problem. The $\mathscr{C}$-norm of the semi-discrete solution $||u_{S^p_{\Delta_h}}||_{\mathscr{C}}$, and the relative value of $\mathscr{C}$-norm of the error $||e_h||_{\mathscr{C}} \Big/ ||u||_{\mathscr{C}}$, for the semi-discrete solutions of degree $p = 1$, 2 and 3, computed using uniform meshes with mesh size $h = \frac{L}{2^n}$, $n = 1, 2, 3$, and 4 respectively.

$\|\|u\|\|_{\mathscr{C}} = 9.38532401$								
	Mesh I		Mesh II		Mesh III		Mesh IV	
p	$\|\|u_{S^p_{\Delta_h}}\|\|_{\mathscr{C}}$	$\frac{\|\|e_h\|\|_{\mathscr{C}}}{\|\|u\|\|_{\mathscr{C}}}$	$\|\|u_{S^p_{\Delta_h}}\|\|_{\mathscr{C}}$	$\frac{\|\|e_h\|\|_{\mathscr{C}}}{\|\|u\|\|_{\mathscr{C}}}$	$\|\|u_{S^p_{\Delta_h}}\|\|_{\mathscr{C}}$	$\frac{\|\|e_h\|\|_{\mathscr{C}}}{\|\|u\|\|_{\mathscr{C}}}$	$\|\|u_{S^p_{\Delta_h}}\|\|_{\mathscr{C}}$	$\frac{\|\|e_h\|\|_{\mathscr{C}}}{\|\|u\|\|_{\mathscr{C}}}$
1	0.80256	99.85850 %	3.65931	93.16247 %	8.29446	47.43671 %	8.90835	35.58213 %
2	4.27059	89.42646 %	7.50215	60.68975 %	9.01966	34.35868 %	9.34872	11.69422 %
3	6.50270	72.59938 %	7.90165	55.99704 %	9.34128	14.34975 %	9.38465	1.94138 %

$n = 1, 2, 3$, and 4 respectively. It can be observed that the effectivity indices are all close to 1 even for the case where the relative error is close to 100%.

Table 4.4 also lists the effectivity index $\kappa_{S^{p+k}_{\Delta_{h'}}}$ from the computable $\mathfrak{E}_{S^{p+k}_{\Delta_{h'}}}$ where the finite element solution $\hat{u}_{S^{p+k}_{\Delta_{h'}}}$ of the elliptic reconstruction problem is computed by *hp* method, which means $\hat{u}_{S^{p+k}_{\Delta_{h'}}}$ is obtained either by increasing the elements order up to $p + k$, or adopting the nested subdivision of the original mesh Δ_h for the semi-discrete finite element solution $u_{S^p_{\Delta_h}}$ of degree p, or the combination of both procedures. It can be seen that the effectivity indices based on the computable $\mathfrak{E}_{S^{p+k}_{\Delta_{h'}}}$ are all close to 1 as finer mesh and higher order polynomials are adopted to compute $\hat{u}_{S^{p+k}_{\Delta_{h'}}}$, and the effectivity indices from the computable $\mathfrak{E}_{S^{p+k}_{\Delta_{h'}}}$ converge to the ones corresponding to the exact $\mathfrak{E}_{EX}$. Note that in the case of Mesh I with $p = 1$ where relative error is close to 100%, if we only use quadratic element to compute $\hat{u}_{S^{p+k}_{\Delta_{h'}}}$, we have the effectivity index around 0.5. Likewise, if we adopt one level of nested subdivision of the original mesh Δ_h without increasing the polynomial order, we can also expect the effectivity index close to 0.5.

Table 4.4. Two dimensional synthetic problem. The effectivity indices κ based on the exact solution $\hat{u}$ and $\kappa_{S^{p+k}_{\Delta_{h'}}} = \mathfrak{E}_{S^{p+k}_{\Delta_{h'}}}/||e_h||_{\mathscr{E}}$ based on the finite element solution $\hat{u}_{S^{p+k}_{\Delta_{h'}}}$ ($k = 1, 2, 3$, and $\Delta_{h'}$ from the nest subdivision of the original mesh Δ_h) of elliptic reconstruction problem obtained with hp method, for the semi-discrete finite element solution $u_{S^p_{\Delta_h}}$, computed using elements of degree $p = 1$, 2, and 3, and uniform meshes with mesh size $h = \frac{L}{2^n}$, $n = 1, 2, 3$, and 4 respectively.

$\hat{u}_{S^{p+k}_{\Delta_{h'}}}$		Mesh I			Mesh II			Mesh III			Mesh IV		
Mesh	$p+k$	$p=1$	$p=2$	$p=3$	$p=1$	$p=2$	$p=3$	$p=1$	$p=2$	$p=3$	$p=1$	$p=2$	$p=3$
Mesh I	1	-	-	-	-	-	-	-	-	-	-	-	-
	2	0.5266	-	-	-	-	-	-	-	-	-	-	-
	3	0.7094	0.6135	-	-	-	-	-	-	-	-	-	-
	4	0.7475	0.6670	0.3754	-	-	-	-	-	-	-	-	-
Mesh II	1	0.4806	-	-	-	-	-	-	-	-	-	-	-
	2	0.8069	0.7469	-	0.7728	-	-	-	-	-	-	-	-
	3	0.8399	0.7915	0.6518	0.8133	0.4127	-	-	-	-	-	-	-
	4	0.9654	0.9539	0.9269	0.9599	0.8926	0.8671	-	-	-	-	-	-
Mesh III	1	0.8889	-	-	0.8700	-	-	-	-	-	-	-	-
	2	0.9465	0.9297	-	0.9380	0.8327	-	0.7043	-	-	-	-	-
	3	0.9942	0.9902	0.9830	0.9932	0.9747	0.9656	0.9579	0.9008	-	-	-	-
	4	1.0029	1.0010	0.9994	1.0032	0.9983	0.9936	0.9972	0.9794	0.9208	-	-	-
Mesh IV	1	0.9417	-	-	0.9319	-	-	0.6706	-	-	-	-	-
	2	0.9972	0.9939	-	0.9966	0.9828	-	0.9714	0.9282	-	0.9418	-	-
	3	1.0036	1.0010	1.0007	1.0039	1.0001	0.9957	1.0001	0.9850	0.9546	0.9942	0.9675	-
	4	1.0037	1.0018	1.0010	1.0041	1.0005	0.9962	1.0008	0.9863	0.9626	0.9954	0.9794	0.9164
$\kappa = \frac{\mathfrak{E}_{EX}}{\|\|e_h\|\|_{\mathscr{E}(\Omega)}}$		1.0038	1.0022	1.0013	1.0041	1.0008	1.0006	1.0010	1.0004	1.0000	1.0007	1.0000	1.0000

Example 4.3. *L-shaped domain problem.* We consider the L-shaped domain problem as shown in Fig. 4.6a

$$\frac{\partial u}{\partial t} - \frac{\partial^2 u}{\partial x^2} - \frac{\partial^2 u}{\partial y^2} = f \quad \text{on} \quad \Omega_T = \Omega \times (0, T] \tag{4.27a}$$

$$u = 0 \quad \text{on} \quad \Gamma_d \tag{4.27b}$$

$$\frac{\partial u}{\partial n} = \frac{\partial u_{EX}}{\partial n} \quad \text{on} \quad \Gamma_N \tag{4.27c}$$

$$u(x, y, 0) = 0 \tag{4.27d}$$

The exact solution is

$$u_{EX}(r, \theta, t) = 10 r^{\frac{1}{3}} \sin\left(\frac{\theta}{3}\right) \sin(3\pi t) \tag{4.27e}$$

Note that $T = 0.5$, $L = 1$, and $r = \sqrt{x^2 + y^2}$

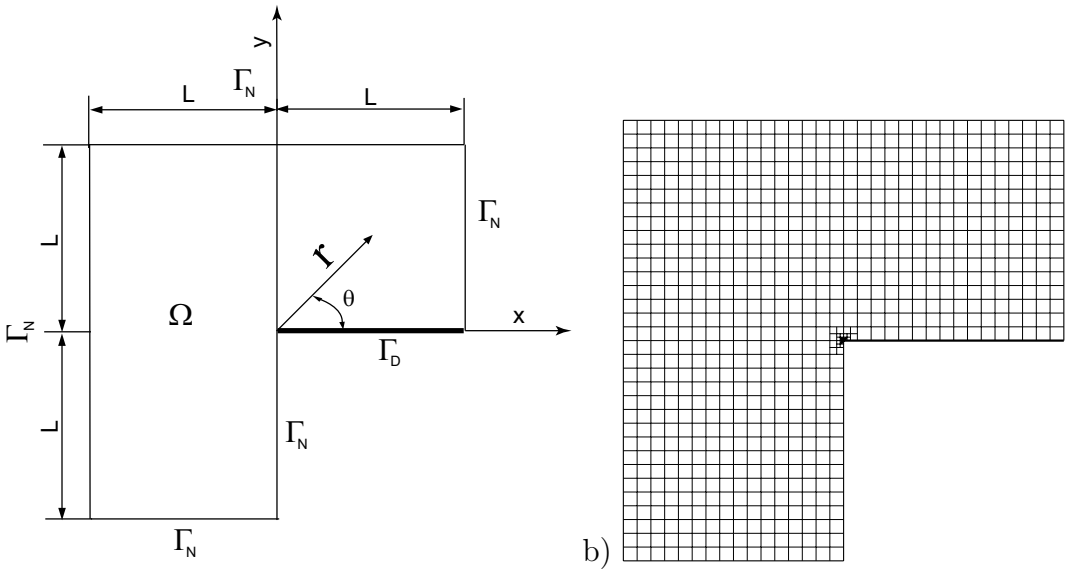

Fig. 4.6. L-shaped domain problem. a)The problem domain and the boundary conditions; b)Mesh employed to obtain overkill solution.

Fig. 4.7 shows the evolution of the exact solution measured in energy norm and L^2 norm respectively. We choose the time instants $t = \frac{T}{16}, \frac{T}{2}$ at which the solution

reflects obvious transient behavior.

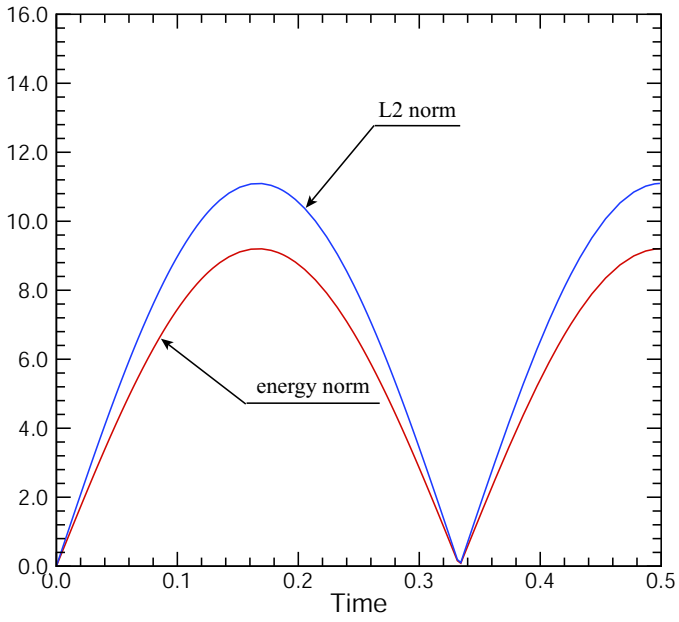

Fig. 4.7. L-shaped domain problem. Plots of evolution of energy norm $||u||_{\mathcal{U}}$ and L^2 norm $||u||_{L^2}$ with respect to time t. Note that $T = 0.5$.

Fig. 4.8 is the illustration of superconvergence properties based on elliptic reconstruction in terms of energy norm and L^2 norm at time instant $t = \frac{T}{16}, \frac{T}{2}$, for the semi-discrete solution $u_{S^p_{\Delta_h}}$ computed using elements of degree $p = 1$, 2, and 3, and uniform meshes with mesh size $h = \frac{L}{2^n}$, $n = 1, 2, 3$, and 4 respectively. At $t = \frac{T}{16}$, it can be seen that for energy norm the convergence rate of $||u - \hat{u}||_{\mathcal{U}}$ is $0.76, 0.71$, and 0.69 while the convergence rate of $||u - u_{S^p_{\Delta_h}}||_{\mathcal{U}}$ is 0.36, 0.35, and 0.34 corresponding to element order $p = 1, 2$, and 3 respectively. For L^2 norm, $||u - \hat{u}||_{L^2}$ has convergence rate 0.76, 0.71, and 0.69 while $||u - u_{S^p_{\Delta_h}}||_{L^2}$ converges at the rate 0.83, 0.74 and 0.71 for element order $p = 1, 2$, and 3 respectively. Similar convergence rate can be observed at time instant $t = \frac{T}{2}$.

It can be noted that in the case of energy norm $u - \hat{u}$ has improved convergence

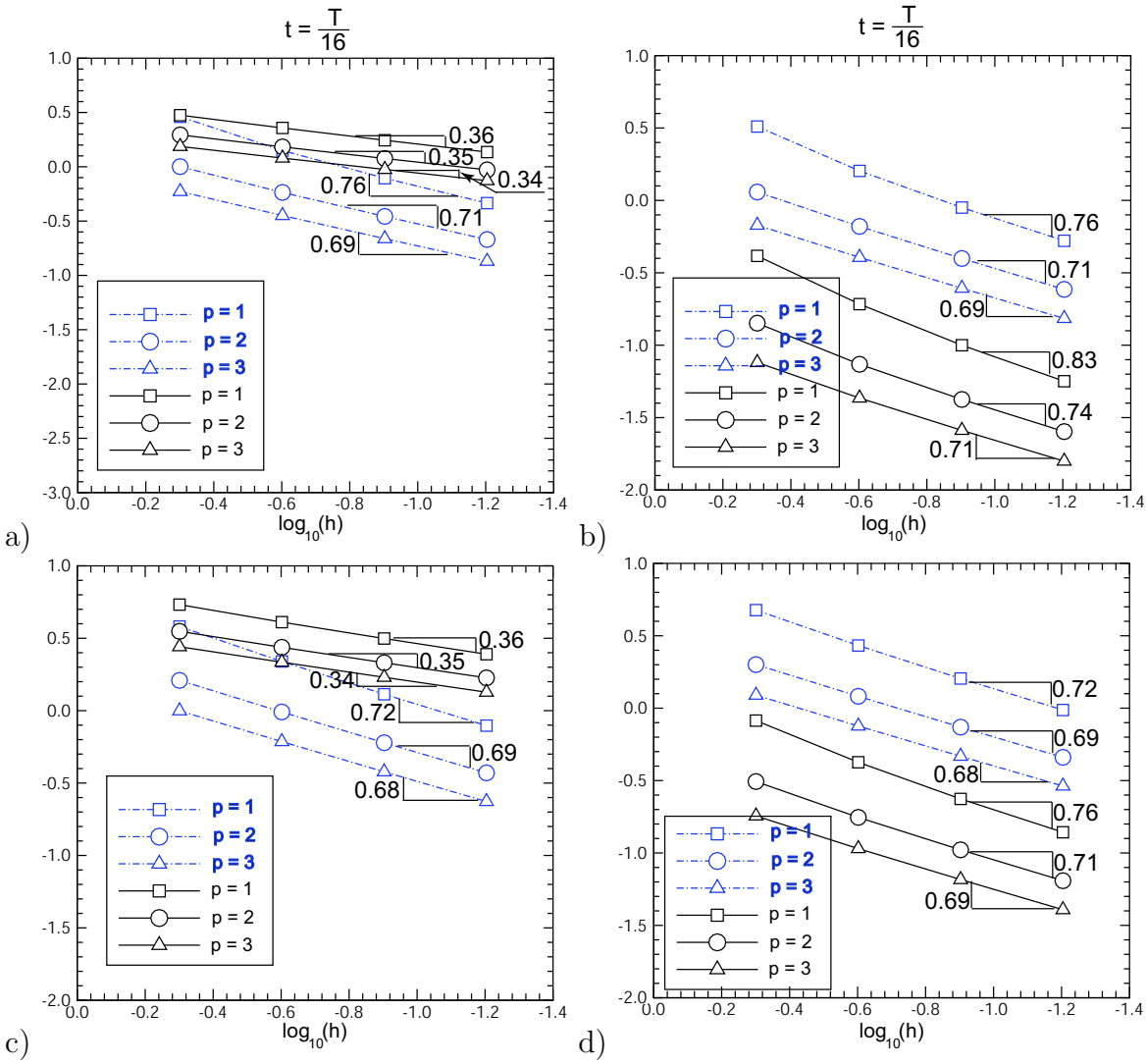

Fig. 4.8. L-shaped domain problem. a) $||u-\hat{u}||_{\mathcal{U}}$ and $||u-u_{S^p_{\Delta_h}}||_{\mathcal{U}}$ at $t=\frac{T}{16}$; b) $||u-\hat{u}||_{L^2}$ and $||u-u_{S^p_{\Delta_h}}||_{L^2}$ at $t=\frac{T}{16}$; c) $||u-\hat{u}||_{\mathcal{U}}$ and $||u-u_{S^p_{\Delta_h}}||_{\mathcal{U}}$ at $t=\frac{T}{2}$; d) $||u-\hat{u}||_{L^2}$ and $||u-u_{S^p_{\Delta_h}}||_{L^2}$ at $t=\frac{T}{2}$, for the semi-discrete finite element solutions of degree $p=1,2$, and 3 with mesh size $h \overset{\text{def}}{=} \frac{L}{2^n}$, $n=1,2,3$, and 4 respectively. The dashdot line is about $u-\hat{u}$ measured in energy norm and L^2 norm while the solid line about $u-u_{S^p_{\Delta_h}}$.

rate over $u - u_{S^p_{\Delta_h}}$ while in L^2 norm there is no improvement in terms of convergence. Moreover the magnitude of the term $u - \hat{u}$ measured in energy norm is smaller than $u - u_{S^p_{\Delta_h}}$ while in L^2 norm the magnitude of $u - \hat{u}$ much bigger than $u - u_{S^p_{\Delta_h}}$. Note that the exact solution $\hat{u}$ is computed with the overkill mesh as shown in Fig. 4.6b and with polynomial order equal to 8, and adaptive refinement is adopted around the singularity located at the origin.

Table 4.5 gives the space-time $\mathscr{C}$-norm of the semi-discrete finite element solution $||u_{S^p_{\Delta_h}}||_{\mathscr{C}}$, and the relative value of the $\mathscr{C}$-norm of the error $||e_h||_{\mathscr{C}} \Big/ ||u||_{\mathscr{C}}$, for the semi-discrete solution of degree $p = 1$, 2 and 3, computed using uniform meshes with mesh size $h = \frac{L}{2^n}$, $n = 1, 2, 3$, and 4 respectively. Note that Mesh I, II, III, and IV correspond to the refinement level $n = 1, 2, 3$,and 4 respectively. It can be seen that even for finer mesh such as Mesh IV and element order $p = 3$, the relative error is still about 5%.

Table 4.5. L-shaped domain problem. The $\mathscr{C}$-norm of the semi-discrete solution $||u_{S^p_{\Delta_h}}||_{\mathscr{C}}$, and the relative value of $\mathscr{C}$-norm of the error $||e_h||_{\mathscr{C}} \Big/ ||u||_{\mathscr{C}}$, for the semi-discrete solutions of degree $p = 1$, 2 and 3, computed using uniform meshes with mesh size $h = \frac{L}{2^n}$, $n = 1, 2, 3$, and 4 respectively.

$\|\|u\|\|_{\mathscr{C}} = 5.98729130$								
	Mesh I		Mesh II		Mesh III		Mesh IV	
p	$\|\|u_{S^p_{\Delta_h}}\|\|_{\mathscr{C}}$	$\frac{\|\|e_h\|\|_{\mathscr{C}}}{\|\|u\|\|_{\mathscr{C}}}$	$\|\|u_{S^p_{\Delta_h}}\|\|_{\mathscr{C}}$	$\frac{\|\|e_h\|\|_{\mathscr{C}}}{\|\|u\|\|_{\mathscr{C}}}$	$\|\|u_{S^p_{\Delta_h}}\|\|_{\mathscr{C}}$	$\frac{\|\|e_h\|\|_{\mathscr{C}}}{\|\|u\|\|_{\mathscr{C}}}$	$\|\|u_{S^p_{\Delta_h}}\|\|_{\mathscr{C}}$	$\frac{\|\|e_h\|\|_{\mathscr{C}}}{\|\|u\|\|_{\mathscr{C}}}$
1	6.08007	22.80031 %	6.04384	16.95901 %	6.02197	12.96582 %	6.00874	10.06376 %
2	6.02944	14.58408 %	6.01365	11.24924 %	6.00372	8.77569 %	5.99756	6.89181 %
3	6.01410	11.35307 %	6.00400	8.85357 %	5.99773	6.95159 %	5.99383	5.48064 %

Table 4.6 shows the effectivity index κ based on the exact solution $\hat{u}$ of the elliptic reconstruction problem, for the semi-discrete finite element solution $u_{S^p_{\Delta_h}}$, computed using elements of degree $p = 1, 2$, and 3, and uniform meshes with mesh size $h = \frac{L}{2^n}$, $n = 1, 2, 3$, and 4 respectively. It can be observed that the effectivity indices are all close to 1 even for the coarse mesh such as Mesh I and element order $p = 1$ where the relative error is about 23%.

Table 4.6 also lists the effectivity index $\kappa_{S^{p+k}_{\Delta_{h'}}}$ from the computable $\mathfrak{E}_{S^{p+k}_{\Delta_{h'}}}$ where the finite element solution $\hat{u}_{S^{p+k}_{\Delta_{h'}}}$ of the elliptic reconstruction problem is computed by hp method, which means $\hat{u}_{S^{p+k}_{\Delta_{h'}}}$ is obtained either by increasing the elements order up to $p + k$, or adopting the nested subdivision of the original mesh Δ_h for the semi-discrete finite element solution $u_{S^p_{\Delta_h}}$ of degree p, or the combination of both procedures. It can be seen that the effectivity indices based on the computable $\mathfrak{E}_{S^{p+k}_{\Delta_{h'}}}$ are all close to 1 as finer mesh and higher order polynomials are adopted to compute $\hat{u}_{S^{p+k}_{\Delta_{h'}}}$, and the effectivity indices from the computable $\mathfrak{E}_{S^{p+k}_{\Delta_{h'}}}$ converge to the ones corresponding to the exact $\mathfrak{E}_{EX}$.

Table 4.6. L-shaped domain problem. The effectivity indices κ based on the exact solution $\hat{u}$ and $\kappa_{S^{p+k}_{\Delta_{h'}}} = \mathfrak{E}_{S^{p+k}_{\Delta_{h'}}}/||e_h||_{\mathscr{E}}$ based on the finite element solution $\hat{u}_{S^{p+k}_{\Delta_{h'}}}$ ($k = 1, 2, 3$, and $\Delta_{h'}$ from the nest subdivision of the original mesh Δ_h) of elliptic reconstruction problem obtained with hp method, for the semi-discrete finite element solution $u_{S^p_{\Delta_h}}$, computed using elements of degree $p = 1$, 2, and 3, and uniform meshes with mesh size $h = \frac{L}{2^n}$, $n = 1, 2, 3$, and 4 respectively.

$\hat{u}_{S^{p+k}_{\Delta_{h'}}}$		Mesh I			Mesh II			Mesh III			Mesh IV		
Mesh	$p+k$	$p=1$	$p=2$	$p=3$	$p=1$	$p=2$	$p=3$	$p=1$	$p=2$	$p=3$	$p=1$	$p=2$	$p=3$
Mesh I	1	-	-	-	-	-	-	-	-	-	-	-	-
	2	0.8657	-	-	-	-	-	-	-	-	-	-	-
	3	1.0071	0.6425	-	-	-	-	-	-	-	-	-	-
	4	1.0718	0.7898	0.5507	-	-	-	-	-	-	-	-	-
Mesh II	1	0.7313	-	-	-	-	-	-	-	-	-	-	-
	2	1.0109	0.6520	-	0.7904	-	-	-	-	-	-	-	-
	3	1.0922	0.8324	0.6345	0.9209	0.6247	-	-	-	-	-	-	-
	4	1.1314	0.9105	0.7735	0.9806	0.7673	0.5421	-	-	-	-	-	-
Mesh III	1	0.9397	-	-	0.6678	-	-	-	-	-	-	-	-
	2	1.0946	0.8371	-	0.9245	0.6340	-	0.7588	-	-	-	-	-
	3	1.1439	0.9346	0.8137	0.9994	0.8084	0.6243	0.8828	0.6149	-	-	-	-
	4	1.1680	0.9801	0.8873	1.0351	0.8835	0.7602	0.9392	0.7544	0.5370	-	-	-
Mesh IV	1	1.0529	-	-	0.8595	-	-	0.6421	-	-	-	-	-
	2	1.1453	0.9373	-	1.0015	0.8130	-	0.8862	0.6240	-	0.7421	-	-
	3	1.1757	0.9945	0.9100	1.0465	0.9066	0.7995	0.9569	0.7946	0.6182	0.8620	0.6091	-
	4	1.1907	0.9801	0.9528	1.0684	0.9501	0.8712	0.9905	0.8677	0.7522	0.9164	0.7467	0.5339
$\kappa = \frac{\mathfrak{E}_{EX}}{\|\|e_h\|\|_{\mathscr{E}(\Omega)}}$		1.2290	1.0905	1.0562	1.1235	1.0552	1.0348	1.0731	1.0342	1.0217	1.0447	1.0213	1.0135

Example 4.4. *Transient diffusion problem in a thermal battery.* We will also consider the problem of the transient heat conduction in a thermal battery [19] modeled as a problem of orthotropic transient heat conduction in the multi-material domain Ω, consisting of five material subdomains Ω_k, $\overline{\Omega} = \bigcup_{k=1}^{5} \overline{\Omega}_k$, with boundary $\Gamma_N = \partial\Omega$, consisting of four parts Γ_N^i, $\overline{\Gamma}_N = \bigcup_{k=1}^{5} \overline{\Gamma}_N^i$, as shown in Fig. 2.1, and $t \in (0, 3000)$, namely,

$$\gamma \frac{\partial u}{\partial t} - \nabla \cdot \big(\mathbf{K}\ \nabla u\big) = f(:,t) \stackrel{\text{def}}{=} \begin{cases} 1 & \text{in } \Omega_2,\ \Omega_3 \\ 0 & \text{elsewhere} \end{cases} \tag{4.28a}$$

with $\mathbf{K}$, and γ constant in each material subdomain Ω_k given below, and boundary condition

$$\mathbf{K}\nabla u \cdot \mathbf{n} = g^{(i)}(:,t) - \alpha^{(i)}(:,t)\ u \qquad \text{on } \Gamma_N^i \tag{4.28b}$$

for $i = 1, 2, 3,$ and 4, where $\alpha^{(i)}(:,t) = \alpha^{(i)}$ and $g^{(i)}(:,t) = g^{(i)}$ are defined as follows,where

$$\alpha^{(i)} = \begin{cases} 0, & i = 1 \\ 1, & i = 2 \\ 2, & i = 3 \\ 3, & i = 4 \end{cases} \qquad g^{(i)} = \begin{cases} 0, & i = 1 \\ 3, & i = 2 \\ 2, & i = 3 \\ 1, & i = 4 \end{cases} \tag{4.28c}$$

for $0 < t \leq 3000$, and with the initial condition

$$u(:,0) = 0 \text{ in } \Omega. \tag{4.28d}$$

We will consider the orthotropic case and $\mathbf{K}$ is constant in each Ω_k, with value $\mathbf{K}^{(k)}_{\text{Orth}} = \begin{bmatrix} K_x^{(k)} & 0 \\ 0 & K_y^{(k)} \end{bmatrix}$ and

$$K_x^{(k)} = \begin{cases} 25.0, & k = 1 \\ 7.0, & k = 2 \\ 5.0, & k = 3 \\ 0.2, & k = 4 \\ 0.05, & k = 5 \end{cases} \qquad K_y^{(k)} = \begin{cases} 25.0, & k = 1 \\ 0.8, & k = 2 \\ 0.0001, & k = 3 \\ 0.2, & k = 4 \\ 0.05, & k = 5 \end{cases} \tag{4.28e}$$

We will also consider the isotropic case in which $\mathbf{K}^{(k)}_{\text{Iso}} = \begin{bmatrix} K_x^{(k)} & 0 \\ 0 & K_x^{(k)} \end{bmatrix}$ and the following γ are employed:

$$\gamma^{(k)} = \begin{cases} 4.0, & k = 1 \\ 1.8, & k = 2 \\ 3.2, & k = 3 \\ 0.1, & k = 4 \\ 0.3, & k = 5 \end{cases} \tag{4.28f}$$

Fig 4.9 is the evolution of the overkill solution $u_{S^7_{\Delta_h^{ovk}}}$ in terms of energy norm $\left|\left|u_{S^7_{\Delta_h^{ovk}}}\right|\right|_{\mathcal{U}}$ and L^2 norm $\left|\left|u_{S^7_{\Delta_h^{ovk}}}\right|\right|_{L^2}$ with respect to time for the isotropic, and the orthotropic case. Note that for the orthotropic case the solution reaches the steady state at a slower rate compared to the isotropic case. For both the isotropic case and the orthotropic case, the solution reflects significant transient behavior for time $t \leq 500$.

Table 4.7 gives the $\mathscr{E}$-norm of the semi-discrete finite element solution $||u_{S^p_{\Delta_h}}||_{\mathscr{E}}$, and the relative value of the $\mathscr{E}$-norm of the error $||e_h||_{\mathscr{E}} \Big/ \left|\left|u_{S^7_{\Delta_h^{ovk}}}\right|\right|_{\mathscr{E}}$, for the semi-discrete solution of degree $p = 1$, 2 and 3, computed using Mesh I, and Mesh II as illustrated in Fig. 2.2. The overkill solutions are computed with $p = 8$, on the meshes Δ_h^{ovk} and $\Delta_h^{ovk'}$ as shown in Fig. 2.2.

Remark 4.5. For both the isotropic case and the orthotropic case, we have multi-material singularities denoted by A_i, $i = 1, ..., 19$ as shown in Fig. 2.1.

Remark 4.6. For orthotropic case there are two interface layers on the top and bottom of domain Ω_3 at the interfaces between Ω_2 and Ω_3 due to the high orthotropy of Ω_3.

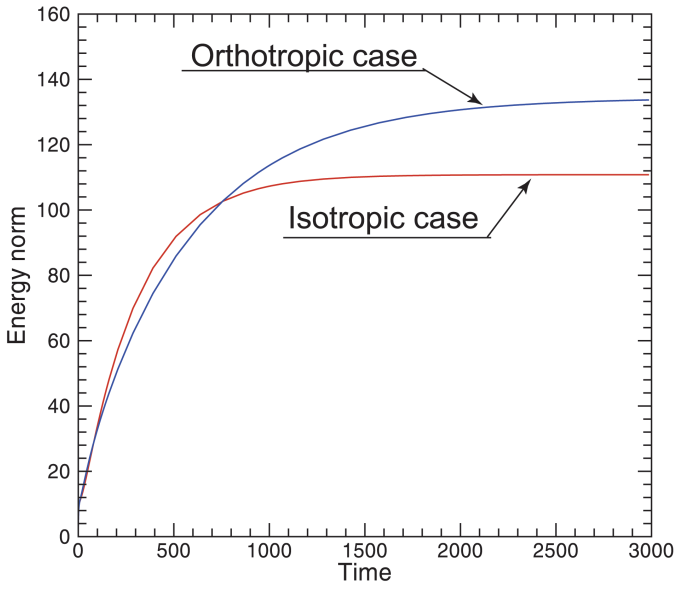

a)

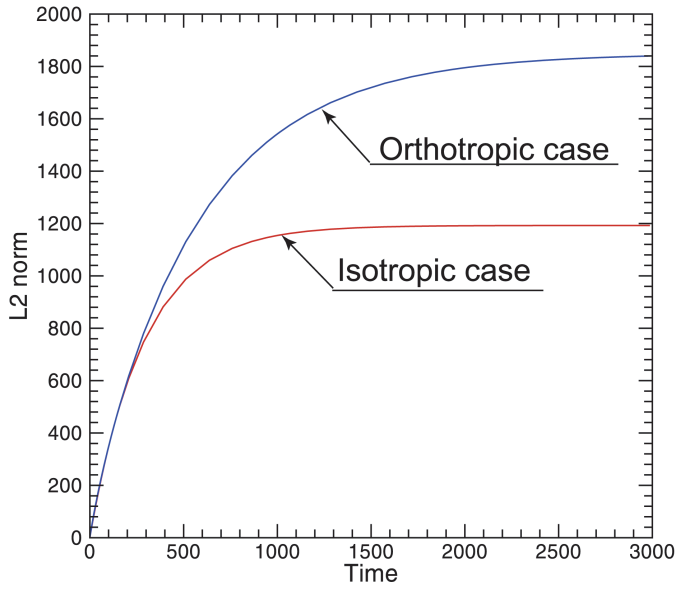

b)

Fig. 4.9. Transient diffusion problem in a thermal battery. a) The evolution of energy norm $\left|\left|u_{S^7_{\Delta_h^{ovk}}}\right|\right|_{\mathcal{U}}$ with respect to time for isotropic and orthotropic cases; b) The evolution of L^2 norm $\left|\left|u_{S^7_{\Delta_h^{ovk}}}\right|\right|_{L^2}$ with respect to time for isotropic and orthotropic cases.

Table 4.7. Transient diffusion problem in a thermal battery. The $\mathscr{C}$-norm of the semi-discrete solution $||u_{S^p_{\Delta_h}}||_{\mathscr{C}}$, and the relative value of $\mathscr{C}$-norm of the error $||e_h||_{\mathscr{C}} \Big/ ||u_{S^7_{\Delta_h^{ovk}}}||_{\mathscr{C}}$, for the semi-discrete solutions of degree $p = 1$, 2 and 3, computed using Mesh I, and Mesh II, for the isotropic and the orthotropic case.

	Isotropic case				Orthotropic case			
	$\|\|u_{S^7_{\Delta_h^{ovk}}}\|\|_{\mathscr{C}} = 2.24075002E5$				$\|\|u_{S^7_{\Delta_h^{ovk}}}\|\|_{\mathscr{C}} = 2.61372111E5$			
	Mesh I		Mesh II		Mesh I		Mesh II	
p	$\|\|u_{S^p_{\Delta_h}}\|\|_{\mathscr{C}}$	$\dfrac{\|\|e_h\|\|_{\mathscr{C}}}{\|\|u_{S^7_{\Delta_h^{ovk}}}\|\|_{\mathscr{C}}}$	$\|\|u_{S^p_{\Delta_h}}\|\|_{\mathscr{C}}$	$\dfrac{\|\|e_h\|\|_{\mathscr{C}}}{\|\|u_{S^7_{\Delta_h^{ovk}}}\|\|_{\mathscr{C}}}$	$\|\|u_{S^p_{\Delta_h}}\|\|_{\mathscr{C}}$	$\dfrac{\|\|e_h\|\|_{\mathscr{C}}}{\|\|u_{S^7_{\Delta_h^{ovk}}}\|\|_{\mathscr{C}}}$	$\|\|u_{S^p_{\Delta_h}}\|\|_{\mathscr{C}}$	$\dfrac{\|\|e_h\|\|_{\mathscr{C}}}{\|\|u_{S^7_{\Delta_h^{ovk}}}\|\|_{\mathscr{C}}}$
1	$2.22163E5$	12.42345%	$2.23199E5$	8.40942%	$2.52214E5$	25.45529%	$2.57158E5$	17.23978%
2	$2.23547E5$	6.52553%	$2.23840E5$	4.35227%	$2.58666E5$	13.87615%	$2.60139E5$	9.14114%
3	$2.23835E5$	4.39573%	$2.23967E5$	2.94321%	$2.60130E5$	9.19611%	$2.60702E5$	6.58230%

Adaptive refinement is adopted for the interface layers with the smallest mesh size close to the magnitude of the characteristic thickness of the interface layers which is $\sqrt{\frac{K_y^3}{K_x^3}}$ in this case. For details about the interface layers of the thermal battery problem, refer to [1]. It can be observed that the interface layers have negligible influence on the overkill solution and relative error as it can be seen from Table 4.8. For simplicity, the overkill solution based on overkill mesh Δ_h^{ovk} as shown in Fig. 2.2d) is employed for the orthotropic case.

Table 4.8. Transient diffusion problem in a thermal battery. The $\mathscr{C}$-norm of the semi-discrete solution $||u_{S^p_{\Delta_h}}||_{\mathscr{C}}$, and the relative value of $\mathscr{C}$-norm of the error $||e_h||_{\mathscr{C}} \Big/ ||u_{S^7_{\Delta_h^{ovk}}}||_{\mathscr{C}}$, for the semi-discrete solutions of degree $p = 1$, 2 and 3, computed using Mesh I, and Mesh II, for the orthotropic case. In this case, to obtain the overkill mesh, the adaptive refinement is adopted at the interface layers located at the top and bottom of highly orthotropic domain Ω_3 such that the smallest mesh size at the the interface layers is about the same magnitude of the characteristic thickness of the interface layers.

Orthotropic case				
$\|\|u_{S^7_{\Delta_h^{ovk}}}\|\|_{\mathscr{C}} = 2.61415216E5$				
	Mesh I		Mesh II	
p	$\|\|u_{S^p_{\Delta_h}}\|\|_{\mathscr{C}}$	$\frac{\|\|e_h\|\|_{\mathscr{C}}}{\|\|u_{S^7_{\Delta_h^{ovk}}}\|\|_{\mathscr{C}}}$	$\|\|u_{S^p_{\Delta_h}}\|\|_{\mathscr{C}}$	$\frac{\|\|e_h\|\|_{\mathscr{C}}}{\|\|u_{S^7_{\Delta_h^{ovk}}}\|\|_{\mathscr{C}}}$
1	$2.52214E5$	25.51157%	$2.57158E5$	17.32494%
2	$2.58666E5$	13.98115%	$2.60139E5$	9.29963%
3	$2.60130E5$	9.35304%	$2.60702E5$	6.79922%

Table 4.9 lists the effectivity index κ from the exact solution $\hat{u}$ of elliptic reconstruction problem based on the semi-discrete finite element solution $u_{S^p_{\Delta_h}}$, computed with the Mesh I, and Mesh II using elements of degree $p = 1$, 2, and 3, for the isotropic case, and the orthotropic case. It can be seen that for both the isotropic case and the orthotropic case the effectivity indices are all close to 1.

Table 4.9 also shows the effectivity indices from the computed $\hat{u}_{S^{p+k}_{\Delta_{h'}}}$ which results from from the nested subdivision of the original mesh (h method), or the increase of polynomial order (p method), or the combination of the two (hp method). It can be seen that the worst effectivity indices are around 0.6, which happens to the cubic element. For semi-discrete finite element solution $u_{S^p_{\Delta_h}}$ of linear order the increase of polynomial order and further refinement of the original mesh yield the best effectivity indices for both the isotropic and orthotropic case. Note that in the case of h method, for the finite element solution $u_{S^p_{\Delta_h}}$ computed with Mesh I, we employ Mesh II and Mesh III as shown in Fig. 2.2 b) and c) to obtain $\hat{u}_{S^{p+k}_{\Delta_{h'}}}$ while for $u_{S^p_{\Delta_h}}$ from Mesh II, we use Mesh III.

Table 4.9. Transient diffusion problem in a thermal battery. The effectivity indices κ based on the exact solution $\hat{u}$ and $\kappa_{S^{p+k}_{\Delta_{h'}}}$ based on the finite element solution $\hat{u}_{S^{p+k}_{\Delta_{h'}}}$ of elliptic reconstruction problem, for the Mesh I, and Mesh II, semi-discrete solution $u_{S^{p}_{\Delta_h}}$ computed using elements of degree $p = 1$, 2, and 3, for the isotropic and orthotropic case.

		Orthotropic						Isotropic					
$\hat{u}_{S^{p+k}_{\Delta_{h'}}}$		Mesh I			Mesh II			Mesh I			Mesh II		
Mesh	$p+k$	$p=1$	$p=2$	$p=3$	$p=1$	$p=2$	$p=3$	$p=1$	$p=2$	$p=3$	$p=1$	$p=2$	$p=3$
Mesh I	1	-	-	-	-	-	-	-	-	-	-	-	-
	2	0.8537	-	-	-	-	-	0.8499	-	-	-	-	-
	3	0.9603	0.7533	-	-	-	-	0.9346	0.7388	-	-	-	-
	4	0.9839	0.8611	0.6068	-	-	-	0.9635	0.8622	0.6597	-	-	-
Mesh II	1	0.7473	-	-	-	-	-	0.7348	-	-	-	-	-
	2	0.9590	0.7593	-	0.8552	-	-	0.9359	0.7449	-	0.8554	-	-
	3	0.9883	0.8888	0.6934	0.9347	0.6851	-	0.9711	0.8924	0.7428	0.9366	0.7366	-
	4	1.0053	0.9364	0.8198	0.9647	0.8149	0.5997	0.9835	0.9402	0.8629	0.9644	0.8599	0.6559
Mesh III	1	0.9162	-	-	0.7541	-	-	0.8884	-	-	0.7367		-
	2	0.9938	0.8956	-	0.9389	0.7056	-	0.9718	0.8953	-	0.9383	0.7446	-
	3	1.0104	0.9534	0.8613	0.9757	0.8571	0.7009	0.9869	0.9531	0.8935	0.9720	0.8912	0.7417
	4	1.0182	0.9793	0.9225	0.9926	0.9192	0.8341	0.9925	0.9736	0.9410	0.9842	0.9398	0.8628
$\kappa = \frac{\mathfrak{E}_{EX}}{\|\|e_h\|\|_{\mathscr{C}(\Omega)}}$		1.0299	1.0175	1.0082	1.0177	1.0060	1.0006	1.0025	0.9997	1.0000	1.0000	1.0000	1.0000

4.4 Bounds based on implicit residual estimators for semi-discrete finite element solutions

Let

$$\hat{e}_h \stackrel{\text{def}}{=} \hat{u} - u_{S^p_{\Delta_h}} \tag{4.29}$$

Then we have the following residual for the elliptic recontruction problem (4.5)

$$\mathcal{B}_\Omega(\hat{e}_h, v) = \mathcal{R}(v) \stackrel{\text{def}}{=} \mathcal{L}(v) - \left(\gamma \frac{\partial u_{S^p_{\Delta_h}}}{\partial t}, v\right)_{L^2(\Omega)} - \mathcal{B}_\Omega(u_{S^p_{\Delta_h}}, v) \qquad \forall v \in \mathcal{U}(\Omega) \tag{4.30}$$

Noting that

$$\mathcal{R}(v) = 0, \qquad \forall v \in S^p_{\Delta_h} \tag{4.31}$$

and similar to the Neumann subdomain residual estimator as defined in (2.15a) for the elliptic problem, we have by following [1]

$$||\hat{e}_h||_{\mathcal{U}} \leq \mathscr{E}^U_{Sub} \stackrel{\text{def}}{=} \sqrt{\sum_{\tau \in \Delta_h} \Big|\Big| \sum_{X \in \mathcal{N}(\Delta_h)} \breve{e}_{\omega_X^{\Delta_h}} \Big|\Big|^2_{\mathcal{U}}} \tag{4.32}$$

where $\omega_X^{\Delta_h} = \text{supp}(\phi_X^{\Delta_h})$ and $\phi_X^{\Delta_h}$ is the piecewise bilinear basis function supported over $\omega_X^{\Delta_h}$, which employs the subdomain residual problems:

Find $\breve{e}_{\omega_X^{\Delta_h}} \in \mathcal{U}_0(\omega_X^{\Delta_h}) \stackrel{\text{def}}{=} \left\{ v \in \mathcal{U}(\omega_X^{\Delta_h}) \middle| \; v|_{\partial\omega_X^{\Delta_h} \cap \Gamma_D} = 0 \text{ or } \int_{\omega_X^{\Delta_h}} v = 0 \right\}$ such that

$$\mathcal{B}_{\omega_X^{\Delta_h}}(\breve{e}_{\omega_X^{\Delta_h}}, v) \stackrel{\text{def}}{=} \int_{\omega_X^{\Delta_h}} \nabla v^T \mathbf{K} \nabla \breve{e}_{\omega_X^{\Delta_h}} + \int_{\partial\omega_X^{\Delta_h}} \alpha \, \breve{e}_{\omega_X^{\Delta_h}} \, v = \mathcal{R}_{\omega_X^{\Delta_h}}(\phi_X^{\Delta_h} \, v) \qquad \forall v \in \mathcal{U}_0(\omega_X^{\Delta_h}) \tag{4.33}$$

Note that

$$\mathcal{R}(v) = \sum_{X \in \mathcal{N}(\Delta_h)} \mathcal{R}_{\omega_X^{\Delta_h}}(\phi_X^{\Delta_h} \, v) \tag{4.34}$$

When we employ the p-version with elements of degree $p+k$ to approximate the indicator function $\breve{e}_{\omega_X^{\Delta}}$, and then we have the computed subdomain residual estimator

defined as

$$\mathscr{C}^{U}_{Sub,p+k} \stackrel{\text{def}}{=} \sqrt{\sum_{\tau\in\Delta_h} \Big|\Big| \sum_{X\in\mathcal{N}(\Delta_h)} \breve{e}_{\omega_X^{\Delta_h},p+k}\Big|\Big|^2_{\mathscr{U}}} \tag{4.35}$$

where $\breve{e}_{\omega_X^{\Delta_h},p+k}$ denotes the $p+k$ degree finite element approximation of the exact indicator function $\breve{e}_{\omega_X^{\Delta_h}}$.

From the computed error indicator function $\breve{e}_{\omega_X^{\Delta_h},p+k}$ of subdomain residual problem, the lower bound $\mathscr{C}^{L}_{Sub,p+k}$ of the error $||\hat{e}_h||_{\mathscr{U}}$ of the elliptic reconstruction problem can be constructed by smoothening the error indicator function with the introduction of the partition of unity used in the construction of the estimator

$$\tilde{e}_{p+k} = \sum_{X\in\mathcal{N}(\Delta_h)} \phi_X^{\Delta_h}\ \breve{e}_{\omega_X^{\Delta_h},p+k} \tag{4.36}$$

With the smoothened error indicator function $\tilde{e}_{p+k}$, we obtain the duality based lower bounds, namely

$$\mathscr{C}^{L}_{Sub,p+k} \stackrel{\text{def}}{=} \frac{\mathscr{R}(\tilde{e}_{p+k})}{||\tilde{e}_{p+k}+q_h||_{\mathscr{U}}} \leq ||\hat{e}_h||_{\mathscr{U}} \tag{4.37}$$

where $q_h \in S^p_{\Delta_h}$ can be obtained by solving the following variational problem

$$\mathscr{B}(q_h,q_h) = -\mathscr{B}(\tilde{e}_{p+k},q_h) \qquad \forall q_h \in S^p_{\Delta_h} \tag{4.38}$$

It should be noted that q_h is the function satisfying

$$||\tilde{e}_{p+k}+q_h||_{\mathscr{U}} = \min_{\chi\in S^p_{\Delta_h}} ||\tilde{e}_{p+k}+\chi||_{\mathscr{U}} \tag{4.39}$$

Upper Estimates for Space-Time Norm:

$$||e_h||_{\mathscr{C}} \leq \mathscr{F}^{U}_{Sub} \stackrel{\text{def}}{=} \sqrt{\int_0^T (T-t)\ \left(\mathscr{C}^{U}_{Sub}\right)^2\ dt + T\ ||\sqrt{\gamma}e_h(0)||^2_{L^2}} \tag{4.40}$$

Proof: Given the identity as shown in the equation (4.20), the $\mathscr{C}$-norm of the exact

error of the semi-discrete finite element solution of the parabolic problem satisfies the following

$$||e_h||_{\mathscr{C}} = \sqrt{\int_0^T (T-t)\bigg(||\hat{e}_h||^2_{\mathscr{U}} - ||u-\hat{u}||^2_{\mathscr{U}} \bigg)\, dt + T||\sqrt{\gamma}e_h(0)||^2_{L^2}} \tag{4.41}$$

Therefore we have by replacing the error $||\hat{e}_h||_{\mathscr{U}}$ with its upper bound $\mathscr{E}^U$

$$\begin{aligned} ||e_h||_{\mathscr{C}} &\leq \sqrt{\int_0^T (T-t)\bigg(\big(\mathscr{E}^U_{Sub}\big)^2 - ||u-\hat{u}||^2_{\mathscr{U}} \bigg)\, dt + T||\sqrt{\gamma}e_h(0)||^2_{L^2}} \\ &\leq \sqrt{\int_0^T (T-t)\big(\mathscr{E}^U_{Sub}\big)^2\, dt + T||\sqrt{\gamma}e_h(0)||^2_{L^2}} \end{aligned} \tag{4.42}$$

□

With the computed residual estimator $\mathscr{E}^U_{Sub,p+k}$, the $\mathscr{C}$-norm of the exact error $||e_h||_{\mathscr{C}}$ can be estimated by the following

$$\mathscr{F}^U_{Sub,p+k} \stackrel{\text{def}}{=} \sqrt{\int_0^T (T-t)\, \big(\mathscr{E}^U_{Sub,p+k}\big)^2\, dt + T\, ||\sqrt{\gamma}e_h(0)||^2_{L^2}} \tag{4.43}$$

where we replaced the exact upper bound $\mathscr{E}^U_{Sub}$ in (4.40) with its computable version $\mathscr{E}^U_{Sub,p+k}$

If we replace the error $||\hat{e}_h||_{\mathscr{U}}$ in (5.63) with its duality based lower bound $\mathscr{E}^L_{Sub,p+k}$. we have

$$||e_h||_{\mathscr{C}} \geq \sqrt{\int_0^T (T-t)\bigg(\big(\mathscr{E}^L_{Sub,p+k}\big)^2 - ||u-\hat{u}||^2_{\mathscr{U}} \bigg)\, dt + T||\sqrt{\gamma}e_h(0)||^2_{L^2}} \tag{4.44}$$

A guaranteed lower bound is obtained assuming that $\int_0^T (T-t)||u-\hat{u}||^2_{\mathscr{U}} dt$ is negligible in comparison of $\int_0^T (T-t)\big(\mathscr{E}^L_{Sub,p+k}\big)^2 dt$, thus we have

$$||e_h||_{\mathscr{C}} \geq \mathscr{F}^L_{Sub,p+k} \stackrel{\text{def}}{=} \sqrt{\int_0^T (T-t)\big(\mathscr{E}^L_{Sub,p+k}\big)^2\, dt + T||\sqrt{\gamma}e_h(0)||^2_{L^2}} \tag{4.45}$$

Remark 4.7. $\mathscr{F}^U_{Sub,p+k}$ is not guaranteed upper bound of $||e_h||_{\mathscr{C}}$ since the computable estimator $\mathscr{E}^U_{Sub,p+k}$ is not a guaranteed upper bound of the exact error $||\hat{e}_h||_{\mathscr{U}}$.

Remark 4.8. Note that in [31–33] the duality approach based on space-time $\mathscr{A}$-norm does not yield lower bound while in our case we can have lower bound.

As shown in (4.44), in order to have a meaningful lower bound, the term $\int_0^T (T-t)||u-\hat{u}||^2_{\mathscr{U}}dt$ has to be negligible in comparison with the term $\int_0^T (T-t)\big(\mathscr{E}^L_{Sub,p+k}\big)^2$. To evaluate the ratio of the two, let us define

$$\epsilon^L_{p+k} \overset{\text{def}}{=} \frac{\displaystyle\int_0^T (T-t)||u-\hat{u}||^2_{\mathscr{U}}dt}{\displaystyle\int_0^T (T-t)\big(\mathscr{E}^L_{Sub,p+k}\big)^2 dt} \times 100\% \tag{4.46}$$

Let us analyze the accuracy of $\mathscr{F}^U_{Sub}$, $\mathscr{F}^U_{Sub,p+k}$, and $\mathscr{F}^L_{Sub,p+k}$ based on the sub-domain residual problem, for $\mathscr{C}$-norm of the exact error $||e_h||_{\mathscr{C}}$ using the following examples. In the meantime, we will also check the performance of the ratio ϵ^L_{p+k}.

Example 4.5. *Heat transition problem in one dimension.* Table 4.10 lists the effectivity indices

$$\kappa^U \stackrel{\text{def}}{=} \frac{\mathscr{F}^U_{Sub}}{||e_h||_{\mathscr{C}}}, \qquad \kappa^U_{p+k} \stackrel{\text{def}}{=} \frac{\mathscr{F}^U_{Sub,p+k}}{||e_h||_{\mathscr{C}}}, \qquad \kappa^L_{p+k} \stackrel{\text{def}}{=} \frac{\mathscr{F}^L_{Sub,p+k}}{||e_h||_{\mathscr{C}}} \tag{4.47}$$

for the $\mathscr{C}$-norm of the error $||e_h||_{\mathscr{C}}$ in the semi-discrete finite element solution $u_{S^p_{\Delta_h}}$ using elements of degree $p = 1, 2$ and 3, computed using Mesh I, Mesh II, Mesh III, and Mesh IV.

It can be seen that the effectivity indices κ^U are close to 1 and κ^U_{p+k}, κ^L_{p+k} are likewise. As mentioned before the computable upper bound $\mathscr{F}^U_{Sub,p+k}$ is not a guaranteed upper bound of $||e_h||_{\mathscr{C}}$ and thus $\kappa^U_{p+k} < 1$ can happen. It can also be observed that κ^U_{p+k} converges to κ^U with the increase of polynomail order $p+k$. For κ^L_{p+k} in the case of linear element if we use coarse mesh, e.g., Mesh I, we can expect the effectivity index greater than 1 for the lower bound, which corresponds to $\epsilon^L_{p+k} \approx 6\%$. With the increase of polynomial order and the finer mesh, we can see that ϵ^L_{p+k} is close to 0, which means $\int_0^T (T-t)||u-\hat{u}||^2_{\mathscr{U}}$ is negligible in comparison with $\int_0^T (T-t)\big(\mathscr{E}^L_{Sub,p+k}\big)^2 dt$, and we should expect good effectivity indices from the lower bound $\mathscr{F}^L_{Sub,p+k}$.

Table 4.10. Heat transition problem in one dimension. The values of the effectivity index κ^U, κ^U_{p+k}, κ^L_{p+k} and the ratio ϵ^L_{p+k} based on the subdomain residual estimators of the elliptic reconstruction problem, for the semi-discrete finite element solutions of degree $p = 1, 2$,and 3 computed using Mesh I, Mesh II, Mesh III, and Mesh IV corresponding respectively to mesh size $h = \frac{L}{2^n}$, $n = 1, 2, 3$, and 4 with $L = 4$.

		Mesh I			Mesh II			Mesh III			Mesh IV		
	k	p=1	p=2	p=3	p=1	p=2	p=3	p=1	p=2	p=3	p=1	p=2	p=3
κ^U_{p+k}	1	1.0122	0.9942	0.9957	1.0024	0.9980	0.9988	1.0006	0.9995	0.9997	1.0001	0.9999	0.9999
	2	1.0294	1.0027	1.0006	1.0073	1.0002	1.0000	1.0018	1.0000	1.0000	1.0005	1.0000	1.0000
	3	1.0304	1.0030	1.0007	1.0073	1.0002	1.0000	1.0018	1.0000	1.0000	1.0005	1.0000	1.0000
κ^U	∞	1.0304	1.0030	1.0007	1.0073	1.0002	1.0000	1.0018	1.0000	1.0000	1.0005	1.0000	1.0000
κ^L_{p+k}	1	1.0130	0.9784	0.9727	0.9930	0.9834	0.9732	0.9882	0.9855	0.9734	0.9870	0.9861	0.9734
	2	1.0111	0.9673	0.9592	0.9870	0.9717	0.9592	0.9811	0.9736	0.9593	0.9796	0.9741	0.9593
	3	1.0093	0.9652	0.9562	0.9832	0.9688	0.9554	0.9770	0.9707	0.9553	0.9754	0.9712	0.9553
ϵ^L_{p+k}	1	6.0160	0.6253	0.1442	1.4942	0.0404	0.0103	0.3762	0.0025	0.0007	0.0942	0.0002	0.0000
	2	6.0384	0.6397	0.1483	1.5127	0.0414	0.0106	0.3816	0.0026	0.0007	0.0957	0.0002	0.0000
	3	6.0598	0.6425	0.1492	1.5241	0.0416	0.0107	0.3849	0.0026	0.0007	0.0965	0.0002	0.0000

Example 4.6. *Two dimensional synthetic problem.* Table 4.11 lists the effectivity index κ^U , κ^U_{p+k}, κ^L_{p+k}, and the ratio ϵ^L_{p+k} for the $\mathscr{C}$-norm of the error $||e_h||_{\mathscr{C}}$ in the semi-discrete finite element solution $u_{S^p_{\Delta_h}}$ using elements of degree $p = 1, 2$ and 3, computed using Mesh I, Mesh II, Mesh III, and Mesh IV.

It can be seen that κ^U are all close to 1. Even for the coarse mesh, e.g., Mesh I where the relative error is about 100%, the effectivity index is still close to 1. For κ^U_{p+k}, it can be observed that for the coarse mesh such as Mesh I and Mesh II the upper bound $\mathscr{F}^U_{Sub,p+k}$ can grossly underestimate the exact error $||e_h||_{\mathscr{C}}$ in the case of $p = 3, k = 1$ which has the effectivity index as small as 0.3762. However with the increase of polynomial order $p+k$ the effectivity indices can be improved dramatically. Again note that the computable upper bound $\mathscr{F}^U_{p+k}$ is not a guaranteed upper bound. The effectivity index κ^L_{p+k} has good performance and the worst number is about 0.5 as in the case of Mesh I, $p = 3, k = 1$. It should be noted that the lower bound $\mathscr{F}^L_{Sub,p+k}$ can be greater than the computable upper bound $\mathscr{F}^U_{Sub,p+k}$, which is the case for $k = 1$. It can be noted that ϵ^L_{p+k} is small and the maximum value is about 3%, which indicates that the lower bound can be sharp if $\mathscr{E}^L_{Sub,p+k}$ is a sharp lower bound of the exact error $||\hat{e}_h||_{\mathscr{U}}$.

Table 4.11. Two dimensional synthetic problem. The values of the effectivity index κ^U, κ^U_{p+k}, κ^L_{p+k} and the ratio ϵ^L_{p+k} based on the subdomain residual estimators of the elliptic reconstruction problem, for the semi-discrete finite element solutions of degree $p = 1, 2$,and 3 computed using Mesh I, Mesh II, Mesh III, and Mesh IV corresponding respectively to mesh size $h = \frac{L}{2^n}$, $n = 1, 2, 3$, and 4 with $L = 1$.

		Mesh I			Mesh II			Mesh III			Mesh IV		
	k	p=1	p=2	p=3	p=1	p=2	p=3	p=1	p=2	p=3	p=1	p=2	p=3
κ^U_{p+k}	1	0.5326	0.6140	0.3762	0.7826	0.4135	0.8717	0.7085	0.9147	0.9564	0.9483	0.9872	0.9485
	2	0.7144	0.6674	0.6258	0.8226	0.8933	0.8986	0.9617	0.9947	0.9879	1.0012	0.9993	0.9991
	3	0.7525	0.7757	0.8440	0.9683	0.9152	0.9798	1.0010	0.9998	0.9999	1.0025	1.0006	1.0001
κ^U	∞	1.0010	1.0024	1.0015	1.0121	1.0013	1.0013	1.0046	1.0019	1.0007	1.0026	1.0006	1.0001
κ^L_{p+k}	1	0.6253	0.6221	0.5285	0.7712	0.7372	0.8625	0.8206	0.9324	0.9469	0.9544	0.9680	0.9483
	2	0.7018	0.6644	0.6949	0.8258	0.8715	0.8592	0.9308	0.9568	0.9420	0.9720	0.9607	0.9597
	3	0.7319	0.7986	0.8294	0.9230	0.8746	0.9391	0.9552	0.9606	0.9594	0.9733	0.9634	0.9617
ϵ^L_{p+k}	1	3.1094	1.3817	1.1665	1.6097	0.3423	0.3228	0.3418	0.3338	0.1463	0.2806	0.0911	0.0200
	2	2.1968	1.1764	0.6383	1.3771	0.2424	0.3254	0.2641	0.3169	0.1479	0.2704	0.0925	0.0195
	3	1.9537	0.7661	0.4384	1.0743	0.2407	0.2714	0.2505	0.3144	0.1425	0.2697	0.0920	0.0195

Example 4.7. *L-shaped domain problem.* Table 4.12 lists the effectivity index κ^U , κ^U_{p+k}, κ^L_{p+k}, and the ratio ϵ^L_{p+k} for the $\mathscr{C}$-norm of the error $||e_h||_{\mathscr{C}}$ in the semi-discrete finite element solution $u_{S^p_{\Delta_h}}$ using elements of degree $p = 1, 2$ and 3, computed using Mesh I, Mesh II, Mesh III, and Mesh IV.

It can be seen that κ^U are all close to 1. The worst effectivity index is around 1.3 which happens to Mesh I and element degree $p = 1$. For κ^U_{p+k}, in the case of $p = 3$ and $k = 1$, the effectivity index can be as small as 0.5. However with the increase of polynomial order $p+k$ the effectivity indices can be improved to be around 0.8. Again note that the computable upper bound $\mathscr{F}^U_{p+k}$is not a guaranteed upper bound. For the effectivity index κ^L_{p+k}, we can see that ϵ^L_{p+k} is over 10% except for Mesh III and IV with element order $p = 2, 3$, which means that the term $\int_0^T (T-t)||u-\hat{u}||^2_{\mathscr{U}}dt$ as shown in (5.66) is not negligible in comparison of $\int_0^T (T-t)\big(\mathscr{C}^L_{Sub,p+k}\big)^2 dt$. Therefore κ^L_{p+k} is a guaranteed lower bound even though it happens that κ^L_{p+k} can be good effectivity indices close to 1. In the case that ϵ^L_{p+k} is small number, such as $\epsilon^L_{p+k} = 7.1\%$ in the case of Mesh III and $p = 3$, we can expect guaranteed lower bound, which is 0.8 in this case. It should be noted that the lower bound $\mathscr{F}^L_{Sub,p+k}$ can be greater than the computable upper bound $\mathscr{F}^U_{Sub,p+k}$.

Table 4.12. L-shaped domain problem. The values of the effectivity index κ^U, κ^U_{p+k}, κ^L_{p+k} and the ratio ϵ^L_{p+k} based on the subdomain residual estimators of the elliptic reconstruction problem, for the semi-discrete finite element solutions of degree $p = 1, 2$,and 3 computed using Mesh I, Mesh II, Mesh III, and Mesh IV corresponding respectively to mesh size $h = \frac{L}{2^n}$, $n = 1, 2, 3$, and 4 with $L = 1$.

		Mesh I			Mesh II			Mesh III			Mesh IV		
	k	p=1	p=2	p=3	p=1	p=2	p=3	p=1	p=2	p=3	p=1	p=2	p=3
κ^U_{p+k}	1	0.8869	0.6511	0.5555	0.8197	0.6357	0.5480	0.7929	0.6274	0.5436	0.7792	0.6225	0.5409
	2	1.0339	0.7997	0.7019	0.9605	0.7817	0.6926	0.9302	0.7717	0.6871	0.9142	0.7658	0.6837
	3	1.1020	0.8776	0.7841	1.0265	0.8583	0.7738	0.9945	0.8474	0.7677	0.9774	0.8409	0.7640
κ^U	∞	1.2643	1.0965	1.0478	1.1994	1.0878	1.0472	1.1630	1.0744	1.0392	1.1432	1.0661	1.0341
κ^L_{p+k}	1	0.9430	0.7250	0.6277	0.8610	0.7046	0.6177	0.8257	0.6932	0.6117	0.8068	0.6863	0.6080
	2	1.0375	0.8354	0.7456	0.9500	0.8113	0.7331	0.9104	0.7974	0.7255	0.8885	0.7890	0.7208
	3	1.0835	0.8897	0.8063	0.9925	0.8635	0.7922	0.9504	0.8483	0.7837	0.9271	0.8390	0.7785
ϵ^L_{p+k}	1	57.392	35.988	29.322	35.368	22.851	18.558	22.237	14.478	11.728	14.060	9.1565	7.4105
	2	47.411	27.099	20.781	29.057	17.237	13.175	18.295	10.941	8.3368	11.592	6.9288	5.2725
	3	43.467	23.895	17.773	26.622	15.217	11.281	16.785	9.6690	7.1433	10.647	6.1276	4.5200

Example 4.8. *Heat equation in a thermal battery.* Table 4.13 lists the effectivity index κ^U , κ^U_{p+k}, κ^L_{p+k}, and the ratio ϵ^L_{p+k} for the $\mathscr{C}$-norm of the error $||e_h||_{\mathscr{C}}$ in the semi-discrete finite element solutions $u_{S^p_{\Delta_h}}$ of degree $p = 1, 2$ and 3, computed using Mesh I and Mesh II as shown in Fig. 2.2, for the orthotropic case and the isotropic case.

It can be seen that κ^U is close to 1 for isostropic case. However for orthotropic case, the effectivity index κ^U deteriorates and $\mathscr{F}^U_{Sub}$ severely overestimates the exact error $||e_h||_{\mathscr{C}}$, and the culprit of the deterioration is the interface layers at the top and bottom of the highly orthotropic subdomain Ω_3. For details about the effect of interface layers on the robustness of residual estimators, refer to [1]. Note that the exact upper bound $\mathscr{F}^U_{Sub}$ is constructed from the "exact" indicator functions $\breve{e}_{\omega_X^{\Delta_h}}$ computed by employing the restriction of the overkill space $S^7_{\Delta^{ovk}}$ in the elements and subdomains.

The effectivity index κ^U_{p+k} based on the computable upper bound $\mathscr{F}^U_{p+k}$ converges to the corresponding exact one κ^U based on the exact upper bound $\mathscr{F}^U$. Again the computable upper bound $\mathscr{F}^U_{Sub,p+k}$ based on the subdomain residual estimator $\mathscr{E}^U_{Sub,p+k}$ may underestimate the exact error $||e_h||_{\mathscr{C}}$ for the isotropic case. In the orthotropic case, $\mathscr{F}^U_{Sub,p+k}$ grossly overestimates the exact error $||e_h||_{\mathscr{C}}$ because of interface layers in the highly orthotropic domain which causes the severe overestimation of $\mathscr{E}^U_{Sub,p+k}$ about the exact error of the elliptic reconstruction problem.

In the case of κ^L_{p+k}, it can be seen that $\mathscr{F}^L_{Sub,p+k}$ based on the subdomain residual of elliptic reconstruction problem grossly underestimates the exact error $||e_h||_{\mathscr{E}}$ for the orthotropic case. The reason is that the lower bound $\mathscr{E}^L_{p+k}$ severely underestimates the exact error of the elliptic reconstruction problem due to the presence of the interface layers. However, in the isotropic case, for finer mesh and higher order of polynomial, e.g., Mesh II and $p = 2, 3$, the lower bound can yield pretty good effectivity indices close to 0.9.

For the ratio of ϵ^L_{p+k}, in the isotropic case ϵ^L_{p+k} is close to 0, which means the neglected term $\displaystyle\int_0^T (T-t)||u-\hat{u}||^2_{\mathscr{U}}dt$ in (5.66) is negligible in comparison of the term $\displaystyle\int_0^T (T-t)\big(\mathscr{E}^L_{Sub,p+k}\big)^2 dt$. Therefore if $\mathscr{E}^L_{Sub,p+k}$ is a good lower bound for the exact error of $||\hat{e}_h||_{\mathscr{U}}$ of the elliptic reconstruction problem, the effectivity index κ^L_{p+k} is good. In the orthotropic case the ratio ϵ^L_{p+k} can be as worse as 300% and in the meantime $\mathscr{E}^L_{Sub,p+k}$ severely underestimates the exact error of $||\hat{e}_h||_{\mathscr{U}}$, the corresponding effectivity index κ^L_{p+k} is close to 0.15. Even in the case when ϵ^L_{p+k} is 5%, the effectivity index κ^L_{p+k} is still 0.3 due to the underestimate of $\mathscr{E}^L_{Sub,p+k}$ over $||\hat{e}_h||_{\mathscr{U}}$.

Table 4.13. Transient diffusion problem in a thermal battery. The values of the effectivity index κ^U, κ^U_{p+k}, κ^L_{p+k} and the ratio ϵ^L_{p+k} based on the subdomain residual estimators of the elliptic reconstruction problem, for the semi-discrete finite element solutions of degree $p = 1, 2$,and 3 computed using Mesh I, and Mesh II as shown in Fig. 2.2, for the orthotropic and the isotropic case.

		Orthotropic						Isotropic					
		Mesh I			Mesh II			Mesh I			Mesh II		
	k	p=1	p=2	p=3	p=1	p=2	p=3	p=1	p=2	p=3	p=1	p=2	p=3
κ^U_{p+k}	1	6.8930	5.0605	4.2962	8.9716	6.4718	4.6249	0.9823	0.7974	0.6862	0.9743	0.8026	0.6936
	2	8.5241	6.5257	5.6635	9.9363	7.5684	5.6048	1.0698	0.9210	0.8269	1.0550	0.9259	0.8345
	3	8.5272	6.5312	5.6722	9.9373	7.5711	5.6095	1.0985	0.9718	0.8922	1.0832	0.9772	0.9004
κ^U	∞	8.5368	6.5476	5.6997	9.9398	7.5781	5.6227	1.1336	1.0575	1.0261	1.1185	1.0644	1.0338
κ^L_{p+k}	1	0.1498	0.1866	0.2219	0.1945	0.2470	0.2508	0.6548	0.7613	0.7143	0.7254	0.7689	0.7131
	2	0.1696	0.2189	0.2642	0.2117	0.2869	0.2990	0.7142	0.8551	0.8234	0.7872	0.8624	0.8244
	3	0.1719	0.2240	0.2721	0.2135	0.2923	0.3069	0.7379	0.8921	0.8694	0.8087	0.8979	0.8707
ϵ^L_{p+k}	1	278.88	101.55	32.781	95.484	19.664	7.6115	0.2606	0.0518	0.0269	0.0957	0.0227	0.0122
	2	217.53	73.797	23.127	80.575	14.572	5.3554	0.2191	0.0411	0.0202	0.0813	0.0180	0.0091
	3	211.84	70.503	21.799	79.219	14.034	5.0841	0.2053	0.0377	0.0181	0.0770	0.0166	0.0082

4.5 Error estimation at any time instant

As we have already seen in (4.12) except the linear element in the L^2 norm, due to the superconvergence properties of the term $u - \hat{u}$, we have

$$||e_h||_H = ||u - u_{S^p_{\Delta_h}}||_H \approx ||\hat{u} - u_{S^p_{\Delta_h}}||_H \tag{4.48}$$

for $H = L^2$, and $H = \mathcal{U}$.

Let us define the effectivity index at any time instant as

$$\eta(t) \stackrel{\text{def}}{=} \frac{||\hat{u} - u_{S^p_{\Delta_h}}||_{\mathcal{U}}}{||e_h||_{\mathcal{U}}}, \qquad \zeta(t) \stackrel{\text{def}}{=} \frac{||\hat{u} - u_{S^p_{\Delta_h}}||_{L^2}}{||e_h||_{L^2}} \tag{4.49}$$

Similarly $\eta_{S^{p+k}_{\Delta_{h'}}}(t)$ and $\zeta_{S^{p+k}_{\Delta_{h'}}}(t)$ when $\hat{u}$ is replaced by $\hat{u}_{S^{p+k}_{\Delta_{h'}}}$.

Further, we let

$$\bar{\eta}^U(t) \stackrel{\text{def}}{=} \frac{\mathscr{E}^U_{Sub}}{||e_h||_{\mathcal{U}}}, \qquad \bar{\eta}^L_{p+k}(t) \stackrel{\text{def}}{=} \frac{\mathscr{E}^L_{Sub,p+k}}{||e_h||_{\mathcal{U}}} \tag{4.50}$$

where $\mathscr{E}^U_{Sub}$ is the exact estimator of $||\hat{u} - u_{S^p_{\Delta_h}}||_{\mathcal{U}}$, and $\bar{\eta}^U_{p+k}(t)$ for the computable "bound"

In the case of the exact error measured in L^2 norm, we can also calculate the effectivity index based on the exact and computed error indicator function. Thus we have

$$\bar{\zeta}(t) \stackrel{\text{def}}{=} \frac{\sqrt{\sum_{\tau\in\Delta_h} \Big|\Big| \sum_{X\in\mathcal{N}(\Delta_h)} \hat{e}_{\omega^{\Delta_h}_X} \Big|\Big|^2_{L^2}}}{||e_h||_{L^2}} \tag{4.51}$$

and $\bar{\zeta}_{p+k}(t)$ when the computable indicator is used.

Let us use the above effectivity indices to analyze the quality of the error estimators at all time instants.

Example 4.9. *Heat transition problem in one dimension.* For this problem, we focus on uniform coarse mesh consisting of 16 elements with mesh size equal to $h = \frac{L}{2^2}, L = 4$.

Fig. 4.10 is the variation of effectivity index $\eta(t)$ and its computable version $\eta_{S^{p+k}_{\Delta_{h'}}}(t)$ corresponding to the exact solution $\hat{u}$ and its approximate solution $\hat{u}_{S^{p+k}_{\Delta_{h'}}}$ from p method, for the elliptic reconstruction problem constructed from the semi-discrete finite element solutions of degree $p = 1, 2$, and 3 with mesh size $h = \frac{L}{2^2}$. It can be seen that the effectivity index is close to 1 except for the time instants close to $t = 0$ at which the boundary condition and initial condition are suddenly applied. Note that with the increase of polynomial order $p + k$ in the approximate solution $\hat{u}_{S^{p+k}_{\Delta_{h'}}}$, the computable version $\eta_{S^{p+k}_{\Delta_{h'}}}(t)$ is close to the exact one $\eta(t)$.

Fig. 4.11 is the variation of effectivity index $\zeta(t)$ and its computable version $\zeta_{S^{p+k}_{\Delta_{h'}}}(t)$ corresponding to the exact solution $\hat{u}$ and its approximate solution $\hat{u}_{S^{p+k}_{\Delta_{h'}}}$ from p method, for the elliptic reconstruction problem constructed from the semi-discrete finite element solutions of degree $p = 1, 2$, and 3 with mesh size $h = \frac{L}{2^2}$. Except the linear element ($p = 1$) where $||u - \hat{u}||_{L^2}$ does not have superconvergence property, it can be seen that the effectivity index is close to 1 except for the time instants close to $t = 0$ at which the boundary condition and initial condition are suddenly applied. Note that with the increase of polynomial order $p + k$ in the approximate solution $\hat{u}_{S^{p+k}_{\Delta_{h'}}}$, the computable version $\zeta_{S^{p+k}_{\Delta_{h'}}}(t)$ is close to the exact one $\zeta(t)$.

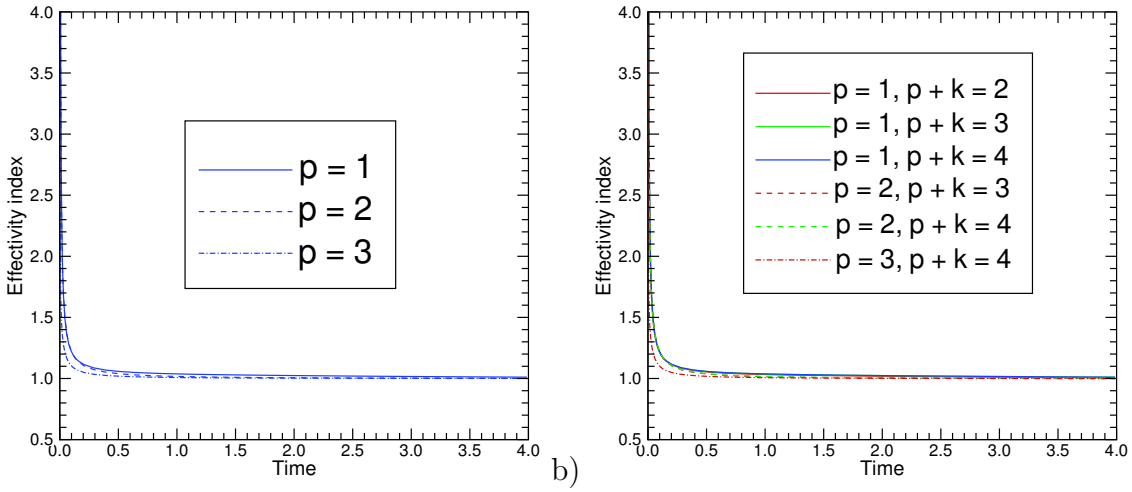

Fig. 4.10. Heat transition problem in one dimension. a) The evolution of effectivity index $\eta(t)$ based on the exact solution $\hat{u}$ of the elliptic reconstruction problem; b) The evolution of effectivity index $\eta_{S^{p+k}_{\Delta_{h'}}}(t)$ based on the approximate solution $\hat{u}_{S^{p+k}_{\Delta_{h'}}}$ of the elliptic reconstruction problem. Note that the elliptic reconstruction problem is constructed from the semi-discrete finite element solutions of degree $p = 1, 2$, and 3 with mesh size $h = \frac{L}{2^2}$.

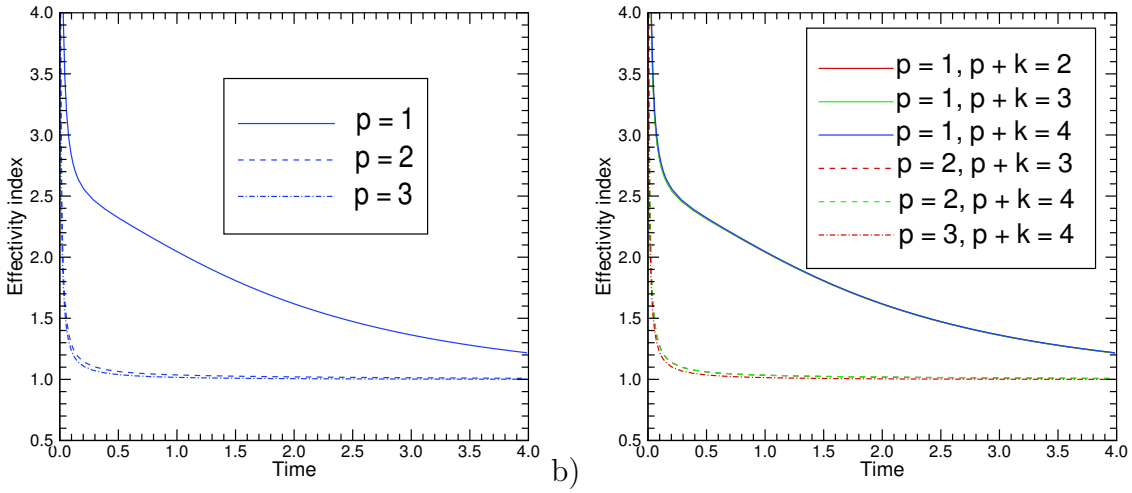

Fig. 4.11. Heat transition problem in one dimension. a) The evolution of effectivity index $\zeta(t)$ based on the exact solution $\hat{u}$ of the elliptic reconstruction problem; b) The evolution of effectivity index $\zeta_{S^{p+k}_{\Delta_{h'}}}(t)$ based on the approximate solution $\hat{u}_{S^{p+k}_{\Delta_{h'}}}$ of the elliptic reconstruction problem. Note that the elliptic reconstruction problem is constructed from the semi-discrete finite element solutions of degree $p = 1, 2$, and 3 with mesh size $h = \frac{L}{2^2}$.

Fig. 4.12 is the evolution of effectivity index $\bar{\eta}^U(t)$, $\bar{\eta}^U_{p+k}(t)$, and $\bar{\eta}^L_{p+k}(t)$) for the exact error measured in energy norm, where the exact error indicator function and its computed version are obtained from the subdomain residual problem of the elliptic reconstruction problems corresponding to the semi-discrete finite element solution $u_{S^p_{\Delta_h}}$ of degree $p = 1, 2$, and 3. It can be observed that except at time instants close to $t = 0$ the effecitivity indices are all close to 1. Note that $\bar{\eta}^L_{p+k}(t)$ is greater than 1 which means that the duality-based lower bound $\mathscr{E}^L_{Sub,p+k}$ is not necessary a guaranteed lower bound for the exact error $||e_h||_{\mathscr{U}}$ even though it is indeed a lower bound for the exact error $||\hat{u} - u_{S^p_{\Delta_h}}||_{\mathscr{U}}$ of the elliptic reconstruction problem.

Fig. 4.13 is the evolution of effectivity index $\bar{\zeta}(t)$ and $\bar{\zeta}_{p+k}(t)$ for the exact error measured in L^2norm, where the exact error indicator function and its computed version are obtained from the subdomain residual problem of the elliptic reconstruction problem. It can be seen that except the linear element case, the effecitivity indices are all close to 1.

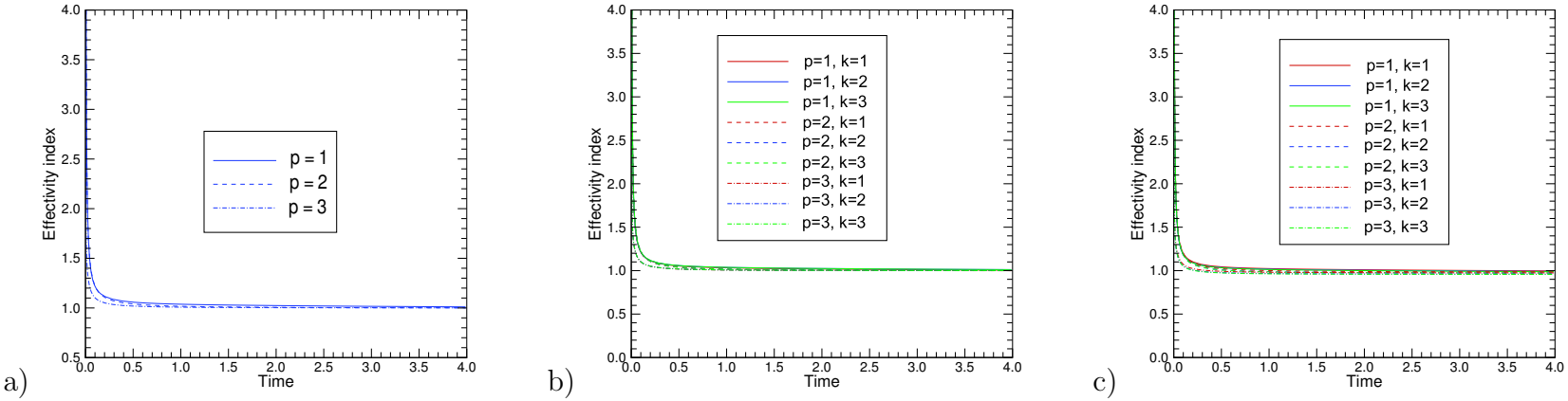

Fig. 4.12. Heat transition problem in one dimension. The evolution of effectivity index for the exact error measured in energy norm based on the subdomain residual problem of the elliptic reconstruction problem. a) $\bar{\eta}^U(t)$; b) $\bar{\eta}^U_{p+k}(t)$; c) $\bar{\eta}^L_{p+k}(t)$.

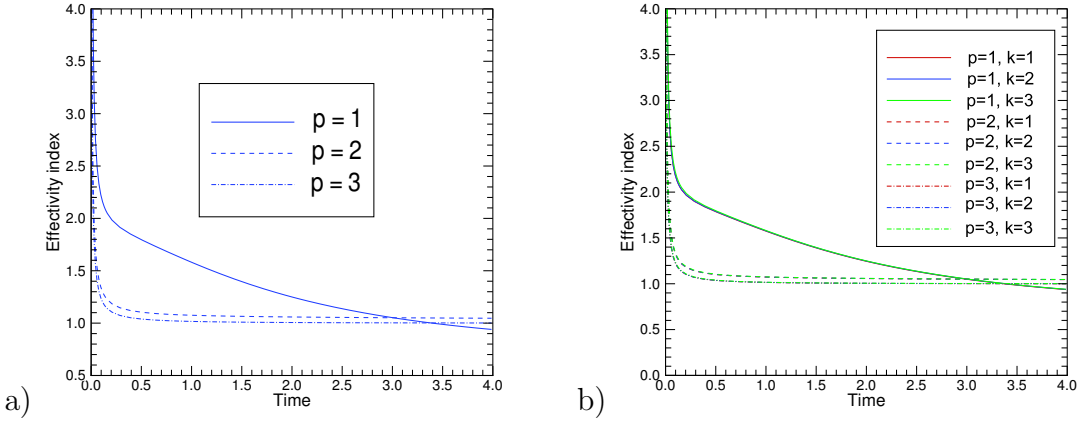

Fig. 4.13. Heat transition problem in one dimension. The evolution of effectivity index for the exact error measured in L^2 norm based on the subdomain residual problem of the elliptic reconstruction problem. a)$\bar{\zeta}(t)$; b) $\bar{\zeta}_{p+k}(t)$.

Fig. 4.14 is the comparison of the exact error $u - u_{S^p_{\Delta_h}}$ in value with its approximate $\hat{u} - u_{S^p_{\Delta_h}}$ at time instant $t = \frac{T}{16}$ for the exact solution $\hat{u}$ of the elliptic reconstruction problem constructed from the semi-discrete finite element solutions of degree $p = 1, 2,$ and 3 with mesh size $h = \frac{L}{2^2}$. It can be seen that except the linear element case $p = 1$, the exact error $u - u_{S^p_{\Delta_h}}$ can be approximated very well by $\hat{u} - u_{S^p_{\Delta_h}}$. We can see similar behavior as shown in Fig. 4.15 if we use approximated solution $\hat{u}_{S^{p+k}_{\Delta_{h'}}}$ of degree $p = k$ to the elliptic reconstruction problem instead of the exact solution $\hat{u}$. Note that the solid line denotes the quantities related to u while discontinuous line related to $\hat{u}$ or its computable version $\hat{u}_{S^{p+k}_{\Delta_{h'}}}$

Fig. 4.16 is the comparison of the exact error $\frac{\partial u}{\partial x} - \frac{\partial u_{S^p_{\Delta_h}}}{\partial x}$ in derivative with its approximate $\frac{\partial \hat{u}}{\partial x} - \frac{\partial u_{S^p_{\Delta_h}}}{\partial x}$ at time instant $t = \frac{T}{16}$. It can be seen that the difference between the two is small. Likewise for the case when we replace the exact solution $\hat{u}$ with computable $\hat{u}_{S^{p+k}_{\Delta_{h'}}}$ as shown in Fig. 4.17.

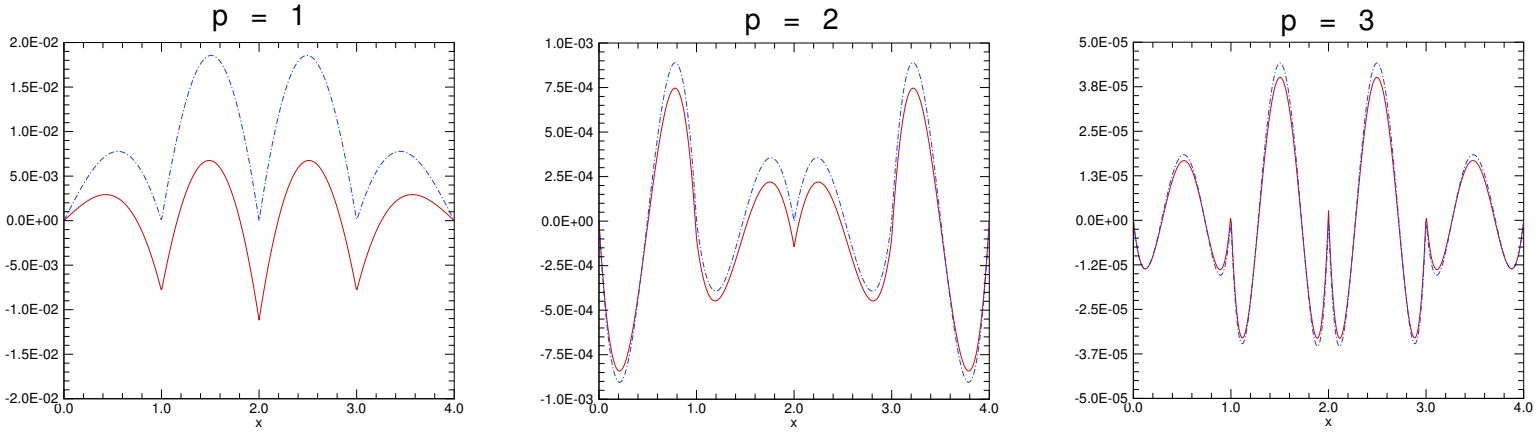

Fig. 4.14. Heat transition problem in one dimension. The comparison of $\hat{u} - u_{S^p_{\Delta_h}}$ with $u - u_{S^p_{\Delta_h}}$ at $t = \frac{T}{16}$.

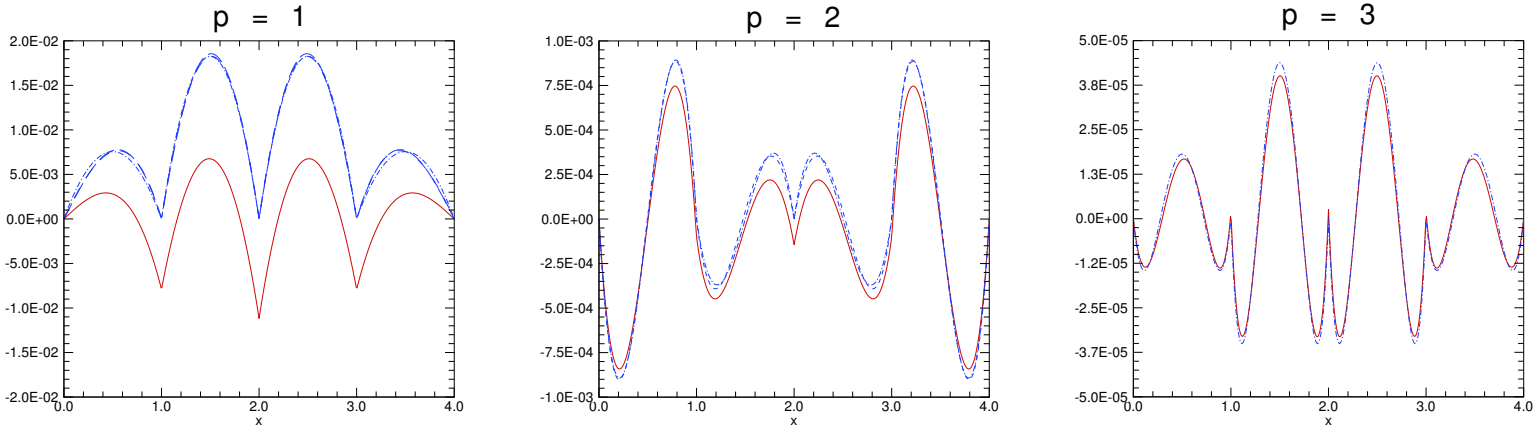

Fig. 4.15. Heat transition problem in one dimension. The comparison of $\hat{u}_{S^{p+k}_{\Delta_{h'}}} - u_{S^p_{\Delta_h}}$ with $u - u_{S^p_{\Delta_h}}$ at $t = \frac{T}{16}$.

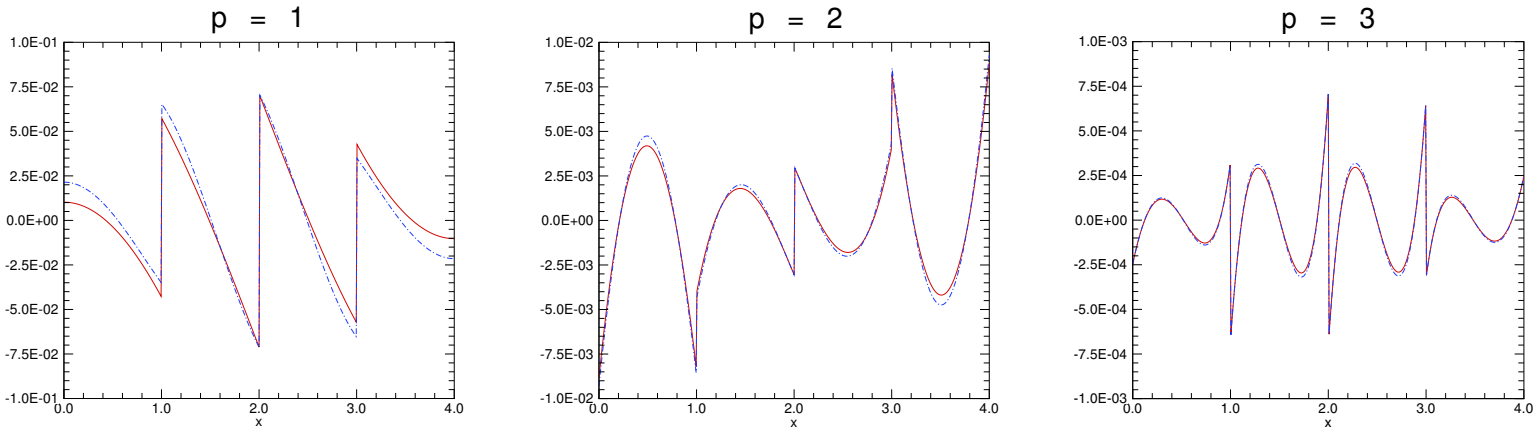

Fig. 4.16. Heat transition problem in one dimension. The comparison of $\frac{\partial \hat{u}}{\partial x} - \frac{\partial u_{S^p_{\Delta_h}}}{\partial x}$ with $\frac{\partial u}{\partial x} - \frac{\partial u_{S^p_{\Delta_h}}}{\partial x}$ at $t = \frac{T}{16}$.

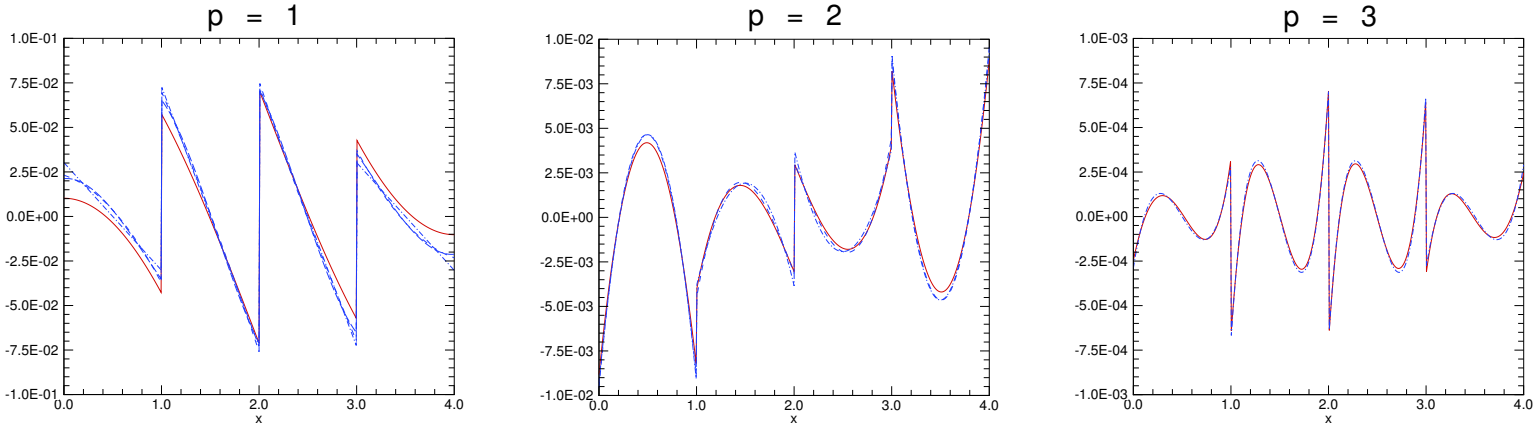

Fig. 4.17. Heat transition problem in one dimension. The comparison of $\frac{\partial \hat{u}_{S^{p+k}_{\Delta_{h'}}}}{dx} - \frac{\partial u_{S^p_{\Delta_h}}}{dx}$ with $\frac{\partial u}{\partial x} - \frac{\partial u_{S^p_{\Delta_h}}}{\partial x}$ at $t = \frac{T}{16}$.

Example 4.10. *Two dimensional synthetic problem.* For this problem, we also choose uniform coarse mesh (Mesh 2) with the number of elements equal to 16. As shown in Fig. 4.5 at time instants $t = \frac{T}{16}, \frac{T}{2}$, the term $u - \hat{u}$ measured in energy norm and L^2 norm does not exhibit superconvergence properties over $u - u_{S^p_{\Delta_h}}$. However its magnitude is much smaller than that of $u - u_{S^p_{\Delta_h}}$.

Fig. 4.18 is the variation of effectivity index $\eta(t)$ and its computable version $\eta_{S^{p+k}_{\Delta_{h'}}}(t)$ corresponding to the exact solution $\hat{u}$ and its approximate solution $\hat{u}_{S^{p+k}_{\Delta_{h'}}}$ from p method, for the elliptic reconstruction problem constructed from the semi-discrete finite element solutions of degree $p = 1, 2$, and 3 with mesh size $h = \frac{L}{2^2}$. It can be seen that the effectivity index is close to 1 except for the time instants close to $t = 0$ at which the boundary condition and initial condition are suddenly applied. Note that with the increase of polynomial order $p + k$ in the approximate solution $\hat{u}_{S^{p+k}_{\Delta_{h'}}}$, the computable version $\eta_{S^{p+k}_{\Delta_{h'}}}(t)$ converges to its corresponding exact one $\eta(t)$.

Fig. 4.19 is the variation of effectivity index $\zeta(t)$ and its computable version $\zeta_{S^{p+k}_{\Delta_{h'}}}(t)$ corresponding to the exact solution $\hat{u}$ and its approximate solution $\hat{u}_{S^{p+k}_{\Delta_{h'}}}$ from p method, for the elliptic reconstruction problem constructed from the semi-discrete finite element solutions of degree $p = 1, 2$, and 3 with mesh size $h = \frac{L}{2^2}$. For elements of degree $p \geq 2$, it can be seen that the effectivity index is close to 1 except for the time instants close to $t = 0$ at which the boundary condition and initial condition are suddenly applied. In the case of linear element $p = 1$, the effectivity index is also close to 1. This is due to the fact that except at the beginning time instant the magnitude of $||u - \hat{u}||_{L^2}$ is much smaller than that of $||\hat{u} - u_{S^p_{\Delta_h}}||_{L^2}$ as shown in Fig. 4.5 even though $||u - \hat{u}||_{L^2}$ does not have superconvergence property. Note that with the increase of polynomial order $p + k$ in the approximate solution $\hat{u}_{S^{p+k}_{\Delta_{h'}}}$, the computable version $\zeta_{S^{p+k}_{\Delta_{h'}}}(t)$ is close to the exact one $\zeta(t)$.

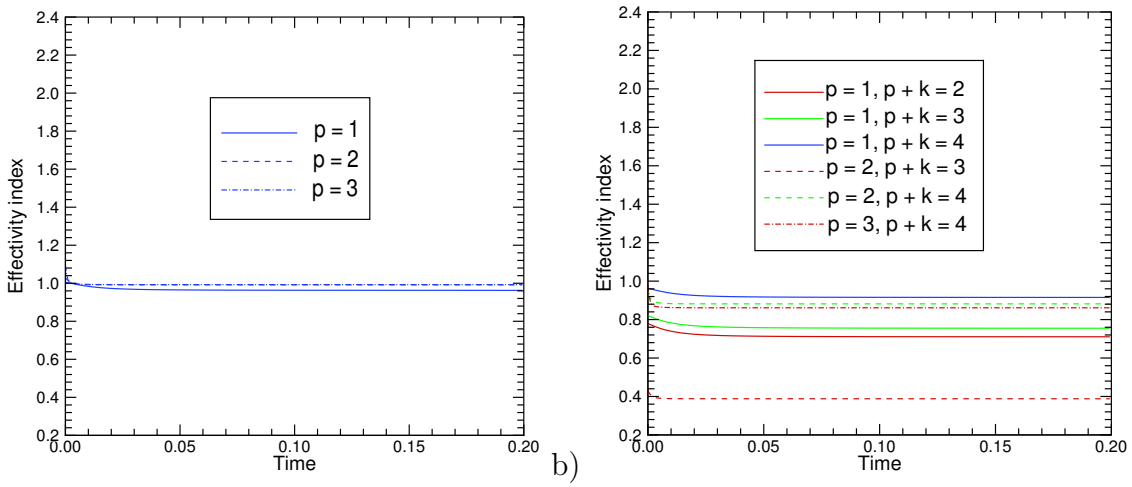

a) b)

Fig. 4.18. Two dimensional synthetic problem. a) The evolution of effectivity index $\eta(t)$ based on the exact solution $\hat{u}$ of the elliptic reconstruction problem; b) The evolution of effectivity index $\eta_{S^{p+k}_{\Delta_{h'}}}(t)$ based on the approximate solution $\hat{u}_{S^{p+k}_{\Delta_{h'}}}$ of the elliptic reconstruction problem. Note that the elliptic reconstruction problem is constructed from the semi-discrete finite element solutions of degree $p = 1, 2$, and 3 with mesh size $h = \frac{L}{2^2}$.

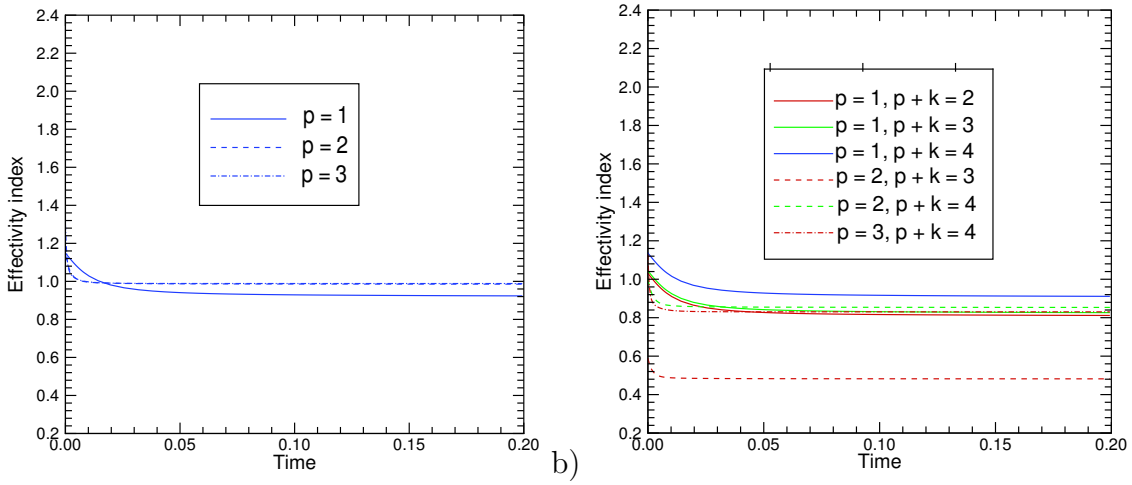

a) b)

Fig. 4.19. Two dimensional synthetic problem. a) The evolution of effectivity index $\zeta(t)$ based on the exact solution $\hat{u}$ of the elliptic reconstruction problem; b) The evolution of effectivity index $\zeta_{S^{p+k}_{\Delta_{h'}}}(t)$ based on the approximate solution $\hat{u}_{S^{p+k}_{\Delta_{h'}}}$ of the elliptic reconstruction problem. Note that the elliptic reconstruction problem is constructed from the semi-discrete finite element solutions of degree $p = 1, 2$, and 3 with mesh size $h = \frac{L}{2^2}$.

Fig. 4.20 is the evolution of effectivity index $\bar{\eta}^U(t)$, $\bar{\eta}^U_{p+k}(t)$, and $\bar{\eta}^L_{p+k}(t)$) for the exact error measured in energy norm, where the exact error indicator function and its computed version are obtained from the subdomain residual problem of the elliptic reconstruction problems corresponding to the semi-discrete finite element solution $u_{S^p_{\Delta_h}}$ of degree $p = 1, 2$, and 3. It can be seen that $\bar{\eta}^U(t)$ is close 1 even at the time instants close to $t = 0$. For the computable version $\bar{\eta}^U_{p+k}(t)$ and $\bar{\eta}^L_{p+k}(t)$) converge to 1 with the increase of order $p+k$. Note that $\bar{\eta}^U_{p+k}(t)$ is not a guarantted upper bound and it can happen that $\bar{\eta}^U_{p+k}(t)$ is smaller than the lower bound $\bar{\eta}^U_{p+k}(t)$. For instance, for $p = 2$ and $k = 1$, $\bar{\eta}^U_{p+k}(t)$ is about 0.4 while $\bar{\eta}^U_{p+k}(t)$ about 0.72.

Fig. 4.21 is the evolution of effectivity index $\bar{\zeta}(t)$ and $\bar{\zeta}_{p+k}(t)$ for the exact error measured in L^2norm, where the exact error indicator function and its computed version are obtained from the subdomain residual problem of the elliptic reconstruction problem. It can be seen that for linear element, $\bar{\zeta}(t)$ is close to 2 while for quadratic and cubic element $\bar{\zeta}(t)$ is 1 except at the time instants close to $t = 0$. The computed version $\bar{\zeta}_{p+k}(t)$ converges to the values corresponding to $\bar{\zeta}(t)$. Note that for $p = 2$ and $k = 1$, $\bar{\zeta}_{p+k}(t)$ can be as small as 0.5 and its value can be improved significantly with the increase of order k. For example, for $k = 2$, $\bar{\zeta}_{p+k}(t)$ is around 0.88.

Fig. 4.22 (resp. Fig. 4.23) is the contour plot of the exact error $|u - u_{S^p_{\Delta_h}}|$ (resp. $|\hat{u} - u_{S^p_{\Delta_h}}|$) in absolute value at time instant $t = \frac{T}{16}$ for the semi-discrete finite element solutions of degree $p = 1, 2$, and 3 and the exact solution $\hat{u}$ of the elliptic reconstruction problem based on these finite element solutions. It can be seen that the contour plots match each other well even in the case of linear element $p = 1$.

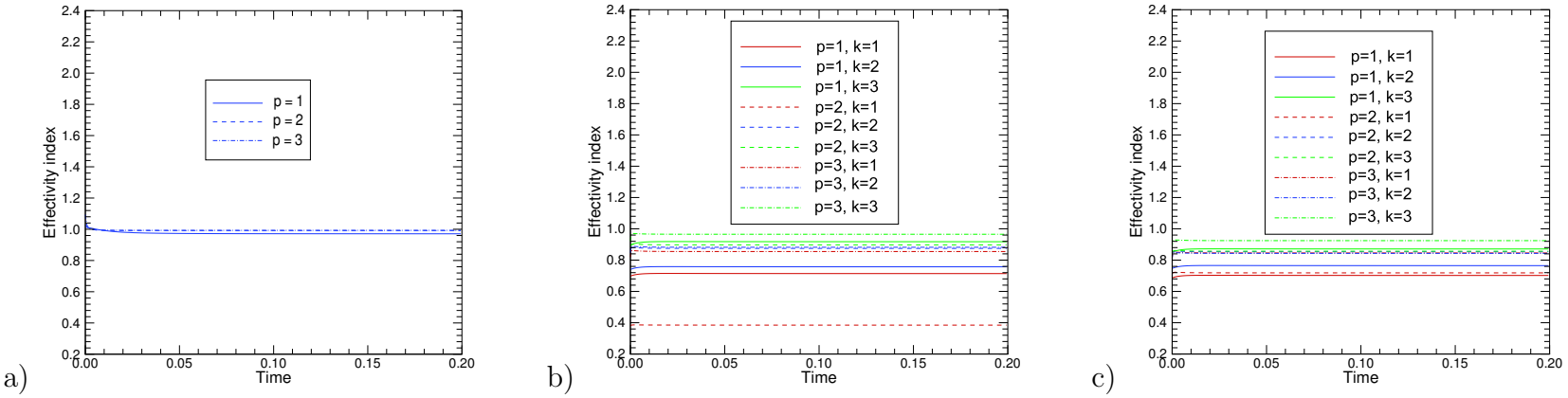

Fig. 4.20. Two dimensional synthetic problem. The evolution of effectivity index for the exact error measured in energy norm based on the subdomain residual problem of the elliptic reconstruction problem. a) $\bar{\eta}^U(t)$; b) $\bar{\eta}^U_{p+k}(t)$; c) $\bar{\eta}^L_{p+k}(t)$.

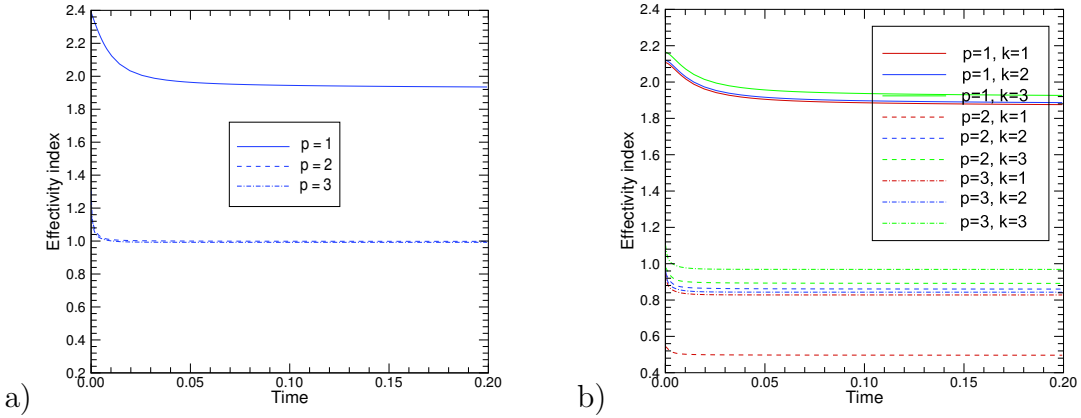

Fig. 4.21. Two dimensional synthetic problem. The evolution of effectivity index for the exact error measured in L^2 norm based on the subdomain residual problem of the elliptic reconstruction problem. a)$\bar{\zeta}(t)$; b) $\bar{\zeta}_{p+k}(t)$.

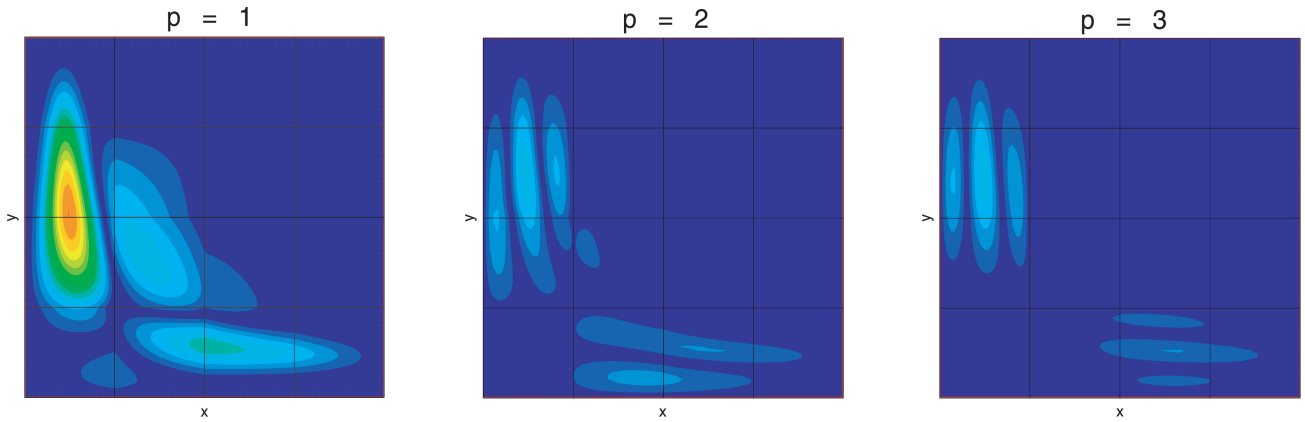

Fig. 4.22. Two dimensional synthetic problem. The contour plot of $|u - u_{S^p_{\Delta_h}}|$ at $t = \frac{T}{16}$.

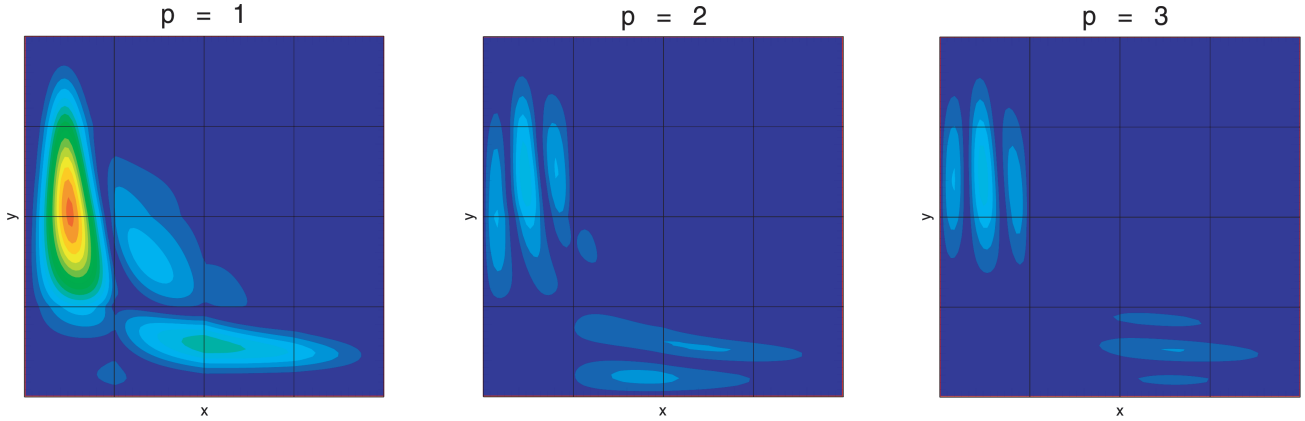

Fig. 4.23. Two dimensional synthetic problem. The contour plot of $|\hat{u} - u_{S^p_{\Delta_h}}|$ at $t = \frac{T}{16}$.

Fig. 4.24 is the contour plot of $|\hat{u}_{S^{p+k}_{\Delta_{h'}}} - u_{S^p_{\Delta_h}}|$ based on the approximate solution $\hat{u}_{S^{p+k}_{\Delta_{h'}}}$ of degree $p+k$ to the elliptic reconstruction problem. It can be seen that as the increase of polynomial order $p+k$ the contour plot of $|\hat{u}_{S^{p+k}_{\Delta_{h'}}} - u_{S^p_{\Delta_h}}|$ is close to the one from $|\hat{u} - u_{S^p_{\Delta_h}}|$.

Fig. 4.25 (resp. Fig. 4.26) is the contour plot of the modulus $|\nabla(u - u_{S^p_{\Delta_h}})|$ of the exact error (resp. Fig. 4.26) at time instant $t = \frac{T}{16}$ for the semi-discrete finite element solutions of degree $p = 1, 2$, and 3 and the exact solution $\hat{u}$ of the elliptic reconstruction problem constructed from these finite element solutions. It can be seen that these contour plots are close between $|\nabla(u - u_{S^p_{\Delta_h}})|$ and $|\nabla(\hat{u} - u_{S^p_{\Delta_h}})|$.

Fig. 4.27 is the contour plot of the modulus $|\nabla(\hat{u}_{S^{p+k}_{\Delta_{h'}}} - u_{S^p_{\Delta_h}})|$ based on the approximate solution $\hat{u}_{S^{p+k}_{\Delta_{h'}}}$ of degree $p+k$ to the elliptic reconstruction problem from the semi-discrete finite element solutions of degree $p = 1, 2$, and 3. It can be seen that with the increase of polynomial order $p+k$ in $\hat{u}_{S^{p+k}_{\Delta_{h'}}}$ the contour plots of $|\nabla(\hat{u}_{S^{p+k}_{\Delta_{h'}}} - u_{S^p_{\Delta_h}})|$ are close to $|\nabla(\hat{u} - u_{S^p_{\Delta_h}})|$.

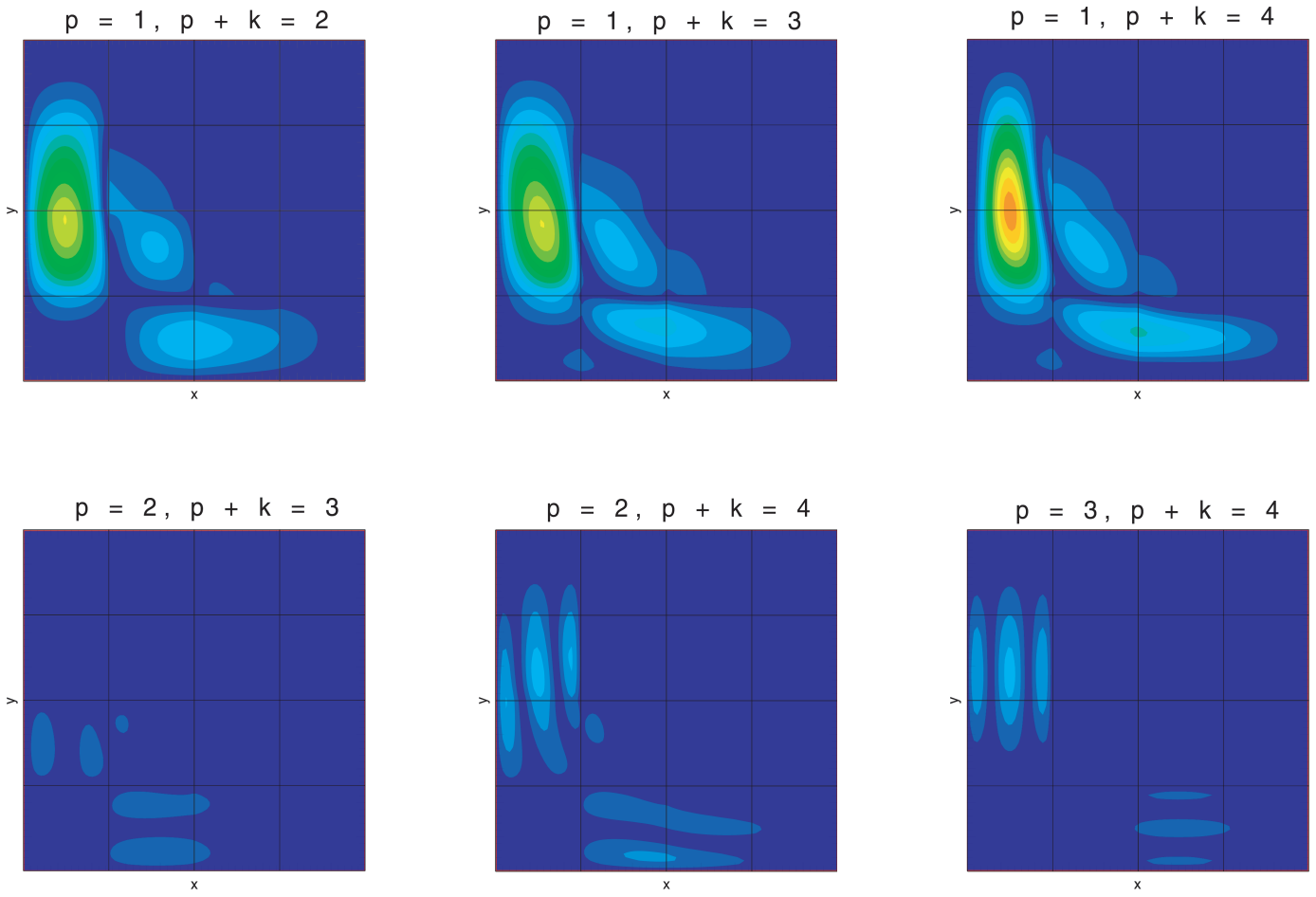

Fig. 4.24. Two dimensional synthetic problem. The contour plot of $|\hat{u}_{S^{p+k}_{\Delta_{h'}}} - u_{S^{p}_{\Delta_h}}|$ at $t = \frac{T}{16}$, where $\hat{u}_{S^{p+k}_{\Delta_{h'}}}$ is the exact solution of the elliptic reconstruction problem constructed from the semi-discrete finite element solutions of degree $p = 1, 2$, and 3 with mesh size $h = \frac{L}{2^2}$.

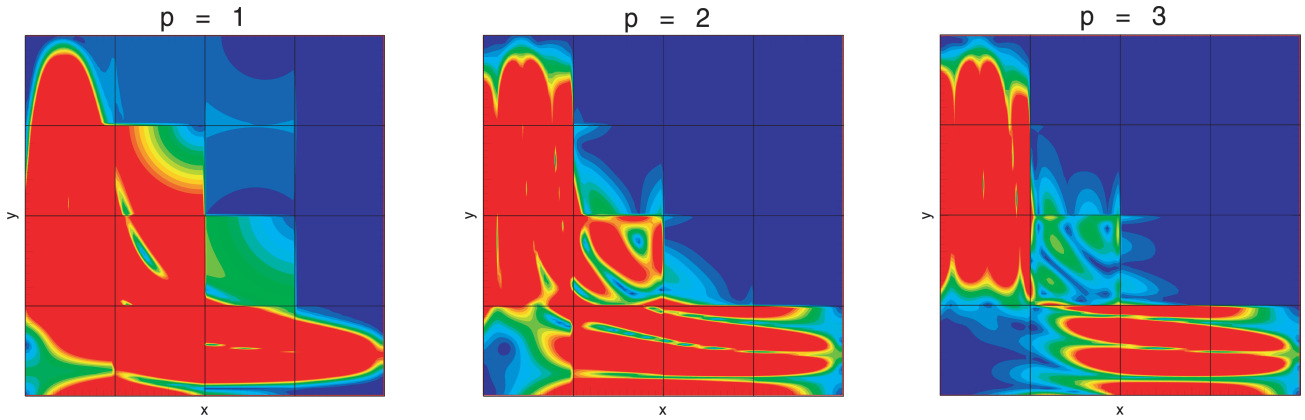

Fig. 4.25. Two dimensional synthetic problem. The contour plot of the modulus of $|\nabla(u - u_{S^p_{\Delta_h}})|$ at $t = \frac{T}{16}$.

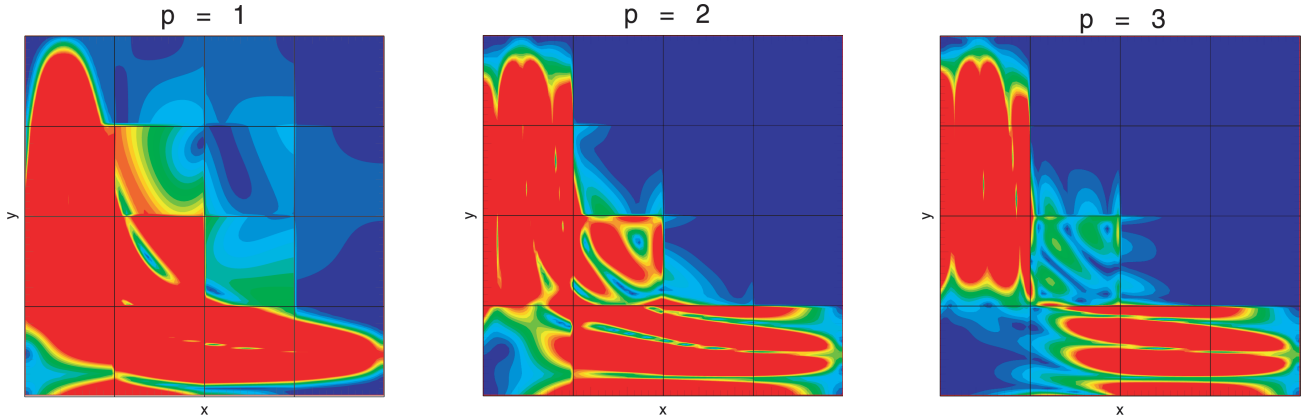

Fig. 4.26. Two dimensional synthetic problem. The contour plot of the modulus of $|\nabla(\hat{u} - u_{S^p_{\Delta_h}})|$ at $t = \frac{T}{16}$.

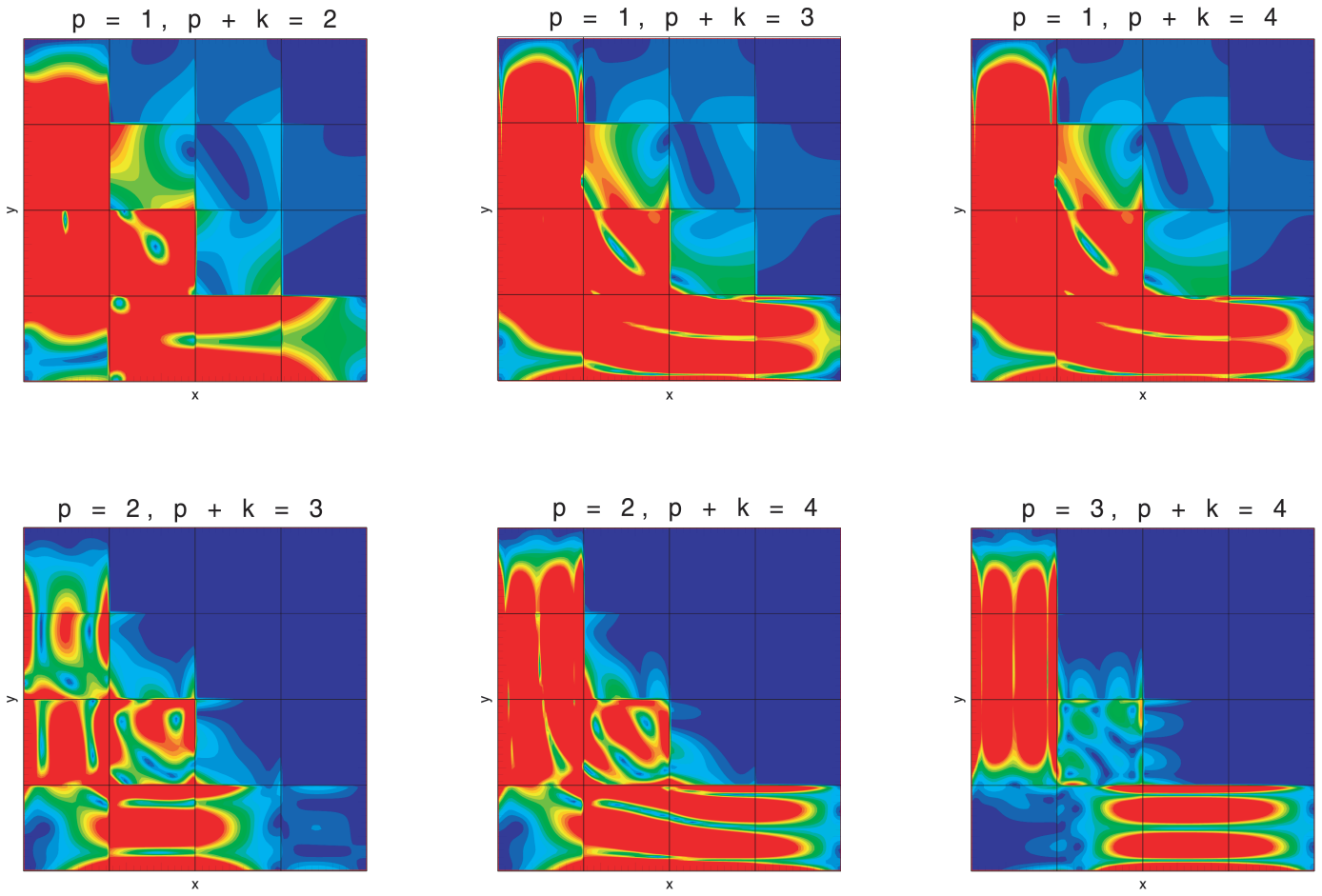

Fig. 4.27. Two dimensional synthetic problem. The contour plot of the modulus of $|\nabla(\hat{u}_{S^{p+k}_{\Delta_{h'}}} - u_{S^{p}_{\Delta_h}})|$ at $t = \frac{T}{16}$, where $\hat{u}_{S^{p+k}_{\Delta_{h'}}}$ is the exact solution of the elliptic reconstruction problem constructed from the semi-discrete finite element solutions of degree $p = 1, 2$, and 3 with mesh size $h = \frac{L}{2^2}$.

Fig. 4.28 is the contour plot of the absolute value of the exact error indicator function $\hat{e}_{\omega_X^{\Delta_h}}$ and its computable version $\hat{e}_{\omega_X^{\Delta_h},p+k}$ based on the subdomain residual of the elliptic recontruction problem based on the semi-discrete finite element solution of degree $p = 2$. It can be seen that the contour of the exact $|\hat{e}_{\omega_X^{\Delta_h}}|$ matches the corresponding exact error as shown in Fig. 4.22 and with the increase of polynomial order $p + k$ the contour of computable $|\hat{e}_{\omega_X^{\Delta_h},p+k}|$ converges to the one from the exact error indicator function.

Fig. 4.29 is the contour plot of the modulus of the exact error indicator function $\hat{e}_{\omega_X^{\Delta_h}}$ and its computable version $\hat{e}_{\omega_X^{\Delta_h},p+k}$ based on the subdomain residual of the elliptic recontruction problem based on the semi-discrete finite element solution of degree $p = 2$. we can see that the modulus of the exact error indicator function $|\nabla\hat{e}_{\omega_X^{\Delta_h}}|$ matches the modulus of the exact error as shown in Fig. 4.25 and its computable version $|\nabla\hat{e}_{\omega_X^{\Delta_h},p+k}|$ converges to the exact one with the increase of degree $p + k$.

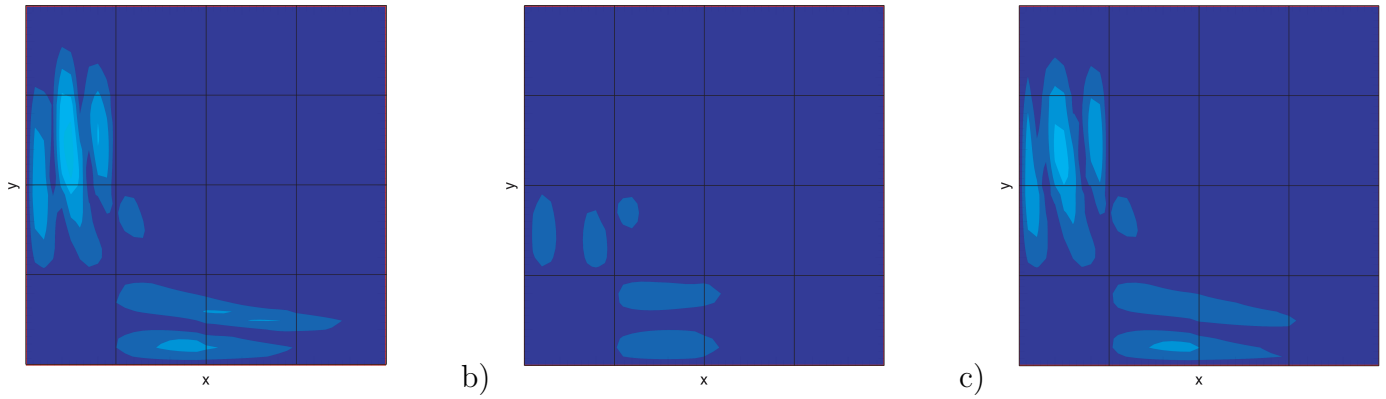

Fig. 4.28. Two dimensional synthetic problem. The contour plots of the absolute value of the error indicator function. a) $|\hat{e}_{\omega_X^{\Delta_h}}|$; b) $|\hat{e}_{\omega_X^{\Delta_h},p+k}|, p=2, k=1$; c) $|\hat{e}_{\omega_X^{\Delta_h},p+k}|, p=2, k=3$.

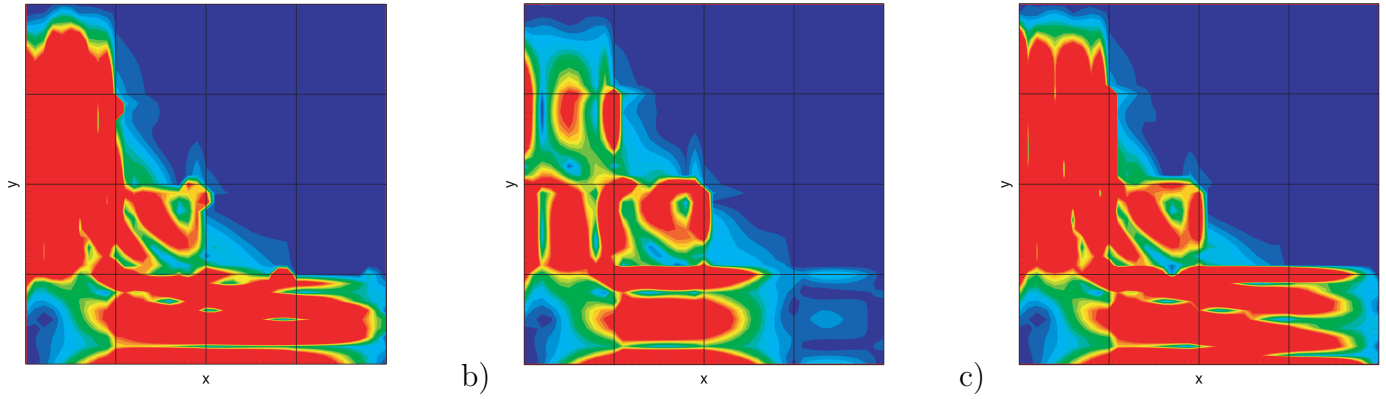

Fig. 4.29. Two dimensional synthetic problem. The contour plots of the modulus of the error indicator function. a) $|\nabla\hat{e}_{\omega_X^{\Delta_h}}|$; b) $|\nabla\hat{e}_{\omega_X^{\Delta_h},p+k}|, p=2, k=1$; c) $|\nabla\hat{e}_{\omega_X^{\Delta_h},p+k}|, p=2, k=3$.

Example 4.11. *L-shaped domain problem.* Fig. 4.30 is the variation of effectivity index $\eta(t)$ and its computable version $\eta_{S^{p+k}_{\Delta_{h'}}}(t)$ corresponding to the exact solution $\hat{u}$ and its approximate solution $\hat{u}_{S^{p+k}_{\Delta_{h'}}}$ from p method, for the elliptic reconstruction problem constructed from the semi-discrete finite element solutions of degree $p = 1, 2,$ and 3 with mesh size $h = \frac{L}{2^2}$. It can be seen that the effectivity index is close to 1 except for the time instants close to $t = 0$ at which the boundary condition and initial condition are suddenly applied, and the time instants $t = \frac{1}{3}$ at which the exact solution is 0. Note that with the increase of polynomial order $p+k$ in the approximate solution $\hat{u}_{S^{p+k}_{\Delta_{h'}}}$, the computable version $\eta_{S^{p+k}_{\Delta_{h'}}}(t)$ converges to its corresponding exact one $\eta(t)$.

Fig. 4.31 is the variation of effectivity index $\zeta(t)$ and its computable version $\zeta_{S^{p+k}_{\Delta_{h'}}}(t)$ corresponding to the exact solution $\hat{u}$ and its approximate solution $\hat{u}_{S^{p+k}_{\Delta_{h'}}}$ from p method, for the elliptic reconstruction problem constructed from the semi-discrete finite element solutions of degree $p = 1, 2,$ and 3 with mesh size $h = \frac{L}{2^2}$. It can be seen that for all the element order $p = 1, 2,$ and 3, $\zeta(t)$ and its computable version $\zeta_{S^{p+k}_{\Delta_{h'}}}(t)$ severely overestimate the exact error except around the time instants $t = \frac{1}{3}$ at which the exact solution is 0, the effectivity indices can be close to 0. Note that with the increase of polynomial order $p + k$ in the approximate solution $\hat{u}_{S^{p+k}_{\Delta_{h'}}}$, the computable version $\zeta_{S^{p+k}_{\Delta_{h'}}}(t)$ is close to the exact one $\zeta(t)$.

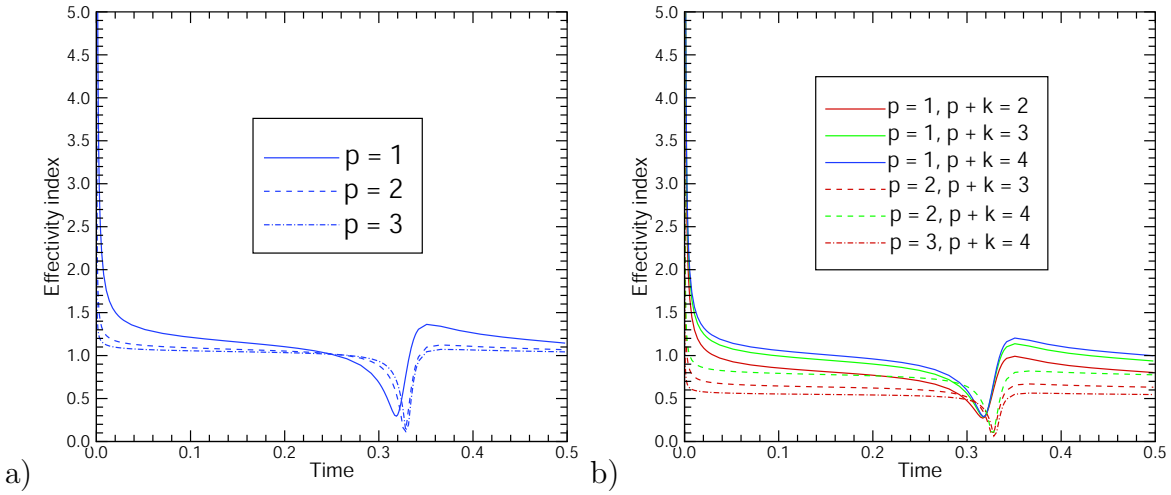

Fig. 4.30. L-shaped domain problem. a) The evolution of effectivity index $\eta(t)$ based on the exact solution $\hat{u}$ of the elliptic reconstruction problem; b) The evolution of effectivity index $\eta_{S^{p+k}_{\Delta_{h'}}}(t)$ based on the approximate solution $\hat{u}_{S^{p+k}_{\Delta_{h'}}}$ of the elliptic reconstruction problem.

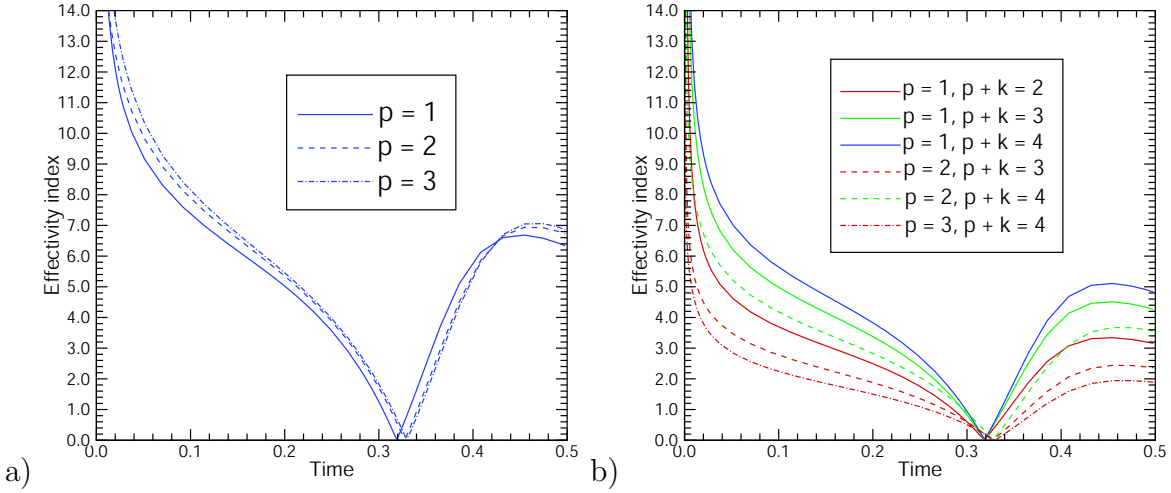

Fig. 4.31. L-shaped domain problem. a) The evolution of effectivity index $\zeta(t)$ based on the exact solution $\hat{u}$ of the elliptic reconstruction problem; b) The evolution of effectivity index $\zeta_{S^{p+k}_{\Delta_{h'}}}(t)$ based on the approximate solution $\hat{u}_{S^{p+k}_{\Delta_{h'}}}$ of the elliptic reconstruction problem.

Fig. 4.32 is the evolution of effectivity index $\bar{\eta}^U(t)$, $\bar{\eta}^U_{p+k}(t)$, and $\bar{\eta}^L_{p+k}(t)$) for the exact error measured in energy norm, where the exact error indicator function and its computed version are obtained from the subdomain residual problem of the elliptic reconstruction problems corresponding to the semi-discrete finite element solution $u_{S^p_{\Delta_h}}$ of degree $p = 1, 2$, and 3. It can be seen that $\bar{\eta}^U(t)$ is close 1 even at the time instants close to $t = 0$ and $t = \frac{1}{3}$. For the computable version $\bar{\eta}^U_{p+k}(t)$ and $\bar{\eta}^L_{p+k}(t)$) converge to 1 with the increase of order $p + k$. Note that $\bar{\eta}^U_{p+k}(t)$ is not a guarantted upper bound.

Fig. 4.33 is the evolution of effectivity index $\bar{\zeta}(t)$ and $\bar{\zeta}_{p+k}(t)$ for the exact error measured in L^2norm, where the exact error indicator function and its computed version are obtained from the subdomain residual problem of the elliptic reconstruction problem. It can be seen that $\bar{\zeta}(t)$ is not a good estimate of the exact error. Again the computed version $\bar{\zeta}_{p+k}(t)$ converges to the values corresponding to $\bar{\zeta}(t)$ with the increase of $p + k$.

Fig. 4.34 (resp. Fig. 4.35) is the contour plot of the exact error $|u - u_{S^p_{\Delta_h}}|$ (resp. $|\hat{u} - u_{S^p_{\Delta_h}}|$) in absolute value at time instant $t = \frac{T}{16}$ for the semi-discrete finite element solutions of degree $p = 1, 2$, and 3 and the exact solution $\hat{u}$ of the elliptic reconstruction problem based on these finite element solutions. It can be seen that the contour plots does not match each other at all.

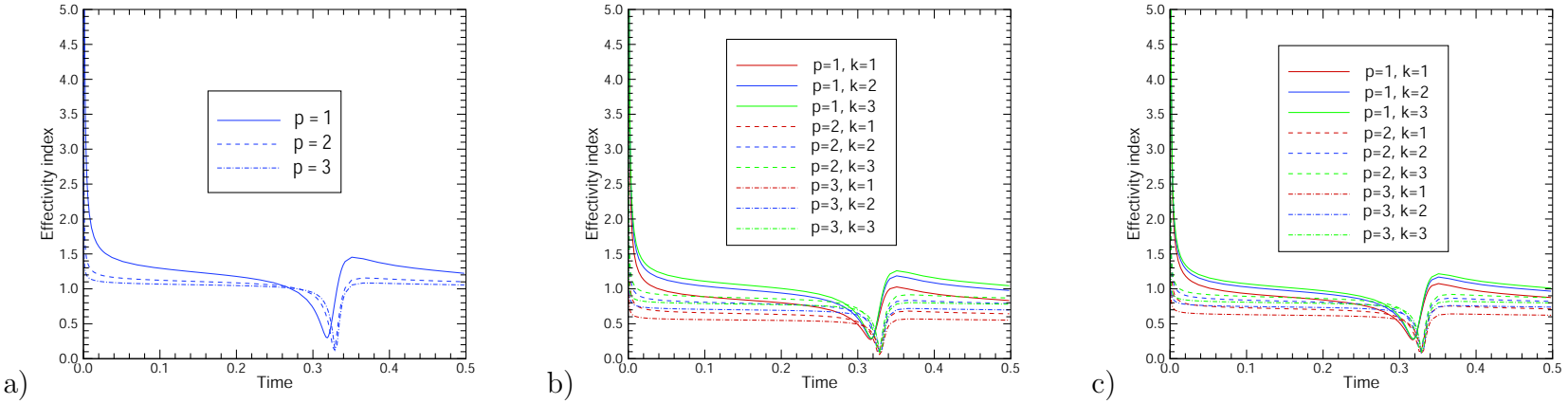

Fig. 4.32. L-shaped domain problem. The evolution of effectivity index for the exact error measured in energy norm based on the subdomain residual problem of the elliptic reconstruction problem. a) $\bar{\eta}^U(t)$; b) $\bar{\eta}^U_{p+k}(t)$; c) $\bar{\eta}^L_{p+k}(t)$.

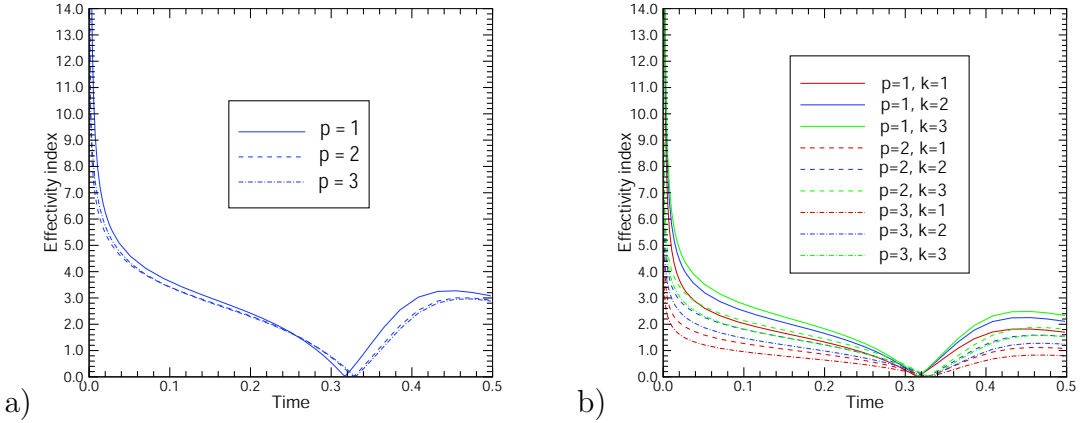

Fig. 4.33. L-shaped domain problem. The evolution of effectivity index for the exact error measured in L^2 norm based on the subdomain residual problem of the elliptic reconstruction problem. a)$\bar{\zeta}(t)$; b) $\bar{\zeta}_{p+k}(t)$.

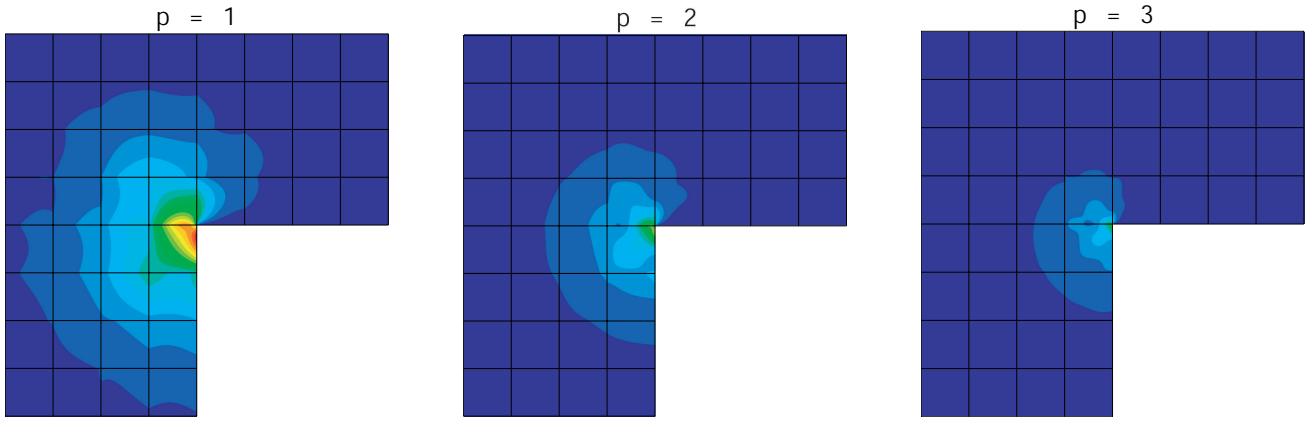

Fig. 4.34. L-shaped domain problem. The contour plot of $|u - u_{S^p_{\Delta_h}}|$ at $t = \frac{T}{16}$.

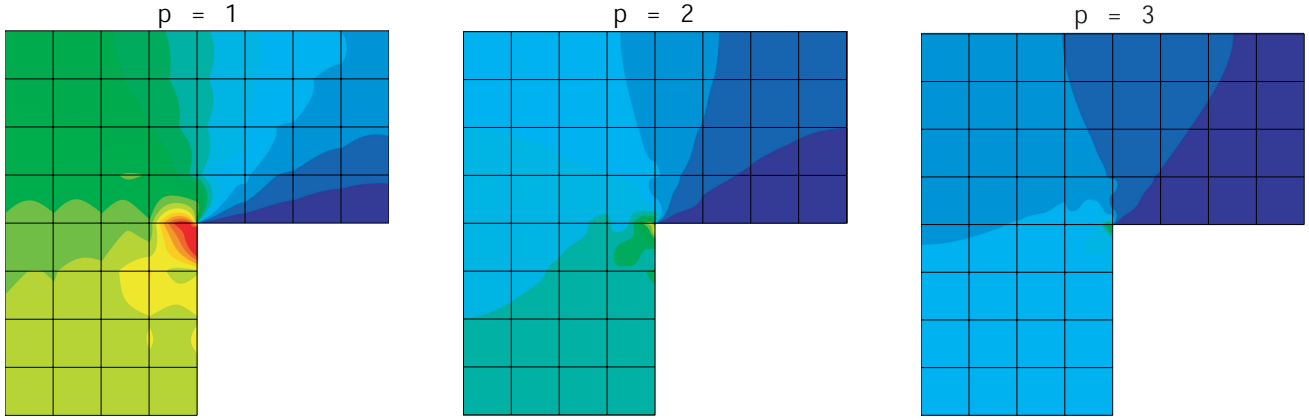

Fig. 4.35. L-shaped domain problem. The contour plot of $|\hat{u} - u_{S^p_{\Delta_h}}|$ at $t = \frac{T}{16}$.

Fig. 4.36 is the contour plot of $|\hat{u}_{S^{p+k}_{\Delta_{h'}}} - u_{S^p_{\Delta_h}}|$ based on the approximate solution $\hat{u}_{S^{p+k}_{\Delta_{h'}}}$ of degree $p+k$ to the elliptic reconstruction problem. It can be seen that as the increase of polynomial order $p+k$ the contour plot of $|\hat{u}_{S^{p+k}_{\Delta_{h'}}} - u_{S^p_{\Delta_h}}|$ is close to the one from $|\hat{u} - u_{S^p_{\Delta_h}}|$, which is especially obvious in the case of $p = 1$.

Fig. 4.37 (resp. Fig. 4.38) is the contour plot of the modulus $|\nabla(u - u_{S^p_{\Delta_h}})|$ of the exact error (resp. Fig. 4.38) at time instant $t = \frac{T}{16}$ for the semi-discrete finite element solutions of degree $p = 1, 2$, and 3 and the exact solution $\hat{u}$ of the elliptic reconstruction problem constructed from these finite element solutions. It can be seen that these contour plots are close between $|\nabla(u - u_{S^p_{\Delta_h}})|$ and $|\nabla(\hat{u} - u_{S^p_{\Delta_h}})|$.

Fig. 4.39 is the contour plot of the modulus $|\nabla(\hat{u}_{S^{p+k}_{\Delta_{h'}}} - u_{S^p_{\Delta_h}})|$ based on the approximate solution $\hat{u}_{S^{p+k}_{\Delta_{h'}}}$ of degree $p+k$ to the elliptic reconstruction problem from the semi-discrete finite element solutions of degree $p = 1, 2$, and 3. It can be seen that with the increase of polynomial order $p+k$ in $\hat{u}_{S^{p+k}_{\Delta_{h'}}}$ the contour plots of $|\nabla(\hat{u}_{S^{p+k}_{\Delta_{h'}}} - u_{S^p_{\Delta_h}})|$ are close to $|\nabla(\hat{u} - u_{S^p_{\Delta_h}})|$.

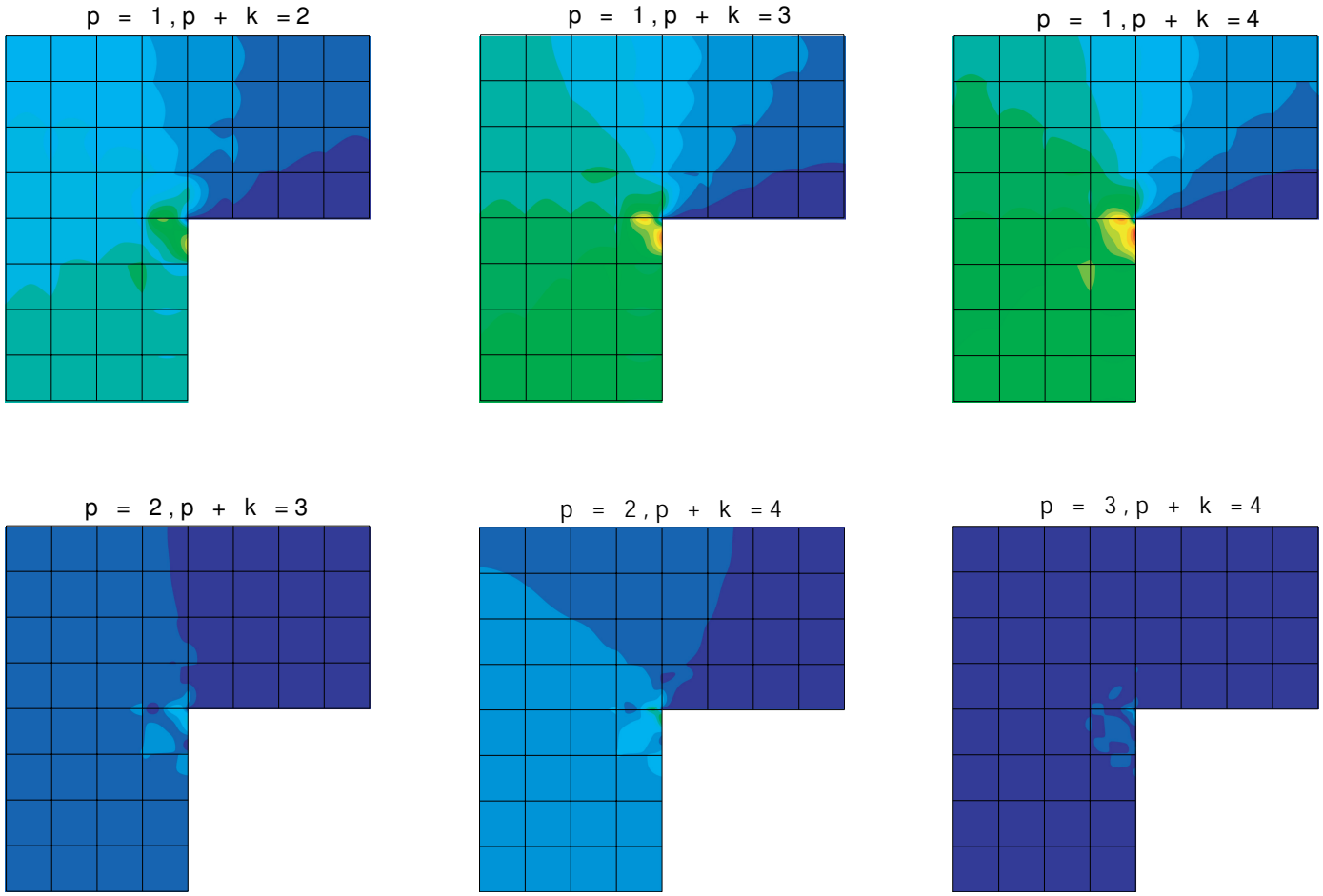

Fig. 4.36. L-shaped domain problem. The contour plot of $|\hat{u}_{S^{p+k}_{\Delta_{h'}}} - u_{S^{p}_{\Delta_h}}|$ at $t = \frac{T}{16}$, where $\hat{u}_{S^{p+k}_{\Delta_{h'}}}$ is the exact solution of the elliptic reconstruction problem constructed from the semi-discrete finite element solutions of degree $p = 1, 2$, and 3 with mesh size $h = \frac{L}{2^2}$.

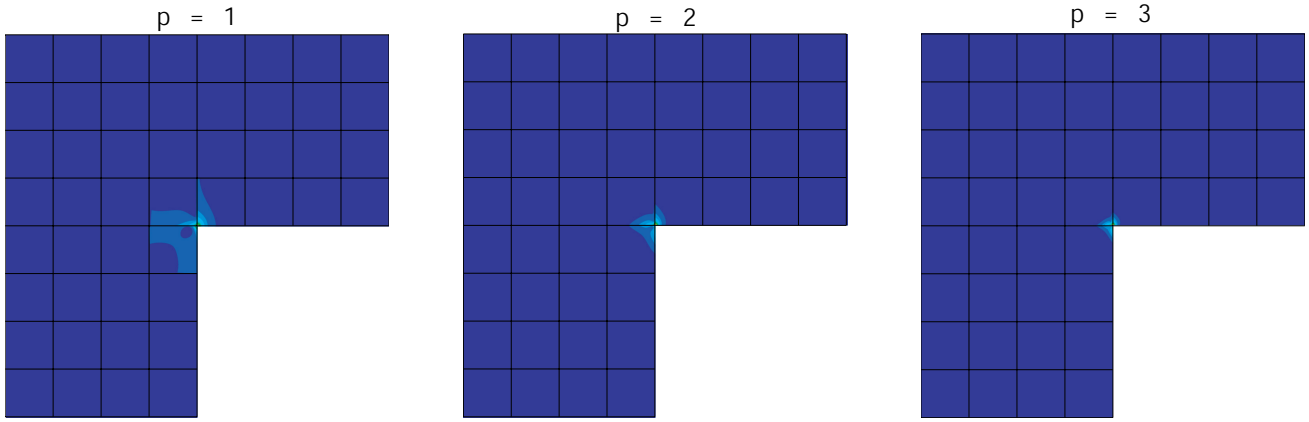

Fig. 4.37. L-shaped domain problem. The contour plot of $|\nabla(u - u_{S^p_{\Delta_h}})|$ at $t = \frac{T}{16}$.

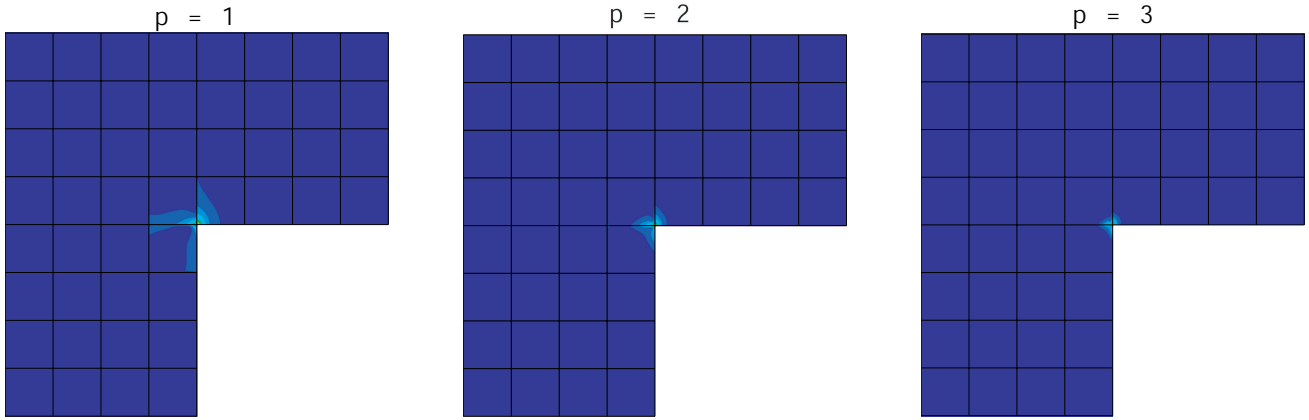

Fig. 4.38. L-shaped domain problem. The contour plot of $|\nabla(\hat{u} - u_{S^p_{\Delta_h}})|$ at $t = \frac{T}{16}$.

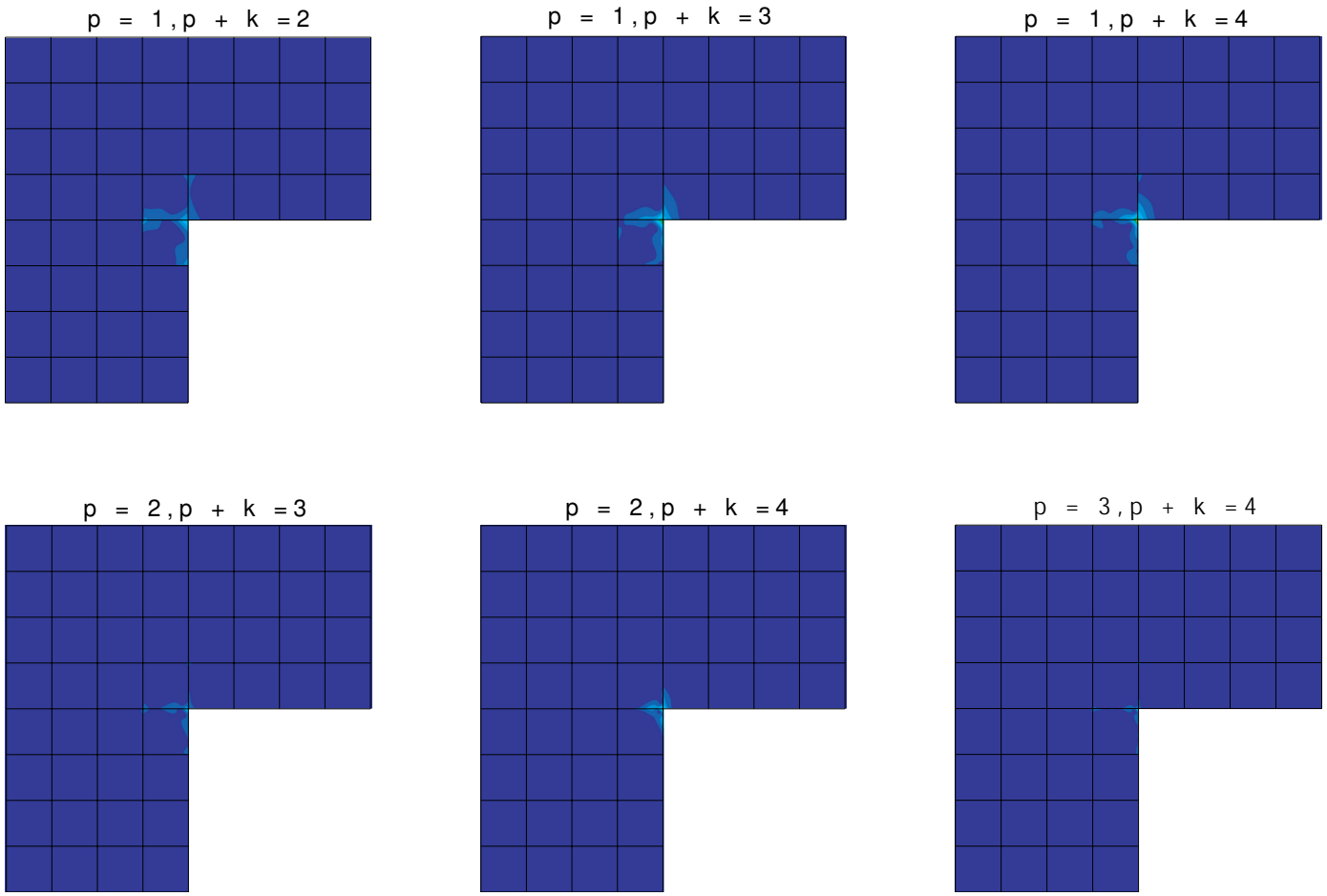

Fig. 4.39. L-shaped domain problem. The contour plot of the modulus of $|\nabla(\hat{u}_{S^{p+k}_{\Delta_{h'}}} - u_{S^p_{\Delta_h}})|$ at $t = \frac{T}{16}$, where $\hat{u}_{S^{p+k}_{\Delta_{h'}}}$ is the exact solution of the elliptic reconstruction problem constructed from the semi-discrete finite element solutions of degree $p = 1, 2$, and 3 with mesh size $h = \frac{L}{2^2}$.

Fig. 4.40 is the contour plot of the absolute value of the exact error indicator function $\hat{e}_{\omega_X^{\Delta_h}}$ and its computable version $\hat{e}_{\omega_X^{\Delta_h},p+k}$ based on the subdomain residual of the elliptic recontruction problem based on the semi-discrete finite element solution of degree $p = 2$. It can be seen that the contour of the exact $|\hat{e}_{\omega_X^{\Delta_h}}|$ does not match the corresponding exact error as shown in Fig. 4.34 in the case of $p = 2$ and with the increase of polynomial order $p+k$ the contour of computable $|\hat{e}_{\omega_X^{\Delta_h},p+k}|$ converges to the one from the exact error indicator function. Note that as shown in Fig. 4.8, $||u - \hat{u}||_{L^2}$ and $||u - u_{S^p_{\Delta_h}}||_{L^2}$ have the same convergence rate, which explains why $|\hat{e}_{\omega_X^{\Delta_h}}|$ does not have good performance.

Fig. 4.41 is the contour plot of the modulus of the exact error indicator function $\hat{e}_{\omega_X^{\Delta_h}}$ and its computable version $\hat{e}_{\omega_X^{\Delta_h},p+k}$ based on the subdomain residual of the elliptic recontruction problem based on the semi-discrete finite element solution of degree $p = 2$. we can see that the modulus of the exact error indicator function $|\nabla\hat{e}_{\omega_X^{\Delta_h}}|$ matches the modulus of the exact error as shown in Fig. 4.37 and its computable version $|\nabla\hat{e}_{\omega_X^{\Delta_h},p+k}|$ converges to the exact one with the increase of degree $p + k$.

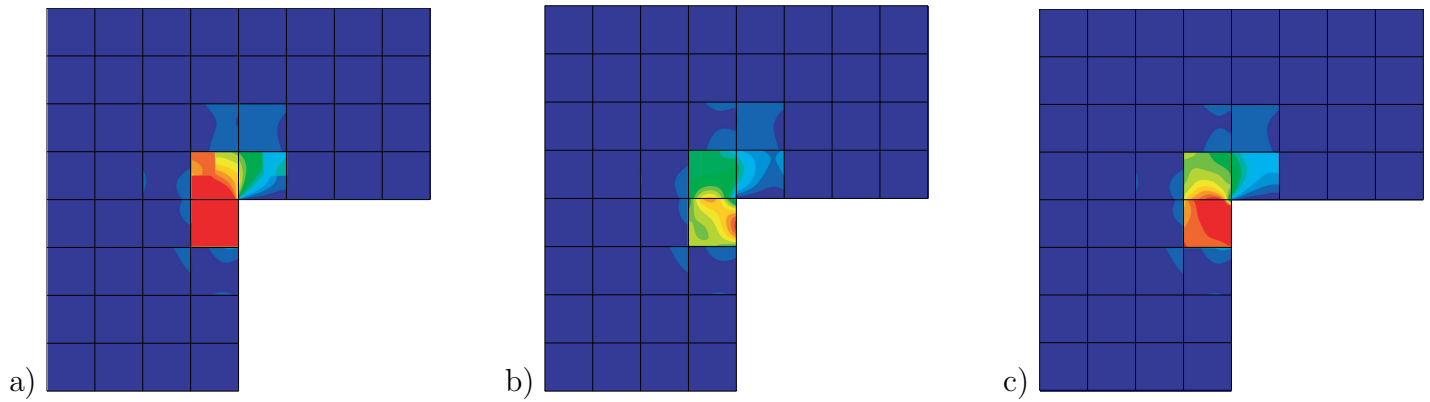

Fig. 4.40. L-shaped domain problem. The contour plots of the absolute value of the error indicator function. a) $|\hat{e}_{\omega_X^{\Delta_h}}|$; b) $|\hat{e}_{\omega_X^{\Delta_h},p+k}|, p=2, k=1$; c) $|\hat{e}_{\omega_X^{\Delta_h},p+k}|, p=2, k=3$.

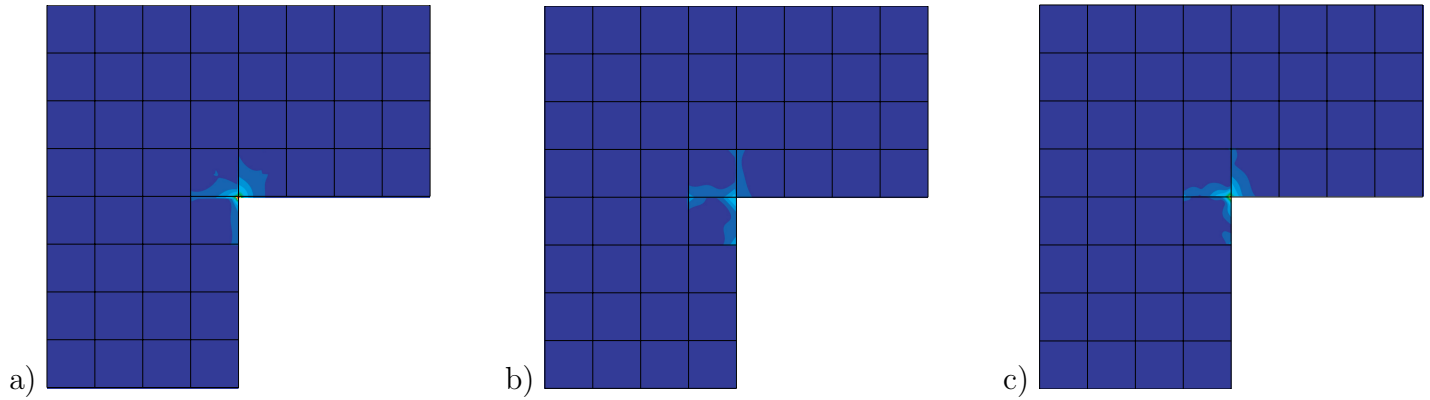

Fig. 4.41. L-shaped domain problem. The contour plots of the modulus of the error indicator function. a) $|\nabla\hat{e}_{\omega_X^{\Delta_h}}|$; b) $|\nabla\hat{e}_{\omega_X^{\Delta_h},p+k}|, p=2, k=1$; c) $|\nabla\hat{e}_{\omega_X^{\Delta_h},p+k}|, p=2, k=3$.

Example 4.12. *Transient diffusion problem in a thermal battery.* Here we focus on the semi-discrete finite element solution $u_{S^p_{\Delta_h}}$ computed with elements of order $p = 1, 2$ and Mesh I as shown in Fig. 2.2. It should be noted that the solution has significant transient behavior for time instant $t \leq 500$ as shown in Fig. 4.9.

Fig. 4.42 is the variation of effectivity index $\eta(t)$ corresponding to the exact solution $\hat{u}$ of the elliptic reconstruction problem constructed from the semi-discrete finite element solutions of degree $p = 1, 2$, and 3. It can be seen that the effectivity index is close to 1 at all time instants for the isotropic case while for the orthotropic case except at the time instant close to $t = 0$ where the effectivity index can be much greater than 1, the effectivity index is close to 1.

Fig. 4.43 is the variation of effectivity index $\eta_{S^{p+k}_{\Delta_{h'}}}(t)$ corresponding to the approximate solution $\hat{u}_{S^{p+k}_{\Delta_{h'}}}$ of the elliptic reconstruction problem constructed from the semi-discrete finite element solutions of degree $p = 1, 2$, and 3. It can be seen that the effectivity index $\eta_{S^{p+k}_{\Delta_{h'}}}(t)$ has the performance similar to the exact version of $\eta(t)$. Note that with the increase of polynomial order $p + k$ in the approximate solution $\hat{u}_{S^{p+k}_{\Delta_{h'}}}$, the computable version $\eta_{S^{p+k}_{\Delta_{h'}}}(t)$ converges to the exact version $\eta(t)$.

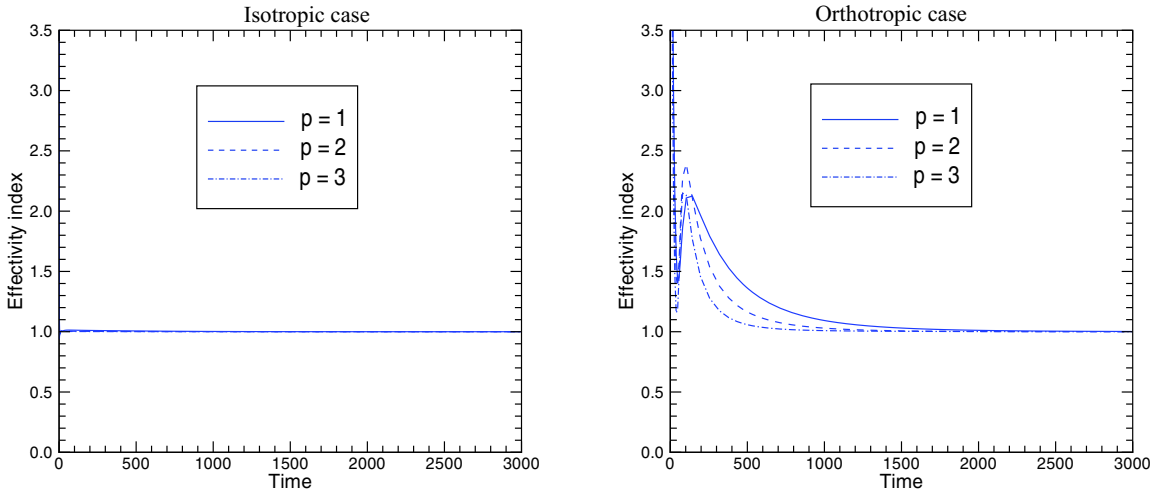

Fig. 4.42. Transient diffusion problem in a thermal battery. The evolution of effectivity index $\eta(t)$ based on the exact solution $\hat{u}$ of the elliptic reconstruction problem constructed from the semi-discrete finite element solutions of degree $p = 1, 2$, and 3 for isotropic case and orthotropic case.

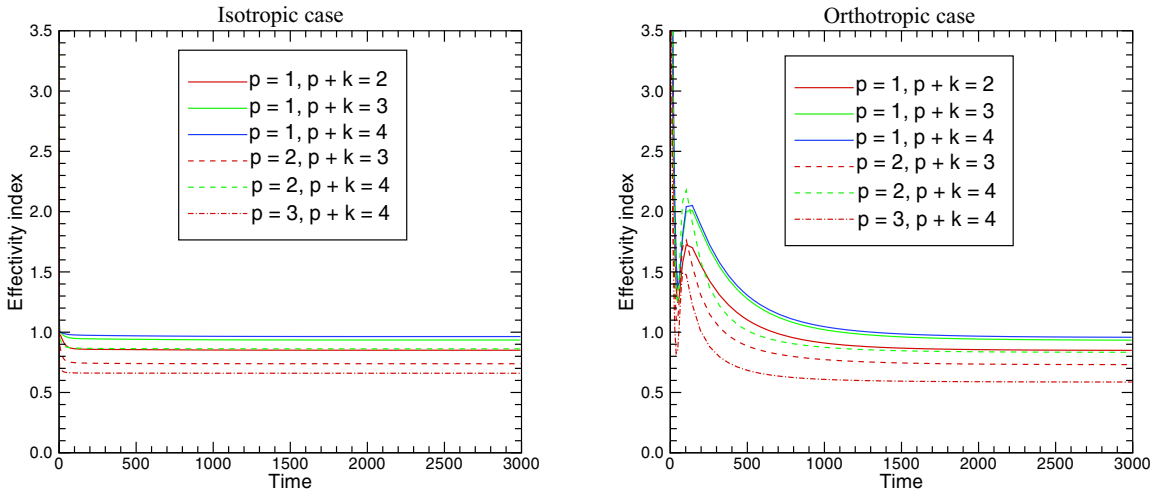

Fig. 4.43. Transient diffusion problem in a thermal battery. The evolution of effectivity index $\eta_{S^{p+k}_{\Delta_{h'}}}(t)$ based on the approximate solution $\hat{u}_{S^{p+k}_{\Delta_{h'}}}$ of the elliptic reconstruction problem from the semi-discrete finite element solutions of degree $p = 1, 2$, and 3 for isotropic case and orthotropic case.

Fig. 4.44 (resp. Fig. 4.45) is the variation of effectivity index $\zeta(t)$ (resp. its computable version $\zeta_{S^{p+k}_{\Delta_{h'}}}(t)$) corresponding to the exact solution $\hat{u}$ (resp. its approximate solution $\hat{u}_{S^{p+k}_{\Delta_{h'}}}$), for the elliptic reconstruction problem constructed from the semi-discrete finite element solutions of degree $p = 1, 2$, and 3 and Mesh I for the isotropic case and the orthotropic case. It can be seen that for the isotropic case $\zeta(t)$ based on $\hat{u}$ is close to 1 even in the case of linear element where there is no superconvergence for the term $||u - \hat{u}||_{L^2(\Omega)}$. For orthotropic case, $\zeta(t)$ has poor performance at the time instants close to $t = 0$. But as time evolves, $\zeta(t)$ improves. The effectivity index $\zeta_{S^{p+k}_{\Delta_{h'}}}(t)$ has performance similar to its corresponding exact version $\zeta(t)$ for both the isotropic case and the orthotropic case.

Fig. 4.46 (resp. Fig. 4.47) is the evolution of effectivity index $\bar{\eta}^U(t)$, $\bar{\eta}^U_{p+k}(t)$, and $\bar{\eta}^L_{p+k}(t)$ for the exact error measured in energy norm, where the exact error indicator function and its computed version are obtained from the subdomain residual problem of the elliptic reconstruction problems corresponding to the semi-discrete finite element solution $u_{S^p_{\Delta_h}}$ of degree $p = 1, 2$, and 3 with Mesh I for the isotropic case (resp. the orthotropic case). It can be seen that for the isotropic case, we have good effecviity index for $\bar{\eta}^U(t)$, $\bar{\eta}^U_{p+k}(t)$, and $\bar{\eta}^L_{p+k}(t)$ at all time instants. However for the orthotropic case, it can be seen that $\bar{\eta}^U(t)$ and $\bar{\eta}^U_{p+k}(t)$ severely overestimate the exact error while $\bar{\eta}^L_{p+k}(t)$ severely underestimate the exact error, and the culprit is the interface layers in the highly orthotropic domain Ω_3.

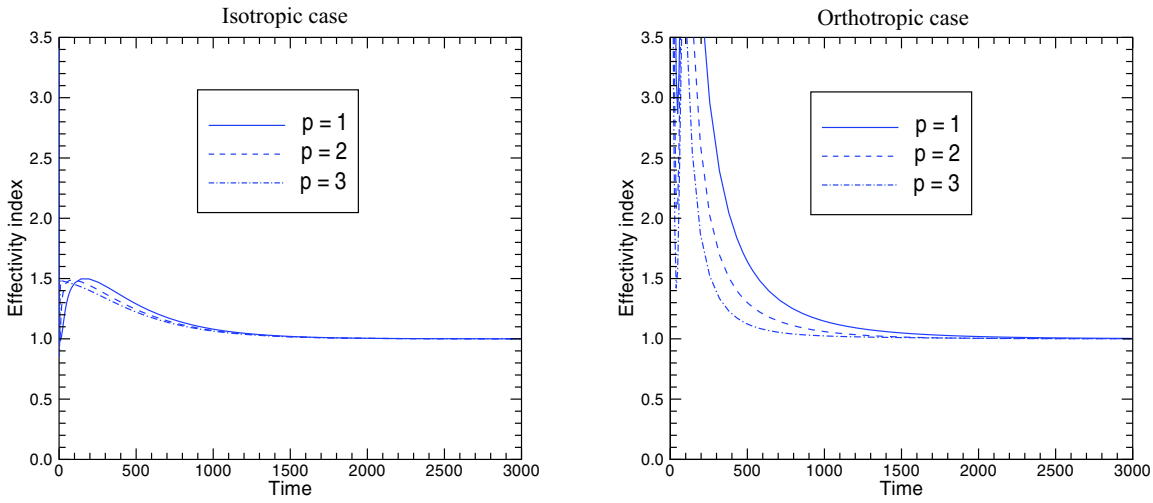

Fig. 4.44. Transient diffusion problem in a thermal battery. The evolution of effectivity index $\zeta(t)$ based on the exact solution $\hat{u}$ of the elliptic reconstruction problem constructed from the semi-discrete finite element solutions of degree $p = 1, 2$, and 3 for isotropic case and orthotropic case.

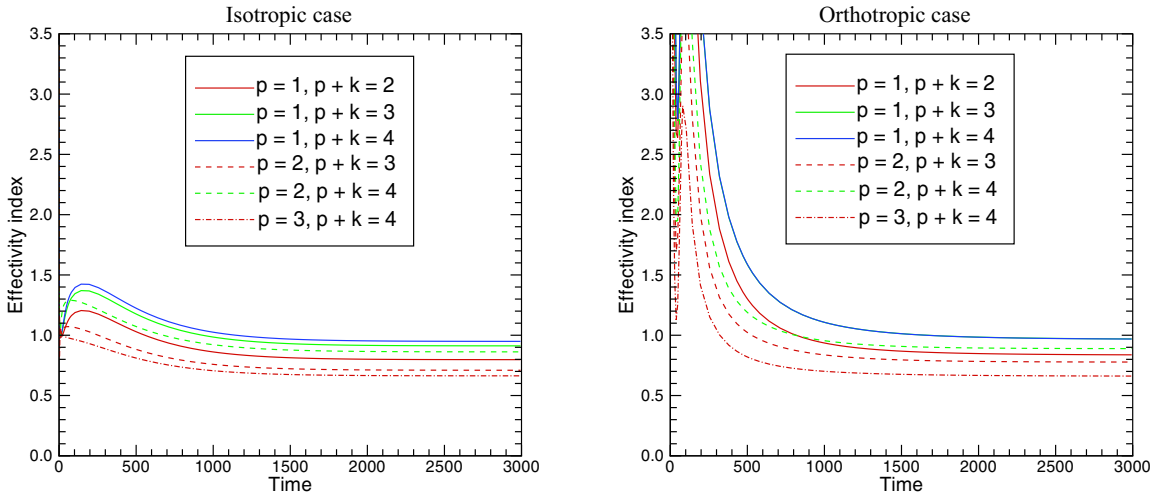

Fig. 4.45. Transient diffusion problem in a thermal battery. The evolution of effectivity index $\zeta_{S^{p+k}_{\Delta_{h'}}}(t)$ based on the approximate solution $\hat{u}_{S^{p+k}_{\Delta_{h'}}}$ of the elliptic reconstruction problem from the semi-discrete finite element solutions of degree $p = 1, 2$, and 3 for isotropic case and orthotropic case.

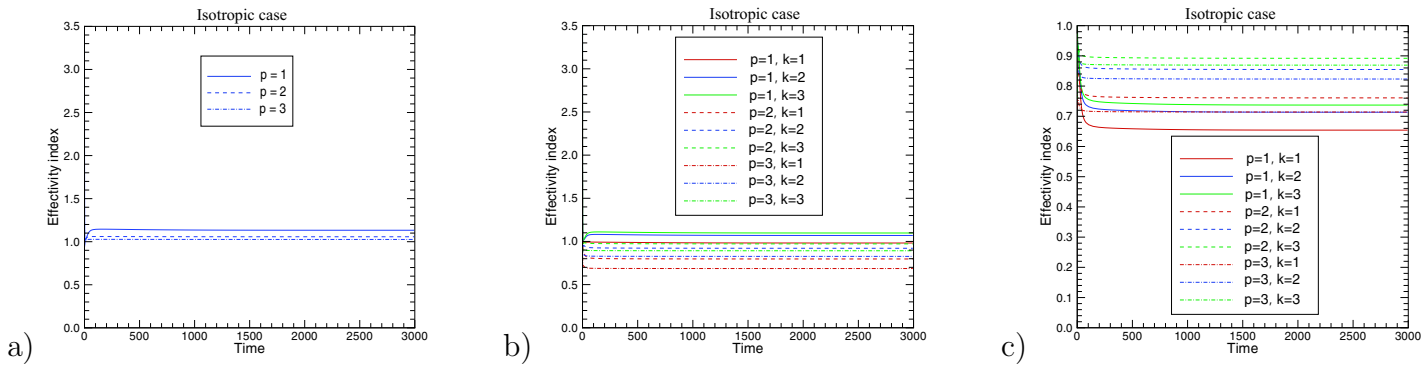

Fig. 4.46. Transient diffusion problem in a thermal battery. The evolution of effectivity index for the exact error measured in energy norm based on the subdomain residual problem of the elliptic reconstruction problem for the isotropic case. a) $\bar{\eta}^U(t)$; b) $\bar{\eta}^U_{p+k}(t)$; c) $\bar{\eta}^L_{p+k}(t)$.

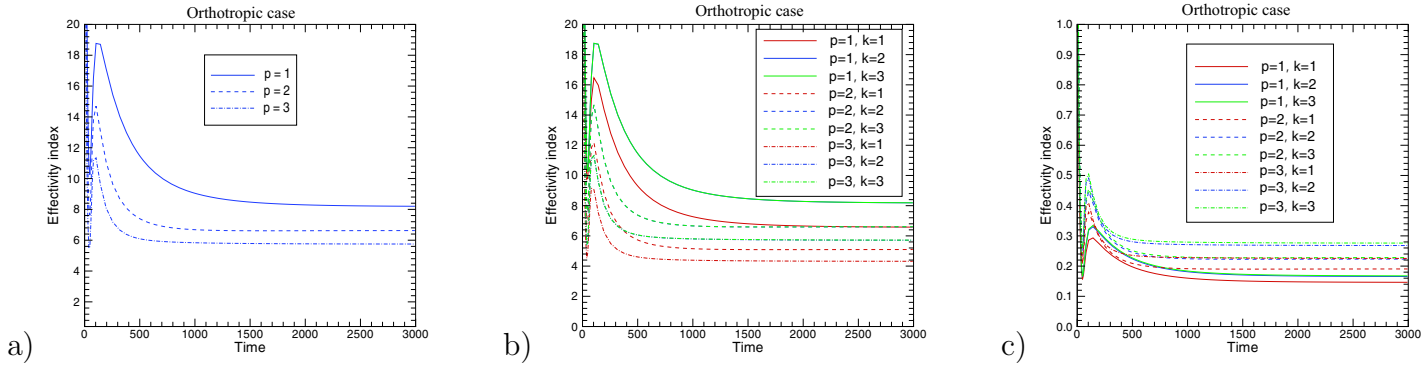

Fig. 4.47. Transient diffusion problem in a thermal battery. The evolution of effectivity index for the exact error measured in energy norm based on the subdomain residual problem of the elliptic reconstruction problem for the orthotropic case. a) $\bar{\eta}^U(t)$; b) $\bar{\eta}^U_{p+k}(t)$; c) $\bar{\eta}^L_{p+k}(t)$.

Fig. 4.48 (resp. Fig. 4.49) is the evolution of effectivity index $\bar{\zeta}(t)$ and $\bar{\zeta}_{p+k}(t)$ for the exact error measured in L^2norm, where the exact error indicator function and its computed version are obtained from the subdomain residual problem of the elliptic reconstruction problem corresponding to the semi-discrete finite element solution $u_{S^p_{\Delta_h}}$ of degree $p = 1, 2$, and 3 with Mesh I for the isotropic case (resp. the orthotropic case). It can be seen that for the isotropic case in the case of linear element $p = 1$ the effectivity index can be as worse as 3.0. However for $p \geq 2$, both $\bar{\zeta}(t)$ and $\bar{\zeta}_{p+k}(t)$ are close to 1. For the orthotropic case, both $\bar{\zeta}(t)$ and $\bar{\zeta}_{p+k}(t)$ severely overestimate the exact error measured in L^2 norm. The best effectivity index is still close 100.

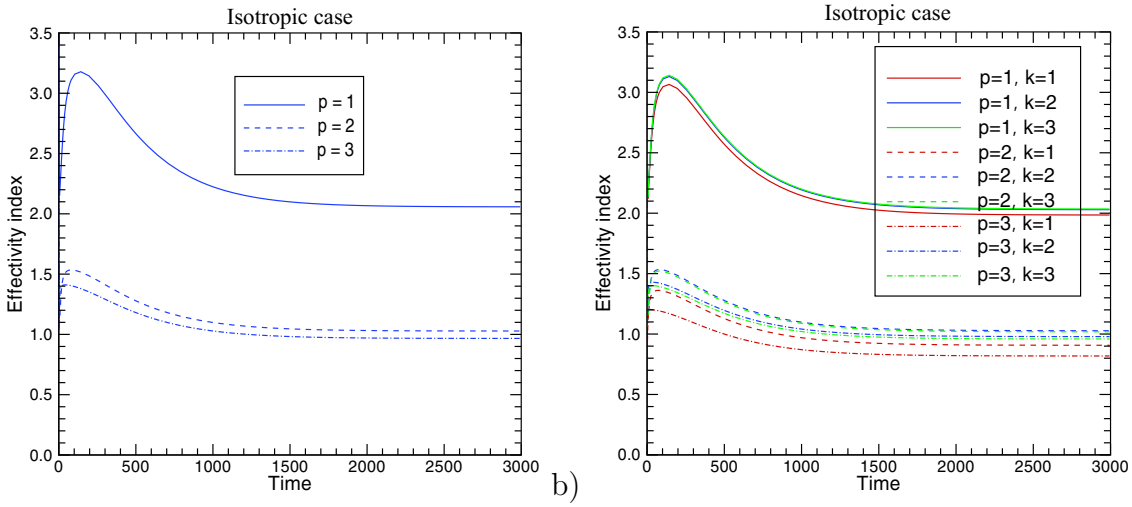

a) b)

Fig. 4.48. Transient diffusion problem in a thermal battery. The evolution of effectivity index for the exact error measured in L^2 norm based on the subdomain residual problem of the elliptic reconstruction problem for the isotropic case. a)$\bar{\zeta}(t)$; b) $\bar{\zeta}_{p+k}(t)$.

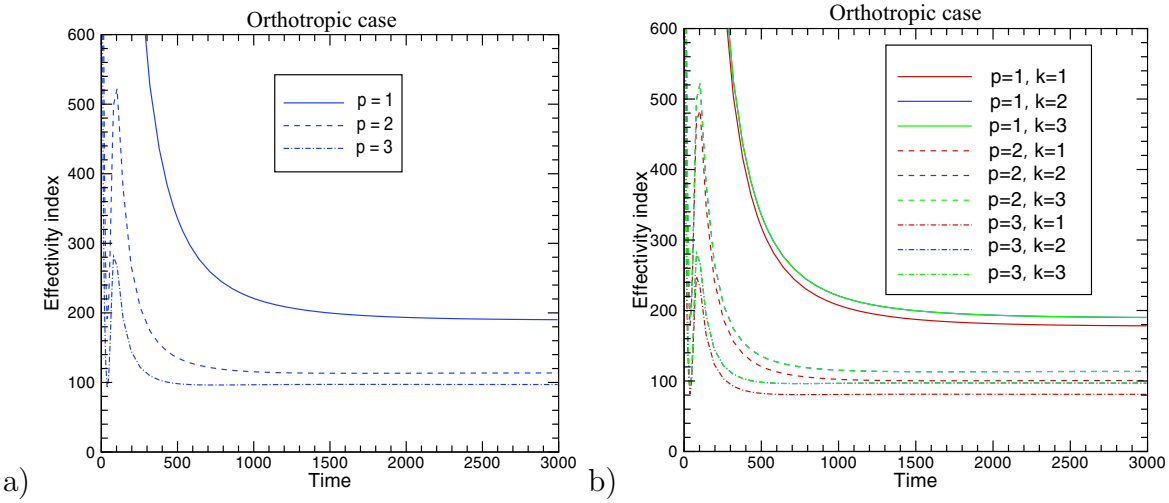

Fig. 4.49. Transient diffusion problem in a thermal battery. The evolution of effectivity index for the exact error measured in L^2 norm based on the subdomain residual problem of the elliptic reconstruction problem for the orthotropic. a)$\bar{\zeta}(t)$; b) $\bar{\zeta}_{p+k}(t)$.

Figs. 4.50 and 4.51 (resp. Figs. 4.52 and 4.53) are the contour plots of the exact error $|u - u_{S^p_{\Delta_h}}|$ and its approximations $|\hat{u} - u_{S^p_{\Delta_h}}|$ and $|\hat{u}_{S^{p+k}_{\Delta_{h'}}} - u_{S^p_{\Delta_h}}|$ based on the exact and approximate solutions of the elliptic reconstruction problem for isotropic case (resp. orthotropic case) for the semi-discrete finite element solution $u_{S^p_{\Delta_h}}$ computed with degree of $p = 1, 2$ and Mesh II. It can be seen that even in the case of linear element where there is no superconvergence property in $||u - \hat{u}||_{L^2(\Omega)}$ the contour plots match each other well. This is even more obvious in the case of quadratic element given that fact that $||u - \hat{u}||_{L^2(\Omega)}$ possesses superconvergence property. Note that for orthotropic case, the high orthotropy does not affect the performance of approximations based on elliptic reconstruction problem.

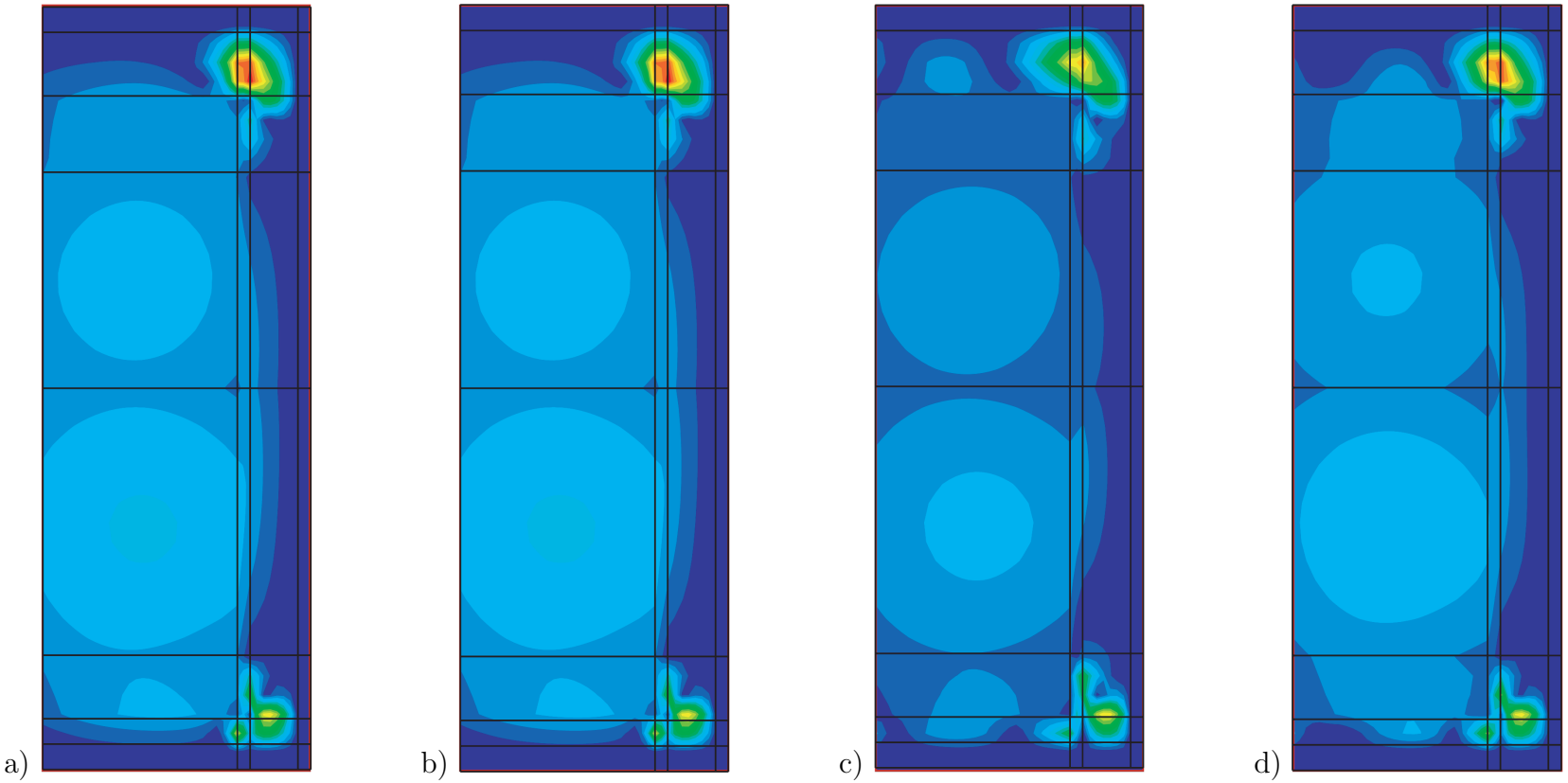

Fig. 4.50. Transient diffusion problem in a thermal battery. The contour plots for isotropic case related to the semi-discrete finite element solution $u_{S^p_{\Delta_h}}$ of degree $p = 1$ at time instant $t = \frac{T}{6}$ for quantities: a) The exact error $|u - u_{S^p_{\Delta_h}}|$; b) The approximation of the exact error $|\hat{u} - u_{S^p_{\Delta_h}}|$ based on the exact solution $\hat{u}$ of the elliptic reconstruction problem; c) The approximation of the exact error $|\hat{u}_{S^{p+k}_{\Delta_{h'}}} - u_{S^p_{\Delta_h}}|$ based on the approximate solution $\hat{u}_{S^{p+k}_{\Delta_{h'}}}$ of the elliptic reconstruction problem with $k = 1$; d) The approximation of the exact error $|\hat{u}_{S^{p+k}_{\Delta_{h'}}} - u_{S^p_{\Delta_h}}|$ based on the approximate solution $\hat{u}_{S^{p+k}_{\Delta_{h'}}}$ of the elliptic reconstruction problem with $k = 2$.

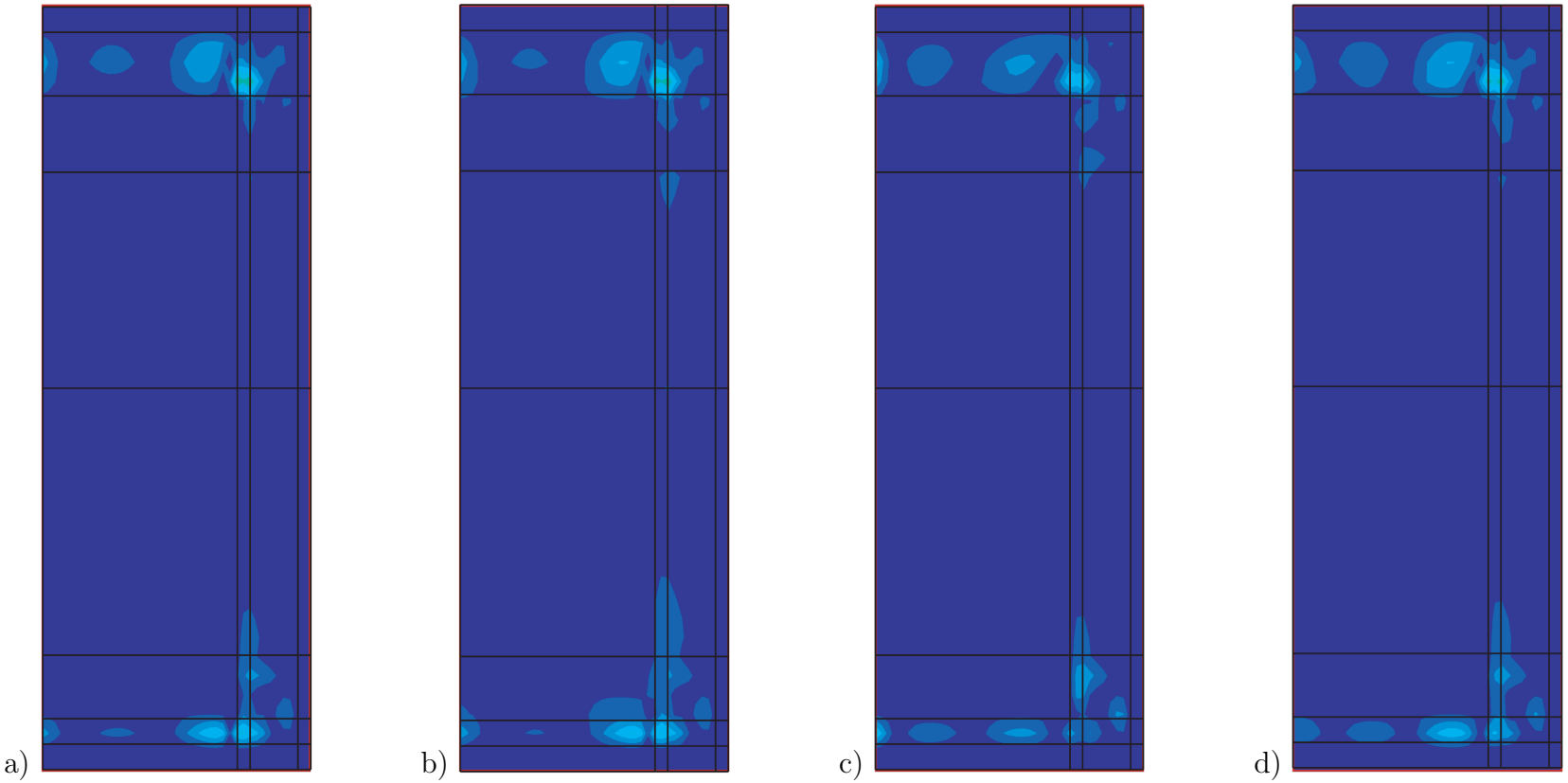

Fig. 4.51. Transient diffusion problem in a thermal battery. The contour plots for isotropic case related to the semi-discrete finite element solution $u_{S^p_{\Delta_h}}$ of degree $p = 2$ at time instant $t = \frac{T}{6}$ for quantities: a) The exact error $|u - u_{S^p_{\Delta_h}}|$; b) The approximation of the exact error $|\hat{u} - u_{S^p_{\Delta_h}}|$ based on the exact solution $\hat{u}$ of the elliptic reconstruction problem; c) The approximation of the exact error $|\hat{u}_{S^{p+k}_{\Delta_{h'}}} - u_{S^p_{\Delta_h}}|$ based on the approximate solution $\hat{u}_{S^{p+k}_{\Delta_{h'}}}$ of the elliptic reconstruction problem with $k = 1$; d) The approximation of the exact error $|\hat{u}_{S^{p+k}_{\Delta_{h'}}} - u_{S^p_{\Delta_h}}|$ based on the approximate solution $\hat{u}_{S^{p+k}_{\Delta_{h'}}}$ of the elliptic reconstruction problem with $k = 2$.

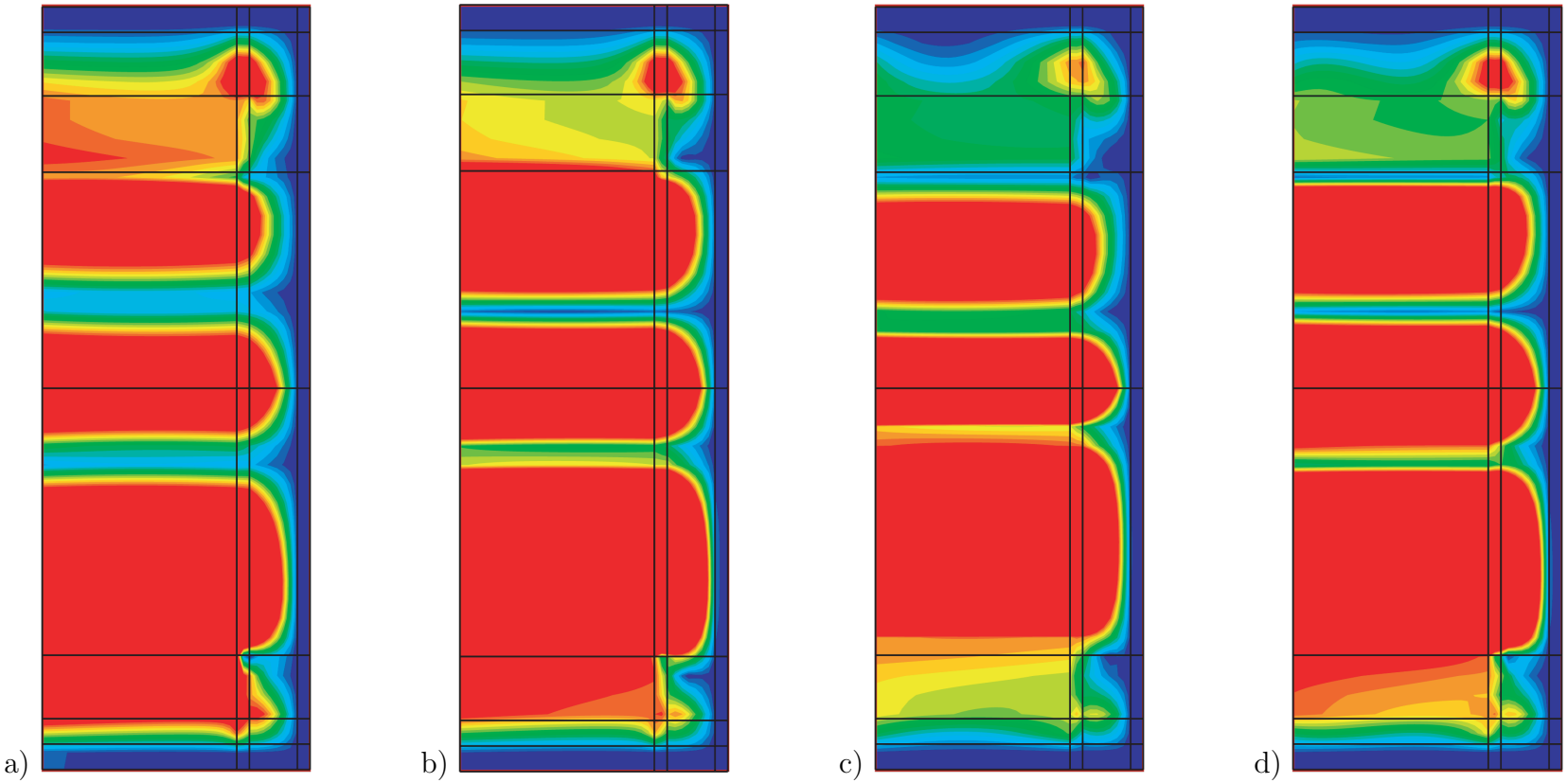

Fig. 4.52. Transient diffusion problem in a thermal battery. The contour plots for orthotropic case related to the semi-discrete finite element solution $u_{S^p_{\Delta_h}}$ of degree $p = 1$ at time instant $t = \frac{T}{6}$ for quantities: a) The exact error $|u - u_{S^p_{\Delta_h}}|$; b) The approximation of the exact error $|\hat{u} - u_{S^p_{\Delta_h}}|$ based on the exact solution $\hat{u}$ of the elliptic reconstruction problem; c) The approximation of the exact error $|\hat{u}_{S^{p+k}_{\Delta_{h'}}} - u_{S^p_{\Delta_h}}|$ based on the approximate solution $\hat{u}_{S^{p+k}_{\Delta_{h'}}}$ of the elliptic reconstruction problem with $k = 1$; d) The approximation of the exact error $|\hat{u}_{S^{p+k}_{\Delta_{h'}}} - u_{S^p_{\Delta_h}}|$ based on the approximate solution $\hat{u}_{S^{p+k}_{\Delta_{h'}}}$ of the elliptic reconstruction problem with $k = 2$.

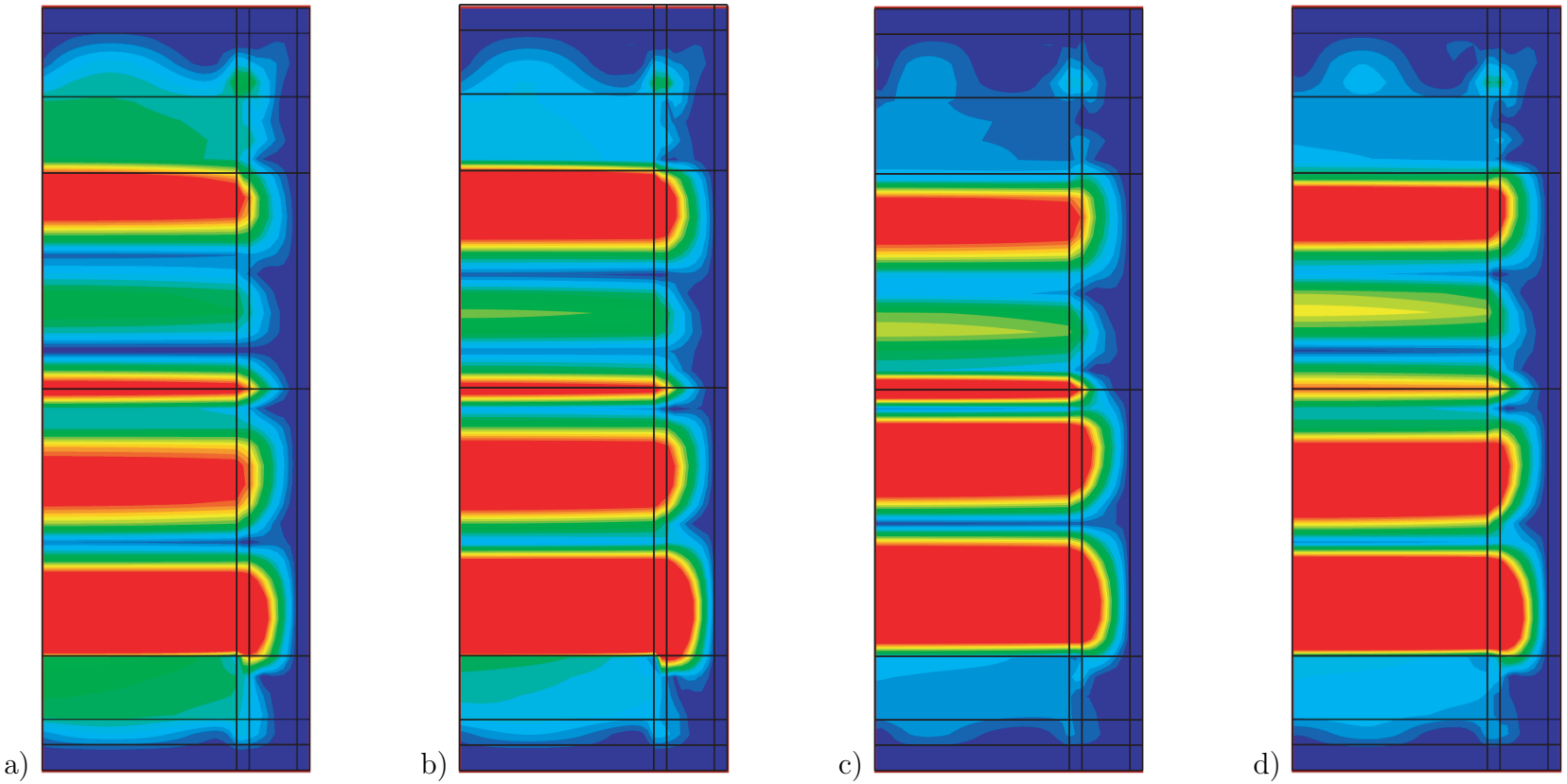

Fig. 4.53. Transient diffusion problem in a thermal battery. The contour plots for orthotropic case related to the semi-discrete finite element solution $u_{S^p_{\Delta_h}}$ of degree $p = 2$ at time instant $t = \frac{T}{6}$ for quantities: a) The exact error $|u - u_{S^p_{\Delta_h}}|$; b) The approximation of the exact error $|\hat{u} - u_{S^p_{\Delta_h}}|$ based on the exact solution $\hat{u}$ of the elliptic reconstruction problem; c) The approximation of the exact error $|\hat{u}_{S^{p+k}_{\Delta_{h'}}} - u_{S^p_{\Delta_h}}|$ based on the approximate solution $\hat{u}_{S^{p+k}_{\Delta_{h'}}}$ of the elliptic reconstruction problem with $k = 1$; d) The approximation of the exact error $|\hat{u}_{S^{p+k}_{\Delta_{h'}}} - u_{S^p_{\Delta_h}}|$ based on the approximate solution $\hat{u}_{S^{p+k}_{\Delta_{h'}}}$ of the elliptic reconstruction problem with $k = 2$.

Figs. 4.54 and 4.55 are the contour plots of the modulus of the exact error $|\mathbf{K}\nabla(u - u_{S^p_{\Delta_h}})|$ and its approximations $|\mathbf{K}\nabla(\hat{u} - u_{S^p_{\Delta_h}})|$ and $|\mathbf{K}\nabla(\hat{u}_{S^{p+k}_{\Delta_{h'}}} - u_{S^p_{\Delta_h}})|$ based on the exact and approximate solutions of the elliptic reconstruction problem for isotropic case for the semi-discrete finite element solution $u_{S^p_{\Delta_h}}$ computed with degree of $p = 1, 2$ and Mesh II.

Figs. 4.56 and 4.57 are the contour plots of the modulus of the exact error $|\mathbf{K}\nabla(u - u_{S^p_{\Delta_h}})|$ and its approximations $|\mathbf{K}\nabla(\hat{u} - u_{S^p_{\Delta_h}})|$ and $|\mathbf{K}\nabla(\hat{u}_{S^{p+k}_{\Delta_{h'}}} - u_{S^p_{\Delta_h}})|$ based on the exact and approximate solutions of the elliptic reconstruction problem for orthotropic case for the semi-discrete finite element solution $u_{S^p_{\Delta_h}}$ computed with degree of $p = 1, 2$ and Mesh II. It can be seen that for both the isotropic case and orthotropic case the contour plots match each other well. Clearly with the increase of polynomial order $p + k$, the approximate value of $|\mathbf{K}\nabla(\hat{u}_{S^{p+k}_{\Delta_{h'}}} - u_{S^p_{\Delta_h}})|$ converges to the exact value of $|\mathbf{K}\nabla(\hat{u} - u_{S^p_{\Delta_h}})|$.

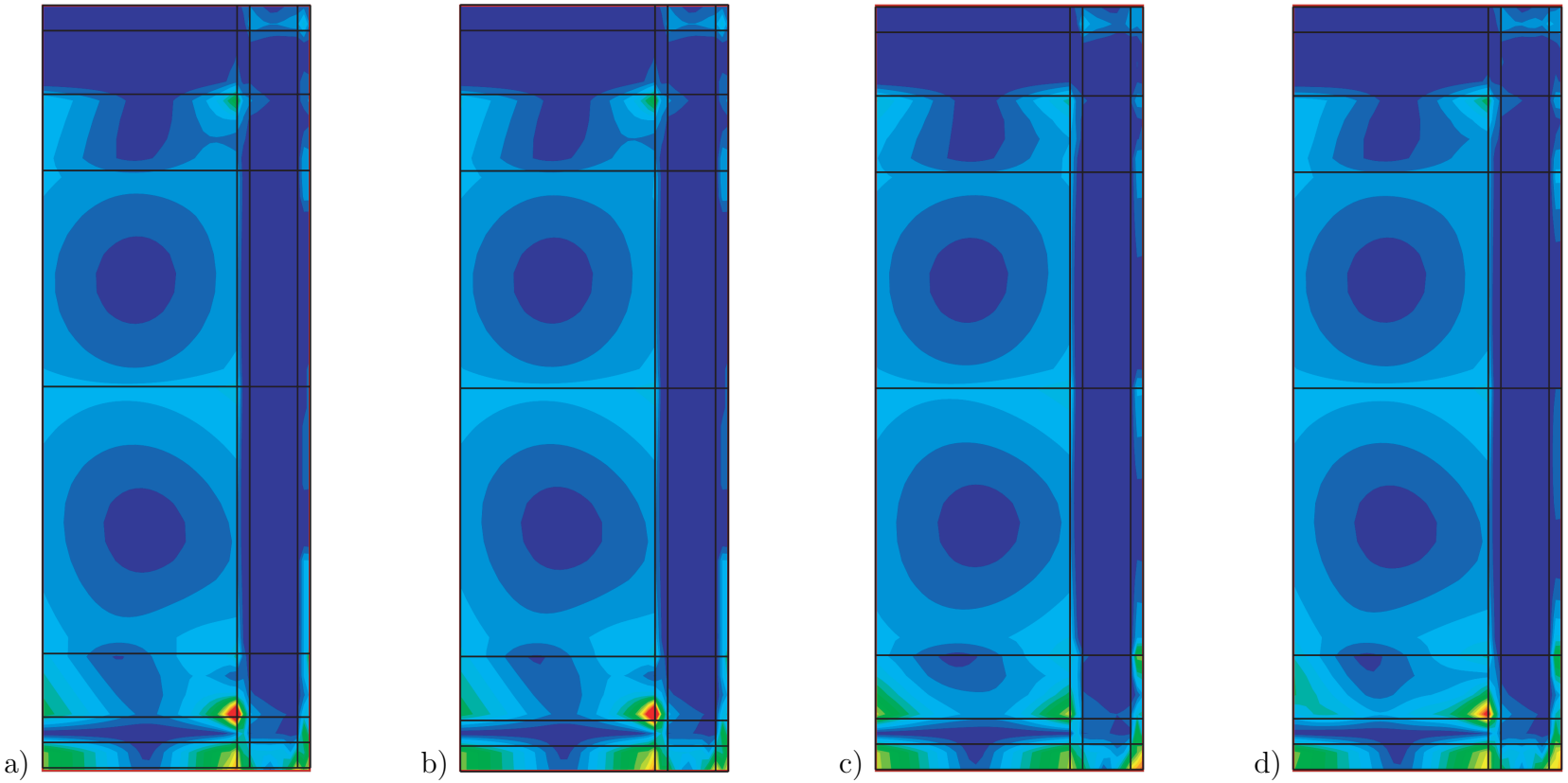

Fig. 4.54. Transient diffusion problem in a thermal battery. The contour plots for isotropic case related to the semi-discrete finite element solution $u_{S^p_{\Delta_h}}$ of degree $p = 1$ at time instant $t = \frac{T}{6}$ for quantities: a) The modulus of exact error $|\mathbf{K}\nabla(u - u_{S^p_{\Delta_h}})|$; b) The approximate modulus of the exact error $|\mathbf{K}\nabla(\hat{u} - u_{S^p_{\Delta_h}})|$ based on the exact solution $\hat{u}$ of the elliptic reconstruction problem; c) The approximate modulus of the exact error $|\mathbf{K}\nabla(\hat{u}_{S^{p+k}_{\Delta_{h'}}} - u_{S^p_{\Delta_h}})|$ based on the approximate solution $\hat{u}_{S^{p+k}_{\Delta_{h'}}}$ of the elliptic reconstruction problem with $k = 1$; d) The approximate modulus of the exact error $|\mathbf{K}\nabla(\hat{u}_{S^{p+k}_{\Delta_{h'}}} - u_{S^p_{\Delta_h}})|$ based on the approximate solution $\hat{u}_{S^{p+k}_{\Delta_{h'}}}$ of the elliptic reconstruction problem with $k = 2$.

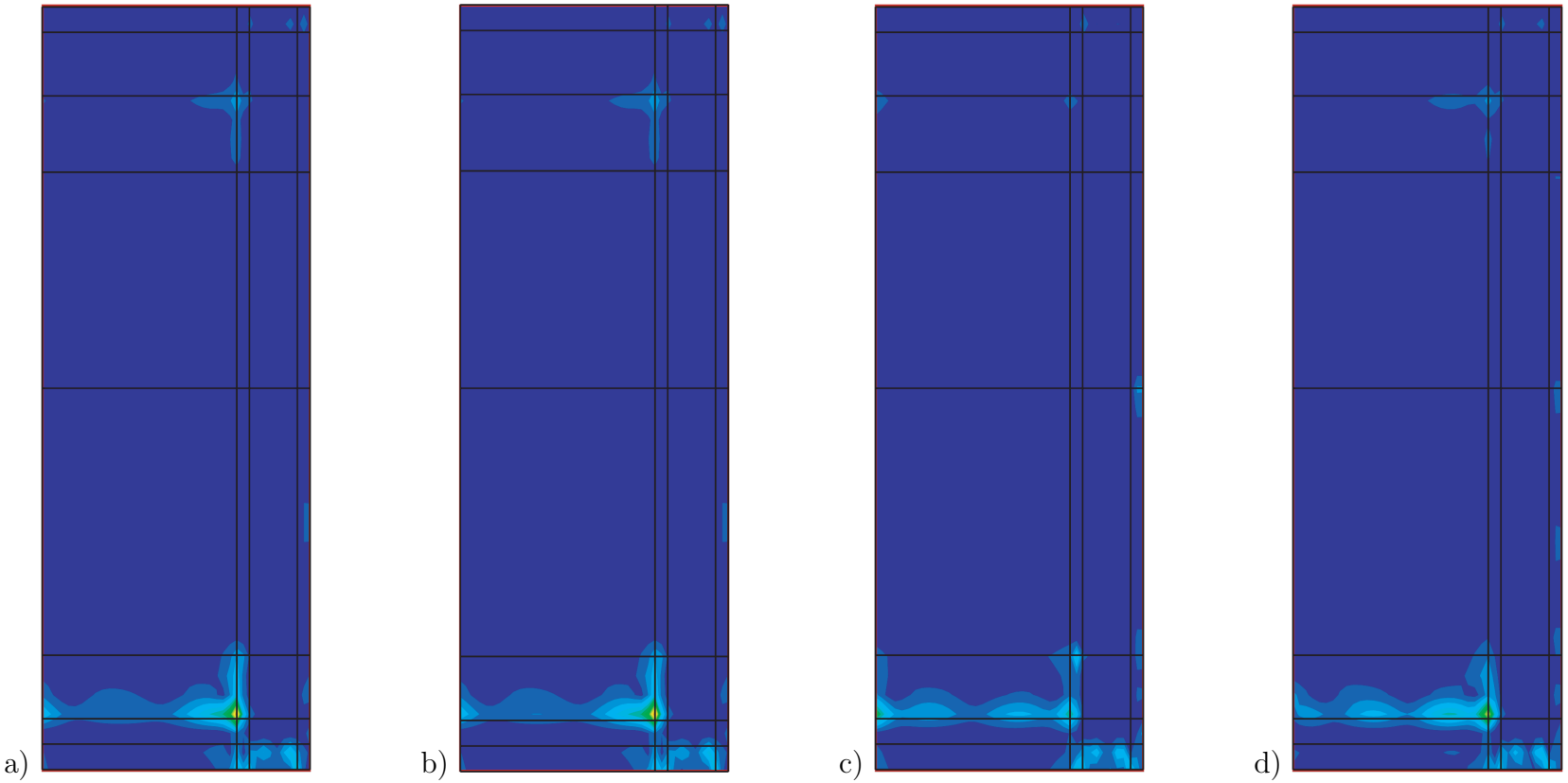

Fig. 4.55. Transient diffusion problem in a thermal battery. The contour plots for isotropic case related to the semi-discrete finite element solution $u_{S^p_{\Delta_h}}$ of degree $p = 2$ at time instant $t = \frac{T}{6}$ for quantities: a) The modulus of exact error $|\mathbf{K}\nabla(u - u_{S^p_{\Delta_h}})|$; b) The approximate modulus of the exact error $|\mathbf{K}\nabla(\hat{u} - u_{S^p_{\Delta_h}})|$ based on the exact solution $\hat{u}$ of the elliptic reconstruction problem; c) The approximate modulus of the exact error $|\mathbf{K}\nabla(\hat{u}_{S^{p+k}_{\Delta_{h'}}} - u_{S^p_{\Delta_h}})|$ based on the approximate solution $\hat{u}_{S^{p+k}_{\Delta_{h'}}}$ of the elliptic reconstruction problem with $k = 1$; d) The approximate modulus of the exact error $|\mathbf{K}\nabla(\hat{u}_{S^{p+k}_{\Delta_{h'}}} - u_{S^p_{\Delta_h}})|$ based on the approximate solution $\hat{u}_{S^{p+k}_{\Delta_{h'}}}$ of the elliptic reconstruction problem with $k = 2$.

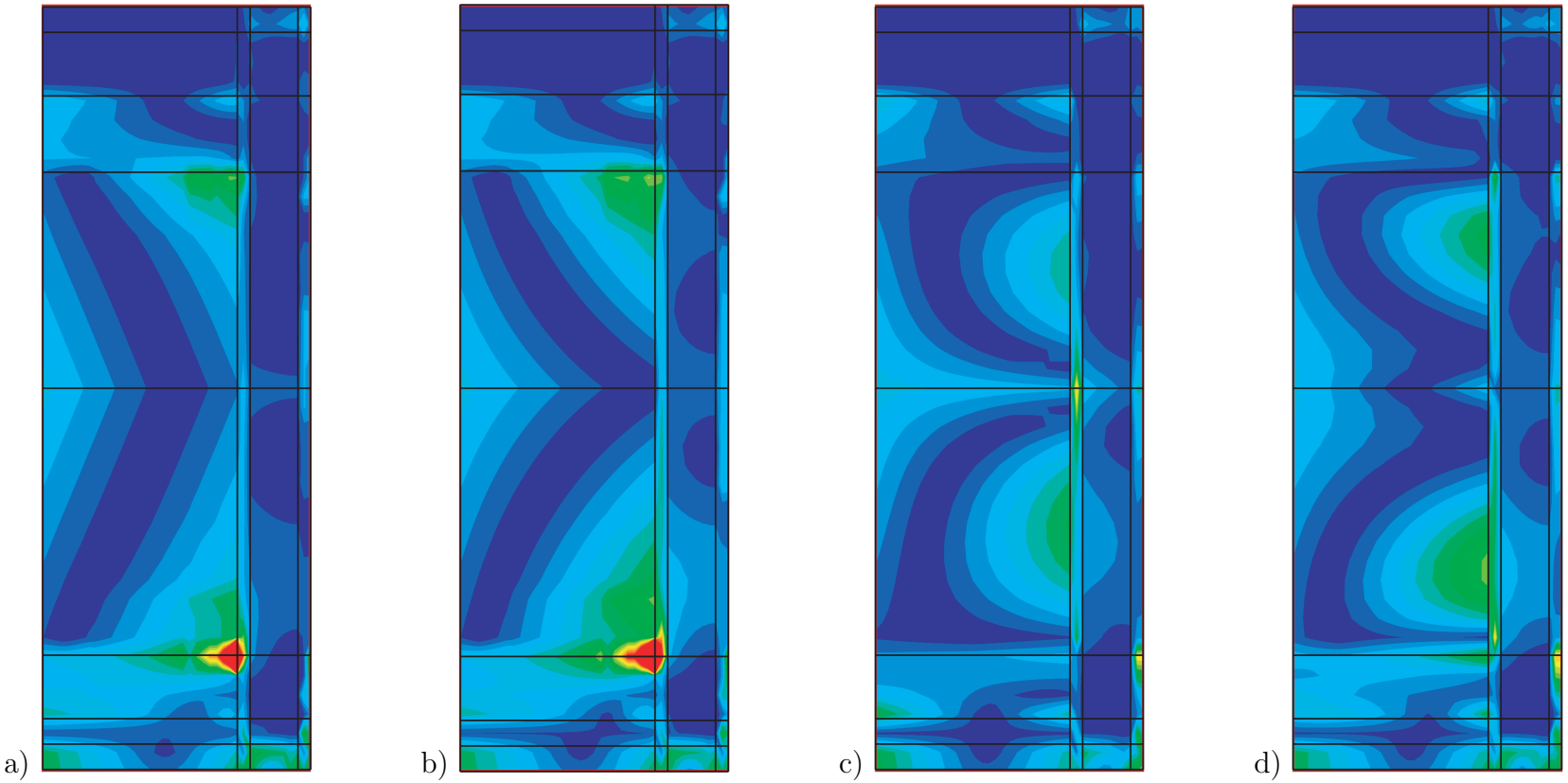

Fig. 4.56. Transient diffusion problem in a thermal battery. The contour plots for orthotropic case related to the semi-discrete finite element solution $u_{S^p_{\Delta_h}}$ of degree $p = 1$ at time instant $t = \frac{T}{6}$ for quantities: a) The modulus of exact error $|\mathbf{K}\nabla(u - u_{S^p_{\Delta_h}})|$; b) The approximate modulus of the exact error $|\mathbf{K}\nabla(\hat{u} - u_{S^p_{\Delta_h}})|$ based on the exact solution $\hat{u}$ of the elliptic reconstruction problem; c) The approximate modulus of the exact error $|\mathbf{K}\nabla(\hat{u}_{S^{p+k}_{\Delta_{h'}}} - u_{S^p_{\Delta_h}})|$ based on the approximate solution $\hat{u}_{S^{p+k}_{\Delta_{h'}}}$ of the elliptic reconstruction problem with $k = 1$; d) The approximate modulus of the exact error $|\mathbf{K}\nabla(\hat{u}_{S^{p+k}_{\Delta_{h'}}} - u_{S^p_{\Delta_h}})|$ based on the approximate solution $\hat{u}_{S^{p+k}_{\Delta_{h'}}}$ of the elliptic reconstruction problem with $k = 2$.

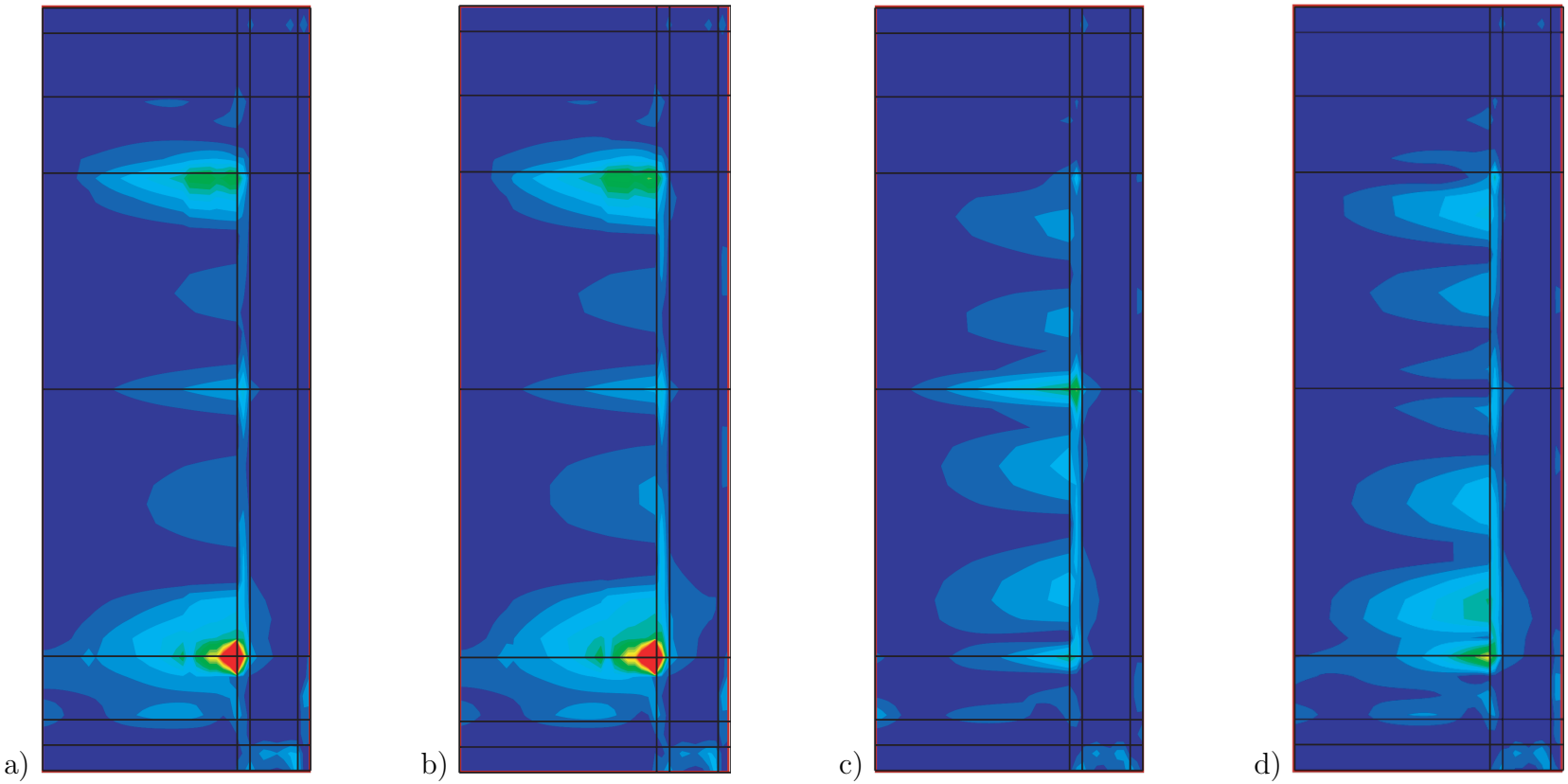

Fig. 4.57. Transient diffusion problem in a thermal battery. The contour plots for orthotropic case related to the semi-discrete finite element solution $u_{S^p_{\Delta_h}}$ of degree $p = 2$ at time instant $t = \frac{T}{6}$ for quantities: a) The modulus of exact error $|\mathbf{K}\nabla(u - u_{S^p_{\Delta_h}})|$; b) The approximate modulus of the exact error $|\mathbf{K}\nabla(\hat{u} - u_{S^p_{\Delta_h}})|$ based on the exact solution $\hat{u}$ of the elliptic reconstruction problem; c) The approximate modulus of the exact error $|\mathbf{K}\nabla(\hat{u}_{S^{p+k}_{\Delta_{h'}}} - u_{S^p_{\Delta_h}})|$ based on the approximate solution $\hat{u}_{S^{p+k}_{\Delta_{h'}}}$ of the elliptic reconstruction problem with $k = 1$; d) The approximate modulus of the exact error $|\mathbf{K}\nabla(\hat{u}_{S^{p+k}_{\Delta_{h'}}} - u_{S^p_{\Delta_h}})|$ based on the approximate solution $\hat{u}_{S^{p+k}_{\Delta_{h'}}}$ of the elliptic reconstruction problem with $k = 2$.

Fig. 4.58 (resp. Fig. 4.59) is the contour plot of the absolute value of the exact and computed error indicator functions $|\hat{e}_{\omega_X^{\Delta_h}}|$ and $|\hat{e}_{\omega_X^{\Delta_h},p+k}|$ for isotropic case (resp. orthotropic case), where the error indicator functions are based on the subdomain residual of the elliptic reconstruction problem constructed from the semi-discrete finite element solution computed with element of degree $p = 2$ and Mesh I. It can be seen that for isotropic case the contour plot based on the error indicator function matches the exact error well. However for orthotropic case, the contour plots between the error indicator function and the exact error are completely different.

Fig. 4.60 (resp. Fig. 4.61) is the contour plot of the modulus from the exact and computed error indicator functions $|\hat{e}_{\omega_X^{\Delta_h}}|$ and $|\hat{e}_{\omega_X^{\Delta_h},p+k}|$ for isotropic case (resp. orthotropic case), where the error indicator functions are based on the subdomain residual of the elliptic reconstruction problem constructed from the semi-discrete finite element solution computed with element of degree $p = 2$ and Mesh I. Again for isotropic case, the modulus based on the error indicator function matches the exact error well. However this is the case for orthotropic case.

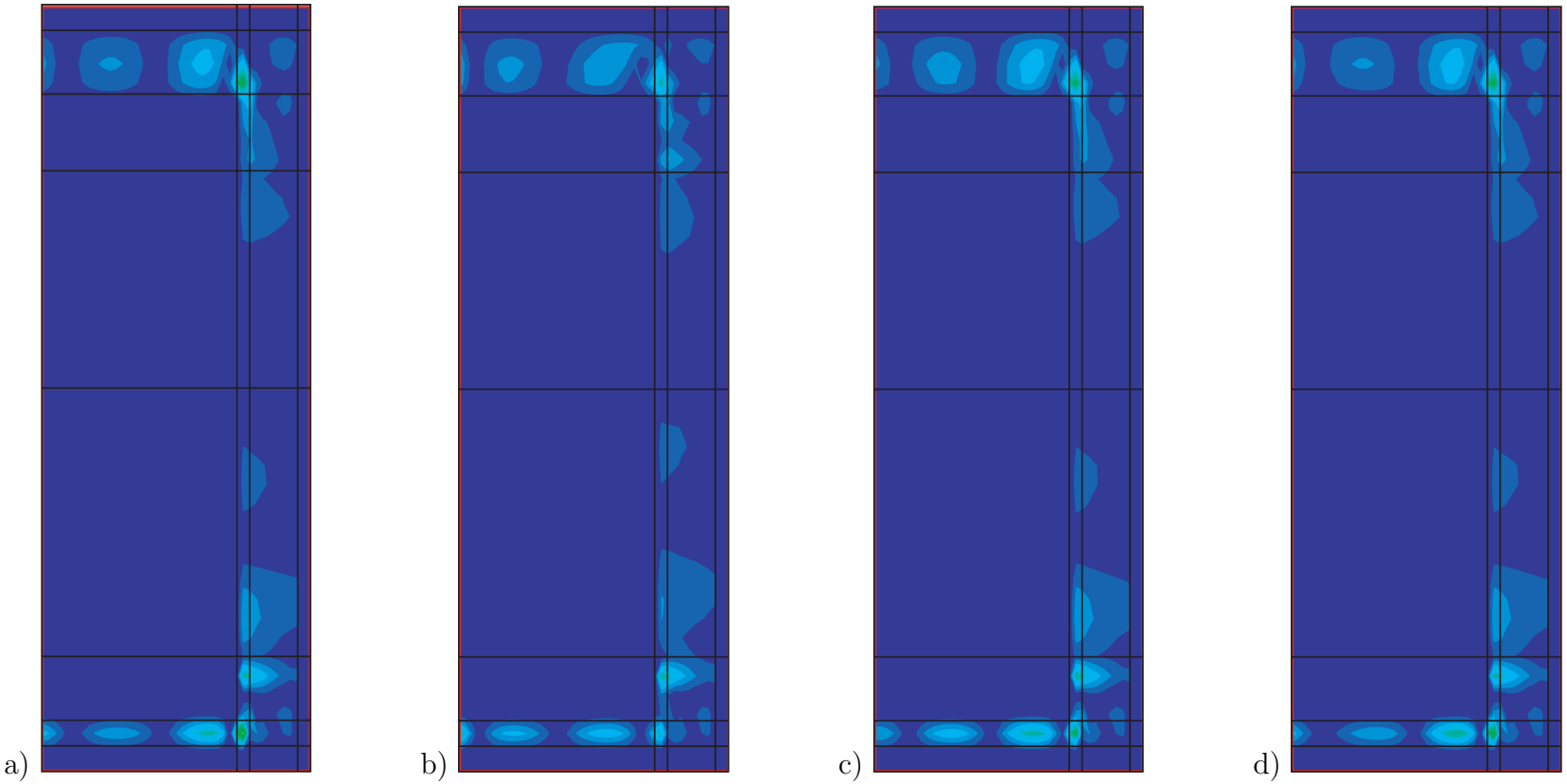

Fig. 4.58. Transient diffusion problem in a thermal battery. The contour plots for isotropic case related to the semi-discrete finite element solution $u_{S^p_{\Delta_h}}$ of degree $p = 2$ at time instant $t = \frac{T}{6}$ for quantities: a) The absolute value of exact error indicator function $|\hat{e}_{\omega_X^{\Delta_h}}|$; b) The absolute value of the computed error indicator function $|\hat{e}_{\omega_X^{\Delta_h},p+k}|, k = 1$; c) The absolute value of the computed error indicator function $|\hat{e}_{\omega_X^{\Delta_h},p+k}|, k = 2$; d) The absolute value of the computed error indicator function $|\hat{e}_{\omega_X^{\Delta_h},p+k}|, k = 3$.

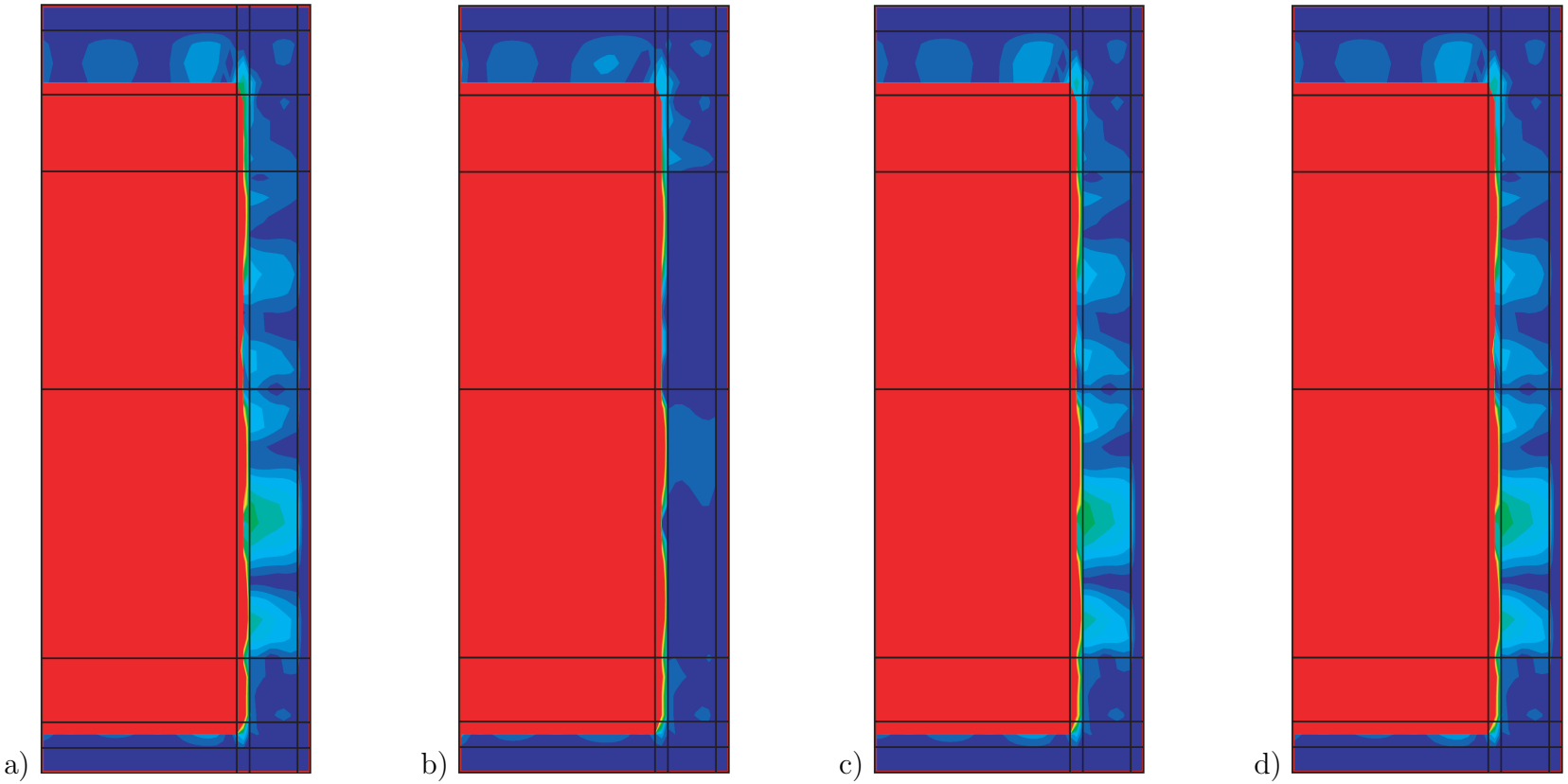

Fig. 4.59. Transient diffusion problem in a thermal battery. The contour plots for orthotropic case related to the semi-discrete finite element solution $u_{S^p_{\Delta_h}}$ of degree $p = 2$ at time instant $t = \frac{T}{6}$ for quantities: a) The absolute value of exact error indicator function $|\hat{e}_{\omega_X^{\Delta_h}}|$; b) The absolute value of the computed error indicator function $|\hat{e}_{\omega_X^{\Delta_h},p+k}|, k = 1$; c) The absolute value of the computed error indicator function $|\hat{e}_{\omega_X^{\Delta_h},p+k}|, k = 2$; d) The absolute value of the computed error indicator function $|\hat{e}_{\omega_X^{\Delta_h},p+k}|, k = 3$.

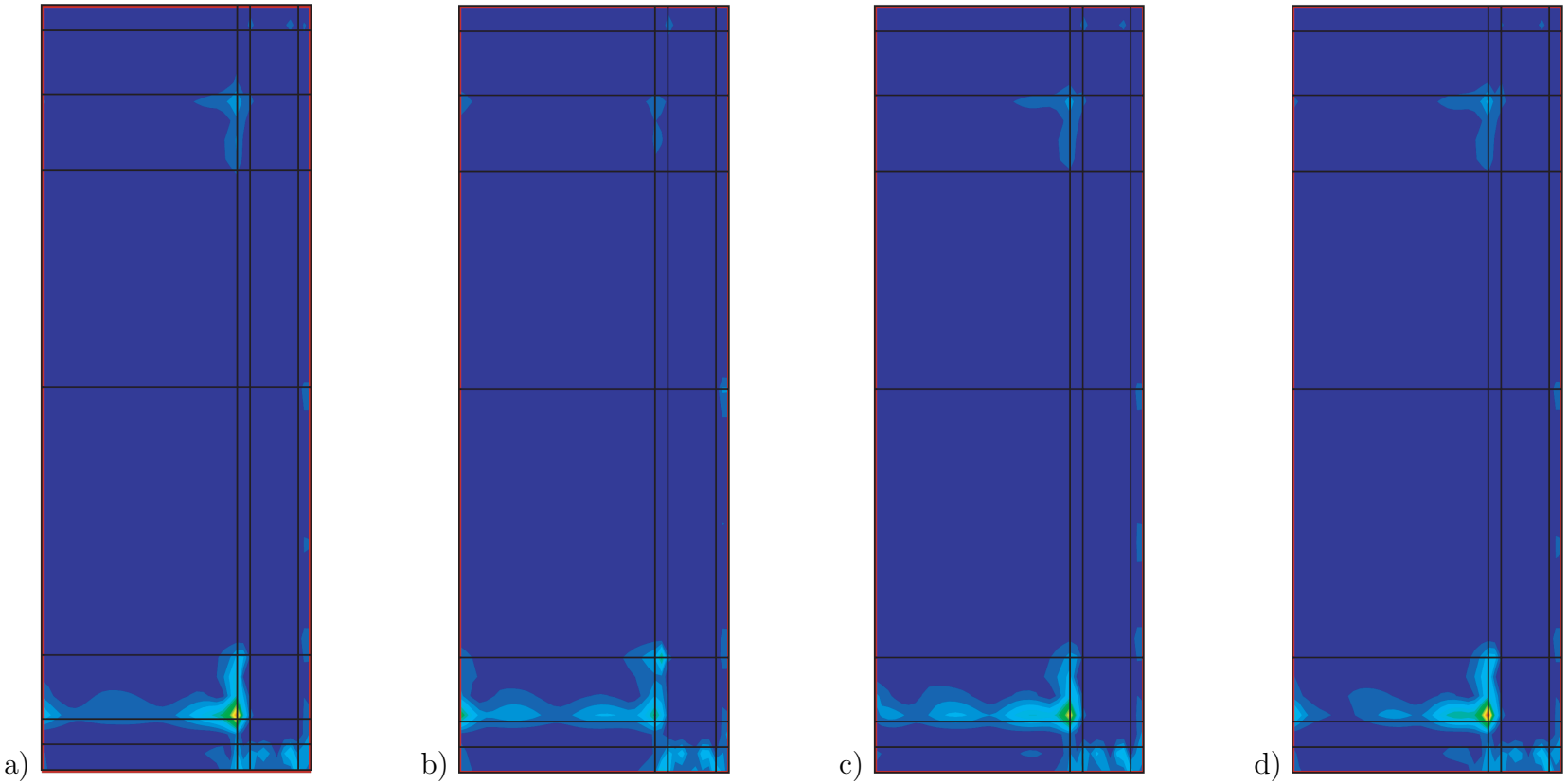

Fig. 4.60. Transient diffusion problem in a thermal battery. The contour plots for isotropic case related to the semi-discrete finite element solution $u_{S^p_{\Delta_h}}$ of degree $p = 2$ at time instant $t = \frac{T}{6}$ for quantities: a) The modulus value of exact error indicator function $|\mathbf{K}\nabla\hat{e}_{\omega_X^{\Delta_h}}|$; b) The modulus of the computed error indicator function $|\mathbf{K}\nabla\hat{e}_{\omega_X^{\Delta_h},p+k}|, k = 1$; c) The modulus of the computed error indicator function $|\mathbf{K}\nabla\hat{e}_{\omega_X^{\Delta_h},p+k}|, k = 2$; d) The modulus of the computed error indicator function $|\mathbf{K}\nabla\hat{e}_{\omega_X^{\Delta_h},p+k}|, k = 3$.

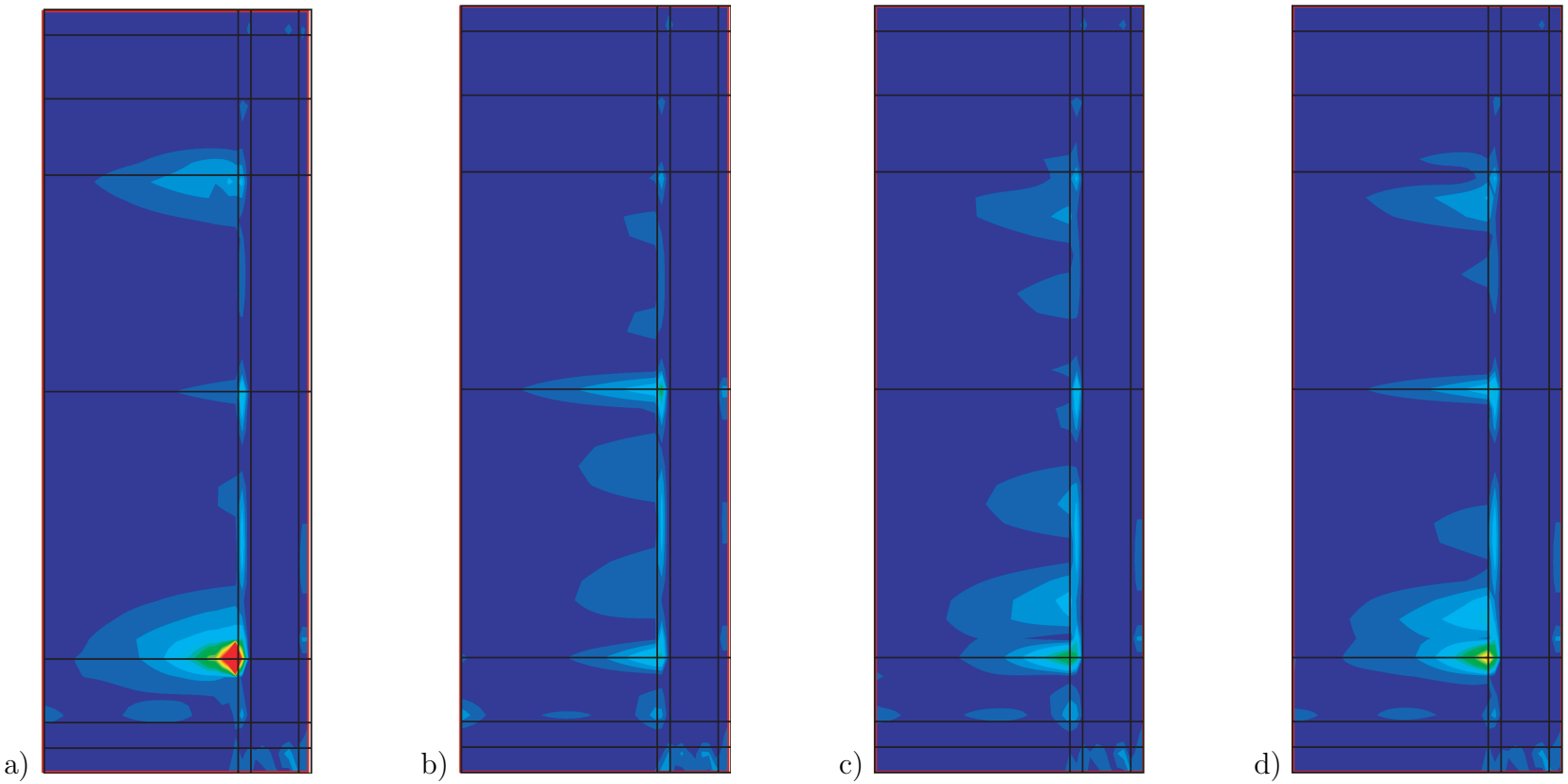

Fig. 4.61. Transient diffusion problem in a thermal battery. The contour plots for orthotropic case related to the semi-discrete finite element solution $u_{S^p_{\Delta_h}}$ of degree $p = 2$ at time instant $t = \frac{T}{6}$ for quantities: a) The modulus value of exact error indicator function $|\mathbf{K}\nabla\hat{e}_{\omega_X^{\Delta_h}}|$; b) The modulus of the computed error indicator function $|\mathbf{K}\nabla\hat{e}_{\omega_X^{\Delta_h},p+k}|, k = 1$; c) The modulus of the computed error indicator function $|\mathbf{K}\nabla\hat{e}_{\omega_X^{\Delta_h},p+k}|, k = 2$; d) The modulus of the computed error indicator function $|\mathbf{K}\nabla\hat{e}_{\omega_X^{\Delta_h},p+k}|, k = 3$.

CHAPTER V

GUARANTEED ERROR ESTIMATION FOR FULLY DISCRETE SOLUTIONS OF PARABOLIC PROBLEMS BASED ON ELLIPTIC RECONSTRUCTION

5.1 Fully discrete finite element solution of the transient heat conduction problem, and postprocessing based on elliptic reconstruction

The formulation of the fully discrete finite element solution corresponding to (4.1) is the following.

Let $\mathcal{I} \stackrel{\text{def}}{=} \{I_n\}_{n=1}^{N}$, be a partition of the time interval $[0,T]$ into N uniform time steps $I_n = (t_{n-1}, t_n]$, $n = 1, ..., N$, $0 = t_0 < t_1 .... < t_N = T$, and we denote by $\Delta t \stackrel{\text{def}}{=} t_n - t_{n-1}$ the time step size. Thus for $t \in I_n$, the standard backward Euler-Galerkin method for the discretization of problem (4.1) associated with the finite element spaces $S^p_{\Delta_h}$ is defined as follows:

Find $U^n_{S^p_{\Delta_h}} \in S^p_{\Delta_h}$, such that

$$\gamma\left(\frac{U^n_{S^p_{\Delta_h}} - U^{n-1}_{S^p_{\Delta_h}}}{\Delta t}, v\right)_{L^2(\Omega)} + \mathcal{B}_\Omega(U^n_{S^p_{\Delta_h}}, v) = \mathcal{L}^n(v) \qquad \forall v \in S^p_{\Delta_h}, \qquad \forall t \in (t_{n-1}, t_n] \tag{5.1}$$

where

$$\mathcal{L}^n(v) \stackrel{\text{def}}{=} \int_\Omega f^n v + \int_{\Gamma_N} g^n v \tag{5.2}$$

Note that for simplicity $U^n_{S^p_{\Delta_h}} \stackrel{\text{def}}{=} U^n_{S^p_{\Delta_h}}(\mathbf{x}, t_n)$, $U^{n-1}_{S^p_{\Delta_h}} \stackrel{\text{def}}{=} U^{n-1}_{S^p_{\Delta_h}}(\mathbf{x}, t_{n-1})$, $f^n \stackrel{\text{def}}{=} f(\mathbf{x}, t_n)$, $g^n \stackrel{\text{def}}{=} g(\mathbf{x}, t_n)$ and $S^p_{\Delta_h} \subset \mathcal{U}(\Omega)$ is the finite element space defined using tensor-product rectangular elements of degree p over mesh Δ_h.

Given the discrete function of time $U^n_{S^p_{\Delta_h}}$ at time node t_n and $U^{n-1}_{S^p_{\Delta_h}}$ at t_{n-1}, we can build a continuous function of time $U_{S^p_{\Delta_h}} \stackrel{\text{def}}{=} U_{S^p_{\Delta_h}}(\mathbf{x}, t)$ for time interval $[t_{n-1}, t_n]$

by piecewise linear interpolation, e.g.,

$$U_{S^p_{\Delta_h}} \stackrel{\text{def}}{=} l_{n-1}(t)U^{n-1}_{S^p_{\Delta_h}} + l_n(t)U^n_{S^p_{\Delta_h}} \quad \text{for} \quad t \in [t_{n-1}, t_n] \tag{5.3}$$

where

$$l_{n-1}(t) \stackrel{\text{def}}{=} \frac{t_n - t}{\Delta t} \qquad \text{and} \qquad l_n(t) \stackrel{\text{def}}{=} \frac{t - t_{n-1}}{\Delta t} \tag{5.4}$$

Let us address the elliptic reconstruction problems as formulated in [36, 37] in terms of the fully discrete finite element solution to the equation (4.1) which is defined as follows:

Find $\hat{U} = \hat{U}(\mathbf{x}, t)$, such that

$$\mathscr{B}_\Omega(\hat{U}, v) = \mathscr{L}(v) - \big(\gamma \frac{\partial}{\partial t} U_{S^p_{\Delta_h}}, v\big)_{L^2(\Omega)} \qquad \forall v \in \mathfrak{u}(\Omega), \qquad \forall t \in (0, T) \tag{5.5}$$

The finite element approximation of (5.5) in space $S^p_{\Delta_h}$ is the following

$$\mathscr{B}_\Omega(\hat{U}_{S^p_{\Delta_h}}, v) = \mathscr{L}(v) - \big(\gamma \frac{\partial}{\partial t} U_{S^p_{\Delta_h}}, v\big)_{L^2(\Omega)} \qquad \forall v \in S^p_{\Delta_h}, \qquad \forall t \in (0, T) \tag{5.6}$$

Note that unlike the semi-discrete finite element solution where the equation (4.6) holds at any time instant $t \in (0, T]$, the finite element solution $\hat{U}_{S^p_{\Delta_h}}$ of the equation (5.5) is equivalent to the fully discrete finite element solution $U_{S^p_{\Delta_h}}$ only at time instant $t = t_n, n = 0, 1, ..., N$, namely,

$$\mathscr{B}_\Omega(\hat{U}^n_{S^p_{\Delta_h}}, v) = \mathscr{L}^n(v) - \big(\gamma \frac{\partial}{\partial t} U_{S^p_{\Delta_h}}, v\big)_{L^2(\Omega)} = \mathscr{B}_\Omega(U^n_{S^p_{\Delta_h}}, v) \qquad \forall v \in S^p_{\Delta_h} \tag{5.7}$$

with

$$\frac{\partial}{\partial t} U_{S^p_{\Delta_h}} = \frac{U^n_{S^p_{\Delta_h}} - U^{n-1}_{S^p_{\Delta_h}}}{\Delta t} \tag{5.8}$$

If we define the exact error between the exact solution u and its fully discrete

finite element approximation $U_{S^p_{\Delta_h}}$ at any time instant t as follows

$$E_h \stackrel{\text{def}}{=} u - U_{S^p_{\Delta_h}} \tag{5.9}$$

then at time instant $t = t_n, n = 0, 1, ..., N$, we have by triangle inequality

$$||E^n_h||_{H^l} = ||u^n - U^n_{S^p_{\Delta_h}}||_{H^l} \leq ||u^n - \hat{U}^n||_{H^l} + ||\hat{U}^n - U^n_{S^p_{\Delta_h}}||_{H^l} \qquad l = 0, 1 \tag{5.10}$$

where $\hat{U}^n$ is the exact solution of equation (5.5) at time instant t_n.

Since $U^n_{S^p_{\Delta_h}}$ is finite element approximation of $\hat{U}^n$ based on finite element space $S^p_{\Delta_h}$, we know that $||\hat{U}^n - U^n_{S^p_{\Delta_h}}||_l$ is spatial error term with the following bounds

$$||\hat{U}^n - U^n_{S^p_{\Delta_h}}||_{H^l} \leq Ch^{p+1-l} \qquad l = 0, 1 \tag{5.11}$$

By introducing the exact solution $\hat{u}^n$ of equation (4.5) at time instant t_n, we can split $u^n - \hat{U}^n$ the following way,

$$u^n - \hat{U}^n = u^n - \hat{u}^n + \hat{u}^n - \hat{U}^n \tag{5.12}$$

Therefore

$$||u^n - \hat{U}^n||_{H^l} \leq ||u^n - \hat{u}^n||_{H^l} + ||\hat{u}^n - \hat{U}^n||_{H^l} \qquad l = 0, 1 \tag{5.13}$$

Clearly $||u^n - \hat{u}^n||_{H^l}$ is the spatial error term and its convergence rate is defined by the theorem 4.1 while $||\hat{u}^n - \hat{U}^n||_{H^l}$ is the temporal term and for quasi-uniform meshes and uniform time step size Δt, we have the following bounds if the temporal discretization scheme is backward difference [40]

$$||\hat{u}^n - \hat{U}^n||_{H^l} \leq C\Delta t \qquad l = 0, 1 \tag{5.14}$$

Therefore we have

$$||E_h^n||_{H^l} \leq C(h^{p+1-l} + h^{p+2-l}|\log h| + \Delta t) \quad p > 1, \quad l = 0, 1 \tag{5.15a}$$

$$||E_h^n||_{H^l} \leq C(h^{2-l} + h^2|\log h|^l + \Delta t) \quad p = 1, \quad l = 0, 1 \tag{5.15b}$$

Clearly it can be seen that if the temporal error term $||\hat{u}^n - \hat{U}^n||_{H^l}$ is negligible and the term $||u^n - \hat{u}^n||_{H^l}$ is superconvergent, we have

$$||E_h^n||_{H^l} \approx ||\hat{U}^n - U^n_{S^p_{\Delta_h}}||_{H^l} \qquad l = 0, 1 \tag{5.16}$$

Let us illustrate the convergence behaviors of $||E_h^n||_{H^l}$ and $||\hat{u}^n - \hat{U}^n||_{H^l}$ with the following examples.

Example 5.1. *Heat transition problem in one dimension.* We choose the time instant $t = \frac{T}{2}$ at which the solution reflects obvious transient behavior to study the relevant convergence behaviors as shown in Fig. 4.1.

Fig. 5.1 (resp. Fig. 5.2) is the convergence plot of $||u^n - U^n_{S^p_{\Delta_h}}||_{H^1}$ and $||\hat{u}^n - \hat{U}^n||_{H^1}$ $(l = 0, 1)$ with respect to time step size $\Delta t = \frac{T}{2^n}, n = 2, 3, 4$, and 5, at time instant $t = \frac{T}{2}$ for the fully discrete finite element solutions of degree $p = 1, 2$, and 3 for uniform meshes $h = \frac{L}{2^m}, m = 1, 2, 3$, and 4. It can be seen that $||\hat{u}^n - \hat{U}^n||_{H^l}$ $(l = 0, 1)$ has a convergence rate of 1 with respect time step size Δt. As the mesh density and polynomial order increase, the convergence behavior of $||u^n - U^n_{S^p_{\Delta_h}}||_{H^l}$ $(l = 0, 1)$ is dominated by the temporal error term $||\hat{u}^n - \hat{U}^n||_{H^l}$ $(l = 0, 1)$, which is obvious in the case of $p = 3$.

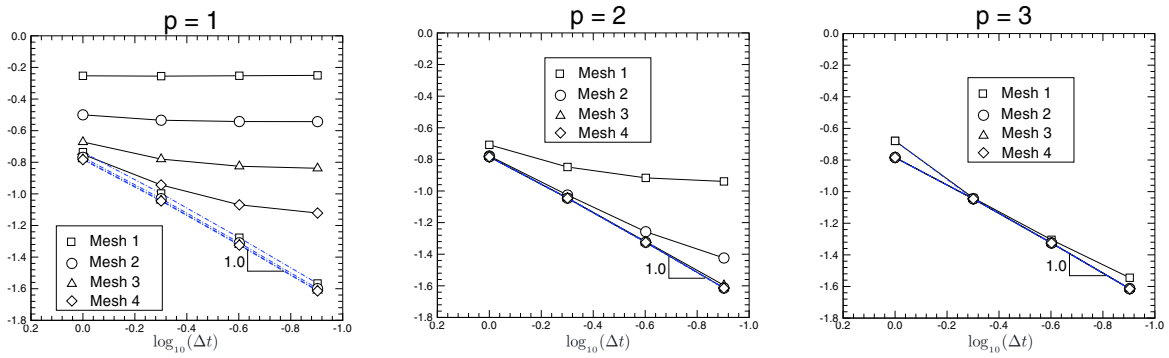

Fig. 5.1. Heat transition problem in one dimension. The convergence of $||u^n - U^n_{S^p_{\Delta_h}}||_{H^1}$ and $||\hat{u}^n - \hat{U}^n||_{H^1}$ vs. time step size $\Delta t = \frac{T}{2^n}, n = 2, 3, 4$, and 5, at time instant $t = \frac{T}{2}$ for the fully discrete finite element solutions of degree $p = 1, 2$, and 3 computed with mesh size $h = \frac{L}{2^m}, m = 1, 2, 3$, and 4.

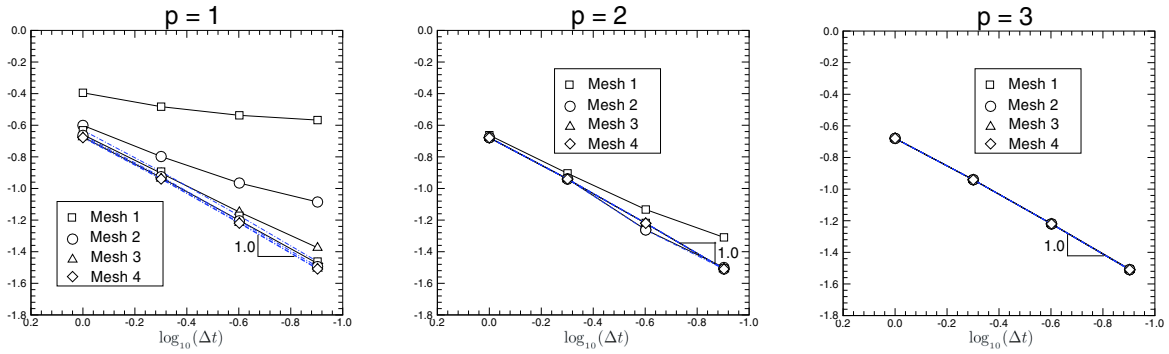

Fig. 5.2. Heat transition problem in one dimension. The convergence of $||u^n - U^n_{S^p_{\Delta_h}}||_{H^0}$ and $||\hat{u}^n - \hat{U}^n||_{H^0}$ vs. time step size $\Delta t = \frac{T}{2^n}, n = 2, 3, 4$, and 5, at time instant $t = \frac{T}{2}$ for the fully discrete finite element solutions of degree $p = 1, 2$, and 3 computed with mesh size $h = \frac{L}{2^m}, m = 1, 2, 3$, and 4.

Fig. 5.3 (resp. Fig. 5.4) is the convergence plot of $||u^n - U^n_{S^p_{\Delta_h}}||_{H^l}$ and $||\hat{u}^n - \hat{U}^n||_{H^l}$ $(l = 0, 1)$ with respect to mesh size h at time instant $t = \frac{T}{2}$ for the fully discrete finite element solutions of degree $p = 1, 2$, and 3 for uniform meshes $h = \frac{L}{2^m}, m = 1, 2, 3$, and 4. It can be seen that $||\hat{u}^n - \hat{U}^n||_{H^l}$ $(l = 0, 1)$ is not sensitive to the mesh density since it is related to temporal error only. With the increase of the number of time

steps, the magnitude of $||\hat{u}^n - \hat{U}^n||_{H^l}$ $(l = 0, 1)$ is reduced. Again for $p = 3$ where the temporal error is dominant, we can see that $||\hat{u}^n - \hat{U}^n||_{H^l}$ $(l = 0, 1)$ is about the same as $||\hat{u}^n - \hat{U}^n||_{H^l}$ $(l = 0, 1)$.

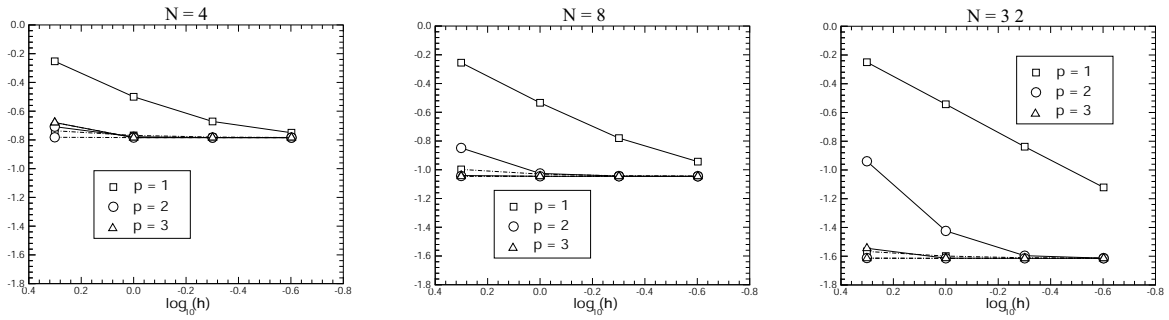

Fig. 5.3. Heat transition problem in one dimension. The convergence of $||u^n - U^n_{S^p_{\Delta_h}}||_{H^1}$ and $||\hat{u}^n - \hat{U}^n||_{H^1}$ vs. mesh size $h = \frac{L}{2^m}, m = 1, 2, 3$, and 4, at time instant $t = \frac{T}{2}$ for the fully discrete finite element solutions of degree $p = 1, 2$, and 3 computed with time step size $\Delta t = \frac{T}{2^n}, n = 2, 3, 4$, and 5.

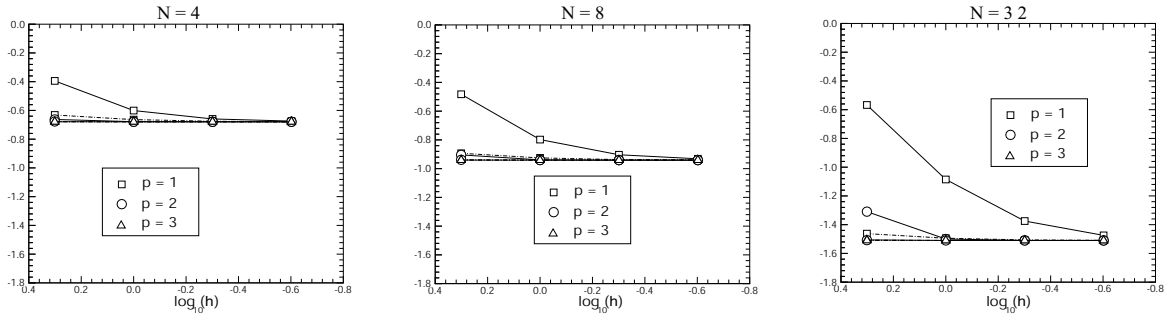

Fig. 5.4. Heat transition problem in one dimension. The convergence of $||u^n - U^n_{S^p_{\Delta_h}}||_{H^0}$ and $||\hat{u}^n - \hat{U}^n||_{H^0}$ vs. mesh size $h = \frac{L}{2^m}, m = 1, 2, 3$, and 4, at time instant $t = \frac{T}{2}$ for the fully discrete finite element solutions of degree $p = 1, 2$, and 3 computed with time step size $\Delta t = \frac{T}{2^n}, n = 2, 3, 4$, and 5.

Example 5.2. *Two dimensional synthetic problem.* We choose the time instant $t = \frac{T}{2}$ at which the solution contour as shown in Fig. 4.3 reflects obvious transient behavior.

Fig. 5.5 (resp. Fig. 5.6) is the convergence plot of $||u^n - U^n_{S^p_{\Delta_h}}||_{H^l}$ and $||\hat{u}^n - \hat{U}^n||_{H^l}$ $(l = 0, 1)$ with respect to time step size $\Delta t = \frac{T}{2^n}, n = 2, 3, 4,$ and 5, at time instant $t = \frac{T}{2}$ for the fully discrete finite element solutions of degree $p = 1, 2,$ and 3 for uniform meshes $h = \frac{L}{2^m}, m = 1, 2, 3,$ and 4. It can be seen that $||\hat{u}^n - \hat{U}^n||_{H^1}$ $(l = 0, 1)$ has a convergence rate of 1 with respect to time step size Δt. The exact error $||u^n - U^n_{S^p_{\Delta_h}}||_{H^l}$ $(l = 1)$ is not sensitive to the variation in time step size Δt which indicates that the spatial error is dominant. In the case of $||u^n - U^n_{S^p_{\Delta_h}}||_{H^l}$ $(l = 0)$, we can see the convergence behavior of $||u^n - U^n_{S^p_{\Delta_h}}||_{H^l}$ $(l = 0)$ is controlled by $||\hat{u}^n - \hat{U}^n||_{H^l}$ $(l = 0)$ for $p = 2, 3$ and Mesh 4 since the temporal error is dominant in this case.

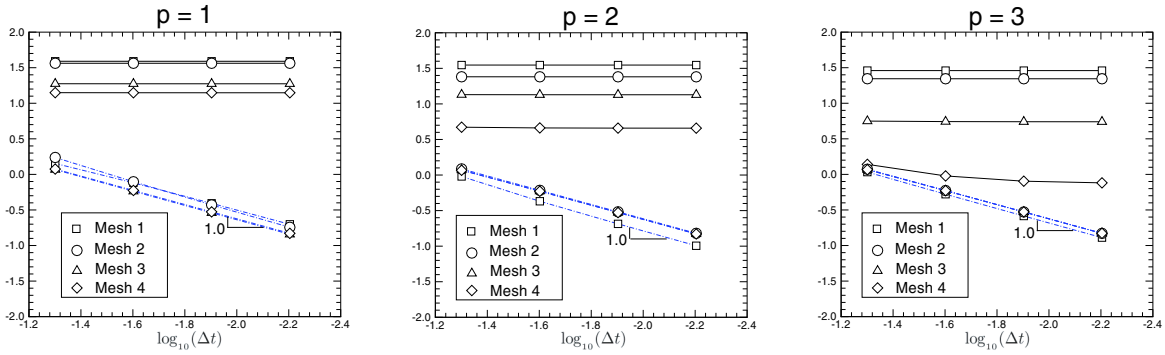

Fig. 5.5. Two dimensional synthetic problem. The convergence of $||u^n - U^n_{S^p_{\Delta_h}}||_{H^1}$ and $||\hat{u}^n - \hat{U}^n||_{H^1}$ vs. time step size $\Delta t = \frac{T}{2^n}, n = 2, 3, 4,$ and 5, at time instant $t = \frac{T}{2}$ for the fully discrete finite element solutions of degree $p = 1, 2,$ and 3 computed with mesh size $h = \frac{L}{2^m}, m = 1, 2, 3,$ and 4.

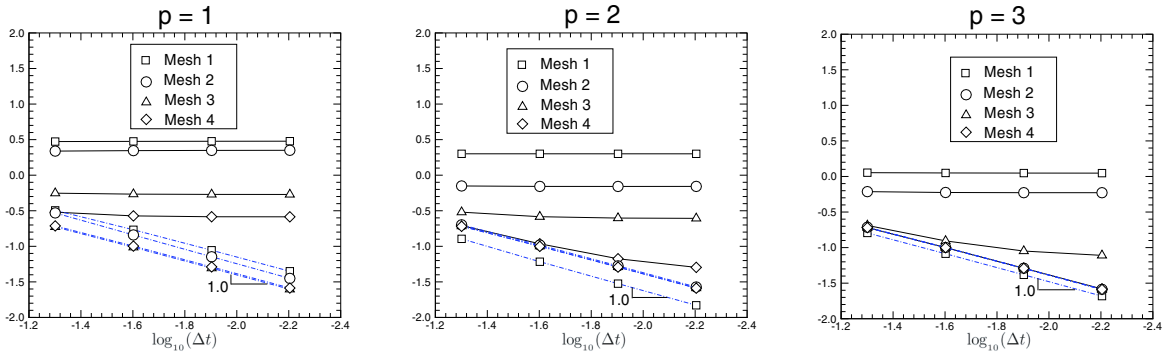

Fig. 5.6. Two dimensional synthetic problem. The convergence of $||u^n - U^n_{S^p_{\Delta_h}}||_{H^0}$ and $||\hat{u}^n - \hat{U}^n||_{H^0}$ vs. time step size $\Delta t = \frac{T}{2^n}, n = 2, 3, 4$, and 5, at time instant $t = \frac{T}{2}$ for the fully discrete finite element solutions of degree $p = 1, 2$, and 3 computed with mesh size $h = \frac{L}{2^m}, m = 1, 2, 3$, and 4.

Fig. 5.7 (resp. Fig. 5.8) is the convergence plot of $||u^n - U^n_{S^p_{\Delta_h}}||_{H^l}$ $(l = 0, 1)$ and $||\hat{u}^n - \hat{U}^n||_{H^l}$ $(l = 0, 1)$ with respect to mesh size h at time instant $t = \frac{T}{2}$ for the fully discrete finite element solutions of degree $p = 1, 2$, and 3 for uniform meshes $h = \frac{L}{2^m}, m = 1, 2, 3$, and 4. It can be seen that $||\hat{u}^n - \hat{U}^n||_{H^l}$ $(l = 0, 1)$ is not sensitive to the mesh size since it is related to the temporal error only and with the increase of the number of time steps its magnitude is reduced. When the spatial error is dominant, $||u^n - U^n_{S^p_{\Delta_h}}||_{H^l}$ $(l = 0, 1)$ converges as the mesh is refined. In the case where the temporal error is dominant, $||u^n - U^n_{S^p_{\Delta_h}}||_{H^l}$ $(l = 0, 1)$ and $||\hat{u}^n - \hat{U}^n||_{H^l}$ $(l = 0, 1)$ are about the same. For example, we can observe this in the case of $p = 3$, Mesh 4 and the number of time steps N equal to 4.

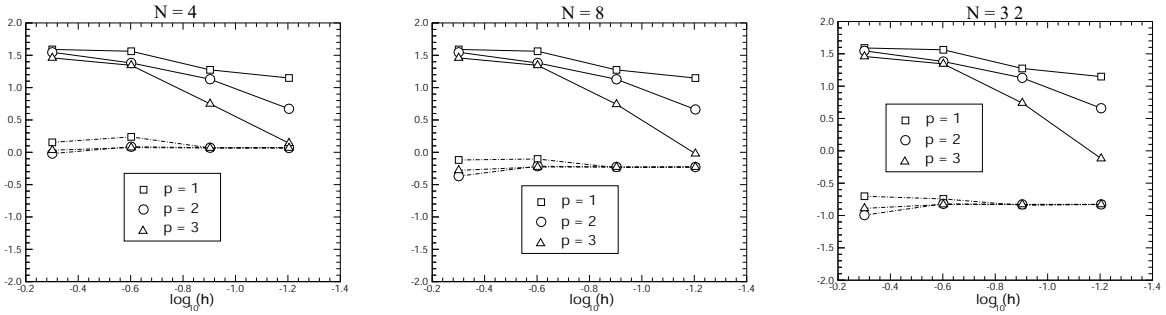

Fig. 5.7. Two dimensional synthetic problem. The convergence of $||u^n - U^n_{S^p_{\Delta_h}}||_{H^1}$ and $||\hat{u}^n - \hat{U}^n||_{H^1}$ vs. mesh size $h = \frac{L}{2^m}, m = 1, 2, 3,$ and 4, at time instant $t = \frac{T}{2}$ for the fully discrete finite element solutions of degree $p = 1, 2,$ and 3 computed with time step size $\Delta t = \frac{T}{2^n}, n = 2, 3, 4,$ and 5.

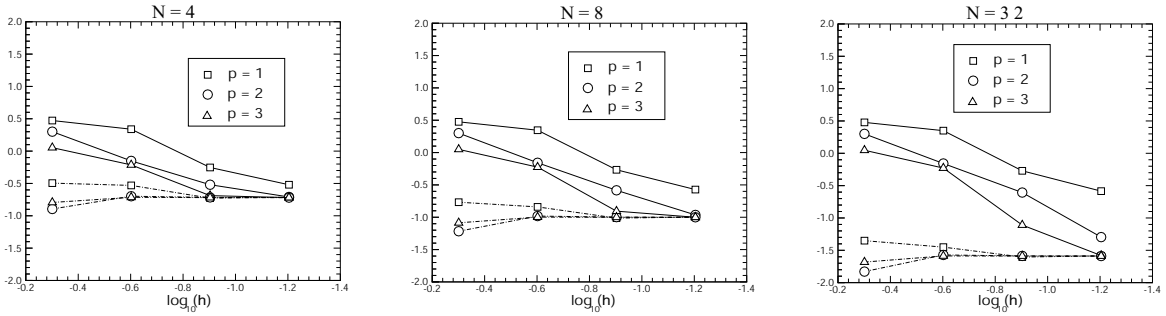

Fig. 5.8. Two dimensional synthetic problem. The convergence of $||u^n - U^n_{S^p_{\Delta_h}}||_{H^0}$ and $||\hat{u}^n - \hat{U}^n||_{H^0}$ vs. mesh size $h = \frac{L}{2^m}, m = 1, 2, 3,$ and 4, at time instant $t = \frac{T}{2}$ for the fully discrete finite element solutions of degree $p = 1, 2,$ and 3 computed with time step size $\Delta t = \frac{T}{2^n}, n = 2, 3, 4,$ and 5.

Example 5.3. *L-shaped domain problem.* We choose the time instant $t = \frac{T}{2}$ at which the solution reflects obvious transient behavior as shown in Fig. 4.7. Fig. 5.9 (resp. Fig. 5.10) is the convergence plot of $||u^n - U^n_{S^p_{\Delta_h}}||_{H^l}$ and $||\hat{u}^n - \hat{U}^n||_{H^l}$ $(l = 0, 1)$ with respect to time step size $\Delta t = \frac{T}{2^n}, n = 2, 3, 4,$ and 5, at time instant $t = \frac{T}{2}$ for the fully discrete finite element solutions of degree $p = 1, 2,$ and 3 for uniform meshes $h = \frac{L}{2^m}, m = 1, 2, 3,$ and 4. It can be seen that $||\hat{u}^n - \hat{U}^n||_{H^l}$ $(l = 0, 1)$ has a convergence rate of 1 with respect to time step size Δt. In the case of $l = 1$, the exact error $||u^n - U^n_{S^p_{\Delta_h}}||_{H^l}$ is not sensitive to the variation of time step size Δt, which means the spatial error is dominant for the given number of time steps. Moreover its magnitude is greater than $||\hat{u}^n - \hat{U}^n||_{H^l}$. However for $l = 0$, we can see that $||u^n - U^n_{S^p_{\Delta_h}}||_{H^l}$ is about the same as $||\hat{u}^n - \hat{U}^n||_{H^l}$ except the case of $p = 1$ and Mesh 1, which indicates that the temporal error in $||u^n - U^n_{S^p_{\Delta_h}}||_{H^l}$ is dominant for $l = 0$.

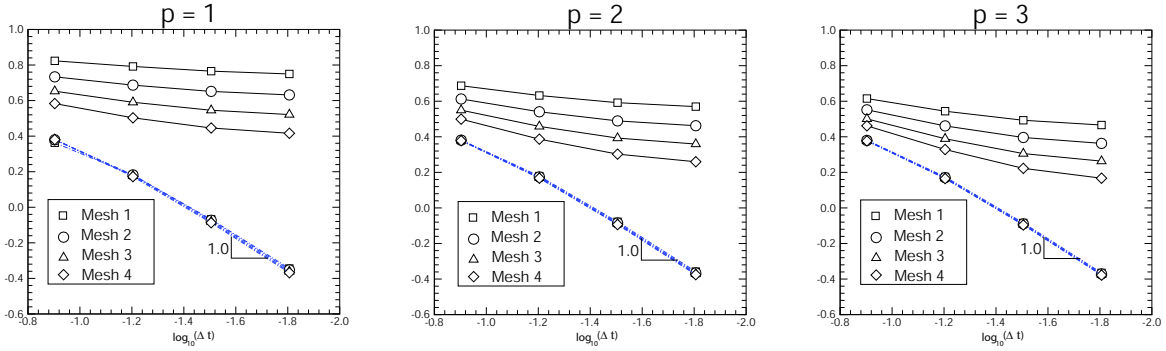

Fig. 5.9. L-shaped domain problem. The convergence of $||u^n - U^n_{S^p_{\Delta_h}}||_{H^1}$ and $||\hat{u}^n - \hat{U}^n||_{H^1}$ vs. time step size $\Delta t = \frac{T}{2^n}, n = 2, 3, 4,$ and 5, at time instant $t = \frac{T}{2}$ for the fully discrete finite element solutions of degree $p = 1, 2,$ and 3 computed with mesh size $h = \frac{L}{2^m}, m = 1, 2, 3,$ and 4.

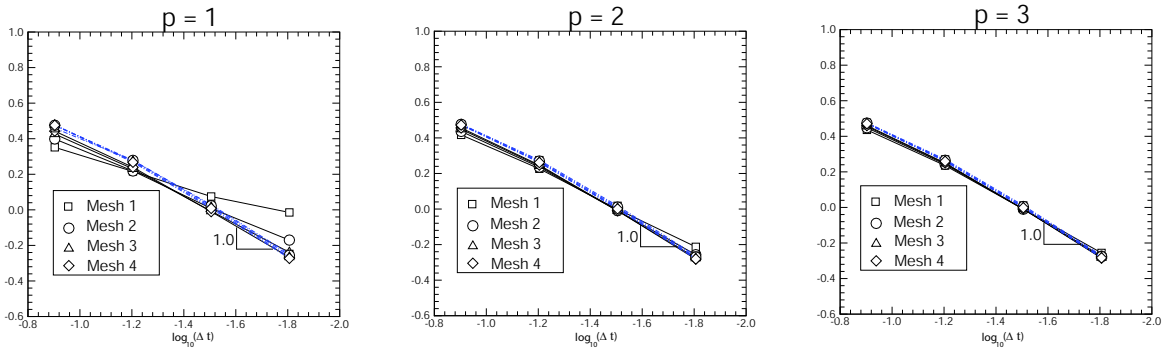

Fig. 5.10. L-shaped domain problem. The convergence of $||u^n - U^n_{S^p_{\Delta_h}}||_{H^0}$ and $||\hat{u}^n - \hat{U}^n||_{H^0}$ vs. time step size $\Delta t = \frac{T}{2^n}, n = 2, 3, 4,$ and 5, at time instant $t = \frac{T}{2}$ for the fully discrete finite element solutions of degree $p = 1, 2,$ and 3 computed with mesh size $h = \frac{L}{2^m}, m = 1, 2, 3,$ and 4.

Fig. 5.11 (resp. Fig. 5.12) is the convergence plot of $||u^n - U^n_{S^p_{\Delta_h}}||_{H^l}$ and $||\hat{u}^n - \hat{U}^n||_{H^l}$ $(l = 0, 1)$ with respect to mesh size h at time instant $t = \frac{T}{2}$ for the fully discrete finite element solutions of degree $p = 1, 2,$ and 3 for uniform meshes $h = \frac{L}{2^m}, m = 1, 2, 3,$ and 4. It can be seen that $||\hat{u}^n - \hat{U}^n||_{H^l}$ is temporal error dependent and is not sensitive to the mesh size, and with the increase of the number of time steps its magnitude is reduced. Since the spatial error is dominant for $l = 1$, we can see that $||u^n - U^n_{S^p_{\Delta_h}}||_{H^l}$ converges as the mesh is refined. Again in the case of $l = 0$ where the temporal error is dominant except the case of $p = 1$, Mesh 1 and $N = 32$, we can see that $||u^n - U^n_{S^p_{\Delta_h}}||_{H^l}$ is about the same as $||\hat{u}^n - \hat{U}^n||_{H^l}$.

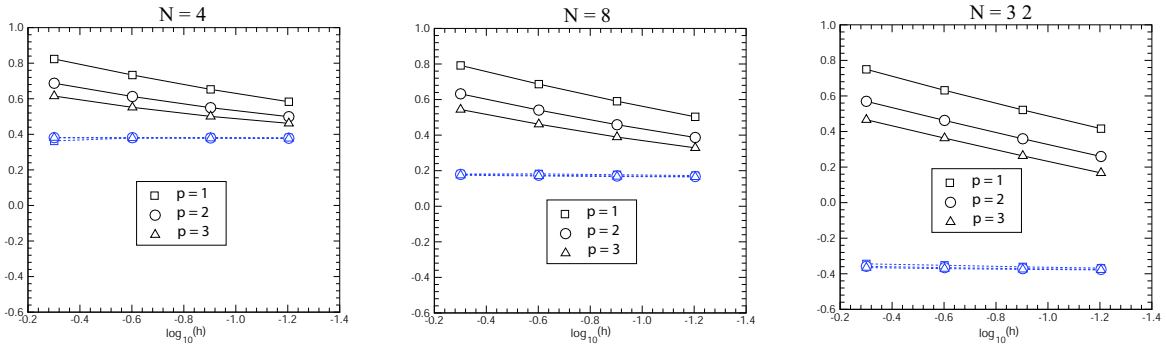

Fig. 5.11. L-shaped domain problem. The convergence of $||u^n - U^n_{S^p_{\Delta_h}}||_{H^1}$ and $||\hat{u}^n - \hat{U}^n||_{H^1}$ vs. mesh size $h = \frac{L}{2^m}, m = 1, 2, 3$, and 4, at time instant $t = \frac{T}{2}$ for the fully discrete finite element solutions of degree $p = 1, 2$, and 3 computed with time step size $\Delta t = \frac{T}{2^n}, n = 2, 3, 4$, and 5.

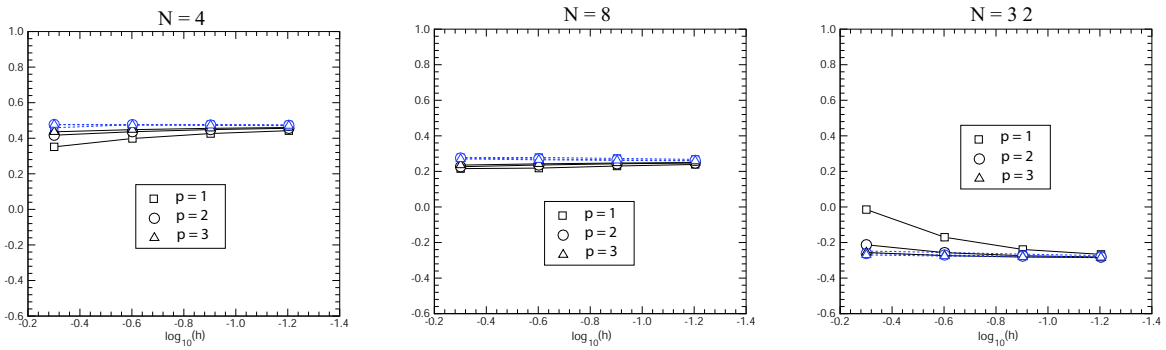

Fig. 5.12. L-shaped domain problem. The convergence of $||u^n - U^n_{S^p_{\Delta_h}}||_{H^0}$ and $||\hat{u}^n - \hat{U}^n||_{H^0}$ vs. mesh size $h = \frac{L}{2^m}, m = 1, 2, 3$, and 4, at time instant $t = \frac{T}{2}$ for the fully discrete finite element solutions of degree $p = 1, 2$, and 3 computed with time step size $\Delta t = \frac{T}{2^n}, n = 2, 3, 4$, and 5.

5.2 Upper bound in space-time norm for the exact error in fully discrete finite element solutions

Upper Bound in Space-Time Norm: The error E_h measured in $\mathscr{C}$-norm has the upper bound as follows

$$||E_h||_{\mathscr{C}} \leq \mathfrak{E}_{EX}^{\mathrm{FD}} \stackrel{\mathrm{def}}{=} \sqrt{\int_0^T (T-t)\big(||\hat{U} - \hat{U}_{S^p_{\Delta_h}}||^2_{\mathscr{U}} + ||\hat{U}_{S^p_{\Delta_h}} - U_{S^p_{\Delta_h}}||^2_{\mathscr{U}}\big)\, dt + T||\sqrt{\gamma}E_h(0)||^2_{L^2}} \tag{5.17}$$

where $E_h(0)$ denotes the exact error at time instant $t = 0$.

Proof: Substracting equation (5.5) from the equation (4.2), we have

$$(\gamma\frac{\partial}{\partial t}E_h, v)_{L^2(\Omega)} + \mathscr{B}_\Omega(u - \hat{U}, v) = 0 \qquad \forall v \in \mathscr{U}(\Omega), \qquad \forall t \in (0,T) \tag{5.18}$$

Let $v = E_h$, we have

$$\frac{1}{2}\frac{d}{dt}||\sqrt{\gamma}E_h||^2_{L^2} + \mathscr{B}_\Omega(u - \hat{U}, E_h) = 0 \qquad \forall t \in (0,T) \tag{5.19}$$

It can be shown that

$$\mathscr{B}_\Omega(u - \hat{U}, E_h) = ||u - \hat{U}||^2_{\mathscr{U}} - ||\hat{U} - U_{S^p_{\Delta_h}}||^2_{\mathscr{U}} + ||E_h||^2_{\mathscr{U}} - \mathscr{B}_\Omega(E_h, u - \hat{U}) \tag{5.20}$$

Then we obtain

$$\mathscr{B}_\Omega(u - \hat{U}, E_h) = \frac{1}{2}\big(||E_h||^2_{\mathscr{U}} + ||u - \hat{U}||^2_{\mathscr{U}} - ||\hat{U} - U_{S^p_{\Delta_h}}||^2_{\mathscr{U}}\big) \tag{5.21}$$

Therefore we have

$$\frac{d}{dt}||\sqrt{\gamma}E_h||^2_{L^2} + ||E_h||^2_{\mathscr{U}} + ||u - \hat{U}||^2_{\mathscr{U}} = ||\hat{U} - U_{S^p_{\Delta_h}}||^2_{\mathscr{U}} \tag{5.22}$$

Note that $\hat{U}_{S^p_{\Delta_h}}$ is the finite element approximation of (5.5) in $S^p_{\Delta_h}$ and we have the

following orthogonality

$$\mathcal{B}_\Omega(\hat{U} - \hat{U}_{S^p_{\Delta_h}}, \hat{U}_{S^p_{\Delta_h}} - U_{S^p_{\Delta_h}}) = 0 \tag{5.23}$$

Thus

$$||\hat{U} - U_{S^p_{\Delta_h}}||^2_{\mathcal{U}} = ||\hat{U} - \hat{U}_{S^p_{\Delta_h}}||^2_{\mathcal{U}} + ||\hat{U}_{S^p_{\Delta_h}} - U_{S^p_{\Delta_h}}||^2_{\mathcal{U}} \tag{5.24}$$

Take time integration $\int_0^T \int_0^\tau$ on both sides of (5.22) and employ Fubini's theorem, we have

$$\begin{aligned} &\int_0^T \big(||\sqrt{\gamma}E_h||^2_{L^2} + (T-t)||E_h||^2_{\mathcal{U}}\big)dt + \int_0^T (T-t)||u - \hat{U}||^2_{\mathcal{U}}\, dt \\ &= \int_0^T (T-t)\big(||\hat{U} - \hat{U}_{S^p_{\Delta_h}}||^2_{\mathcal{U}} + ||\hat{U}_{S^p_{\Delta_h}} - U_{S^p_{\Delta_h}}||^2_{\mathcal{U}}\big)\, dt + T||\sqrt{\gamma}E_h(0)||^2_{L^2} \end{aligned} \tag{5.25}$$

By dropping the term $||u - \hat{U}||^2_{\mathcal{U}}$, (5.25) immediately yields (5.17)

□

Remark 5.1. If $\int_0^T (T-t)||u-\hat{U}||^2_{\mathcal{U}}\, dt$ is negligible in comparison of $\int_0^T \big(||\sqrt{\gamma}E_h||^2_{L^2} + (T-t)||E_h||^2_{\mathcal{U}}\big)dt$, the upper bound $\mathfrak{E}_{EX}$ is sharp.

With the introduction of $\mathfrak{E}^{\text{FD}}_{EX}$, we can define effectivity index to measure the error E_h of the fully discrete finite element solution $U_{S^p_{\Delta_h}}$ as shown below

$$\kappa^{\text{FD}} \overset{\text{def}}{=} \frac{\mathfrak{E}^{\text{FD}}_{EX}}{||E_h||_{\mathcal{E}}} \tag{5.26}$$

In practice the exact solution $\hat{U}$ of elliptic reconstruction problem (5.5) is not computable and thus the upper bound $\mathfrak{E}^{\text{FD}}_{EX}$ is unknown. However $\hat{U}$ can be approximated by the nested refinement of the finite element mesh for $U_{S^p_{\Delta_h}}$ (h method) or the increase of polynomial order (p method), or both (hp method). We will refer to $\hat{U}_{S^{p+k}_{\Delta_{h'}}}$ as the approximation of the exact solution $\hat{U}$ where $p+k$ denotes the polynomial space of degree $p+k$ and the mesh $\Delta_{h'}$ is obtained from the uniform nested subdivision of

the mesh Δ_h employed to obtain the fully discrete finite element solution $U_{S^p_{\Delta_h}}$.

Thus we can define the following computable version of upper bound $\mathfrak{E}^{\mathrm{FD}}_{EX}$

$$\mathfrak{E}^{\mathrm{FD}}_{S^{p+k}_{\Delta_{h'}}} \stackrel{\mathrm{def}}{=} \sqrt{\int_0^T (T-t)\ ||\hat{U}_{S^{p+k}_{\Delta_{h'}}} - U_{S^p_{\Delta_h}}||^2_{\mathbb{U}}\ dt + T\ ||\sqrt{\gamma}E_h(0)||^2_{L^2}} \tag{5.27}$$

It should be noted that $\mathfrak{E}^{\mathrm{FD}}_{S^{p+k}_{\Delta_{h'}}}$ is not necessary a guaranteed upper bound.

Let us define the effectivity index of the $\mathfrak{E}^{\mathrm{FD}}_{S^{p+k}_{\Delta_{h'}}}$ as

$$\kappa^{\mathrm{FD}}_{S^{p+k}_{\Delta_{h'}}} \stackrel{\mathrm{def}}{=} \frac{\mathfrak{E}^{\mathrm{FD}}_{S^{p+k}_{\Delta_{h'}}}}{||E_h||_{\mathscr{E}}} \tag{5.28}$$

Let us split the error of fully discrete finite element solution E_h into two parts as follows

$$E_h = \rho_h + \theta_h \tag{5.29}$$

where ρ_h is the spatial error defined as

$$\rho_h \stackrel{\mathrm{def}}{=} u - u_{S^p_{\Delta_h}} \tag{5.30}$$

and θ_h is the temporal error defined as

$$\theta_h \stackrel{\mathrm{def}}{=} u_{S^p_{\Delta_h}} - U_{S^p_{\Delta_h}} \tag{5.31}$$

We define the ratio of the spatial error to the total error as

$$\alpha \stackrel{\mathrm{def}}{=} \frac{||\rho_h||_{\mathscr{E}}}{||E_h||_{\mathscr{E}}} \times 100\% \tag{5.32}$$

and the ratio of the temporal error to the total error as

$$\beta \stackrel{\mathrm{def}}{=} \frac{||\theta_h||_{\mathscr{E}}}{||E_h||_{\mathscr{E}}} \times 100\% \tag{5.33}$$

Upper Bound for Temporal Error in Space-Time Norm: The temporal error θ_h measured in space-time $\mathscr{C}$-norm has the following upper bound:

$$||\theta_h||_{\mathscr{C}} \leq \mathfrak{T}^{\mathrm{FD}}_{S^p_{\Delta_h}} \stackrel{\mathrm{def}}{=} \sqrt{\int_0^T (T-t)||\hat{U}_{S^p_{\Delta_h}} - U_{S^p_{\Delta_h}}||^2_{\mathscr{U}}\, dt} \tag{5.34}$$

Proof: Substracting equation (5.6) from the equation (4.4), we have

$$(\gamma \frac{\partial}{\partial t}\theta_h, v)_{L^2(\Omega)} + \mathscr{B}_\Omega(u_{S^p_{\Delta_h}} - \hat{U}_{S^p_{\Delta_h}}, v) = 0 \qquad \forall v \in S^p_{\Delta_h}, \qquad \forall t \in (0,T) \tag{5.35}$$

Let $v = \theta_h$, we have

$$\frac{1}{2}\frac{d}{dt}||\sqrt{\gamma}\theta_h||^2_{L^2} + \mathscr{B}_\Omega(u_{S^p_{\Delta_h}} - \hat{U}_{S^p_{\Delta_h}}, \theta_h) = 0 \qquad \forall t \in (0,T) \tag{5.36}$$

It can be shown that

$$2\mathscr{B}_\Omega(u_{S^p_{\Delta_h}} - \hat{U}_{S^p_{\Delta_h}}, \theta_h) = ||u_{S^p_{\Delta_h}} - \hat{U}_{S^p_{\Delta_h}}||^2_{\mathscr{U}} - ||\hat{U}_{S^p_{\Delta_h}} - U_{S^p_{\Delta_h}}||^2_{\mathscr{U}} + ||\theta_h||^2_{\mathscr{U}} \tag{5.37}$$

Therefore, we have

$$\frac{d}{dt}||\sqrt{\gamma}\theta_h||^2_{L^2} + ||\theta_h||^2_{\mathscr{U}} + ||u_{S^p_{\Delta_h}} - \hat{U}_{S^p_{\Delta_h}}||^2_{\mathscr{U}} = ||\hat{U}_{S^p_{\Delta_h}} - U_{S^p_{\Delta_h}}||^2_{\mathscr{U}} \tag{5.38}$$

Take time integration $\int_0^T \int_0^\tau$ on both sides of (5.38) and employ Fubini's theorem, we have

$$\begin{aligned}\int_0^T \left(||\sqrt{\gamma}\theta_h||^2_{L^2} + (T-t)||\theta_h||^2_{\mathscr{U}}\right)dt + \int_0^T (T-t)||u_{S^p_{\Delta_h}} - \hat{U}_{S^p_{\Delta_h}}||^2_{\mathscr{U}}\, dt \\ = \int_0^T (T-t)||\hat{U}_{S^p_{\Delta_h}} - U_{S^p_{\Delta_h}}||^2_{\mathscr{U}}\, dt\end{aligned} \tag{5.39}$$

Note that the temporal error at time instant $t = 0$ satisfies $\theta_h(0) = 0$.

By dropping the term $\int_0^T (T-t)||u_{S^p_{\Delta_h}} - \hat{U}_{S^p_{\Delta_h}}||^2_{\mathscr{U}}\, dt$, we have the upper bound

for the temporal error $||\theta_h||_{\mathscr{C}(\Omega)}$.

□

Remark 5.2. Note that $\mathfrak{T}^{\mathrm{FD}}_{S^p_{\Delta_h}} \leq \mathfrak{E}^{\mathrm{FD}}_{EX}$ since

$$\mathfrak{E}^{\mathrm{FD}}_{EX} = \sqrt{\int_0^T (T-t)||\hat{U} - \hat{U}_{S^p_{\Delta_h}}||^2_{\mathscr{U}} dt + \left(\mathfrak{T}^{\mathrm{FD}}_{S^p_{\Delta_h}}\right)^2 + T||\sqrt{\gamma}E_h(0)||^2_{L^2}} \tag{5.40}$$

according to (5.17) and (5.34). And the terms $||\hat{U} - \hat{U}_{S^p_{\Delta_h}}||_{\mathscr{U}}$ and $||\sqrt{\gamma}E_h(0)||^2_{L^2}$ have spatial error only.

Remark 5.3. It should be noted that unlike $\mathfrak{E}^{\mathrm{FD}}_{EX}$ which is not computable, here $\mathfrak{T}^{\mathrm{FD}}_{S^p_{\Delta_h}}$ is computable and unlike the computable version $\mathfrak{E}^{\mathrm{FD}}_{S^{p+k}_{\Delta_{h'}}}$ which might not be a guaranteed upper bound, $\mathfrak{T}^{\mathrm{FD}}_{S^p_{\Delta_h}}$ is a guaranteed upper bound for the temporal error.

Remark 5.4. Note that at each time integration point an elliptic problem of (5.6) has to be solved for $\hat{U}_{S^p_{\Delta_h}}$. However the global stiffness matrix of (5.6) only needs to be factorized once and saved on the hard disk for the whole time interval $(0, T]$, and the only computational cost is to form the right-hand-side load vector of (5.6).

At any time instant, the term $||u_{S^p_{\Delta_h}} - \hat{U}_{S^p_{\Delta_h}}||^2_{\mathscr{U}}$ is bounded as follows

$$||u_{S^p_{\Delta_h}} - \hat{U}_{S^p_{\Delta_h}}||_{\mathscr{U}} \leq ||\hat{u} - \hat{U}||_{\mathscr{U}} \tag{5.41}$$

Proof: Since $u_{S^p_{\Delta_h}} - \hat{U}_{S^p_{\Delta_h}} \in S^p_{\Delta_h}$, for semi-discrete finite element solution $u_{S^p_{\Delta_h}}$, we have the orthogonality condition

$$\mathscr{B}_\Omega(\hat{u} - u_{S^p_{\Delta_h}}, u_{S^p_{\Delta_h}} - \hat{U}_{S^p_{\Delta_h}}) = 0 \tag{5.42}$$

while for fully discrete finite element solution $\hat{U}_{S^p_{\Delta_h}}$, the orthogonality condition is

$$\mathscr{B}_\Omega(\hat{U} - \hat{U}_{S^p_{\Delta_h}}, u_{S^p_{\Delta_h}} - \hat{U}_{S^p_{\Delta_h}}) = 0 \tag{5.43}$$

Subtract (5.43) from (5.42), we have

$$\mathcal{B}_{\Omega}(\hat{u}-\hat{U}, u_{S^p_{\Delta_h}}-\hat{U}_{S^p_{\Delta_h}}) = ||u_{S^p_{\Delta_h}}-\hat{U}_{S^p_{\Delta_h}}||^2_{\mathcal{U}} \tag{5.44}$$

Given the fact

$$\mathcal{B}_{\Omega}(\hat{u}-\hat{U}, u_{S^p_{\Delta_h}}-\hat{U}_{S^p_{\Delta_h}}) \leq ||\hat{u}-\hat{U}||_{\mathcal{U}}\ ||u_{S^p_{\Delta_h}}-\hat{U}_{S^p_{\Delta_h}}||_{\mathcal{U}} \tag{5.45}$$

we can see (5.41) holds.

□

We can define effectivity index to measure the temporal error θ_h as follows

$$\zeta^{\mathrm{FD}}_{S^p_{\Delta_h}} \stackrel{\mathrm{def}}{=} \frac{\mathfrak{T}^{\mathrm{FD}}_{S^p_{\Delta_h}}}{||\theta_h||_{\mathscr{C}(\Omega)}} \tag{5.46}$$

Note that $\mathfrak{T}^{\mathrm{FD}}_{S^p_{\Delta_h}}$ is guaranteed computable upper bound for the temporal error.

It can be seen that for total error $||E_h||_{\mathscr{C}}$ we have the estimate $\mathfrak{E}^{\mathrm{FD}}_{EX}$ while for temporal error the estimate is $\mathfrak{T}^{\mathrm{FD}}_{S^p_{\Delta_h}}$. Therefore we have the following estimate for the exact temporal error ratio β

$$\beta^{\mathrm{FD}} \stackrel{\mathrm{def}}{=} \frac{\mathfrak{T}^{\mathrm{FD}}_{S^p_{\Delta_h}}}{\mathfrak{E}^{\mathrm{FD}}_{EX}} \times 100\% \tag{5.47}$$

If we employ the computable version of $\mathfrak{E}^{\mathrm{FD}}_{EX}$, we have

$$\beta^{\mathrm{FD}}_{S^{p+k}_{\Delta_{h'}}} \stackrel{\mathrm{def}}{=} \frac{\mathfrak{T}^{\mathrm{FD}}_{S^p_{\Delta_h}}}{\mathfrak{E}^{\mathrm{FD}}_{S^{p+k}_{\Delta_{h'}}}} \times 100\% \tag{5.48}$$

Remark 5.5. If temporal error $||\theta_h||_{\mathscr{C}}$ is dominant in the total error $||E_h||_{\mathscr{C}}$, namely, $||\theta_h||_{\mathscr{C}} \approx ||E_h||_{\mathscr{C}}$, we have according to (5.40)

$$\mathfrak{E}^{\mathrm{FD}}_{EX} \approx \mathfrak{T}^{\mathrm{FD}}_{S^p_{\Delta_h}} \tag{5.49}$$

and hence

$$\kappa^{\mathrm{FD}} \approx \zeta^{\mathrm{FD}}_{S^p_{\Delta_h}} \tag{5.50}$$

Let us illustrate the upper bounds with some examples.

Example 5.4. *Heat transition problem in one dimension.* Fig. 5.13 is the relative error

$$\varepsilon \stackrel{\mathrm{def}}{=} \frac{||E_h||_{\mathscr{C}}}{||u||_{\mathscr{C}}} \times 100\% \tag{5.51}$$

while Fig. 5.14 illustrates the ratio of spatial error to the total error α and the ratio of the temporal error to the total error β, for the fully discrete finite element solution $U_{S^p_{\Delta_h}}$.

It can be seen that with the increase in mesh refinement level, polynomial order p, the number of time steps, the relative error ε goes down. In the case of $p = 3$, the mesh refinement has no effect on the relative error which indicates that the temporal error is dominant as shown in Fig. 5.14 for $p = 3$. For linear element $p = 1$, we can see from Fig. 5.14 that with the increase of time steps, the spatial error becomes dominant. As a matter of fact, for coarse mesh, Mesh 1, the spatial error is dominant for all four types of time step size. In case of cubic element $p = 3$, the spatial error is killed and temporal error is dominant.

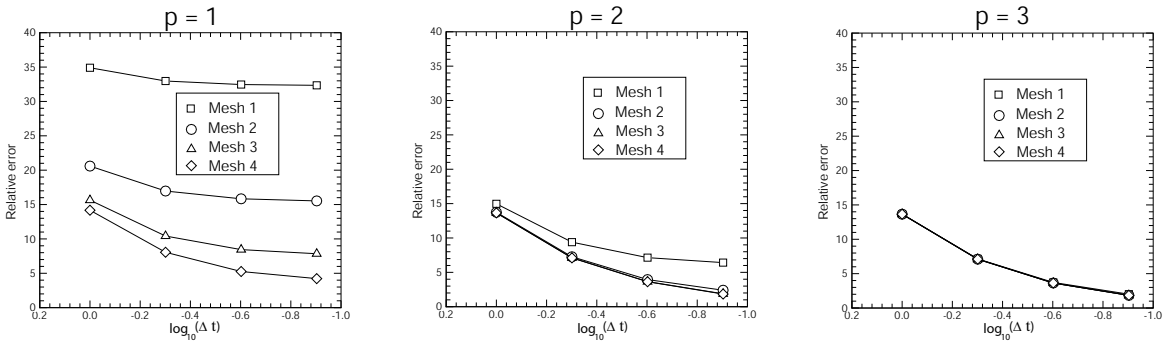

Fig. 5.13. Heat transition problem in one dimension. The relative error ε for the fully discrete finite element solutions of degree $p = 1, 2$, and 3 computed with four different mesh sizes and four different time step sizes.

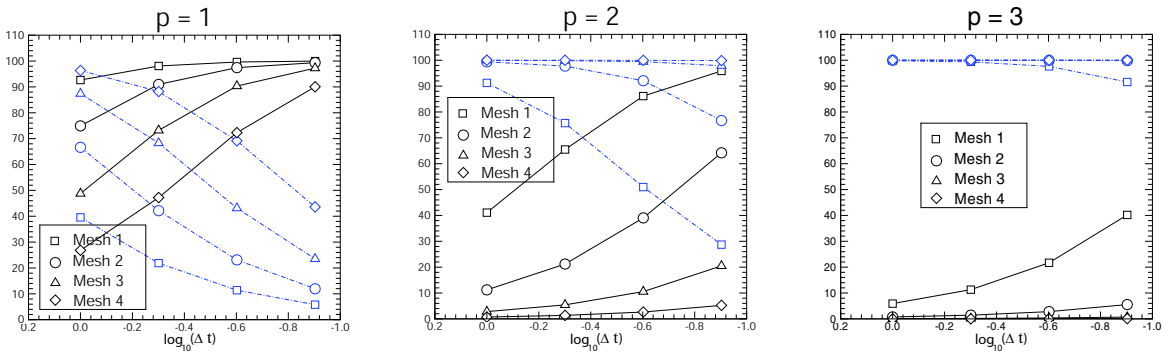

Fig. 5.14. Heat transition problem in one dimension. The ratio of temporal error β (dash-dot line) and the ratio of spatial error α (solid line) for the fully discrete finite element solutions of degree $p = 1, 2$, and 3 computed with four different mesh sizes and four different time step sizes.

Fig. 5.15 is the illustration of the effectivity index κ^{FD} for the total error $||E_h||_{\mathscr{C}}$ and the effectivity index $\zeta^{\mathrm{FD}}_{S^p_{\Delta_h}}$ for the temporal error $||\theta_h||_{\mathscr{C}}$ for the fully discrete finite element solutions $U_{S^p_{\Delta_h}}$ of degree $p = 1, 2$, and 3. It can be seen that as the spatial error is killed, the effectivity index κ^{FD} converges to the effectivity index $\zeta^{\mathrm{FD}}_{S^p_{\Delta_h}}$ for the temporal error around the value of 1.65 as shown in the case of $p = 3$. Based on Fig. 5.14, we can also see that κ^{FD} is close to 1 as long as the spatial error is dominant.

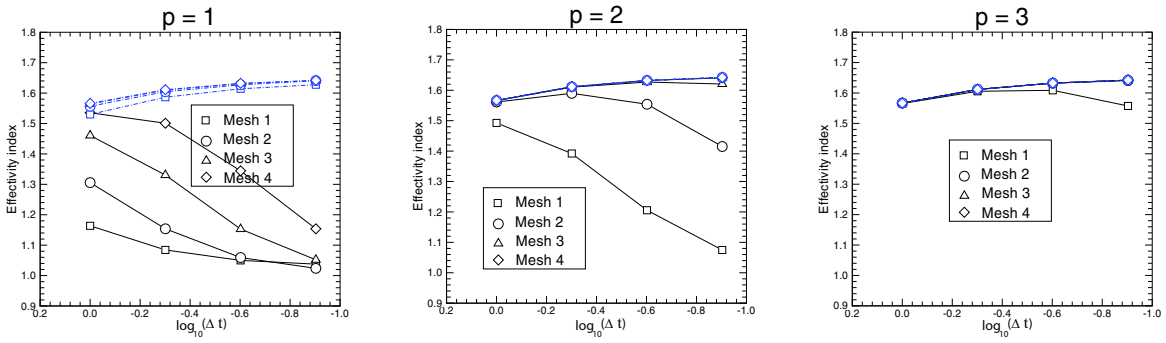

Fig. 5.15. Heat transition problem in one dimension. The effectivity index κ^{FD} (solid line) for the total error $||E_h||_{\mathscr{C}}$ and the effectivity index $\zeta^{\mathrm{FD}}_{S^p_{\Delta_h}}$ (dash-dot line) for the temporal error $||\theta_h||_{\mathscr{C}}$ for the fully discrete finite element solutions of degree $p = 1, 2$, and 3 computed with four different mesh sizes and four different time step sizes.

Fig. 5.16 is the illustration of the effectivity index $\kappa^{\mathrm{FD}}_{S^{p+k}_{\Delta_{h'}}}$ based on $\hat{U}_{S^{p+k}_{\Delta_{h'}}}$ which is the finite element approximation of the exact solution $\hat{U}$ of degree $p + k$, $k = 1, 2$, and 3, computed with mesh $\Delta_{h'}$ obtained from the uniform nested subdivision of the mesh Δ_h employed to obtain the fully discrete finite element solution $U_{S^p_{\Delta_h}}$. Here for simplicity, we fix the mesh, i.e., $\Delta_{h'} = \Delta_h$, and only increase the polynomial order from p to $p + k$ with $k = 1, 2$, and 3 respectively. It can be seen that $\kappa^{\mathrm{FD}}_{S^{p+k}_{\Delta_{h'}}}$ has the performance similar to its exact version κ^{FD} and it converges to κ^{FD} even for $k = 1$.

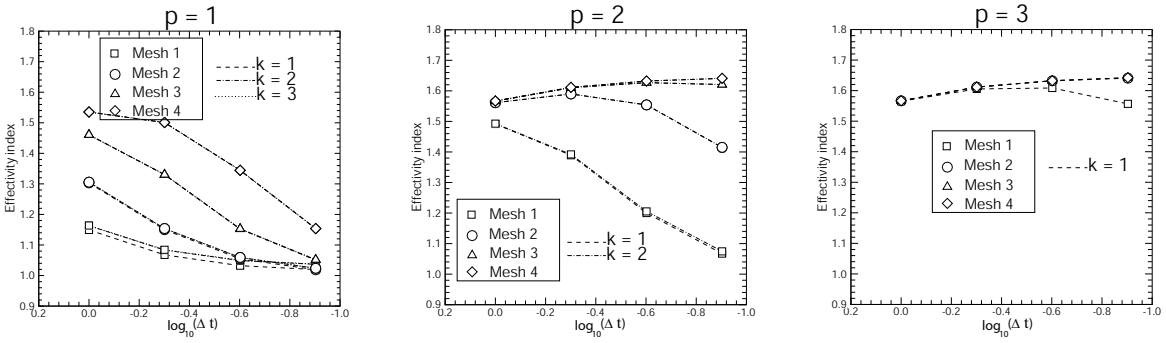

Fig. 5.16. Heat transition problem in one dimension. The effectivity index $\kappa^{\mathrm{FD}}_{S^{p+k}_{\Delta_{h'}}}$ for the total error $||E_h||_{\mathscr{C}}$ for the fully discrete finite element solutions of degree $p = 1, 2$, and 3 computed with four different mesh sizes and four different time step sizes.

Fig. 5.17 is the illustration of the exact temporal error ratio β and its estimate β^{FD}. In the case of linear element $p = 1$ whose spatial error is significant, we can see that β^{FD} is good approximation of β. Again we can see that as the temporal error becomes dominant, β^{FD} converges to β such as the case of $p = 3$. We can also observe that β is bounded by β^{FD} for this example. Note that β^{FD} is not computable since it employs the exact solution $\hat{U}$ of the elliptic reconstruction problem.

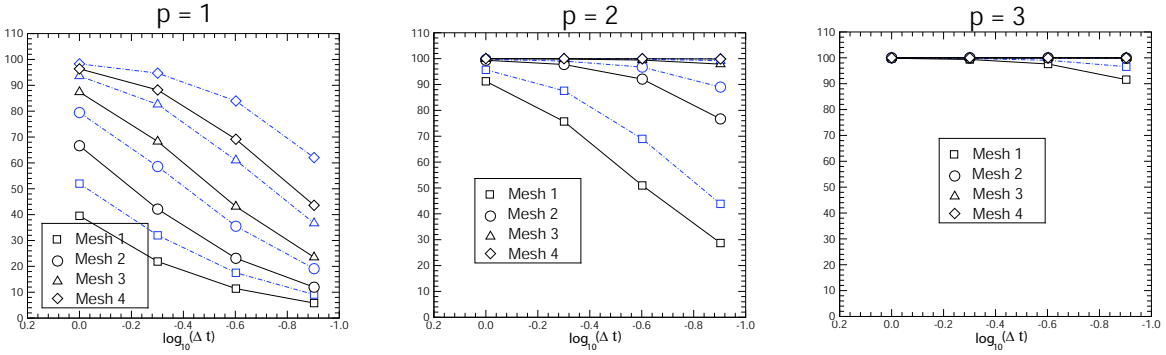

Fig. 5.17. Heat transition problem in one dimension. The exact temporal error ratio β (solid line) and the estimated temporal error ratio β^{FD} (dash-dot line) for the fully discrete finite element solutions of degree $p = 1, 2$, and 3 computed with four different mesh sizes and four different time step sizes.

Fig. 5.18 is the comparison of the exact temporal error ratio β and its approximation $\beta^{\mathrm{FD}}_{S^{p+k}_{\Delta_{h'}}}$. It can be seen that $\beta^{\mathrm{FD}}_{S^{p+k}_{\Delta_{h'}}}$ converges to its exact version β^{FD} as shown in Fig. 5.17 even with $k = 1$. Note that $\beta^{\mathrm{FD}}_{S^{p+k}_{\Delta_{h'}}}$ is computable since it is based on $\hat{U}_{S^{p+k}_{\Delta_{h'}}}$.

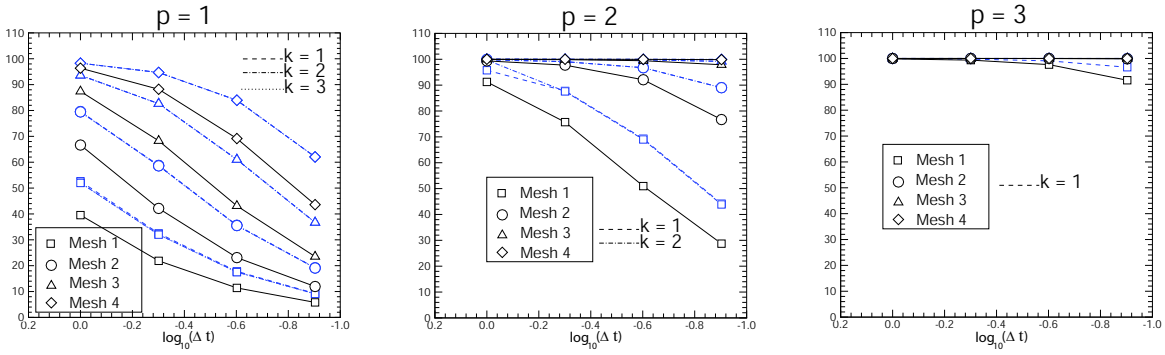

Fig. 5.18. Heat transition problem in one dimension. The exact temporal error ratio β (solid line) and the estimated temporal error ratio $\beta^{\mathrm{FD}}_{S^{p+k}_{\Delta_{h'}}}$ (dash-dot line) for the fully discrete finite element solutions of degree $p = 1, 2$, and 3 computed with four different mesh sizes and four different time step sizes.

Example 5.5. *Two dimensional synthetic problem.* Fig. 5.19 is the relative error ε for the fully discrete finite element solution $U_{S^p_{\Delta_h}}$. It can be seen that the relative error is not sensitive to the time step size which means that the spatial error is dominant as seen in Fig. 5.20 which illustrates the ratio of spatial error to the total error α and the ratio of the temporal error to the total error β. Note that for coarse mesh, such as Mesh 1, the relative error can be close to 100% for element of degree $p = 1$ and 2.

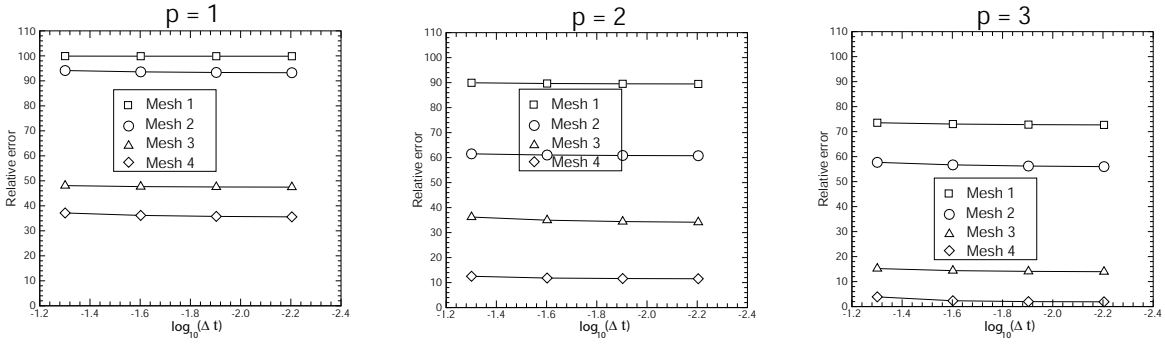

Fig. 5.19. Two dimensional synthetic problem. The relative error ε for the fully discrete finite element solutions of degree $p = 1, 2$, and 3 computed with four different mesh sizes and four different time step sizes.

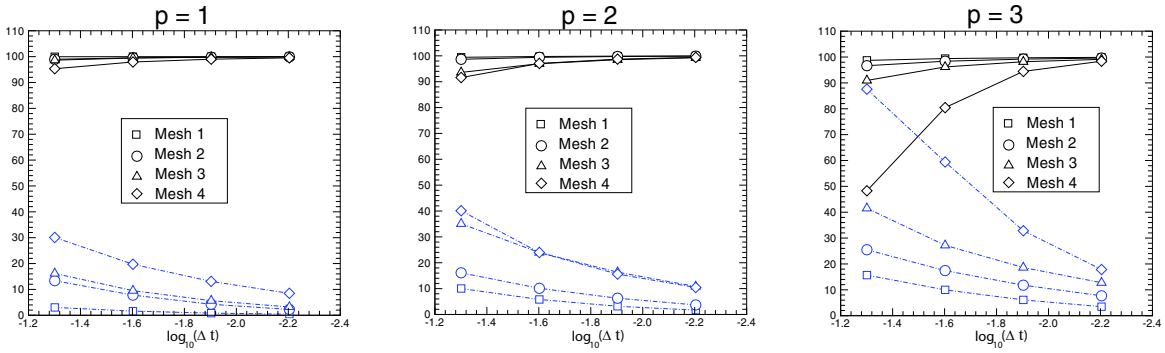

Fig. 5.20. Two dimensional synthetic problem. The ratio of temporal error β (dash-dot line) and the ratio of spatial error α (solid line) for the fully discrete finite element solutions of degree $p = 1, 2$, and 3 computed with four different mesh sizes and four different time step sizes.

Fig. 5.21 is the illustration of the effectivity index κ^{FD} for the total error $||E_h||_{\mathscr{C}}$ and the effectivity index $\zeta^{\mathrm{FD}}_{S^p_{\Delta_h}}$ for the temporal error $||\theta_h||_{\mathscr{C}}$ for the fully discrete finite element solutions $U_{S^p_{\Delta_h}}$. It can be seen that κ^{FD} is close to 1 and not sensitive to the time step size due to the fact that spatial error is dominant. The maximum effectivity index $\zeta^{\mathrm{FD}}_{S^p_{\Delta_h}}$ for the temporal error $||\theta_h||_{\mathscr{C}}$ is less than 1.6 which happens to Mesh 1 and linear element $p = 1$.

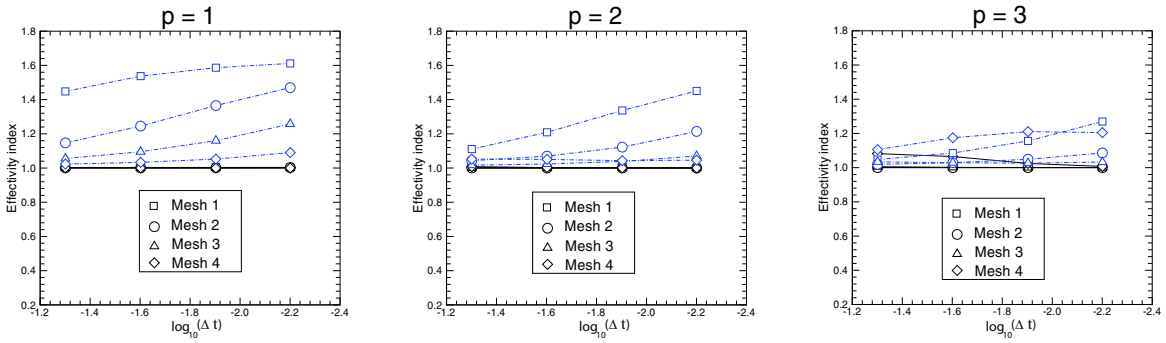

Fig. 5.21. Two dimensional synthetic problem. The effectivity index κ^{FD} (solid line) for the total error $||E_h||_{\mathscr{C}(\Omega)}$ and the effectivity index $\zeta^{\mathrm{FD}}_{S^p_{\Delta_h}}$ (dash-dot line) for the temporal error $||\theta_h||_{\mathscr{C}(\Omega)}$ for the fully discrete finite element solutions of degree $p = 1, 2$, and 3 computed with four different mesh sizes and four different time step sizes.

Fig. 5.22 is the illustration of the effectivity index $\kappa^{\mathrm{FD}}_{S^{p+k}_{\Delta_{h'}}}$ based on $\hat{U}_{S^{p+k}_{\Delta_{h'}}}$ which is the finite element approximation of the exact solution $\hat{U}$ of degree $p+k$, computed with the mesh $\Delta_{h'}$ obtained from the uniform nested subdivision of the mesh Δ_h employed to obtain the fully discrete finite element solution $U_{S^p_{\Delta_h}}$. Here for simplicity, we fix the mesh, i.e., $\Delta_{h'} = \Delta_h$, and only increase the polynomial order from degree p to degree $p + k$ with $k = 1, 2$, and 3 respectively. It can be seen that $\kappa^{\mathrm{FD}}_{S^{p+k}_{\Delta_{h'}}}$ converges to its exact version κ^{FD} with the increase of element order $p + k$. For $k = 1$, the effectivity index $\kappa^{\mathrm{FD}}_{S^{p+k}_{\Delta_{h'}}}$ can be as small as 0.4. However, with the increase of k, the effectivity index is significantly improved.

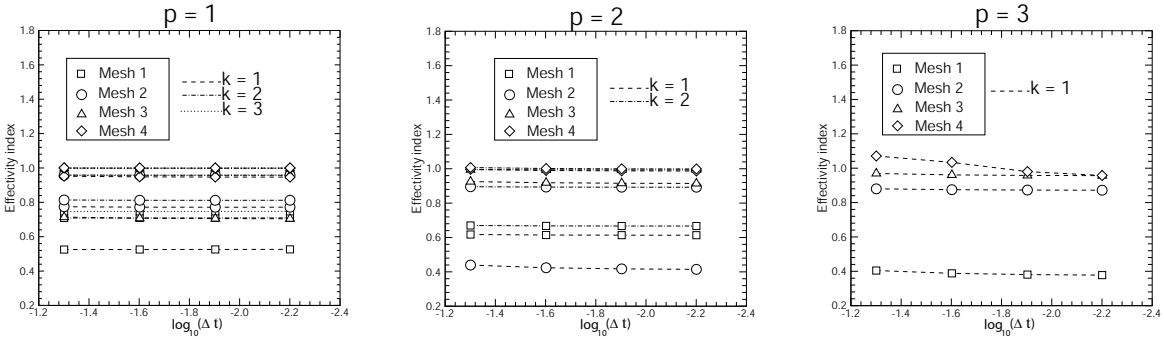

Fig. 5.22. Two dimensional synthetic problem. The effectivity index $\kappa^{\mathrm{FD}}_{S^{p+k}_{\Delta_{h'}}}$ for the total error $||E_h||_{\mathscr{C}}$ for the fully discrete finite element solutions of degree $p = 1, 2$, and 3 computed with four different mesh sizes and four different time step sizes.

Fig. 5.23 is the illustration of the exact temporal error ratio β and its estimate β^{FD}. It can be seen that β^{FD} is a very good approximation of β. Again β^{FD} is not computable since it employs the exact solution $\hat{U}$ of the elliptic reconstruction problem.

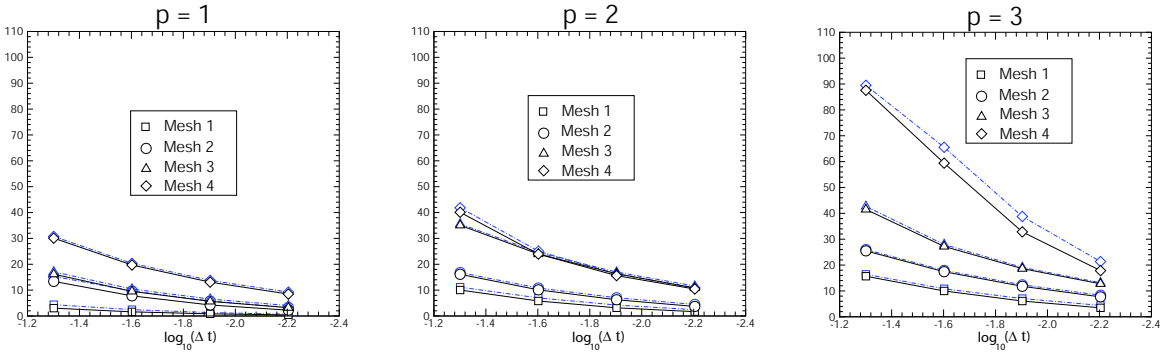

Fig. 5.23. Two dimensional synthetic problem. The exact temporal error ratio β (solid line) and the estimated temporal error ratio β^{FD} (dash-dot line) for the fully discrete finite element solutions of degree $p = 1, 2$, and 3 computed with four different mesh sizes and four different time step sizes.

Fig. 5.24 is the comparison of the exact temporal error ratio β and its approximation $\beta^{\mathrm{FD}}_{S^{p+k}_{\Delta_{h'}}}$. It can be seen that $\beta^{\mathrm{FD}}_{S^{p+k}_{\Delta_{h'}}}$ converges to its exact version β^{FD} as shown

in Fig. 5.23 with the increase of k. Moreover, $\beta^{\mathrm{FD}}_{S^{p+k}_{\Delta_{h'}}}$ is a good approximation of β. Note that β is bounded by $\beta^{\mathrm{FD}}_{S^{p+k}_{\Delta_{h'}}}$ and $\beta^{\mathrm{FD}}_{S^{p+k}_{\Delta_{h'}}}$ is computable since it is based on $\hat{U}_{S^{p+k}_{\Delta_{h'}}}$.

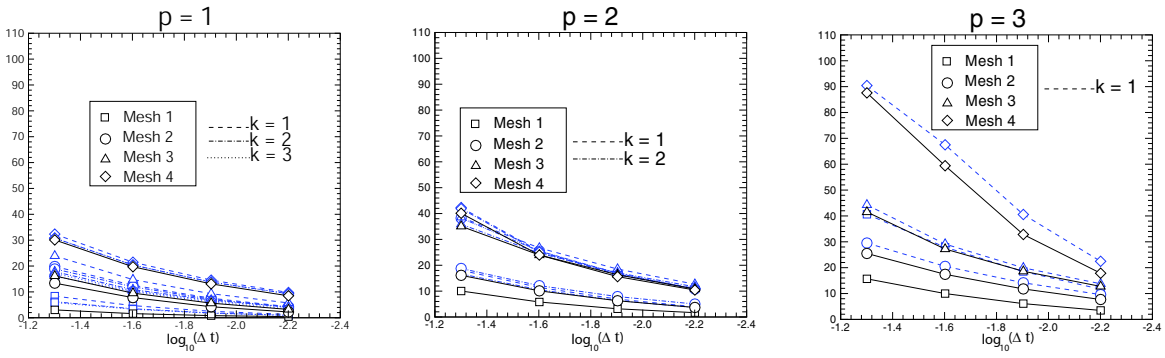

Fig. 5.24. Two dimensional synthetic problem. The exact temporal error ratio β (solid line) and the estimated temporal error ratio $\beta^{\mathrm{FD}}_{S^{p+k}_{\Delta_{h'}}}$ (dash-dot line) for the fully discrete finite element solutions of degree $p = 1, 2$, and 3 computed with four different mesh sizes and four different time step sizes.

Example 5.6. *L-shaped domain problem.* Fig. 5.25 is the relative error ε for the fully discrete finite element solution $U_{S^p_{\Delta_h}}$. It can be seen that the relative error is about 100% when the number of time steps N is equal to 4 and with the increase in time steps the relative error decreases dramatically. The relative error is not sensitive to the polynomial order p and the mesh refinement which indicates that the temporal error is dominant. Fig. 5.20 illustrates the ratio of spatial error to the total error α and the ratio of the temporal error to the total error β. It can be seen that the temporal error is dominant for all the cases except the case where $N = 4$, $p = 1$ and Mesh 1 are employed. where the spatial error becomes dominant.

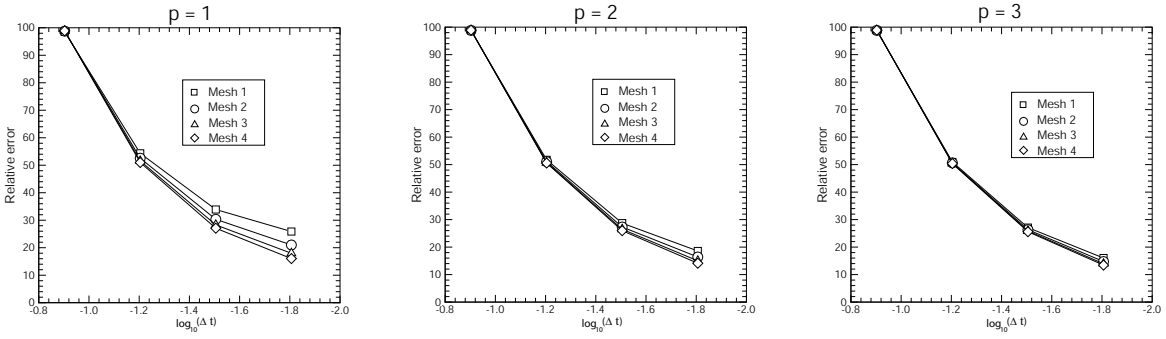

Fig. 5.25. L-shaped domain problem. The relative error ε for the fully discrete finite element solutions of degree $p = 1, 2$, and 3 computed with four different mesh sizes and four different time step sizes.

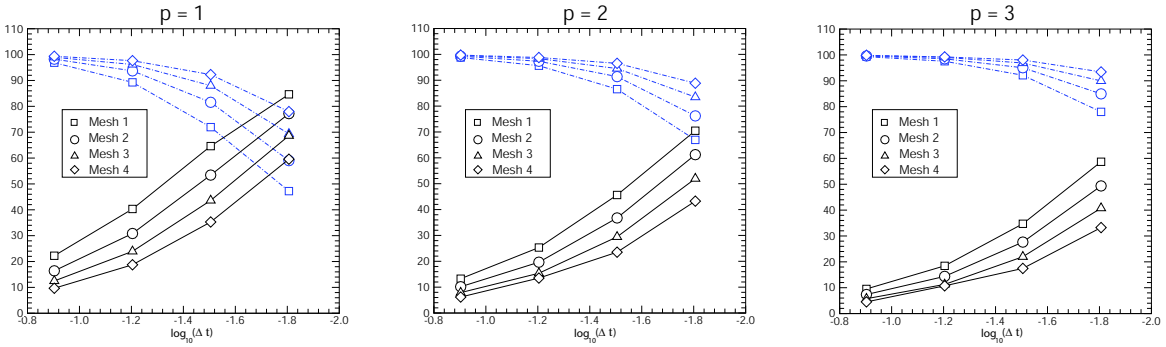

Fig. 5.26. L-shaped domain problem. The ratio of temporal error β (dash-dot line) and the ratio of spatial error α (solid line) for the fully discrete finite element solutions of degree $p = 1, 2$, and 3 computed with four different mesh sizes and four different time step sizes.

Fig. 5.27 is the illustration of the effectivity index κ^{FD} for the total error $||E_h||_{\mathscr{C}}$ and the effectivity index $\zeta^{\mathrm{FD}}_{S^p_{\Delta_h}}$ for the temporal error $||\theta_h||_{\mathscr{C}}$ for the fully discrete finite element solutions $U_{S^p_{\Delta_h}}$. It can be seen that the best number of κ^{FD} is close to 2.4 which happens to the case $N = 32$, $p = 1$ and Mesh 1. In the case that the temporal error is dominant such as $p = 3$ as shown in Fig. 5.20, the effectivity index $\zeta^{\mathrm{FD}}_{S^p_{\Delta_h}}$ for the temporal error $||\theta_h||_{\mathscr{C}}$ is close to κ^{FD}

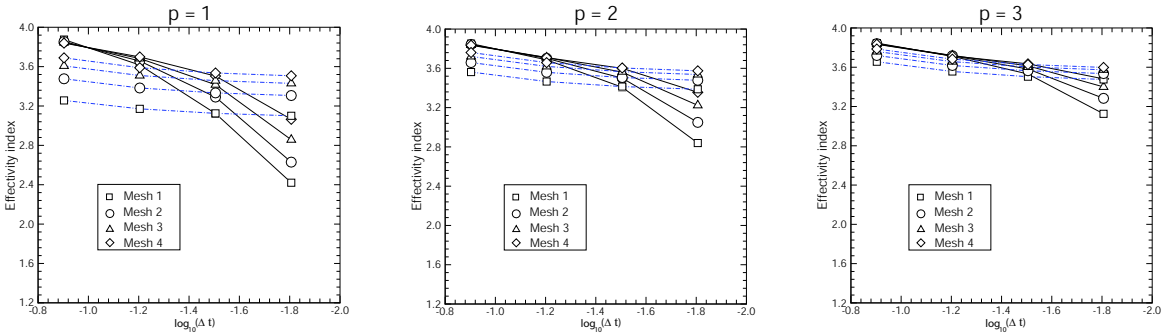

Fig. 5.27. L-shaped domain problem. The effectivity index κ^{FD} (solid line) for the total error $||E_h||_{\mathscr{C}(\Omega)}$ and the effectivity index $\zeta^{\mathrm{FD}}_{S^p_{\Delta_h}}$ (dash-dot line) for the temporal error $||\theta_h||_{\mathscr{C}(\Omega)}$ for the fully discrete finite element solutions of degree $p = 1, 2$, and 3 computed with four different mesh sizes and four different time step sizes.

Fig. 5.28 is the illustration of the effectivity index $\kappa^{\mathrm{FD}}_{S^{p+k}_{\Delta_{h'}}}$ based on $\hat{U}_{S^{p+k}_{\Delta_{h'}}}$ which is the finite element approximation of the exact solution $\hat{U}$ of degree $p+k$, computed with the mesh $\Delta_{h'}$ obtained from the uniform nested subdivision of the mesh Δ_h employed to obtain the fully discrete finite element solution $U_{S^p_{\Delta_h}}$. Here for simplicity, we fix the mesh, i.e., $\Delta_{h'} = \Delta_h$, and only increase the polynomial order from degree p to degree $p + k$ with $k = 1, 2$, and 3 respectively. It can be seen that $\kappa^{\mathrm{FD}}_{S^{p+k}_{\Delta_{h'}}}$ converges to its exact version κ^{FD} with the increase of element order $p + k$.

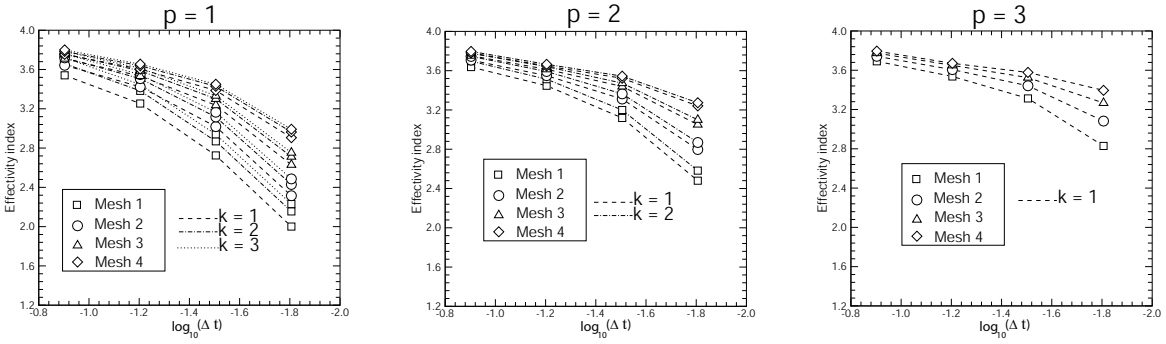

Fig. 5.28. L-shaped domain problem. The effectivity index $\kappa^{\mathrm{FD}}_{S^{p+k}_{\Delta_{h'}}}$ for the total error $||E_h||_{\mathscr{C}}$ for the fully discrete finite element solutions of degree $p = 1, 2$, and 3 computed with four different mesh sizes and four different time step sizes.

Fig. 5.29 is the illustration of the exact temporal error ratio β and its estimate β^{FD}. It can be seen that β^{FD} is a very good approximation of β. Again β^{FD} is not computable since it employs the exact solution $\hat{U}$ of the elliptic reconstruction problem.

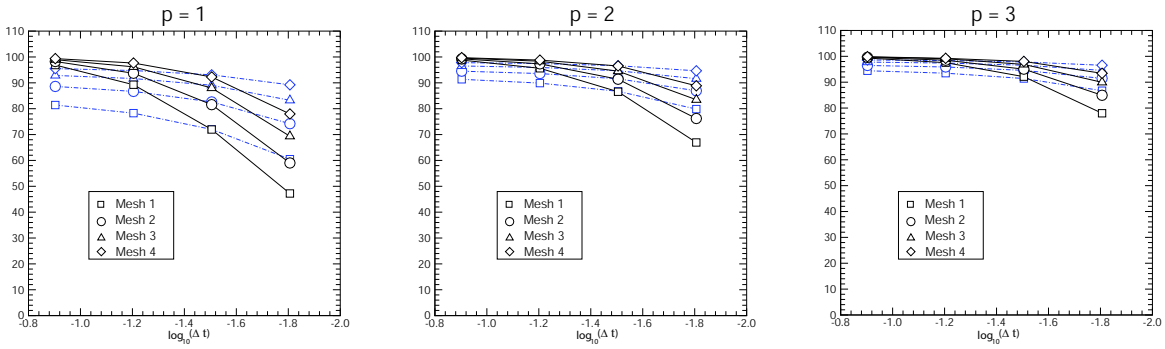

Fig. 5.29. L-shaped domain problem. The exact temporal error ratio β (solid line) and the estimated temporal error ratio β^{FD} (dash-dot line) for the fully discrete finite element solutions of degree $p = 1, 2$, and 3 computed with four different mesh sizes and four different time step sizes.

Fig. 5.30 is the comparison of the exact temporal error ratio β and its approximation $\beta^{\mathrm{FD}}_{S^{p+k}_{\Delta_{h'}}}$. It can be seen that $\beta^{\mathrm{FD}}_{S^{p+k}_{\Delta_{h'}}}$ converges to its exact version β^{FD} as shown in Fig. 5.23 with the increase of k. Moreover, $\beta^{\mathrm{FD}}_{S^{p+k}_{\Delta_{h'}}}$ is a good approximation of β. Note that β is bounded by $\beta^{\mathrm{FD}}_{S^{p+k}_{\Delta_{h'}}}$ and $\beta^{\mathrm{FD}}_{S^{p+k}_{\Delta_{h'}}}$ is computable since it is based on $\hat{U}_{S^{p+k}_{\Delta_{h'}}}$.

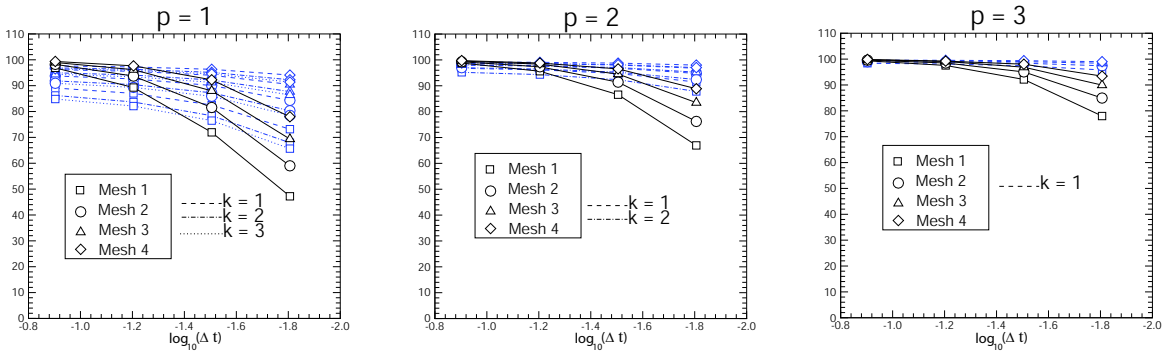

Fig. 5.30. L-shaped domain problem. The exact temporal error ratio β (solid line) and the estimated temporal error ratio $\beta^{\mathrm{FD}}_{S^{p+k}_{\Delta_{h'}}}$ (dash-dot line) for the fully discrete finite element solutions of degree $p = 1, 2$, and 3 computed with four different mesh sizes and four different time step sizes.

Example 5.7. *Transient diffusion problem in a thermal battery.* Fig. 5.31 (resp. 5.32) is the relative error for isotropic case (resp. orthotropic case) where the exact solution u is approximated by the overkill solution $u_{S^{p'}_{\Delta^{ovk}_h}}$ computed with $p' = 8$ and overkill mesh as shown in Fig. 2.2. It can be seen that for both cases the relative error becomes smaller with the increase of the number of time steps.

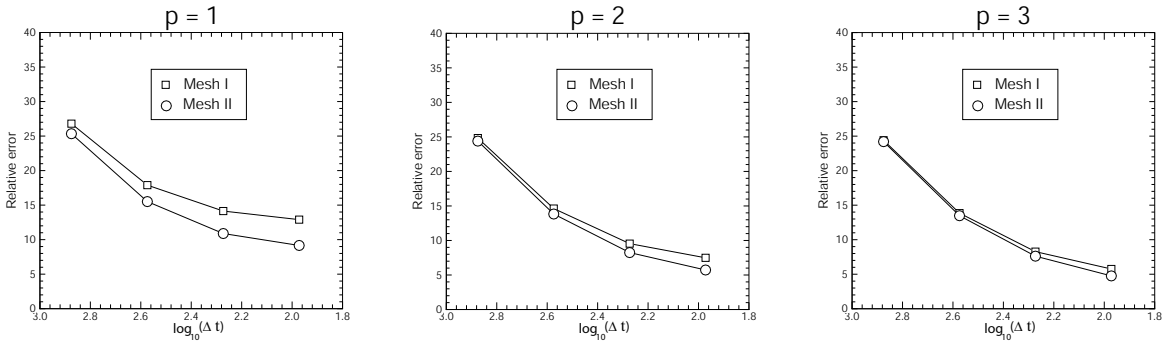

Fig. 5.31. Transient diffusion problem in a thermal battery. The relative error ε for the fully discrete finite element solutions of degree $p = 1, 2$, and 3 computed with Mesh I and II and four different time step sizes in the isotropic case.

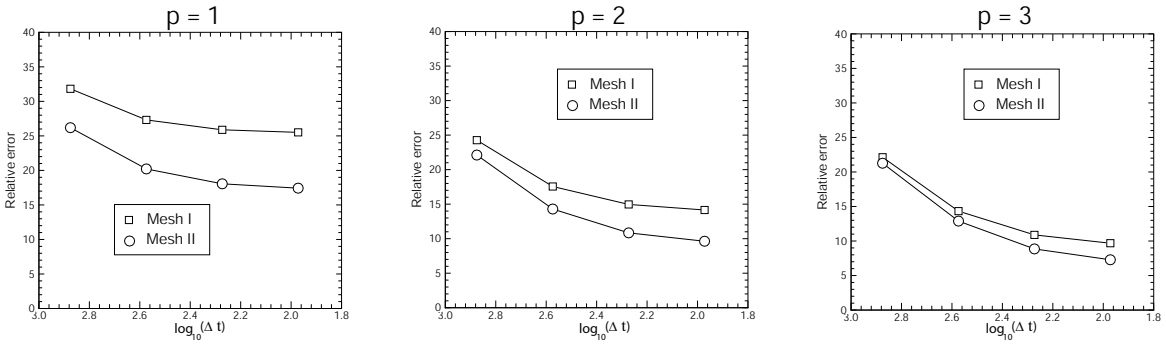

Fig. 5.32. Transient diffusion problem in a thermal battery. The relative error ε for the fully discrete finite element solutions of degree $p = 1, 2$, and 3 computed with Mesh I and II and four different time step sizes in the orthotropic case.

Fig. 5.33 (resp. 5.34) illustrates the ratio of spatial error to the total error α and the ratio of the temporal error to the total error β for the fully discrete finite element solution $U_{S^p_{\Delta_h}}$ in the isotropic case (resp. orthotropic case). For isotropic case, it can be seen that the temporal error is dominant for large step size, e.g., $\Delta t = \frac{T}{2^2}$ and $\frac{T}{2^3}$. With the smaller time step size, the spatial error becomes dominant. For orthotropic case, in the case of linear element $p = 1$, the spatial error is dominant for all the four different time step sizes. In the case of $p = 2$ and 3, the temporal error is dominant for large time step size, e.g., $\Delta t = \frac{T}{2^2}$, and the spatial error becomes dominant once smaller time size is chosen, e.g., $\Delta t = \frac{T}{2^5}$.

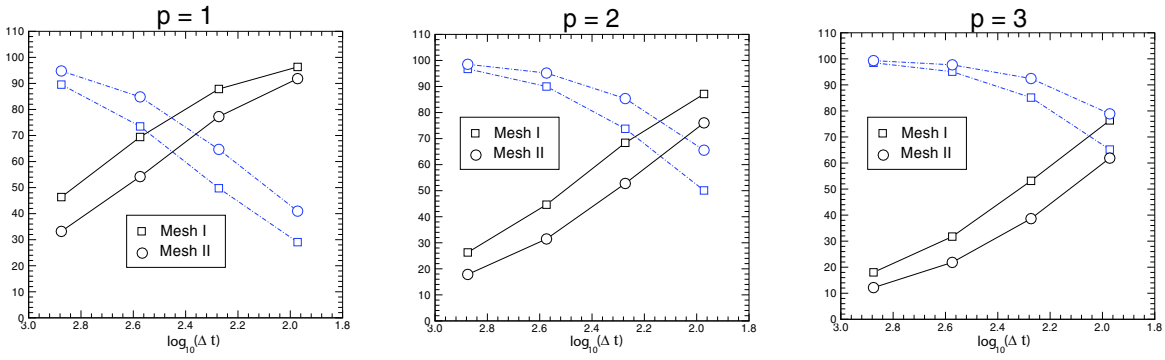

Fig. 5.33. Transient diffusion problem in a thermal battery. The ratio of temporal error β (dash-dot line) and the ratio of spatial error α (solid line) for the fully discrete finite element solutions of degree $p = 1, 2$, and 3 computed with Mesh I and II and four different time step sizes in the isotropic case.

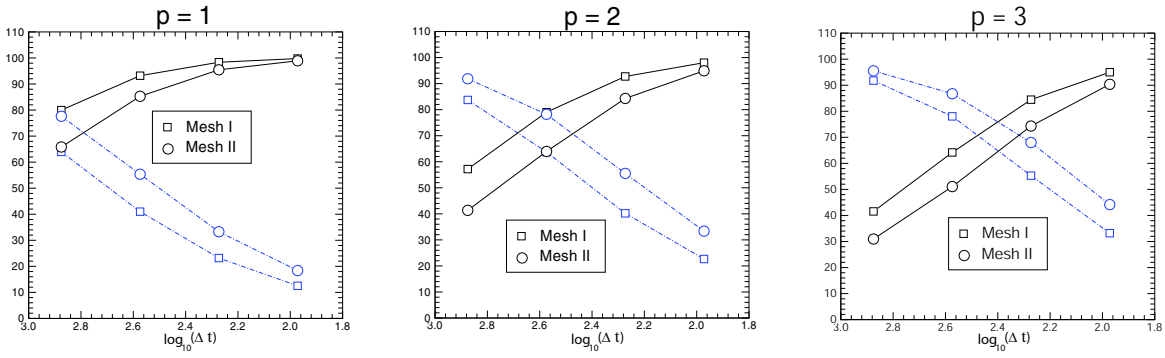

Fig. 5.34. Transient diffusion problem in a thermal battery. The ratio of temporal error β (dash-dot line) and the ratio of spatial error α (solid line) for the fully discrete finite element solutions of degree $p = 1, 2$, and 3 computed with Mesh I and II and four different time step sizes in the orthotropic case.

Fig. 5.35 (resp. 5.36) is the illustration of the effectivity index κ^{FD} for the total error $||E_h||_{\mathscr{C}}$ and the effectivity index $\zeta^{\mathrm{FD}}_{S^p_{\Delta_h}}$ for the temporal error $||\theta_h||_{\mathscr{C}}$ for the fully discrete finite element solutions $U_{S^p_{\Delta_h}}$ of degree $p = 1, 2$, and 3 in the isotropic case (resp. orthotropic case). It can be seen that κ^{FD} is close to 1 for both isotropic case and orthotropic case, and the maximum effectivity index $\zeta^{\mathrm{FD}}_{S^p_{\Delta_h}}$ for the temporal error is less than 1.6. We can also observe that if the temporal error is dominant κ^{FD} is

close to $\zeta^{\mathrm{FD}}_{S^p_{\Delta_h}}$. For example, we can see from Fig. 5.33 that in the isotropic case with time step size $\Delta t = \frac{T}{2^2}$ and $p = 2, 3$, the temporal error is dominant and about 100%. In Fig. 5.35, we find that κ^{FD} is equal to $\zeta^{\mathrm{FD}}_{S^p_{\Delta_h}}$. This phenomenon can also be observed for orthotropic case with $p = 2$ and 3 at time step size $\Delta t = \frac{T}{2^2}$.

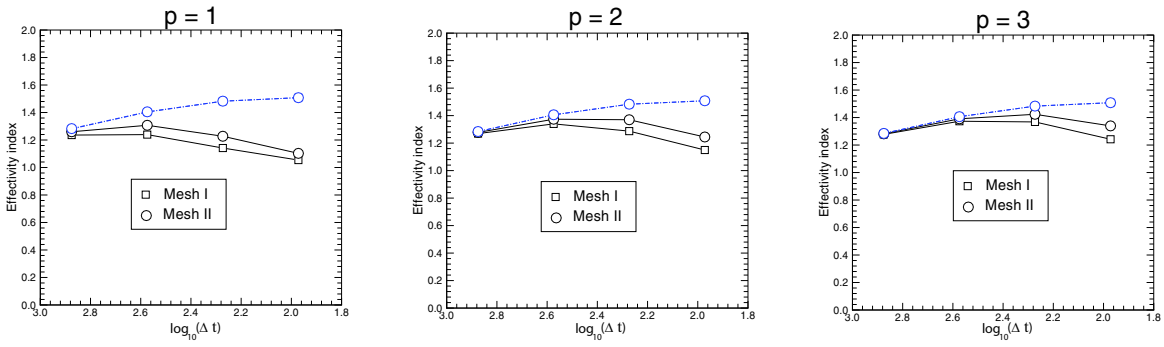

Fig. 5.35. Transient diffusion problem in a thermal battery. The effectivity index κ^{FD} (solid line) for the total error $||E_h||_{\mathscr{C}}$ and the effectivity index $\zeta^{\mathrm{FD}}_{S^p_{\Delta_h}}$ (dash-dot line) for the temporal error $||\theta_h||_{\mathscr{C}}$ for the fully discrete finite element solutions of degree $p = 1, 2$, and 3 computed with Mesh I and II and four different time step sizes in the isotropic case.

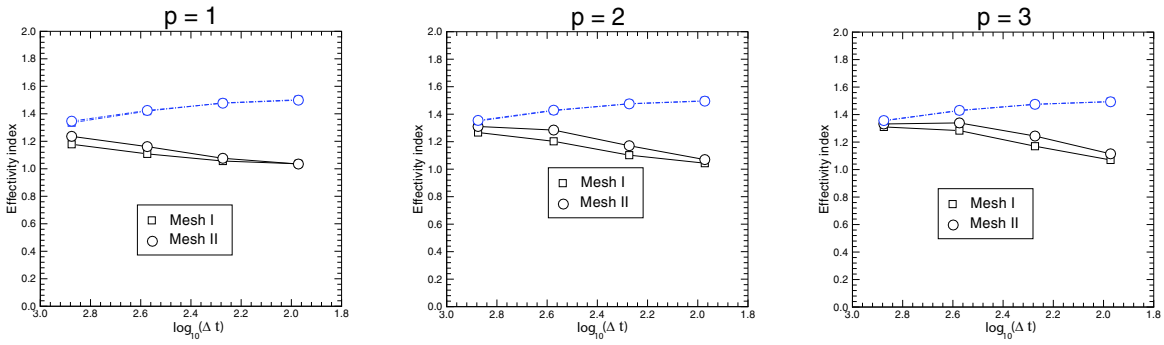

Fig. 5.36. Transient diffusion problem in a thermal battery. The effectivity index κ^{FD} (solid line) for the total error $||E_h||_{\mathscr{C}}$ and the effectivity index $\zeta^{\mathrm{FD}}_{S^p_{\Delta_h}}$ (dash-dot line) for the temporal error $||\theta_h||_{\mathscr{C}}$ for the fully discrete finite element solutions of degree $p = 1, 2$, and 3 computed with Mesh I and II and four different time step sizes in the orthotropic case.

Fig. 5.37 (resp. 5.38) is the illustration of the effectivity index $\kappa^{\mathrm{FD}}_{S^{p+k}_{\Delta_{h'}}}$ based on

$\hat{U}_{S^{p+k}_{\Delta_{h'}}}$ which is the finite element approximation of the exact solution $\hat{U}$ of degree $p+k$, computed with the mesh $\Delta_{h'}$ obtained from the uniform nested subdivision of the mesh Δ_h employed to obtain the fully discrete finite element solution $U_{S^p_{\Delta_h}}$. Here for simplicity, we fix the mesh, i.e., $\Delta_{h'} = \Delta_h$, and only increase the polynomial order from degree p to degree $p+k$ with $k = 1, 2$, and 3 respectively. It can be seen that $\kappa^{\mathrm{FD}}_{S^{p+k}_{\Delta_{h'}}}$ has the performance similar to its exact version κ^{FD} and it converges to κ^{FD} even for $k = 1$.

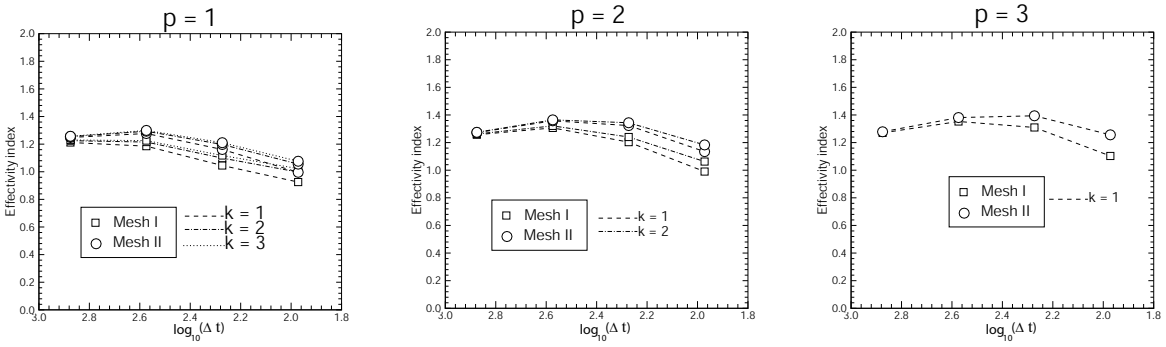

Fig. 5.37. Transient diffusion problem in a thermal battery. The effectivity index $\kappa^{\mathrm{FD}}_{S^{p+k}_{\Delta_{h'}}}$ for the total error $||E_h||_{\mathscr{C}}$ for the fully discrete finite element solutions of degree $p = 1, 2$, and 3 computed with Mesh I and II and four different time step sizes in the isotropic case.

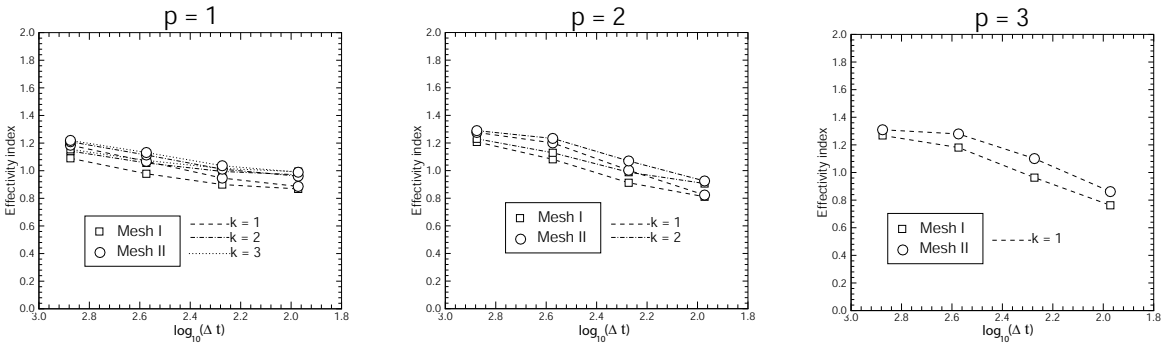

Fig. 5.38. Transient diffusion problem in a thermal battery. The effectivity index $\kappa^{\mathrm{FD}}_{S^{p+k}_{\Delta_{h'}}}$ for the total error $||E_h||_{\mathscr{C}}$ for the fully discrete finite element solutions of degree $p = 1, 2$, and 3 computed with Mesh I and II and four different time step sizes in the orthotropic case.

Fig. 5.39 (resp. 5.40) is the illustration of the exact temporal error ratio β and its estimate β^{FD} for isotropi case (resp. orthotropic case). It can be seen that β is bounded by β^{FD}. For both cases, β^{FD} is good estimate of β. If the temporal error is dominant, we can see that β^{FD} is very close to β. For instance, in the isotropic case with time step size $\Delta t = \frac{T}{2^2}$ and $p = 2, 3$, where the temporal error ratio is about 100%.

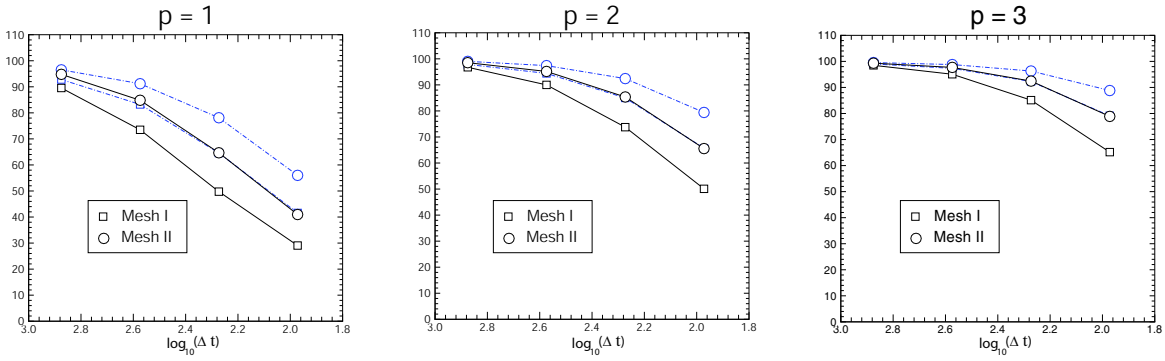

Fig. 5.39. Transient diffusion problem in a thermal battery. The exact temporal error ratio β (solid line) and the estimated temporal error ratio β^{FD} (dash-dot line) for the fully discrete finite element solutions of degree $p = 1, 2$, and 3 computed with Mesh I and II and four different time step sizes in the isotropic case.

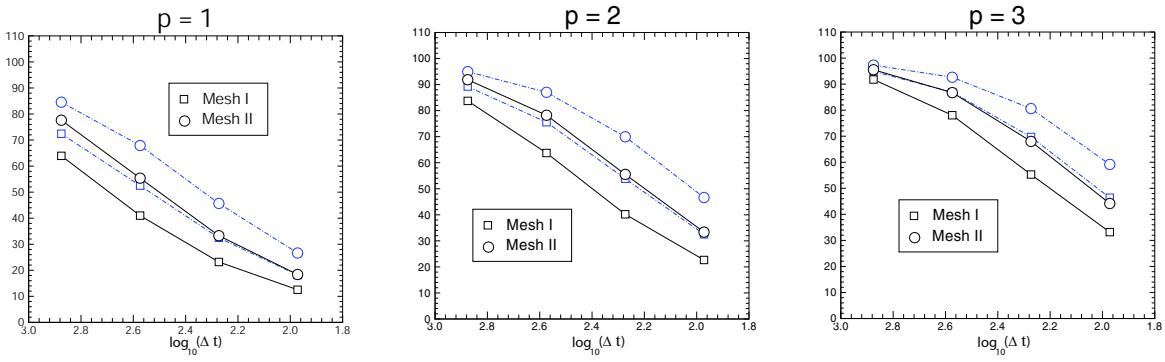

Fig. 5.40. Transient diffusion problem in a thermal battery. The exact temporal error ratio β (solid line) and the estimated temporal error ratio β^{FD} (dash-dot line) for the fully discrete finite element solutions of degree $p = 1, 2$, and 3 computed with Mesh I and II and four different time step sizes in the orthotropic case.

Fig. 5.41 (resp. 5.42) is the comparison of the exact temporal error ratio β and its approximation $\beta^{\mathrm{FD}}_{S^{p+k}_{\Delta_{h'}}}$. It can be seen that $\beta^{\mathrm{FD}}_{S^{p+k}_{\Delta_{h'}}}$ converges to its exact version β^{FD} as shown in Fig. 5.17 even with $k = 1$. Note that $\beta^{\mathrm{FD}}_{S^{p+k}_{\Delta_{h'}}}$ is computable since it is based on $\hat{U}_{S^{p+k}_{\Delta_{h'}}}$.

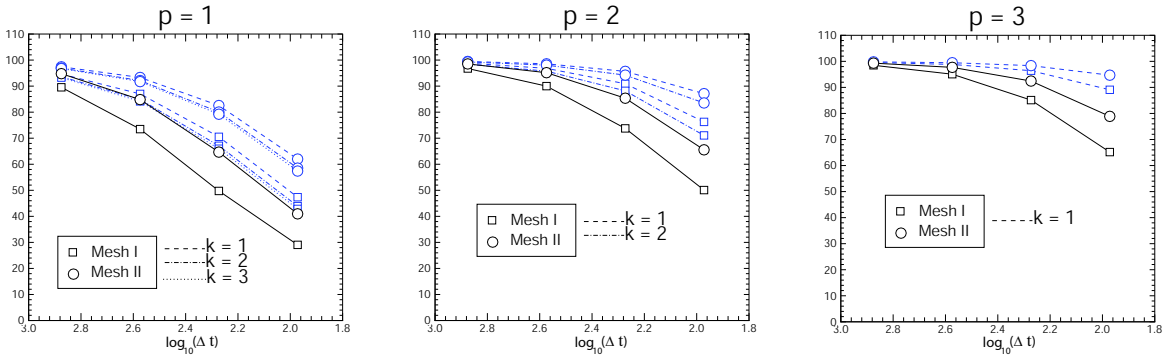

Fig. 5.41. Transient diffusion problem in a thermal battery. The exact temporal error ratio β (solid line) and the estimated temporal error ratio $\beta^{\mathrm{FD}}_{S^{p+k}_{\Delta_{h'}}}$ (dash-dot line) for the fully discrete finite element solutions of degree $p = 1, 2$, and 3 computed with Mesh I and II and four different time step sizes in the isotropic case.

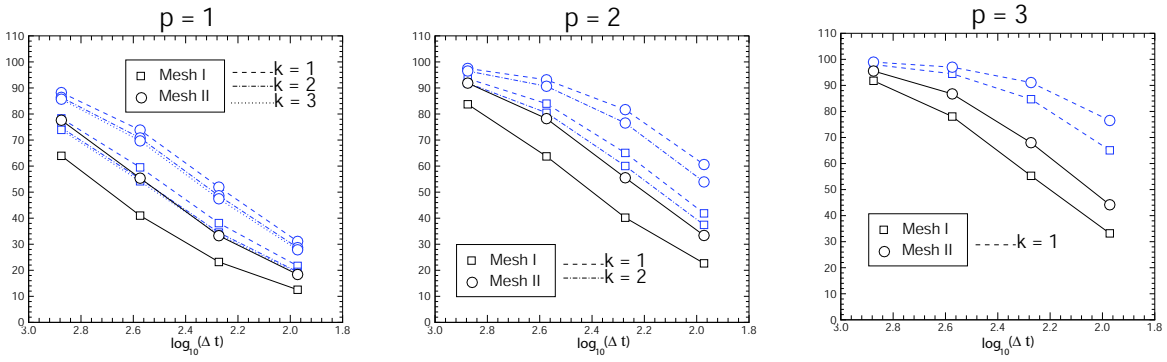

Fig. 5.42. Transient diffusion problem in a thermal battery. The exact temporal error ratio β (solid line) and the estimated temporal error ratio $\beta^{\mathrm{FD}}_{S^{p+k}_{\Delta_{h'}}}$ (dash-dot line) for the fully discrete finite element solutions of degree $p = 1, 2$, and 3 computed with Mesh I and II and four different time step sizes in the orthotropic case.

5.3 Bounds based on implicit residual estimators for fully discrete finite element solutions

Let

$$\hat{E}_h \stackrel{\text{def}}{=} \hat{U} - \hat{U}_{S^p_{\Delta_h}} \tag{5.52}$$

which is the exact error of the elliptic recontruction problem (5.5).

Then we have

$$\mathscr{B}_\Omega(\hat{E}_h, v) = \mathscr{R}(v) = \mathscr{L}(v) - (\gamma \frac{\partial}{\partial t} U_{S^p_{\Delta_h}}, v)_{L^2(\Omega)} - \mathscr{B}_\Omega(\hat{U}_{S^p_{\Delta_h}}, v) \qquad \forall v \in \mathscr{U}(\Omega) \tag{5.53}$$

Noting that

$$\mathscr{R}(v) = 0, \qquad \forall v \in S^p_{\Delta_h} \tag{5.54}$$

and following [1] we have

$$||\hat{E}_h||_{\mathscr{U}} \leq \mathscr{E}^{U,\text{FD}}_{Sub} \stackrel{\text{def}}{=} \sqrt{\sum_{\tau \in \Delta_h} \Big|\Big| \sum_{X \in \mathcal{N}(\Delta_h)} \breve{e}^{\text{FD}}_{\omega_X^{\Delta_h}} \Big|\Big|^2_{\mathscr{U}}} \tag{5.55}$$

which employs the following Neumann subdomain residual problems:

$$\text{Find } \breve{e}^{\text{FD}}_{\omega_X^{\Delta_h}} \in \mathscr{U}_0(\omega_X^{\Delta_h}) = \left\{ v \in \mathscr{U}(\omega_X^{\Delta_h}) \Big|\ v|_{\partial\omega_X^{\Delta_h} \cap \Gamma_D} = 0 \text{ or } \int_{\omega_X^{\Delta_h}} v = 0 \right\} \text{ such that}$$

$$\mathscr{B}_{\omega_X^{\Delta_h}}(\breve{e}^{\text{FD}}_{\omega_X^{\Delta_h}}, v) \stackrel{\text{def}}{=} \int_{\omega_X^{\Delta_h}} \nabla v^T \mathbf{K} \nabla \breve{e}^{\text{FD}}_{\omega_X^{\Delta_h}} + \int_{\partial\omega_X^{\Delta_h}} \alpha\, \breve{e}^{\text{FD}}_{\omega_X^{\Delta_h}}\, v = \mathscr{R}_{\omega_X^{\Delta_h}}(\phi_X^{\Delta_h}\, v) \qquad \forall v \in \mathscr{U}_0(\omega_X^{\Delta_h}) \tag{5.56}$$

When we employ the p-version with elements of degree $p+k$ to approximate the indicator function $\breve{e}^{\text{FD}}_{\omega_X^{\Delta_h}}$, and then we have the computed Neumann subdomain residual estimator defined as

$$\mathscr{E}^{U,\text{FD}}_{Sub,p+k} \stackrel{\text{def}}{=} \sqrt{\sum_{\tau \in \Delta_h} \Big|\Big| \sum_{X \in \mathcal{N}(\Delta_h)} \breve{e}^{\text{FD}}_{\omega_X^{\Delta_h},p+k} \Big|\Big|^2_{\mathscr{U}}} \tag{5.57}$$

where $\breve{e}^{\mathrm{FD}}_{\omega_X^{\Delta_h},p+k}$ denotes the $p+k$ degree finite element approximation of the exact indicator function $\breve{e}^{\mathrm{FD}}_{\omega_X^{\Delta_h}}$.

From the computed error indicator function $\breve{e}^{\mathrm{FD}}_{\omega_X^{\Delta_h},p+k}$ of subdomain residual problem, the lower bound $\mathscr{C}^{L,\mathrm{FD}}_{Sub,p+k}$ of the error $||\hat{E}_h||_{\mathscr{U}}$ of the elliptic reconstruction problem can be constructed by smoothening the error indicator function with the introduction of the partition of unity used in the construction of the estimator

$$\tilde{e}^{\mathrm{FD}}_{p+k} = \sum_{X\in\mathcal{N}(\Delta_h)} \phi_X^{\Delta_h}\ \breve{e}^{\mathrm{FD}}_{\omega_X^{\Delta_h},p+k} \tag{5.58}$$

With the smoothened error indicator function $\tilde{e}^{\mathrm{FD}}_{p+k}$, we obtain the duality based lower bounds, namely

$$\mathscr{C}^{L,\mathrm{FD}}_{Sub,p+k} \overset{\mathrm{def}}{=} \frac{\mathscr{R}(\tilde{e}^{\mathrm{FD}}_{p+k})}{||\tilde{e}^{\mathrm{FD}}_{p+k}+q_h||_{\mathscr{U}}} \leq ||\hat{E}_h||_{\mathscr{U}} \tag{5.59}$$

where $q_h^{\mathrm{FD}} \in S^p_{\Delta_h}$ can be obtained by solving the following variational problem

$$\mathscr{B}(q_h^{\mathrm{FD}}, q_h^{\mathrm{FD}}) = -\mathscr{B}(\tilde{e}^{\mathrm{FD}}_{p+k}, q_h^{\mathrm{FD}}) \qquad \forall q_h^{\mathrm{FD}} \in S^p_{\Delta_h} \tag{5.60}$$

It should be noted that q_h^{FD} is the function satisfying

$$||\tilde{e}^{\mathrm{FD}}_{p+k}+q_h^{\mathrm{FD}}||_{\mathscr{U}} = \min_{\chi\in S^p_{\Delta_h}} ||\tilde{e}^{\mathrm{FD}}_{p+k}+\chi||_{\mathscr{U}} \tag{5.61}$$

Upper Estimates for Space-Time Norm:

$$||E_h||_{\mathscr{C}} \leq \mathscr{F}^{U,\mathrm{FD}}_{Sub} \overset{\mathrm{def}}{=} \sqrt{\int_0^T (T-t)\left(\left(\mathscr{C}^{U,\mathrm{FD}}_{Sub}\right)^2 + ||\hat{U}_{S^p_{\Delta_h}} - U_{S^p_{\Delta_h}}||^2_{\mathscr{U}}\right)\,dt + T||\sqrt{\gamma}E_h(0)||^2_{L^2}} \tag{5.62}$$

Proof: Given the identity as shown in the equation (5.25), the $\mathscr{C}$-norm of the exact error of the fully discrete finite element solution of the parabolic problem satisfies the

following

$$||E_h||_{\mathscr{C}} = \sqrt{\int_0^T (T-t)\big(||\hat{E}_h||_{\mathscr{U}}^2 + ||\hat{U}_{S^p_{\Delta_h}} - U_{S^p_{\Delta_h}}||_{\mathscr{U}}^2 - ||u-\hat{U}||_{\mathscr{U}}^2\big)\, dt + T||\sqrt{\gamma}E_h(0)||_{L^2}^2} \tag{5.63}$$

Therefore we have by replacing the error $||\hat{E}_h||_{\mathscr{U}}$ with its upper bound $\mathscr{E}_{Sub}^{U,\mathrm{FD}}$

$$\begin{aligned} &||E_h||_{\mathscr{C}} \leq \\ &\sqrt{\int_0^T (T-t)\bigg(\big(\mathscr{E}_{Sub}^{U,\mathrm{FD}}\big)^2 + ||\hat{U}_{S^p_{\Delta_h}} - U_{S^p_{\Delta_h}}||_{\mathscr{U}}^2 - ||u-\hat{U}||_{\mathscr{U}}^2\bigg)\, dt + T||\sqrt{\gamma}e_h(0)||_{L^2(\Omega)}^2} \\ &\leq \sqrt{\int_0^T (T-t)\bigg(\big(\mathscr{E}_{Sub}^{U,\mathrm{FD}}\big)^2 + ||\hat{U}_{S^p_{\Delta_h}} - U_{S^p_{\Delta_h}}||_{\mathscr{U}}^2\bigg)\, dt + T||\sqrt{\gamma}e_h(0)||_{L^2}^2} \end{aligned} \tag{5.64}$$

□

With the computed residual estimator $\mathscr{E}_{Sub,p+k}^{U,\mathrm{FD}}$, the $\mathscr{C}$-norm of the exact error $||E_h||_{\mathscr{C}}$ can be estimated by the following

$$\mathscr{F}_{Sub,p+k}^{U,\mathrm{FD}} \stackrel{\mathrm{def}}{=} \sqrt{\int_0^T (T-t)\, \bigg(\big(\mathscr{E}_{Sub,p+k}^{U,\mathrm{FD}}\big)^2 + ||\hat{U}_{S^p_{\Delta_h}} - U_{S^p_{\Delta_h}}||_{\mathscr{U}(\Omega)}^2\bigg)\, dt + T\, ||\sqrt{\gamma}E_h(0)||_{L^2}^2} \tag{5.65}$$

where we replaced the exact upper bound $\mathscr{E}_{Sub}^{U,\mathrm{FD}}$ in (5.62) with its computable version $\mathscr{E}_{Sub,p+k}^{U,\mathrm{FD}}$

If we replace the error $||\hat{E}_h||_{\mathscr{U}}$ in (5.63) with its duality based lower bound $\mathscr{E}_{Sub,p+k}^{L,\mathrm{FD}}$. we have

$$\begin{aligned} &||E_h||_{\mathscr{C}} \geq \\ &\sqrt{\int_0^T (T-t)\bigg(\big(\mathscr{E}_{Sub,p+k}^{L,\mathrm{FD}}\big)^2 + ||\hat{U}_{S^p_{\Delta_h}} - U_{S^p_{\Delta_h}}||_{\mathscr{U}}^2 - ||u-\hat{U}||_{\mathscr{U}}^2\bigg)\, dt + T||\sqrt{\gamma}E_h(0)||_{L^2}^2} \end{aligned} \tag{5.66}$$

A lower bound can be obtained assuming that $||u-\hat{U}||_{\mathscr{U}}^2$ is negligible in comparison

of $\mathscr{E}^{L,\mathrm{FD}}_{Sub,p+k}$ or $||\hat{U}_{S^p_{\Delta_h}} - U_{S^p_{\Delta_h}}||_{\mathscr{U}}$, thus we have

$$||E_h||_{\mathscr{E}} \geq \mathscr{F}^{L,\mathrm{FD}}_{Sub,p+k} \overset{\mathrm{def}}{=} \sqrt{\int_0^T (T-t)\left(\left(\mathscr{E}^{L,\mathrm{FD}}_{Sub,p+k}\right)^2 + ||\hat{U}_{S^p_{\Delta_h}} - U_{S^p_{\Delta_h}}||^2_{\mathscr{U}}\right)\, dt + T||\sqrt{\gamma}E_h(0)||^2_{L^2}} \tag{5.67}$$

Remark 5.6. $\mathscr{F}^{U,\mathrm{FD}}_{Sub,p+k}$ is not guaranteed upper bound of $||E_h||_{\mathscr{E}}$ since the computable estimator $\mathscr{E}^{U,\mathrm{FD}}_{Sub,p+k}$ is not a guaranteed upper bound of the exact error $||\hat{E}_h||_{\mathscr{U}}$.

Remark 5.7. The estimates $\mathscr{F}^{U,\mathrm{FD}}$, $\mathscr{F}^{U,\mathrm{FD}}_{Sub,p+k}$ and $\mathscr{F}^{L,\mathrm{FD}}_{Sub,p+k}$ contain the term $\int_0^T (T-t)||\hat{U}_{S^p_{\Delta_h}} - U_{S^p_{\Delta_h}}||^2_{\mathscr{U}}\, dt$ which is related to the upper bound $\mathfrak{T}^{\mathrm{FD}}_{S^p_{\Delta_h}}$ for the temporal error.

Remark 5.8. Note that in [31–33] the duality approach based on space-time $\mathscr{A}$-norm does not yield lower bound while in our case it is possible that a lower bound can be obtained.

Let us analyze the accuracy of $\mathscr{F}^{U,\mathrm{FD}}_{Sub}$, $\mathscr{F}^{U,\mathrm{FD}}_{Sub,p+k}$, and $\mathscr{F}^{L,\mathrm{FD}}_{Sub,p+k}$ based on the sub-domain residual problem, for $\mathscr{E}$-norm of the exact error $||E_h||_{\mathscr{E}}$ using the following examples.

Example 5.8. *Heat transition problem in one dimension.* Fig. 5.43 (resp. Figs. 5.44 and 5.45) is the illustration of the effectivity indices corresponding to

$$\kappa^{U,\mathrm{FD}} \overset{\mathrm{def}}{=} \frac{\mathscr{F}^{U,\mathrm{FD}}_{Sub}}{||E_h||_{\mathscr{E}}}, \qquad \kappa^{U,\mathrm{FD}}_{p+k} \overset{\mathrm{def}}{=} \frac{\mathscr{F}^{U,\mathrm{FD}}_{Sub,p+k}}{||E_h||_{\mathscr{E}}}, \qquad \kappa^{L,\mathrm{FD}}_{p+k} \overset{\mathrm{def}}{=} \frac{\mathscr{F}^{L,\mathrm{FD}}_{Sub,p+k}}{||E_h||_{\mathscr{E}}} \tag{5.68}$$

vs. time step size $\Delta t = \frac{T}{2^n}(n = 1, 2, 3, 4)$, for the $\mathscr{E}$-norm of the error $||E_h||_{\mathscr{E}}$ in the fully discrete finite element solution $U_{S^p_{\Delta_h}}$ using elements of degree $p = 1, 2$ and 3 and uniform mesh size $h = \frac{L}{2^m}(m = 1, 2, 3, 4)$.

It can be seen that all the effectivity indices are close to the ones defined by (5.26) as shown in Fig. 5.15, due to the fact that the bounds $\mathscr{E}^{U,\mathrm{FD}}_{Sub}$, $\mathscr{E}^{U,\mathrm{FD}}_{Sub,p+k}$, and $\mathscr{E}^{L,\mathrm{FD}}_{Sub,p+k}$ are good estimate of the exact error $||\hat{E}_h||_{\mathscr{U}}$ of the elliptic reconstruction problem (5.5).

The maximum effectivity indes is about 1.65 which corresponds to the case where the temporal error is about 100% of the total error, e.g. $p = 3$ as shown in Fig. 5.14. It should be noted that $\kappa_{p+k}^{L,\mathrm{FD}}$ is not less than 1 since the temporal error term $||u - \hat{U}||_{\mathcal{U}}$ in (5.66) is not negligible in comparison of the other terms.

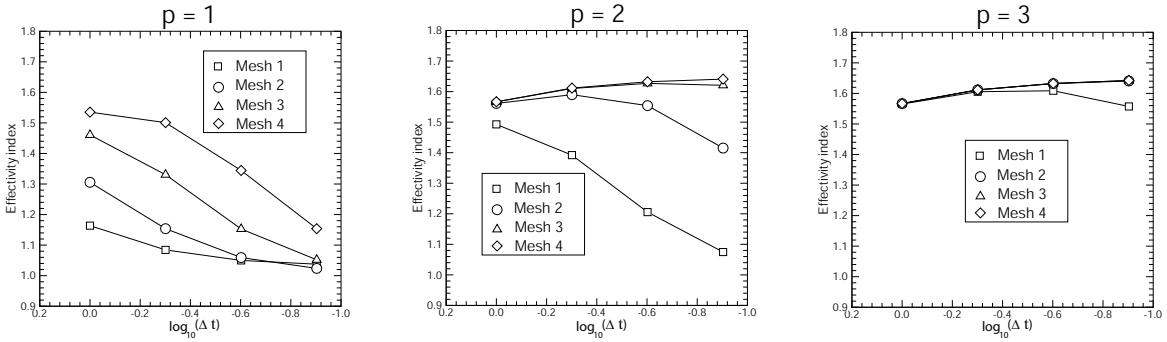

Fig. 5.43. Heat transition problem in one dimension. The variation of effectivity index $\kappa^{U,\mathrm{FD}}$ vs. time step size $\Delta t = \frac{T}{2^n}(n = 1, 2, 3, 4)$ based on exact Neumann subdomain residual estimator of the elliptic reconstruction problem, for the fully discrete finite element solution of degree $p = 1, 2$, and 3 computed with Mesh 1, Mesh 2, Mesh 3, and Mesh 4 corresponding to mesh size $h = \frac{L}{2^m}, m = 1, 2, 3$, and 4 respectively.

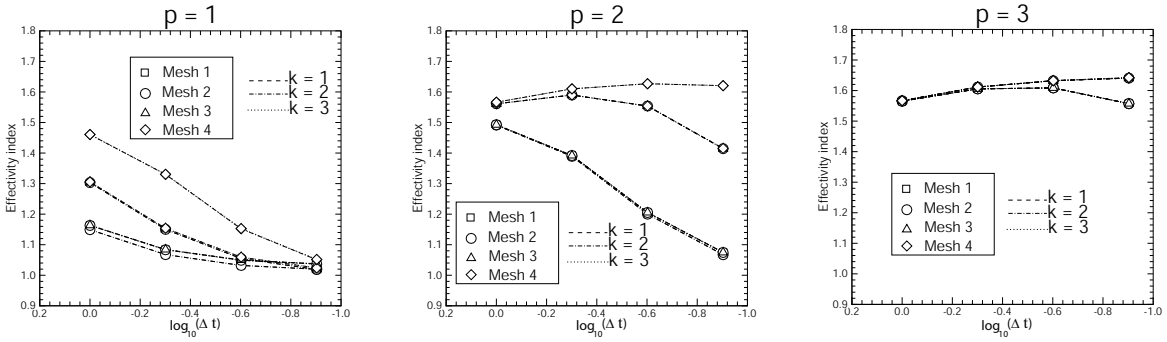

Fig. 5.44. Heat transition problem in one dimension. The variation of effectivity index $\kappa_{p+k}^{U,\mathrm{FD}}$ vs. time step size $\Delta t = \frac{T}{2^n}(n = 1, 2, 3, 4)$ based on computable Neumann subdomain residual estimator of degree $p + k(k = 1, 2, 3)$ of the elliptic reconstruction problem, for the fully discrete finite element solution of degree $p = 1, 2$, and 3 computed with Mesh 1, Mesh 2, Mesh 3, and Mesh 4 corresponding to mesh size $h = \frac{L}{2^m}, m = 1, 2, 3$, and 4 respectively.

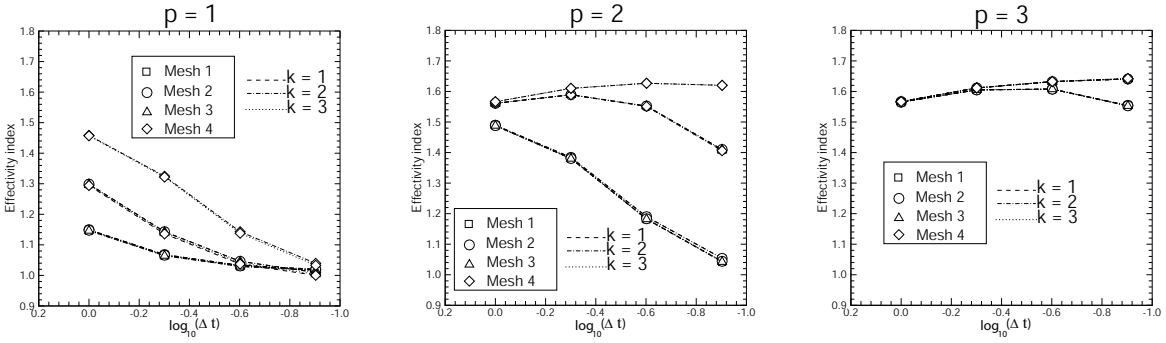

Fig. 5.45. Heat transition problem in one dimension. The variation of effectivity index $\kappa_{p+k}^{L,\mathrm{FD}}$ vs. time step size $\Delta t = \frac{T}{2^n}(n = 1, 2, 3, 4)$ based on computable Neumann subdomain residual estimator of degree $p + k(k = 1, 2, 3)$ of the elliptic reconstruction problem, for the fully discrete finite element solution of degree $p = 1, 2$, and 3 computed with Mesh 1, Mesh 2, Mesh 3, and Mesh 4 corresponding to mesh size $h = \frac{L}{2^m}, m = 1, 2, 3$, and 4 respectively.

Fig. 5.46 (resp. Figs. 5.47 and 5.48) is the estimated temporal error ratio

$$\begin{aligned}
\beta^{U,\mathrm{FD}} &\stackrel{\mathrm{def}}{=} \frac{\mathfrak{T}^{\mathrm{FD}}_{S^p_{\Delta_h}}}{\mathscr{F}^{U,\mathrm{FD}}_{Sub}} \times 100\% \\
\beta^{U,\mathrm{FD}}_{p+k} &\stackrel{\mathrm{def}}{=} \frac{\mathfrak{T}^{\mathrm{FD}}_{S^p_{\Delta_h}}}{\mathscr{F}^{U,\mathrm{FD}}_{Sub,p+k}} \times 100\% \\
\beta^{L,\mathrm{FD}}_{p+k} &\stackrel{\mathrm{def}}{=} \frac{\mathfrak{T}^{\mathrm{FD}}_{S^p_{\Delta_h}}}{\mathscr{F}^{L,\mathrm{FD}}_{Sub,p+k}} \times 100\%
\end{aligned} \tag{5.69}$$

and the corresponding exact temporal error ratio β with respect to time step size $\Delta t = \frac{T}{2^n}(n = 1, 2, 3, 4)$, for the $\mathscr{C}$-norm of the error $||E_h||_{\mathscr{C}}$ in the fully discrete finite element solution $U_{S^p_{\Delta_h}}$ using elements of degree $p = 1, 2$ and 3, computed using uniform mesh size $h = \frac{L}{2^m}(m = 1, 2, 3, 4)$.

It can be seen that the estimated temporal error ratio $\beta^{U,\mathrm{FD}}$, $\beta^{U,\mathrm{FD}}_{p+k}$, and $\beta^{L,\mathrm{FD}}_{p+k}$ are close to the exact ratio β and are also its upper bounds. Moreover they all are about the same in the case that the temporal error is 100%. Note that $\beta^{U,\mathrm{FD}}_{p+k}$ and $\beta^{L,\mathrm{FD}}_{p+k}$ converge to $\beta^{U,\mathrm{FD}}$ with the increase of element order $p + k$.

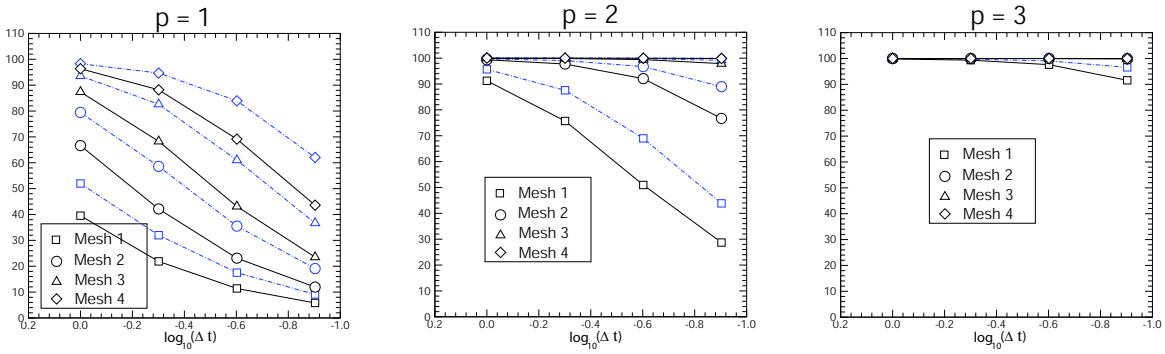

Fig. 5.46. Heat transition problem in one dimension. The exact ratio of temporal error to the total error β and its estimate $\beta^{U,\mathrm{FD}}$ based on exact Neumann subdomain residual estimator of the elliptic reconstruction problem, for the fully discrete finite element solution of degree $p = 1, 2$, and 3 computed with Mesh 1, Mesh 2, Mesh 3, and Mesh 4 corresponding to mesh size $h = \frac{L}{2^m}, m = 1, 2, 3$, and 4 respectively.

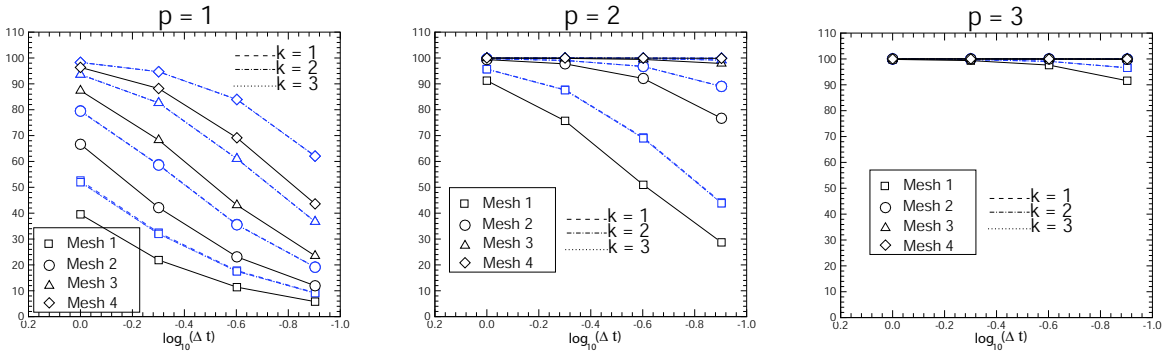

Fig. 5.47. Heat transition problem in one dimension. The exact ratio of temporal error to the total error β and its estimate $\beta^{U,\mathrm{FD}}_{p+k}$ based on computable Neumann subdomain residual estimator of the elliptic reconstruction problem, for the fully discrete finite element solution of degree $p = 1, 2$, and 3 computed with Mesh 1, Mesh 2, Mesh 3, and Mesh 4 corresponding to mesh size $h = \frac{L}{2^m}, m = 1, 2, 3$, and 4 respectively.

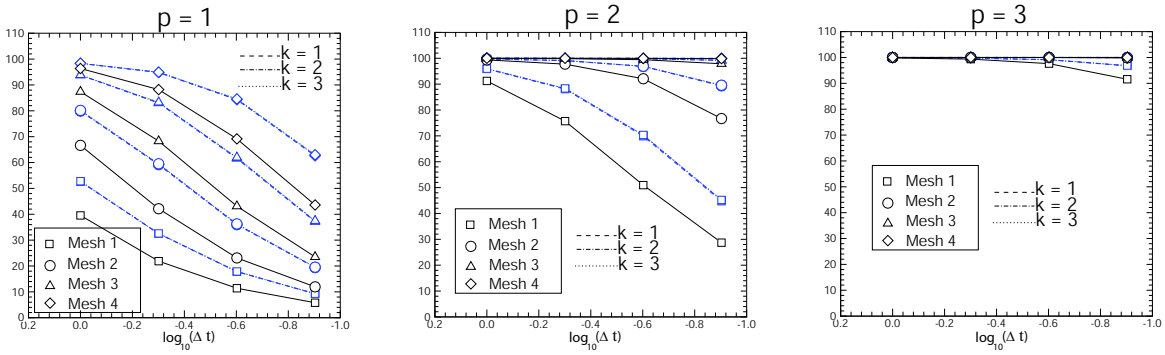

Fig. 5.48. Heat transition problem in one dimension. The exact ratio of temporal error to the total error β and its estimate $\beta_{p+k}^{L,\mathrm{FD}}$ based on computable Neumann subdomain residual estimator of the elliptic reconstruction problem, for the fully discrete finite element solution of degree $p = 1, 2$, and 3 computed with Mesh 1, Mesh 2, Mesh 3, and Mesh 4 corresponding to mesh size $h = \frac{L}{2^m}, m = 1, 2, 3$, and 4 respectively.

Example 5.9. *Two dimensional synthetic problem.* Fig. 5.49 (resp. Figs. 5.50 and 5.51) is the illustration of the effectivity indices $\kappa^{U,\mathrm{FD}}$, $\kappa_{p+k}^{U,\mathrm{FD}}$, and $\kappa_{p+k}^{L,\mathrm{FD}}$ vs. time step size $\Delta t = \frac{T}{2^n}(n = 1, 2, 3, 4)$, for the $\mathscr{C}$-norm of the error $||E_h||_{\mathscr{C}}$ in the fully discrete finite element solution $U_{S_{\Delta_h}^p}$ using elements of degree $p = 1, 2$ and 3 and uniform mesh size $h = \frac{L}{2^m}(m = 1, 2, 3, 4)$.

It can be seen that $\kappa^{U,\mathrm{FD}}$ is basically 1. The minimum value of $\kappa_{p+k}^{U,\mathrm{FD}}$ is about 0.4 and is improved dramatically with the increase of element order $p+k$ such as the case of $p = 1$ and Mesh 1. The effectivity index $\kappa_{p+k}^{L,\mathrm{FD}}$ is less than 1 for most cases and in the case of $p = 3$ and Mesh 4 where the maximum temporal error is 90% of the total error, it can be seen that $\kappa_{p+k}^{L,\mathrm{FD}}$ is greater than 1. Note that $\kappa_{p+k}^{L,\mathrm{FD}}$ is greater than the computable upper bound $\kappa_{p+k}^{U,\mathrm{FD}}$ which is not a guaranteed one.

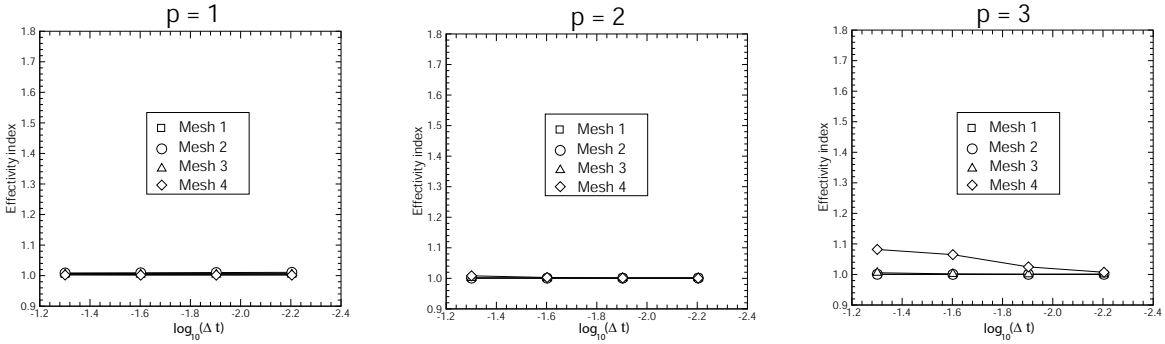

Fig. 5.49. Two dimensional synthetic problem. The variation of effectivity index $\kappa^{U,\mathrm{FD}}$ vs. time step size $\Delta t = \frac{T}{2^n}(n = 1, 2, 3, 4)$ based on exact Neumann subdomain residual estimator of the elliptic reconstruction problem, for the fully discrete finite element solution of degree $p = 1, 2$, and 3 computed with Mesh 1, Mesh 2, Mesh 3, and Mesh 4 corresponding to mesh size $h = \frac{L}{2^m}, m = 1, 2, 3$, and 4 respectively.

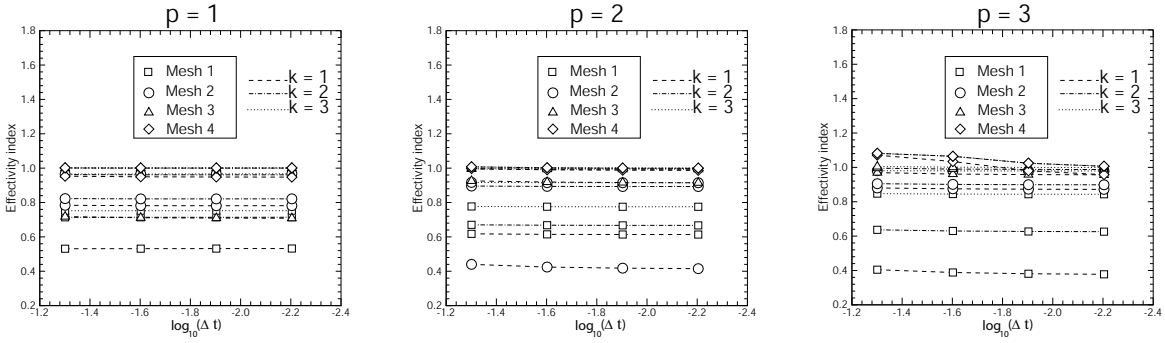

Fig. 5.50. Two dimensional synthetic problem. The variation of effectivity index $\kappa^{U,\mathrm{FD}}_{p+k}$ vs. time step size $\Delta t = \frac{T}{2^n}(n = 1, 2, 3, 4)$ based on computable Neumann subdomain residual estimator of degree $p + k(k = 1, 2, 3)$ of the elliptic reconstruction problem, for the fully discrete finite element solution of degree $p = 1, 2$, and 3 computed with Mesh 1, Mesh 2, Mesh 3, and Mesh 4 corresponding to mesh size $h = \frac{L}{2^m}, m = 1, 2, 3$, and 4 respectively.

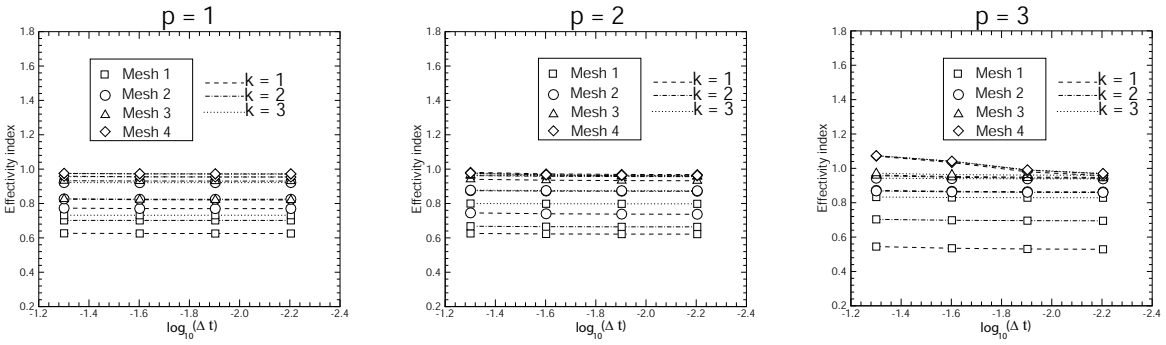

Fig. 5.51. Two dimensional synthetic problem. The variation of effectivity index $\kappa_{p+k}^{L,\mathrm{FD}}$ vs. time step size $\Delta t = \frac{T}{2^n}(n = 1, 2, 3, 4)$ based on computable Neumann subdomain residual estimator of degree $p + k(k = 1, 2, 3)$ of the elliptic reconstruction problem, for the fully discrete finite element solution of degree $p = 1, 2$, and 3 computed with Mesh 1, Mesh 2, Mesh 3, and Mesh 4 corresponding to mesh size $h = \frac{L}{2^m}, m = 1, 2, 3$, and 4 respectively.

Fig. 5.52 (resp. Figs. 5.53 and 5.54) is the estimated temporal error ratio $\beta^{U,\mathrm{FD}}$, $\beta_{p+k}^{U,\mathrm{FD}}$, and $\beta_{p+k}^{L,\mathrm{FD}}$ and the corresponding exact temporal error ratio β with respect to time step size $\Delta t = \frac{T}{2^n}(n = 1, 2, 3, 4)$, for the $\mathscr{C}$-norm of the error $||E_h||_{\mathscr{C}}$ in the fully discrete finite element solution $U_{S_{\Delta_h}^p}$ using elements of degree $p = 1, 2$ and 3, computed using uniform mesh size $h = \frac{L}{2^m}(m = 1, 2, 3, 4)$. It can be seen that we have pretty good estimate for the exact temporal error ratio for all the cases. The computable $\beta_{p+k}^{U,\mathrm{FD}}$ and $\beta_{p+k}^{L,\mathrm{FD}}$ converge to $\beta^{U,\mathrm{FD}}$ with the increase of element order $p + k$.

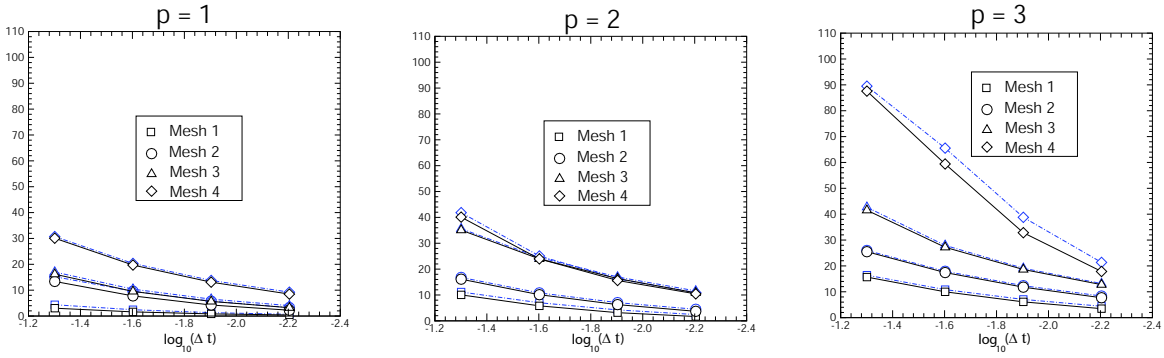

Fig. 5.52. Two dimensional synthetic problem. The exact ratio of temporal error to the total error β and its estimate $\beta^{U,\mathrm{FD}}$ based on computable Neumann subdomain residual estimator of the elliptic reconstruction problem, for the fully discrete finite element solution of degree $p = 1, 2$, and 3 computed with Mesh 1, Mesh 2, Mesh 3, and Mesh 4 corresponding to mesh size $h = \frac{L}{2^m}, m = 1, 2, 3$, and 4 respectively.

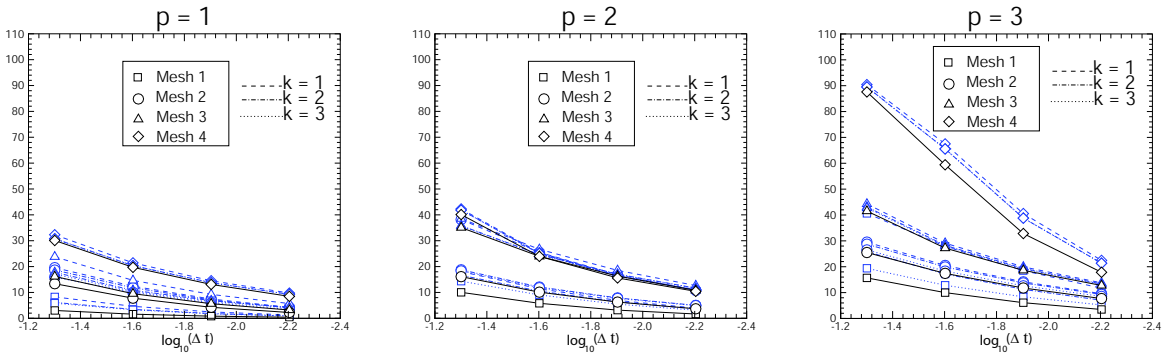

Fig. 5.53. Two dimensional synthetic problem. The exact ratio of temporal error to the total error β and its estimate $\beta^{U,\mathrm{FD}}_{p+k}$ based on computable Neumann subdomain residual estimator of the elliptic reconstruction problem, for the fully discrete finite element solution of degree $p = 1, 2$, and 3 computed with Mesh 1, Mesh 2, Mesh 3, and Mesh 4 corresponding to mesh size $h = \frac{L}{2^m}, m = 1, 2, 3$, and 4 respectively.

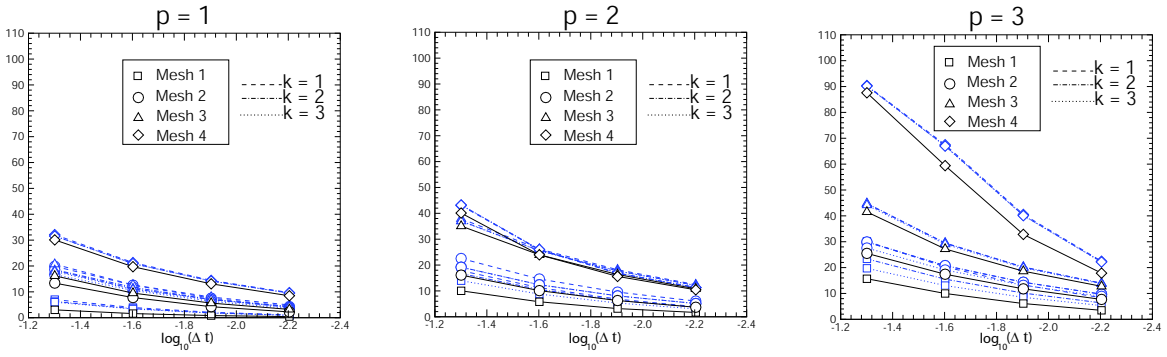

Fig. 5.54. Two dimensional synthetic problem. The exact ratio of temporal error to the total error β and its estimate $\beta_{p+k}^{L,\mathrm{FD}}$ based on computable Neumann subdomain residual estimator of the elliptic reconstruction problem, for the fully discrete finite element solution of degree $p = 1, 2$, and 3 computed with Mesh 1, Mesh 2, Mesh 3, and Mesh 4 corresponding to mesh size $h = \frac{L}{2^m}, m = 1, 2, 3$, and 4 respectively.

Example 5.10. *L-shaped domain problem.* Fig. 5.55 (resp. Figs. 5.56 and 5.57) is the illustration of the effectivity indices $\kappa^{U,\mathrm{FD}}$, $\kappa_{p+k}^{U,\mathrm{FD}}$, and $\kappa_{p+k}^{L,\mathrm{FD}}$ vs. time step size $\Delta t = \frac{T}{2^n}(n = 1, 2, 3, 4)$, for the $\mathscr{C}$-norm of the error $||E_h||_{\mathscr{C}}$ in the fully discrete finite element solution $U_{S_{\Delta_h}^p}$ using elements of degree $p = 1, 2$ and 3 and uniform mesh size $h = \frac{L}{2^m}(m = 1, 2, 3, 4)$.

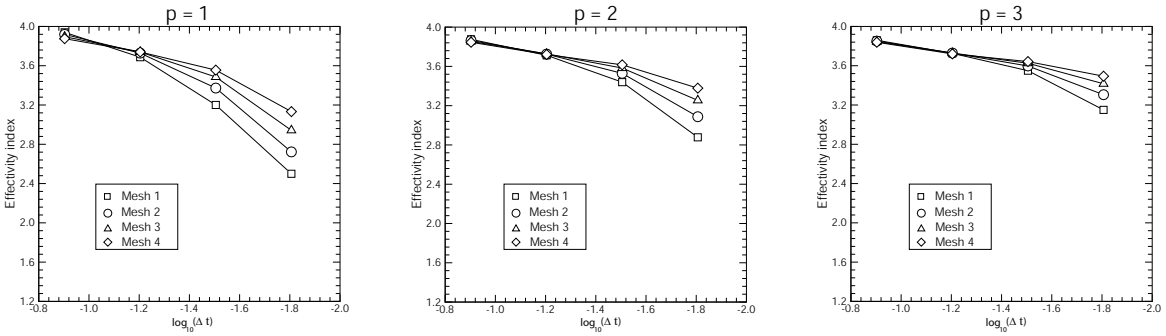

Fig. 5.55. L-shaped domain problem. The variation of effectivity index $\kappa^{U,\mathrm{FD}}$ vs. time step size $\Delta t = \frac{T}{2^n}(n = 1, 2, 3, 4)$ based on exact Neumann subdomain residual estimator of the elliptic reconstruction problem, for the fully discrete finite element solution of degree $p = 1, 2$, and 3 computed with Mesh 1, Mesh 2, Mesh 3, and Mesh 4 corresponding to mesh size $h = \frac{L}{2^m}, m = 1, 2, 3$, and 4 respectively.

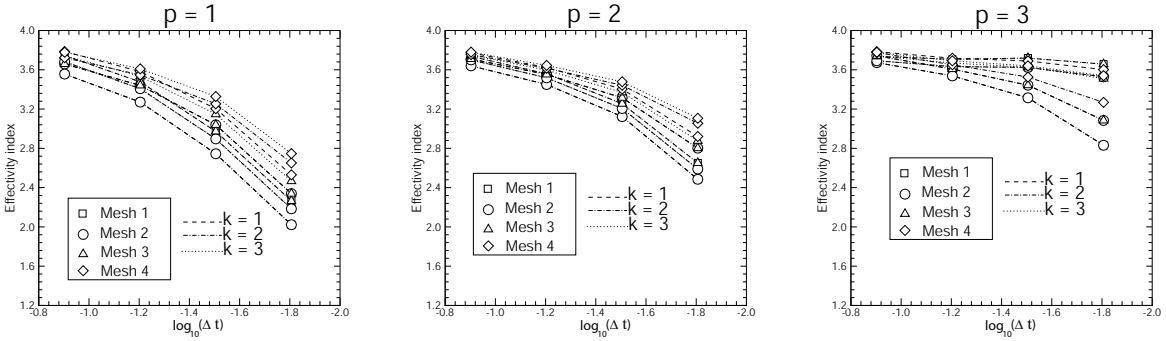

Fig. 5.56. L-shaped domain problem. The variation of effectivity index $\kappa_{p+k}^{U,\mathrm{FD}}$ vs. time step size $\Delta t = \frac{T}{2^n}(n = 1, 2, 3, 4)$ based on computable Neumann subdomain residual estimator of degree $p + k(k = 1, 2, 3)$ of the elliptic reconstruction problem, for the fully discrete finite element solution of degree $p = 1, 2$, and 3 computed with Mesh 1, Mesh 2, Mesh 3, and Mesh 4 corresponding to mesh size $h = \frac{L}{2^m}, m = 1, 2, 3$, and 4 respectively.

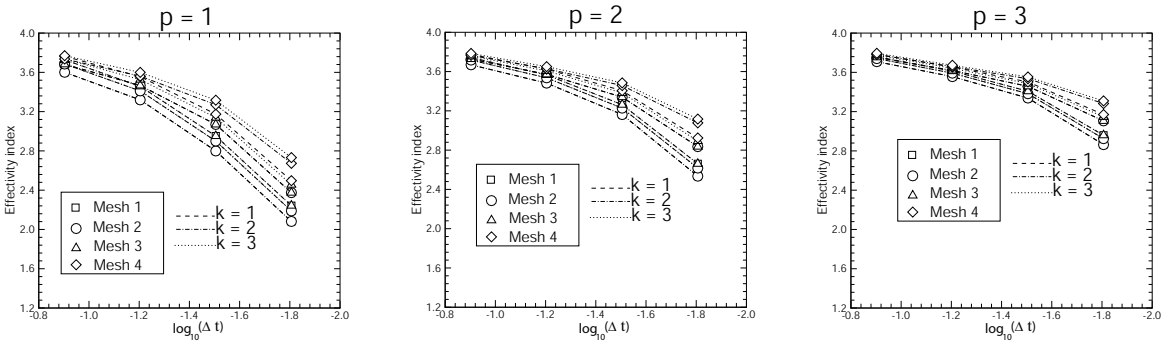

Fig. 5.57. L-shaped domain problem. The variation of effectivity index $\kappa_{p+k}^{L,\mathrm{FD}}$ vs. time step size $\Delta t = \frac{T}{2^n} (n = 1, 2, 3, 4)$ based on computable Neumann subdomain residual estimator of degree $p+k (k = 1, 2, 3)$ of the elliptic reconstruction problem, for the fully discrete finite element solution of degree $p = 1, 2$, and 3 computed with Mesh 1, Mesh 2, Mesh 3, and Mesh 4 corresponding to mesh size $h = \frac{L}{2^m}, m = 1, 2, 3$, and 4 respectively.

It can be seen that the largest effectivity index $\kappa^{U,\mathrm{FD}}$ is about 4 which happens to the case when the number of time steps is equal to 4, and with the increase of time steps $\kappa^{U,\mathrm{FD}}$ is reduced. However, the smallest effectivity index $\kappa^{U,\mathrm{FD}}$ is about 2.4 when the number of time steps is equal to 32 and $p = 1$. It can also be observed that $\kappa_{p+k}^{U,\mathrm{FD}}$ converges to $\kappa^{U,\mathrm{FD}}$ with the increase of polynomial order $p + k$ and has behavior similar to $\kappa^{U,\mathrm{FD}}$. The effectivity indices $\kappa_{p+k}^{L,\mathrm{FD}}$ are all above 1 which is not a lower bound. As a matter of fact $\kappa_{p+k}^{L,\mathrm{FD}}$ is close $\kappa_{p+k}^{U,\mathrm{FD}}$. The reason that $\kappa^{U,\mathrm{FD}}$, $\kappa_{p+k}^{U,\mathrm{FD}}$, and $\kappa_{p+k}^{L,\mathrm{FD}}$ have poor performance is due to the fact that the temporal error term $\int_0^T (T-t) || \hat{U}_{S_{\Delta_h}^p} - U_{S_{\Delta_h}^p} ||_{\mathcal{U}(\Omega)}^2 dt$ is dominant in (5.62), (5.65), and (5.67) as shown in Figs. 5.58, 5.59 and 5.60 by the discontinuous lines. We can also observe that the estimated temporal error ratio $\beta^{U,\mathrm{FD}}$, $\beta_{p+k}^{U,\mathrm{FD}}$, and $\beta_{p+k}^{L,\mathrm{FD}}$ are good approximation of the exact temporal error ratio β which is close to 100% except for $p = 1$ and $N = 32$.

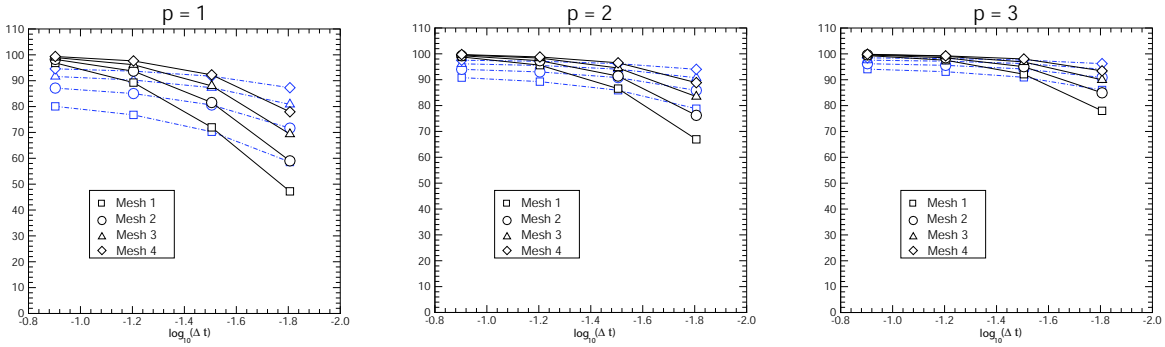

Fig. 5.58. L-shaped domain problem. The exact ratio of temporal error to the total error β and its estimate $\beta^{U,\mathrm{FD}}$ based on computable Neumann subdomain residual estimator of the elliptic reconstruction problem, for the fully discrete finite element solution of degree $p = 1, 2$, and 3 computed with Mesh 1, Mesh 2, Mesh 3, and Mesh 4 corresponding to mesh size $h = \frac{L}{2^m}, m = 1, 2, 3$, and 4 respectively.

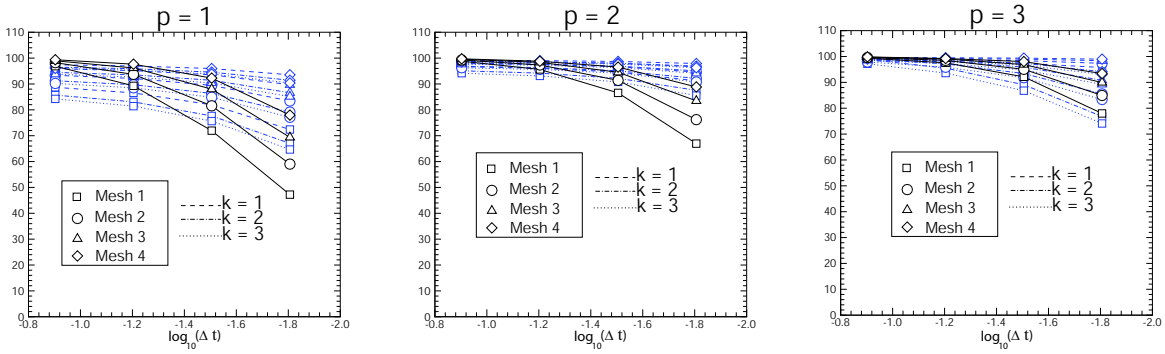

Fig. 5.59. L-shaped domain problem. The exact ratio of temporal error to the total error β and its estimate $\beta^{U,\mathrm{FD}}_{p+k}$ based on computable Neumann subdomain residual estimator of the elliptic reconstruction problem, for the fully discrete finite element solution of degree $p = 1, 2$, and 3 computed with Mesh 1, Mesh 2, Mesh 3, and Mesh 4 corresponding to mesh size $h = \frac{L}{2^m}, m = 1, 2, 3$, and 4 respectively.

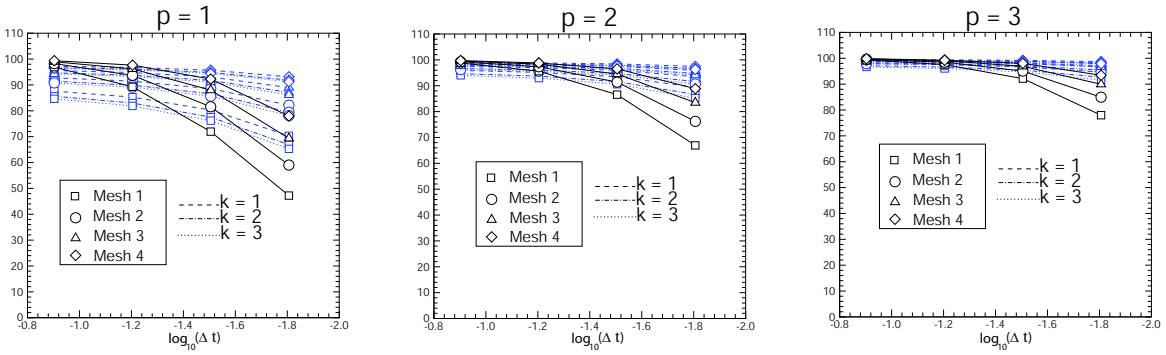

Fig. 5.60. L-shaped domain problem. The exact ratio of temporal error to the total error β and its estimate $\beta_{p+k}^{L,\mathrm{FD}}$ based on computable Neumann subdomain residual estimator of the elliptic reconstruction problem, for the fully discrete finite element solution of degree $p = 1, 2$, and 3 computed with Mesh 1, Mesh 2, Mesh 3, and Mesh 4 corresponding to mesh size $h = \frac{L}{2^m}, m = 1, 2, 3$, and 4 respectively.

Example 5.11. *Transient diffusion problem in a thermal battery.* Figs. 5.61, 5.62 and 5.63 (resp. Figs. 5.64, 5.65 and 5.66) are the illustrations of the effectivity indices $\kappa^{U,\mathrm{FD}}$, $\kappa_{p+k}^{U,\mathrm{FD}}$, and $\kappa_{p+k}^{L,\mathrm{FD}}$ vs. time step size $\Delta t = \frac{T}{2^n}(n = 1, 2, 3, 4)$, for the $\mathscr{C}$-norm of the error $||E_h||_{\mathscr{C}}$ in the fully discrete finite element solution $U_{S_{\Delta_h}^p}$ using elements of degree $p = 1, 2$ and 3 and Mesh I and II in the isotropic case (resp. orthotropic case).

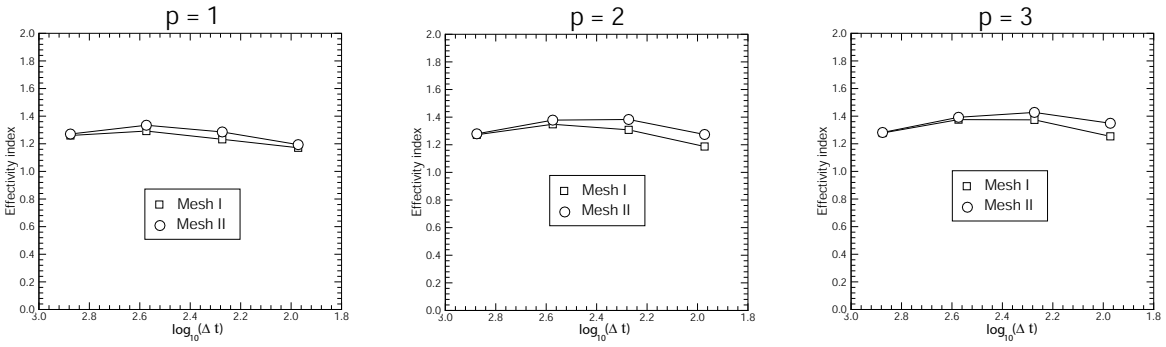

Fig. 5.61. Transient diffusion problem in a thermal battery. The variation of effectivity index $\kappa^{U,\mathrm{FD}}$ vs. time step size $\Delta t = \frac{T}{2^n}(n = 1, 2, 3, 4)$ based on exact Neumann subdomain residual estimator of the elliptic reconstruction problem, for the fully discrete finite element solution of degree $p = 1, 2$, and 3 computed with Mesh I and II for isotropic case.

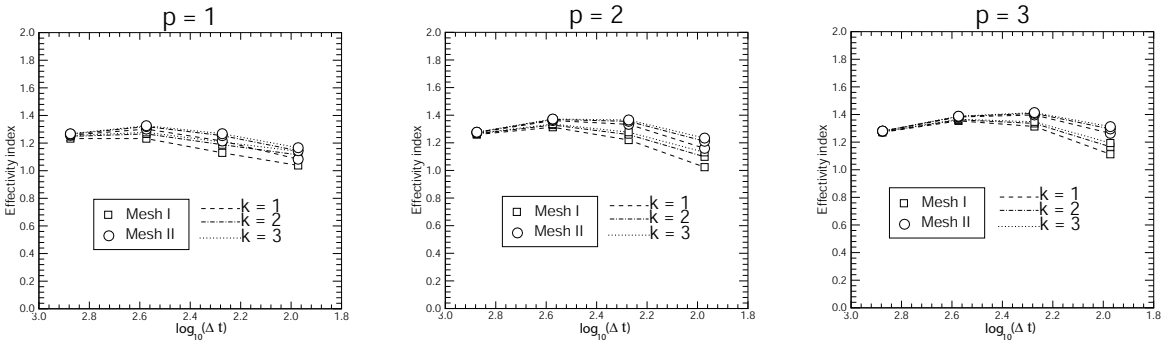

Fig. 5.62. Transient diffusion problem in a thermal battery. The variation of effectivity index $\kappa_{p+k}^{U,\mathrm{FD}}$ vs. time step size $\Delta t = \frac{T}{2^n} (n = 1, 2, 3, 4)$ based on computable Neumann subdomain residual estimator of degree $p + k (k = 1, 2, 3)$ of the elliptic reconstruction problem, for the fully discrete finite element solution of degree $p = 1, 2$, and 3 computed with Mesh I and II for isotropic case.

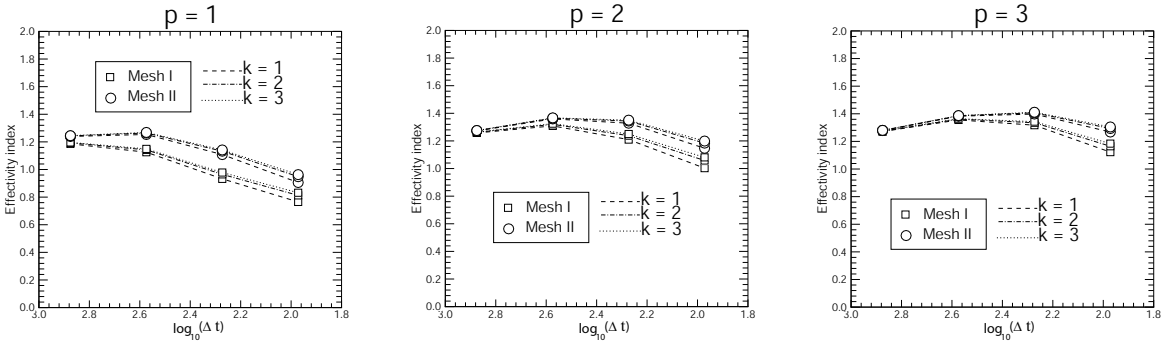

Fig. 5.63. Transient diffusion problem in a thermal battery. The variation of effectivity index $\kappa_{p+k}^{L,\mathrm{FD}}$ vs. time step size $\Delta t = \frac{T}{2^n} (n = 1, 2, 3, 4)$ based on computable Neumann subdomain residual estimator of degree $p + k (k = 1, 2, 3)$ of the elliptic reconstruction problem, for the fully discrete finite element solution of degree $p = 1, 2$, and 3 computed with Mesh I and II for isotropic case.

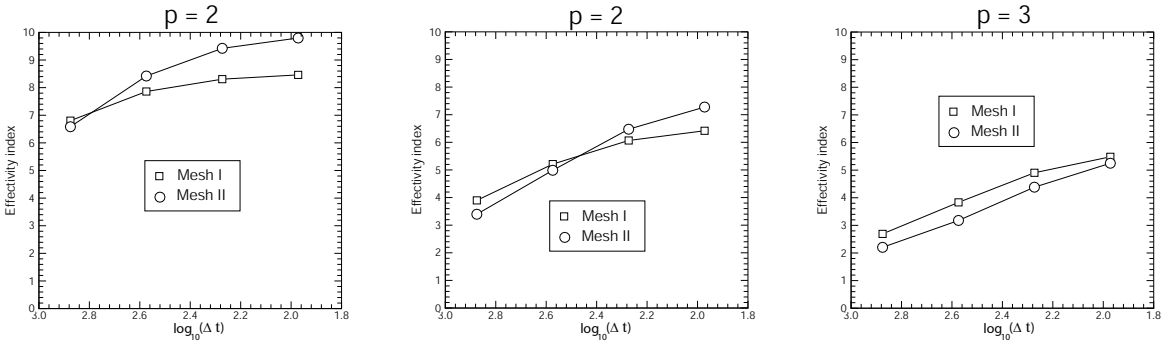

Fig. 5.64. Transient diffusion problem in a thermal battery. The variation of effectivity index $\kappa^{U,\mathrm{FD}}$ vs. time step size $\Delta t = \frac{T}{2^n}(n = 1, 2, 3, 4)$ based on exact Neumann subdomain residual estimator of the elliptic reconstruction problem, for the fully discrete finite element solution of degree $p = 1, 2$, and 3 computed with Mesh I and II for orthotropic case.

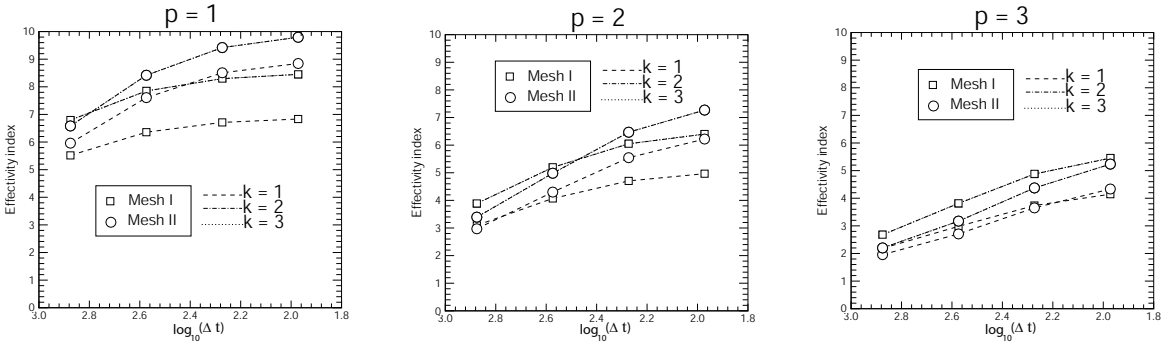

Fig. 5.65. Transient diffusion problem in a thermal battery. The variation of effectivity index $\kappa^{U,\mathrm{FD}}_{p+k}$ vs. time step size $\Delta t = \frac{T}{2^n}(n = 1, 2, 3, 4)$ based on computable Neumann subdomain residual estimator of degree $p + k(k = 1, 2, 3)$ of the elliptic reconstruction problem, for the fully discrete finite element solution of degree $p = 1, 2$, and 3 computed with Mesh I and II for orthotropic case.

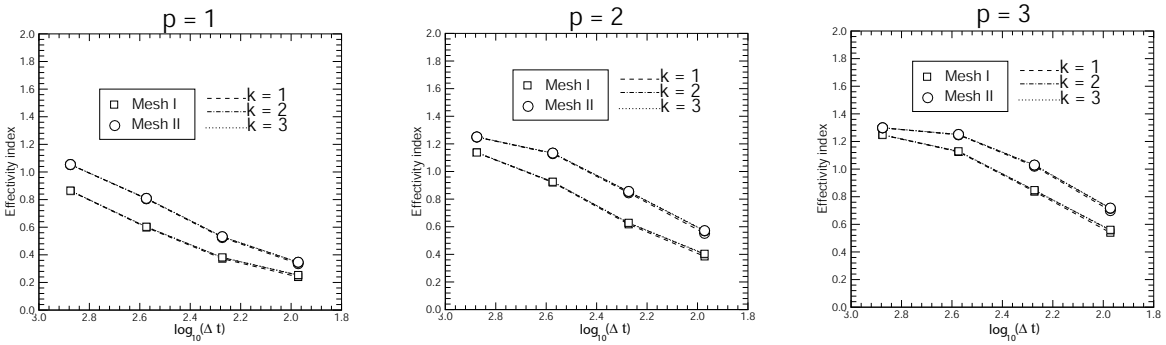

Fig. 5.66. Transient diffusion problem in a thermal battery. The variation of effectivity index $\kappa_{p+k}^{L,\mathrm{FD}}$ vs. time step size $\Delta t = \frac{T}{2^n} (n = 1, 2, 3, 4)$ based on computable Neumann subdomain residual estimator of degree $p + k (k = 1, 2, 3)$ of the elliptic reconstruction problem, for the fully discrete finite element solution of degree $p = 1, 2$, and 3 computed with Mesh I and II for orthotropic case.

It can be seen that $\kappa^{U,\mathrm{FD}}$ has good performance in the isotropic case and the maximum value is 1.4 while in the orthotropic case $\kappa^{U,\mathrm{FD}}$ can be as big as 10 since $\mathscr{E}_{Sub}^{U,\mathrm{FD}}$ severely overestimates the exact error $||\hat{E}_h||_{\mathscr{U}}$ and the culprit is the existence of interface layers at the top and bottom of the highly orthotropic domain Ω_3 as shown in Fig. 2.2. For details about the effect of interface layers on the robustness of elliptic residual estimators, refer to [1]. Likewise we can observe similar performance for $\kappa_{p+k}^{U,\mathrm{FD}}$ for both the isotropic case and the orthotropic case, and with the increase of element order $p + k$, $\kappa_{p+k}^{U,\mathrm{FD}}$ converges to $\kappa^{U,\mathrm{FD}}$. Note that for orthotropic case, the results are the same in the case of $k = 2$ and $k = 3$.

In the case of $\kappa_{p+k}^{L,\mathrm{FD}}$, we can see that for isotropic case $\kappa_{p+k}^{L,\mathrm{FD}}$ can be greater than 1. For orthotropic case, $\mathscr{E}_{Sub,p+k}^{L,\mathrm{FD}}$ is greater than 1 for coarse time step size. However with the increase in the number of time steps the temporal error diminishes and spatial error becomes dominant as shown in Fig. 5.34, $\kappa_{p+k}^{L,\mathrm{FD}}$ can be as small as 0.2 because the existence of interface layers on Ω_3 causes the severe underestimation of $\mathscr{E}_{Sub,p+k}^{L,\mathrm{FD}}$ over the exact error $||\hat{E}_h||_{\mathscr{U}}$ in the elliptic reconstruction problem (5.5).

Figs. 5.67, 5.68 and 5.69(resp. Figs. 5.70, 5.71 and 5.72) are the illustrations of the estimated temporal error ratio $\beta^{U,\mathrm{FD}}$, $\beta_{p+k}^{U,\mathrm{FD}}$, and $\beta_{p+k}^{L,\mathrm{FD}}$ and the corresponding exact temporal error ratio β with respect to time step size $\Delta t = \frac{T}{2^n}(n = 1, 2, 3, 4)$ for isotropic case (resp. orthotropic case). It can be seen that in isotropic case, $\beta^{U,\mathrm{FD}}$, $\beta_{p+k}^{U,\mathrm{FD}}$, and $\beta_{p+k}^{L,\mathrm{FD}}$ are good estimate of the exact temporal error ratio β and also its upper bounds. $\beta_{p+k}^{U,\mathrm{FD}}$ and $\beta_{p+k}^{L,\mathrm{FD}}$ converge to $\beta^{U,\mathrm{FD}}$ with the increase of element order $p + k$. However in the orthotropic case, $\beta^{U,\mathrm{FD}}$ and $\beta_{p+k}^{U,\mathrm{FD}}$ can grossly underestimate the exact temporal error ratio β and $\beta_{p+k}^{L,\mathrm{FD}}$ can grossly overestimate β, which is because of the severe overestimation of $\mathscr{E}_{Sub,p+k}^{U,\mathrm{FD}}$ over the exact error $||\hat{E}_h||_{\mathscr{U}}$ and gross underestimation of $\mathscr{E}_{Sub,p+k}^{L,\mathrm{FD}}$ over the exact error $||\hat{E}_h||_{\mathscr{U}}$.

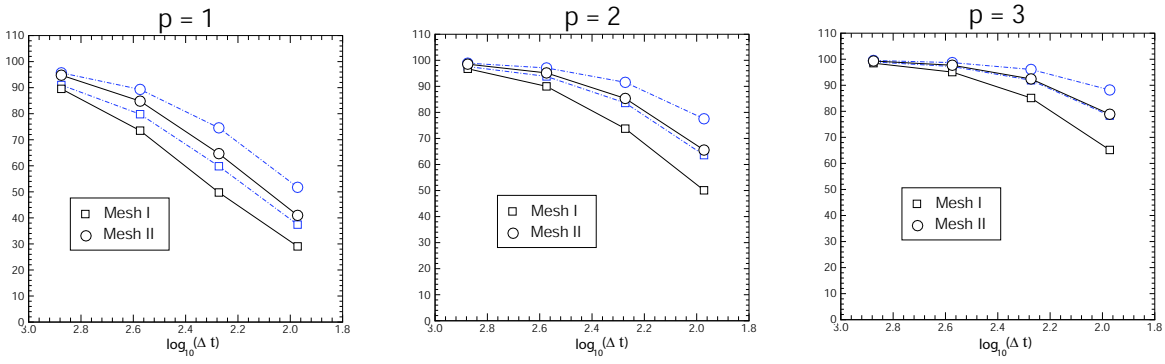

Fig. 5.67. Transient diffusion problem in a thermal battery. The exact ratio of temporal error to the total error β and its estimate $\beta^{U,\mathrm{FD}}$ based on exact Neumann subdomain residual estimator of the elliptic reconstruction problem, for the fully discrete finite element solution of degree $p = 1, 2$, and 3 computed with Mesh I and II for isotropic case.

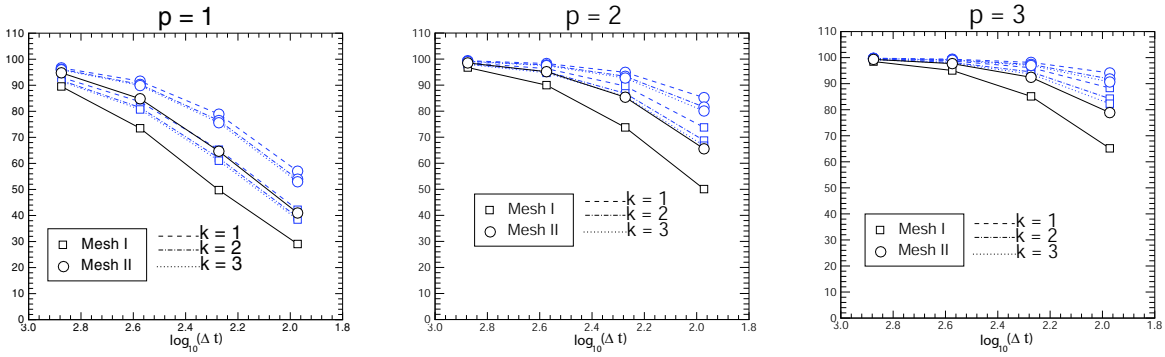

Fig. 5.68. Transient diffusion problem in a thermal battery. The exact ratio of temporal error to the total error β and its estimate $\beta^{U,\mathrm{FD}}_{p+k}$ based on computable Neumann subdomain residual estimator of the elliptic reconstruction problem, for the fully discrete finite element solution of degree $p = 1, 2$, and 3 computed with Mesh I and II for isotropic case.

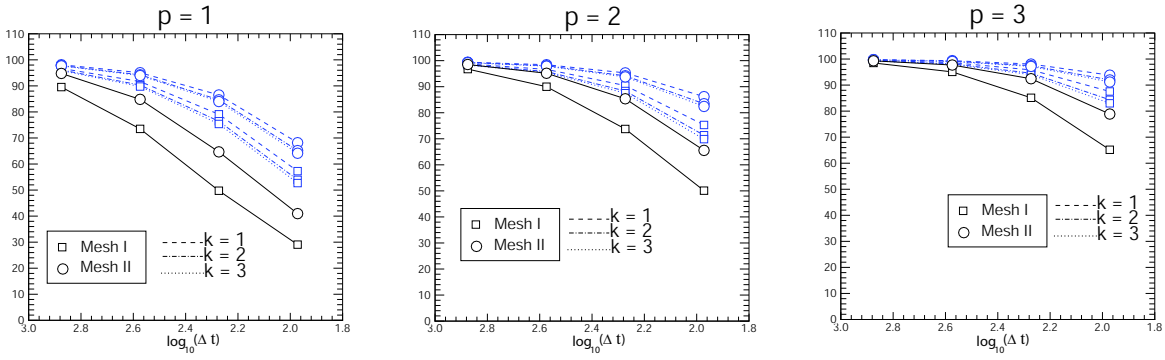

Fig. 5.69. Transient diffusion problem in a thermal battery. The exact ratio of temporal error to the total error β and its estimate $\beta_{p+k}^{L,\mathrm{FD}}$ based on computable Neumann subdomain residual estimator of the elliptic reconstruction problem, for the fully discrete finite element solution of degree $p = 1, 2$, and 3 computed with Mesh I and II for isotropic case.

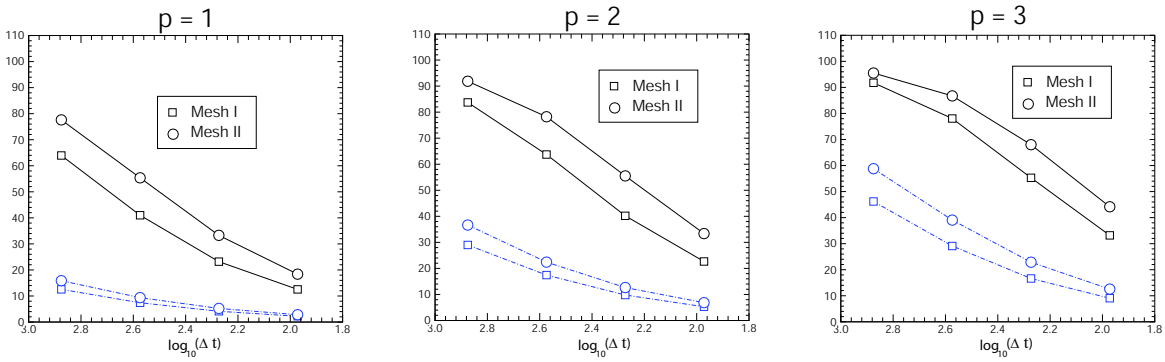

Fig. 5.70. Transient diffusion problem in a thermal battery. The exact ratio of temporal error to the total error β and its estimate $\beta^{U,\mathrm{FD}}$ based on exact Neumann subdomain residual estimator of the elliptic reconstruction problem, for the fully discrete finite element solution of degree $p = 1, 2$, and 3 computed with Mesh I and II for orthotropic case.

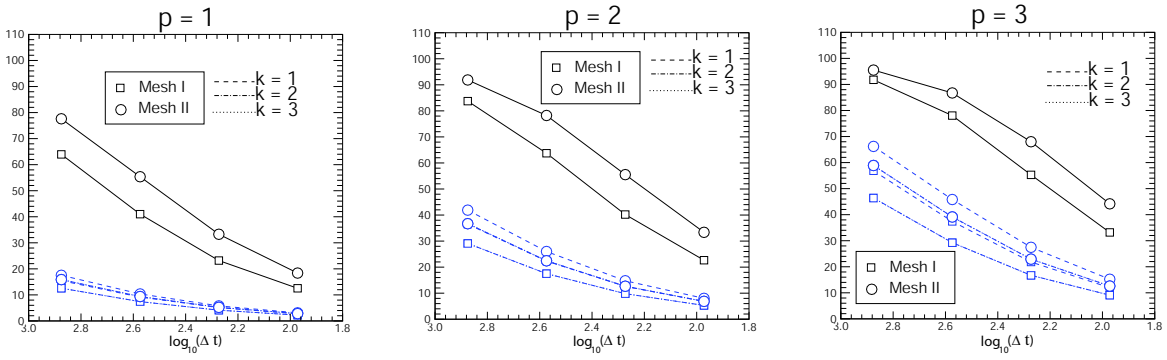

Fig. 5.71. Transient diffusion problem in a thermal battery. The exact ratio of temporal error to the total error β and its estimate $\beta_{p+k}^{U,\mathrm{FD}}$ based on computable Neumann subdomain residual estimator of the elliptic reconstruction problem, for the fully discrete finite element solution of degree $p = 1, 2$, and 3 computed with Mesh I and II for orthotropic case.

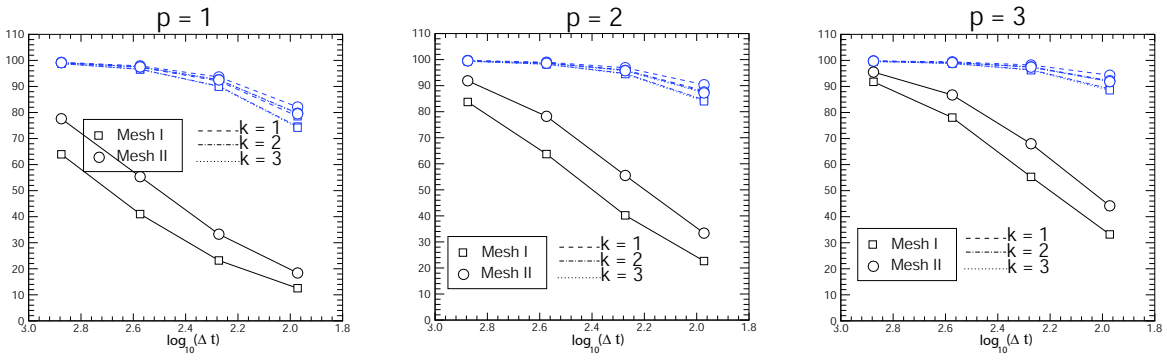

Fig. 5.72. Transient diffusion problem in a thermal battery. The exact ratio of temporal error to the total error β and its estimate $\beta_{p+k}^{L,\mathrm{FD}}$ based on computable Neumann subdomain residual estimator of the elliptic reconstruction problem, for the fully discrete finite element solution of degree $p = 1, 2$, and 3 computed with Mesh I and II for orthotropic case.

5.4 Error estimation at any time instant for fully discrete finite element solutions

For the exact error E_h, we have

$$||E_h||_H = ||u - U_{S^p_{\Delta_h}}||_H \leq ||u - \hat{u}||_H + ||\hat{u} - \hat{U}||_H + ||\hat{U} - U_{S^p_{\Delta_h}}||_H \tag{5.70}$$

for $H = L^2$, and $H = \mathbb{U}$. As we have already known that except the linear element in the L^2 norm, due to the superconvergence properties of the term $u - \hat{u}$, we have

$$||E_h||_H \approx ||\hat{u} - \hat{U}||_H + ||\hat{U} - U_{S^p_{\Delta_h}}||_H \tag{5.71}$$

The term $||\hat{u} - \hat{U}||_H$ represents temporal error. It can be seen that at any time instant t if the temporal error $||\hat{u} - \hat{U}||_H$ is negligible in comparison of the term $||\hat{U} - U_{S^p_{\Delta_h}}||_H$, we have

$$||E_h||_H \approx ||\hat{U} - U_{S^p_{\Delta_h}}||_H \tag{5.72}$$

Let us define the effectivity index at any time instant as

$$\eta^{FD}(t) \stackrel{\text{def}}{=} \frac{||\hat{U} - U_{S^p_{\Delta_h}}||_{\mathbb{U}}}{||E_h||_{\mathbb{U}}}, \qquad \zeta^{FD}(t) \stackrel{\text{def}}{=} \frac{||\hat{U} - U_{S^p_{\Delta_h}}||_{L^2}}{||E_h||_{L^2}} \tag{5.73}$$

Similarly $\eta^{FD}_{S^{p+k}_{\Delta_{h'}}}(t)$ and $\zeta^{FD}_{S^{p+k}_{\Delta_{h'}}}(t)$ when $\hat{U}$ is replaced by $\hat{U}_{S^{p+k}_{\Delta_{h'}}}$.

If we introduce the finite element approximation of $\hat{U}$, we have

$$||\hat{U} - U_{S^p_{\Delta_h}}||^2_{\mathbb{U}} = ||\hat{U} - \hat{U}_{S^p_{\Delta_h}}||^2_{\mathbb{U}} + ||\hat{U}_{S^p_{\Delta_h}} - U_{S^p_{\Delta_h}}||^2_{\mathbb{U}} = ||\hat{E}_h||^2_{\mathbb{U}} + ||\hat{U}_{S^p_{\Delta_h}} - U_{S^p_{\Delta_h}}||^2_{\mathbb{U}} \tag{5.74}$$

because of orthogonality condition and

$$||\hat{U} - U_{S^p_{\Delta_h}}||_{L^2} \leq ||\hat{U} - \hat{U}_{S^p_{\Delta_h}}||_{L^2} + ||\hat{U}_{S^p_{\Delta_h}} - U_{S^p_{\Delta_h}}||_{L^2} = ||\hat{E}_h||_{L^2} + ||\hat{U}_{S^p_{\Delta_h}} - U_{S^p_{\Delta_h}}||_{L^2} \tag{5.75}$$

because of triangle inequality.

Furthermore, if we employ the Neumann subdomain residual estimator to esti-

mate the exact error of $\hat{E}_h$

$$\bar{\eta}^{U,\mathrm{FD}}(t) \stackrel{\mathrm{def}}{=} \frac{\sqrt{\left(\mathscr{E}_{Sub}^{U,\mathrm{FD}}\right)^2 + ||\hat{U}_{S^p_{\Delta_h}} - U_{S^p_{\Delta_h}}||^2_{\mathscr{U}}}}{||E_h||_{\mathscr{U}}},\ \bar{\eta}^{L,\mathrm{FD}}_{p+k}(t) \stackrel{\mathrm{def}}{=} \frac{\sqrt{\left(\mathscr{E}_{Sub,p+k}^{L,\mathrm{FD}}\right)^2 + ||\hat{U}_{S^p_{\Delta_h}} - U_{S^p_{\Delta_h}}||^2_{\mathscr{U}}}}{||E_h||_{\mathscr{U}}} \tag{5.76}$$

where $\mathscr{E}_{Sub}^{U,\mathrm{FD}}$ is the exact estimator of $||\hat{U} - \hat{U}_{S^p_{\Delta_h}}||_{\mathscr{U}}$, and $\bar{\eta}^{U,\mathrm{FD}}_{p+k}(t)$ for the computable "bound"

In the case of the exact error measured in L^2 norm, we can also calculate the effectivity index based on the exact and computed error indicator function. Thus we have

$$\bar{\zeta}^{\mathrm{FD}}(t) \stackrel{\mathrm{def}}{=} \frac{\sqrt{\sum_{\tau\in\Delta_h} \left|\left| \sum_{X\in\mathcal{N}(\Delta_h)} \hat{e}^{\mathrm{FD}}_{\omega_X^{\Delta_h}} \right|\right|^2_{L^2}} + ||\hat{U}_{S^p_{\Delta_h}} - U_{S^p_{\Delta_h}}||_{L^2}}{||E_h||_{L^2}} \tag{5.77}$$

and $\bar{\zeta}^{\mathrm{FD}}_{p+k}(t)$ when the computable indicator is used.

Remark 5.9. Note that according to (5.7), at certain time instant, i.e., $t = t_n$, we have $\hat{U}_{S^p_{\Delta_h}} = U_{S^p_{\Delta_h}}$. Thus the term $||\hat{U}_{S^p_{\Delta_h}} - U_{S^p_{\Delta_h}}||_H$ disappears at $t = t_n$.

Example 5.12. *Heat transition problem in one dimension.* Fig. 5.73 and 5.74 are the evolution plots of the relative error measured in energy and L^2 norm respectively defined as follows

$$\phi^{\mathrm{FD}}(t) \stackrel{\mathrm{def}}{=} \frac{||E_h||_{\mathscr{U}}}{||u||_{\mathscr{U}}} \times 100\% \qquad \psi^{\mathrm{FD}}(t) \stackrel{\mathrm{def}}{=} \frac{||E_h||_{L^2}}{||u||_{L^2}} \times 100\% \tag{5.78}$$

while Fig. 5.75 and 5.76 are the evolution plots of spatial and temporal ratios with respect to the total error in energy norm

$$\mu^{\mathrm{FD}}(t) \stackrel{\mathrm{def}}{=} \frac{||\rho_h||_{\mathscr{U}}}{||E_h||_{\mathscr{U}}} \times 100\% \qquad \nu^{\mathrm{FD}}(t) \stackrel{\mathrm{def}}{=} \frac{||\theta_h||_{\mathscr{U}}}{||E_h||_{\mathscr{U}}} \times 100\% \tag{5.79}$$

and in L^2 norm

$$\delta^{\mathrm{FD}}(t) \stackrel{\mathrm{def}}{=} \frac{||\rho_h||_{L^2}}{||E_h||_{L^2}} \times 100\% \qquad \vartheta^{\mathrm{FD}}(t) \stackrel{\mathrm{def}}{=} \frac{||\theta_h||_{L^2}}{||E_h||_{L^2}} \times 100\% \tag{5.80}$$

, for the fully discrete finite element solutions of degree $p = 1, 2, 3$, computed with uniform mesh size $h = \frac{L}{2^2}$ and time steps $N = 4$, 8, and 32 respectively.

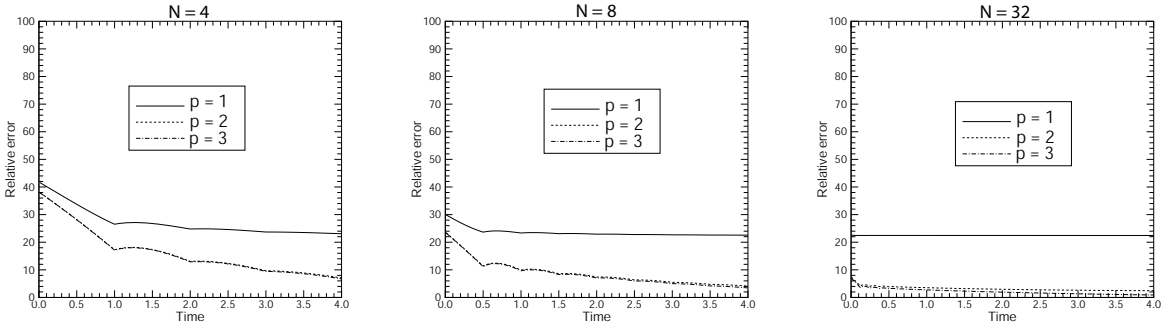

Fig. 5.73. Heat transition problem in one dimension. The evolution of the relative error $\phi^{\mathrm{FD}}(t)$ for the fully discrete finite element solutions of degree $p = 1, 2$, and 3, computed with mesh size $h = \frac{L}{2^2}$ and time steps $N = 4$, 8, and 32 respectively.

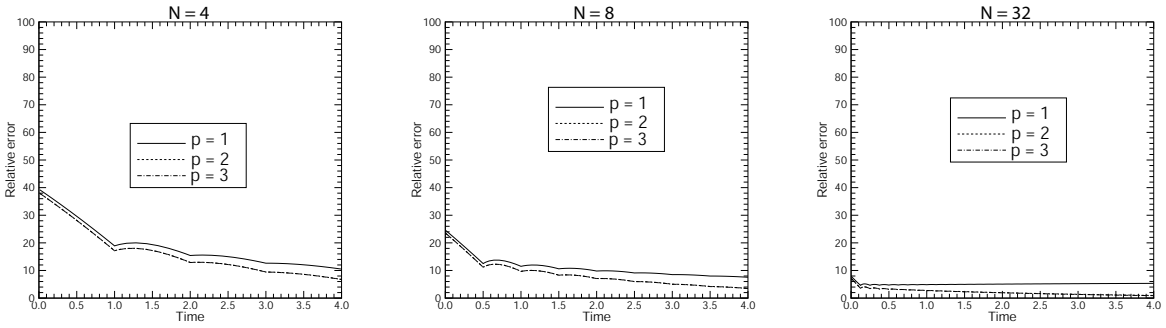

Fig. 5.74. Heat transition problem in one dimension. The evolution of the relative error $\psi^{\mathrm{FD}}(t)$ for the fully discrete finite element solutions of degree $p = 1, 2$, and 3, computed with mesh size $h = \frac{L}{2^2}$ and time steps $N = 4$, 8, and 32 respectively.

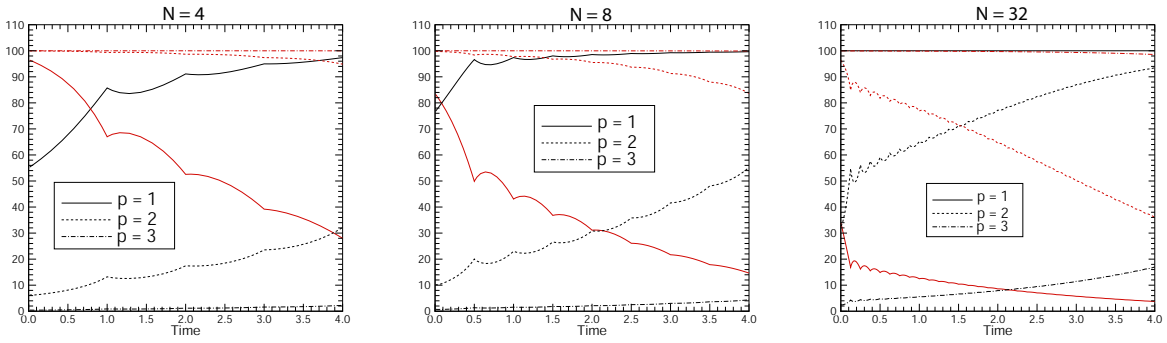

Fig. 5.75. Heat transition problem in one dimension. The evolution of the spatial error ratio $\mu^{\mathrm{FD}}(t)$ (black-color line) and the temporal error ratio $\nu^{\mathrm{FD}}(t)$ (red-color line) for the fully discrete finite element solutions of degree $p = 1, 2$, and 3, computed with mesh size $h = \frac{L}{2^2}$ and time steps $N = 4$, 8, and 32 respectively.

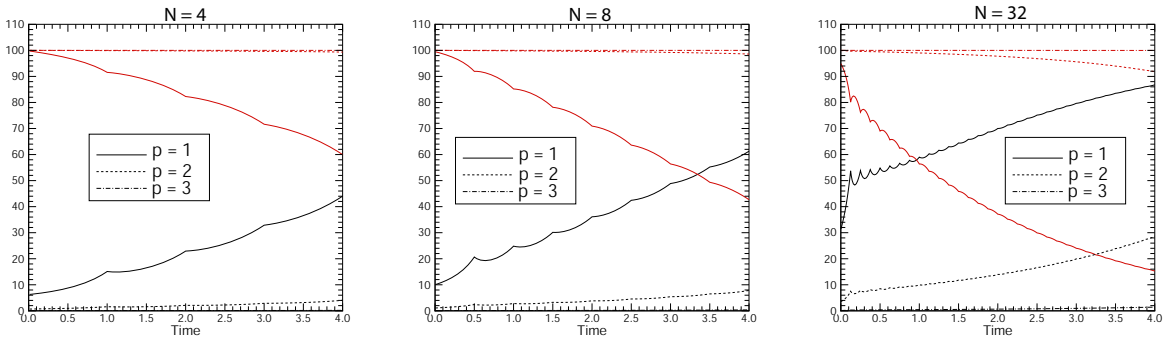

Fig. 5.76. Heat transition problem in one dimension. The evolution of the spatial error ratio $\delta^{\mathrm{FD}}(t)$ (black-color line) and the temporal error ratio $\vartheta^{\mathrm{FD}}(t)$ (red-color line) for the fully discrete finite element solutions of degree $p = 1, 2$, and 3 computedwith mesh size $h = \frac{L}{2^2}$ and time steps $N = 4$, 8, and 32 respectively.

In the case of energy norm, it can be seen from Fig. 5.75 that for cubic element $p = 3$, the temporal error is about 100% of the total error and spatial error is negligible. For quadratic element, the temporal error is dominant for time steps equal to 4 and 8 while in the case of time steps equal to 32 the temporal error is dominant at time instants close to $t = 0$ and as time evolves the spatial error becomes dominant. For linear element, the spatial error is 100% of the total error in the case of time

steps equal to 32 while for time steps equal to 4 and 8 the temporal error is dominant at time instants close to $t = 0$ and as time evolves the spatial error is dominant and close to 100%.

In the case of L^2 norm, it can be that for quadratic and cubic element $p = 2, 3$ the temporal error is dominant and about 100% of the total error. For linear element $p = 1$ and time steps equal to 4, the temporal error is dominant for the whole time interval and as time evolves it starts decreasing while spatial error increases. In the case of time steps equal to 8 and 32, in the beginning the temporal error is dominant and as time evolves temporal error starts decreasing and the spatial error becomes dominant. It takes less time for spatial error to be dominant for time steps equal to 32 than for time steps equal to 8.

Fig. 5.77 (resp. Fig. 5.78) is the evolution of effectivity index $\zeta^{\mathrm{FD}}(t)$ (resp. its computable version $\eta^{\mathrm{FD}}_{S^{p+k}_{\Delta_{h'}}}(t)$) based on the elliptic reconstruction problem from the fully discrete finite element solution. It can be seen that except at time instants close to $t = 0$ we can expect good effectivity indices equal to 1 as long as the spatial error is close to 100% of the total error, which is obvious in the case of linear element $p = 1$ and time steps equal to 32. Moreover, we also have good effectivity indices at the end of each time interval, namely $t = t_n$, if spatial error becomes dominant. However, if temporal error is dominant, we can expect $\zeta^{\mathrm{FD}}(t)$ and $\eta^{\mathrm{FD}}_{S^{p+k}_{\Delta_{h'}}}(t)$ close to 0 at $t = t_n$. Note that the element order $p + k$ increases, $\eta^{\mathrm{FD}}_{S^{p+k}_{\Delta_{h'}}}(t)$ converges to its exact value $\zeta^{\mathrm{FD}}(t)$. In the case of the error measured in L^2 norm, we can observe similar behavior in the performance of effectivity index $\zeta^{\mathrm{FD}}(t)$ and $\zeta^{\mathrm{FD}}_{S^{p+k}_{\Delta_{h'}}}(t)$ as shown in Figs. 5.79 and 5.80.

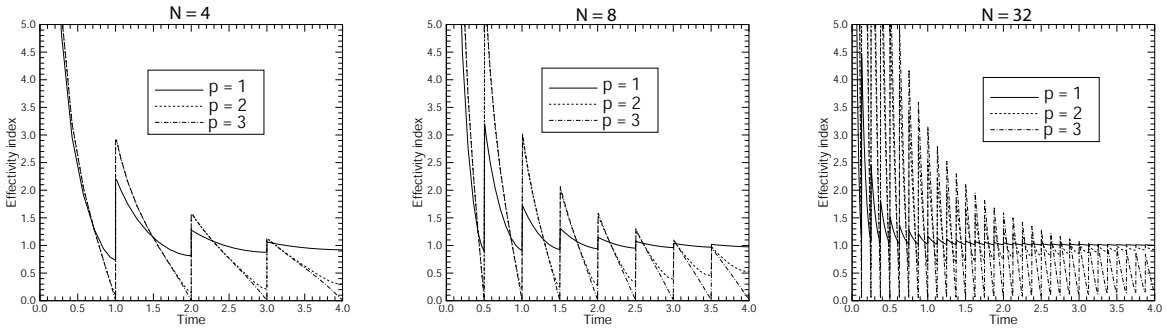

Fig. 5.77. Heat transition problem in one dimension. The evolution of effectivity index $\eta^{\mathrm{FD}}(t)$ based on the exact solution $\hat{U}$ of the elliptic reconstruction problem. Note that the elliptic reconstruction problem is constructed from the fully discrete finite element solutions of degree $p = 1, 2$, and 3, computed with mesh size $h = \frac{L}{2^2}$ and time steps $N = 4$, 8, and 32 respectively.

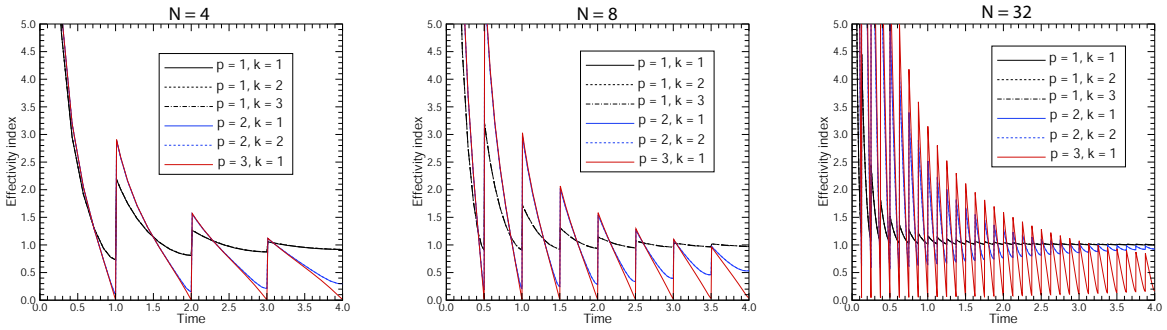

Fig. 5.78. Heat transition problem in one dimension. The evolution of effectivity index $\eta^{\mathrm{FD}}_{S^{p+k}_{\Delta_{h'}}}(t)$ based on the approximate solution $\hat{U}_{S^{p+k}_{\Delta'_h}}$ of the elliptic reconstruction problem. Note that the elliptic reconstruction problem is constructed from the fully discrete finite element solutions of degree $p = 1, 2$, and 3, computed with mesh size $h = \frac{L}{2^2}$ and time steps $N = 4$, 8, and 32 respectively.

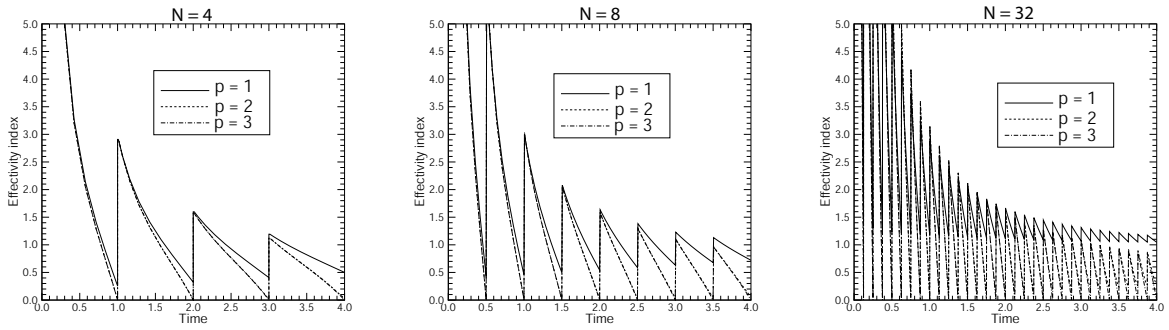

Fig. 5.79. Heat transition problem in one dimension. The evolution of effectivity index $\zeta^{\mathrm{FD}}(t)$ based on the exact solution $\hat{U}$ of the elliptic reconstruction problem. Note that the elliptic reconstruction problem is constructed from the fully discrete finite element solutions of degree $p = 1, 2$, and 3, computed with mesh size $h = \frac{L}{2^2}$ and time steps $N = 4$, 8, and 32 respectively.

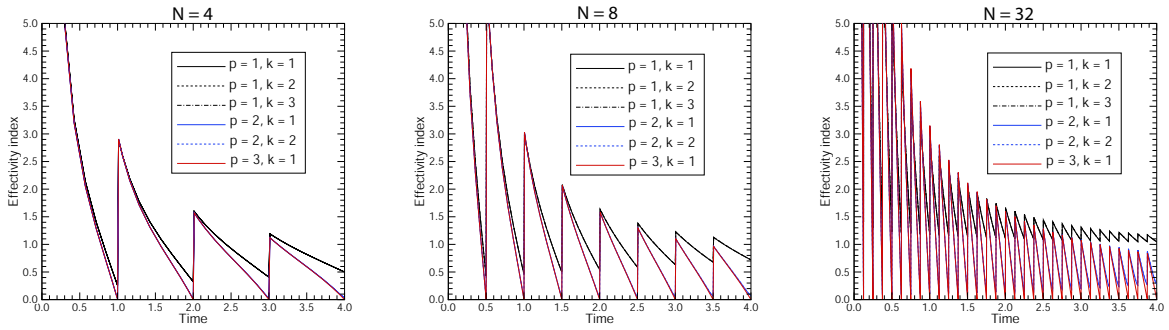

Fig. 5.80. Heat transition problem in one dimension. The evolution of effectivity index $\zeta^{\mathrm{FD}}_{S^{p+k}_{\Delta_{h'}}}(t)$ based on the approximate solution $\hat{U}_{S^{p+k}_{\Delta'_h}}$ of the elliptic reconstruction problem. Note that the elliptic reconstruction problem is constructed from the fully discrete finite element solutions of degree $p = 1, 2$, and 3, computed with mesh size $h = \frac{L}{2^2}$ and time steps $N = 4$, 8, and 32 respectively.

Fig. 5.81 (resp. Figs. 5.82 and 5.83) is the evolution of effectivity index $\bar{\eta}^{U,\mathrm{FD}}(t)$ (resp. $\bar{\eta}^{U,\mathrm{FD}}_{p+k}(t)$ and $\bar{\eta}^{L,\mathrm{FD}}_{p+k}(t)$) for the exact error measured in energy norm, where the exact error indicator function and its computed version are obtained from the subdomain residual problem of the elliptic reconstruction problems corresponding to the fully discrete finite element solution $U_{S^p_{\Delta_h}}$ of degree $p = 1, 2$, and 3 with $N = 4, 8$,

and 32.

It can be observed that when the temporal error is negligible in comparison of the spatial error such as the case of $p = 1, N = 32$, the effectivity index $\bar{\eta}^{U,\mathrm{FD}}(t)$ is close to 1 and this especially holds at the time instant $t = t_n$ for each time interval $(t_{n-1}, t_n]$. Similar behavior can be observed for $\bar{\eta}^{U,\mathrm{FD}}_{p+k}(t)$ and $\bar{\eta}^{L,\mathrm{FD}}_{p+k}(t)$ which converge to the exact $\bar{\eta}^{U,\mathrm{FD}}(t)$ with the increase of polynomial order $p+k$. Note that $\bar{\eta}^{L,\mathrm{FD}}_{p+k}(t)$ is greater than 1 which means that the lower bound is not necessary a guaranteed lower bound for the exact error $||E_h||_{\mathcal{U}(\Omega)}$ even though $\mathscr{E}^{L,\mathrm{FD}}_{Sub,p+k}$ is indeed a lower bound for the exact error $||\hat{U} - U_{S^p_{\Delta_h}}||_{\mathcal{U}(\Omega)}$ of the elliptic reconstruction problem.

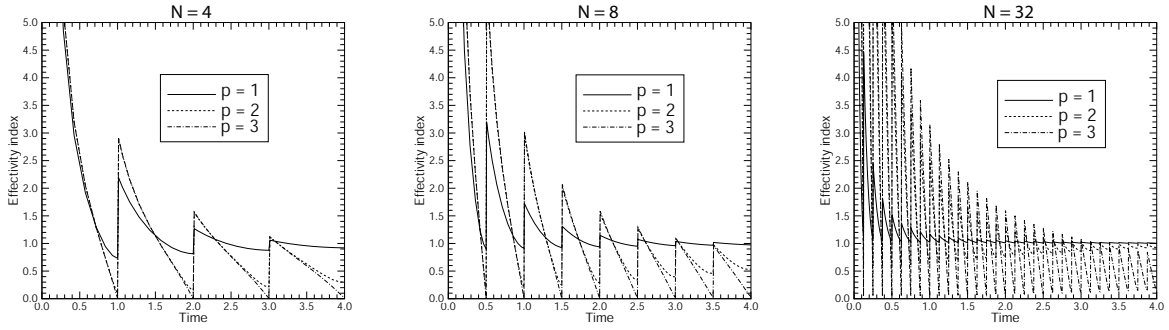

Fig. 5.81. Heat transition problem in one dimension. The evolution of effectivity index $\bar{\eta}^{U,\mathrm{FD}}(t)$ for the exact error measured in energy norm based on exact estimator of the subdomain residual problem of the elliptic reconstruction problem.

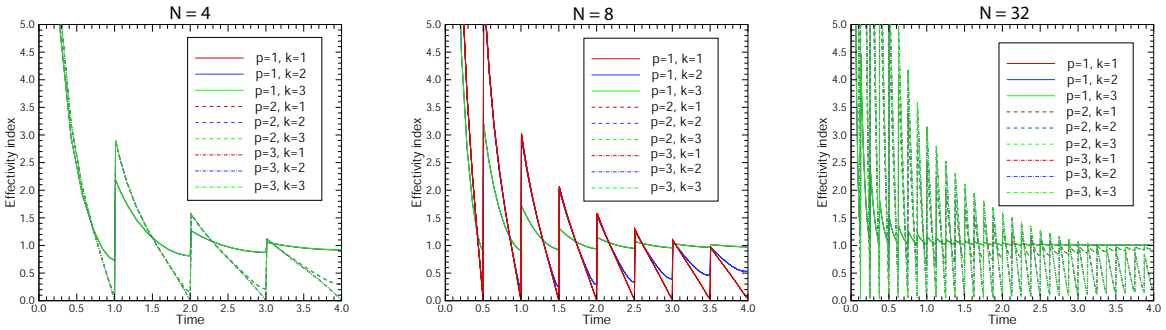

Fig. 5.82. Heat transition problem in one dimension. The evolution of effectivity index $\bar{\eta}_{p+k}^{U,\mathrm{FD}}(t)$ for the exact error measured in energy norm based on exact estimator of the subdomain residual problem of the elliptic reconstruction problem.

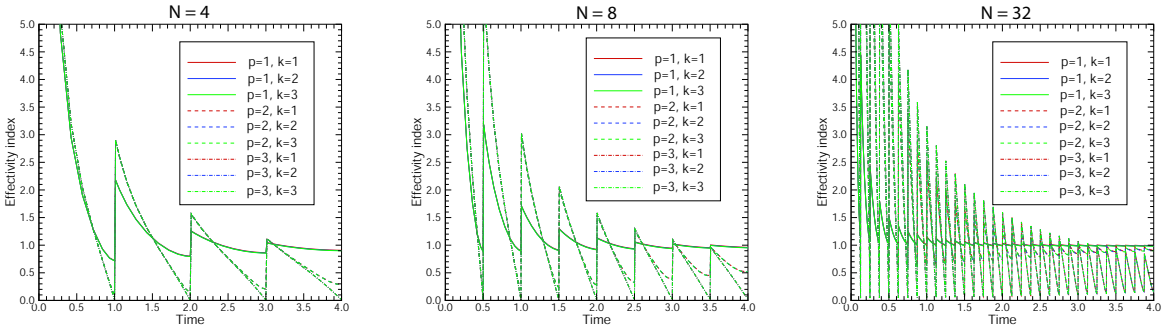

Fig. 5.83. Heat transition problem in one dimension. The evolution of effectivity index $\bar{\eta}_{p+k}^{L,\mathrm{FD}}(t)$ for the exact error measured in energy norm based on exact estimator of the subdomain residual problem of the elliptic reconstruction problem.

Fig. 5.84 is the time evolution of effectivity index $\bar{\zeta}^{\mathrm{FD}}(t)$. It can be seen that when the spatial error is dominant, $\bar{\zeta}^{\mathrm{FD}}(t)$ is close to 1 at time instant $t = t_n$ for each time interval $(t_{n-1}, t_n]$ which is obvious in the case of $N = 32$. The computable version of $\bar{\zeta}_{p+k}^{\mathrm{FD}}(t)$ which converges to the exact version $\bar{\zeta}^{\mathrm{FD}}(t)$ has similar performance as shown in Fig. 5.85.

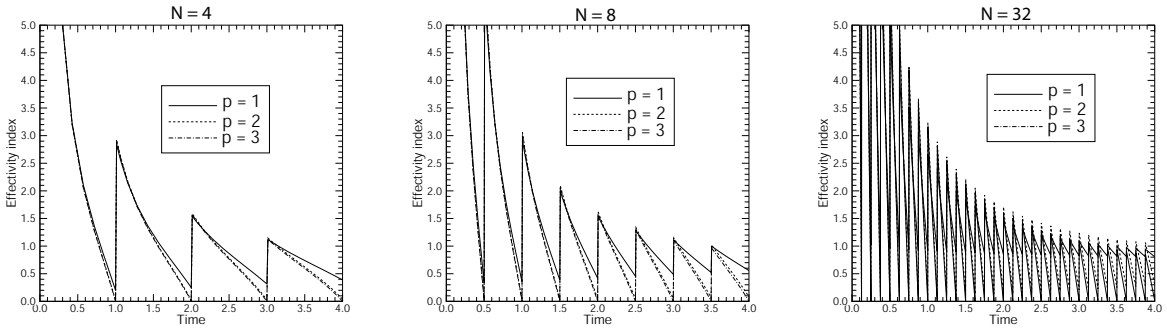

Fig. 5.84. Heat transition problem in one dimension. The evolution of effectivity index $\bar{\zeta}^{\mathrm{FD}}(t)$ for the exact error measured in L^2 norm based on the exact estimator of the subdomain residual problem of the elliptic reconstruction problem.

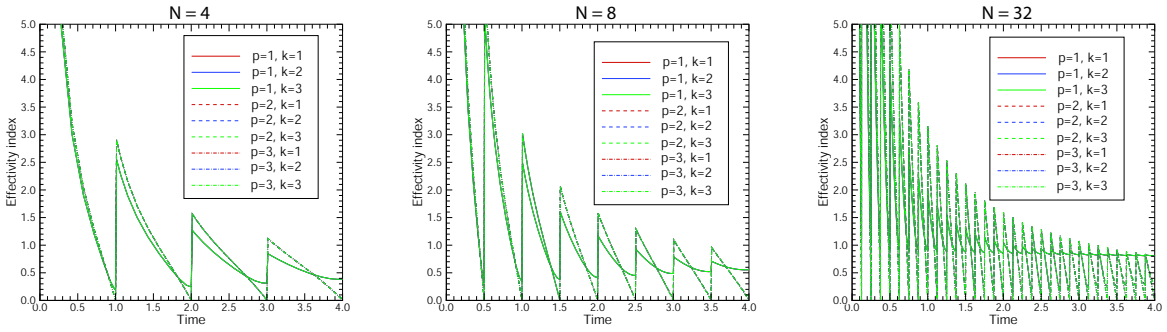

Fig. 5.85. Heat transition problem in one dimension. The evolution of effectivity index $\bar{\zeta}^{\mathrm{FD}}_{p+k}(t)$ for the exact error measured in L^2 norm based on the exact estimator of the subdomain residual problem of the elliptic reconstruction problem.

Example 5.13. *Two dimensional synthetic problem.* Figs. 5.86 and 5.87 are the evolution plots of the relative error $\phi^{\mathrm{FD}}(t)$ and $\psi^{\mathrm{FD}}(t)$, and Figs. 5.88 and 5.89 are the evolution plots of spatial and temporal ratios with respect to the total error for $\mu^{\mathrm{FD}}(t)$ and $\nu^{\mathrm{FD}}(t)$ in energy norm and for $\delta^{\mathrm{FD}}(t)$ and $\vartheta^{\mathrm{FD}}(t)$ in L^2 norm, for the fully discrete finite element solutions of degree $p = 1, 2, 3$, computed with uniform mesh size $h = \frac{L}{2^2}$ and time steps $N = 4$, 8, and 32 respectively.

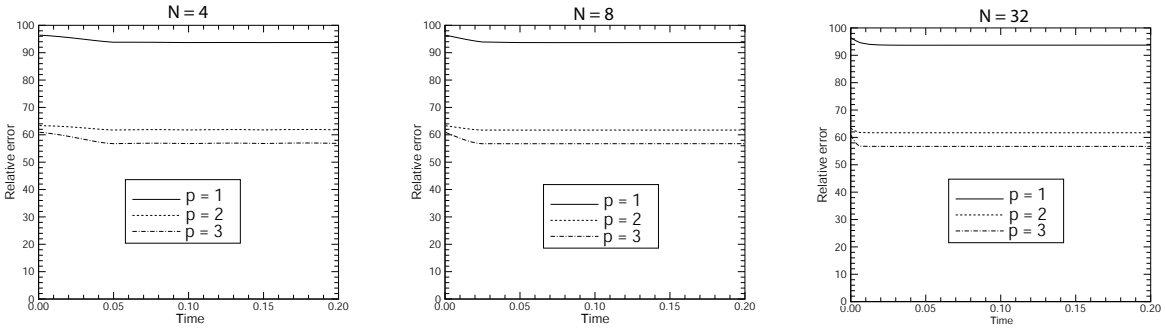

Fig. 5.86. Two dimensional synthetic problem. The evolution of the relative error $\phi^{\mathrm{FD}}(t)$ for the fully discrete finite element solutions of degree $p = 1, 2$, and 3, computed with mesh size $h = \frac{L}{2^2}$ and time steps $N = 4$, 8, and 32 respectively.

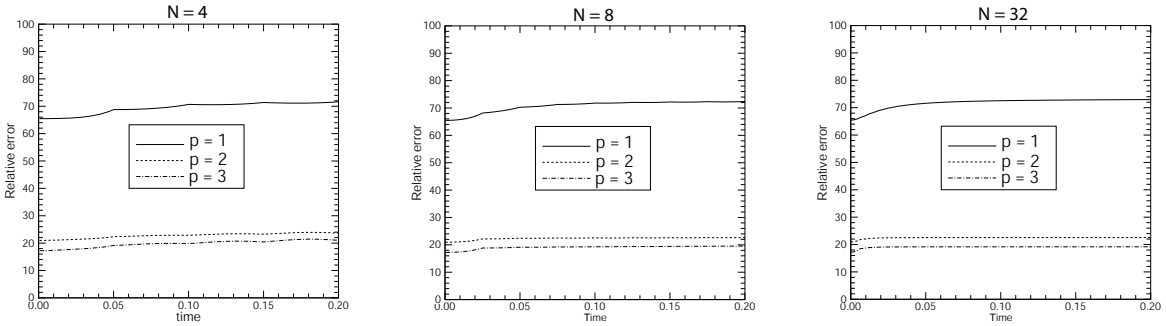

Fig. 5.87. Two dimensional synthetic problem. The evolution of the relative error $\psi^{\mathrm{FD}}(t)$ for the fully discrete finite element solutions of degree $p = 1, 2$, and 3, computed with mesh size $h = \frac{L}{2^2}$ and time steps $N = 4$, 8, and 32 respectively.

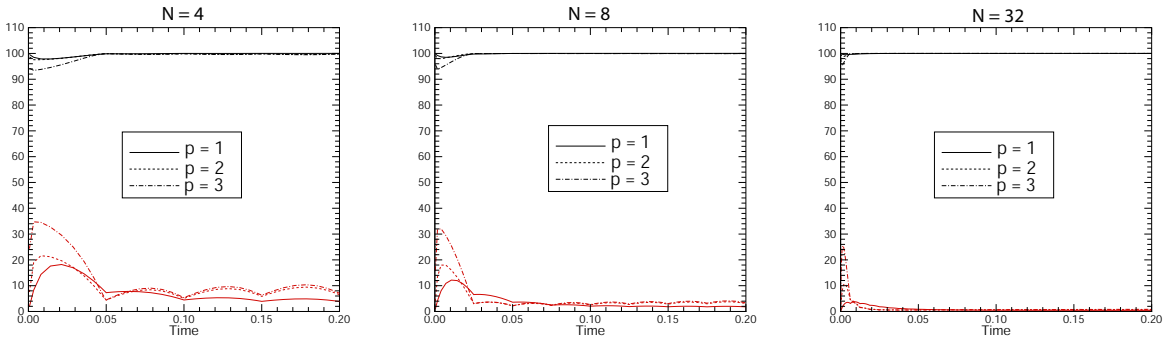

Fig. 5.88. Two dimensional synthetic problem. The evolution of the spatial error ratio $\mu^{\mathrm{FD}}(t)$ (black-color line) and the temporal error ratio $\nu^{\mathrm{FD}}(t)$ (red-color line) for the fully discrete finite element solutions of degree $p = 1, 2$, and 3, computed with mesh size $h = \frac{L}{2^2}$ and time steps $N = 4$, 8, and 32 respectively.

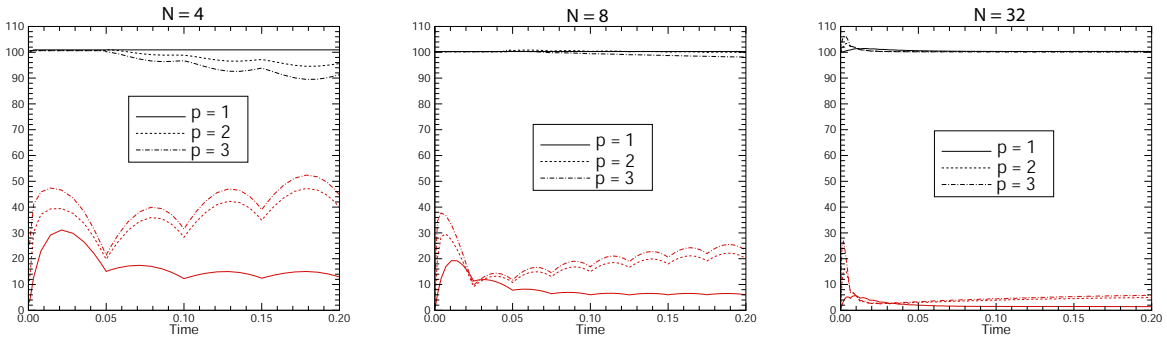

Fig. 5.89. Two dimensional synthetic problem. The evolution of the spatial error ratio $\delta^{\mathrm{FD}}(t)$ (black-color line) and the temporal error ratio $\vartheta^{\mathrm{FD}}(t)$ (red-color line) for the fully discrete finite element solutions of degree $p = 1, 2$, and 3, computed with mesh size $h = \frac{L}{2^2}$ and time steps $N = 4$, 8, and 32 respectively.

It can be seen that the relative error is not sensitive to the variation in the number of time steps, and the spatial error is dominant and about 100% of the total error during the whole solution time interval. It should be noted that the temporal error ratio is reduced with the increase of time steps as shown in Figs. 5.88 and 5.89.

Fig. 5.90 (resp. Fig. 5.91) is the evolution of effectivity index $\eta^{\mathrm{FD}}(t)$ (resp. its computable version $\eta^{\mathrm{FD}}_{S^{p+k}_{\Delta_{h'}}}(t)$) based on the elliptic reconstruction problem from the

fully discrete finite element solution for the exact error measured in energy norm. $\zeta^{\mathrm{FD}}(t)$ is basically 1 for the whole solution time interval due to the fact that the spatial error is dominant and about 100% of the total error as shown in Fig. 5.86. The computable $\eta^{\mathrm{FD}}_{S^{p+k}_{\Delta_{h'}}}(t)$ converges to the exact value $\zeta^{\mathrm{FD}}(t)$ very fast with the increase of element order $p+k$. For instance, for $p=2$ and $k=1$, $\eta^{\mathrm{FD}}_{S^{p+k}_{\Delta_{h'}}}(t)$ is about 0.4 while it is close to 0.9 with $k=2$. We can observe similar behavior in $\zeta^{\mathrm{FD}}(t)$ and its computable version $\zeta^{\mathrm{FD}}_{S^{p+k}_{\Delta_{h'}}}(t)$ for the exact error measured in L^2 norm as shown in Figs. 5.92 and 5.93.

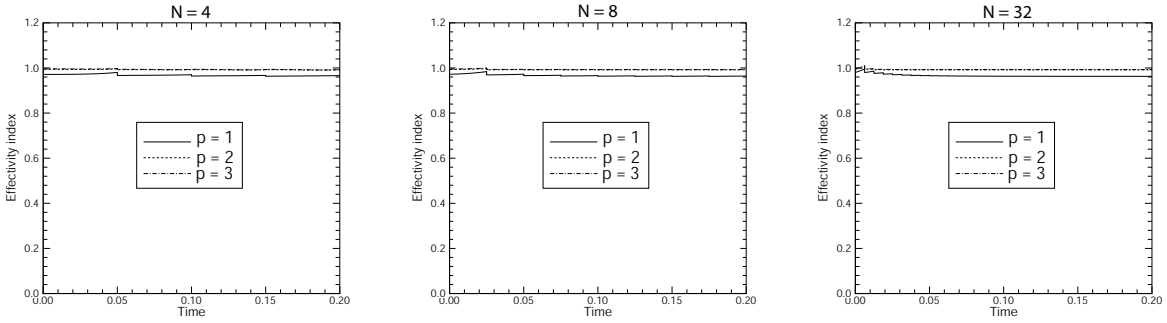

Fig. 5.90. Two dimensional synthetic problem. The evolution of effectivity index $\eta^{\mathrm{FD}}(t)$ based on the exact solution $\hat{U}$ of the elliptic reconstruction problem. Note that the elliptic reconstruction problem is constructed from the fully discrete finite element solutions of degree $p=1,2$, and 3, computed with mesh size $h=\frac{L}{2^2}$ and time steps $N=4$, 8, and 32 respectively.

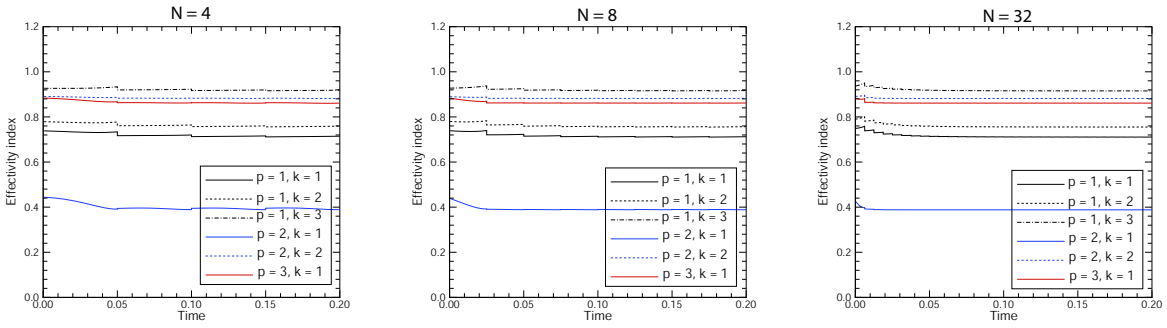

Fig. 5.91. Two dimensional synthetic problem. The evolution of effectivity index $\eta^{\mathrm{FD}}_{S^{p+k}_{\Delta_{h'}}}(t)$ based on the approximate solution $\hat{U}_{S^{p+k}_{\Delta'_h}}$ of the elliptic reconstruction problem. Note that the elliptic reconstruction problem is constructed from the fully discrete finite element solutions of degree $p = 1, 2$, and 3, computed with mesh size $h = \frac{L}{2^2}$ and time steps $N = 4$, 8, and 32 respectively.

Fig. 5.94 (resp. Figs. 5.95 and 5.96) is the evolution of effectivity index $\bar{\eta}^{U,\mathrm{FD}}(t)$ (resp. $\bar{\eta}^{U,\mathrm{FD}}_{p+k}(t)$ and $\bar{\eta}^{L,\mathrm{FD}}_{p+k}(t)$) for the exact error measured in energy norm, where the exact error indicator function and its computed version are obtained from the subdomain residual problem of the elliptic reconstruction problems corresponding to the fully discrete finite element solution $U_{S^p_{\Delta_h}}$ of degree $p = 1, 2$, and 3 with $N = 4, 8$, and 32. It can be observed that $\bar{\eta}^{U,\mathrm{FD}}(t)$ is close to 1 since the spatial error is dominant as shown in Fig. 5.88. The computable upper bound $\bar{\eta}^{U,\mathrm{FD}}_{p+k}(t)$ and lower bound $\bar{\eta}^{L,\mathrm{FD}}_{p+k}(t)$ have performance similar to $\bar{\eta}^{U,\mathrm{FD}}(t)$. Note that $\bar{\eta}^{L,\mathrm{FD}}_{p+k}(t)$ is indeed lower bound.

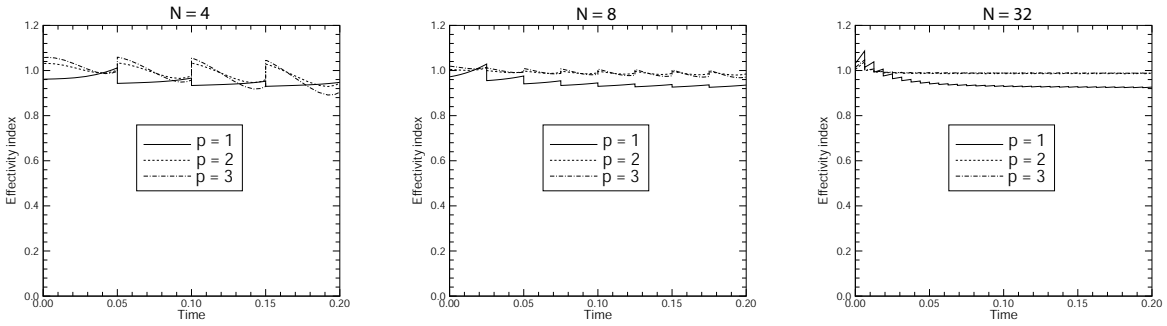

Fig. 5.92. Two dimensional synthetic problem. The evolution of effectivity index $\zeta^{\mathrm{FD}}(t)$ based on the exact solution $\hat{U}$ of the elliptic reconstruction problem. Note that the elliptic reconstruction problem is constructed from the fully discrete finite element solutions of degree $p = 1, 2$, and 3, computed with mesh size $h = \frac{L}{2^2}$ and time steps $N = 4$, 8, and 32 respectively.

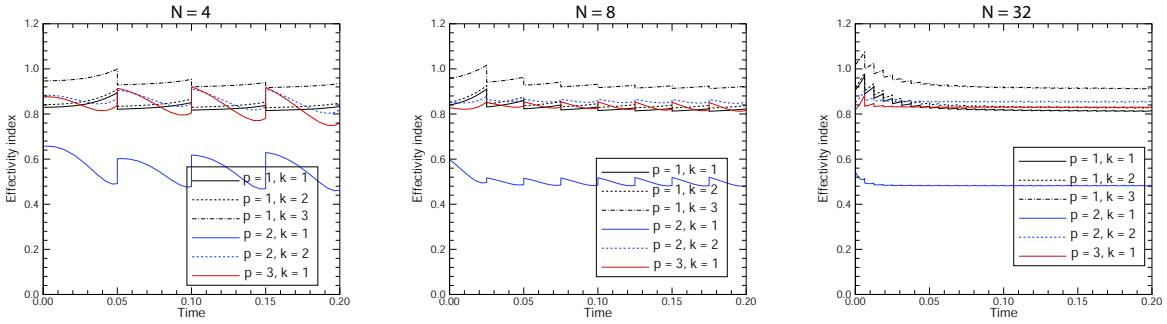

Fig. 5.93. Two dimensional synthetic problem. The evolution of effectivity index $\zeta^{\mathrm{FD}}_{S^{p+k}_{\Delta_{h'}}}(t)$ based on the approximate solution $\hat{U}_{S^{p+k}_{\Delta'_h}}$ of the elliptic reconstruction problem. Note that the elliptic reconstruction problem is constructed from the fully discrete finite element solutions of degree $p = 1, 2$, and 3, computed with mesh size $h = \frac{L}{2^2}$ and time steps $N = 4$, 8, and 32 respectively.

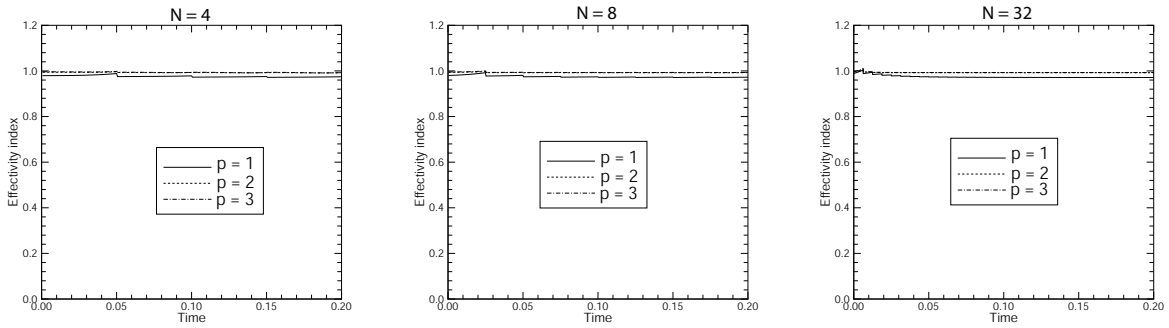

Fig. 5.94. Two dimensional synthetic problem. The evolution of effectivity index $\bar{\eta}^{U,\mathrm{FD}}(t)$ for the exact error measured in energy norm based on exact estimator of the subdomain residual problem of the elliptic reconstruction problem.

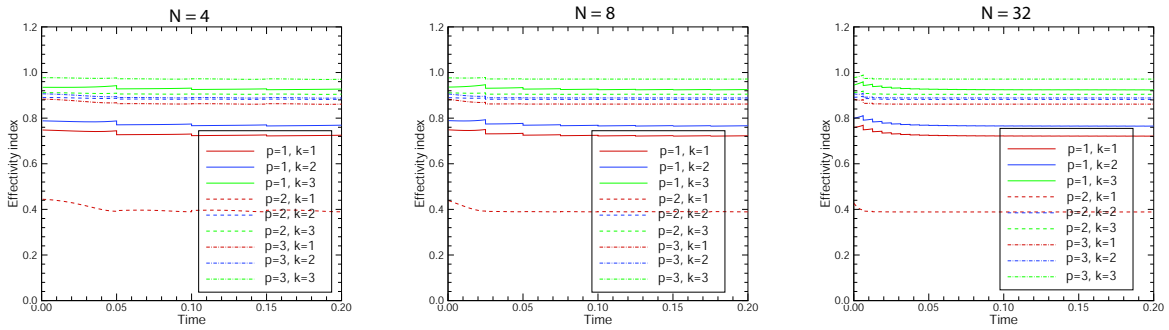

Fig. 5.95. Two dimensional synthetic problem. The evolution of effectivity index $\bar{\eta}^{U,\mathrm{FD}}_{p+k}(t)$ for the exact error measured in energy norm based on exact estimator of the subdomain residual problem of the elliptic reconstruction problem.

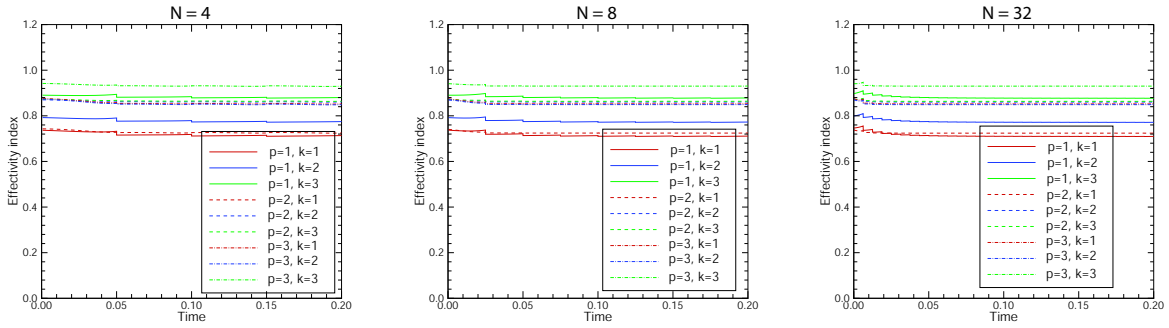

Fig. 5.96. Two dimensional synthetic problem. The evolution of effectivity index $\bar{\eta}^{L,\mathrm{FD}}_{p+k}(t)$ for the exact error measured in energy norm based on exact estimator of the subdomain residual problem of the elliptic reconstruction problem.

Fig. 5.97 is the time evolution of effectivity index $\bar{\zeta}^{\mathrm{FD}}(t)$. It can be seen that in the case of $p = 1$, $\bar{\zeta}^{\mathrm{FD}}(t)$ overestimates the exact error $||E_h||_{L^2(\Omega)}$. For $p = 2, 3$, the effectivity index $\bar{\zeta}^{\mathrm{FD}}(t)$ is close to 1 for the whole time interval $(0, T]$ and at time instant $t = t_n$, $\bar{\zeta}^{\mathrm{FD}}(t)$ is basically 1. The computable version of $\bar{\zeta}^{\mathrm{FD}}_{p+k}(t)$ which converges to the exact version $\bar{\zeta}^{\mathrm{FD}}(t)$ has similar performance as shown in Fig. 5.98.

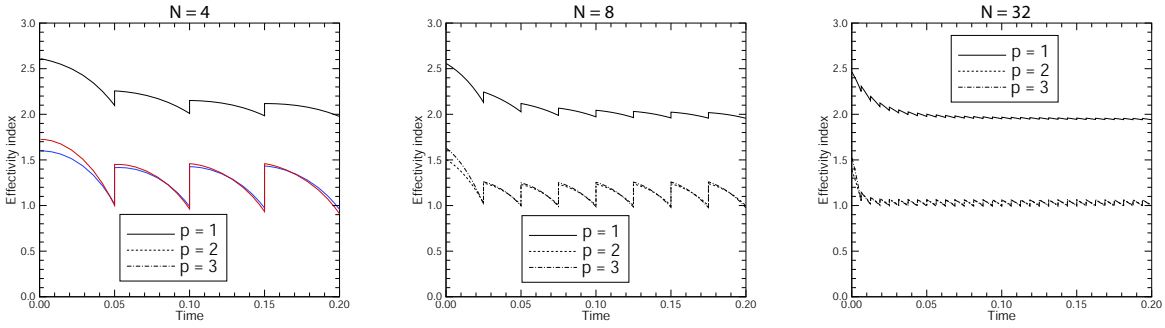

Fig. 5.97. Two dimensional synthetic problem. The evolution of effectivity index $\bar{\zeta}^{\mathrm{FD}}(t)$ for the exact error measured in L^2 norm based on the exact estimator of the subdomain residual problem of the elliptic reconstruction problem.

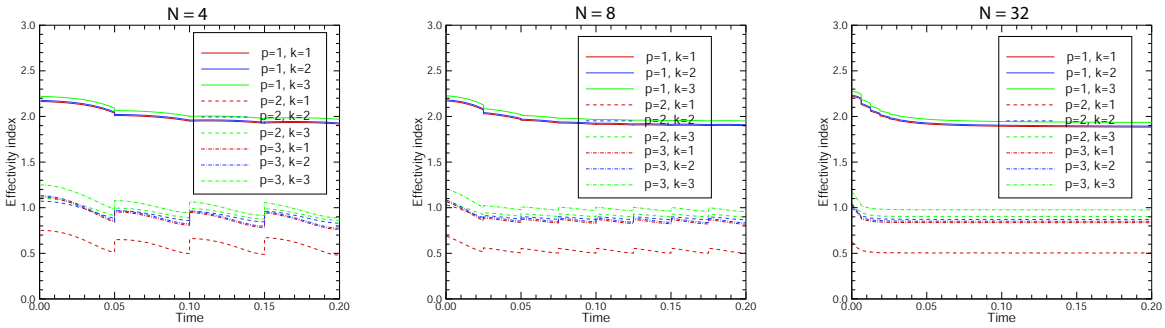

Fig. 5.98. Two dimensional synthetic problem. The evolution of effectivity index $\bar{\zeta}^{\mathrm{FD}}_{p+k}(t)$ for the exact error measured in L^2 norm based on the exact estimator of the subdomain residual problem of the elliptic reconstruction problem.

Example 5.14. *L-shaped domain problem.* Figs. 5.99 and 5.100 are the evolution plots of the relative error $\phi^{\mathrm{FD}}(t)$ and $\psi^{\mathrm{FD}}(t)$, and Figs. 5.101 and 5.102 are the

evolution plots of spatial and temporal ratios with respect to the total error for $\mu^{\mathrm{FD}}(t)$ and $\nu^{\mathrm{FD}}(t)$ in energy norm and for $\delta^{\mathrm{FD}}(t)$ and $\vartheta^{\mathrm{FD}}(t)$ in L^2 norm, for the fully discrete finite element solutions of degree $p = 1, 2, 3$, computed with uniform mesh size $h = \frac{L}{2^2}$ and time steps $N = 4$, 8, and 32 respectively.

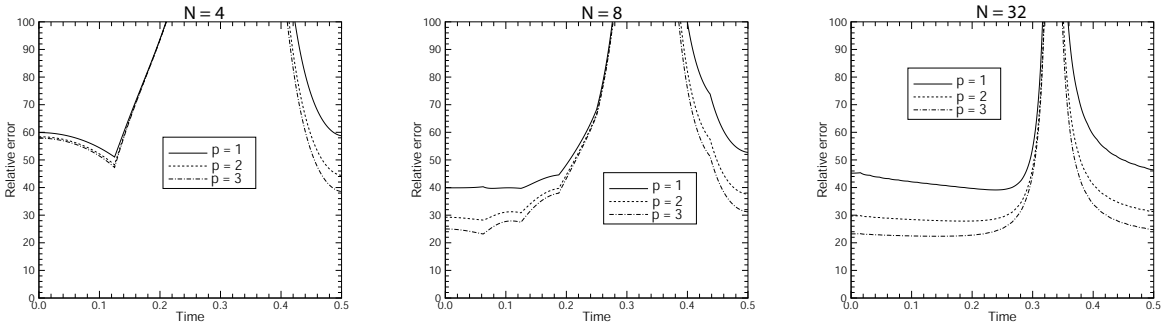

Fig. 5.99. L-shaped domain problem. The evolution of the relative error $\phi^{\mathrm{FD}}(t)$ for the fully discrete finite element solutions of degree $p = 1, 2$, and 3, computed with mesh size $h = \frac{L}{2^2}$ and time steps $N = 4$, 8, and 32 respectively.

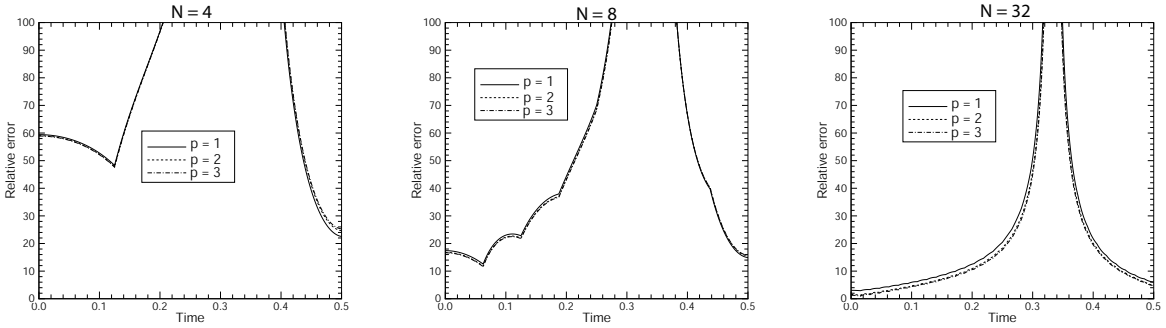

Fig. 5.100. L-shaped domain problem. The evolution of the relative error $\psi^{\mathrm{FD}}(t)$ for the fully discrete finite element solutions of degree $p = 1, 2$, and 3, computed with mesh size $h = \frac{L}{2^2}$ and time steps $N = 4$, 8, and 32 respectively.

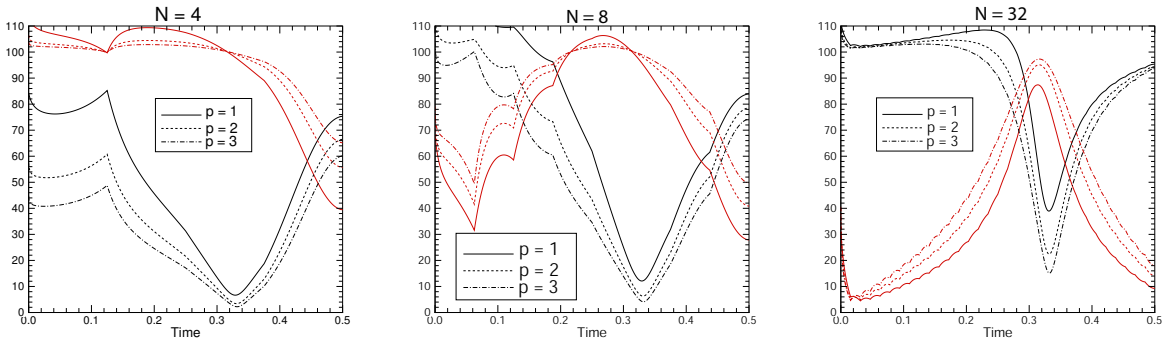

Fig. 5.101. L-shaped domain problem. The evolution of the spatial error ratio $\mu^{\mathrm{FD}}(t)$ (black-color line) and the temporal error ratio $\nu^{\mathrm{FD}}(t)$ (red-color line) for the fully discrete finite element solutions of degree $p = 1, 2$, and 3, computed with mesh size $h = \frac{L}{2^2}$ and time steps $N = 4$, 8, and 32 respectively.

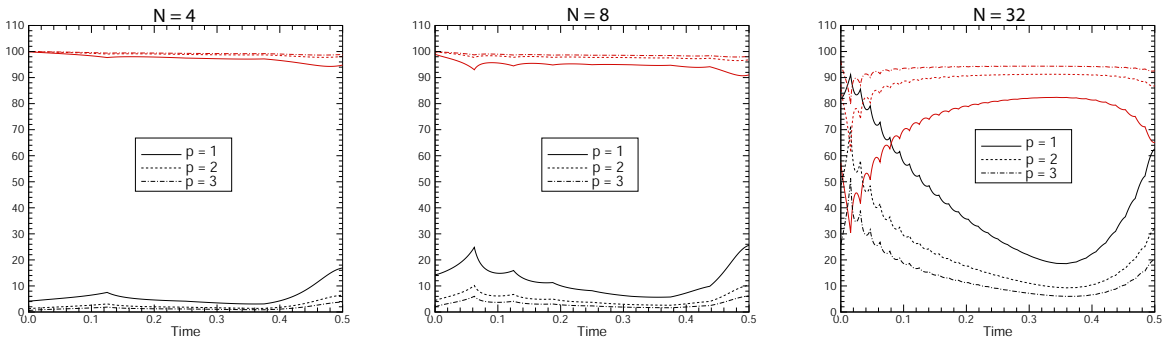

Fig. 5.102. L-shaped domain problem. The evolution of the spatial error ratio $\delta^{\mathrm{FD}}(t)$ (black-color line) and the temporal error ratio $\vartheta^{\mathrm{FD}}(t)$ (red-color line) for the fully discrete finite element solutions of degree $p = 1, 2$, and 3, computed with mesh size $h = \frac{L}{2^2}$ and time steps $N = 4$, 8, and 32 respectively.

First it can be seen that the relative error both in energy and L^2 norm tends to go to infinity as the time is close to the instant $t = \frac{1}{3}$ at which the exact solution is zero. In the energy norm case, the temporal error is dominant for almost all the whole time interval except the time instants close to the final time T when the number of time steps $N = 4$ is employed. As the number of time steps increases, it can be seen that the spatial error becomes dominant except those time intervals which are close to the

time instant at which the exact solution is zero, which can be observed obviously for $N = 32$. In the L^2 norm case, it can be seen that for $N = 4, 8$, the temporal error is about 100% of the total error. Even in the case of $N = 32$, except those time instants close to $t = 0$, the temporal error is still dominant most of the time.

Fig. 5.103 (resp. Fig. 5.104) is the evolution of effectivity index $\eta^{\mathrm{FD}}(t)$ (resp. its computable version $\eta^{\mathrm{FD}}_{S^{p+k}_{\Delta_{h'}}}(t)$) based on the elliptic reconstruction problem from the fully discrete finite element solution for the exact error measured in energy norm. In comparison of Fig. 5.101, it can be seen that $\zeta^{\mathrm{FD}}(t)$ has good effectivity index at the time instant $t = t_n$ for each time interval $(t_{n-1}, t_n]$. For example, in the case of $N = 32$, we have $\zeta^{\mathrm{FD}}(t)$ close to 1.2 at time instant $t = t_n$ if the temporal error at $t = t_n$ is negligible compared with the spatial error. However, this is not the case for the time instants within the time interval $(t_{n-1}, t_n]$. We can observe similar behavior in the computable version $\eta^{\mathrm{FD}}_{S^{p+k}_{\Delta_{h'}}}(t)$ which converges to $\zeta^{\mathrm{FD}}(t)$ with the increase of polynomial order $p + k$.

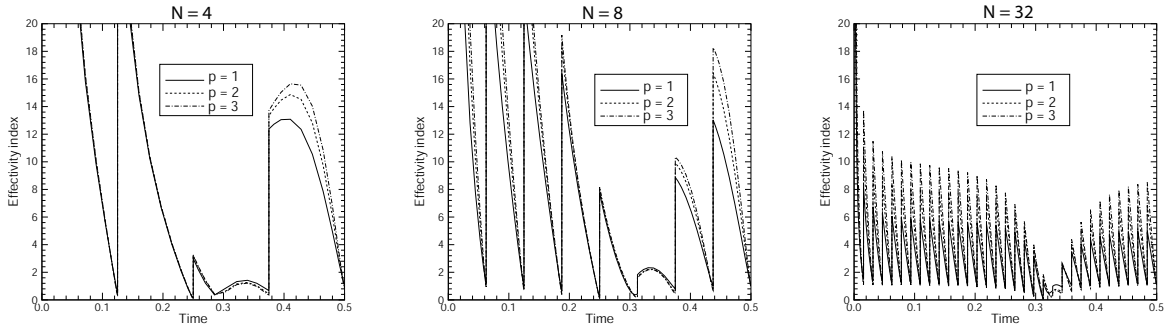

Fig. 5.103. L-shaped domain problem. The evolution of effectivity index $\eta^{\mathrm{FD}}(t)$ based on the exact solution $\hat{U}$ of the elliptic reconstruction problem. Note that the elliptic reconstruction problem is constructed from the fully discrete finite element solutions of degree $p = 1, 2$, and 3, computed with mesh size $h = \frac{L}{2^2}$ and time steps $N = 4$, 8, and 32 respectively.

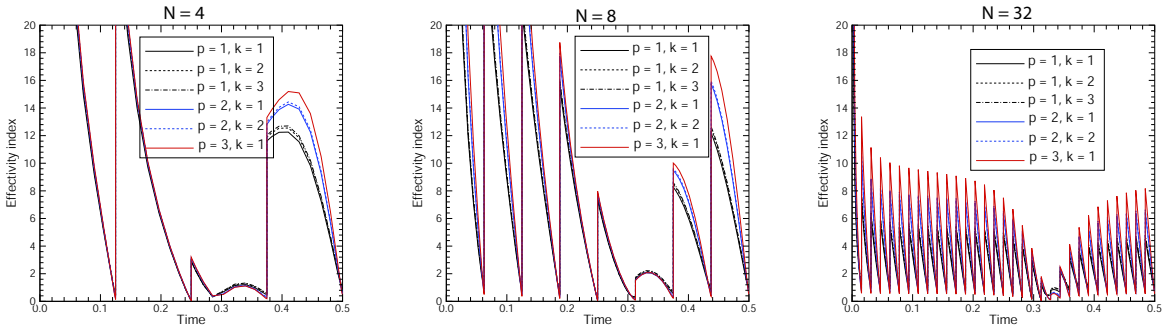

Fig. 5.104. L-shaped domain problem. The evolution of effectivity index $\eta^{\mathrm{FD}}_{S^{p+k}_{\Delta_{h'}}}(t)$ based on the approximate solution $\hat{U}_{S^{p+k}_{\Delta'_h}}$ of the elliptic reconstruction problem. Note that the elliptic reconstruction problem is constructed from the fully discrete finite element solutions of degree $p = 1, 2$, and 3, computed with mesh size $h = \frac{L}{2^2}$ and time steps $N = 4$, 8, and 32 respectively.

Fig. 5.105 (resp. Fig. 5.106) is the evolution of effectivity index $\zeta^{\mathrm{FD}}(t)$ (resp. its computable version $\zeta^{\mathrm{FD}}_{S^{p+k}_{\Delta_{h'}}}(t)$) based on the elliptic reconstruction problem from the fully discrete finite element solution for the exact error measured in L^2 norm. As shown in Fig. 5.102, the temporal error is dominant for $N = 4, 8$ and $\zeta^{\mathrm{FD}}(t)$ does not have good effectivity index. In the case of $N = 32$, we can see from Fig. 5.102 that for $p = 1$ the spatial error is dominant at those time instants close to $t = 0$. However $\zeta^{\mathrm{FD}}(t)$ is still not good number even at the time instant $t = t_n$ for each time interval $(t_{n-1}, t_n]$. Similar performance happens to the computable version of $\zeta^{\mathrm{FD}}_{S^{p+k}_{\Delta_{h'}}}(t)$ which converges to $\zeta^{\mathrm{FD}}(t)$ with the increase of $p + k$.

Fig. 5.107 (resp. Figs. 5.108 and 5.109) is the evolution of effectivity index $\bar{\eta}^{U,\mathrm{FD}}(t)$ (resp. $\bar{\eta}^{U,\mathrm{FD}}_{p+k}(t)$ and $\bar{\eta}^{L,\mathrm{FD}}_{p+k}(t)$) for the exact error measured in energy norm, where the exact error indicator function and its computed version are obtained from the subdomain residual problem of the elliptic reconstruction problems corresponding to the fully discrete finite element solution $U_{S^p_{\Delta_h}}$ of degree $p = 1, 2$, and 3 with $N = 4, 8$, and 32. It can be observed that $\bar{\eta}^{U,\mathrm{FD}}(t)$ severely overestimates the exact

error in the case $N = 4, 8$. In the case of $N = 32$ for the time instants $t = t_n$ where the spatial error is dominant, we have $\bar{\eta}^{U,\mathrm{FD}}(t)$ close to 1.2. The computable upper bound $\bar{\eta}^{U,\mathrm{FD}}_{p+k}(t)$ and lower bound $\bar{\eta}^{L,\mathrm{FD}}_{p+k}(t)$ have performance similar to $\bar{\eta}^{U,\mathrm{FD}}(t)$ and converge to $\bar{\eta}^{U,\mathrm{FD}}(t)$ with the increase of polynomial order $p + k$. Note that $\bar{\eta}^{L,\mathrm{FD}}_{p+k}(t)$ is indeed lower bound.

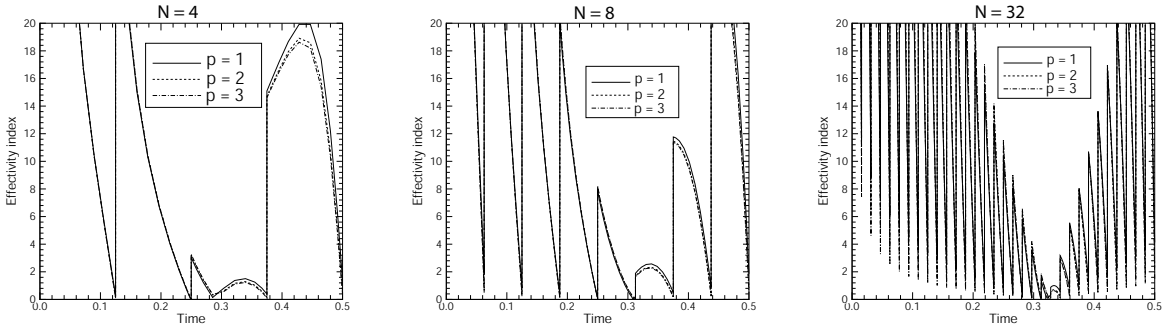

Fig. 5.105. L-shaped domain problem. The evolution of effectivity index $\zeta^{\mathrm{FD}}(t)$ based on the exact solution $\hat{U}$ of the elliptic reconstruction problem. Note that the elliptic reconstruction problem is constructed from the fully discrete finite element solutions of degree $p = 1, 2,$ and 3, computed with mesh size $h = \frac{L}{2^2}$ and time steps $N = 4$, 8, and 32 respectively.

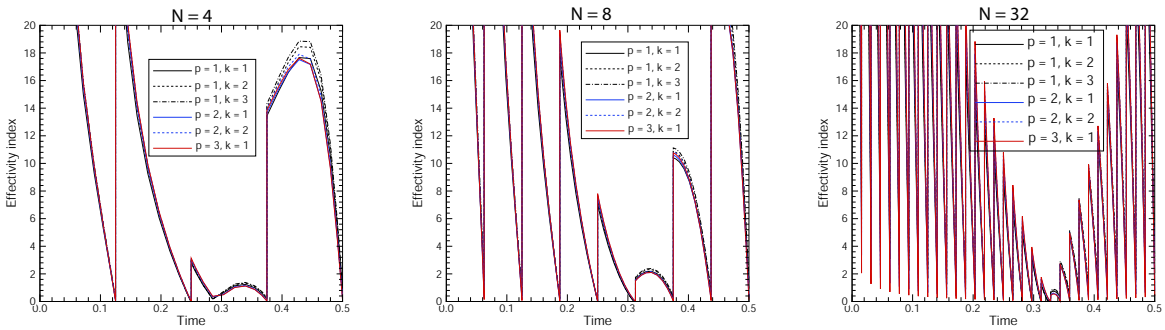

Fig. 5.106. L-shaped domain problem. The evolution of effectivity index $\zeta^{\mathrm{FD}}_{S^{p+k}_{\Delta_{h'}}}(t)$ based on the approximate solution $\hat{U}_{S^{p+k}_{\Delta'_h}}$ of the elliptic reconstruction problem. Note that the elliptic reconstruction problem is constructed from the fully discrete finite element solutions of degree $p = 1, 2,$ and 3, computed with mesh size $h = \frac{L}{2^2}$ and time steps $N = 4$, 8, and 32 respectively.

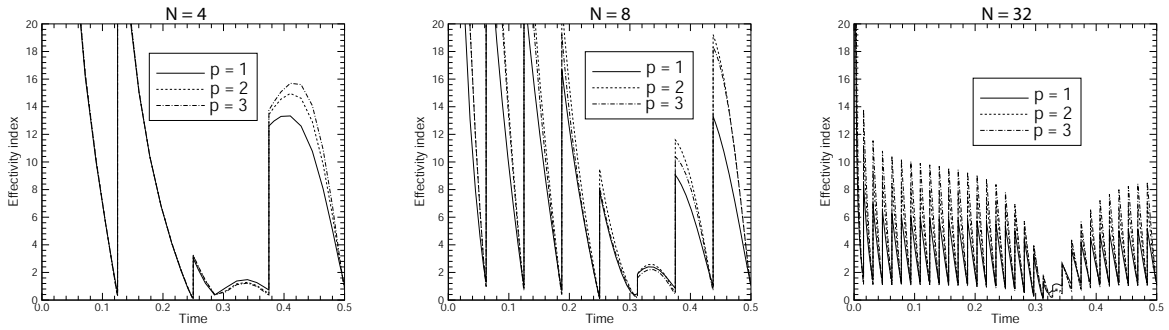

Fig. 5.107. L-shaped domain problem. The evolution of effectivity index $\bar{\eta}^{U,\mathrm{FD}}(t)$ for the exact error measured in energy norm based on exact estimator of the subdomain residual problem of the elliptic reconstruction problem.

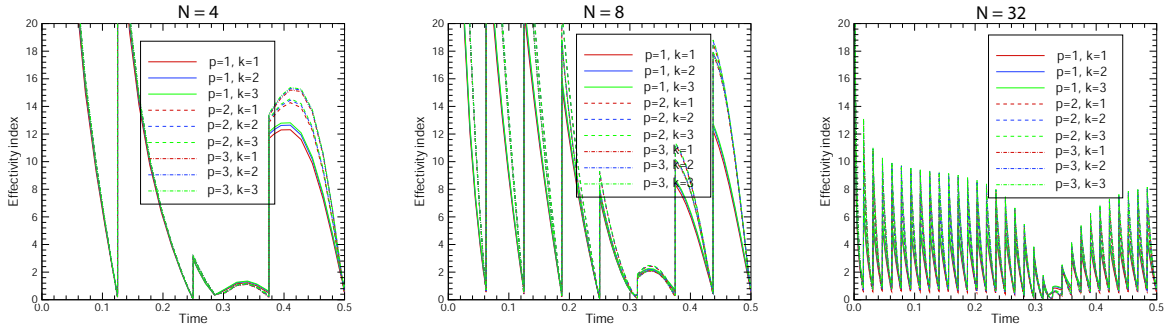

Fig. 5.108. L-shaped domain problem. The evolution of effectivity index $\bar{\eta}^{U,\mathrm{FD}}_{p+k}(t)$ for the exact error measured in energy norm based on exact estimator of the subdomain residual problem of the elliptic reconstruction problem.

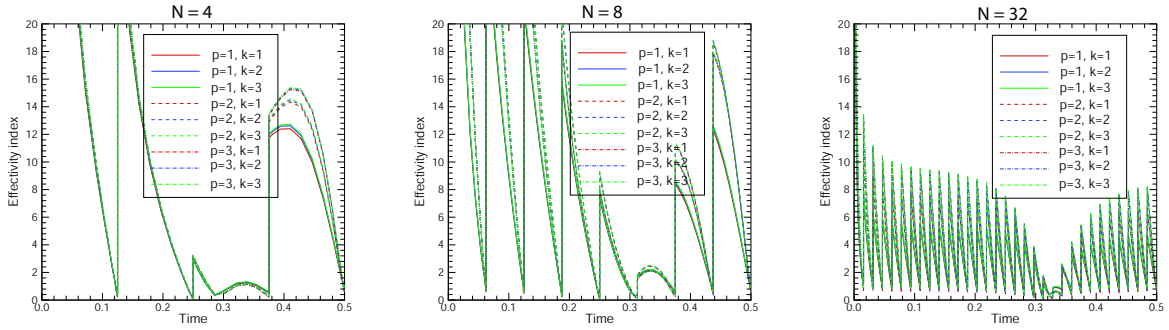

Fig. 5.109. L-shaped domain problem. The evolution of effectivity index $\bar{\eta}^{L,\mathrm{FD}}_{p+k}(t)$ for the exact error measured in energy norm based on exact estimator of the subdomain residual problem of the elliptic reconstruction problem.

Fig. 5.110 is the time evolution of effectivity index $\bar{\zeta}^{\mathrm{FD}}(t)$. It can be seen that $\bar{\zeta}^{\mathrm{FD}}(t)$ has poor performance and overestimates the exact error $||E_h||_{L^2(\Omega)}$ since the temporal error is dominant. The computable version of $\bar{\zeta}^{\mathrm{FD}}_{p+k}(t)$ which converges to the exact version $\bar{\zeta}^{\mathrm{FD}}(t)$ has similar performance as shown in Fig. 5.111.

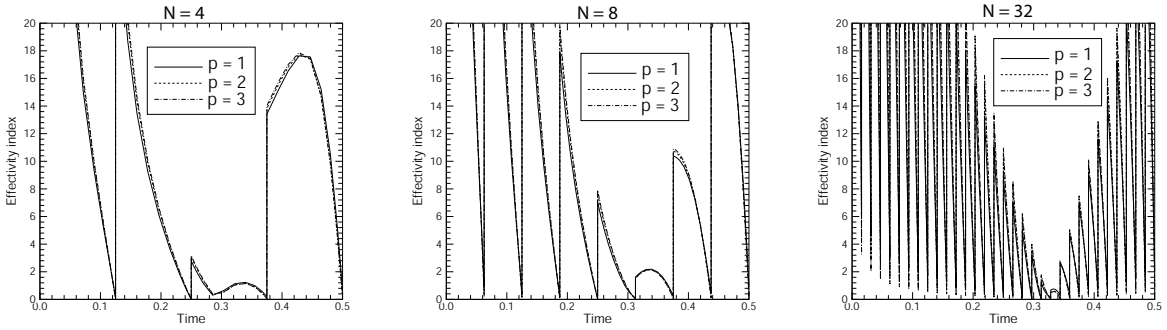

Fig. 5.110. L-shaped domain problem. The evolution of effectivity index $\bar{\zeta}^{\mathrm{FD}}(t)$ for the exact error measured in L^2 norm based on the exact estimator of the subdomain residual problem of the elliptic reconstruction problem.

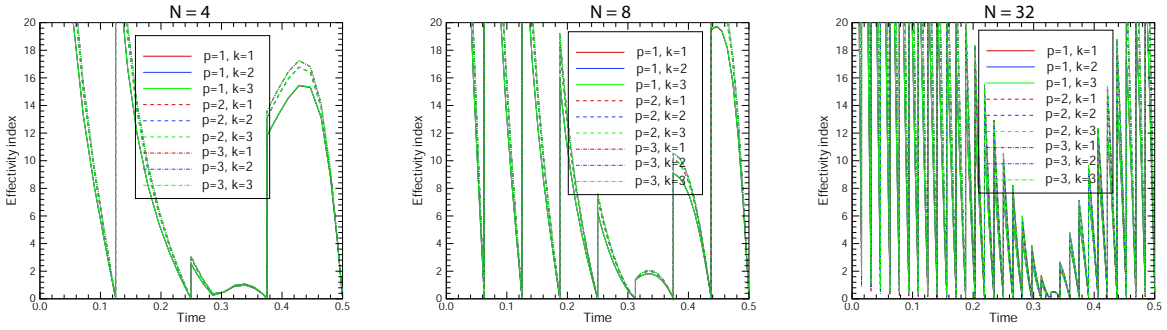

Fig. 5.111. L-shaped domain problem. The evolution of effectivity index $\bar{\zeta}^{\mathrm{FD}}_{p+k}(t)$ for the exact error measured in L^2 norm based on the exact estimator of the subdomain residual problem of the elliptic reconstruction problem.

Example 5.15. *Transient diffusion problem in a thermal battery.* Figs. 5.112 and 5.113 (resp. Figs. 5.114 and 5.115) are the evolution plots of the relative error $\phi^{\mathrm{FD}}(t)$ and $\psi^{\mathrm{FD}}(t)$, for the fully discrete finite element solutions of degree $p = 1, 2, 3$,

computed with Mesh I and time steps $N = 4$, 8, and 32 respectively for isotropic case (resp. orthotropic case). It can be seen that for both the istropic case and the orthotropic case the relative error is big at the time instants close to $t = 0$ and decreases as time evolves, and after $t \geq 1000$ the relative error remains stable since the solution is close to the steady-state as shown in Fig. 4.9, which is obvious in the case of time steps equal to 8 and 32.

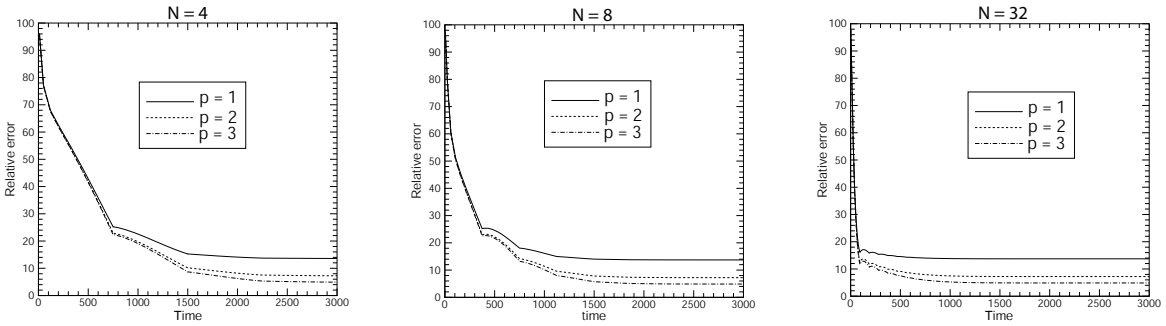

Fig. 5.112. Transient diffusion problem in a thermal battery. The evolution of the relative error $\phi^{\mathrm{FD}}(t)$ for the fully discrete finite element solutions of degree $p = 1, 2$, and 3, computed with Mesh I and time steps $N = 4$, 8, and 32 respectively for isotropic case.

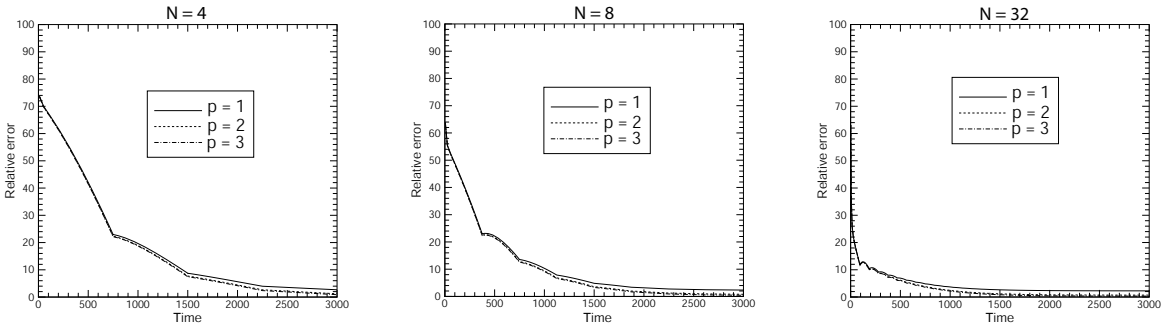

Fig. 5.113. Transient diffusion problem in a thermal battery. The evolution of the relative error $\psi^{\mathrm{FD}}(t)$ for the fully discrete finite element solutions of degree $p = 1, 2$, and 3, computed with Mesh I and time steps $N = 4$, 8, and 32 respectively for isotropic case.

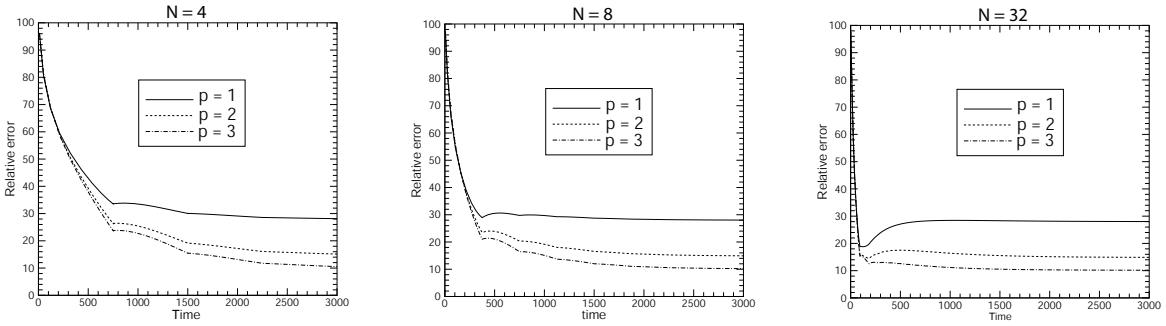

Fig. 5.114. Transient diffusion problem in a thermal battery. The evolution of the relative error $\phi^{\mathrm{FD}}(t)$ for the fully discrete finite element solutions of degree $p = 1, 2$, and 3, computed with Mesh I and time steps $N = 4$, 8, and 32 respectively for orthotropic case.

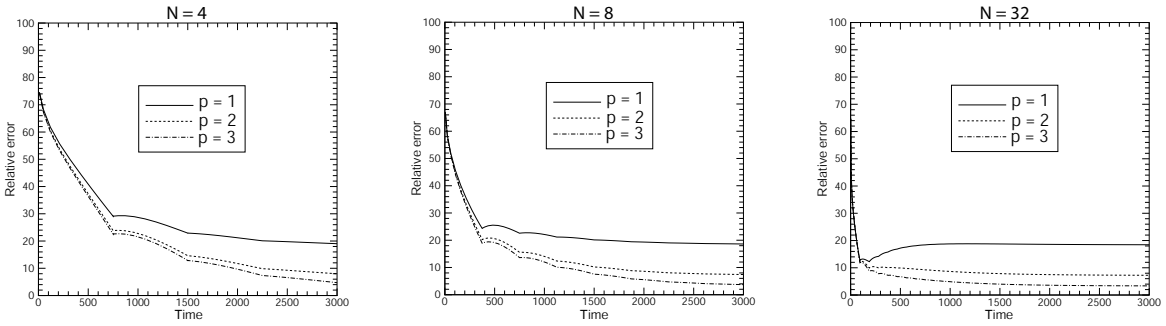

Fig. 5.115. Transient diffusion problem in a thermal battery. The evolution of the relative error $\psi^{\mathrm{FD}}(t)$ for the fully discrete finite element solutions of degree $p = 1, 2$, and 3, computed with Mesh I and time steps $N = 4$, 8, and 32 respectively for orthotropic case.

Figs. 5.116 and 5.117 (resp. Figs. 5.118 and 5.119) are the evolution plots of spatial and temporal ratios with respect to the total error for $\mu^{\mathrm{FD}}(t)$ and $\nu^{\mathrm{FD}}(t)$ in energy norm and for $\delta^{\mathrm{FD}}(t)$ and $\vartheta^{\mathrm{FD}}(t)$ in L^2 norm in the isotropic case (resp. orthotropic case). In the case of energy norm for both the isotropic case and the orthotropic case, it can be seen that with the increase in the number of time steps, it takes less time for the spatial error to become dominant and once the solution is close to steady-state, the spatial error is about 100% and the temporal error becomes negligible. In the case of L^2 norm, the spatial error ratio $\delta^{\mathrm{FD}}(t)$ and the temporal

error ratio $\vartheta^{\mathrm{FD}}(t)$ in the isotropic case is not as sensitive as in the orthotropic with respect to the increase in the time steps. Again we can see that the spatial error is about 100% of the total error as the solution is close to the steady-state.

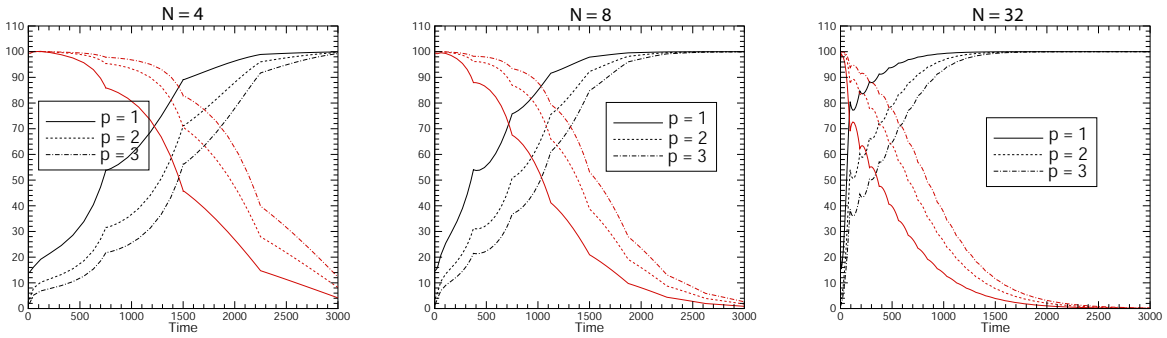

Fig. 5.116. Transient diffusion problem in a thermal battery. The evolution of the spatial error ratio $\mu^{\mathrm{FD}}(t)$ (black-color line) and the temporal error ratio $\nu^{\mathrm{FD}}(t)$ (red-color line) for the fully discrete finite element solutions of degree $p = 1, 2$, and 3, computed with Mesh I and time steps $N = 4$, 8, and 32 respectively for isotropic case.

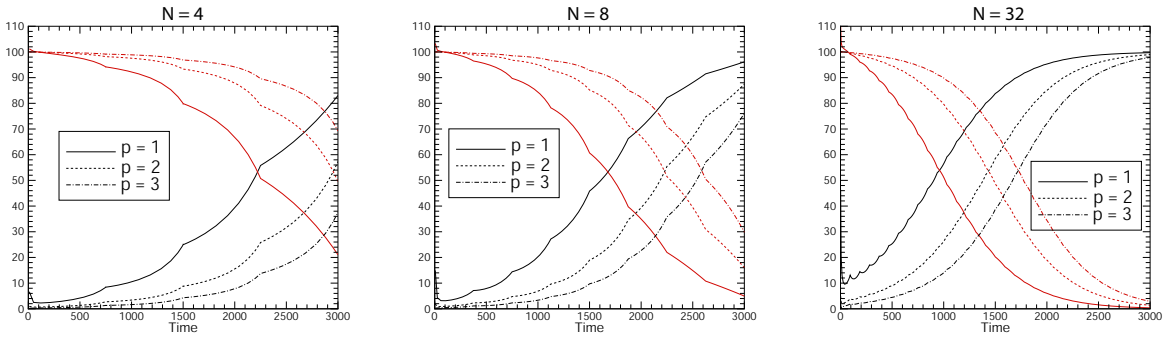

Fig. 5.117. Transient diffusion problem in a thermal battery.The evolution of the spatial error ratio $\delta^{\mathrm{FD}}(t)$ (black-color line) and the temporal error ratio $\vartheta^{\mathrm{FD}}(t)$ (red-color line) for the fully discrete finite element solutions of degree $p = 1, 2$, and 3, computed with Mesh I and time steps $N = 4$, 8, and 32 respectively for isotropic case.

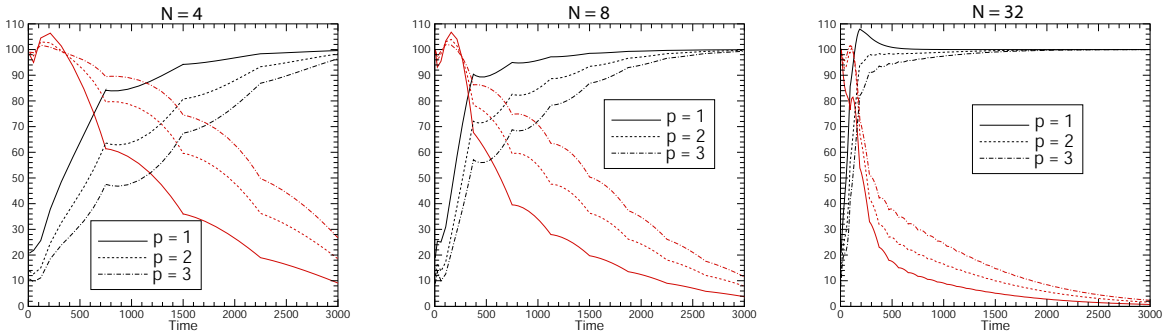

Fig. 5.118. Transient diffusion problem in a thermal battery. The evolution of the spatial error ratio $\mu^{\mathrm{FD}}(t)$ (black-color line) and the temporal error ratio $\nu^{\mathrm{FD}}(t)$ (red-color line) for the fully discrete finite element solutions of degree $p = 1, 2$, and 3, computed with Mesh I and time steps $N = 4$, 8, and 32 respectively for orthotropic case.

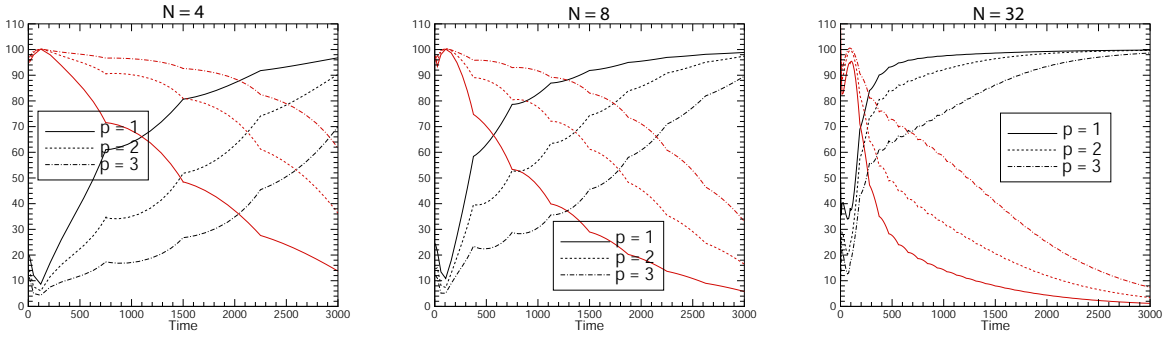

Fig. 5.119. Transient diffusion problem in a thermal battery. The evolution of the spatial error ratio $\delta^{\mathrm{FD}}(t)$ (black-color line) and the temporal error ratio $\vartheta^{\mathrm{FD}}(t)$ (red-color line) for the fully discrete finite element solutions of degree $p = 1, 2$, and 3, computed with Mesh I and time steps $N = 4$, 8, and 32 respectively for orthotropic case.

Figs. 5.120 and 5.121 (resp. Figs. 5.122 and 5.123) is the evolution of effectivity index $\eta^{\mathrm{FD}}(t)$ and its computable version $\eta^{\mathrm{FD}}_{S^{p+k}_{\Delta_{h'}}}(t))$ based on the elliptic reconstruction problem from the fully discrete finite element solution for the exact error measured in energy norm in the isotropic case (resp. orthotropic case). In comparison of Fig. 5.116 (resp. Fig. 5.118) for istoropic case (resp. orthotropic case), it can be seen as long as the spatial error becomes dominant, the effectivity indices $\eta^{\mathrm{FD}}(t)$ and $\eta^{\mathrm{FD}}_{S^{p+k}_{\Delta_{h'}}}(t))$ start to improve. For instance in the isotropic case, for $p = 1$ and time steps equal to

8, we can see from Fig. 5.116 that the spatial error becomes dominant after $t \geq 750$ while in Fig. 5.120 we can see the effectivity index $\eta^{\mathrm{FD}}(t)$ close to 1. Similarly in the orthotropic case, for $p = 1$ and time steps equal to 8, we can see from Fig. 5.118 that the spatial error becomes dominant after $t \geq 500$ and in Fig. 5.122 it can be seen the effectivity index $\eta^{\mathrm{FD}}(t)$ starts to improve and eventually is close to 1 at the end of time interval $t = t_n$. The effectivity index $\eta^{\mathrm{FD}}_{S^{p+k}_{\Delta_{h'}}}(t)$ converges to its exact value $\eta^{\mathrm{FD}}(t)$ with the increase of element order $p + k$.

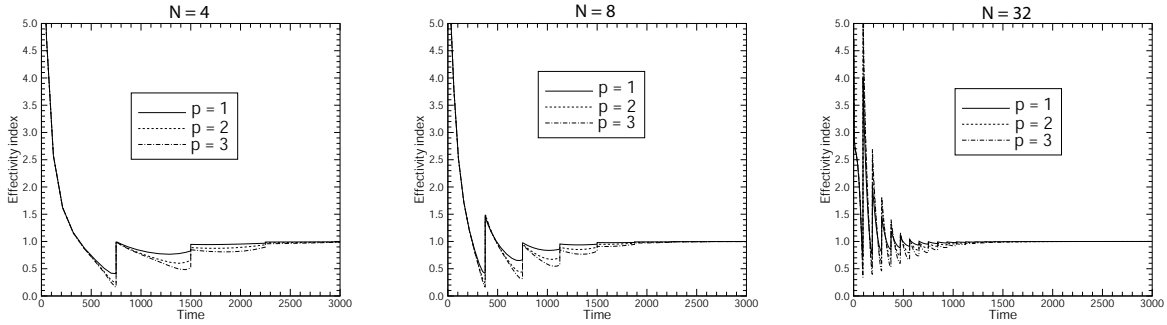

Fig. 5.120. Transient diffusion problem in a thermal battery. The evolution of effectivity index $\eta^{\mathrm{FD}}(t)$ based on the exact solution $\hat{U}$ of the elliptic reconstruction problem. Note that the elliptic reconstruction problem is constructed from the fully discrete finite element solutions of degree $p = 1, 2$, and 3, computed with Mesh I and time steps $N = 4$, 8, and 32 respectively for isotropic case.

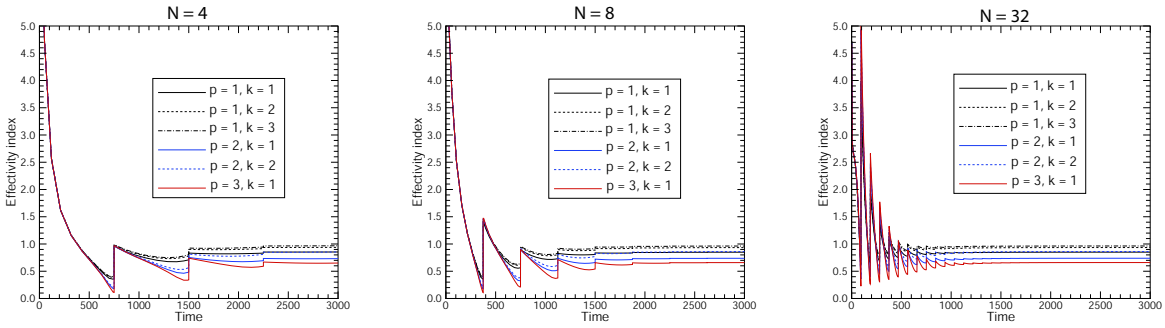

Fig. 5.121. Transient diffusion problem in a thermal battery. The evolution of effectivity index $\eta^{\mathrm{FD}}_{S^{p+k}_{\Delta_{h'}}}(t)$ based on the approximate solution $\hat{U}_{S^{p+k}_{\Delta'_h}}$ of the elliptic reconstruction problem. Note that the elliptic reconstruction problem is constructed from the fully discrete finite element solutions of degree $p = 1, 2$, and 3, computed with Mesh I and time steps $N = 4$, 8, and 32 respectively for isotropic case.

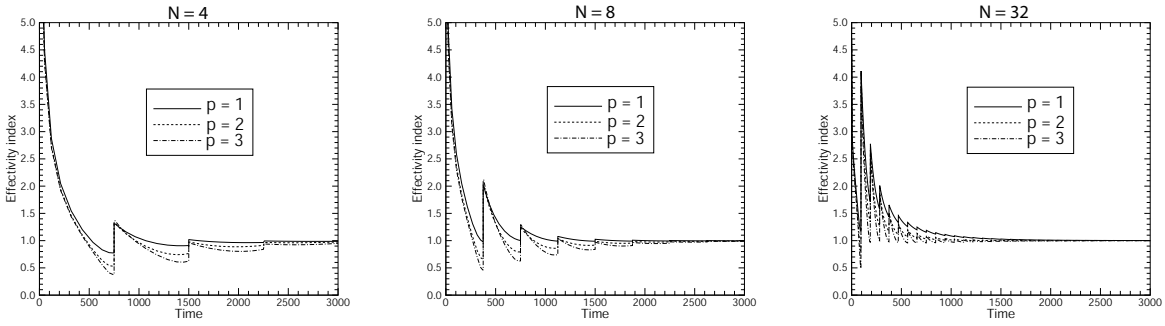

Fig. 5.122. Transient diffusion problem in a thermal battery. The evolution of effectivity index $\eta^{\mathrm{FD}}(t)$ based on the exact solution $\hat{U}$ of the elliptic reconstruction problem. Note that the elliptic reconstruction problem is constructed from the fully discrete finite element solutions of degree $p = 1, 2$, and 3, computed with Mesh I and time steps $N = 4$, 8, and 32 respectively for orthotropic case.

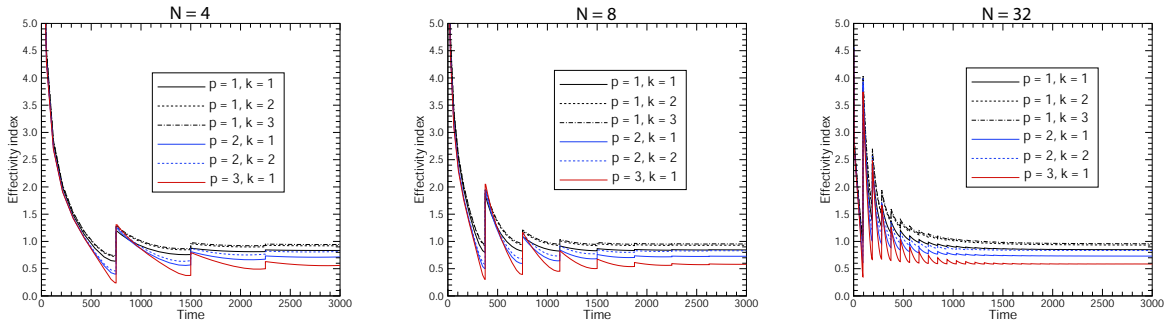

Fig. 5.123. Transient diffusion problem in a thermal battery. The evolution of effectivity index $\eta^{\mathrm{FD}}_{S^{p+k}_{\Delta_{h'}}}(t)$ based on the approximate solution $\hat{U}_{S^{p+k}_{\Delta'_h}}$ of the elliptic reconstruction problem. Note that the elliptic reconstruction problem is constructed from the fully discrete finite element solutions of degree $p = 1, 2$, and 3, computed with Mesh I and time steps $N = 4$, 8, and 32 respectively for orthotropic case.

Figs. 5.124 and 5.125 (resp. Figs. 5.126 and 5.127) is the evolution of effectivity index $\zeta^{\mathrm{FD}}(t)$ and its computable version $\zeta^{\mathrm{FD}}_{S^{p+k}_{\Delta_{h'}}}(t)$ based on the elliptic reconstruction problem from the fully discrete finite element solution for the exact error measured in L^2 norm in the isotropic case (resp. orthotropic case). Again, in comparison of Fig. 5.117 (resp. Fig. 5.119) for istoropic case (resp. orthotropic case), we can observe that as long as the spatial error becomes dominant, the effectivity indices $\zeta^{\mathrm{FD}}(t)$ and $\zeta^{\mathrm{FD}}_{S^{p+k}_{\Delta_{h'}}}(t)$ also start to improve. For instance in the isotropic case, for $p = 1$ and time steps equal to 8, we can see from Fig. 5.117 that the spatial error becomes dominant after $t \geq 1500$ while in Fig. 5.124 we can see the effectivity index $\eta^{\mathrm{FD}}(t)$ close to 1. Similarly in the orthotropic case, for $p = 1$ and time steps equal to 8, we can see from Fig. 5.119 that the spatial error becomes dominant after $t \geq 500$ and in Fig. 5.126 it can be seen the effectivity index $\eta^{\mathrm{FD}}(t)$ starts to improve and eventually is close to 1 at the end of time interval $t = t_n$. The effectivity index $\zeta^{\mathrm{FD}}_{S^{p+k}_{\Delta_{h'}}}(t)$ converges to its exact value $\zeta^{\mathrm{FD}}(t)$ with the increase of element order $p + k$.

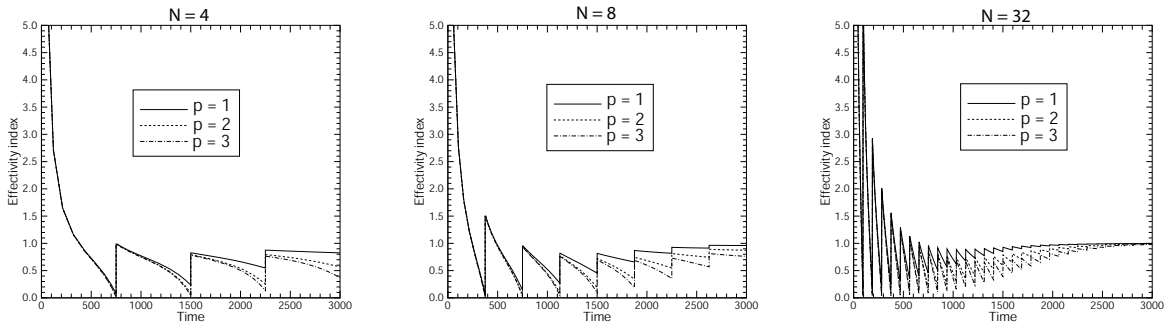

Fig. 5.124. Transient diffusion problem in a thermal battery. The evolution of effectivity index $\zeta^{\mathrm{FD}}(t)$ based on the exact solution $\hat{U}$ of the elliptic reconstruction problem. Note that the elliptic reconstruction problem is constructed from the fully discrete finite element solutions of degree $p = 1, 2$, and 3, computed with mesh II and time steps $N = 4$, 8, and 32 respectively for isotropic case.

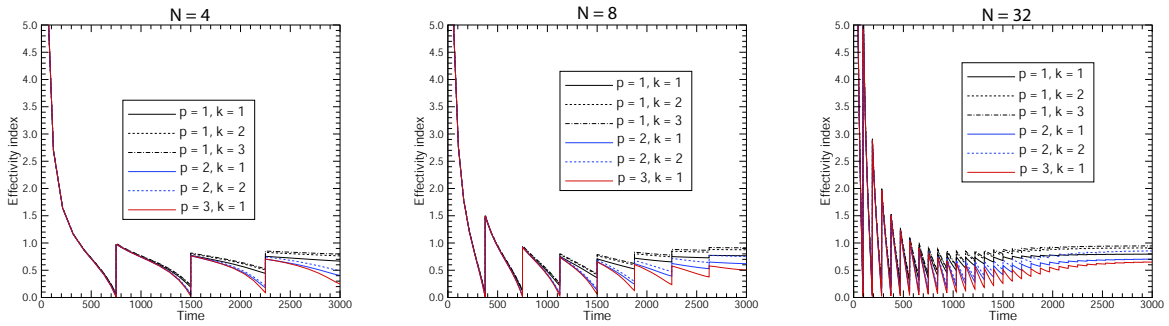

Fig. 5.125. Transient diffusion problem in a thermal battery. The evolution of effectivity index $\zeta^{\mathrm{FD}}_{S^{p+k}_{\Delta_{h'}}}(t)$ based on the approximate solution $\hat{U}_{S^{p+k}_{\Delta'_h}}$ of the elliptic reconstruction problem. Note that the elliptic reconstruction problem is constructed from the fully discrete finite element solutions of degree $p = 1, 2$, and 3, computed with mesh II and time steps $N = 4$, 8, and 32 respectively for isotropic case.

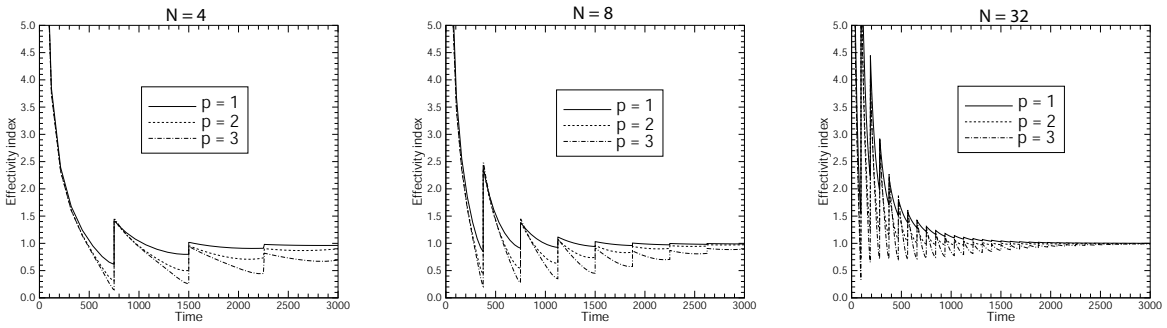

Fig. 5.126. Transient diffusion problem in a thermal battery. The evolution of effectivity index $\zeta^{\mathrm{FD}}(t)$ based on the exact solution $\hat{U}$ of the elliptic reconstruction problem. Note that the elliptic reconstruction problem is constructed from the fully discrete finite element solutions of degree $p = 1, 2$, and 3, computed with mesh II and time steps $N = 4$, 8, and 32 respectively for orthotropic case.

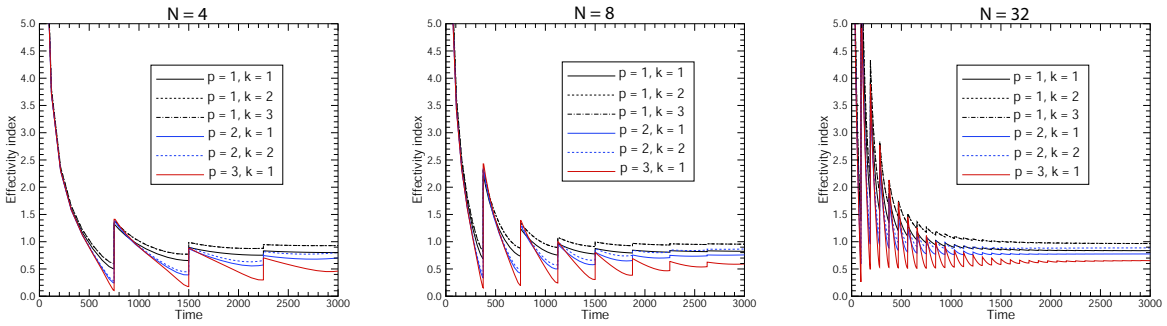

Fig. 5.127. Transient diffusion problem in a thermal battery. The evolution of effectivity index $\zeta^{\mathrm{FD}}_{S^{p+k}_{\Delta_{h'}}}(t)$ based on the approximate solution $\hat{U}_{S^{p+k}_{\Delta'_h}}$ of the elliptic reconstruction problem. Note that the elliptic reconstruction problem is constructed from the fully discrete finite element solutions of degree $p = 1, 2$, and 3, computed with mesh II and time steps $N = 4$, 8, and 32 respectively for orthotropic case.

Figs. 5.128, 5.129 and 5.130 (resp. Figs. 5.131, 5.132 and 5.133) are the evolution of effectivity index $\bar{\eta}^{U,\mathrm{FD}}(t)$, $\bar{\eta}^{U,\mathrm{FD}}_{p+k}(t)$ and $\bar{\eta}^{L,\mathrm{FD}}_{p+k}(t)$ for the exact error measured in energy norm, where the exact error indicator function and its computed version are obtained from the subdomain residual problem of the elliptic reconstruction problems corresponding to the fully discrete finite element solution $U_{S^p_{\Delta_h}}$ of degree $p = 1, 2$, and

3 with $N = 4, 8$, and 32, in the isotropic case (resp. orthotropic case). For isotropic case it can be seen that $\bar{\eta}^{U,\mathrm{FD}}(t)$ is close to 1 for $t > 1000$ since the solution falls into the range of steady state as shown in Fig. 4.9 and the spatial error is about 100% of the total error as illustrated in Fig. 5.116. For $t \leq 1000$ where the solution reflects obvious transient behavior, we find that as long as the spatial error is dominant we have effectivity index $\bar{\eta}^{U,\mathrm{FD}}(t)$ close to 1 at time instant $t = t_n$ for each time interval $(t_{n-1}, t_n]$, which can be observed in the case of $p = 1$ and $N = 32$. The computable bounds $\bar{\eta}^{U,\mathrm{FD}}_{p+k}(t)$ and $\bar{\eta}^{L,\mathrm{FD}}_{p+k}(t)$ have the performance similar to $\bar{\eta}^{U,\mathrm{FD}}(t)$. It can also be found that the lower bound $\bar{\eta}^{L,\mathrm{FD}}_{p+k}(t)$ is less than 1 for $t > 1000$ as the solution is close to steady state. For orthotropic case, we can see that $\bar{\eta}^{U,\mathrm{FD}}(t)$ severely overestimates the exact error even at the time instant $t = t_n$ where the spatial error is dominant as illustrated in Fig. 5.118. The poor performance of $\bar{\eta}^{U,\mathrm{FD}}(t)$ is because of the lack of robustness of the subdomain residual estimator for the elliptic reconstruction problem due to the existence of interface layers caused by the highly orthotropic domain. Likewise the computable version of $\bar{\eta}^{U,\mathrm{FD}}_{p+k}(t)$. The lower bound $\bar{\eta}^{L,\mathrm{FD}}_{p+k}(t)$ severely underestimates the exact error. Again the culprit of severe underestimation is because of the interface layer.

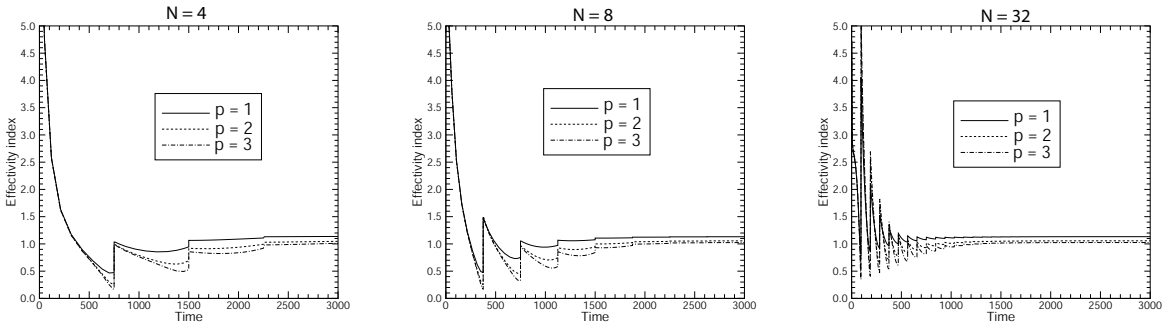

Fig. 5.128. Transient diffusion problem in a thermal battery. The evolution of effectivity index $\bar{\eta}^{U,\mathrm{FD}}(t)$ for the exact error measured in energy norm based on exact estimator of the subdomain residual problem of the elliptic reconstruction problem for isotropic case.

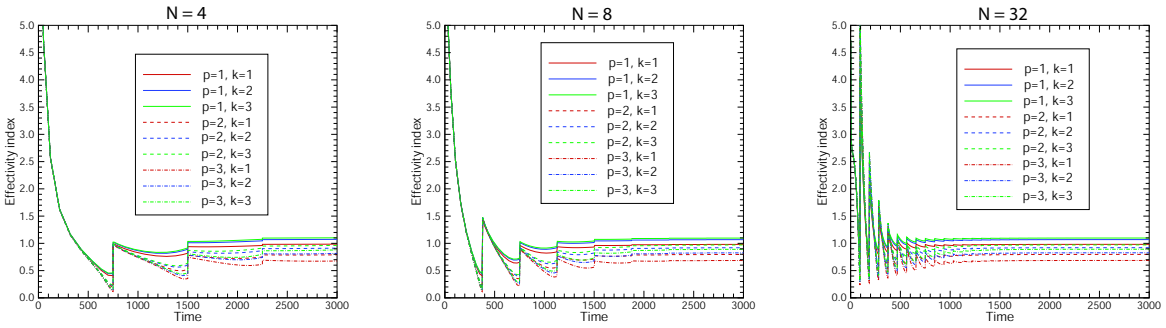

Fig. 5.129. Transient diffusion problem in a thermal battery. The evolution of effectivity index $\bar{\eta}^{U,\mathrm{FD}}_{p+k}(t)$ for the exact error measured in energy norm based on exact estimator of the subdomain residual problem of the elliptic reconstruction problem for isotropic case.

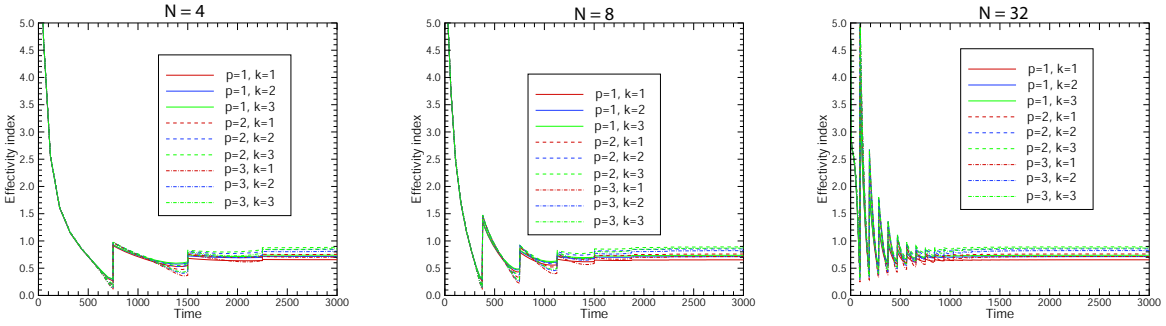

Fig. 5.130. Transient diffusion problem in a thermal battery. The evolution of effectivity index $\bar{\eta}^{L,\mathrm{FD}}_{p+k}(t)$ for the exact error measured in energy norm based on exact estimator of the subdomain residual problem of the elliptic reconstruction problem for isotropic case.

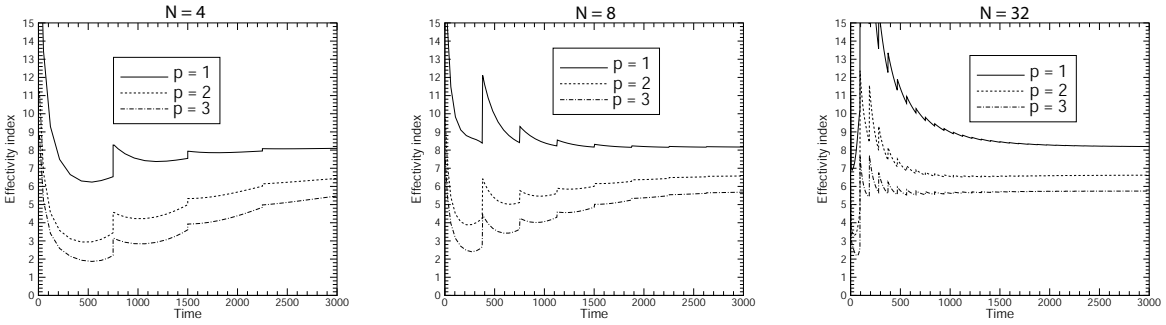

Fig. 5.131. Transient diffusion problem in a thermal battery. The evolution of effectivity index $\bar{\eta}^{U,\mathrm{FD}}(t)$ for the exact error measured in energy norm based on exact estimator of the subdomain residual problem of the elliptic reconstruction problem for orthotropic case.

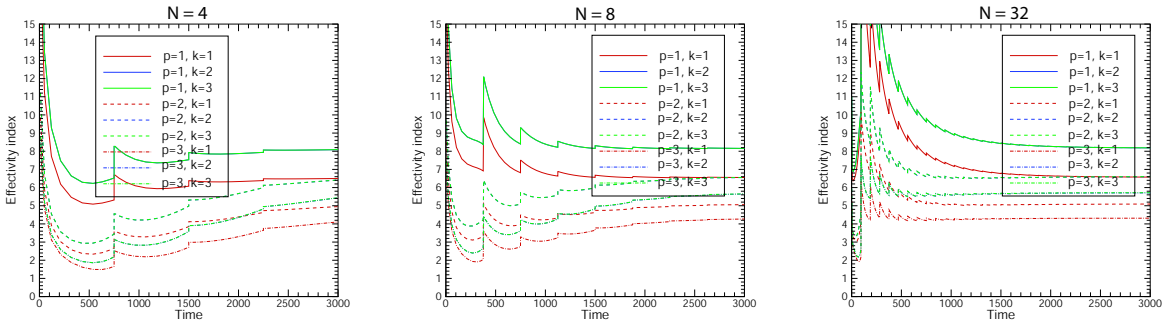

Fig. 5.132. Transient diffusion problem in a thermal battery. The evolution of effectivity index $\bar{\eta}_{p+k}^{U,\mathrm{FD}}(t)$ for the exact error measured in energy norm based on exact estimator of the subdomain residual problem of the elliptic reconstruction problem for orthotropic case.

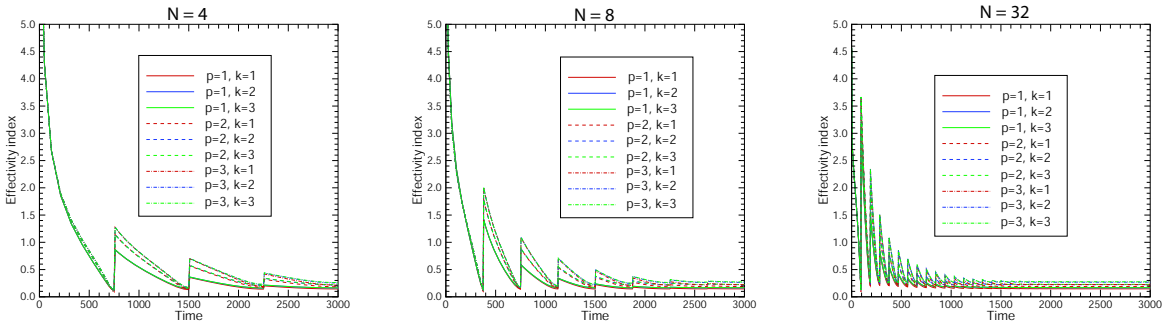

Fig. 5.133. Transient diffusion problem in a thermal battery. The evolution of effectivity index $\bar{\eta}_{p+k}^{L,\mathrm{FD}}(t)$ for the exact error measured in energy norm based on exact estimator of the subdomain residual problem of the elliptic reconstruction problem for orthotropic case.

Figs. 5.134 and 5.135 (resp. Figs. 5.136 and 5.137) are the time evolution of effectivity index $\bar{\zeta}^{\mathrm{FD}}(t)$ and its computable version $\bar{\zeta}^{\mathrm{FD}}_{p+k}(t)$ for isotropic case (resp. orthotropic case). For istropic case, it can be seen that $\bar{\zeta}^{\mathrm{FD}}(t)$ and $\bar{\zeta}^{\mathrm{FD}}_{p+k}(t)$ have poor performance at $t = t_n$ for each time interval $(t_{n-1}, t_n]$ even when the solution is close to steady state. In the orthotropic case, both $\bar{\zeta}^{\mathrm{FD}}(t)$ and $\bar{\zeta}^{\mathrm{FD}}_{p+k}(t)$ severely overestimates the exact error to such an extent that they have no practical meaning.

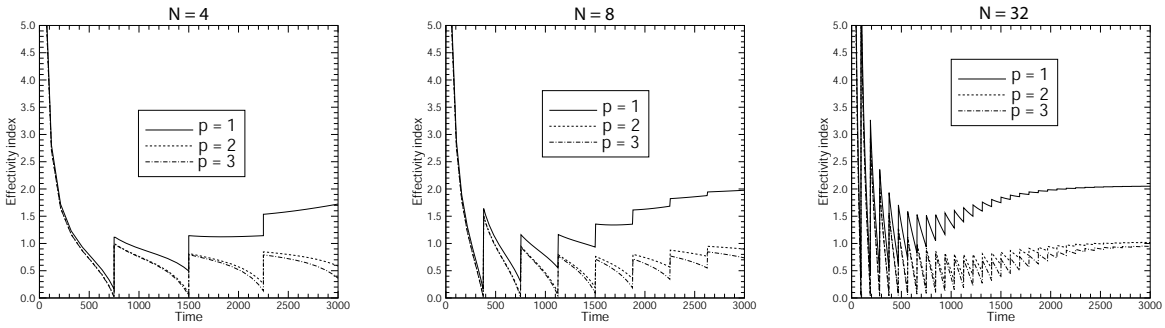

Fig. 5.134. Transient diffusion problem in a thermal battery. The evolution of effectivity index $\bar{\zeta}^{\mathrm{FD}}(t)$ for the exact error measured in L^2 norm based on the exact estimator of the subdomain residual problem of the elliptic reconstruction problem for isotropic case.

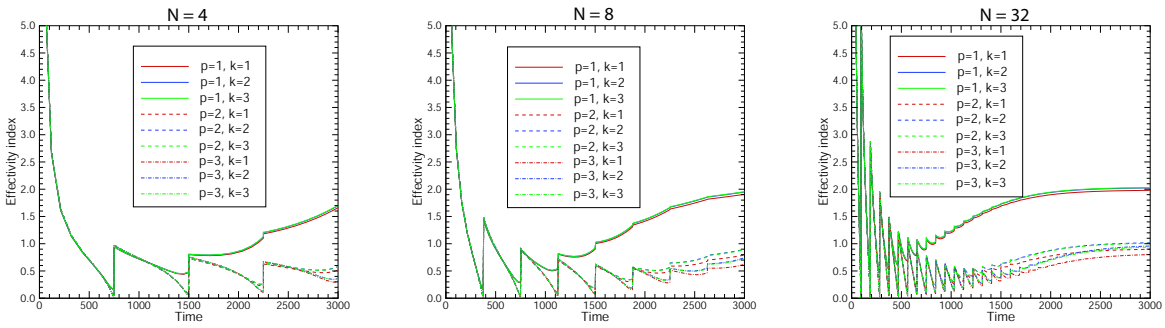

Fig. 5.135. Transient diffusion problem in a thermal battery. The evolution of effectivity index $\bar{\zeta}^{\mathrm{FD}}_{p+k}(t)$ for the exact error measured in L^2 norm based on the exact estimator of the subdomain residual problem of the elliptic reconstruction problem for isotropic case.

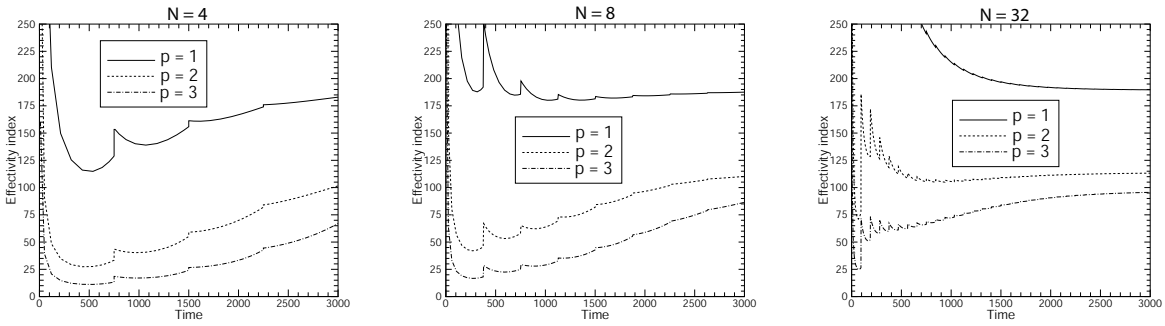

Fig. 5.136. Transient diffusion problem in a thermal battery. The evolution of effectivity index $\bar{\zeta}^{\mathrm{FD}}(t)$ for the exact error measured in L^2 norm based on the exact estimator of the subdomain residual problem of the elliptic reconstruction problem for orthotropic case.

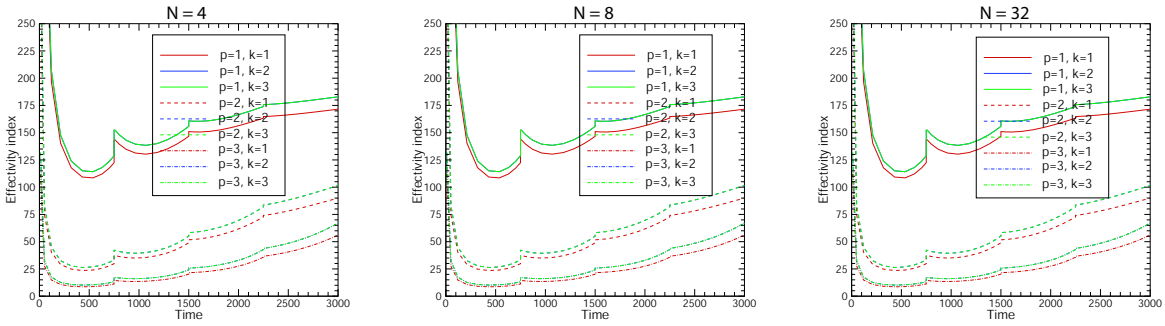

Fig. 5.137. Transient diffusion problem in a thermal battery. The evolution of effectivity index $\bar{\zeta}^{\mathrm{FD}}_{p+k}(t)$ for the exact error measured in L^2 norm based on the exact estimator of the subdomain residual problem of the elliptic reconstruction problem for orthotropic case.

CHAPTER VI

CONCLUSIONS AND RECOMMENDATIONS FOR FUTURE WORK

6.1 Conclusions

In this dissertation we first presented what can be called a careful benchmark study of the robustness of residual estimators for a class of problems with very high orthotropy. The conclusions can be summarized as follows:

1. We first employed as our model problem the heat conduction in a thermal battery which includes a highly orthotropic subdomain. We considered the exact versions of four implicit residual estimators, namely, a Neumann element residual estimators, all three leading to constant-free upper estimators of the error, and a Dirichlet subdomain residual estimator which is the first estimator ever introduced. We employed overkills to obtain the "exact" solution of the model problem and also the exact solutions of all the local residual problems, and we analyzed the effectivity indices of the estimators as a function of material orthotropy for meshes of rectangles and elements of degrees $p = 1, 2, 3$. The main characteristic of the meshes is that they are dictated by the geometry, and seem to be sufficiently refined for the intended computations especially when $p = 3$ degree elements are employed. Our intention was to analyze the estimators for finite element approximations in settings likely to occur in practical computations where the analyst is not aware of all the details of the problem that he is trying to solve, as it is often the case in engineering practice. From the analysis of the results obtained in this setting we concluded:

   a) All four estimators give reliable results in the isotropic case for all the employed meshes.

b) All four estimators deteriorate significantly with high orthotropy for all the meshes and degrees p. All three Neumann estimators, the exact versions of which are upper bounds, grossly overestimate, while the Dirichlet subdomain estimator underestimates and seems to perform better for high orthotropy in this particular benchmark.

c) The computed versions of all four estimators lead to smaller values of the effectivity index. Nevertheless, the trend is very similar with that of the exact versions and, in general, it is not possible to improve the robustness of the estimators by computing the indicators with less accuracy.

d) All the lower estimators constructed from the four types of residual indicators functions employed here, also deteriorate significantly with the increase in orthotropy albeit less than the upper bounds.

e) The optimization of the lower estimators achieved by computing an additional finite element solution at a negligible cost of a resolution of the already factorized stiffness matrix, leads to significant improvement of the lower estimators, especially in the isotropic case, where the obtained lower estimate has effectivity close to one.

2. To clearly illustrate the culprit in the deterioration of the estimates, which is the size of the mesh relative to the size of the sharp layers in the solution close to the high orthotropy, we employed the simplest possible model problem with boundary layer derived by simplifying the original model problem. In addition to being able to obtain analytical expressions for the exact solutions of this problem, we are also able to obtain an analytical expression for the finite element solution. By this we mean the finite element solution computed analytically in terms of a formula without the need to factorize the stiffness

matrix. This helps us avoid the effect of the roundoff error when the mesh is refined many times before reaching the sufficiently small mesh size needed for asymptotic behavior depending on the employed orthotropy. We used this setting to analyze the explicit residual estimator which is directly calculated from the residuals and can be formulated as an asymptotically exact estimator for the energy, H^1 and L^2 norm of the error. We noted the following:

a) Until the size of the mesh is sufficiently small to get several elements across the thickness of the boundary layer the explicit estimator grossly overestimates.

b) Similar behavior is expected for the implicit residual estimators which lead to constant-free upper bounds.

c) The estimation of the L^2-norm of the error in bilinear finite element solution ($p = 1$) is not reliable because of the global pollution in the value.

3. We also considered another simplified model problem which has an interface layer and is closer to the original model problem of the thermal battery. Once more the accuracy of the error estimation is governed by the size of the mesh relative to the size of the interface layer due to the high orthotropy, however here we have also another factor which is the contribution to the global norm of the error from the error in the highly orthotropic subdomain. Extrapolating from this example, we can say that the behavior of the effectivity of the estimators for the thermal battery problem is much more complicated because it involves the effectivity of the estimators at multimaterial points.

Another important issue that must be always addressed is the difference between the exact and computed versions of the various residual estimators, especially for the case of high orthotropy.

4. The main point of the robustness analysis for the thermal battery problem is that asymptotic analyses of the estimators may not be relevant for practical computations where the mesh is chosen somehow based on the experience of the user and on the available mesh generator. As we have seen in the model examples above, the relative error can be in the acceptable range of engineering accuracy e.g. 5%. However the bounds could indicate that it is big, e.g. nearly 100% leading the user to possibly unnecessary refinements and additional computations until much higher accuracy e.g. 0.5% is obtained at which instant the bounds also become efficient (the ratio $\frac{\mathscr{E}^U}{\mathscr{E}^L}$ is close to one), the user realizes that a much higher than the desired accuracy has been reached and decides to terminate the computation. In our view it is for this case namely when the error is in the range of engineering accuracy 5% that we need to construct efficient bounds for the error and not when the mesh is sufficiently refined for the bounds to approach their asymptotic values.

Secondly, we carried out the *a-posteriori* error estimation for the semi-discrete finite element solution of linear transient problem based on the elliptic reconstruction procedure. The conclusions can be drawn as follows:

1. For smooth solution, the difference between the exact solution of the linear transient problem and the exact solution of the elliptic reconstruction problem based on the semi-discrete finite element solution, namely $u - \hat{u}$, has improved convergence rate in comparison of the exact error in the semi-discrete finite element solution when measured in energy norm or L^2 norm. However, in the L^2 norm case, the superconvergence does not exist for linear finite element solution. For nonsmooth solution such as the L-shaped domain problem, $u - \hat{u}$ has improved convergence rate only for the energy or H^1 norm. In the case of

L^2 norm, $u - \hat{u}$ has the same convergence rate as the exact error $u - u_{S^p_{\Delta_h}}$ even for quadratic and cubic finite element solutions.

2. The space-time based error estimator we invented has robust performance even for nonsmooth solution.

3. With the introduction of elliptic reconstruction problem, all the available elliptic residual estimators can be employed for the error estimation of linear parabolic problem. Furthermore, we can even obtain lower bound for the error measured in space-time $\mathscr{C}$-norm.

4. Except the case where the exact error in linear finite element solution is measured in L^2 norm, $u - u_{S^p_{\Delta_h}}$ can be approximated well at any time instant by $\hat{u} - u_{S^p_{\Delta_h}}$ if the solution is smooth. In the case of nonsmooth solution, $\hat{u} - u_{S^p_{\Delta_h}}$ is good approximation for $u - u_{S^p_{\Delta_h}}$ measured in H^1 norm.

Thirdly, we employed the elliptic reconstruction procedure for the error estimation of fully discrete finite element solution to the linear parabolic problem obtained from backward-difference time discretization scheme. We can draw the following conclusions:

1. The exact error in the fully discrete finite element solution $u - U_{S^p_{\Delta_h}}$ can be approximated well by $\hat{U} - U_{S^p_{\Delta_h}}$ at time instant $t = t_n$ for each time interval $(t_{n-1}, t_n]$ only under the condition that the temporal error is negligible in comparison of the spatial error.

2. We invented an estimator which can be employed to evaluate the temporal error in space-time $\mathscr{C}$-norm.

3. Similar to the semi-discrete case, a space-time error estimator also exists for fully discrete case and can have good performance if the temporal error is not dominant.

6.2 Future work

The elliptic reconstruction procedure has a great potential that can be tapped, which can be listed as follows:

1. For error estimation of quantity of interest for linear parabolic problem, the prevalent scheme is to solve the a dual problem backwards in time which can be tricky and even prohibitively expensive if three-dimensional problem is considered. The elliptic reconstruction procedure is appealing in this respect.

2. The procedure can also be extended to the reaction-convection-diffusion type equation.

3. Given the new error estimator for the temporal error, it is practical now to design adaptive time-stepping scheme in order to control the temporal error.

4. The time-discretization scheme employed in the dissertation is backward difference. The other discretization schemes, such as forward difference, Crank-Nicholson, and discontinuous Galerkin method, can also be employed.

REFERENCES

[1] T. Strouboulis, D. L. Wang, I. Babuška, Robustness of error estimators for finite element solutions of problems with high orthotropy, Comp. Meth. Appl. Mech. Engr. 198 (2009) 1946–1966.

[2] I. Babuška, J. T. Oden, Verification and validation in computational engineering and science: basic concepts, Comp. Meth. Appl. Mech. Engr. 193 (2004) 4057–4066.

[3] P. Roache, Verification and Validation in Computational Science and Engineering, Hermosa Publishers, Albuquerque, 1998.

[4] M. Ainsworth, J.T. Oden, A posteriori Error Estimation in Finite Element Analysis, John Wiley, London, 2000.

[5] P. Ladevèze, J. P. Pelle, Mastering Calculations in linear and Nonlinear Mechanics, Springer, New York, 2005.

[6] I. Babuška, T. Strouboulis, The Finite Element Method and Its Reliability, Oxford University Press, London, 2001.

[7] P. Ladeveze, D. Leguillon, Error estimate procedure in the finite element method and applications, SIAM J. Numer. Anal. 20 (3) (1983) 485–509.

[8] J. L. Synge, The Hypercircle in Mathematical Physics, Cambridge at the University Press, Cambridge, UK, 1957.

[9] P. Ladevèze, J. P. Pelle, La Maitrise du Calcul en Mécanique Lineaire et Non-Linéaire, Hermès-Lavoisier, Cachan Cedex, France, 2001.

[10] P. Ladevèze, Upper error bounds on calculated outputs of interest for linear and nonlinear structural problems, Comptes Rendus - Mecanique 334 (7) (2006) 399–407.

[11] L. Chamoin, P. Ladevèze, Bounds on history-dependent or independent local quantities in viscoelasticity problems solved by approximate methods, Int. J. Numer. Meth. Engr. 71 (2007) 1387–1411.

[12] L. Chamoin, P. Ladevèze, A non-intrusive method for the calculation of strict and efficient bounds of calculated outputs of interest in linear viscoelasticity problems, Comp. Meth. Appl. Mech. Engr. 197 (2008) 994–1014.

[13] P. Ladevèze, Strict upper error bounds on computed outputs of interest in computational structural mechanics, Comput. Mech. 42 (2008) 271–286.

[14] S. Prudhomme, F. Nobile, L. Chamoin, J. T. Oden, Analysis of a subdomain-based error estimator for finite element approximations of elliptic problems, Numer. Methods Partial Differential Eq. 20 (2004) 165–192.

[15] N. Parés, J. Bonnet, A. Huerta, J. Peraire, The computation of bounds for linear-functional outputs of weak solutions to the two-dimensional elasticity equations, Comp. Meth. Appl. Mech. Engr. 195 (2006) 406–429.

[16] N. Parés, P. Diez, A. Huerta, Subdomain-based flux-free a posteriori error estimation, Comp. Meth. Appl. Mech. Engr. 195 (2006) 297–323.

[17] T. Strouboulis, L. Zhang, D. L. Wang, I. Babuška, a posteriori error estimation for generalized finite element methods, Comp. Meth. Appl. Mech. Engr. 195 (2006) 852–879.

[18] C. Carstensen, J. Thiele, Partition of unity for localization in implicit a posteriori finite element error control for linear elasticity, Int. J. Numer. Meth. Engr. 73 (2008) 71–95.

[19] R. R. Lober, Thermal battery life test problem for residual method error measure development, Tech. rep., Sandia National Laboratories, Albuquerque, NM, February 1999.

[20] D. K. Datta, Computer analysis of error estimation in finite element computations for elliptic and parabolic problems, Ph.D. thesis, Texas A&M University, College Station, Texas, August 2001.

[21] M. Biterman, I. Babuška, The finite element method for parabolic equations: (I) a posteriori estimation, Numer. Math. 40 (1982) 339–371.

[22] M. Biterman, I. Babuška, The finite element method for parabolic equations: (II) a posteriori estimation and adaptive approach, Numer. Math. 40 (1982) 373–406.

[23] P. K. Moore, A posteriori error estimation with finite element semi- and fully discrete methods for nonlinear parabolic equations in one space dimension, SIAM J. Numer. Anal. 31 (1994) 149–169.

[24] M. Picasso, Adaptive finite elements for a linear parabolic problem, Comp. Meth. Appl. Mech. Engr. 167 (1998) 223–237.

[25] K. Eriksson, C. Johnson, Adaptive finite element methods for parabolic problems I: a linear model problem, SIAM J. Numer. Anal. 28 (1) (1991) 43–77.

[26] K. Eriksson, C. Johnson, Adaptive finite element methods for parabolic problems IV: nonlinear problems, SIAM J. Numer. Anal. 32 (6) (1995) 1729–1749.

[27] R. H. Nochetto, G. Savaré, C. Verdi, A posteriori error estimates for variable time-step discretizations of nonlinear evolution equations, Comm. Pure Appl. Math. 53 (5) (2000) 525–589.

[28] R. Verfürth, A posteriori error estimates for nonlinear problems: finite element discretizations of parabolic equations, Math. Comp. 67 (224) (1998) 1335–1360.

[29] R. Verfürth, A posteriori error estimates for nonlinear problems: finite element discretizations of parabolic equations, Numer. Meth. Part. Differ. Eq. 14 (4) (1998) 487–518.

[30] R. Verfurth, A posteriori error estimates for nonlinear problems: finite element discretizations of elliptic equations, Math. Comp. 62 (206) (1994) 445–475.

[31] I. Babuška, S. Ohnimus, A posteriori error estimation for the semidiscrete finite element method of parabolic differential equations, Comp. Meth. Appl. Mech. Engr. 190 (35-36) (2001) 4691–4712.

[32] I. Babuška, P. Feistauer, M. Šolin, On one approach to a posteriori error estimates for evolution problems solved by the method of lines, Numerische Mathematik 89 (2) (2001) 225–256.

[33] T. Strouboulis, I. Babŭka, D. K. Datta, Guaranteed a posteriori error estimation for fully discrete solutions of parabolic problems, Int. J. Numer. Meth. Engr. 56 (2003) 1243–1259.

[34] Z. Chen, R. H. Nochetto, A. Schmidt, A characteristic Galerkin method with adaptive error control for continuous casting problem, Comp. Meth. Appl. Mech. Engr. 189 (2000) 249–276.

[35] R. H. Nochetto, A. Schmidt, C. Verdi, A posteriori error estimation and adaptivity for degenerate parabolic problems, Math. Comp. 69 (2000) 1–24.

[36] B. García-Archilla, E. S. Titi, Postprocessing the Galerkin method: the finite-element case, SIAM J. Numer. Anal. 37 (2) (2000) 470–499.

[37] J. de Frutos, J. Novo, Postprocessing the linear finite element method, SIAM J. Numer. Anal. 40 (3) (2002) 805–819.

[38] J. de Frutos, J. Novo, A posteriori error estimation with the p-version of the finite element method for nonlinear parabolic differential equation, Comp. Meth. Appl. Mech. Engr. 191 (2002) 4893–4904.

[39] J. de Frutos, J. Novo, Element-wise a posteriori estimates based on hierarchical bases for nonlinear parabolic problems, Int. J. Numer. Meth. Engr. 63 (2005) 1146–1173.

[40] J. de Frutos, B. García-Archilla, J. Novo, A posteriori error estimates for fully discrete nonlinear parabolic problems, Comp. Meth. Appl. Mech. Engr. 196 (2007) 3462–3474.

[41] C. Makridakis, R. H. Nochetto, Elliptic reconstruction and a posteriori error estimates for parabolic problems, SIAM J. Numer. Anal. 41 (4) (2003) 1585–1594.

[42] O. Lakkis, C. Makridakis, Elliptic reconstruction and a posteriori error estimates for fully discrete linear parabolic problems, Math. Comput. 75 (2006) 1627–1658.

[43] L. Machiels, A posteriori finite element bounds for output functionals of discontinuous Galerkin discretizations of parabolic problems, Comp. Meth. Appl. Mech. Engr. 190 (2001) 3401–3411.

[44] A. M. Sauer-Budge, J. Peraire, Computing bounds for linear functionals of exact weak solutions to the advection-diffusion-reaction equation, SIAM J. Sci. Comput. 26 (2) (2004) 636–652.

[45] N. Parés, P. Díez, A. Huerta, Bounds of functional outputs for parabolic problems. Part I: exact bounds of the discontinuous Galerkin time discretization, Comp. Meth. Appl. Mech. Engr. 197 (2008) 1641–1660.

[46] N. Parés, P. Díez, A. Huerta, Bounds of functional outputs for parabolic problems. Part II: bounds of the exact solution, Comp. Meth. Appl. Mech. Engr. 197 (2008) 1661–1679.

[47] I. Babuška, M. Suri, On locking and robustness in the finite element method, SIAM J. Numer. Anal. 29 (5) (1992) 1261–1293.

[48] P. Morin, R. H. Nochetto, K. G. Siebert, Local problems on stars: a posteriori error estimators, convergence, and performance, Math. of Comp. 72 (243) (2002) 1067–1097.

[49] V. Thomée, Galerkin Finite Element Methods for Parabolic Problems, Springer Verlag, New York, 1997.

[50] C. Makridakis, R. H. Nochetto, Elliptic reconstruction and a posteriori error estimates for parabolic problems, SIAM J. Numer. Anal. 41 (4) (2003) 1585–1594.

[51] T. Werder, K. Gerdes, D. Schötzau, C. Schwab, *hp*-discontinuous galerkin time stepping for parabolic problems, Comp. Meth. Appl. Mech. Engr. 190 (2001) 6685–6708.

[52] T. Strouboulis, I. Babuška, D. K. Datta, Guaranteed a posteriori error estimation for fully discrete solutions of parabolic problems, Int. J. Numer. Meth. Engr. 56 (2003) 1243–1259.

[53] P. Díez, G. Calderón, Goal-oriented error estimation for transient parabolic problems, Comput. Mech. 29 (2007) 633–646.

APPENDIX A

EXACT FINITE ELEMENT SOLUTION FOR BOUNDARY LAYER PROBLEM

For a uniform mesh as shown in Fig. A.1, the number of subdivisions along both x and y axis is chosen to be n and the mesh sizes along x and y axes are denoted by $h_1 \stackrel{\text{def}}{=} \frac{a}{n}$ and $h_2 \stackrel{\text{def}}{=} \frac{b}{n}$ respectively. The nodal degrees of freedom is denoted by the index i $(i = 0, 1, 2, ..., n)$ along x axis and the index j $(j = 0, 1, 2, ..., n)$ along y axis. In the global stiffness matrix, we have the following discretization form corresponding

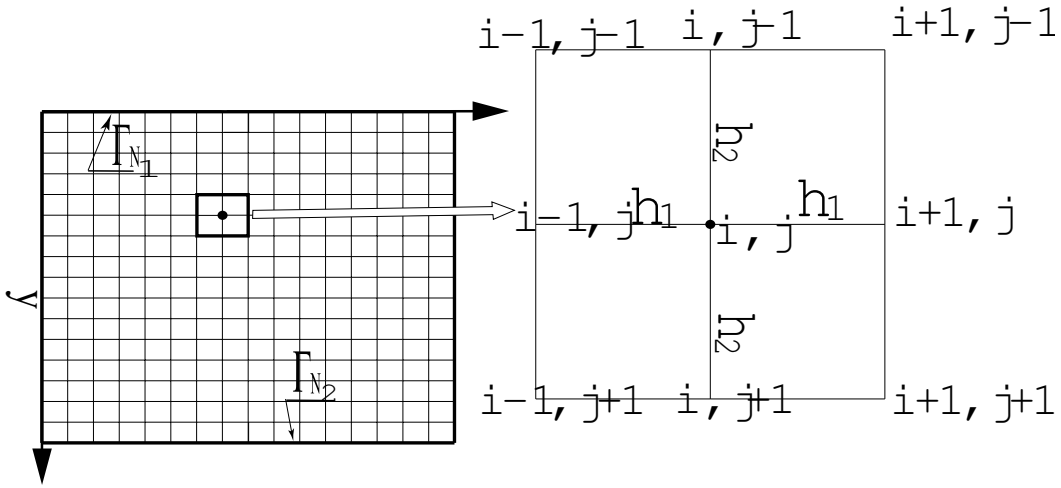

Fig. A.1. Uniform mesh for model problem with boundary layer

to an arbitrary node denoted by (i, j) not on the boundaries.

$$\begin{aligned}
&\Big(-k_x\frac{h_2}{6h_1} - k_y\frac{h_1}{6h_2}\Big)u_{i-1,j-1} + 2\Big(k_x\frac{h_2}{6h_1} - k_y\frac{h_1}{3h_2}\Big)u_{i,j-1}+\\
&\Big(-k_x\frac{h_2}{6h_1} - k_y\frac{h_1}{6h_2}\Big)u_{i+1,j-1} + 2\Big(-k_x\frac{h_2}{3h_1} + k_y\frac{h_1}{6h_2}\Big)u_{i-1,j}+\\
&4\Big(k_x\frac{h_2}{3h_1} + k_y\frac{h_1}{3h_2}\Big)u_{i,j} + 2\Big(-k_x\frac{h_2}{3h_1} + k_y\frac{h_1}{6h_2}\Big)u_{i+1,j}+\\
&\Big(-k_x\frac{h_2}{6h_1} - k_y\frac{h_1}{6h_2}\Big)u_{i-1,j+1} + 2\Big(k_x\frac{h_2}{6h_1} - k_y\frac{h_1}{3h_2}\Big)u_{i,j+1}+\\
&\Big(-k_x\frac{h_2}{6h_1} - k_y\frac{h_1}{6h_2}\Big)u_{i+1,j+1} = 0
\end{aligned} \tag{A.1}$$

At the boundary Γ_{N_1}, we have

$$\begin{aligned}
&\Big(-k_x\frac{h_2}{3h_1} + k_y\frac{h_1}{6h_2}\Big)u_{i-1,0} + \Big(-k_x\frac{h_2}{6h_1} - k_y\frac{h_1}{6h_2}\Big)u_{i-1,1}\\
&+ 2\Big(k_x\frac{h_2}{3h_1} + k_y\frac{h_1}{3h_2}\Big)u_{i,0} + 2\Big(k_x\frac{h_2}{6h_1} - k_y\frac{h_1}{3h_2}\Big)u_{i,1}+\\
&\Big(-k_x\frac{h_2}{3h_1} + k_y\frac{h_1}{6h_2}\Big)u_{i+1,0} + \big(-k_x\frac{h_2}{6h_1} - k_2\frac{h_1}{6h_2}\Big)u_{i+1,1}\\
&= \int_{s_1} k_y\frac{\partial u}{\partial y}\phi_i\big|_{\tau_1} + \int_{s_2} k_y\frac{\partial u}{\partial y}\phi_i\big|_{\tau_2}
\end{aligned} \tag{A.2}$$

where the shape functions at node $(i, 0)$ defined at the two elements τ_1 and τ_2 are $\phi_i\big|_{\tau_1} = \frac{x-x_{i-1}}{x_i-x_{i-1}}$ and $\phi_i\big|_{\tau_2} = \frac{x-x_{i+1}}{x_i-x_{i+1}}$ respectively.

Similarly at the boundary Γ_{N_2}, we have

$$\begin{aligned}
&\Big(-k_x\frac{h_2}{6h_1} - k_y\frac{h_1}{6h_2}\Big)u_{i-1,n-1} + \Big(-k_x\frac{h_2}{3h_1} + k_y\frac{h_1}{6h_2}\Big)u_{i-1,n}+\\
&2\Big(k_x\frac{h_2}{6h_1} - k_y\frac{h_1}{3h_2}\Big)u_{i,n-1} + 2\Big(k_x\frac{h_2}{3h_1} + k_y\frac{h_1}{3h_2}\Big)u_{i,n}+\\
&\Big(-k_x\frac{h_2}{6h_1} - k_y\frac{h_1}{6h_2}\Big)u_{i+1,n-1} + \Big(-k_x\frac{h_2}{3h_1} + k_y\frac{h_1}{6h_2}\Big)u_{i+1,n} = 0
\end{aligned} \tag{A.3}$$

It should be noted that in equation A.3 the right-hand-side is zero due to homogeneous Newumann boundary condition.

Using separation of variables and assuming the degrees of freedom $u_{i,j} = X_i Y_j$, from equation A.1 we have

$$\frac{Y_{j+1} + Y_{j-1}}{Y_j} = C$$
$$-\frac{2\Big(k_x\frac{h_2}{6h_1} - k_y\frac{h_1}{3h_2}\Big)X_{i-1} + 4\Big(k_x\frac{h_2}{3h_1} + k_y\frac{h_1}{3h_2}\Big)X_i + 2\Big(k_x\frac{h_2}{6h_1} - k_y\frac{h_1}{3h_2}\Big)X_{i+1}}{\Big(-k_x\frac{h_2}{6h_1} - k_y\frac{h_1}{6h_2}\Big)X_{i-1} + 2\Big(-k_x\frac{h_2}{3h_1} + k_y\frac{h_1}{6h_2}\Big)X_i + \Big(-k_x\frac{h_2}{6h_1} - k_y\frac{h_1}{6h_2}\Big)X_{i+1}} = C \tag{A.4}$$

From equation A.4, we have the following form for X_{i-1}, X_i, and X_{i+1}.

$$\begin{aligned}
&\Big(2\Big(k_x\frac{h_2}{6h_1} - k_y\frac{h_1}{3h_2}\Big) - C\Big(k_x\frac{h_2}{6h_1} + k_y\frac{h_1}{6h_2}\Big)\Big)X_{i+1} + \\
&\Big(4\Big(k_x\frac{h_2}{3h_1} + k_y\frac{h_1}{3h_2}\Big) + 2C\Big(-k_x\frac{h_2}{3h_1} + k_y\frac{h_1}{6h_2}\Big)\Big)X_i \\
&+ \Big(2\Big(k_x\frac{h_2}{6h_1} - k_y\frac{h_1}{3h_2}\Big) - C\Big(k_x\frac{h_2}{6h_1} + k_y\frac{h_1}{6h_2}\Big)\Big)X_{i-1} = 0
\end{aligned} \tag{A.5}$$

Assume $X_i = \gamma^i$ and plug it into equation A.5, we have a quadratic equation for γ

$$\begin{aligned}
&\Big(2\Big(k_x\frac{h_2}{6h_1} - k_y\frac{h_1}{3h_2}\Big) - C\Big(k_x\frac{h_2}{6h_1} + k_y\frac{h_1}{6h_2}\Big)\Big)\gamma^2 + \\
&\Big(4\Big(k_x\frac{h_2}{3h_1} + k_y\frac{h_1}{3h_2}\Big) + 2C\Big(-k_x\frac{h_2}{3h_1} + k_y\frac{h_1}{6h_2}\Big)\Big)\gamma \\
&+ \Big(2\Big(k_x\frac{h_2}{6h_1} - k_y\frac{h_1}{3h_2}\Big) - C\Big(k_x\frac{h_2}{6h_1} + k_y\frac{h_1}{6h_2}\Big)\Big) = 0
\end{aligned} \tag{A.6}$$

Assume γ_1 and γ_2 are the two roots of equation A.6 and X_j can be expressed as a linear combination of γ_1 and γ_2 as follows

$$X_i = D_1\gamma_1^i + D_2\gamma_2^i \tag{A.7}$$

At the boundary $x = 0$ and $x = a$ which corresponds to the indices $i = 0$ and $i = n$, we have

$$\begin{aligned} X_0 &= D_1 + D_2 = 0 \quad \text{at } i = 0 \\ X_n &= D_1\gamma_1^n + D_2\gamma_2^n \quad \text{at } i = n \end{aligned} \tag{A.8}$$

To have nontrivial constants D_1 and D_2, the two roots γ_1 and γ_2 have to be conjugate complex. Thus by assuming $\gamma_1 = re^{I\psi}$ and $\gamma_2 = re^{-I\psi}$ and using Vieta's theorem, we have

$$\begin{aligned} \gamma_1 + \gamma_2 &= -\frac{4\Big(k_x\frac{h_2}{3h_1} + k_y\frac{h_1}{3h_2}\Big) + 2C\Big(-k_x\frac{h_2}{3h_1} + k_y\frac{h_1}{6h_2}\Big)}{2\Big(k_x\frac{h_2}{6h_1} - k_y\frac{h_1}{3h_2}\Big) - C\Big(k_x\frac{h_2}{6h_1} + k_y\frac{h_1}{6h_2}\Big)} = 2\cos(\psi) \\ \gamma_1\ \gamma_2 &= r^2 = 1 \end{aligned} \tag{A.9}$$

Therefore, X_i has the following form by noting $D_1 + D_2 = 0$ and $r = 1$

$$X_i = D_1e^{Ii\psi} + D_2e^{-Ii\psi} = (D_1 + D_2)\cos(i\psi) + I(D_1 - D_2)\sin(i\psi) = I(D_1 - D_2)\sin(i\psi) \tag{A.10}$$

According to boundary condition $X_n = 0$, we have

$$X_n = I(D_1 - D_2)\sin(n\psi) = 0 \tag{A.11}$$

Thus we have $\psi = \frac{k}{n}\pi$ with $k = 1, 2, ..., n-1$.

Since D_1 and D_2 are arbitrary constants and by setting $I(D_1 - D_2)$ to be unity, we have

$$X_i^k = \sin\big(\frac{i}{n}k\pi\big) \tag{A.12}$$

The constant C_k can be determined by plugging $\phi = \frac{\pi}{n}$ into equation A.9, which has the form as follows

$$C_k = 2\frac{\frac{k_x}{6}\frac{h_2}{h_1}\big(2+\cos(\frac{k}{n}\pi)\big) + \frac{k_y}{3}\frac{h_1}{h_2}\big(1-\cos(\frac{k}{n}\pi)\big)}{\frac{k_x}{6}\frac{h_2}{h_1}\big(2+\cos(\frac{k}{n}\pi)\big) - \frac{k_y}{6}\frac{h_1}{h_2}\big(1-\cos(\frac{k}{n}\pi)\big)} \tag{A.13}$$

According to equation A.4, we have

$$Y_{j+1}^k - C_k Y_j^k + Y_{j-1}^k = 0 \tag{A.14}$$

Let $Y_j^k = \lambda_k^j$, we have a quadratic equation

$$\lambda_k^2 - C_k\lambda_k + 1 = 0 \tag{A.15}$$

and its two roots are

$$\begin{aligned} \lambda_{1,k} &= \frac{C_k + \sqrt{C_k^2 - 4}}{2} \\ \lambda_{2,k} &= \frac{C_k - \sqrt{C_k^2 - 4}}{2} \end{aligned} \tag{A.16}$$

Likewise, put Y_j^k as a linear combintaion of the two roots $\lambda_{1,k}$ and $\lambda_{2,k}$, we have

$$Y_j^k = \alpha_1^k\lambda_{1,k}^j + \alpha_2^k\lambda_{2,k}^j \tag{A.17}$$

Let $u_{i,j} = \sum_{k=1}^{n-1} X_i^k Y_j^k$ and plugging it into the equations A.2 and A.3 corresponding to Neumann boundary conditions which are $Y_0^k = \alpha_1^k + \alpha_2^k$ and $Y_n^k = \alpha_1^k\lambda_{1,k}^n + \alpha_2^k\lambda_{2,k}^n$ respectively. Thus we have after simplification

$$\begin{aligned} &\sum_{k=1}^{n-1}\sin(\frac{i}{n}k\pi)\big\{(A^k + B^k\lambda_{1,k})\alpha_1^k + (A^k + B^k\lambda_{2,k})\alpha_2^k\big\} = \sin(\frac{i}{n}\pi)S \\ &\sum_{k=1}^{n-1}\sin(\frac{i}{n}k\pi)\big\{(A^k\lambda_{1,k} + B^k)\lambda_{1,k}^{n-1}\alpha_1^k + (A^k\lambda_{2,k} + B^k)\lambda_{2,k}^{n-1}\alpha_2^k\big\} = 0 \end{aligned} \tag{A.18}$$

where

$$
\begin{aligned}
A^k &= k_x \frac{2h_2}{3h_1}\Big(1-\cos(\frac{k}{n}\pi)\Big) + k_y \frac{h_1}{3h_2}\Big(2+\cos(\frac{k}{n}\pi)\Big) \\
B^k &= k_x \frac{h_2}{3h_1}\Big(1-\cos(\frac{k}{n}\pi)\Big) - k_y \frac{h_1}{3h_2}\Big(2+\cos(\frac{k}{n}\pi)\Big) \\
S &= 2\frac{a^2}{\pi^2 h_1}\Big(1-\cos(\frac{\pi}{n})\Big)
\end{aligned}
\tag{A.19}
$$

From equation A.18, it can be seen that $k = 1$. For simplification, the index k is dropped and we have

$$
\begin{aligned}
&(A + B\lambda_{_1})\alpha_{_1} + (A + B\lambda_{_2})\alpha_{_2} = S \\
&(A\lambda_{_1} + B)\lambda_{_1}^{n-1}\alpha_{_1} + (A\lambda_{_2} + B)\lambda_{_2}^{n-1}\alpha_{_2} = 0
\end{aligned}
\tag{A.20}
$$

where

$$
\begin{aligned}
A &= k_x \frac{2h_2}{3h_1}\Big(1-\cos(\frac{\pi}{n})\Big) + k_y \frac{h_1}{3h_2}\Big(2+\cos(\frac{\pi}{n})\Big) \\
B &= k_x \frac{h_2}{3h_1}\Big(1-\cos(\frac{\pi}{n})\Big) - k_y \frac{h_1}{3h_2}\Big(2+\cos(\frac{\pi}{n})\Big) \\
S &= 2\frac{a^2}{\pi^2 h_1}\Big(1-\cos(\frac{\pi}{n})\Big)
\end{aligned}
\tag{A.21}
$$

After solving the two equations, the constants $C_{_1}$ and $C_{_2}$ have the following form

$$
\begin{aligned}
\alpha_{_1} &= -\frac{S}{T_j}\Big(A\lambda_{_2} + B\Big)\lambda_{_2}^{n-1} \\
\alpha_{_2} &= \frac{S}{T_j}\Big(A\lambda_{_1} + B\Big)\lambda_{_1}^{n-1}
\end{aligned}
\tag{A.22}
$$

where

$$
T = \lambda_{_1}^{n-1}\Big(A\lambda_{_1} + B\Big)\Big(A + B\lambda_{_2}\Big) - \lambda_{_2}^{n-1}\Big(A + B\lambda_{_1}\Big)(A\lambda_{_2} + B\Big) \tag{A.23}
$$

Therefore for linear finite element solution, the explicit expression of degree of freedom at node (i, j) is

$$
u_{i,j} = X_i Y_j = \sin(\frac{i}{n}\pi)\big(\alpha_{_1}\lambda_{_1}^j + \alpha_{_2}\lambda_{_2}^j\big) \tag{A.24}
$$

For an element defined by (i, j), $(i, j+1)$, $(i+1, j+1)$, and $(i+1, j)$ as shown in Figure A.1, the finite element solution can be put as

$$u_{\Delta}^{p,\mathrm{ex}} = u_{i,j}\phi_{i,j} + u_{i,j+1}\phi_{i,j+1} + u_{i+1,j+1}\phi_{i+1,j+1} + u_{i+1,j}\phi_{i+1,j} \tag{A.25}$$

where $\phi_{i,j}$, $\phi_{i,j+1}$, $\phi_{i+1,j+1}$, and $\phi_{i+1,j}$ are linear shape functions corresponding to nodes (i, j), $(i, j+1)$, $(i+1, j+1)$, and $(i+1, j)$ respectively. Let us note that u_{Δ}^{p} computed by the stiffness matrix, and $u_{\Delta}^{p,\mathrm{ex}}$, are identical up to the roundoff error.

It can be observed that the procedures to derive an explicit expression of nodal degree of freedom is identical with those to derive the exact solution to the partial differential equation. The only difference between the two is that the former works on discrete equation while the latter works on continuous equation. It should also be noted that unlike the finite element solution u_{Δ}^{p} obtained from Fortran code, the solution $u_{\Delta}^{p,\mathrm{ex}}$ which can be called exact finite element solution has no numerical integration and factorization error since all the computations are symbolic. To validate the above derivations, the comparision of energy norm of u_{Δ}^{p} and $u_{\Delta}^{p,\mathrm{ex}}$ is listed in Table A.1. It is obvious that the results from the solution $u_{\Delta}^{p,\mathrm{ex}}$ based on explicit formula are consistent with those from Fortran code.

Table A.1. Model problem with boundary layer. The comparisons of energy norm u_{Δ}^{p} and $u_{\Delta}^{p,\mathrm{ex}}$ vs. the different orthotropies $\frac{k_x}{k_y}$ and mesh refinements n with $k_y = \epsilon$, $h_1 = \frac{a}{2^n}$, $h_2 = \frac{b}{2^n}$, and $n = 1, 2, 3, 4, 5$.

	$\epsilon = 1$		$\epsilon = 0.1$	
n	$\|\|u_{\Delta}^{p}\|\|_{\mathcal{U}}$	$\|\|u_{\Delta}^{p,\mathrm{ex}}\|\|_{\mathcal{U}}$	$\|\|u_{\Delta}^{p}\|\|_{\mathcal{U}}$	$\|\|u_{\Delta}^{p,\mathrm{ex}}\|\|_{\mathcal{U}}$
n=1	1.175884664	1.175895274	1.292884998	1.292884999
n=2	1.471496181	1.471496163	1.891691080	1.891691081
n=3	1.583604860	1.583604886	2.422598743	2.422598743
n=4	1.616090273	1.616090324	2.734684253	2.734684254
n=5	1.624556788	1.624556847	2.849963701	2.849963701
	$\epsilon = 0.01$		$\epsilon = 0.001$	
n	$\|\|u_{\Delta}^{p}\|\|_{\mathcal{U}}$	$\|\|u_{\Delta}^{p,\mathrm{ex}}\|\|_{\mathcal{U}}$	$\|\|u_{\Delta}^{p}\|\|_{\mathcal{U}}$	$\|\|u_{\Delta}^{p,\mathrm{ex}}\|\|_{\mathcal{U}}$
n=1	1.310153826	1.310153827	1.308532420	1.308532422
n=2	1.994326378	1.994326380	1.983797585	1.983797585
n=3	2.870217704	2.870217706	2.810196627	2.810196628
n=4	4.048925527	4.048925528	3.759091133	3.759091134
n=5	5.578182413	5.578182413	4.557968568	4.557968568
	$\epsilon = 0.0001$		$\epsilon = 0.00001$	
n	$\|\|u_{\Delta}^{p}\|\|_{\mathcal{U}}$	$\|\|u_{\Delta}^{p,\mathrm{ex}}\|\|_{\mathcal{U}}$	$\|\|u_{\Delta}^{p}\|\|_{\mathcal{U}}$	$\|\|u_{\Delta}^{p,\mathrm{ex}}\|\|_{\mathcal{U}}$
n=1	1.310316559	1.310316641	1.310332838	1.310332858
n=2	1.995394775	1.995394798	1.995501772	1.995501867
n=3	2.876582346	2.876582364	2.877222702	2.877222706
n=4	4.084720654	4.084720651	4.088388200	4.088388228
n=5	5.766436026	5.766436040	5.787087794	5.787087800

APPENDIX B

DETERMINATION OF CONSTANTS IN EXPLICIT ESTIMATOR

We determine constants C_2 and α based on interpolation error of a smooth quadratic polynomial which satifies the following governing equation and boundary condition defined on the domain of equation 3.1.

$$\begin{aligned} -k_x\frac{\partial^2 u}{\partial x^2} - k_y\frac{\partial^2 u}{\partial y^2} &= 0 \quad \text{on } \Omega_1 = (0,a)\times(0,b) \\ -k_x\frac{\partial u}{\partial x} &= -2x \quad \text{at } x = 0, a \\ -k_y\frac{\partial u}{\partial y} &= -2y \quad \text{at } y = 0, b \end{aligned} \tag{B.1}$$

where

$$u_{EX}(x,y) = \frac{x^2}{k_x} - \frac{y^2}{k_y} \tag{B.2}$$

For an arbitrary element τ defined by nodes (i,j), $(i,j+1)$, $(i+1,j+1)$, and $(i+1,j)$ as shown in Figure A.1, we define an linear interpolation function as

$$u_{\text{I}} = u^{\text{I}}_{i,j}\phi_{i,j} + u^{\text{I}}_{i,j+1}\phi_{i,j+1} + u^{\text{I}}_{i+1,j+1}\phi_{i+1,j+1} + u^{\text{I}}_{i+1,j+1}\phi_{i+1,j} \tag{B.3}$$

where $\phi_{i,j}$, $\phi_{i,j+1}$, $\phi_{i+1,j+1}$, and $\phi_{i+1,j}$ are linear shape functions corresponding to nodes (i,j), $(i,j+1)$, $(i+1,j+1)$, and $(i+1,j)$ respectively and $u^{\text{I}}_{i,j}$, $u^{\text{I}}_{i,j+1}$, $u^{\text{I}}_{i+1,j+1}$, and $u^{\text{I}}_{i+1,j+1}$ are the exact values of u_{EX} at the corresponding nodes.

Therefore we can get at element τ the explicit formulae for the interpolation error $e_{\Delta}^{\mathrm{I}} \stackrel{\text{def}}{=} u_{EX} - u_{\mathrm{I}}$ in energy norm, H_1 norm and L^2 norm

$$\begin{aligned}
||e_{\Delta}^{\mathrm{I}}||_{\mathcal{U}(\tau)}^2 &= \frac{h_1 h_2 (k_x h_2^2 + k_y h_1^2)}{3 k_x k_y} \\
||e_{\Delta}^{\mathrm{I}}||_{H_1(\tau)}^2 &= \frac{h_1 h_2 (k_x^2 h_2^2 + k_y^2 h_1^2)}{3 k_x^2 k_y^2} \\
||e_{\Delta}^{\mathrm{I}}||_{L^2(\tau)}^2 &= \frac{h_1 h_2 (-5 k_x k_y h_1^2 h_2^2 + 3 k_x^2 h_2^4 + 3 k_y^2 h_1^4)}{90 k_x^2 k_y^2}
\end{aligned} \tag{B.4}$$

It can be seen that the interpolation error among all the elements is identical for the uniform mesh refinement. On element τ, the jump due to interpolation has the form of

$$\sum_{\varepsilon \subset \partial\tau} h_{\epsilon}^{\alpha} \Big|\Big| \frac{J_{\varepsilon}^{\tau}}{\sqrt{2}} \Big|\Big|_{L^2(\varepsilon)}^2 = 4\Big(h_1^{\alpha+1} h_2^2 + h_2^{\alpha+1} h_1^2 \Big) \tag{B.5}$$

By assuming the total number of elements is N, we have the following for interpolation error according to equation 3.5

$$||e_{\Delta}^{\mathrm{I}}||_{\Omega}^2 = N ||e_{\Delta}^{\mathrm{I}}||_{\tau}^2 \leq 4 N C_2 \Big(h_1^{\alpha+1} h_2^2 + h_2^{\alpha+1} h_1^2 \Big) \tag{B.6}$$

Given the explicit form of $||e_{S_{\Delta_h}^p}^{\mathrm{I}}||_{\tau}^2$ in different norms as shown in equation B.4, we can determine the constant C_2 by taking the equal sign in equation B.6, which can be expressed as follows

$$\begin{aligned}
C_2^{\mathcal{U}} &= \frac{k_x \beta + \frac{k_y}{\beta}}{24 k_x k_y} \quad \text{and} \quad \alpha = 1 \\
C_2^{H^1} &= \frac{k_x^2 \beta + \frac{k_y^2}{\beta}}{24 k_x^2 k_y^2} \quad \text{and} \quad \alpha = 1 \\
C_2^{L^2} &= \frac{3 k_x^2 \beta^4 - 5 k_1 k_y \beta^2 + 3 k_y^2}{360\Big(\beta^3 + \beta\Big) k_x^2 k_y^2} \quad \text{and} \quad \alpha = 3
\end{aligned} \tag{B.7}$$

where $\beta \overset{\text{def}}{=} \frac{h_2}{h_1}$ is defined as aspect ratio and $C_2^{\mathscr{U}}$, $C_2^{H^1}$, and $C_2^{L^2}$ denote the constant C_2 for error measured in energy norm, H_1 norm, and L^2 norm respectively. It can be seen that the constant C_2 is the function of mesh aspect ratio and material properties. Therefore we have the following explicit estimators

$$\begin{aligned}
\mathscr{E}_{\mathscr{U}}^{EXPL} &\overset{\text{def}}{=} \sqrt{C_2^{\mathscr{U}}\Big(\sum_{\tau}\big(\sum_{\varepsilon\subset\partial\tau} h_\varepsilon \Big|\Big|\frac{J_\varepsilon^\tau}{\sqrt{2}}\Big|\Big|^2_{L^2(\varepsilon)}\big)\Big)} \\
\mathscr{E}_{H^1}^{EXPL} &\overset{\text{def}}{=} \sqrt{C_2^{H^1}\Big(\sum_{\tau}\big(\sum_{\varepsilon\subset\partial\tau} h_\varepsilon \Big|\Big|\frac{J_\varepsilon^\tau}{\sqrt{2}}\Big|\Big|^2_{L^2(\varepsilon)}\big)\Big)} \\
\mathscr{E}_{L^2}^{EXPL} &\overset{\text{def}}{=} \sqrt{C_2^{L^2}\Big(\sum_{\tau}\big(\sum_{\varepsilon\subset\partial\tau} h_\varepsilon^3 \Big|\Big|\frac{J_\varepsilon^\tau}{\sqrt{2}}\Big|\Big|^2_{L^2(\varepsilon)}\big)\Big)}
\end{aligned} \tag{B.8}$$

which correspond to the error measured in energy norm, H^1 norm, and L^2 norm respectively.

APPENDIX C

EXACT FINITE ELEMENT SOLUTION FOR INTERFACE LAYER PROBLEM

For a uniform mesh as shown in Figure C.1, the number of subdivisions for domain Ω_1 and domain Ω_2 is chosen to be n and the mesh sizes along x and y axes are denoted by $h_1 \stackrel{\text{def}}{=} \frac{a}{n}$ and $h_2 \stackrel{\text{def}}{=} \frac{b}{n}$ for domain Ω_1, and $h_1' \stackrel{\text{def}}{=} \frac{a}{n}$ and $h_2' \stackrel{\text{def}}{=} \frac{d}{n}$ for domain Ω_2. It should be noted that h_1' is equal to h_1. The nodal degrees of freedom for nodes on domain Ω_1 are denoted by the index i $(i = 0, 1, 2, ..., n)$ along x axis and the index j $(j = 0, 1, 2, ..., n)$ along y axis while for nodes on domain Ω_2 the nodal degrees of freedom denoted by the index i $(i = 0, 1, 2, ..., n)$ along x axis and the index l $(l = 0, 1, 2, ..., n)$ along y axis. It should be noted that the node indices for both domains along x axis are denoted by the same index i since the number of refinement level along x axis is the same for domain Ω_1 and Ω_2.

In the global stiffness matrix, we have the following discretization form corresponding to an arbitrary node on domain Ω_1 denoted by (i, j) not on the boundaries.

$$
\begin{aligned}
&\left(-k_x\frac{h_2}{6h_1} - k_y\frac{h_1}{6h_2}\right)u_{i-1,j-1} + 2\left(k_x\frac{h_2}{6h_1} - k_y\frac{h_1}{3h_2}\right)u_{i,j-1} + \\
&\left(-k_x\frac{h_2}{6h_1} - k_y\frac{h_1}{6h_2}\right)u_{i+1,j-1} + 2\left(-k_x\frac{h_2}{3h_1} + k_y\frac{h_1}{6h_2}\right)u_{i-1,j} + \\
&4\left(k_x\frac{h_2}{3h_1} + k_y\frac{h_1}{3h_2}\right)u_{i,j} + 2\left(-k_x\frac{h_2}{3h_1} + k_y\frac{h_1}{6h_2}\right)u_{i+1,j} + \\
&\left(-k_x\frac{h_2}{6h_1} - k_y\frac{h_1}{6h_2}\right)u_{i-1,j+1} + 2\left(k_x\frac{h_2}{6h_1} - k_y\frac{h_1}{3h_2}\right)u_{i,j+1} + \\
&\left(-k_x\frac{h_2}{6h_1} - k_y\frac{h_1}{6h_2}\right)u_{i+1,j+1} = 0
\end{aligned}
\tag{C.1}
$$

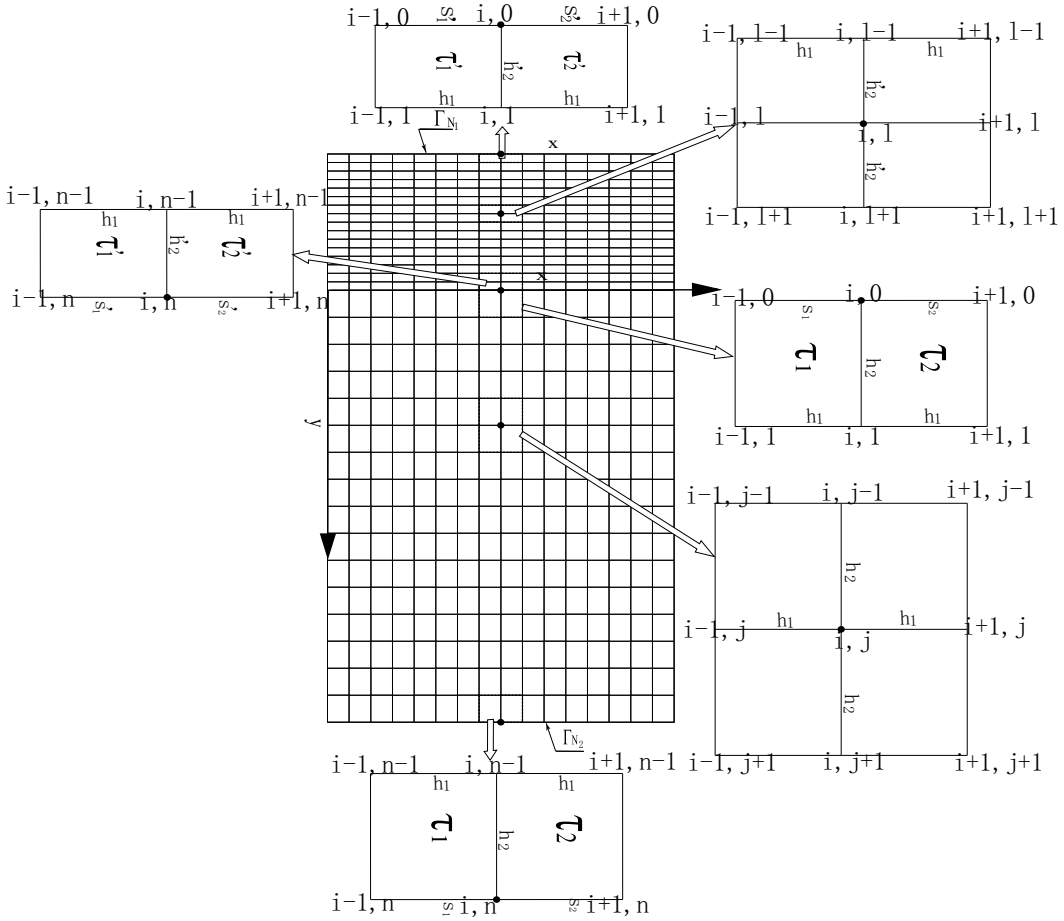

Fig. C.1. Uniform mesh for model problem with interface layer

while an arbitrary node on domain Ω_2 denoted by (i, l) not located on the boundaries has the following discrete form in the global stiffness matrix.

$$
\begin{aligned}
&\left(-k'_x\frac{h'_2}{6h_1} - k'_y\frac{h_1}{6h'_2}\right)u_{i-1,l-1} + 2\left(k'_x\frac{h'_2}{6h_1} - k'_y\frac{h_1}{3h'_2}\right)u_{i,l-1} + \\
&\left(-k'_x\frac{h'_2}{6h_1} - k'_y\frac{h_1}{6h'_2}\right)u_{i+1,l-1} + 2\left(-k'_x\frac{h'_2}{3h_1} + k'_y\frac{h_1}{6h'_2}\right)u_{i-1,l} + \\
&4\left(k'_x\frac{h'_2}{3h_1} + k'_y\frac{h_1}{3h'_2}\right)u_{i,l} + 2\left(-k'_x\frac{h'_2}{3h_1} + k'_y\frac{h_1}{6h'_2}\right)u_{i+1,l} + \\
&\left(-k'_x\frac{h'_2}{6h_1} - k'_y\frac{h_1}{6h'_2}\right)u_{i-1,l+1} + 2\left(k'_x\frac{h'_2}{6h_1} - k'_y\frac{h_1}{3h'_2}\right)u_{i,l+1} + \\
&\left(-k'_x\frac{h'_2}{6h_1} - k'_y\frac{h_1}{6h'_2}\right)u_{i+1,l+1} = 0
\end{aligned}
\tag{C.2}
$$

At the boundary Γ_{N_1}, we have for $l = 0$ and $l = 1$

$$\begin{aligned}
&\Big(- k'_x \frac{h'_2}{3h_1} + k'_y \frac{h_1}{6h'_2} \Big) u_{i-1,0} + \Big(- k'_x \frac{h'_2}{6h_1} - k'_y \frac{h_1}{6h'_2} \Big) u_{i-1,1} + \\
&2 \Big(k'_x \frac{h'_2}{3h_1} + k'_y \frac{h_1}{3h'_2} \Big) u_{i,0} + 2 \Big(k'_x \frac{h'_2}{6h_1} - k'_y \frac{h_1}{3h'_2} \Big) u_{i,1} + \\
&\Big(- k'_x \frac{h'_2}{3h_1} + k'_y \frac{h_1}{6h'_2} \Big) u_{i+1,0} + \big(- k'_x \frac{h'_2}{6h_1} - k'_2 \frac{h_1}{6h'_2} \Big) u_{i+1,1} \\
&= \int_{s'_1} k'_y \frac{\partial u}{\partial y} \phi'_i \big|_{\tau'_1} + \int_{s'_2} k'_y \frac{\partial u}{\partial y} \phi'_i \big|_{\tau'_2}
\end{aligned} \tag{C.3}$$

where the shape functions at node $(i, 0)$ defined at the two elements τ'_1 and τ'_2 are $\phi'_i\big|_{\tau'_1} = \frac{x - x_{i-1}}{x_i - x_{i-1}}$ and $\phi'_i\big|_{\tau'_2} = \frac{x - x_{i+1}}{x_i - x_{i+1}}$ respectively.

Similarly at the homogeneous Neumann boundary Γ_{N_2}, we have for $i = n - 1$ and $i = n$

$$\begin{aligned}
&\Big(- k_x \frac{h_2}{6h_1} - k_y \frac{h_1}{6h_2} \Big) u_{i-1,n-1} + \Big(- k_x \frac{h_2}{3h_1} + k_y \frac{h_1}{6h_2} \Big) u_{i-1,n} + \\
&2 \Big(k_x \frac{h_2}{6h_1} - k_y \frac{h_1}{3h_2} \Big) u_{i,n-1} + 2 \Big(k_x \frac{h_2}{3h_1} + k_y \frac{h_1}{3h_2} \Big) u_{i,n} + \\
&\Big(- k_x \frac{h_2}{6h_1} - k_y \frac{h_1}{6h_2} \Big) u_{i+1,n-1} + \Big(- k_x \frac{h_2}{3h_1} + k_y \frac{h_1}{6h_2} \Big) u_{i+1,n} = 0
\end{aligned} \tag{C.4}$$

At the interface of the two domains for $l = n-1, n$ and $j = 0, 1$, we have the following discrete form for the common node (i, n) on domain Ω_2 which is $(i, 0)$ on domain Ω_1

$$\begin{aligned}
&\Big(-k'_x\frac{h'_2}{6h_1} - k'_y\frac{h_1}{6h'_2}\Big)u_{i-1,n-1} + \Big(-k'_x\frac{h'_2}{3h_1} + k'_y\frac{h_1}{6h'_2}\Big)u_{i-1,n} + \\
&2\Big(k'_x\frac{h'_2}{6h_1} - k'_y\frac{h_1}{3h'_2}\Big)u_{i,n-1} + 2\Big(k'_x\frac{h'_2}{3h_1} + k'_y\frac{h_1}{3h'_2}\Big)u_{i,n} + \\
&\Big(-k'_x\frac{h'_2}{6h_1} - k'_y\frac{h_1}{6h'_2}\Big)u_{i+1,n-1} + \Big(-k'_x\frac{h'_2}{3h_1} + k'_y\frac{h_1}{6h'_2}\Big)u_{i+1,n} + \\
&\Big(-k_x\frac{h_2}{3h_1} + k_y\frac{h_1}{6h_2}\Big)u_{i-1,0} + \Big(-k_x\frac{h_2}{6h_1} - k_y\frac{h_1}{6h_2}\Big)u_{i-1,1} + \\
&2\Big(k_x\frac{h_2}{3h_1} + k_y\frac{h_1}{3h_2}\Big)u_{i,0} + 2\Big(k_x\frac{h_2}{6h_1} - k_y\frac{h_1}{3h_2}\Big)u_{i,1} + \\
&\Big(-k_x\frac{h_2}{3h_1} + k_y\frac{h_1}{6h_2}\Big)u_{i+1,0} + \big(-k_x\frac{h_2}{6h_1} - k_2\frac{h_1}{6h_2}\Big)u_{i+1,1} = 0
\end{aligned} \tag{C.5}$$

By noting the nodal degrees of freedom $u_{i-1,n}$, $u_{i,n}$, and $u_{i+1,n}$ defined on domain Ω' are equal to their counterparts $u_{i-1,0}$, $u_{i,0}$, and $u_{i+1,0}$ defined on domain Ω, we have

$$\begin{aligned}
&\Big(-k'_x\frac{h'_2}{6h_1} - k'_y\frac{h_1}{6h'_2}\Big)u_{i-1,n-1} - \Big(k'_x\frac{h'_2}{3h_1} - k'_y\frac{h_1}{6h'_2} + k_x\frac{h_2}{3h_1} - k_y\frac{h_1}{6h_2}\Big)u_{i-1,n} - \\
&\Big(k_x\frac{h_2}{6h_1} + k_y\frac{h_1}{6h_2}\Big)u_{i-1,1} + 2\Big(k'_x\frac{h'_2}{6h_1} - k'_y\frac{h_1}{3h'_2}\Big)u_{i,n-1} + \\
&2\Big(k'_x\frac{h'_2}{3h_1} + k'_y\frac{h_1}{3h'_2} + k_x\frac{h_2}{3h_1} + k_y\frac{h_1}{3h_2}\Big)u_{i,n} + 2\Big(k_x\frac{h_2}{6h_1} - k_y\frac{h_1}{3h_2}\Big)u_{i,1} - \\
&\Big(k'_x\frac{h'_2}{6h_1} + k'_y\frac{h_1}{6h'_2}\Big)u_{i+1,n-1} - \Big(k'_x\frac{h'_2}{3h_1} - k'_y\frac{h_1}{6h'_2} + k_x\frac{h_2}{3h_1} - k_y\frac{h_1}{6h_2}\Big)u_{i+1,n} - \\
&\Big(k_x\frac{h_2}{6h_1} + k_2\frac{h_1}{6h_2}\Big)u_{i+1,1} = 0
\end{aligned} \tag{C.6}$$

Assuming $u_{i,l} = X_i Y_l$, $u_{i,j} = X_i Y_j$, following the same procedures as in the case of one battery domain problem, and plugging them into the equations C.2 and C.1, we have

$$X_i^k = \sin\big(\frac{i}{n}k\pi\big) \tag{C.7}$$

and

$$
\begin{aligned}
C_k &= 2\frac{\frac{k_x}{6}\frac{h_2}{h_1}\big(2+\cos(\frac{k}{n}\pi)\big)+\frac{k_y}{3}\frac{h_1}{h_2}\big(1-\cos(\frac{k}{n}\pi)\big)}{\frac{k_x}{6}\frac{h_2}{h_1}\big(2+\cos(\frac{k}{n}\pi)\big)-\frac{k_y}{6}\frac{h_1}{h_2}\big(1-\cos(\frac{k}{n}\pi)\big)} \quad \text{on } \Omega_1 \\
C'_k &= 2\frac{\frac{k'_x}{6}\frac{h'_2}{h_1}\big(2+\cos(\frac{k}{n}\pi)\big)+\frac{k'_y}{3}\frac{h_1}{h'_2}\big(1-\cos(\frac{k}{n}\pi)\big)}{\frac{k'_x}{6}\frac{h'_2}{h_1}\big(2+\cos(\frac{k}{n}\pi)\big)-\frac{k'_y}{6}\frac{h_1}{h'_2}\big(1-\cos(\frac{k}{n}\pi)\big)} \quad \text{on } \Omega_2
\end{aligned}
\tag{C.8}
$$

with $k = 0, 1, 2, ..., n$ Therefore we have

$$
\begin{aligned}
Y^k_{j+1} - C_k Y^k_j + Y^k_{j-1} = 0 \quad \text{on } \Omega_1 \\
Y^k_{l+1} - C'_k Y^k_l + Y^k_{l-1} = 0 \quad \text{on } \Omega_2
\end{aligned}
\tag{C.9}
$$

Let $Y^k_l = \eta^l_k$ and $Y^k_j = \lambda^j_k$, we have two quadratic equations

$$
\begin{aligned}
\lambda^2_k - C_k\lambda_k + 1 = 0 \quad \text{on } \Omega_1 \\
\eta^2_k - C'_k\eta_k + 1 = 0 \quad \text{on } \Omega_2
\end{aligned}
\tag{C.10}
$$

and on domain Ω_1, the roots are

$$
\begin{aligned}
\lambda_{1,k} &= \frac{C_k + \sqrt{C^2_k - 4}}{2} \\
\lambda_{2,k} &= \frac{C_k - \sqrt{C^2_k - 4}}{2}
\end{aligned}
\tag{C.11}
$$

while on domain Ω_2, the roots are

$$
\begin{aligned}
\eta_{1,k} &= \frac{C'_k + \sqrt{{C'_k}^2 - 4}}{2} \\
\eta_{2,k} &= \frac{C'_k - \sqrt{{C'_k}^2 - 4}}{2}
\end{aligned}
\tag{C.12}
$$

Likewise, put Y_l^k and Y_j^k as a linear combintaion of the their corresponding roots, we have

$$\begin{aligned} Y_j^k &= \beta_1^k \lambda_{1,k}^j + \beta_2^k \lambda_{2,k}^j \quad \text{on } \Omega_1 \\ Y_l^k &= \alpha_1^k \eta_{1,k}^l + \alpha_2^k \eta_{2,k}^l \quad \text{on } \Omega_2 \end{aligned} \tag{C.13}$$

Let $u_{i,l} = \sum_{k=1}^{n-1} X_i^k Y_l^k$ and $l = 0$ and plug it into the equations C.3 corresponding to Neumann boundary conditions, we have after simplification

$$\sum_{k=1}^{n-1} \sin(\frac{i}{n}k\pi)\big\{(E^k + F^k\eta_{1,k})\alpha_1^k + (E^k + F^k\eta_{2,k})\alpha_2^k\big\} = \sin(\frac{i}{n}\pi)S \tag{C.14}$$

where

$$\begin{aligned} E^k &= k'_x \frac{2h'_2}{3h_1}\Big(1 - \cos(\frac{k}{n}\pi)\Big) + k'_y \frac{h_1}{3h'_2}\Big(2 + \cos(\frac{k}{n}\pi)\Big) \\ F^k &= k'_x \frac{h'_2}{3h_1}\Big(1 - \cos(\frac{k}{n}\pi)\Big) - k'_y \frac{h_1}{3h'_2}\Big(2 + \cos(\frac{k}{n}\pi)\Big) \\ S &= 2\frac{a^2}{\pi^2 h_1}\Big(1 - \cos(\frac{\pi}{n})\Big) \end{aligned} \tag{C.15}$$

Let $u_{i,j} = \sum_{k=1}^{n-1} X_i^k Y_j^k$ and plug it into the equations C.4, we have after simplification

$$\sum_{k=1}^{n-1} \sin(\frac{i}{n}k\pi)\big\{(G^k\lambda_{1,k} + H^k)\lambda_{1,k}^{n-1}\beta_1^k + (G^k\lambda_{2,k} + H^k)\lambda_{2,k}^{n-1}\beta_2^k\big\} = 0 \tag{C.16}$$

where

$$\begin{aligned} G^k &= k_x \frac{2h_2}{3h_1}\Big(1 - \cos(\frac{k}{n}\pi)\Big) + k_y \frac{h_1}{3h_2}\Big(2 + \cos(\frac{k}{n}\pi)\Big) \\ H^k &= k_x \frac{h_2}{3h_1}\Big(1 - \cos(\frac{k}{n}\pi)\Big) - k_y \frac{h_1}{3h_2}\Big(2 + \cos(\frac{k}{n}\pi)\Big) \end{aligned}$$

From equation C.14, it can be seen that $k = 1$. For simplification, the index k is dropped and we have

$$(E + F\eta_1)\alpha_1 + (E + F\eta_2)\alpha_2 = S \tag{C.17}$$

$$(G\lambda_1 + H)\lambda_1^{n-1}\beta_1 + (G\lambda_2 + H)\lambda_2^{n-1}\beta_2 = 0 \tag{C.18}$$

where

$$
\begin{aligned}
E &= k'_x \frac{2h'_2}{3h_1}\Big(1-\cos(\frac{\pi}{n})\Big) + k'_y \frac{h_1}{3h'_2}\Big(2+\cos(\frac{\pi}{n})\Big) \\
F &= k'_x \frac{h'_2}{3h_1}\Big(1-\cos(\frac{\pi}{n})\Big) - k'_y \frac{h_1}{3h'_2}\Big(2+\cos(\frac{\pi}{n})\Big) \\
G &= k_x \frac{2h_2}{3h_1}\Big(1-\cos(\frac{\pi}{n})\Big) + k_y \frac{h_1}{3h_2}\Big(2+\cos(\frac{\pi}{n})\Big) \\
H &= k_x \frac{h_2}{3h_1}\Big(1-\cos(\frac{\pi}{n})\Big) - k_y \frac{h_1}{3h_2}\Big(2+\cos(\frac{\pi}{n}) \\
S &= 2\frac{a^2}{\pi^2 h_1}\Big(1-\cos(\frac{\pi}{n})\Big)
\end{aligned}
\tag{C.19}
$$

Therefore at the interface of the two domains, we have for domain Ω_2 by letting $l = n-1, n$

$$
\begin{aligned}
Y_{n-1} &= \alpha_{_1}\eta_{_1}^{n-1} + \alpha_{_2}\eta_{_2}^{n-1} \\
Y_n &= \alpha_{_1}\eta_{_1}^{n} + \alpha_{_2}\eta_{_2}^{n}
\end{aligned}
\tag{C.20}
$$

while for domain Ω_1 with $j = 0, 1$

$$
\begin{aligned}
Y_0 &= \beta_{_1} + \beta_{_2} \\
Y_1 &= \beta_{_1}\lambda_{_1} + \beta_{_2}\lambda_{_2}
\end{aligned}
\tag{C.21}
$$

Plug the equation C.20 and C.21 into the equation C.6, we have after simplification

$$
(E\eta_{_1}^{n} + F\eta_{_1}^{n-1})\alpha_{_1} + (E\eta_{_2}^{n} + F\eta_{_2}^{n-1})\alpha_{_2} + (G + H\lambda_{_1})\beta_{_1} + (G + H\lambda_{_2})\beta_{_2} = 0 \tag{C.22}
$$

It should be noted also that at node (i, n) on Ω' which coincides with node $(i, 0)$ on Ω, we have $u_{i,n} = u_{i,0}$ which means

$$
\alpha_{_1}\eta_{_1}^{n} + \alpha_{_2}\eta_{_2}^{n} = \beta_{_1} + \beta_{_2} \tag{C.23}
$$

The derivation of equations C.22 and C.23 is similiar to the enforcement of the continuity conditions of heat flux and temperature at the interface of two domains in

deriving the exact solution.

The constants $\alpha_1, \alpha_2, \beta_1$, and β_2 can be obtained by solving the linear system equations of C.17, C.18, C.22, and C.23, which have the following form

$$\begin{aligned}
\alpha_1 &= \frac{-\lambda_1^{n-1}\eta_2^{n-1}(G\lambda_1 + H)\big(E\eta_2 + F + \eta_2(G + H\lambda_2)\big)}{\chi} \\
&\quad + \frac{\lambda_2^{n-1}\eta_2^{n-1}(G\lambda_2 + H)\big(E\eta_2 + F + \eta_2(G + H\lambda_1)\big)}{\chi} \\
\alpha_2 &= \frac{-\lambda_1^{n-1}\eta_1^{n-1}(G\lambda_1 + H)\big(E\eta_1 + F + \eta_1(G + H\lambda_2)\big)}{\chi} \\
&\quad + \frac{\lambda_2^{n-1}\eta_1^{n-1}(G\lambda_2 + H)\big(E\eta_1 + F + \eta_1(G + H\lambda_1)\big)}{\chi} \\
\beta_1 &= \frac{\eta_1^{n-1}\eta_2^{n-1}\lambda_2^{n-1}(\eta_1 - \eta_2)F(G\lambda_2 + H)}{\chi} \\
\beta_2 &= \frac{\eta_1^{n-1}\eta_2^{n-1}\lambda_1^{n-1}(\eta_2 - \eta_1)F(G\lambda_1 + H)}{\chi}
\end{aligned} \tag{C.24}$$

where

$$\begin{aligned}
\chi &= \lambda_1^{n-1}\eta_1^{n-1}(G\lambda_1 + H)(E + F\eta_2)\big(E\eta_1 + F + \eta_1(G + H\lambda_2)\big) \\
&\quad - \lambda_1^{n-1}\eta_2^{n-1}(G\lambda_1 + H)(E + F\eta_1)\big(E\eta_2 + F + \eta_2(G + H\lambda_2)\big) \\
&\quad + \lambda_2^{n-1}\eta_2^{n-1}(G\lambda_2 + H)(E + F\eta_1)\big(E\eta_2 + F + \eta_2(G + H\lambda_1)\big) \\
&\quad - \lambda_2^{n-1}\eta_1^{n-1}(G\lambda_2 + H)(E + F\eta_2)\big(E\eta_1 + F + \eta_1(G + H\lambda_1)\big)
\end{aligned} \tag{C.25}$$

Therefore for linear finite element solution, the explicit expression of degree of freedom at node (i, j) on Ω_1 is

$$u_{i,j} = X_i Y_j = \sin(\frac{i}{n}\pi)\big(\beta_1\lambda_1^j + \beta_2\lambda_2^j\big) \tag{C.26}$$

and for node (i, l) on Ω_2 the expression is

$$u_{i,l} = X_i Y_l = \sin(\frac{i}{n}\pi)\big(\alpha_1\eta_1^l + \alpha_2\eta_2^l\big) \tag{C.27}$$

For an arbitrary element on Ω_1 defined by (i,j), $(i,j+1)$, $(i+1,j+1)$, and $(i+1,j)$ as shown in Figure C.1, the finite element solution can be put as

$$u_{\Delta}^{p,\mathrm{ex}} = u_{i,j}\phi_{i,j} + u_{i,j+1}\phi_{i,j+1} + u_{i+1,j+1}\phi_{i+1,j+1} + u_{i+1,j}\phi_{i+1,j} \tag{C.28}$$

where $\phi_{i,j}$, $\phi_{i,j+1}$, $\phi_{i+1,j+1}$, and $\phi_{i+1,j}$ are linear shape functions corresponding to nodes (i,j), $(i,j+1)$, $(i+1,j+1)$, and $(i+1,j)$ respectively.

Likewise for the element on Ω_2 defined by (i,l), $(i,l+1)$, $(i+1,l+1)$, and $(i+1,l)$ the exact finite element solution has the form of

$$u_{\Delta}^{p,\mathrm{ex}} = u_{i,l}\phi_{i,l} + u_{i,l+1}\phi_{i,l+1} + u_{i+1,l+1}\phi_{i+1,l+1} + u_{i+1,l}\phi_{i+1,l} \tag{C.29}$$

where $\phi_{i,l}$, $\phi_{i,l+1}$, $\phi_{i+1,l+1}$, and $\phi_{i+1,l}$ are linear shape functions corresponding to nodes (i,l), $(i,l+1)$, $(i+1,l+1)$, and $(i+1,l)$ respectively.

The comparison of energy norm of u_{Δ}^{p} and $u_{\Delta}^{p,\mathrm{ex}}$ is listed in Table C.1. It is obvious that the results from the solution $u_{\Delta}^{p,\mathrm{ex}}$ based on explicit formula are consistent with those from Fortran code for the two battery domains problem.

Table C.1. Model problem with interface layer. The comparisons of energy norm u_{Δ}^{p} and $u_{\Delta}^{p,\mathrm{ex}}$ vs. the different orthotropies $\frac{k_x}{k_y}$ on Ω and mesh refinements n with $k_y = \epsilon$, $h_1 = \frac{a}{2^n}$, $h_2 = \frac{b}{2^n}$, and $n = 1, 2, 3, 4, 5$.

	$\epsilon = 1$		$\epsilon = 0.1$	
n	$\|\|u_{\Delta}^{p}\|\|_{\mathcal{U}}$	$\|\|u_{\Delta}^{p,\mathrm{ex}}\|\|_{\mathcal{U}}$	$\|\|u_{\Delta}^{p}\|\|_{\mathcal{U}}$	$\|\|u_{\Delta}^{p,\mathrm{ex}}\|\|_{\mathcal{U}}$
n=1	1.390409148	1.390408936	1.390411040	1.390411858
n=2	1.534023198	1.534022056	1.534171977	1.534177000
n=3	1.569990885	1.569989397	1.570356027	1.570363288
n=4	1.578984117	1.578982532	1.579462890	1.579471009
n=5	1.581232541	1.581230931	1.581748790	1.581757166
	$\epsilon = 0.01$		$\epsilon = 0.001$	
n	$\|\|u_{\Delta}^{p}\|\|_{\mathcal{U}}$	$\|\|u_{\Delta}^{p,\mathrm{ex}}\|\|_{\mathcal{U}}$	$\|\|u_{\Delta}^{p}\|\|_{\mathcal{U}}$	$\|\|u_{\Delta}^{p,\mathrm{ex}}\|\|_{\mathcal{U}}$
n=1	1.390411298	1.390412232	1.390411325	1.390412271
n=2	1.534199244	1.534205123	1.534202245	1.534208215
n=3	1.570462708	1.570471576	1.570476693	1.570485750
n=4	1.579665705	1.579676088	1.579702201	1.579712925
n=5	1.582014337	1.582025370	1.582083071	1.582094643
	$\epsilon = 0.0001$		$\epsilon = 0.00001$	
n	$\|\|u_{\Delta}^{p}\|\|_{\mathcal{U}}$	$\|\|u_{\Delta}^{p,\mathrm{ex}}\|\|_{\mathcal{U}}$	$\|\|u_{\Delta}^{p}\|\|_{\mathcal{U}}$	$\|\|u_{\Delta}^{p,\mathrm{ex}}\|\|_{\mathcal{U}}$
n=1	1.390411327	1.390412275	1.390411328	1.390412275
n=2	1.534202548	1.534208527	1.534202579	1.534208559
n=3	1.570478140	1.570487217	1.570478286	1.570487364
n=4	1.579706272	1.579717033	1.579706685	1.579717448
n=5	1.582092317	1.582103957	1.582093281	1.582104929

VITA

Delin Wang was born in Shandong Province, China. After graduating from Qingdao University of Science & Technology in 1993 with a B.E. in mechanical engineering, he continued his study in Jilin University as a graduate student in the major of computational mechanics in 1993. In 1996, he joined a research institute as a structural reliability engineer after he obtained M.S. degree in computational mechanics. In 2001, he enrolled in the Department of Aerospace Engineering, Texas A&M University. He first obtained a M.E. degree in 2005, and then took a full-time job in a finite element software company while registering as a part-time student to finish his Ph.D. degree. He received his Ph.D. in aerospace engineering in 2011 under the guidance of Dr. Theofanis Strouboulis. Dr. Wang may be contacted at:

Delin Wang

c/o Dr. Theofanis Strouboulis

Department of Aerospace Engineering

H.R. Bright Building, Ross Street-TAMU 3141

Texas A&M University

College Station TX 77843-3141